



Study of ORAI protein remodeling with CRISPR and quantitative microscopy

Alexandre Bokhobza

► To cite this version:

Alexandre Bokhobza. Study of ORAI protein remodeling with CRISPR and quantitative microscopy. Cellular Biology. Université de Lille, 2022. English. NNT : 2022ULILS100 . tel-03889489

HAL Id: tel-03889489

<https://theses.hal.science/tel-03889489>

Submitted on 8 Dec 2022

HAL is a multi-disciplinary open access archive for the deposit and dissemination of scientific research documents, whether they are published or not. The documents may come from teaching and research institutions in France or abroad, or from public or private research centers.

L'archive ouverte pluridisciplinaire **HAL**, est destinée au dépôt et à la diffusion de documents scientifiques de niveau recherche, publiés ou non, émanant des établissements d'enseignement et de recherche français ou étrangers, des laboratoires publics ou privés.

Année 2022

UNIVERSITÉ DE LILLE
ÉCOLE DOCTORALE BIOLOGIE ET SANTÉ

THÈSE
Discipline : Aspects moléculaires et cellulaires de la Biologie

Présentée et soutenue publiquement par
ALEXANDRE BOKHOBZA

**STUDY OF ORAI PROTEIN REMODELING WITH CRISPR AND QUANTITATIVE
MICROSCOPY**

**ETUDE DU REMODELAGE DES PROTEINES ORAI GRACE A L'UTILISATION DE
LA TECHNIQUE CRISPR/CAS9 ET DE LA MICROSCOPIE QUANTITATIVE**

Thèse dirigée par le docteur Fabien Vanden Abeele, HDR

Soutenue le 31 Janvier 2022

Jury:

Prof. Natalia Prevarskaya, HDR, Université de Lille
Dr. Giulia Bertolin, HDR, Université de Rennes 1
Dr. Sébastien Roger, HDR, Université de Tours
Prof. Philippe Delannoy HDR, Université de Lille
Prof. Mathieu Gautier, HDR, Université de Picardie
Dr. Fabien Vanden Abeele, HDR, Université de Lille

Présidente
Rapporteur
Rapporteur
Examineur
Examineur
Examineur

Remerciements

Je tiens tout d'abord à sincèrement remercier les membres de mon jury de thèse : Prof. Natalia Prevarskaya, Dr Giulia Bertolin, Dr Sébastien Roger, Prof Morad Roudbaraki et le Prof Mathieu Gautier, pour avoir accepté d'évaluer mes travaux de thèse.

Je souhaite également remercier mon tuteur de thèse Dr Fabien Vanden Abeele, pour les conseils qu'il m'a prodigué pendant ces années de thèse.

Je tiens à remercier particulièrement le Prof Prevarskaya de m'avoir autorisé à réaliser une thèse en parallèle à mes activités d'ingénieur au sein du laboratoire, sans votre accord et votre compréhension, je n'en serais pas là aujourd'hui. Je me souviens du jour où vous m'aviez indiqué de la potentielle ouverture d'un poste d'ingénieur au sein du laboratoire auquel je pourrais postuler, vous m'aviez dit qu'il y avait le temps de faire la thèse plus tard. Vous aviez raison ! Merci encore.

Je tiens également à remercier spécifiquement certains membres du laboratoire qui ont su me faire grandir en tant que scientifique de par leur conseil :

Je souhaite adresser un grand merci au Dr Dimitra Gkika (Myrto), que de chemin parcouru depuis mon premier stage sous ta direction au sein de l'unité 1003 il y a 10 ans ! Merci de m'avoir appris les bases des techniques de biologie moléculaire de m'avoir soutenu durant mon Master2, de m'avoir permis d'obtenir mon poste d'ingénieur au sein du laboratoire, je te suis extrêmement redevable, et comme pour Natacha, je n'en serais pas là où j'en suis aujourd'hui sans ton aide, merci.

Je tiens à remercier les étudiantes en thèse lors de mon arrivée dans le laboratoire : Dr Marine Warnier et Dr Sandra Derouiche, nous n'avons pas toujours été sérieux, mais vos conseils sur la manière de réaliser mes expériences m'ont grandement aidé. Merci également de m'avoir aidé à m'intégrer au sein du laboratoire et merci pour toutes les parties de rigolade que nous avons partagées.

Je remercie également Mr Etienne Dewailly et le Dr Christian Slomianny, vous m'avez apporté un aide immense dès mon arrivée dans le laboratoire. Etienne, merci de m'avoir appris les secrets des techniques de biochimie ! Christian, merci pour l'aide que tu m'as apportée lorsque j'apprenais à maîtriser les microscopes confocaux du laboratoire. Merci également à vous deux pour votre bonne humeur.

Merci à Elodie Richard, pour son aide sur la plateforme microscopie du laboratoire.

Je tiens à remercier le Dr Loïc Lemonnier et le Prof Morad Roudbaraki, nous étions les derniers « survivants » des repas au RU lorsque j'ai quitté le laboratoire, j'ai grandement apprécié nos discussions scientifiques (et pas que scientifiques) lors de nos repas. Vous avez su m'apporter de nombreux conseils, me donner de nouvelles idées, merci beaucoup ! (Je dois même avouer que les repas du RU me manquent parfois).

Merci à Dr Dmitrii Grodienko pour ses conseils avisés en matière de microscopie.

Je tiens également à remercier les Dr Pascal Mariot, Emmanuelle Germain, Ingrid Fliniaux, et Christophe Tastet, pour la bonne ambiance qu'ils ont su maintenir dans l'unité.

Merci à Lucile, Valério, Emilie, Pauline, Guillaume, Michela, Eric, Abigael, Antoine, Katya, Artem, pour les moments passés en votre présence dans la laboratoire et l'ambiance chaleureuse que vous avais apporté à l'unité.

Un grand merci à mes deux acolytes Laurent Allart et Nathalie Ziental-Gelus, vous avez su m'aider et m'assister dans mes nombreuses manip de clonage et de screening, je vous en remercie grandement.

Je souhaite adresser un merci tout particulier aux Dr Gabriel Bidaux et Laurent Heliot. Gabriel, je ne pense pas te l'avoir dit mais je t'ai toujours considéré comme un modèle scientifique. Je me souviens de ta présentation d'HDR lorsque tu as présenté tes travaux de FLIM réalisés dans le laboratoire de Laurent, j'avais été particulièrement impressionné, et je me disais que j'aimerais être capable de maîtriser des techniques aussi pointues ! Laurent, merci beaucoup de m'avoir laissé accéder aux microscopes, et de m'avoir « intégré » dans ton équipe au P5. Merci également de m'avoir permis de participer à MiFoBio et de m'avoir permis d'entrer dans le monde de microscopie. Merci à vous deux pour votre aide lors de mes comités de suivi de thèse, je vous considère comme mes co-encadrants, un grand merci.

Je tiens également à remercier les anciens membres du laboratoire du Dr Laurent Héliot : Dr Dorian Champelovier, Dr Marie Fournier, et Dr Alessandro Furlan, merci de m'avoir accueilli au sein du laboratoire et merci de m'avoir chaque jour de manip chez vous ! Vos conseils ont été plus que précieux.

Finalement, merci aux personnes qui ont été à mes côtés toutes ces années :

Merci à ma « famille Ukrainienne », merci Yourii, Andrii, Luda, Sasha, Vika et Yulia pour votre soutien. Un merci spécial pour Viktoriia, sans votre présence pendant ces deux derniers mois, je n'aurais jamais réussi à rédiger cette thèse, je vous dois énormément.

Merci à mes parents de m'avoir toujours soutenu, Papa et Maman, merci de m'avoir toujours permis d'être dans les meilleures dispositions pour que je progresse dans mes études. Merci à ma sœur Laurane et à Morgan, pour leur soutien. Merci à mamie Jojo, Hélène, Nathalie, Alexandra, Valentin pour votre soutien. Merci à Guy pour avoir su me motiver à terminer ma thèse. Merci à Stéphanie et Patrick (et les lapins) de nous avoir aidé à nous installer en Suisse ! Merci également aux membres de la famille Dumoulin. Merci à mon parrain Gilles Grégoire pour ses encouragements. Vous tous m'avez permis de décompresser à un moment ou un autre durant mes travaux.

Enfin, merci à ma femme le Dr Oksana Iamshanova, tu as été là dès le début pour me soutenir, me motiver et me pousser à terminer cette thèse. Je n'aurais jamais pu accomplir tout cela sans toi. Tu es un modèle scientifique pour moi et tu es certainement la personne qui a eu la plus grande importance dans la conduite de ces travaux, merci ! Thank you for your wisest advice day after day: Start writing up your PhD Alex! 😊

Merci à ma fille Mila Bokhobza, merci pour le bonheur que tu me procure chaque jour. J'ai maintenant une longue histoire à te raconter pour t'endormir le soir !

TITRE DE LA THESE EN FRANÇAIS :

Etude du remodelage des protéines ORAI grâce à l'utilisation de la technique CRISPR/Cas9 et de la microscopie quantitative.

RÉSUMÉ DE LA THÈSE EN FRANÇAIS :

L'entrée capacitive de calcium (Ca^{2+}), appelée SOCE en anglais (store operated Ca^{2+} entry) représente une entrée d'ions Ca^{2+} dans la cellule consécutive à la vidange des stocks calciques réticulaires. Ce processus constitue l'un des mécanismes d'entrée majeure de Ca^{2+} dans les cellules non-excitables. L'importance physiologique de ce processus est soulignée par la gravité des syndromes induits par des mutations des canaux responsables du SOCE : le syndrome sévère d'immunodéficience combinée induit par des mutations de types perte de fonction du SOCE et les syndromes d'agrégation tubulaire myopathique (TAM) et de Stormorken induit par des mutations de type gain de fonction du SOCE. Le SOCE résulte de l'interaction de deux familles de protéines appelées STIM (Stromal interaction protein, 1,2) localisées dans la membrane du réticulum endoplasmique (RE) et ORAI (1-3) situées dans la membrane plasmique. Le processus classique d'apparition du SOCE dans les cellules peut être décrit de la sorte : La protéine STIM1, qui possède des motifs EF-hand sensible au Ca^{2+} dans la lumière du RE, détecte une diminution de la concentration en Ca^{2+} . En réponse, la protéine STIM subit un changement conformationnel qui conduit à son oligomérisation et sa translocation au niveau des jonctions membrane plasmique – RE. Les protéines STIM vont ensuite interagir, regrouper et activer les protéines ORAI1 qui forment le canal appelé Ca^{2+} -release activated Ca^{2+} (CRAC) aboutissant à la production du SOCE. Cependant, de nombreuses publications ont démontré l'implication des autres isoformes des protéines STIM et ORAI dans ce processus. De manière intéressante, l'intervention des protéines STIM2 et ORAI2/3 dans le mécanisme du SOCE permet de moduler le signal produit et ainsi de réguler finement les effets physiologiques de l'entrée de Ca^{2+} dans les cellules. En particulier, notre laboratoire a démontré que les canaux hétéromériques formés par les protéines ORAI1 et ORAI3 définissent un "interrupteur" oncogénique dans les cellules cancéreuses prostatiques permettant l'apparition d'un phénotype plus agressif. L'étude des mécanismes amenant à la formation de ces canaux hétéromériques est complexe en raison des limites des techniques à disposition. Par exemple, la plupart des moyens d'études reposent sur des systèmes de surexpression ou de sous expression, qui ne permettent pas de supprimer totalement l'expression des protéines endogènes. La présence de ces protéines endogènes rend difficile l'interprétation des résultats obtenus. Le but de cette thèse était donc d'utiliser des techniques de pointe pour étudier les mécanismes d'association des protéines ORAI. Ainsi, nous avons utilisé la technique CRISPR/Cas9 afin de générer des cellules doubles knockout (KO) pour les protéines ORAI1 et ORAI3. Ces cellules, KO pour ORAI1 et ORAI3 ont été utilisées pour réaliser des expériences de microscopie quantitative. Nous avons notamment ré-exprimé des versions fluorescentes des protéines ORAI1 et ORAI3 dans ces cellules avant de réaliser des expériences de mesure de temps de vie de

fluorescence via la technique de FLIM-FRET (fluorescence lifetime imaging microscopy - Förster resonance energy transfer). Cette technique nous a permis de suivre l'évolution des interactions entre les protéines ORAI1 et ORAI3 lors de différentes stimulations cellulaires. De la sorte nous avons pu montrer que l'interaction entre les protéines ORAI1 et ORAI3 est dynamique en fonction de la stimulation appliquée. De plus, nous avons tiré profit des cellules KO générées afin d'étudier le rôle des protéines ORAI1/3 et du SOCE dans les lignées HEK-293 et PC3. Nous avons ainsi démontré que, dans les cellules HEK, la protéine ORAI1 et le SOCE jouent un rôle limité dans le maintien de leur physiologie, alors que dans les cellules PC3, ORAI1 et ORAI3 sont importantes pour le maintien du phénotype migratoire de ces cellules.

TITLE OF THE THESIS IN ENGLISH:

Study of ORAI protein remodeling with CRISPR and quantitative microscopy.

ABSTRACT OF THE THESIS IN ENGLISH:

The store operated calcium (Ca^{2+}) entry (SOCE) represents the entry of Ca^{2+} through the cell's plasma membrane consecutive to an endoplasmic reticulum (ER) Ca^{2+} store depletion. This process is described as one of the main calcium (Ca^{2+}) pathway in the cells. Its importance is highlighted by the severe syndromes induced by loss or gain of function mutation of its constituent named severe combined immunodeficiency (SCID) and tubular aggregate myopathy (TAM)/Stormorken syndrome (STRMK) respectively. SOCE is the result of interaction between two families of proteins, the ER residing protein family Stromal interaction molecule (STIM 1&2) and the plasmalemmal proteins called ORAI (1-3). The classic molecular choreography of SOCE activation is described as follow: a drop in ER- Ca^{2+} content is detected by the EF-hand domain present in the STIM protein. Following ER Ca^{2+} depletion, STIM protein oligomerize and translocate to ER- plasma membrane (PM) junctions where they bind and activate ORAI1 composed channel called Ca^{2+} release activated Ca^{2+} channel providing SOCE. Interestingly, it appears that this choreography is much more complex than initially thought with the involvement of other STIM and ORAI isoforms (STIM2 and ORAI2,3). The involvement of these isoforms affects the properties of SOCE by modulating its Ca^{2+} signature resulting in different cellular answers. Especially, it was shown that heteromeric channels composed of ORAI1 and ORAI3 protein are defining an oncogenic switch in prostate cancer cell lines that lead to the more aggressive phenotype. However, the study of the mechanisms leading to the creation of ORAI1/3 channels at the expense of ORAI1-only channels is problematic due to technical limitations. For example, most of investigations are performed in overexpression or downregulation system where endogenous protein are still present and might blur the results of experiments. The goal of this PhD was to use high end techniques in order to study the mechanisms of ORAI1/3 interactions without facing the limitations mentioned above. Specifically, we implemented and used CRISPR/Cas9 technique to generate double knockout (KO) cell lines for ORAI1 and 3 proteins. We used these "ORAI1/3 free cells" to perform quantitative microscopy experiments. Specifically, we expressed fluorescently tagged ORAI1 and ORAI3 proteins and performed FLIM-FRET (fluorescence lifetime imaging microscopy - Förster resonance energy transfer) experiments enabling us to follow their association process in answer to different stimulations. We thus demonstrated that the association between ORAI1 and ORAI3 is a dynamic process in the cells. Additionally, we took advantage of these KO cell lines to study the role of ORAI1/3 protein and SOCE in HEK-293 and PC3 cells physiology. We thus demonstrated that ORAI1 protein and SOCE only presented a limited role in the maintenance of HEK-293 physiology, while ORAI1 and ORAI3 are important to maintain migrative properties of the cancerous PC3 cells.

A ma femme, à ma fille,

1. Introduction	18
1.1. General overview of ion channels	18
1.1.1. Common features	18
1.1.2. Functional diversity	18
1.1.3. Ion channel structure diversity	19
1.1.3.1. Primary structure	19
1.1.3.2. Secondary structure	19
1.1.3.3. Tertiary structure	22
1.1.3.4. Quaternary structure	22
1.1.4. Conclusion on the diversity of ion channels	27
1.2. Store operated Ca^{2+} entry (SOCE) and its components	28
1.2.1. Discovery of SOCE	28
1.2.2. STIM proteins	30
1.2.2.1. Discovery of STIM proteins	30
1.2.2.2. Structure of STIM proteins	30
1.2.2.2.1. Common characteristics between STIM proteins	30
1.2.2.2.2. STIM1 isoforms	32
1.2.2.2.3. STIM2 isoforms	33
1.2.2.3. STIM activation during SOCE	33
1.2.3. ORAI proteins and their associated channels	35
1.2.3.1. Discovery of ORAI proteins	35
1.2.3.2. Phylogenetic origin of ORAI proteins	35
1.2.3.3. ORAI proteins structure	37
1.2.3.3.1. ORAI1	39
1.2.3.3.2. ORAI2	39
1.2.3.3.3. ORAI3	42
1.2.3.4. ORAI channels activation during SOCE	42
1.2.3.4.1. I_{CRAC}	42
1.2.3.4.2. CRAC channel detailed structure	43
1.2.3.4.3. CRAC channel gating by STIM1	45
1.2.3.4.4. I_{SOC}	48
1.2.3.5. Other ORAI channel	48
1.2.3.5.1. Homomeric ORAI2 – ORAI3 channels	48
1.2.3.5.2. Heteromeric ORAI channels in SOCE	50
1.2.3.5.3. Heteromeric non-SOCE channel, ARC/LTR	52
1.2.4. Role of ORAI proteins in the physiology and pathology	54
1.2.4.1. Physiology	54

1.2.4.1.1.	Role of ORAI and SOCE in physiology	54
1.2.4.1.2.	Role of ORAI and store independent Ca^{2+} entry (SICE) in physiology	54
1.2.4.2.	Pathology	55
1.2.4.2.1.	Role of ORAI and SOCE in pathology	55
1.2.4.2.2.	Role of ORAI and store independent Ca^{2+} entry (SICE) in pathology	57
1.2.5.	Evidence for an ORAI proteins dynamic associations	57
1.3.	Microscopy to study ion channels	59
1.3.1.	Invention and popularization of the microscopes.	59
1.3.2.	Characteristics of optical microscopes.	62
1.3.3.	Fluorescence microscopy	64
1.3.3.1.	Fluorescence discovery and principle	64
1.3.3.2.	Fluorescent proteins	67
1.3.3.2.1.	GFP discovery	67
1.3.3.2.2.	Structure and properties of GFP	67
1.3.3.2.3.	Properties of fluorescent proteins (FP)	71
1.3.3.3.	Types of fluorescence microscopy	77
1.3.3.3.1.	Widefield fluorescence microscopy	77
1.3.3.3.2.	Confocal microscopy	85
1.3.3.3.3.	Total internal reflection fluorescence (TIRF) microscopy	90
1.3.3.4.	Summary of the advantage and limitations of fluorescence microscopy techniques	90
1.3.4.	Study of properties of ORAI proteins with microscopy techniques	92
1.3.4.1.	Calcium entry	92
1.3.4.1.1.	Ca^{2+} imaging with Fura-2	93
1.3.4.1.2.	Ca^{2+} imaging with genetically encoded Ca^{2+} indicators (GECI)	95
1.3.4.2.	Localization and diffusion properties of ORAI proteins	97
1.3.4.2.1.	Usage of TIRF microscopy	97
1.3.4.2.2.	Usage of FRAP and FCS	99
1.3.4.2.3.	Usage of super resolution microscopy techniques	101
1.3.4.3.	Protein-protein interactions	103
1.3.4.3.1.	Usage of Bimolecular fluorescence complementation (BiFC)	103
1.3.4.3.2.	Usage of Förster resonance energy transfer (FRET)	106
1.3.5.	Fluorescence lifetime imaging (FLIM) – FRET	115
1.3.5.1.	FLIM-FRET principles	115
1.3.5.2.	FLIM-FRET measurements	116
1.3.5.3.	FLIM-FRET analysis	118
1.3.6.	Summary on the use of microscopy techniques for the study of ORAI proteins	122
1.4.	The CRISPR-Cas9 system	123

1.4.1.	Discovery of the CRISPR-Cas system	123
1.4.2.	Mechanism of CRISPR-Cas9 system	123
1.4.2.1.	Physiological mechanism of CRISPR-Cas9	123
1.4.2.2.	Usage of CRISPR-Cas9 for genome editing	125
2.	Aim and scope of the PhD	129
3.	Material and methods	130
3.1.	Stocks solution	130
3.1.1.	Buffers and standard solutions	130
3.1.2.	Pharmacological agents	130
3.1.3.	Antibiotics	130
3.2.	Molecular biology	131
3.2.1.	NEBuilder Cloning	131
3.2.2.	Classic expression cloning	131
3.2.2.1.	Bacterial transformation	131
3.2.2.2.	Plasmid isolation	132
3.2.2.3.	Sequencing	132
3.2.2.4.	Restriction digest	132
3.2.2.5.	Agarose gel electrophoresis	132
3.2.2.6.	DNA extraction from agarose gel	132
3.2.2.7.	Ligation	132
3.2.3.	Polymerase chain reaction (PCR)	132
3.2.3.1.	RNA extraction	132
3.2.3.2.	DNase treatment	132
3.2.3.3.	Genomic DNA extraction (gDNA)	133
3.2.3.4.	Reverse transcription	133
3.2.3.5.	Conventional PCR condition	133
3.2.3.6.	Quantitative real-time PCR (qPCR)	135
3.3.	CRISPR/Cas9 related techniques	135
3.3.1.	gRNA design	135
3.3.2.	gRNA cloning	137
3.3.2.1.	Phosphorylation and annealing of the oligonucleotides	138
3.3.2.2.	Ligation of oligonucleotides into CRISPR/Cas plasmids	138
3.3.3.	T7 Endonuclease 1 (T7E1) assay	138
3.3.4.	CRISPR-Cas9 related plasmids construction	140
3.3.4.1.	CRISPR-Cas9 plasmids	140
3.3.4.2.	Recombination plasmids	142

3.3.4.3.	PITCh plasmids	142
3.3.4.4.	mCherry-eGFP Surrogate plasmids	145
3.3.5.	Genomic sequencing	145
3.4.	Oligonucleotides	145
3.4.1.	Primers	145
3.4.1.1.	PCR	145
3.4.1.2.	qPCR	149
3.4.1.3.	Cloning primers	150
3.4.2.	Expression plasmid	151
3.5.	Cell lines, bacterial strains, and growth condition	152
3.5.1.	Cell lines and growth conditions	152
3.5.2.	Bacterial strains and growth conditions	152
3.6.	Cell culture assay	152
3.6.1.	Cell count	152
3.6.2.	Proliferation	152
3.6.3.	Cell cycle analysis	152
3.6.4.	Adhesion Assay	153
3.6.5.	Video microscopy migration assay (Wound healing)	153
3.6.6.	Boyden chamber migration assay (Transwell [®])	153
3.7.	Transfections	154
3.8.	Macromolecule blotting	154
3.8.1.	Protein extraction	154
3.8.2.	Immunoblotting	154
3.9.	Calcium imaging	155
3.10.	FLIM-FRET	155
3.10.1.	Fluorophore choice	155
3.10.2.	Experimental procedure	156
3.10.3.	Acquisition conditions	157
3.11.	Statistical analysis and data presentation	157
4.	Results	159
4.1.	Consideration before performing CRISPR-Cas experiment	159
4.1.1.	Model cell line to edit	159
4.1.2.	Choice of the Cas protein to induce double strand break (DSB)	159
4.1.3.	Delivery of the Cas9 protein in the cells	160

4.2.	Generating gene knockin (KI) with CRISPR-Cas9	160
4.2.1.	Design of gRNA	160
4.2.1.1.	Cutting efficiency	161
4.2.1.2.	Cutting specificity	161
4.2.2.	Assessment of gRNA efficiencies	163
4.2.3.	Recombination method	163
4.2.3.1.	Considerations before conducting homologous direct repair (HDR) experiment	166
4.2.3.2.	Donor plasmid	166
4.2.3.3.	Increasing the endogenous expression level of <i>ORAI1</i> and <i>ORAI3</i>	172
4.2.3.4.	Precise Integration into Target Chromosome (PITCh) technique	172
4.2.4.	Conclusion on the gene KI experiments with CRISPR-Cas9 system.	172
4.3.	Generating knockout (KO) with CRISPR-Cas9 system.	173
4.3.1.	General consideration for creating KO with CRISPR-Cas9	173
4.3.1.1.	Identification of a suitable screening method for KO identification	173
4.3.1.2.	Design of gRNA for <i>ORAI1</i> - and <i>ORAI3</i> - KO	174
4.3.1.3.	Assessment of gRNA efficiencies	174
4.3.2.	Generation of <i>ORAI1</i> KO HEK-293 cells	174
4.3.2.1.	Validation of <i>ORAI1</i> KO in HEK-293 cells	179
4.3.2.1.1.	Ca ²⁺ imaging experiments	179
4.3.2.1.2.	Immunoblotting	179
4.3.2.1.3.	Gene sequencing	183
4.3.2.2.	Conclusion on the generation of HEK ORAI1 KO	183
4.3.3.	Generation of double KO for <i>ORAI1</i> and <i>ORAI3</i> in PC3 cells.	183
4.3.3.1.	Screening and validation of ORAI1 KO in PC3 cells	185
4.3.3.2.	Screening and validation of ORAI3 KO in PC3 cells	185
4.3.4.	General conclusions on the generation of KO cells	185
4.4.	Impact of ORAI1 deletion on the HEK-293 physiology	190
4.4.1.	Different roles for ORAI1 in HEK-293 physiology	190
4.4.2.	Ca ²⁺ signaling	190
4.4.3.	ORAI homologues expression	191
4.4.4.	Proliferation	191
4.4.5.	Adhesion	191
4.4.6.	Migration	197
4.4.7.	Conclusions	197
4.5.	Study of ORAI1 - ORAI3 interactions with FLIM-FRET	201
4.5.1.	Hypotheses on the existence of a dynamic re-arrangement of ORAI protein	201
4.5.2.	Impact of ORAI1 and ORAI3 overexpression modulation on SOCE level	201

4.5.2.1.	Effect of transient overexpression of ORAI1 and ORAI3 on SOCE	201
4.5.2.2.	Effect ORAI1 deletion on SOCE	202
4.5.2.3.	Effect of ORAI3 deletion on SOCE	202
4.5.2.4.	Conclusion on the roles of ORAI1 and ORAI3 in endogenous SOCE	208
4.5.3.	Measurement of ORAI1-ORAI3 interaction with FLIM-FRET	208
4.5.3.1.	In HEK-293	208
4.5.3.1.1.	Basal interaction	209
4.5.3.1.2.	Arachidonic acid activated interaction	209
4.5.3.1.3.	Store dependent interaction	213
4.5.3.1.4.	Sequential activation of ARC and CRAC	213
4.5.3.1.5.	Conclusion on the ORAI1-ORAI3 interaction in HEK-293	216
4.5.3.2.	In PC3	216
4.5.3.2.1.	PC3 WT	216
4.5.3.2.2.	Double KO (ORAI1-ORAI3) PC3	219
4.5.3.3.	Conclusion on the interactions between ORAI1 and ORAI3 in PC3 cells	224
5.	Discussion and perspectives	225
5.1.	Challenges in generating gene KI with the CRISPR/Cas9 system	225
5.1.1.	HDR-based method of KI	225
5.1.2.	Non-HDR based method for KI	225
5.1.3.	Hypothesis on the non-detection of recombination events	226
5.1.4.	Conclusions and perspectives for the generation of gene KI	229
5.2.	Challenges in generating gene KO with the CRISPR/Cas9 system	229
5.2.1.	Design of gRNA	229
5.2.2.	Assessment of gRNA efficiency	229
5.2.3.	Screening method for selection of KO cell lines and validation of KO.	230
5.2.4.	Conclusion on the generation of gene KO with the CRISPR/Cas9 system	231
5.3.	Dispensability of ORAI1 in the control of the HEK-293 physiology.	231
5.3.1.	ORAI1 deletion abolishes SOCE	232
5.3.2.	ORAI1 deletion does not affect proliferative properties of HEK-293	232
5.3.3.	ORAI1 deletion is not fundamental for the control of HEK-293 migration	233
5.3.4.	Conclusion on the role of ORAI1 in HEK-293 physiology.	233
5.3.5.	Perspectives on the role of ORAI1 in HEK-293 physiology.	234
5.4.	Evidence of an ORAI1-ORAI3 dynamic remodeling	234
5.4.1.	Influence of ORAI1 and ORAI3 expression on SOCE level	235
5.4.1.1.	Overexpression of ORAI in WT PC3	235
5.4.1.2.	Effect of ORAI proteins deletion on SOCE in PC3 cells	235

5.4.2.	Study of ORAI1-Orai3 interaction with FLIM-FRET	236
5.4.2.1.	Orai1-Orai3 interaction models in HEK-293	236
5.4.2.1.1.	Putative model N°1: on site assembly of ORAI dimers.	236
5.4.2.1.2.	Putative model N°2: reorganization of pre-formed ORAI channels	237
5.4.2.1.3.	FLIM-FRET results in regard with the interaction models	237
5.4.2.2.	Study of ORAI1-Orai3 interaction in PC3	250
5.4.2.2.1.	Orai1-Orai3 interaction in PC3-WT	250
5.4.2.2.2.	Orai1-Orai3 interactions in double KO (ORAI1+ORAI3) PC3	250
5.4.2.3.	Perspectives on the study of ORAI1-Orai3 interactions	251
5.4.2.3.1.	Additional analysis of the results	251
5.4.2.3.2.	Additional experimental procedures	252
6.	General conclusion	254
6.1.	Generation of KI cell lines with CRISPR/Cas9	254
6.2.	Generation of KO cell lines with CRISPR/Cas9	254
6.3.	Study of ORAI1 role in fundamental physiology of HEK-293	254
6.4.	Study of ORAI1-Orai3 interaction with FLIM-FRET	254
7.	Annexes	256
	<i>Error! Bookmark not defined.</i>	
8.	Bibliography	267

1. Introduction

1.1. General overview of ion channels

1.1.1. Common features

Living organisms are embedded in a structure isolating them from the external medium. Except from some viruses this structure consists in lipidic membrane which provide an impermeable barrier allowing the organism to retain the vital molecules required for its growth. Nonetheless, in order to develop, all organisms need to excrete their waste products and import valuable elements. From all the proteins responsible for these exchanges, ion channels are the one responsible for ion flux across the membrane. The importance of this protein family is highlighted by the fact that ion channels were identified in virtually all living cells, from Bacteria and Archaea to Eukaryote and (Jiang *et al*, 2003) even in some Viruses (Moran *et al*, 2015). Nonetheless, from an evolutionary point of view, there is no evidence that ion channels evolved from a unique ancestor as no sequence homology could be detected within the myriad of ion channel protein identified (Nayak *et al*, 2009). Nevertheless, all ion channels are sharing a number of common features that defines them as members of the ion channel protein family (Anderson & Greenberg, 2001; Nayak *et al*, 2009). These features can be described as follow, ion channels:

- (1) are integral membrane proteins and thus possess hydrophobic segments.
- (2) allow passive transport of ion through membranes, meaning that ion fluxes diffuse according to the electrochemical gradient.
- (3) main structural property is to form ion-permeable tunnel across the membrane, named pore.
- (4) minimal structural constituent is represented by two transmembrane domains (TM) surrounding the pore-forming loop.
- (5) possess a high rate of ion diffusion.

1.1.2. Functional diversity

Ion channels seems to have appeared several times throughout evolution depending on the specific needs of the organisms (Nayak *et al*, 2009). This is probably one of the reasons of their important diversity. Due to this diversity, several systems of classifications for ion channels co-exist. For example, ion channels can be separated in different families depending on their ion selectivity, and thus define the Potassium (K^+), Sodium (Na^+), Chloride (Cl^-), Calcium (Ca^{2+}), Proton (H^+), and non-selective ion channel families. Alternatively, ion channel families can also be distinguished through their gating mechanisms. Of note, the term ‘gating’ refers to the mechanism by which the ion-permeable pore is opening (activation) or closing (by deactivation or inactivation). Apart from constitutively open leak channels, the activation of an ion channel results from a conformational change and thus requires an energetic input to allow their unlocking. The gating mechanism classification of ion channels includes three main families. The first group comprises ligand-gated channels, they can be activated by the

binding of a specific molecule (*e.g.* acetylcholine for acetylcholine receptor), an ion (*e.g.* Ca^{2+} for Ca^{2+} -activated K^+ channels), or another protein (*e.g.* ORAI channels during the store-operated Ca^{2+} entry [SOCE] mechanism). The second group represent pH-gated channels for which the protonation state of specific amino acid determines the opening or closing of the channel (*e.g.* Acid-sensing ion channels [ASIC]). The third group comprises channels which are gated by a physical process and includes the super-families of voltage-, mechano-, and temperature-gated ion channels (**Figure 1**). Importantly, several ion channels fall into multiple groups. For example, the transient receptor potential vanilloid 1 (TRPV1) is a ligand-gated ion channel that also displays voltage-gating properties (Gunthorpe *et al*, 2000). Additionally, the channel H_v1 is a voltage-gated channel but is at the same time strongly regulated by pH, and sensitive to mechanical stimuli (Pathak *et al*, 2016; DeCoursey, 2013). Therefore, there is no unique and formal classification system for ion channels, and in fact, many classification systems co-exist.

1.1.3. Ion channel structure diversity

Protein structure is characterized by four levels organization (**Figure 2**). The primary level is simply the linear chain of amino acid, the secondary level is represented the three-dimensional (3D) shape adopted by groups of amino acid, the tertiary structure of protein represents the 3D organization of the whole protein including its different domains, and the quaternary structure, which is not observed for all proteins, consists of the organization of multiple units of proteins into macromolecules, this process being called oligomerization. In addition to the existing diversity in their ion selectivity and gating mechanisms, ion channel also present heterogeneity at each of these structural levels:

1.1.3.1. Primary structure

From a phylogenetic point of view, ion channel primary structure diversity is evident as no homology in their amino acid sequence could be identified and linked to single ancestor. A good example of ion channel diversity in their primary structure is the large difference in amino acid length observed between the smallest identified ion channel: Kcv (a potassium ion channel identified in virus constituted of 94 amino acid) and some of the longest ion channels such as ryanodine receptor (RyR) which can be composed of more than 5000 amino acids (Kang *et al*, 2004) (**Figure 3 A and B**).

1.1.3.2. Secondary structure

Originally, three types of protein secondary structures were described: α -helix, β -strands, and random coil (Pauling *et al*, 1951; Pauling & Corey, 1951). However, several other non-repetitive secondary structures were later identified (such as turns and loops, for example) (Fetrow, 1995). Yet, no consensus about the description of all secondary (or super secondary) structures organization was reached as demonstrated by the classifications heterogeneity found between different structural

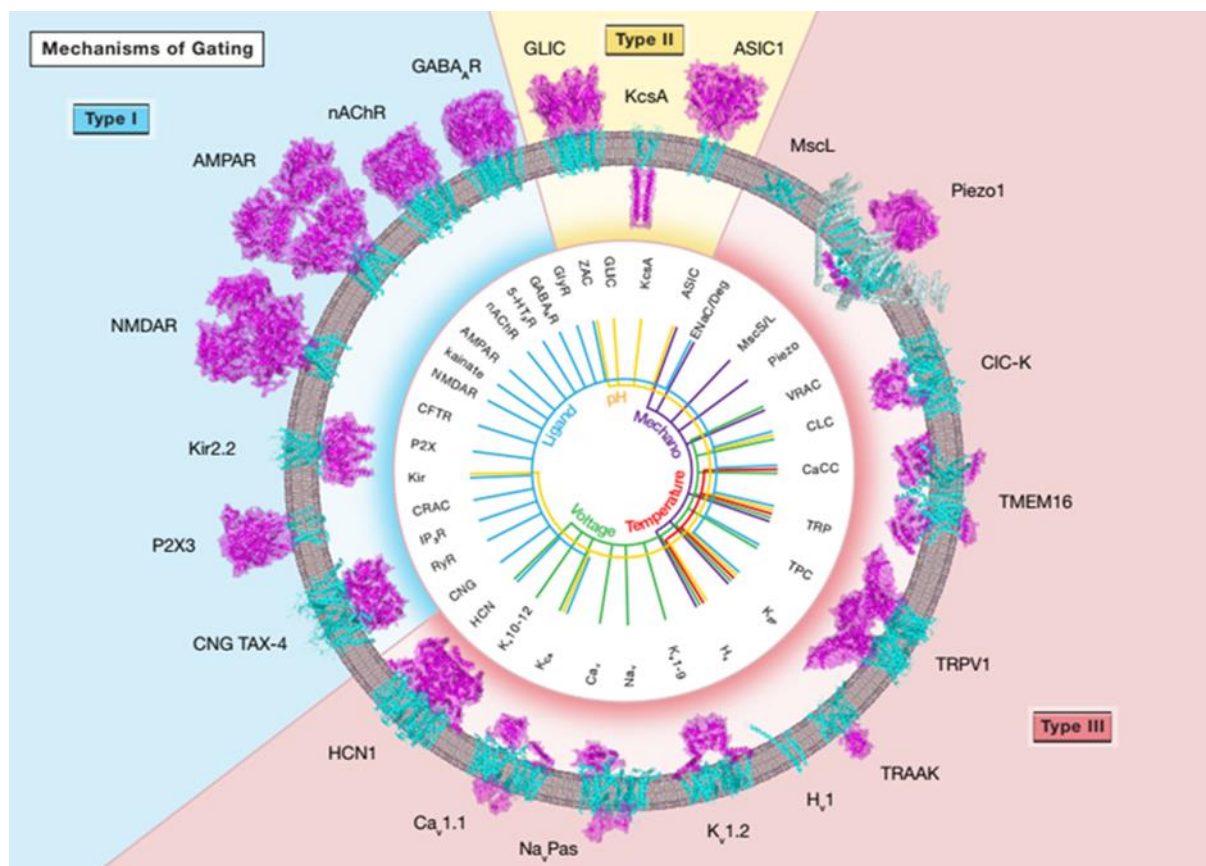


Figure 1 | Ion channel classification by their gating mechanism.

Three types of gating mechanisms allow the classification of ions channels. Type I (in blue) gather ligand-gated ion channel whether ligand consists of neurotransmitter, lipid, intracellular molecule or other protein. Type II (in yellow) includes proton-gated ion channel for which pH modification gates the pore opening. Type III (in violet) comprises channel gated by a physical process such as voltage, temperature or tension modification. Some structures of ion channels are depicted on the circular lipid bilayer with the transmembrane domain in blue and the extracellular (pointing outside of the circle), an intracellular (pointing inside the circle) in violet. The internal wheel diagram presents subdivision of the three types of gating mechanisms and highlights the diversity and complexity of classification system as multiple gating mechanisms might co-exist for a single ion channel.

Adapted from Goldschen-Ohm & Chanda, 2017

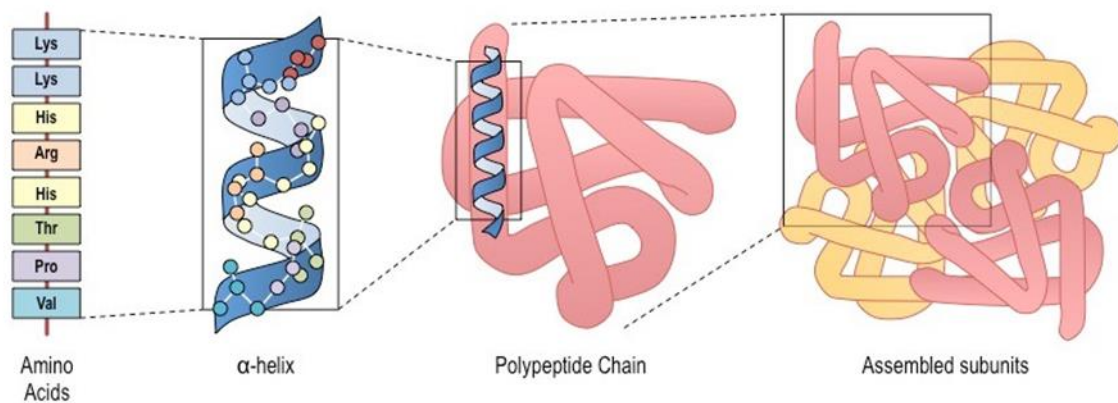


Figure 2 | Structural organization of proteins.

From left to right: The primary structure consists of the amino acid sequence of the protein. The secondary structure represents the local organization of the amino acid chain, the most common secondary structures are α -helix and β -sheets. The tertiary structure can refer to the 3-dimensional shape of the whole polypeptide chain or of its specific domains. The quaternary structure does not exist for all protein, it is restricted to protein assemblies. It corresponds to the 3D organization of multiples subunits (individual polypeptide chains).

Image modified from: <https://ib.bioninja.com.au/higher-level/topic-7-nucleic-acids/73-translation/protein-structure.html>

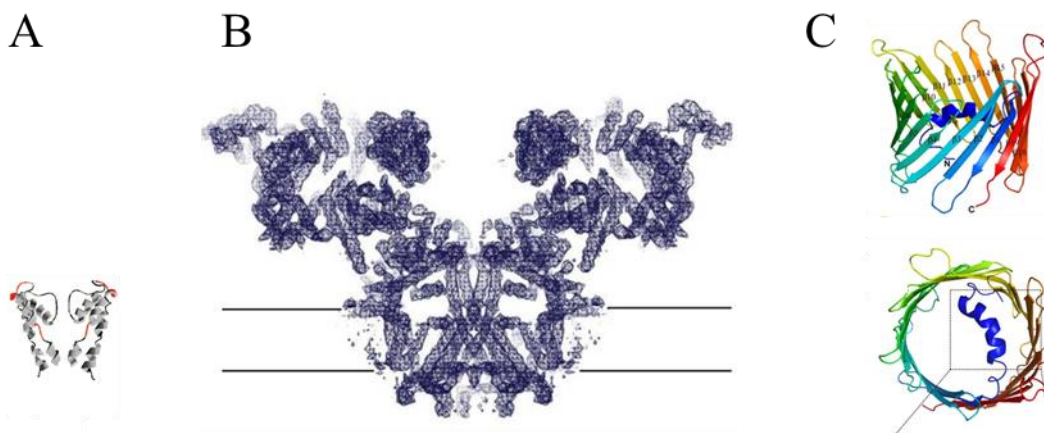


Figure 3 | Ion channel size range.

- Hypothetical model of one of the smallest ion channel identified: the viral potassium channel Kcv (94 amino acids).
- Structure of one of the biggest ion channel identified: the tetrameric mammalian ryanodine receptor (more than 5000 amino acids).
- Structure of the *human* mitochondrial voltage-dependent anion channel (VDAC), side view (top) and top view (bottom). This channel displays a β -barrel organization if its TM domain.

Image modified from: (Gazzarrini et al, 2003; Zalk et al, 2015; Bayrhuber et al, 2008)

databases (Banach *et al*, 2019). It is therefore, difficult to appreciate their representation level within the myriad of ion channel described. Nevertheless, it is interesting to note that TM domains, the structural basic element of ion channel structure, present diversity in their structure. Indeed, most of ion channel present TM domains composed of α -helix. However, some ion channels located in outer membranes of Gram-negative bacteria, chloroplasts or mitochondria such as the voltage-dependent anion channel (VDAC) present TM composed of β -barrel demonstrating that even in their most conserved part, ion channel also present structural heterogeneity (**Figure 3 C**) (Cavalier-Smith, 2000; Moitra & Rapaport, 2021).

1.1.3.3. Tertiary structure

The tertiary structural organization level of proteins usually refers to the spatial arrangement of secondary and super secondary structures of proteins. While this term was initially used to describe the global 3D shape of proteins (Moss, 1996), tertiary structures element can also define protein regions that adopt a specific conformation independently from the rest of the protein structure. Such regions usually exhibit specific functions and are named protein domains (Skipper, 2005). Ion channels present a myriad of different domain depending on their mode of activation, or additional function (such as enzymatic functions). Nonetheless, the channel pore represents a domain which is evidently found in every ion channel. One of the best representations of tertiary structure diversity within ion channels is represented by their various gating mechanisms. Specifically, almost each gating mechanism is associated with its specific domains. For example, voltage-gated ion channel requires the presence of voltage sensing domain; ligand gated ion channel family entails the presence of specific ligand binding domain. In addition, several protein interaction domains are also found in ion channels due to the requirement of some ion channel protein to form oligomer to be active. For example, some ankyrin domains were found on TRPV5 channels and were shown to facilitate their tetramerization (Chang *et al*, 2004). Similarly, coil-coiled domain present in Hv1/VSOP channel are important for their dimerization (Fujiwara *et al*, 2012). Finally, some ion channels are also displaying domains bearing a secondary function, in addition to their ion conduction role, such as enzymatic activity. It is the case for the TRP melastatin 7 (TRPM7) channel which presents kinase activity (Ryazanova *et al*, 2004).

1.1.3.4. Quaternary structure

The last level of protein structure is called quaternary structure, it represents the association between multiple proteins called oligomerization and it enables the proteins to function properly (Ouellette & Rawn, 2015). Most ion channels are oligomeric assemblies of the same protein (homo-oligomers) or of different proteins (hetero oligomers). In fact, the specific oligomerization of an ion channel is usually related to its family and often represent a way of regulating the function or the properties of the channels. The oligomerization process of ion channels represents a way for the cell to tightly control and

modulates their function. To appreciate the complexity in oligomeric assemblies of ion channels, some typical architecture of different ion channel families will be presented below:

- Voltage-gated cation ion channels superfamily.

It was postulated that all the members of this family are originating from a single ancestor ion channel. This prototypic ion channel ancestor underwent several rounds of gene duplication and gene fission leading to the multiplication of its TM domain and to the diversification of its architecture eventually leading to the apparition of a multitude of ion channel presenting distinct properties and different oligomerization states (**Figure 4**). Specifically, it is believed that the Inward-rectifier potassium channels family (K_{ir}), whom members are found from Prokaryotes to Eukaryotes, are the closest example of the typical ion channel ancestor from this family (Anderson & Greenberg, 2001; Moran *et al*, 2015). K_{ir} channels are displaying the simplest ion channel structure with only 2 TM domains. All the members of the superfamily display this similar K_{ir} -like domain but have acquired additional regulatory domain throughout evolution such as voltage-sensing, or ligand binding regions. Overall, due to successive rounds of gene duplication and fusion members of the superfamily can present 2, 4, 6, 12 or 24 TM domain (**Figure 4**) (Nayak *et al*, 2009; Moran *et al*, 2015). Interestingly, despite their different numbers of TM, their pore architecture is somewhat conserved, and it is the number of protein units required to form a functional channel which differs. For example, 2TM, 4 TM and 6TM domain proteins such as K_{ir} , K2P (Two-pore-domain potassium channel) or TRP need to tetramerize in order to form functional channels (**Figure 5 A, C, D**). Remarkably, channel from these sub-family are able to form hetero- or homo-tetramers therefore providing specific properties to the channel they form. At the opposite, 24 TM domain protein from the Ca_v or Na_v family are strictly monomeric and are regulated by accessories subunits. Finally, the members of the two-pore channel (TPC) family present 12TM domain, they can form pseudo-tetramers which consists in the association of 2 homo- or hetero- dimers with each of the dimers forming one individual pore (**Figure 5 E**).

- Pentameric ligand-gated ion channels.

As indicated by their name, members of this family are gated by ligand binding. These channels are functional when assembled as pentamers. This group including the Cys-loop receptors family which are displaying extracellular C- and N- termini responsible for the binding of neurotransmitters that gate the channel. They possess 4TM domains and the pore is constituted primarily of the TM N°2 of each protein. While they can associate as homo-pentamers, their preferred assembly consist of hetero-pentamers as the association of different subunit types confers different properties to the formed channel (**Figure 5 G**) (Sine & Engel, 2006; Jaiteh *et al*, 2016).

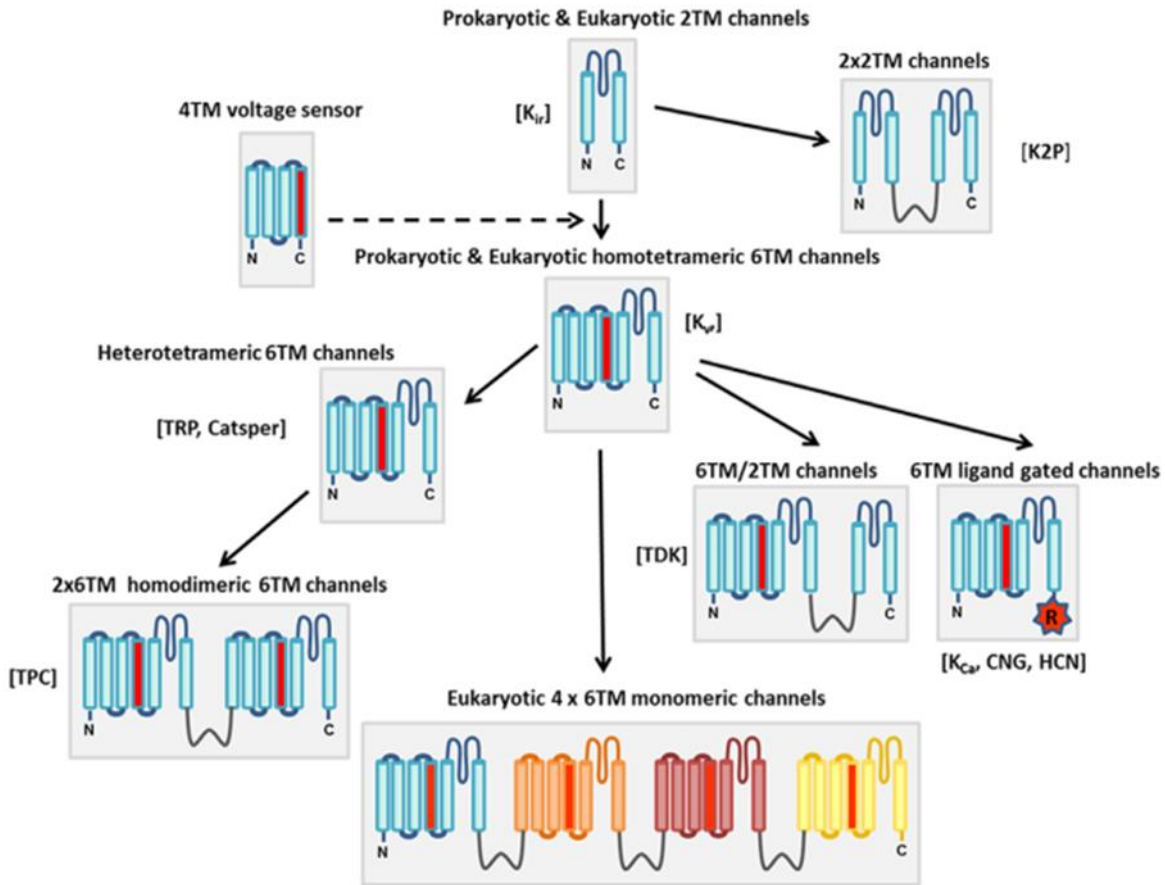


Figure 4 | Evolution scheme of the cation voltage-gated ion channels superfamily.

The K_{ir} family ion channel represents the simplest structure of ion channel with 2TM separated by a loop containing the pore domain. These protein associates in tetramer to form functional ion channel. The ancestor of this family was probably bearing the same simple channel structure as similar ion channel are found across many Prokaryotes and Eukaryotes. From this ancestor gene duplication and fusion gave birth to 4TM channel protein that dimerize to form ion channel such as the K2P family. On the other hand, fusion of the ancestor ion channel to a voltage sensing domain of a non-channel protein formed 6 TM ion channels which forms homo- or hetero- tetrameric assemblies (K_v, TRP channels respectively). Subsequent gene duplication and fusion of 6TM heterotetrameric channels lead to the emergence of 2x6TM homodimeric channels such as TPC. Homotetrameric 6TM channels are at the basis of: 6TM ligand gated ion channel due to fusion to specific ligand binding domain; 6TM/2TM channels after fusion to simple 2TMchannel; and 24TM monomeric channels thanks to two successive rounds of duplication and fusion.

Image adapted from: Amey et al, 2015

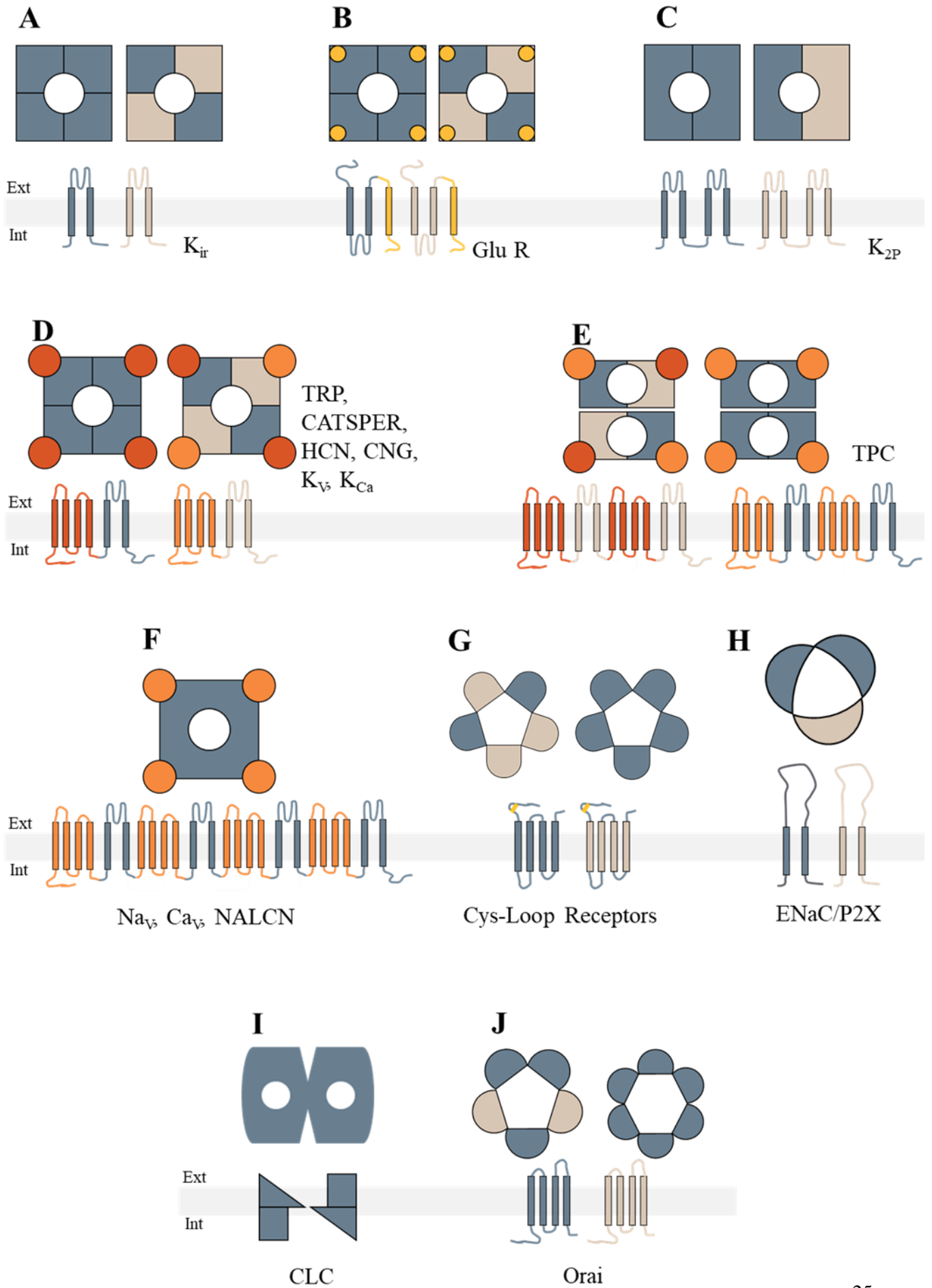


Figure 5 | Structural diversity of ion channels.

The overall channel structure viewed from above is depicted at the top of each panel. At the bottom, the proteins are represented with their TM domains as rectangles.

- A. K_{ir} -like ion channel possess 2 TM domain and are assembled as homo- or hetero- tetramers to form functional channel.
- B. Glu R present an inverted K_{ir} -like domain fused to an additional TM domain (in yellow), they can also form functional channels as homo- or hetero- tetramers.
- C. K2P channels presents 4TM resulting from the fusion of 2 K_{ir} -like elements, they assemble as homo- or hetero- dimers.
- D. 6TM domain channels derived from the voltage-gated ion channels super-family possess a 4 TM voltage-sensing domain (in dark and light orange) plus a 2TM K_{ir} -like prototypic domain. They form functional channels as homo- or hetero- tetramers depending on their family type.
- E. TPC are bearing 12TM domain results from the fusion of two 6TM domain (containing a 4TM domain voltage-sensing like and a 2 TM domain resembling a K_{ir} -like domain). They form pseudo tetramers (association of homo- or hetero- dimers) and bear two individual pores when assembled.
- F. Na^+ voltage-gated, Ca^{2+} voltage-gated and Sodium leak channel NALCN are 4X 6TM proteins and form monomeric channel. Their structure results from successive rounds of gene duplication and fusion.
- G. Ion channels from the Cys-loop ligand-gated superfamily such as GABA (GABAR) or nicotine acetylcholine (nAChR) receptors present 4 TM as well as extracellular termini. Additionally, they present a disulfide bridge which confers its name to the family. They form functional channel when assembled as homo- or hetero- pentamers.
- H. Members of the ENaC/P2X superfamily ion channel are formed by homo- or hetero- trimeric association of 2TM domain proteins.
- I. Chloride channels from CLC family possess atypical and complex structure with α -helix that do not cross entirely the plasma membrane. The functional channel is a dimer of two protein assembled in an anti-parallel symmetry with each protein bearing its own pore.
- J. ORAI protein do not show homology with any other ion channel. They possess 4TM domain and have been shown to possess the ability to form homo-hexamers as well as hetero-pentamers.

Abbreviations: K_{ir} : Inward-rectifier potassium channel, Glu R: Ionotropic Glutamate Receptors, K2P: Two-pore-domain potassium channel, TRP: Transient receptor potential, CATSPER: Cation channels of sperm, HCN: Hyperpolarization-activated cyclic nucleotide-gated channel, CNG: Cyclic nucleotide-gated ion channel, K_v : Voltage-Gated K^+ Channels, K_{Ca} : Calcium-activated potassium channel, TPC: Two-pore channel, Nav: Voltage-gated sodium channels, Cav: Voltage-gated calcium channels, NALCN: Sodium leak channel non-selective, ENaC/P2X: Epithelial sodium channel / ATP-gated P2X receptor cation channel family, CLC: Chloride channel

- Epithelial sodium channel (ENaC) /P2X family.

This superfamily includes members of the Enac, the P2X and Acid sensing ion channel (ASICs) families, these proteins present 2TM domain proteins with the pore mainly constituted by the TM N°2. They associate as trimers to form functional channel. Similarly, to the group above, proteins can adopt hetero- or homo-trimers form in order to modulate the properties of the channel they form (**Figure 5 H**). (Jasti *et al*, 2007; Barrera *et al*, 2005; Horikawa, 2015; Kaczmarek-Hájek *et al*, 2012).

- Chloride Carrier/Channel family

The members of the chloride channel family display a very complex structure. They possess membrane domain which are not spanning the entire membrane and the number of 'real' TM is variable. They assemble as dimers in an anti-parallel way and each individual protein bears its individual pore. The functional channels are hetero- or homo- dimers(**Figure 5 I**) (Jentsch *et al*, 2002; Poroca *et al*, 2017).

- Ca^{2+} release-activated Ca^{2+} channel (CRAC-C) family

This unique family of ion channel protein count three members named ORAI1, 2 and 3. They show no sequence homology with any other known ion channels which explain their relatively recent discovery in 2006. The 3 *human* members of this family possess 4TM domains, and the pore-forming unit is constituted by their first TM1. They show a unique property as their stoichiometry can be different depending on the channel they form. As such, it was demonstrated that the Ca^{2+} release activated Ca^{2+} (CRAC) channel, responsible for the store operated Ca^{2+} entry (SOCE), consists of a homo-hexameric assembly of ORAI1 protein whereas the Arachidonate-regulated channel (ARC) present a hetero-pentameric structure composed of ORAI1 and ORAI3 proteins (**Figure 5J**) (Mignen *et al*, 2008a; Lis *et al*, 2007a).

1.1.4. Conclusion on the diversity of ion channels

To conclude, ion channels are an extremely diverse protein family. Within this family, multimerization is a common process which is found across several ion channel families. Indeed, oligomerization process presents the advantage of allowing an adjustment of channel properties by simply modifying its subunit composition. Nonetheless, the modification of the channel composition usually does not affect their stoichiometry and thus leaves their pore architecture intact. Thus, within all ion channel identified, the ORAI protein family present a unique property since it was described that they can assemble in distinct channels of different stoichiometry bearing specific properties. The following part of the dissertation will be devoted to the description of ORAI proteins. Especially, ORAI proteins are essential component of one of the central mechanisms of Ca^{2+} signaling in the cells called SOCE. Thus, we will start by describing the SOCE process and its specific molecular components before reporting the other types of channels that can be formed by ORAI proteins.

1.2. Store operated Ca^{2+} entry (SOCE) and its components

1.2.1. Discovery of SOCE

The ORAI proteins were identified as the effector part of the cellular process called Store Operated Calcium Entry (SOCE). The SOCE correspond to an entry of Ca^{2+} from the extracellular space into the cytoplasm in response to an endoplasmic reticulum (ER) Ca^{2+} store depletion. The existence of a link between the Ca^{2+} release from the ER, and the Ca^{2+} entry through the plasma membrane (PM) was first postulated in 1977 by Dr Putney who named this process the capacitative entry. Indeed, Dr Putney predicted the existence of an intermediate step between the Ca^{2+} release from the ER stores and the subsequent Ca^{2+} entry across the PM. Thus, he used the term capacitative as an homology with the “electrical circuit where a charge must load a capacitor before current can flow through it” (Putney, 2007). Even though it was thought, at first, that the SOCE was allowing a direct refilling of the intracellular stock of Ca^{2+} (*i.e.*: the ER) from the exterior of the cells (Casteels & Droogmans, 1981). This hypothesis was later invalidated by a study conducted by Dr Kwan indicating that the refilling of the store was not a direct route (Rosado, 2006; Kwan *et al*, 1990). In the following years, it was also demonstrated that the role of SOCE was not limited to the sole refilling of intracellular Ca^{2+} store but that it was also of extreme importance for a variety of cellular processes such as differentiation, secretion, proliferation, migration in multiple cell types (Darbellay *et al*, 2009; Concepcion *et al*, 2016; Abdullaev *et al*, 2008; Potier *et al*, 2009). Despite its physiological importance and the growing number of studies related to SOCE, the identification of its molecular component took almost 20 years (Putney, 1986; Roos *et al*, 2005; Liou *et al*, 2005; Prakriya *et al*, 2006; Vig *et al*, 2006). Thus, in 2005 and 2006, the discoveries and identification of STIM and ORAI proteins respectively enabled the description of the molecular choreography leading to the generation of SOCE. The simplified mechanism leading to SOCE generation could be described as follow: (1) The stimulation of a cell surface receptor results in the production of the second messenger inositol triphosphate (IP3). (2) The binding of IP3 on its ER receptor induces ER Ca^{2+} release. (3) The decrease in Ca^{2+} concentration induces a conformational change in the ER resident protein STIM. (4) The STIM protein starts diffusing to in ER-PM junction where it binds the Ca^{2+} channel composed of ORAI1 protein named Ca^{2+} release-activated Ca^{2+} channel (CRAC). (5) Binding of STIM1 to CRAC channel induce a conformational change which opens the channel and thus allows the Ca^{2+} entry in the cytoplasm through the PM in a process called the SOCE (**Figure 6**). The precise molecular mechanisms leading to the activation of STIM and ORAI proteins have been extensively studied. In order to detail this mechanism, the structural elements present in ORAI and STIM proteins will be detailed thereafter.

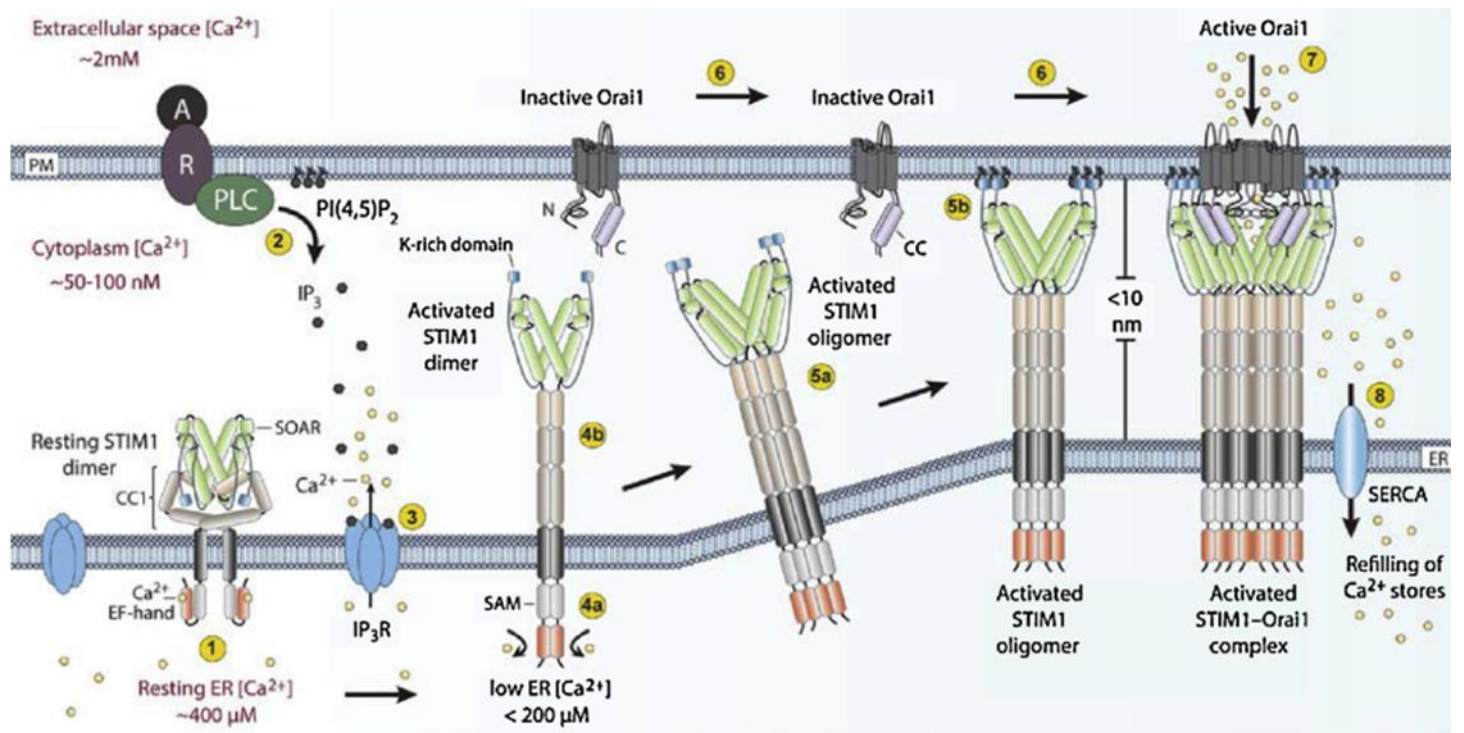


Figure 6 | Store operated Ca^{2+} entry (SOCE) mechanism.

In resting state, the dimeric ER residing STIM1 protein adopts a packed conformation due to the Ca^{2+} binding on its EF-hand domain (1). The binding of an agonist (A) on a cell surface receptor (R) induces the activation of the phospholipase C (PLC) leading to the creation of phosphatidyl inositol biphosphate (PI(4,5)P₂) and inositol triphosphate (IP₃) (2). The binding of IP₃ on the IP₃ receptor (IP₃R) induces Ca^{2+} release from the ER (3). The decrease in the ER Ca^{2+} concentration induces release of Ca^{2+} from STIM1 EF-hand and leading to a conformational change of the STIM1 dimer provoking the deployment of its cytosolic extremities (4a, 4b). The deployed STIM1 are oligomerizing, binding ORAI1 proteins, and migrating to ER-PM junction (5a, 5b, 6) and ultimately activating the ORAI1 channel (7), allowing Ca^{2+} entry in the cytoplasm, that enable ER store refilling due to the SERCA pump activity (8).

Image adapted from: Bhardwaj et al, 2016

1.2.1.STIM proteins

1.2.1.1. Discovery of STIM proteins

The *STIM* gene was cloned in 1996 by two independent teams (Oritani & Kincade, 1996; Parker *et al*, 1996). If Parker's team cloned the gene and named it *GOK*, they did not find any function for the newly discovered protein as it was not showing any sequence homology with other known proteins at the time. On contrary, Oritani & Kincade were the first to identify a role for the protein coded by *GOK* gene. They found that this protein played a role in the interaction process between stromal and pre-B cells, it is the reason why they initially named this protein SIM (Stromal Interaction Molecule) which was later renamed STIM (STromal Interaction Molecule). Even though the exact role of STIM protein was not identified by these teams, they both correctly identified important topological domain of the STIM protein, such as its transmembrane domain, its coil-coiled interaction domain and a signal peptide sequence. In 2001, a gene database screening revealed the existence of a homologue gene to *STIM* contributing to the creation of the STIM family including *STIM1* and *STIM2* genes (Williams *et al*, 2001). It is only, in 2005 that two teams have independently discovered the essential role of STIM proteins in the SOCE process (Roos *et al*, 2005; Liou *et al*, 2005). Since this date, the STIM proteins (1&2) have been extensively studied (with more almost 200 publications including STIM in their title since 2005), and the structure of these proteins is well described, and will be recapitulated below.

1.2.1.2. Structure of STIM proteins

1.2.1.2.1. Common characteristics between STIM proteins

STIM1 and STIM2 are homologous proteins encoded by two different genes. In humans, at least 3 isoforms of each *STIM* gene were described: *STIM1*, *STIM1L* and *STIM1B* for the *STIM1* homologues, and *STIM2.1* (also named STIM2 β), *STIM2.2*, which is the regular *STIM2* isoform (also named STIM α), and *STIM 2.3* (Darbellay *et al*, 2011; Ramesh *et al*, 2021; Miederer *et al*, 2015; Rana *et al*, 2015). All STIM isoforms present the same overall structure constituted of a short N-terminus facing the ER lumen, a single-pass transmembrane domain, and a long C-terminus region facing the cytosol. In human, the predominant form of STIM1 and STIM2 (STIM1 and STIM2.2 respectively) are ubiquitously expressed. These protein are mainly found in the ER membrane even though few publications have identified STIM proteins in PM (Spasova *et al*, 2006) and acidic stores (Zbidi *et al*, 2011). STIM proteins possess a dual role of sensing the Ca²⁺ concentration in the ER and activating the ORAI1 channel in the PM. In addition, STIM proteins present several domains including (**Figure 7**):

- On the N-terminal extremity, facing the ER lumen:
 - A canonical and a non-canonical EF hand motif (cEF and nEF respectively) associated with a sterile alpha motif (SAM). This domain called EF-SAM allows the STIM protein to detect variation in the ER Ca²⁺ concentration. Of note, these domains are not identical for all the STIM isoforms. As a consequence, the

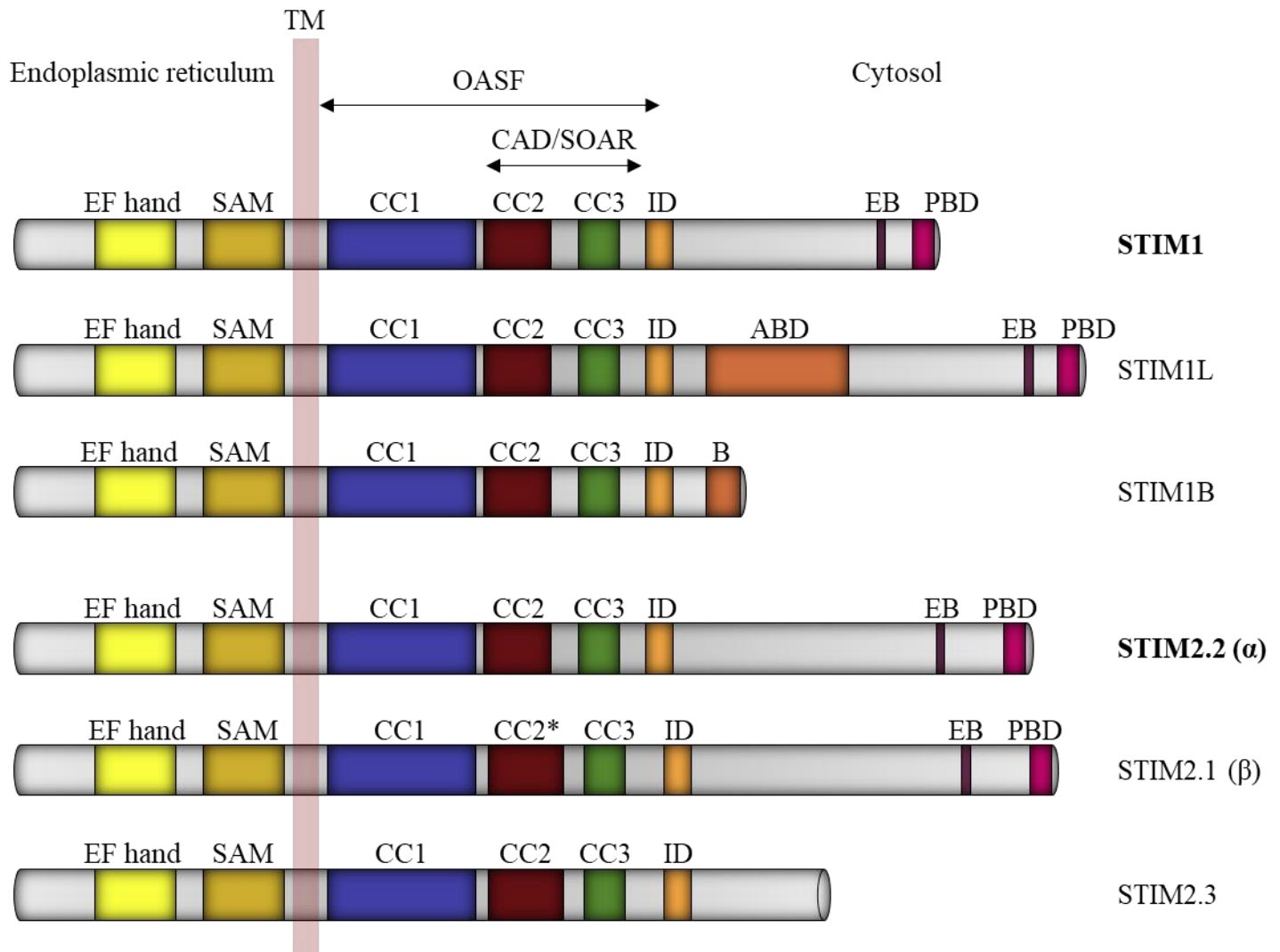


Figure 7 | The STIM protein family structural features.

Schematic representation of STIM protein family domains. The three isoforms of STIM1 and STIM are represented (main isoform in bold). Colored boxes indicates specific domains. All isoforms present the following domains: EF hand domain (yellow rectangle includes a canonical and a non canonical EF hand domains), the sterile alpha motif is represented in golden (SAM), the purple inserts represent the transmembrane domain (TM), coil-coiled region are displayed in blue, red, and green (CC1, CC2, and CC3, respectively). Of note the CC1 is usually subdivided in three region named $\alpha 1$, $\alpha 2$, and $\alpha 3$; the inactivation domain (ID) is represented in bright orange, and poly basic domains (PBD) are displayed in purple. The microtubule end binding domain (EB, dark purple) are missing in STIM1B and STIM2.3. STIM1L possess a unique domain actin-binding domain (ABD, dark orange). STIM1B present an additional domain named domain B (B, dark orange). The CC2 of STIM2.1 possess an 8 amino acid insertion due to specific splicing. Of note, the region spanning CC2 and CC3 represent the CRAC activating domain (CAD) also called STIM-ORAI1 activating region (SOAR). Finally, the region spanning the CC to the ID defines the ORAI-activating small fragment (OASF).

Image adapted from: Grabmayr et al, 2021

- differences in EF hands sequence confers different sensitivities of the STIM isoforms to ER Ca^{2+} concentration and thus allow for their selective activation depending on the level of Ca^{2+} depletion.
- A transmembrane domain
- On the C-terminal extremity facing the cytosol:
 - 3 successive coil-coiled (CC) domains: CC1, CC2 and CC3. The last two being involved in the ORAI channel gating, as such, they constitute the CRAC-activating domain (CAD) also called the STIM-ORAI-activating region (SOAR).
 - A STIM inactivation domain (ID) which is important for the Ca^{2+} dependent inactivation (CDI) of the CRAC channel.
 - A microtubule end binding (EB) domain (absent in STIM2.3) which interact with microtubules and allows the fast movements of the STIM proteins. Nonetheless, it was shown that this domain also reduces the ability of STIM to migrate towards the PM. Thus, it is not absolutely required for SOCE activation as it was demonstrated that Ca^{2+} store depletion leads to the dissociation of microtubules from EB domains (Chang *et al*, 2018; Wang *et al*, 2018a; Pozo-Guisado *et al*, 2013)(Pozo-Guisado *et al*, 2013).
 - A polybasic rich domain (PBD) (absent in STIM2.3) in the end of the C-terminal extremity which enables the interaction of STIM with the PIP2 from the PM and thus promotes its localization to ER-PM junctions.

In addition to these prevalent domains, the different STIM isoforms also present structural features which are specific to each isoform.

1.2.1.2.2. STIM1 isoforms

The classically described STIM1 protein possesses two isoforms. Both isoforms are displaying their own specific additional domains:

- STIM1L possesses an additional actin-binding domain (ABD), leading to the permanent formation of STIM1L clusters, which enable an almost instantaneous SOCE activation (Darbellay *et al*, 2011). Of note, this isoform has been exclusively found in skeletal muscle. Interestingly, it was demonstrated that the STIM1L isoform was able to interact with other proteins than ORAI, namely TRP canonical channels (TRPC1,3,4 and 6) (Horinouchi *et al*, 2012; Antigny *et al*, 2017; Dyrda *et al*, 2020).
- STIM1B, the latest STIM1 isoform identified, displays an additional domain named domain B. This isoform is the result of the incorporation of an alternative exon (13B) which leads to the insertion of this domain just after the ID domain of STIM1. Of note this insertion induces a shift in the open reading frame of STIM1, thereby inducing the apparition of an early STOP codon resulting in the production of a shorter isoform lacking the EB and PBD

domain. This isoform is mainly found in brain tissue where it slows SOCE activation (Ramesh *et al*, 2021).

1.2.1.2.3. STIM2 isoforms

The STIM2 protein (STIM2.2) presents a strong sequence homology with STIM1. Specifically, the main difference between STIM1 and 2 lies in their Ca^{2+} affinity. In fact, STIM2 is more sensitive to changes in ER- Ca^{2+} concentration since its EF-hand domain displays a lower affinity for Ca^{2+} than the one of STIM1 (Zheng *et al*, 2008). In addition, it was shown that the CAD/SOAR domain of STIM2 also diverges from the one of STIM1 leading to a weaker coupling with ORAI1 (Zheng *et al*, 2018). This reduced affinity for Ca^{2+} and lower gating to ORAI1 enable a fine-tuning of SOCE which is even accentuated by the fact that STIM1 and STIM2 are able to form heterodimers (Subedi *et al*, 2018). In addition to the classic STIM2, two alternatively spliced STIM2 protein have also been described:

- The STIM2.1 variant presents an additional exon resulting in an 8 amino acid insertion localized in the CC2 domain of the CAD/SOAR region of STIM2. This insertion prevents the association of STIM2.1 with ORAI (Miederer *et al*, 2015; Rana *et al*, 2015). Thus, STIM2.1 possesses an inhibitory effect on SOCE but the mechanisms leading to this inactivation are not totally understood. Of note, as STIM2.2, the STIM2.1 protein variant is ubiquitously expressed in human but their relative expression levels are tissue specific (Miederer *et al*, 2015).
- STIM2.3 also includes an alternative exon expression. Nonetheless, the insertion of this additional exon induces the apparition of an early STOP codon resulting in the shortest STIM isoform identified. Of note, this isoform has only been detected on mRNA level (Miederer *et al*, 2015).

Overall, the 6 identified STIM isoforms are presenting a strong homology both in their sequences and their domains. While some isoforms possess opposite effects on the SOCE, their global mechanism of activation is believed to be comparable within all STIM isoforms. Since STIM1 represents the most studied of STIM isoforms, the next paragraph will focus on the description of its specific activation mechanism.

1.2.1.3. STIM activation during SOCE

The STIM1 activation processes leading to the generation of SOCE have been extensively studied, and while all the details are not yet understood, a global consensus on the STIM activation process has been reached and will be described thereafter (**Figure 8**). In resting state, STIM proteins are dimers diffusing along the ER membrane. The dimerization of STIM proteins is stabilized by the interaction between their adjacent cytosolic domains CAD/SOAR (Yang *et al*, 2012; Muik *et al*, 2009). The interaction between CAD/SOAR domain of STIM proteins maintain the C-terminus extremities of STIM in a compacted form sequestering the C-terminal ends near the ER membrane (Yang *et al*, 2012;

Muik *et al*, 2009). Of note, in this resting state the N-terminal EF/SAM domain of adjacent domain are not interacting. This absence of interaction is due to the presence of Ca^{2+} bound in the EF hand domains (Li *et al*, 2007; Korzeniowski *et al*, 2017). Following drop in ER Ca^{2+} concentration, Ca^{2+} is unbound from EF hand. The Ca^{2+} liberation from the EF hand motif allows the whole EF-SAM domains from

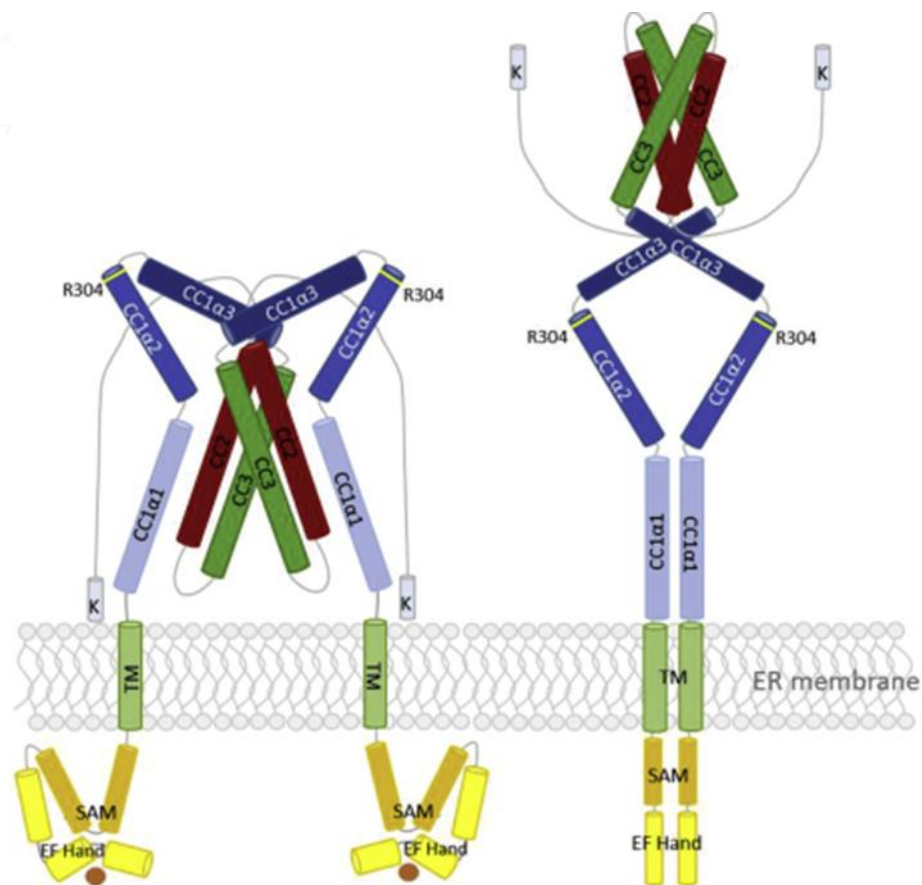


Figure 8 | Structure of the STIM1 protein in the inactive and active forms.

Left: Inactive STIM1 dimer structure representation. The compacted form of the dimer is maintained through interaction of the CAD/SOAR (CRAC-activating domain / STIM-Orai activating region) domains of STIM1 (coil-coiled domain 2 and 3 [CC2 and CC3]), and the binding of Ca^{2+} in the EF hand domains. In this form, the N-terminal extremities of STIM1 are not interacting, and the polybasic domain (K) are bound to the ER membrane

Right: Active STIM1 dimer structure representation. Note that Ca^{2+} is unbound from the EF hand motifs, allowing interaction of the SAM. The deployed STIM1 dimers are still interaction through the CAD/SOAR domain. The extension of the C-terminal extremities occurred due to reorientation of the CC1. In this conformation, the polybasic domain are extended in order to reach the plasma membrane.

Image adapted from: Lunz *et al*, 2019

adjacent STIM proteins to interact together. This conformational change is further propagated through the PM to the cytoplasmic region of STIM (Hirve *et al*, 2018; Ma *et al*, 2015). Due to the conformational change propagation, the interacting CC1 domain of adjacent STIM proteins are modifying their orientation and allowing the liberation of the CAD/SOAR domain. This whole process induces the deployment of STIM C-terminal extremities (Korzeniowski *et al*, 2017; Hirve *et al*, 2018). As a results, PBD are exposed to the phospholipids from the PM which allows the clustering of STIM proteins in higher oligomeric stated in the ER-PM junction (Liou *et al*, 2007; Walsh *et al*, 2010; Korzeniowski *et al*, 2017; Park *et al*, 2009a). Of note, this higher oligomeric state is thought to be promoted due to the extension of C-terminal extremities. Specifically, the new accessibility of the CC3 domains induced by the conformational change is thought to mediates the interaction between STIM protein to form high oligomeric states (Fahrner *et al*, 2014). The STIM protein clustering together with the availability of CAD/SOAR domain to interact with ORAI protein will lead to the opening of ORAI channel and ultimately to the induction of SOCE.

1.2.2. ORAI proteins and their associated channels

1.2.2.1. Discovery of ORAI proteins

ORAI proteins were discovered in 2006 in an effort to identify the molecular component of the SOCE. Specifically, the *ORAI1* gene was cloned during a genome-wide RNA interference experiment performed in *Drosophila* aiming to identify the proteins responsible for SOCE (Feske *et al*, 2006; Vig, 2006). Three homolog genes for *ORAI* were later identified and named *ORAI1*, *ORAI2* and *ORAI3* as a reference to the three keepers of the gate leading to heaven in Greek mythologic. Analysis of their protein sequence revealed the existence of 4 putative TM domains making them good candidates for being the channel accountable for SOCE. However, due to the absence of homology between the newly discovered ORAI proteins and any other ion channels, it was not clear whether they were the channels providing SOCE or auxiliary proteins important for the channel activation. During the year of their discovery, mutagenesis experiments demonstrated that ORAI1 proteins were forming the so-called Ca²⁺ Release-Activated Ca²⁺ (CRAC) channel (Yeromin *et al*, 2006) and were the effector part of the SOCE. It was further demonstrated that when overexpressed, the three homologues were able to generate different level of SOCE, with ORAI1 providing the larger Ca²⁺ entry, ORAI3 the lowest and ORAI2 being intermediate (Mercer *et al*, 2006b). Over the years, studies revealed that the three ORAI homologs are expressed in all human tissues at the mRNA and protein level (**Figure 9**)(Hoth & Niemeyer, 2013; Chalmers & Monteith, 2018).

1.2.2.2. Phylogenetic origin of ORAI proteins

From a phylogenetic perspective, the ORAI protein family is unrelated to any other known ion channel. In fact, it is supposed that the ORAI protein family appeared following an unusual round of retro-evolution. Specifically, it has been shown that the ORAI protein sequences derive from the cation

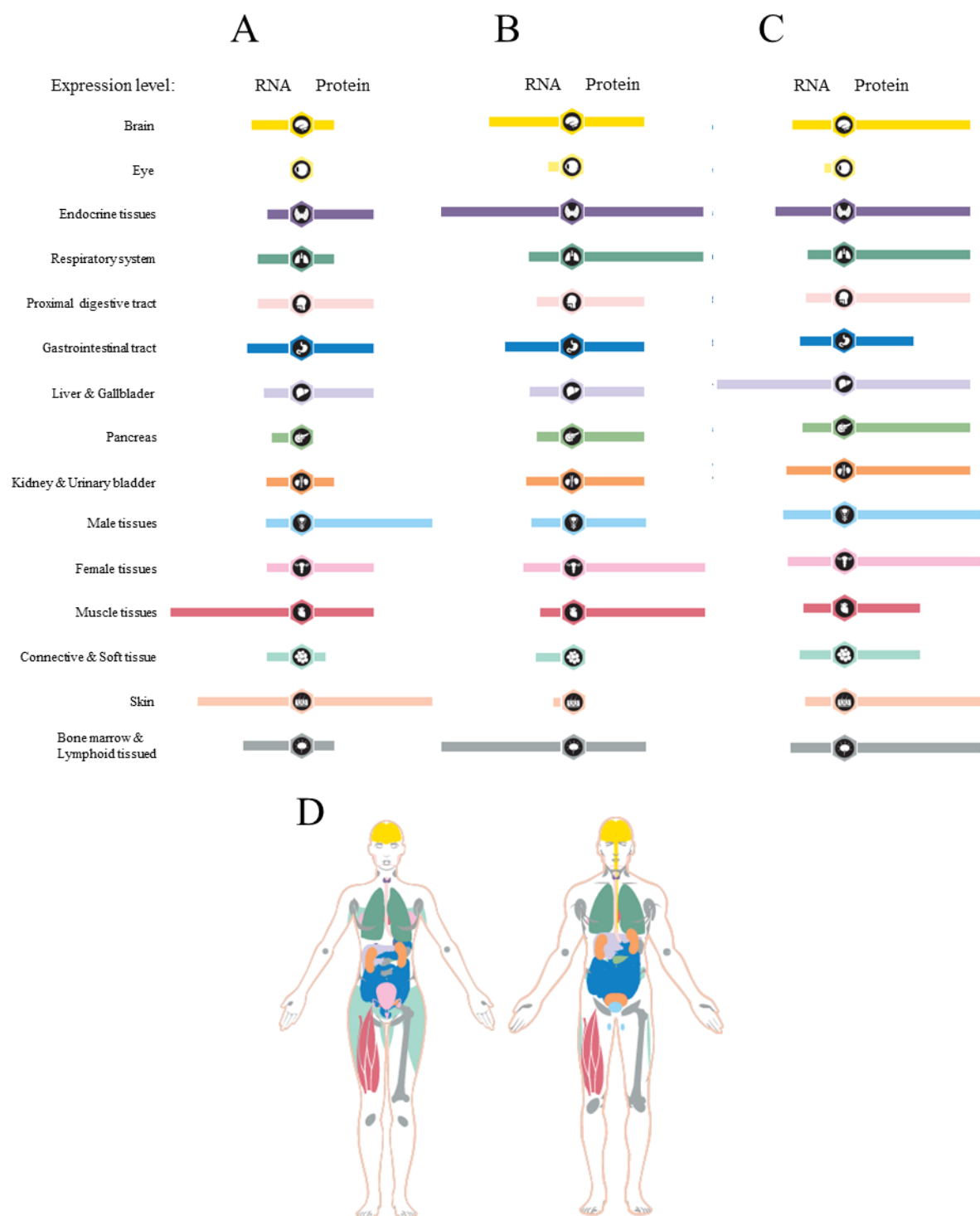


Figure 9 | The three ORAI homologues are ubiquitously expressed in human.

- A. Expression level of ORAI1 RNA (left column) and protein (right column) in human tissues.
- B. Expression level of ORAI2 RNA (left column) and protein (right column) in human tissues.
- C. Expression level of ORAI3 RNA (left column) and protein (right column) in human tissues.
- D. Color-coded tissues representation from the tables in A, B, and C .

Image adapted from Human Protein Atlas proteinatlas.org, (Uhlen et al, 2010)

diffusion facilitator (CDF) carrier protein family (Matias *et al*, 2010). CDF carrier protein are 6TM domain protein involved in transport of metallic ions. Sequence homology was identified between the 4 ORAI TMs and the TMs N°3 to N°6 of CDF carrier. Based on this sequence homology it was proposed that the ORAI proteins originate from the loss, by the CDF carrier protein, of its two first TM domain (Matias *et al*, 2010). Of note, the emergence of the *ORAI2* and *ORAI3* genes are the result of *ORAI1* gene duplication with *ORAI2* appearing earlier than *ORAI3*, and with the latter found only in mammals while *ORAI2* is found in lower vertebrates. Interestingly, it was shown that *ORAI3* is evolving faster than its two homologs, and therefore has acquired distinct features compared to the two other ORAI homologues. This led to the hypothesis that ORAI3 could present distinct functions and properties compared to the two other homologues (Cai, 2007; Shuttleworth, 2012).

1.2.2.3. ORAI proteins structure

The three ORAI proteins are sharing the same global topology: they possess 4 TM domain with both N- and C- termini facing the cytosol. Thus, they present two extracellular and one intracellular loop. Overall, the amino acid sequence homology between the three protein is situated around 60%. Interestingly, this homology shows large discrepancies amongst the different topological domains of ORAI proteins. These variations in sequence homology indicates on the crucial role of the specific conserved domains in the maintenance of ion channel function, but also highlight the existence of unique roles taken by each gene due to their non-conserved domains. Of note, ORAI1 is largely the most studied of all ORAI proteins. Thus, some of its important domains which present high sequence homology with the other homologues are reputed being present in all ORAI. Especially, the three ORAI protein present in their N-terminal extremity a CaM binding domain, responsible for the inactivation of the channels formed by ORAI proteins (Mullins *et al*, 2009; Frischauf *et al*, 2011). In addition, the ORAI1 domain named extended TM ORAI1 NH₂-terminal (ETON), is conserved in the three homologues. This domain consists, as indicated by its name, in an extension of the ORAI first TM into the cytosol and is crucial for the maintenance of the CRAC channel properties. Finally, the C-terminal extremity of all three ORAI present coil-coiled interaction domain (**Figure 10**). Importantly, both the coil-coiled domains and ETON region were shown to play a role in the STIM-ORAI interaction (Derler *et al*, 2013; Park *et al*, 2009b; Frischauf *et al*, 2009c). Overall, the most conserved regions are represented by the TM domains of ORAI proteins: the TM1 is totally conserved among the three human isoforms while TM2 to 4 are overall displaying 81 % and 87 % homology between ORAI1/2 and ORAI1/3 respectively (Hogan & Rao, 2015) (**Figure 11**). The strong homology found in TM domain of ORAI protein helped to understand some of the main features of the channel they form. For example, two glutamic acid residues localized in the 1st and 3rd TM domain of ORAI homologs (E106 and E190 of ORAI1) were identified as crucial for conferring Ca²⁺ selectivity to the CRAC channel. Thus, it was shown that the mutation of one of these residues leads to the expression of negative dominant form of ORAI which abolishes the SOCE (Gwack *et al*, 2007a). Aside from these conserved regions, each of the ORAI proteins also present

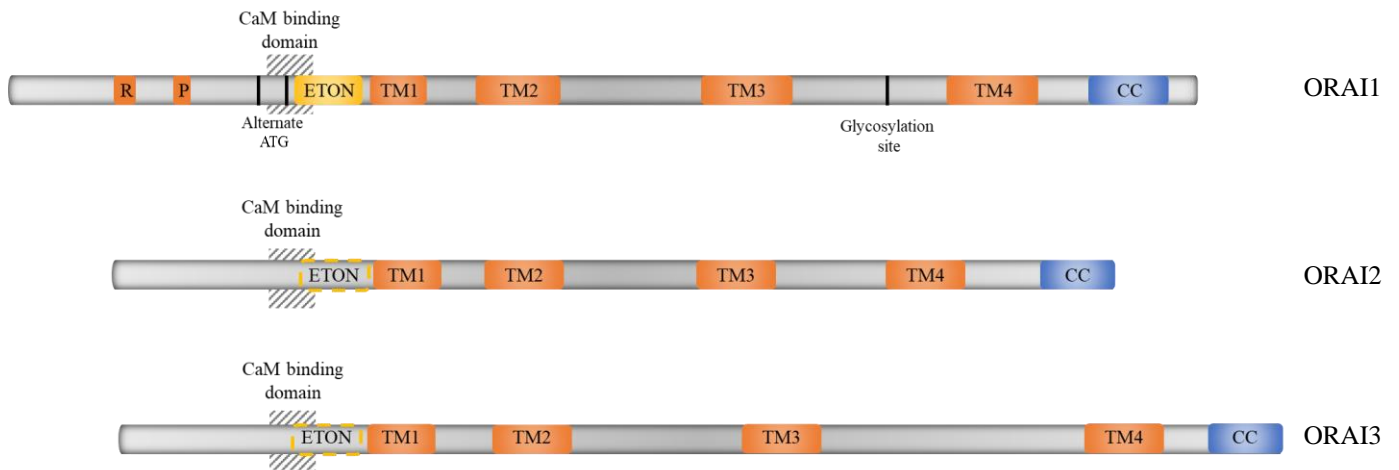


Figure 10 | The ORAI protein family structural features.

Schematic representation of the ORAI protein structural features. The three ORAI protein possess 4 transmembrane domain (TM, orange rectangles), and a coil-coiled domain (CC, blue rectangles) in their C-terminal extremity. The extended transmembrane ORAI1 NH₂ terminal (ETON) domain (yellow rectangle) as well as the CaM binding domain (grey hatched rectangle) are thought to be present in all ORAI due to level of conservation observed between the homologues at these sites. ORAI1 presents an arginine (R, orange box) and proline (P, orange box) in its N-terminal extremity

some unique features. Specifically, the N- and C- termini domain present the lowest homology among the three homologs and these differences are providing specific characteristics to the channels they might form.

1.2.2.3.1. ORAI1

ORAI1 is the longest of the three ORAI proteins with 301 aa compared to the 254 aa of ORAI2 and the 295 aa of ORAI3. This difference in length is due to the presence at the beginning of its N-termini of a unique proline/arginine-rich region. These domains were shown to be responsible for the slow reactivation displayed CRAC channel (Frischauf *et al*, 2011). In addition, some studies revealed that these domains were important for providing strong Ca^{2+} current specific to the CRAC channel (Takahashi *et al*, 2007; Fahrner *et al*, 2009). ORAI1 protein is also the only homologue presenting a site for N-glycosylation localized in the 2nd extracellular loop, between the TM3 and the TM4 (**Figure 10**) (Gwack *et al*, 2007b). Glycosylation at this residue seem to be cell type dependent, and while it is not strictly required for SOCE activity, some studies indicates that the glycosylation status of ORAI1 can affect the SOCE intensity (Gwack *et al*, 2007b; Dörr *et al*, 2016) . Finally, as mentioned above, the three ORAI members possess a coil-coiled interaction domain allowing the interaction between ORAI and STIM proteins (**Figure 12 A**). Nonetheless, it was demonstrated that ORAI1 possess the “weakest” coil-coiled domain. (Frischauf *et al*, 2009a). Indeed, mutagenesis experiments showed that a single point mutation (L273S) is sufficient to suppress ORAI1-STIM1 interaction while ORAI2 and ORAI3 require two mutations (L237S + L244S and L285S + L292S respectively) to produce the same effect (Frischauf *et al*, 2009a). If this coil-coiled region was first demonstrated to be important for ORAI-STIM interaction, the solving of the crystal structure of the CRAC channel formed by ORAI1 in *Drosophila melanogaster* also indicates that this domain is involved in the interaction between ORAI proteins themselves (**Figure 12 B,C**) (Xiaowei Hou, Leanne Pedi, Melinda M. Diver, 2012; Tirado-Lee *et al*, 2015; Hou *et al*, 2018b). Finally, one shorter isoform of the ORAI1 protein was identified named ORAI1 β . This isoform results from the existence of alternative translation initiation codon in the from the *ORAI1* gene (**Figure 10**). This isoform, lacking the proline/arginine rich domain of classic ORAI1, is able to generate classic SOCE but its current present a stronger Ca^{2+} dependent inhibition than the classic one. Of note, it was also demonstrated that ORAI1 β diffusion rate in the PM is higher than the classic ORAI1 protein (Desai *et al*, 2015; Fukushima *et al*, 2012; Zhang *et al*, 2019).

1.2.2.3.2. ORAI2

ORAI2 is the shortest of the ORAI isoform and the less studied of ORAI proteins. From the sequence homology, it is assumed that this homologue contains all the following elements from the ORAI1 proteins: The CaM binding domain and the ETON domain in the N-terminal extremity, and the coil-coiled region in its C-termini. As mentioned earlier, ORAI2 does not present the N-terminal prolin/arginin rich region (**Figure 11**). Overall, ORAI1 and ORAI2 protein present the strongest

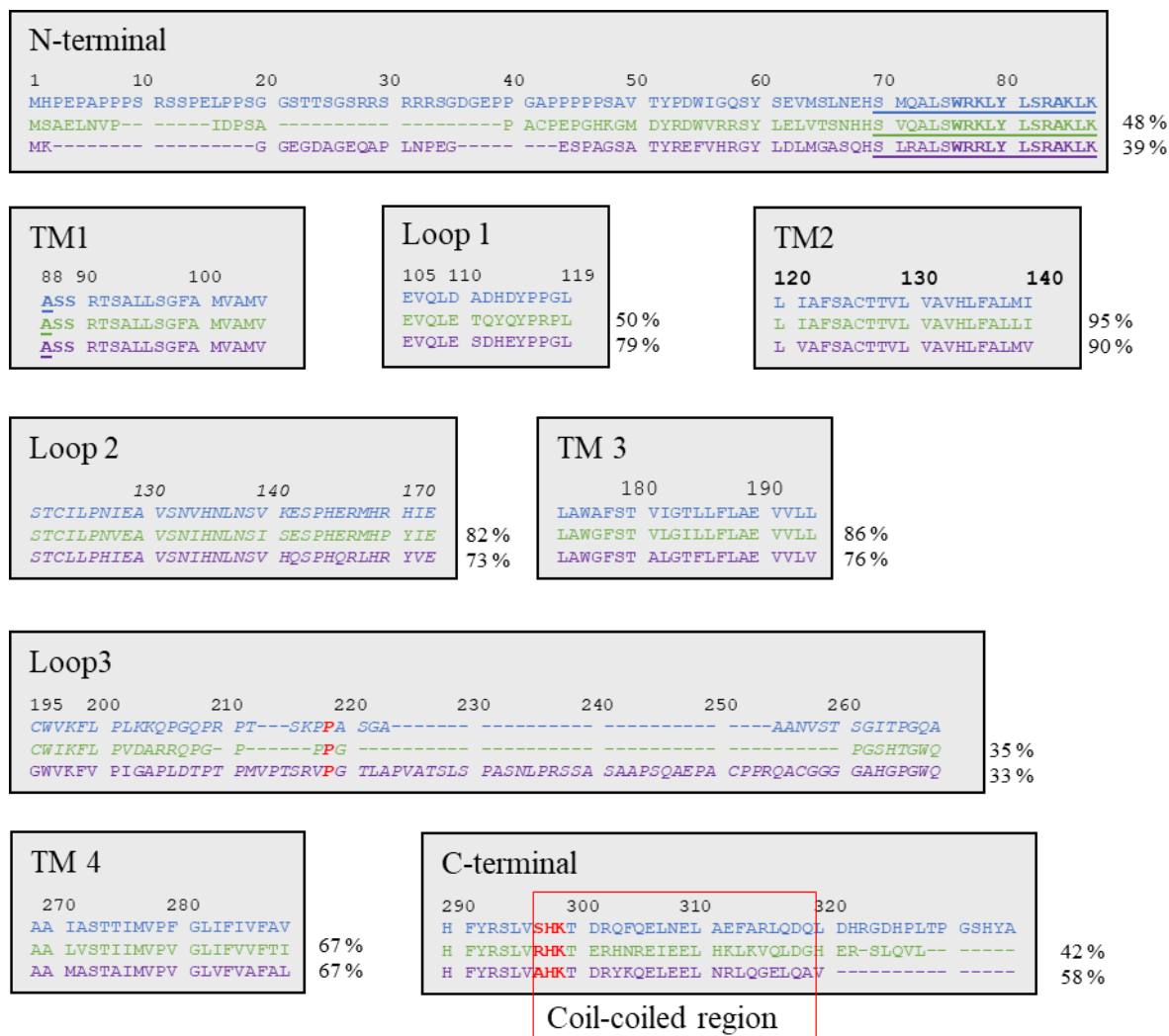


Figure 11 | Alignment of the three ORAI protein sequences.

The protein sequences of the three ORAI homologues are aligned for each region, the number next to each box represent to homology percentage to ORAI1. Regions were defined from the ORAI1 identified domains. The sequences indicated in bold, represent the region corresponding to the ETON of ORAI1. The underlined sequence represent the region corresponding to the calmodulin binding domain of ORAI1. The red box, indicates the position of the coil-coiled region of ORAI1. In red and bold are indicated the amino acid residues corresponding the *drosophila* ORAI1 residues of crucial importance of CRAC channel opening. The different ORAI1 sequence are indicated in different colors: ORAI in blue, ORAI2 in green, ORAI3 in violet.

Alignment performed with Clustal Omega, <https://www.ebi.ac.uk/Tools/msa/clustalo/> (Sievers et al, 2011).

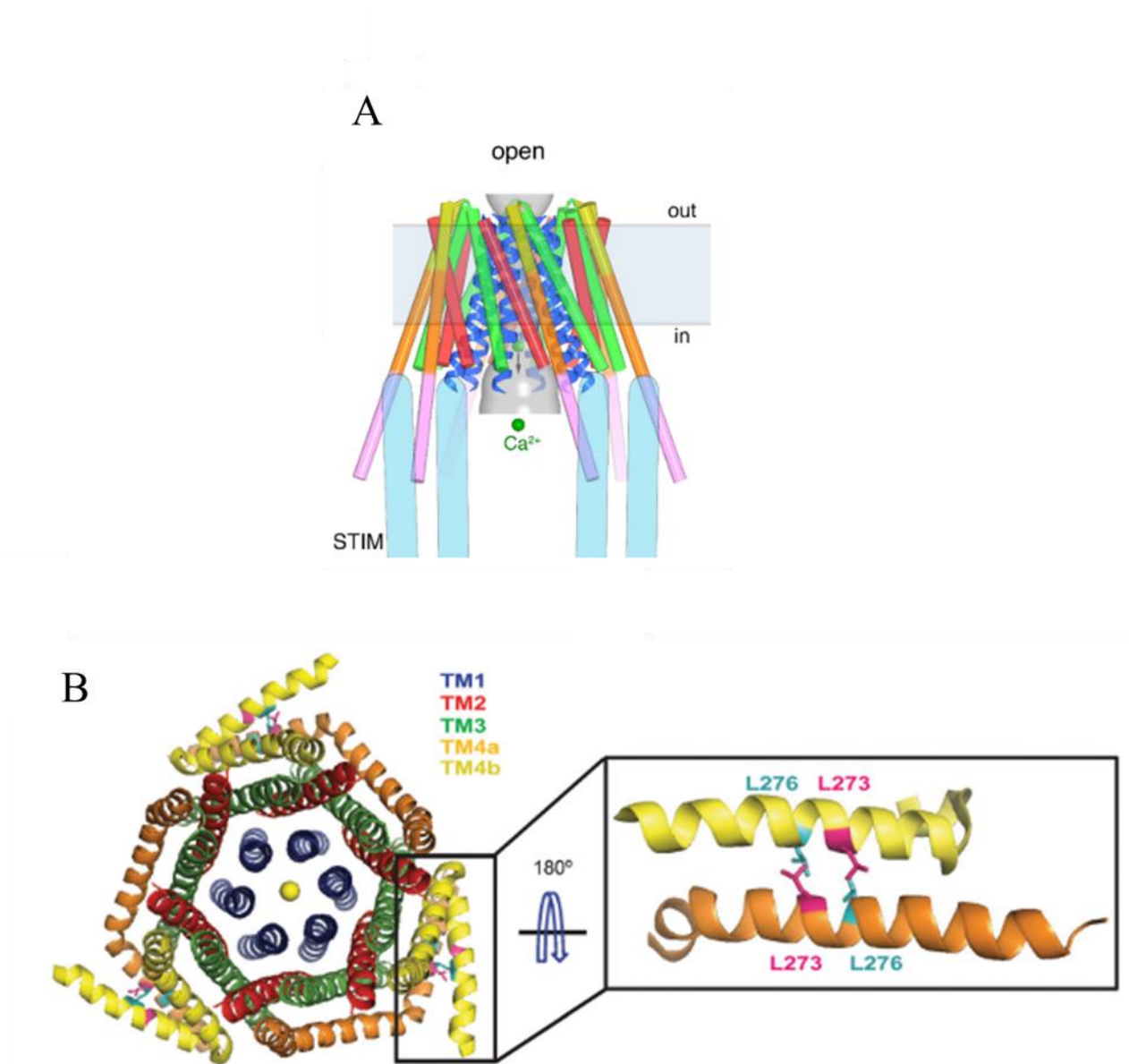


Figure 12 | Structure of the CRAC channel, coil-coiled domain

- A. Representation of the CRAC channel structure as viewed from the side. The different ORAI1 TM are depicted in different colors, the 1st TM forming the displayed as a blue helix. The extension of the 4th TM are displayed in orange, the coil-coiled region allowing the interaction with STIM are represented in pink.
- B. CRAC channel structure visualized from above. The blues helix represent to 1st TM forming the pore. The 4th TM extension are shown in orange and yellow, and are interacting by pari between adjacent ORAI1 proteins (insert on the right)

adapted from Hou et al, 2018, and Tirado-Lee et al, 2015

sequence homology. As a consequence, the biophysical properties of ORAI2 and ORAI1 composed channel are closely related compared to the channel formed by ORAI3 proteins (Gwack *et al*, 2007a; Lis *et al*, 2007a).

1.2.2.3.3. ORAI3

The ORAI3 protein is almost as long as ORAI1 (295 aa and 301 aa respectively) but both proteins are showing differences in their structure. As for ORAI2, it lacks the proline/arginin domain present in ORAI1 but conserves the most important elements displayed across the three proteins (ETON domain; CaM binding domain; coil-coiled region). However, the C and N-termini of ORAI3 only show 34% and 46% sequence homology respectively to ORAI1 (Shuttleworth, 2012). In addition, the 2nd loop, between TM2 and TM3, present non conserved amino acids and simulations demonstrated that this sequence difference was sufficient to alter the structural properties of the channel formed by ORAI3 proteins (Fahrner *et al*, 2018). Finally, the 3rd loop, between the TM domain 3 and 4, is sensibly elongated in ORAI1 compared to ORAI3 (38 amino acids versus 72 respectively) but the role of this difference elongated loop remains elusive (**Figure 11**)(Shuttleworth, 2012). Of note, since the sequence variation between ORAI3 and ORAI1 are mainly present in the non-pore forming region, it was hypothesized that ORAI3 channels possessed different gating properties than ORAI1 and ORAI2 channels.

1.2.2.4. ORAI channels activation during SOCE

1.2.2.4.1. I_{CRAC}

As mentioned earlier, ORAI protein were discovered as the effector part of the physiological Ca^{2+} entry called SOCE. Indeed, SOCE was described long before the identification of its molecular components, and the electrophysiological characteristics of the current it provides were revealed by Hoth and Penner thanks to whole cell patch-clamp recording (Hoth & Penner, 1992). Following its identification, the current responsible for the SOCE was called I_{CRAC} (Ca^{2+} release activated Ca^{2+}) and its characteristics includes:

- An inward rectification (non-voltage-activated) (Hoth & Penner, 1992)
- A high Ca^{2+} selectivity and low single channel conductance in the range of femtosiemens (Zweifach & Lewis, 1993; Hoth, 1995).
- A Ca^{2+} dependent inactivation (CDI) which can be separated in two distinct phases: a fast CDI (FCDI) occurring within milliseconds, and visualized during hyperpolarizing voltage steps, and a slow CDI (SCDI) completed within minutes (Zweifach & Lewis, 1995a, 1995b).

Of note, I_{CRAC} first recording were acquired in mast cells and T lymphocytes. However, in different cell types, the currents evoked by SOCE activation presented alternative characteristics (especially different ionic selectivity) ,and were termed I_{SOC} (Liu *et al*, 2004). It was demonstrated later that TRP

channels were participating in the I_{SOC} currents. This is especially true for the TRPC channels family as it was shown that their activation mechanisms were relying on the Ca^{2+} entry induced by I_{CRAC} (Ong *et al*, 2016; Shin *et al*, 2016). As a consequence, before the ORAI identification, TRPC channels were thought to be responsible for CRAC (Zhu *et al*, 1996; Zitt *et al*, 1996). Nonetheless, following the identification of the three ORAI homologs, it was demonstrated that each ORAI protein was able to produce I_{CRAC} -like currents when overexpressed together with STIM, indicating that ORAI proteins are forming homo-oligomers supporting SOCE entry (Mercer *et al*, 2006a). These studies also revealed that it was the ORAI1 protein who was the main responsible of SOCE due to the increased level of Ca^{2+} entry it was able to provide. Thus, it is the ORAI1 channel structure that was the most studied.

1.2.2.4.2. CRAC channel detailed structure

Early studies aiming to determine the structure of the CRAC channel were using overexpression of concatemers composed of variable number of ORAI1, or single-molecule imaging techniques in combination with biochemical methods. These data pointed out that the CRAC channel was constituted of 4 units of ORAI1 (Mignen *et al*, 2008b; Penna *et al*, 2009). In addition, Dr Penna indicated that in resting cells, ORAI1 were forming dimers and were further assembled in tetramers due to the channel activation. During the following year it remained controversial whether ORAI1 channel were indeed dimers, tetramers or could even possess higher oligomeric states depending on their activation status. While a variety of techniques, such as electron microscopy (Maruyama *et al*, 2009), biochemical analysis (Gwack *et al*, 2007a; Zhou *et al*, 2010), imaging methods like single molecule photobleaching (Ji *et al*, 2008a; Penna *et al*, 2009) or brightness analysis (Madl *et al*, 2010a) were used to elucidate the composition of CRAC channels, its definitive structure was established in 2012 with the crystallization of the *drosophila* CRAC channel (Xiaowei Hou, Leanne Pedi, Melinda M. Diver, 2012) (**Figure 13**). The 1st crystal structure of the CRAC was obtained while the channel was in its close-state ORAI channel, it revealed the CRAC channel was a hexamer of 6 ORAI1 proteins. Since the human and *drosophila* ORAI1 are sharing a strong homology ($\approx 78\%$) it was quickly admitted that the human CRAC channel composition possessed a similar structure. Later, the crystal structure of the open-state CRAC channel was obtained by the same group thanks to constitutively active mutant of *drosophila* ORAI1 (Hou *et al*, 2018a). Finally, a high resolution (3,3 Å versus 6,7 Å previously) picture of the CRAC

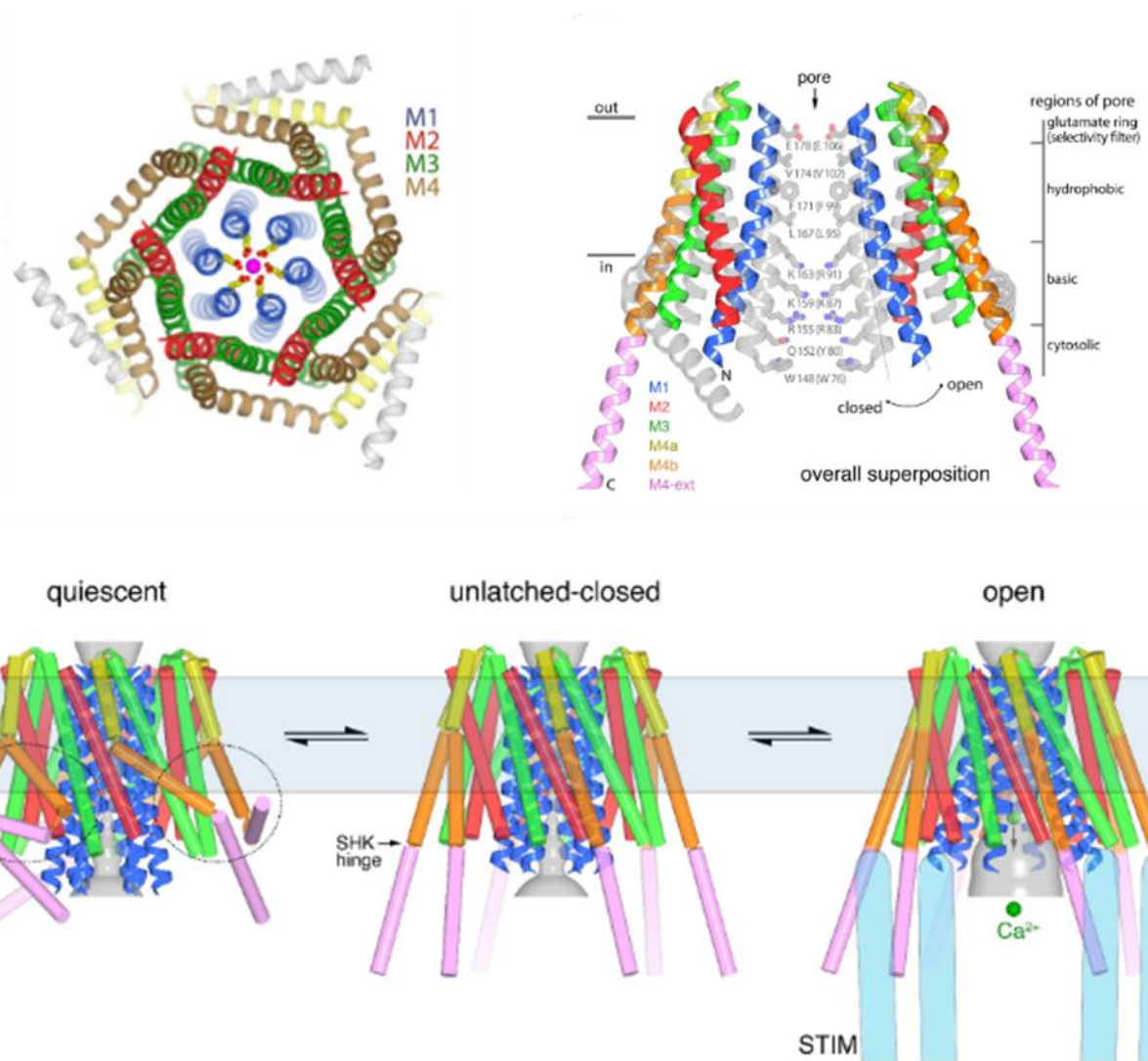


Figure 13 | Global structure of the CRAC channel

For all the figures, the different ORAI1 TM are depicted in different colors, the 1st TM forming the displayed as a blue helix, other TM are displayed in different colors

- Initial structure determination of the *drosophila* CRAC channel (closed-state).
- Over imposition of the initial *drosophila* CRAC channel structure (closed-state in grey) and the open-state structure of the CRAC channel (colored). Note the conformational change induced in the C-terminal part of ORAI1 protein induced dilatation of CRAC pore.
- Model for CRAC channel opening. In the quiescent state, the ORAI1 C-terminal extremities are latched. These extremities need to unlatched before allowing the CRAC channel opening. Note the conformational changes induced at the P288 (corresponding to P261 for *human*) hinge and SHK hinge, as well as the extension of all TM into the cytoplasm.

adapted from Hou et al, 2018, and Tirado-Lee et al, 2015

channel in its open-state structure was obtained with Cryo-EM technique and revealed new structural details (Hou *et al*, 2020). In addition, these new structural data allowed the author to propose a model for the CRAC channel opening involving two strong conformational changes in the middle of the 4th TM and in between the 4th TM and the TM4 extension allowing the unlatching of the channel preceding its opening (**Figure 13**). Taken together, these data allowed a clearer depiction of the CRAC channel and of its important domain. Hence, unlike any other channel the pore of the CRAC channel is formed only by the 1st TM of the six ORAI1 units. The three other TM are forming a shell that surrounds the pore with the 4th TM being at the periphery of the channel. The importance of each TM domain, suggested by their significant degree of conservation across ORAI homologs, was highlighted by their specific structure as they are all presenting a helical extension in the cytoplasm (**Figure 13**). Especially, it is admitted that dilatation of the 1st TM especially its ETON extension is responsible for pore opening (Tiffner & Derler, 2021; Tiffner *et al*, 2021). The specific configuration of the 4th TM and its cytosolic extension was also shown to be essential for STIM binding, conformational change, and pore opening. Specifically, the 4th TM present a bend (at the position P261 for the *human* ORAI1) in its structure dividing it in two regions: TM4a and TM4b. Following the 4th TM, a hinge region consisting of SHK (Serine – Histidine – Lysine) motif links the TM with the TM4 helical extension (Figure 11 and 13). This specific structure was suggested to be important for the transmission of the conformational changes inducing pore opening to the whole protein through modification of its coil-coiled interaction domain (Hou *et al*, 2012a, 2018b). Additionally, the intracellular loop (loop2) was also shown to be particularly important for the maintenance of ORAI1 channel properties through a specific interaction with their N-terminal extremity (Fahrner *et al*, 2018). Importantly, despite the solving of the CRAC channel structure, the exact structural modification leading to pore opening are not yet totally defined. Especially, cryo-EM and the crystal structural data are showing discrepancies in the open-state structure of CRAC channel. Additionally, the open state structure was not obtained due to STIM binding but due to gain of (GoF) function mutation in the ORAI1 sequence leading to a constitutively open state of the channel. Moreover, MD simulation of ORAI1 channel open state due to STIM gating, , suggests a different mechanism for CRAC channel opening and accessory roles for peripheral structures of CRAC channel (Tiffner *et al*, 2021; Tiffner & Derler, 2021; Dong *et al*, 2019). Nonetheless, it is now admitted that CRAC channel opening is due to a conformational change leading to the dilatation of the pore formed by ORAI1 1st TMs.

1.2.2.4.3. CRAC channel gating by STIM1

The unveiling of the CRAC channel structure allowed a better comprehension of its gating by STIM1. Even though some mechanisms are still debated, a global picture of the CRAC activation through STIM1 gating has now emerged. Specifically, following their translocation to ER-PM junction due to Ca²⁺ store depletion, STIM proteins trap ORAI through interaction between their respective coil-coiled domains. Importantly, several mutation of specific amino acids in the CAD/SOAR domain (CC2

and CC3) of STIM1 as well as in the C-terminal coil-coil domain of ORAI1 were shown to impact ORAI1-STIM1 interaction and gating (Park *et al*, 2009b; Muik *et al*, 2008; Stathopulos *et al*, 2013; Navarro-Borelly *et al*, 2008). In addition, N-termini and loop 2 of ORAI were also shown to participate in STIM interaction although to a lesser extent. The current hypothesis point-out the possibility that, following the establishment of a coil-coiled interaction between ORAI1 and STIM1 C-termini, a conformational change is propagated through the ORAI1 loop2 until the 1st TM and the ETON domain leading to pore opening (Palty *et al*, 2017; Liu *et al*, 2019; Niu *et al*, 2020). This hypothesis proposes an explanation to the observations indicating that ORAI1 N-termini and STIM1 are interacting, but that mutation in ORAI1 N-terminal region is not abolishing SOCE (Fahrner *et al*, 2018; Li *et al*, 2007; McNally *et al*, 2013; Butorac *et al*, 2019). In addition, interactions between all cytosolic parts of ORAI1 (N-t, loop2 and C-t) and STIM1 were identified, but their respective contribution to the gating of the channel remains elusive. This can be partially attributed to the “weak” level of interaction between ORAI and STIM preventing the purification of the associated structures and compelling interaction studies to be conducted using fragments of each proteins (Qiu & Lewis, 2019). An additional question arising from the ORAI1-STIM1 gating mechanism is the number of STIM1 and ORAI1 protein required to gate the channel. It is admitted that the trapping of CRAC channels by STIM1 is preceding its activation. For example, it was demonstrated that a single STIM1 dimer was sufficient to trap, but not to activate the CRAC channel (Hoover & Lewis, 2011). However, the exact STIM1:ORAI1 stoichiometry required to activate the CRAC channel remain subject to discussion, and two main hypothesis co-exists named the bimolecular and unimolecular models.

- The dimeric model proposes that SOAR/CAD domain of STIM1 dimers are interacting with two ORAI1 protein from the same CRAC channel, leading to a 1:1 stoichiometry (1 STIM protein for 1 ORAI1 in 1 CRAC channel) (**Figure 14**). This hypothesis is supported by NMR and FRET data (Stathopulos *et al*, 2013; Yen & Lewis, 2018) but it does contradicts the structural evidence from the published CRAC open-state crystal structure. However, one cannot exclude that this contradiction is imputable to the utilization of constitutively active mutant that do not display STIM interaction for the crystallization experiments.
- The alternative unimolecular model proposes that STIM1 dimers are interacting with ORAI1 protein from different CRAC channel assemblies (**Figure 14**). Such model leads to a 2:1 stoichiometry (STIM1:ORAI1) and to clustering of ORAI channel which classically observed in overexpression models (Park *et al*, 2009b; Perni *et al*, 2015; Zhou *et al*, 2018b; Baraniak *et al*, 2021). Interestingly, both model could actually co-exist and their specific proportion be dependent on the activation level of SOCE as proposed by Palty and al (Palty *et al*, 2017).

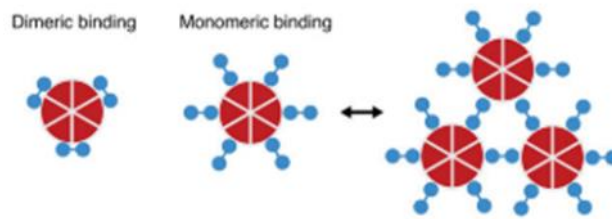


Figure 14 | The ORAI-STIM stoichiometry

Scheme representing the potential stoichiometries of the ORAI-STIM coupling. In the dimeric binding (left), also called bimolecular coupling, STIM1 dimers are binding two adjacent ORAI1 proteins from the same channel. In the monomeric coupling model also named unimolecular model (right), STIM1 dimers are binding ORAI1 protein from two different CRAC channels, resulting in the clustering of CRAC channels

adapted from (Yen & Lewis, 2019)

1.2.2.4.4. I_{SOC}

As mentioned earlier, some cell types, are displaying SOCE current presenting different characteristics than the classic I_{CRAC} . Especially different Ca^{2+} selectivity was observed. This alternative currents were named I_{SOC} (Liu *et al*, 2004, 1998). In fact, depending on the cell types, Ca^{2+} store depletion induces a variety of different Ca^{2+} current suggesting that several channels are participating in SOCE (Parekh & Putney, 2005; Cheng *et al*, 2013). For this reason, it was early suggested that TRPC1 was the channel responsible for SOCE. For example, early data on SOCE showed that absence or downregulation of TRPC1 was leading to impaired SOCE while its overexpression was leading to an increased SOCE in different cell models such as salivary glands, or endothelial cells (Sun *et al*, 2015; Ma *et al*, 2011; Liu *et al*, 2007; Brough *et al*, 2001; Liu *et al*, 2000; Rosado *et al*, 2002). The identification of ORAI proteins together with the decrease in SOCE observed while altering TRPC1 expression led to the hypothesis that both proteins could form a heteromeric channel (Liao *et al*, 2008; Kwong *et al*, 2008; Huang *et al*, 2006; Kim *et al*, 2009), or could form dynamic assemblies all together with STIM1 (Hwei *et al*, 2007). In fact, various microscopy techniques such as FRET and TIRF, demonstrated that STIM1 interacts with TRPC1 (Huang *et al*, 2006; Hwei *et al*, 2007; Alicia *et al*, 2008; Lee *et al*, 2014). Additionally, it was demonstrated that the Ca^{2+} entry induced by CRAC channel activation leads to the addressing of TRPC1 to the plasma membrane, indicating that the gating of TRPC1 is strictly dependent on the presence of both STIM1 and ORAI1 (Lee *et al*, 2010; Cheng *et al*, 2011). In addition, it was later demonstrated that ORAI1 and TRPC1 channel are found in close vicinity, indicating on the existence of dynamic assemblies of protein complexes including ORAI1, TRPC1 and STIM1. Nonetheless, it was demonstrated that ORAI and TRPC1 proteins, both form two different channels ruling-out the existence of heteromeric ORAI1-TRPC1 channels (Ambudkar *et al*, 2017).

1.2.2.5. Other ORAI channel

1.2.2.5.1. Homomeric ORAI2 – ORAI3 channels

Because of the overlapping pattern of expression between all ORAI homologs, endogenous current provided by ORAI2- or ORAI3-only oligomers have never formally been observed. However, early overexpression studies demonstrated that ORAI2 as well as ORAI3 proteins are able to form functional channel allowing SOCE in HEK when overexpressed together with STIM1 (Lis *et al*, 2007a). These data have allowed to define the biophysical characteristics of the currents provided by these homomeric channels (**Table 1**) (Lis *et al*, 2007b; DeHaven *et al*, 2007, 2008). Thus, while ORAI1-only channels (*i.e* the prototypic CRAC channel) are displaying the greatest current amplitude, ORAI2-only channels present an intermediate level of current and ORAI3-only channel the smallest. The activation time also differs within these channels with ORAI2-only channels presenting the fastest activation time while ORAI3-only are displaying the slowest. Additionally, the Ca^{2+} inactivation features of these channel are

	CRACM1	CRACM2	CRACM3
Store-operated	Yes	Yes	Yes
Activation time ($t_{1/2}$)	35 ± 7 s	21 ± 3 s	63 ± 7 s
Ca ²⁺ -dependent inactivation (fast)	Moderate	Moderate	Strong
Ca ²⁺ -dependent inactivation (slow)	Strong	None	None
Ca ²⁺ -dependent reactivation	Yes	No	No
Selectivity	Ca ²⁺ >> Na ⁺ , Ba ²⁺	Ca ²⁺ >> Na ⁺ , Ba ²⁺	Ca ²⁺ >> Na ⁺ , Ba ²⁺
Monovalent permeation in DVF solutions	Moderate	Moderate	Strong
2-APB effect at 50 μ M	Block	Reduction	Potential

Table 1 | Properties of the Mammalian ORAI proteins.

CRACM1, CRACM2, and CRACM3 corresponds to ORAI1, ORAI2, and ORAI3 proteins, specifically.

From (Lis et al, 2007)

also different. Of note, ORAI1 channel display a Ca^{2+} -dependent inactivation (CDI) that is be decomposed in fast inactivation (FCDI) and slow inactivation (SCDI), interspersed by a small reactivation phase. The reactivation phase is absent in both ORAI2- and ORAI3- only channels as well as the SCDI. On the other hand, while the FCDI of ORAI2 is similar to the one observed for ORAI1, FCDI of ORAI3 is significantly stronger. In term of selectivity, all channels are highly selective for Ca^{2+} over other ions. Nonetheless, ORAI3-only channels display larger Na^{+} permeation in DVF solution (DeHaven *et al*, 2007). Finally, all these ORAI channels present different sensitivities to the chemical compound 2-APB (2-aminoethyldiphenyl borate). This compound potentiate I_{CRAC} in ORAI1 channels at low concentration and blocks it at high concentration, ORAI2 channels were shown to be less sensitive to its inhibition, while ORAI3 channels are never inhibited by 2-APB but rather activated (Lis *et al*, 2007b). 2-APB mediating its effect *via* binding on the extracellular motifs of ORAI channels, it was suggested that its specific effect on the ORAI3 channel could be attributed to the significantly longer 2nd extracellular loop (between TM3 and TM4). In addition, it was shown that Orai3-channel activation by 2-APB was modifying its selectivity by allowing entry of monovalent ions probably through widening its pore (Schindl *et al*, 2008). Nonetheless, the physiological relevance of these differences remains under question since ORAI2-only and ORAI3-only channels current were never observed endogenously. In addition, these studies were conducted in HEK-293 cells expressing endogenous ORAI1 protein, and thus allowing the integration of ORAI1 proteins in channels supposedly composed of only ORAI2 or ORAI3 units. Nonetheless, Orai2 was reported to be present into intracellular compartment including the ER (Ikeya *et al*, 2014). Moreover, another study have reported a potential role for endogenous Orai2 channel as ER Ca^{2+} leak channel by using siRNA (Bandara *et al*, 2013). Thus ORAI2-only channels might represent a specific type of ER channels. On a similar note, it has been hypothesized that Orai3 channels exist on the ER membrane. Indeed, few publications described intracellular localization when overexpressing fluorescently labeled Orai3 proteins (Varadarajan *et al*, 2013; Dickson *et al*, 2012). Additionally, it was shown that the absence of the tripeptide EFA in Orai3 C-terminus prevent its addressing to the PM which is dependent of the presence of Orai1 (Alansary *et al*, 2015). Following these clues, Leon-Aparicio and colleagues demonstrated in 2017 that in HeLa cells, Orai3 channels are located on the ER and plays a role in preventing ER Ca^{2+} overloading (Leon-Aparicio *et al*, 2017). On the other hand, the existence of ORAI3-only channels was suggested by Motiani and al., who demonstrated that in estrogen receptor-negative breast cancer cells, ORAI3 was alone responsible for the native SOCE (Motiani *et al*, 2010). Few other publication also demonstrates that ORAI3 was responsible for SOCE in some cancer indicating on a potential existence of ORAI3 channels (Faouzi *et al*, 2011; Ay *et al*, 2015).

1.2.2.5.2. Heteromeric ORAI channels in SOCE

The first studies assessing the physiological properties of ORAI composed channels suggested the existence of ORAI heteromeric channels (Lis *et al*, 2007b; DeHaven *et al*, 2007; Gwack *et al*, 2007a).

Nonetheless, physiological evidence of the existence of such channels were lacking for a long time. Recently, several works have identified heteromeric ORAI1-ORAI2 and ORAI1-ORAI3 channels involved in SOCE.

- ORAI1-ORAI2

In 2015, Inayama and al., demonstrated that ORAI2 is abundantly expressed in the human chondrocyte cell-line OUMS-27. They showed that ORAI2 down-regulation or overexpression was affecting the SOCE amplitude, indicating on a role of ORAI2 in controlling SOCE. They further confirmed their hypothesis that ORAI2 and ORAI1 were forming a functional channel, by using a combination of microscopy techniques such as TIRF, single molecule photobleaching assays and bifunctional complementation assays (BiFC) (Inayama *et al*, 2015a). On a similar note, in 2017 Vaeth and al., demonstrated that ORAI1 and ORAI2 can form heteromeric channel that modulate the SOCE amplitude in mice T-cells. In fact, by overexpressing pore-dead mutant of ORAI1 or ORAI2 protein in knock-out models they were demonstrated that the function of the wild-type remaining ORAI was suppressed. Further patch-clamp analysis demonstrated that ORAI1-ORAI2 channels maintain the essential CRAC channel properties while presenting few differences in their I_{CRAC} current compared to the ORAI1-only channel. Finally, they also show that the inhibitory effect of ORAI2 on the CRAC function was present in multiple human immune cells and that the ratio of expression between ORAI1 and ORAI2 was evolving during maturation process of T-cells. Thus, they hypothesized that the dynamic variation in the CRAC channel stoichiometry could be a mechanism to modulate SOCE (Vaeth *et al*, 2017a).

- ORAI1-ORAI3

The existence of ORAI1-ORAI3 channels responsible for SOCE was mainly proposed in the pathological process of cancer. For example, Motiani *et al.*, were the first to demonstrate that SOCE, in estrogen-receptor positive (ER⁺) breast cancer cell, was mediated by ORAI3, while estrogen-negative (ER⁻) cells were displaying classic ORAI1-mediated SOCE (Motiani *et al*, 2010). A role of ORAI3 in SOCE induction was further demonstrated for other cancer cell lines such as non-small cell lung adenocarcinoma and pancreatic ductal adenocarcinoma (PDAC) cell lines (Ay *et al*, 2015; Dubois *et al*, 2021). Additionally, Dubois *et al.*, also demonstrated a role for ORAI3 in SOCE in normal prostatic cell-line (Dubois *et al*, 2021, 2014a). Finally, Yeast and al., presented the strongest evidence of the existence of native heteromers between ORAI1, 2 and 3 and their role in physiology. By creating single, double and triple knockout cells for these proteins and using agonist leading to incomplete store depletion (mimicking physiological activation), they demonstrated that native CRAC channel are heteromers bearing different sensitivities to Ca²⁺ store depletion. The proportion of these channels in specific cell-line would lead to different physiological answer depending on the intensity of the stimulation they receive. Of note, ORAI1 and ORAI3 are also participating in the formation of a second

channel bearing different properties and being non-Store-Operated named arachidonate-regulated Ca^{2+} (ARC) channel that will be describe thereafter.

1.2.2.5.3. Heteromeric non-SOCE channel, ARC/LTR

Following the identification of ORAI protein, and the discovery that ORAI1 form the CRAC channel responsible for the SOCE, it was suggested that ORAI1 and ORAI3 can form another channel responsible for a store independent Ca^{2+} entry (SICE). This channel was named arachidonate-regulated Ca^{2+} (ARC) channel as it could be activated by low concentration of arachidonic acid (AA) (Mignen *et al*, 2008a). The ARC channel was shown to possess different properties compared to the CRAC channel (**Table 2**). Especially, ARC channels do not show Ca^{2+} -dependent inhibition neither display sensitivity to the pharmacological agent 2-aminoethoxydiphenyl borate (2-APB) (Mignen & Shuttleworth, 2000, 2001). Additionally, ARC channels can exhibit a monovalent cation permeability in the absence of divalent cations (Zhang *et al*, 2014). The composition of this channel was established in 2009, with the usage of concatemeric constructs with different proportion of ORAI1 and ORAI3 subunits. This approach allowed the authors to demonstrate that the properties of the native I_{ARC} current were restored with the expression of hetero-pentameric assemblies of ORAI1 and ORAI3 proteins organized as follow: 31113 or 31311 (where 3 indicates ORAI3 proteins, and 1 ORAI1 proteins) (Mignen *et al*, 2009). It was further demonstrated that this channel could be more robustly activated by leukotriene C_4 (LTC_4), a metabolite product of AA. Therefore, this channel could be referred in literature as ARC, LTC_4 -regulated Ca^{2+} (LRC), or ARC/LRC (González-Cobos *et al*, 2013; Zhang *et al*, 2014). While this channel present distinct feature from CRAC channel, several studies indicated that its activation was dependent on the presence of STIM1 protein although the activation of the channel was shown to be Ca^{2+} store independent. Thus, early studies on ARC channel performed by Mignen and al., claimed that a small pool of STIM1 localized at the PM was required to provide functional ARC current (Mignen *et al*, 2007). Additionally, Trebbak's team indicated that ER-STIM was sufficient to activate ARC/LRC channel and that PM-STIM was simply playing a facilitator role in ARC/LRC activation (Zhang *et al*, 2014). In any way, interaction between ORAI3 and STIM was shown to be mediated through their CC domain and to be mandatory for the ARC-LRC activation by LTC_4 (Zhang *et al*, 2013).

	ARC Channels	LRC Channels	CRAC Channels
Permeability	Ca ²⁺ -selective channel	Ca ²⁺ -selective channel	Ca ²⁺ -selective channel
Activation	Arachidonic acid	LTC ₄	Store depletion
Inhibition	Inhibited by La ³⁺ and Gd ³⁺ , insensitive to 2-APB	Inhibited by Gd ³⁺ , insensitive to 2-APB	Inhibited by Gd ³⁺ and high concentration (30–50 μ M) of 2-APB
Endogenous current size	0.4–0.6 pA/pF at –80 mV	0.1–0.2 pA/pF at –100 mV	0.1–0.2 pA/pF at –100 mV
Direction of current	Inward current	Inward current	Inward current
Component of channel	Orai1, Orai3	Orai1, Orai3	Orai1
Stoichiometry of channel	2 Orai3 and 3 Orai1 (31113 or 31311)	n/d	6 Orai1
pH sensitive	Insensitive to low pH = 6.7	n/d	Sensitive to low pH = 6.7
Fast CDI	Absent	n/d	Present
PKA	Regulated by PKA	n/d	Non-regulated by PKA
Interaction	PM-STIM1	ER-STIM1	ER-STIM1
Site of action	Inner surface of PM	Inner surface of PM	n/a

Notes: CDI, Ca²⁺-dependent inactivation; PM, plasma membrane; ER, endoplasmic reticulum; n/d, not determined; n/a, not applicable.

Table 2 | Biophysical properties of ARC, LRC, and CRAC channel.

1.2.3. Role of ORAI proteins in the physiology and pathology

1.2.3.1. Physiology

1.2.3.1.1. Role of ORAI and SOCE in physiology

SOCE is a ubiquitous process, and its main function is to induce Ca^{2+} store refilling following depletion (Putney *et al*, 2017). Even though this function of store refilling was initially thought to be fundamental, the importance of this process can be questioned since absence of SOCE does not prevent fetal development until birth. Nonetheless, humans presenting SOCE deregulation display strong deficiencies resulting different syndrome ultimately leading to a premature death (Lacruz & Feske, 2015a). ORAI1 representing the principal SOCE effector, its normal functionality is crucial for several cell types. Specifically, ORAI1 is particularly important for the maintenance of normal of immune cell function (Vig *et al*, 2008; Feske, 2009). Aside from immune cells, ORAI1 is also a fundamental actor of the normal physiology of several cell types including cardiomyocytes, endothelial cells, and skeletal muscle (Tiffner & Derler, 2021; Michelucci *et al*, 2018). The physiological functions of ORAI2 and ORAI3 are less clearly define because their expression pattern overlaps with ORAI1, and they are usually expressed at a lower level than the later. than. In fact, it was suggested that the lack of one homologues could be compensated by affecting the expression of another (Feske, 2011). Nonetheless, the strongest indication of a physiological role of ORAI2 is related to the maturation of innates immune cells. Indeed, depending on their maturation level, innate cells present different expression ratio of the different ORAI proteins homologues. It was further demonstrated in murine and human cell line that the inclusion of ORAI2 in the CRAC channel was leading to modification of SOCE and thus modulating the immune responses provided by these cells (Vaeth *et al*, 2017; Inayama *et al*, 2015a; Gross *et al*, 2007). As for a role of ORAI3 in physiology, this homologue has been identified as the main actor of SOCE in rat cardiac hypertrophy model (Saliba *et al*, 2015a). Overall, the main function of ORAI2 and ORAI3 seem to consist in the fine-tuning of Ca^{2+} signals of various cell types such as cardiac and skeletal muscle cells (Tiffner & Derler, 2021). Of note, this fine-tuning mostly results in SOCE impairment, as it was demonstrated in dental enamel, T cells and mast cells (Yoast *et al*, 2020a; Vaeth *et al*, 2017; Eckstein *et al*, 2019a; Tsvilovskyy *et al*, 2017).

1.2.3.1.2. Role of ORAI and store independent Ca^{2+} entry (SICE) in physiology

The physiological role of the ARC/LRC channel is not clearly defined as it was less studied than CRAC channel. Nonetheless, few physiological roles for these channels were identified. For example, AA-induced Ca^{2+} entry was shown to promote proliferation of bovine endothelial cells (Fiorio Pla & Munaron, 2001). In human, it was shown that vascular endothelial growth factor (VEGF) induces ORAI3 expression at the cell surface leading cell remodeling (Li *et al*, 2015) Additionally, it was

proposed that the remodeling of ORAI1/ORAI3 participate in the neointima formation after the vascular injury suggesting the existence of a remodeling mechanism (González-Cobos *et al*, 2013). Finally, ORAI3 knockdowns were shown to impair the migration of vascular smooth muscle cells (Zhang *et al*, 2014) (Zhang *et al*, 2015a).

1.2.3.2. Pathology

1.2.3.2.1. Role of ORAI and SOCE in pathology

Several genetic alterations of the molecular determinants of SOCE (*i.e.*, ORAI and STIM) such as GoF mutations, inducing constant SOCE activation, or loss of function (LoF) mutation, leading to the impossibility of SOCE induction, are linked to the apparition of specific human syndromes. Of note, all the mutations identified are affecting ORAI1 or STIM1 but not their other homologs indicating on their importance in maintenance of normal function compared to other homologs. Specifically, GoF mutations lead to the apparition of the severe combined immunodeficiency (SCID) syndrome, which includes autoimmunity, muscular hypotonia, ectodermal dysplasia, as well as dental enamel defects. At the opposite, patients displaying LoF mutations present the York platelet and Stormorken syndrome along with non-syndromic tubular aggregate myopathy (TAM) consisting of myopathy, thrombocytopenia, thrombopathy and bleeding diathesis (Lacruz & Feske, 2015a). Aside from genetic pathologies, expression deregulation was also shown to be the cause of pathologies. For example, in skeletal muscle, enhanced SOCE level attributed to ORAI1/STIM1 overexpression were linked to promotion of dystrophic phenotype in muscular dystrophia. Additionally, SOCE impairment caused by diminution of STIM/ORAI expression was also associated to muscle aging and fatigue susceptibility (Michelucci *et al*, 2018). Moreover, changes in ORAI channels expression including the relative expression level of the different homologs was also suggested to participate in cancer development (Chalmers & Monteith, 2018) (**Table 3**). For example, deregulations in ORAI1 expression were identified in liver, stomach, renal cancer (Tang *et al*, 2017; Zhu *et al*, 2014; Xia *et al*, 2016; Kim *et al*, 2014). Additionally, ORAI2 was also proposed to undergo expression alteration in acute myeloid leukemia cell line (Diez-Bello *et al*, 2017). Finally, ORAI3 expression has been shown to be increased in estrogen positive breast cancer cells as well as in lung and pancreatic cancer (Ay *et al*, 2015; Benzerdjeb *et al*, 2016; Dubois *et al*, 2021). Importantly, it was also shown that, by modifying Ca²⁺ homeostasis, alteration in ORAI expression was affecting cancer cell properties including proliferation, migration, apoptosis (Chalmers & Monteith, 2018).

ORAI/ STIM isoform	Cancer type	Change with cancer		Change with increasing tumour stage
		mRNA	Protein	
ORAI1	Liver cancer	↑	↑	
	Oesophageal cancer	↑	↑	↑
	Renal cancer		↑	
	Stomach cancer		↑	
	Lung cancer	↑	↑	↑
ORAI3	Renal cancer		↔	
	Breast cancer	↑	↑	
	Lung cancer	↑	↑	↑
STIM1	Cervical cancer		↑	
	Stomach cancer		↑	↔
	Liver cancer	↑	↑	
	Colorectal cancer	↑	↑	
STIM2	Colorectal cancer	↑		

Table 3 | Involvement of ORAI and STIM proteins in cancer.

From (Chalmers & Monteith, 2018)

1.2.3.2.2. Role of ORAI and store independent Ca^{2+} entry (SICE) in pathology

Few studies indicated on a potential involvement of ARC/LRC channels in pathologies. For example, it was suggested that ARC/LRC channels participate in asthma disease by dysregulating the Ca^{2+} signalization (Thompson *et al*, 2014). Additionally, it was shown that cardiomyocytes display a Ca^{2+} permeance when exposed to AA which was increased during cardiac hypertrophy (Saliba *et al*, 2015b). Interestingly, it was shown that ORAI3 was upregulated after vascular injury in vascular smooth muscle cells (VSMC), and it was proposed that the remodeling of ORAI1/ORAI3 participate in the neointima formation after the vascular injury (González-Cobos *et al*, 2013). Finally, remodeling in ORAI1/ORAI3 channel composition was also shown to be implicated in prostate cancer. The authors proposed that the increased expression of ORAI3 observed in prostate cancer cell line favors the formation of heteromeric ORAI1/ORAI3 channels at the expense of the classic CRAC channel therefore providing a new store ARC-like independent Ca^{2+} entry promoting cancer cell proliferation (Dubois *et al*, 2014b).

1.2.4. Evidence for an ORAI proteins dynamic associations

Since their identification 15 years ago, the importance of ORAI proteins in physiology and pathology has been demonstrated several times. Their ability to form channels of different stoichiometry is somewhat unique and studies exploring the functions and mechanisms of ORAI proteins association when forming channels are just emerging. In the recent years, our laboratory suggested that ORAI1 and ORAI3 proteins were responsible for the existence of a heteromeric channel bearing distinct properties than the classically described ARC channel. In addition, this publication highlighted that ORAI channels composition was susceptible to modification during cancerization process, but also depending on the stimulation received by the cell (Dubois *et al*, 2014b). Their conclusions led them to propose the existence of a dynamic remodeling in the ORAI channel composition. A similar hypothesis was latter suggested by another group who suggested that ORAI channels could be assembled “on site” *via* the α -SNAP protein (Li *et al*, 2016a). Finally, the recent demonstration by Trebak’s team that native ORAI channels are heteromeric and that their compositions modulates the properties of SOCE also point towards the existence of mechanisms regulating the composition of ORAI channels (Yeast *et al*, 2020b). Because structural studies on ORAI channels were focusing on the activation of the SOC channel and its specific gating by STIM, the mode of association within ORAI proteins in the formation of functional channels remain elusive. As a consequence, the modifications of interactions between ORAI proteins within a channel are not well documented. While biochemical studies were proven powerful in the study of protein-protein interactions, the identification of modulation of interaction is not straightforward and usually relies on the use of highly specific antibodies which are lacking for OAI homologues. On the other hand, microscopy also represent a powerful tool to study protein-protein interactions. In addition, the development of high-end microscopy techniques and their increased accessibility even for non-

specialist user have made them a powerful alternative strategy for studying ORAI channel specificities. Thus, the main aim of this PhD was to study the interaction between ORAI proteins with microscopy techniques. Especially, we wanted to implement the fluorescence lifetime imaging of Förster resonance energy transfer (FLIM-FRET) for studying the interaction between the ORAI1 and ORAI3 proteins. Before developing the different objectives of this work, we will introduce the main microscopy techniques which were already used to study ORAI protein. In addition, a specific focus on the FLIM FRET technique principle and application will be described. Finally, because some of the limitation in the use of microscopy techniques could be overcome through the use of genome editing techniques, a brief introduction of the CRISPR-Cas9 mechanism will be presented thereafter.

1.3. Microscopy to study ion channels

1.3.1. Invention and popularization of the microscopes.

Allegedly, ancient Chinese texts are reporting the use of water microscope, a tube filled with different level of water depending on the magnification level required, more than 4000 years ago (History of Microscopes | Microscope.com). Nonetheless, the first reference indicating on the existence of microscopic device is dated from the 8th century BC as hieroglyphs dated from this age are thought to be representing glass lenses (Enoch, 1999). The physical proof suggesting the existence of microscopes is dated to 750 BC, and is represented by a polished piece of rock crystal found in the Assyrian palace of Nimrud (**Figure 15A**) (Kriss & Kriss, 1998). Its use as a magnifying glass, a burning glass or simply as ornaments is debated, however it appears evident that this object was deliberately manufactured as a lens. More formal proofs on the usage of magnifying devices are dated from Greeks and Romans writing. For instance, scriptures from the 1st century attributed to Seneca, the Nero emperor's tutor, are reporting the usage of a globe of glass filled with water used to enlarge letters (Kriss & Kriss, 1998; Bardell, 2004). However, it is only in 10th century that the Arab mathematician and physicist Alhazen investigate, in the Book of Optics, the principles leading to magnification of object seen through a lens (**Figure 15B**) (Al Deek, 2004). Three centuries later, a Florentine manuscript describing the use of spectacles represent the first practical application of the magnifying power of lenses (Kriss & Kriss, 1998). Around the same period, Roger Bacon, deepening the work of Alhazen, designed an instrument aiming to "help the aged and those with weak eyes to see enlarged letters" (Bacon, 1267) and named it eyeglass. Shortly after, the basic magnifying constituents of the eyeglasses were called lens (Bardell, 2004). It took three more centuries to appreciate the full potential of lenses for scientific purposes with the development of the first telescopes and microscopes around 1600. Their inventions are closely related since both instruments are relying on the alignment of two lenses to induce image magnification. The discovery of this principle is usually credited either to Hans Lippershey (known as inventor of telescopes) or to the Janssen family (father and son's Hans and Zacharias) who were all Dutch spectacle-maker from Middelburg (Ball, 1966). Specifically, Hans and Zacharias Janssen will use their knowledge to create the first known compound microscope (i.e., a microscope composed by two lenses, as opposed to single lens microscopes) which was able to magnify object around 10 times (**Figure 15 C**). Their instrument consisted in a three tubes device, where the central tube was a sleeve in which the two other tubes (carrying the ocular lens and the objective lens) could be pushed to adjust the focus (Ball, 2018). Because of its relatively simple composition, this new instrument will be reproduced several times in the following years. Thus, a letter from 1625 written by Giovanni Faber, mentions an instrument designed by Galileo that allows "to look at small things". Following this description, Faber will coin the term microscope by contracting the Greek words "micro" (meaning small) and "skopein" (meaning to look at). Quite surprisingly, the firsts microscopes were mostly seen as new toys rather than as scientific instruments allowing new discoveries. It is only in 1661, that

Marcello Malpighi used a compound microscope for a scientific purpose, and thus discovered the blood capillaries (West, 2013). Four year later, Robert Hooke published his famous book *Micrographia* where, using microscopes, he could observe and describes with his drawing new details of insects and plant anatomy that were invisible to the eye. His discoveries led to the coining of the word “cell” which he used to describe the “plant basic structure”. However, in the preface of his book, Robert Hooke indicates that his observations were mostly made using a single lens microscope. Indeed, at that time compound microscopes were suffering from many flaws such as chromatic & spherical aberrations making their usage laborious and preventing their magnification power to overcome the one of single lens microscopes. Nonetheless, Dr. Hooke made many improvements on the compound microscope. Especially, through the addition of a base and screws to hold and modify the position of both the microscope and the samples. Additionally, he thought about improving the illumination of the sample by using a spherical glass filled with water. Thus, he could concentrate the light on the object to magnify (**Figure 15D**) (Bardell, 2004). But even with these improvements the maximal magnification obtained at the time was around 20 to 30x. This probably explains why the major discoveries of the time were obtained with single lens microscope. Indeed, it is the single lens microscope designed by Anton van Leeuwenhoek who enabled not only to make bigger images of an already visible objects but rather discover a whole new world invisible by eyes. Thanks to his skills he produced the lens of his single lens microscope and thus could reach a magnification up to 300x (**Figure 15E**). With his device, he revealed the existence of invisible ‘creatures’ named animalcules and opened the new era of microbiology. He was indeed, the first to discover the existence of protists, bacteria or spermatozoids (Kriss & Kriss, 1998). These discoveries eventually popularized the usage of microscopes in biological studies. During the next century both the single-lens and compound microscopes co-existed and were used amongst their advantages and flaws, until the quality improvement of the lens brought better power of magnification and correction of aberrations leading to the progressive abandon of single lens microscopes in favor of compound microscopes.

A



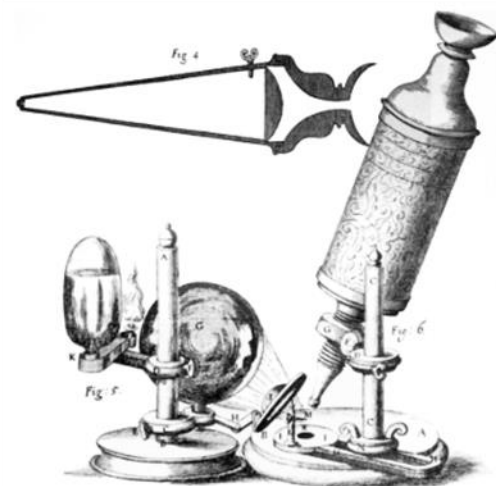
B



C



D



E

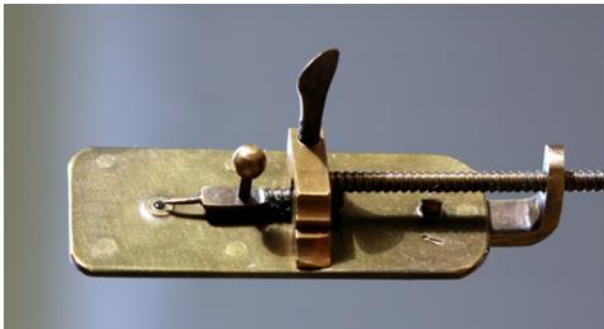


Figure 15 | Evolution of optics towards microscope invention.

- A. The Nimrud lens, might represent the oldest optical device (750-710 BC).
- B. Illustration from the Book of Optics (Alhazen), is the first trace of a valid vision theory. It also describes the principles of image magnification (10th century).
- C. The first compound microscope designed by Hans and Zacharias Janssen (1608).
- D. Illustration of the compound microscope improved by Robert Hooke (1665).
- E. The single lens microscope designed by Antoni Van Leeuwenhoek (1676).

Images from: (A) the British museum (<https://www.britishmuseum.org/>), (B) <https://funci.org/73607/?lang=en>, (C) http://theo.janssen.ca/documents/Janssen/Zacharias%20Janssen/Zacharias_Janssen.htm, (D) Bardell, 2004, and (E) Jeroen Rouwkema via Wikimedia Commons

1.3.2.Characteristics of optical microscopes.

Microscopes are instruments allowing to improve the resolution of the image of an object through its magnification. The resolution represents the ability to distinguish two points as being separated. For example, the resolution of a human eye is approximately of 150 μm , which means that two objects separated by this distance will be visualized as separated entities. Optical microscopes are able to reach the maximal resolution of 0.2 μm , which is usually called the diffraction barrier. The diffraction barrier is the result of the properties of the light (behaving like a wavefront) and of the fundamental laws of physics indicating that wavefront passing through or around an obstacle (*i.e.*, a lens in the case of microscopy) are spreading around this obstacle. To overcome this resolution limit, other types of microscopes were developed which are using alternative source of illumination such as electron microscopes. Thus, three main categories of microscopes can be defined depending on their illumination sources: Optical microscopes using light (photons) as illumination source; electron microscopes using electron as illumination source; and scanning-probes microscopes using metallic tip to scan the surface of an object and measure its electronic and magnetic forces. On the one hand, electron and scanning-probes microscopes display the best resolution (0.1nm and 10nm respectively), but the high level of specialization required to master their use as well as their high cost limits their use in biology. On the other hand, optical microscopes present a lower resolution (0.2 μm) but are more reasonably priced, and their use is more accessible to newcomers. Thus, they are widely used in biology. The elements constituting modern optical microscope are relatively simple, and includes four main components: a light source, a condenser lens, plus two lenses magnifying the desired object (Mualla *et al*, 2018) (**Figure 16**). The lens located the closer to the object is the objective lens, and the one closer to the observer's eye is the eyepiece also called ocular. The objective lens is characterized by its magnification factor, and its numerical aperture (NA). Of note, the NA represents the ability of the lens to gather light. Specifically, it denotes the maximal angle of the incoming light that can be collected by the objective lens (Kubitscheck, 2017). Of note, the resolution of an objective is directly dependent on the quantity of light it collects. Thus, to obtain the maximal resolution with a specific objective, the maximal light should be collected. This highlights the importance of the light source, which should be stable and powerful, and of the condenser lens which focuses the power light onto the object to be studied. Optical microscopes exist in two configurations according to the positions of the light source, and of the objective relative to the object to image. On the one hand, upright microscopes are imaging the sample from the top: the light source is situated below the object and the objective is placed above. On the other hand, in inverted microscopes the objective is placed below the sample and light is coming from above (**Figure 17**). For biological studies, inverted microscopes present a great advantage over upright microscopes as they allow to image samples from below. This specificity enables living samples present in liquid medium to be imaged while they lie on the bottom of Petri dishes or coverslips.

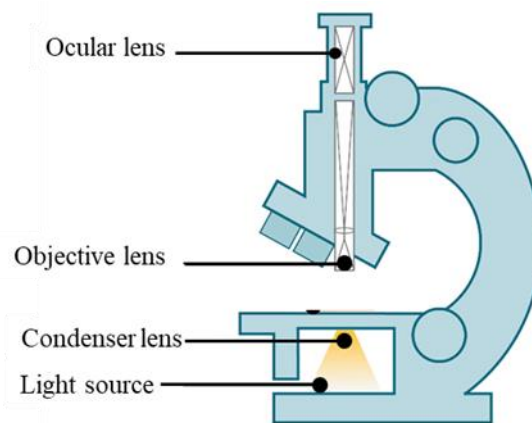


Figure 16 | The simplest microscope design.

Scheme of the simplest optical microscope. It is composed of a light source, a condenser lens focusing the light on the sample, and an objective and ocular lenses allowing the magnification of the sample image.

Image from <https://www.thermofisher.com/blog/microscopy/seeing-with-electrons-the-anatomy-of-an-electron-microscope/>

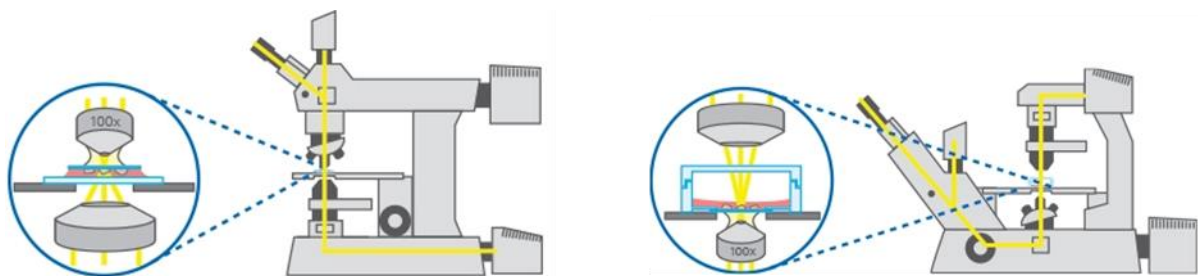


Figure 17 | Upright and inverted microscopes.

In an upright microscope (left), the light source is located below the sample and the objective over the sample.

In an inverted microscope (right), the light source is located above the sample and the objective below the sample. Inverted microscopes are commonly used in biology because they allow imaging of samples lying in Petri dishes.

Images from: <https://ibidi.com/content/212-inverted-and-upright-microscopy>

The simplest optical microscope is represented by the bright-field microscope, it is virtually present in every biological laboratory as a mean to observe cells. In brightfield microscopy, the incident light passes through the object and only structures opaques to photon are visible in gray level over a white background. Nonetheless, cells are relatively transparent to photon, thus they present a very low contrast making their observation arduous. Thus, element enabling phase contrast are often implemented in bright-field microscopes such as diaphragms. Alternatively, histological studies where samples are colored with specific dyes allow the visualization of the specifically colored structures (**Figure 18**) (Davidson & Abramowitz, 2002). Despite these improvements, the evolution of biological studies towards the identification of molecular processes occurring within the cells has outdated brightfield microscopy techniques which were overwhelmed by fluorescence microscopy.

1.3.3. Fluorescence microscopy

The apparition of fluorescent microscopy results from a series of unrelated discoveries in the worlds of physics and biology. First, the identification of fluorescent materials, and the desire of physicists to apprehend the mechanism by which fluorescence occurs led the scientists to develop and use specific materials that will later be implemented in microscopes (such as quartz lenses for example). Second, the observation of tissue auto-fluorescence by August Kohler in 1904, as well as the successful labelling of pneumococcal anti-serum (1941, Coons) and secondary antibodies (Weller and Coons 1954) with fluorescent compounds (fluoresceine), paved the way for a general use of fluorescence in biological studies (Ghiran, 2011). Later, the identification and cloning of the green fluorescent protein (GFP) was another breakthrough expending of the implementation of microscopes in biology laboratories.

1.3.3.1. Fluorescence discovery and principle

Several compounds naturally present fluorescence. The firsts reported observation of this phenomenon are dated from the 16th century by a Spanish scientist, Nicolas Monardes, and a Franciscan missionary, Bernardino de Sahagun. They both reported their observation that infusion of wood (*Lignum nephriticum*, and *Eysenhardtia polystachya* respectively) gives to the water a bluish shade (**Figure 19 A**) (Acuña *et al*, 2009). Other observations of fluorescence were later reported from stones (by Vincenzo Casciarolo in 1603), leaves (by David Brewster in 1833) or chemical compounds (Calcium sulphate, by Edmond Becquerel in 1842 or quinine sulfate, by John Herschel in 1845) (**Figure 19 B,C,& D**). In 1852, the Irish physicist George Gabriel Stokes will coin the fluorescence in his treaty “on the change of refrangibility of light” (Stokes, 1852). Stokes was also the first one to notice that the light emitted by fluorescent compound had a longer wavelength than the one from the excitation light (Ghiran, 2011). Formally, fluorescence is defined as " the emission of electromagnetic radiation, usually visible light, caused by excitation of atoms in a material, which then reemit almost immediately (within about 10⁻⁸ seconds)” (Britanica encyclopedia). In fluorescent microscopy, the material mentioned in the above definition is usually represented by fluorophores (*i.e*, inorganic dyes or genetically encoded fluorescent

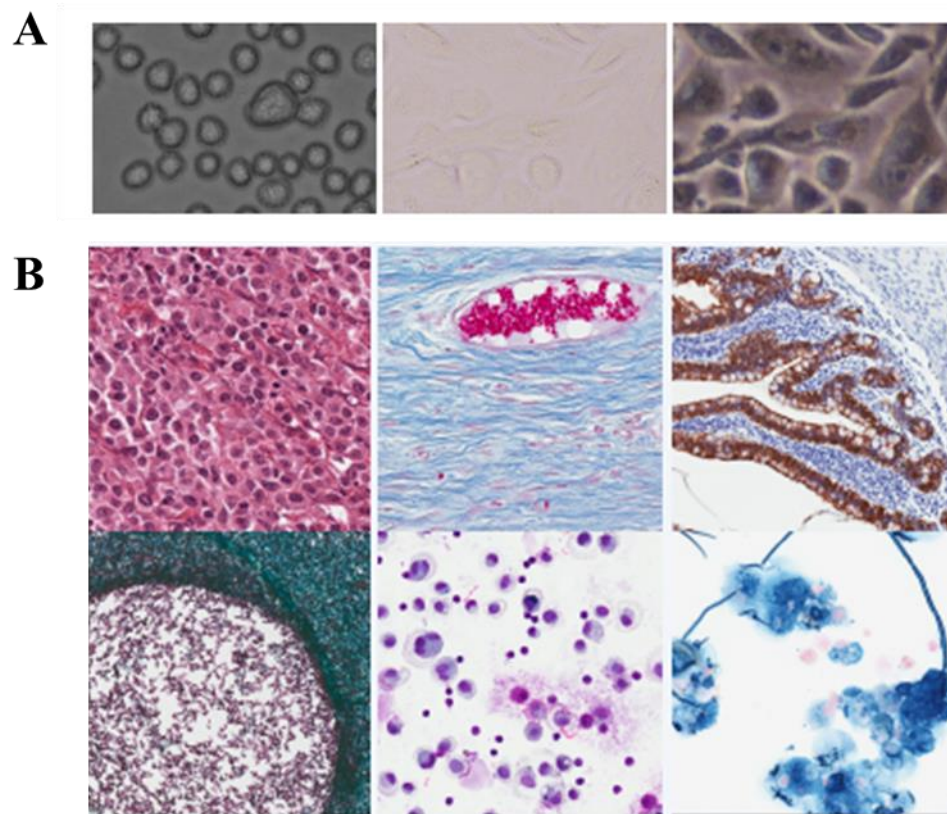


Figure 18 | Contrast enhancement in brightfield microscopy.

- A. Typical brightfield microscopy, with contrast enhancement due to phase contrasting technique.
 - B. Histological staining allowing an increase of contrast in classic brightfield microscopy experiment.
- Images adapted from Mualla et al, 2018*

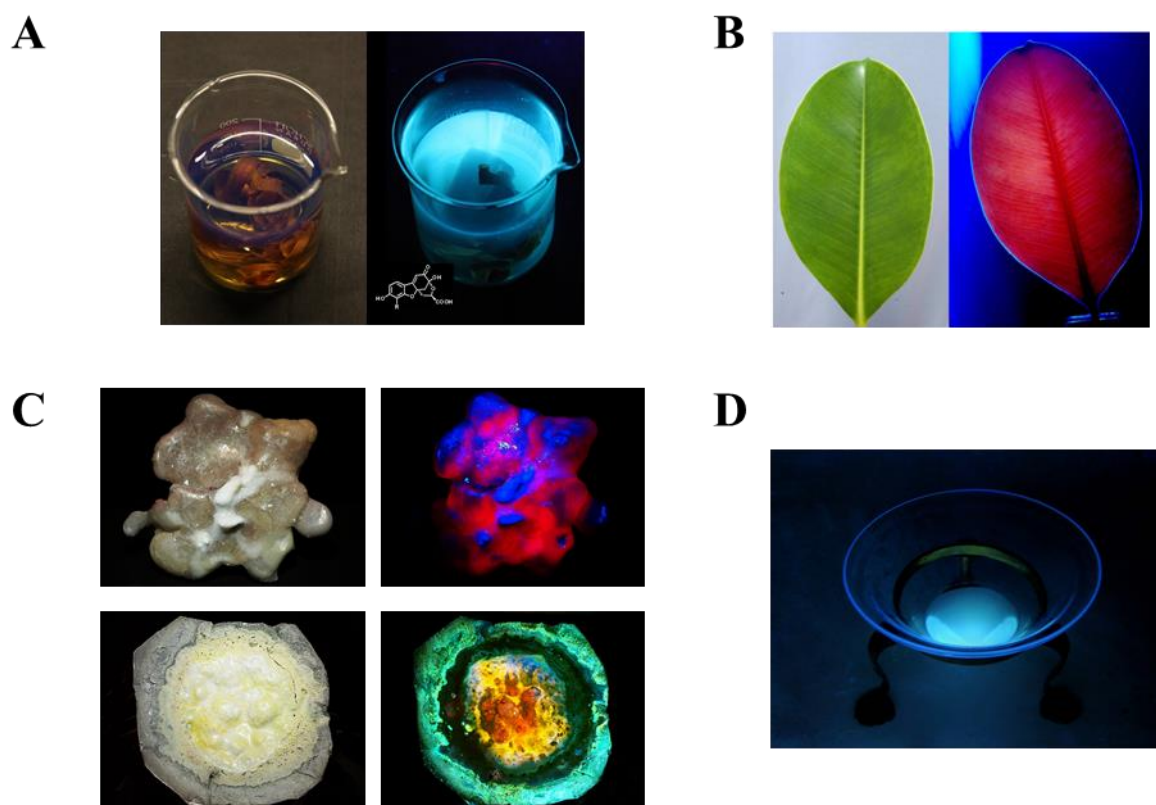


Figure 19 | Different compounds presenting fluorescent properties.

A. *Lignum Nephriticum* fluorescence.

B. Chlorophyll fluorescence from leave exposed to ultraviolet light.

C. Barium sulfate fluorescence (top) and Calcium sulfate fluorescence (bottom).

D. Quinine sulfate fluorescence.

Images from: (A) <https://imgur.com/gallery/uBmzc/comment/751859480>, (B) Lagorio et al, 2015, (C) <https://www.flickr.com/photos/28617364@N04/21435015662/in/photostream/>, and <https://www.flickr.com/photos/28617364@N04/7265309240/in/album-72157629885141550/>, (D) <https://www.flickr.com/photos/14833125@N02/4564370367/in/photostream/>

proteins), and the electromagnetic radiation used to excite the fluorophore correspond to the specific light wavelength allowing its excitation. The physical principle of fluorescence was described by Dr Jablonski and is schematized in the Jablonski diagram (**Figure 20**)(Jablonski, 1933). This principle stipulates that when a fluorophore is hit by a photon, it will absorb its energy. The acquisition of additional energy by the fluorescent molecule is characterized by the passage of its electrons from a ground state energy level (named S_0) to the first excited singlet state (named S_1). Of note, this first excited energy state is itself subdivided in several intermediate vibrational level, and when an electron enters in the excited energy, it reaches one of these intermediate vibrational electronic states. Due to vibrational relaxation the electron will release energy to reach the lowest vibrational energy level from S_1 . This state being by essence unstable, the electrons will eventually return to their ground energy level by dissipating the surplus energy through the emission of a photon carrying less energy than the one being absorbed (due to the loss of energy induced by the vibrational relaxation process mentioned earlier) (**Figure 20**). The difference in energy between the absorbed and emitted photon is called Stokes shift in the honor of Stokes who was the first to describe the phenomenon. Since the energy carried by a photon is associated to its wavelength, with the shortest wavelength representing the highest level of energy, during the fluorescence process the absorbed photon possess a shorter wavelength than the emitted and thus is red shifted (**Figure 21**).

1.3.3.2. Fluorescent proteins

1.3.3.2.1. GFP discovery

The discovery GFP is dated from 1955, when Davenport and al., identified a jellyfish presenting photogenic tissue. At the time the authors did not link this photogenicity to a protein (D. Davenport and J. A. C. Nicol, 1955), and it took almost ten years before the Dr Shimomura established that a protein was responsible for this fluorescence (Shimomura et al, 1962). It took another 30 years, before the first cloning of the GFP gene realized by Dr Prasher in 1992 (Prasher et al, 1992). In addition, to cloning the gene of GFP, Dr Prasher will be the first to have the intuition that GFP could be used as a tag to track proteins in cells. However, unable to pursue his academic career, Dr Prasher will send the cloned GFP gene to Dr Chalfie who will be the first to express the GFP in *Escherichia coli* and *Caenorhabditis elegans* (Chalfie et al, 1994). One year later, Tsien and al., started genetically affecting the GFP and modifying its properties paving the way for its general use in microscopy (Heim et al, 1995). Of note, the importance of the discovery of GFP was recognize as the Dr Shimomura, Dr Chalfie and Dr Tsien were awarded by the Nobel prize in 2008.

1.3.3.2.2. Structure and properties of GFP

The GFP present a cylinder-like structure organized in β -barrel. Of note, the wall of this cylinder is formed by 11 anti-parallel β -sheets with most of the amino acid side chains pointing to the cylinder center (**Figure 22**). This specific arrangement of the side amino acid pointing toward the center of the

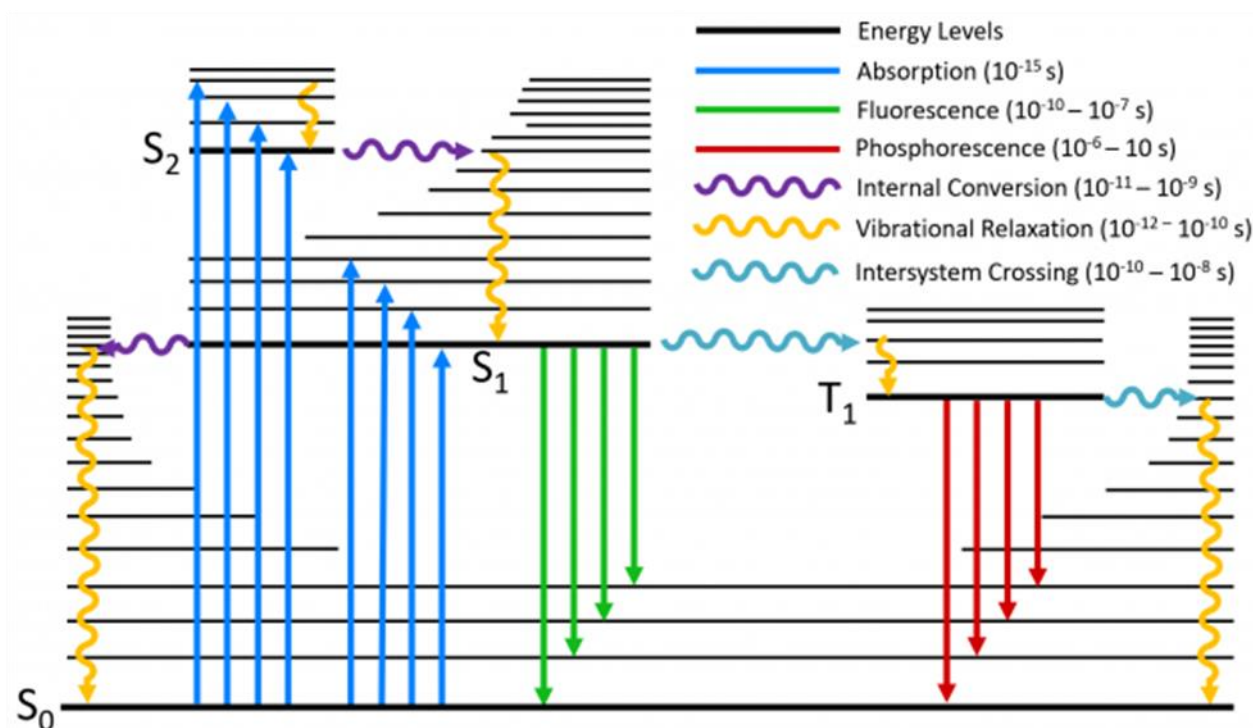


Figure 20 | Jablonski diagram.

The Jablonski diagram allow the visualization of the potential transitions that might occur following excitement of a fluorescent molecule. The horizontal black lines represent the different singlet energy states (S_0 , S_1 , S_2), with the bold lanes representing the lower vibrational level within each state, and the thin lines representing the higher vibrational states (S_0 , S_1 , S_2). At rest, the fluorescent molecules are in the ground state (S_0). When a fluorescent molecule is excited by the absorption of a photo, (blue arrows) it enters a singlet excited state of higher energy level (S_1 or S_2). Following its promotion to higher energy state, the excited fluorescent molecule undergo vibrational relaxation (yellow arrows) leading to its return on the lowest vibrational level of its singlet excited state (S_1 or S_2 , bold lane). The return from the singlet excited state to the ground state usually occurs through the radiative process of fluorescence (green arrow), but non-radiative pathways (such as internal conversion [violet wavelet] followed by vibrational relaxation, or entry in triplet state T_1 through intersystem crossing [blue wavelet], followed by phosphorescence or vibrational relaxation) might also occur. The difference between the energy absorbed and the energy released by the radiative process (due to vibrational relaxation) causes the Stokes shift. Note the different time scales of each of these processes.

Image from: <https://www.edinst.com/blog/jablonski-diagram/>

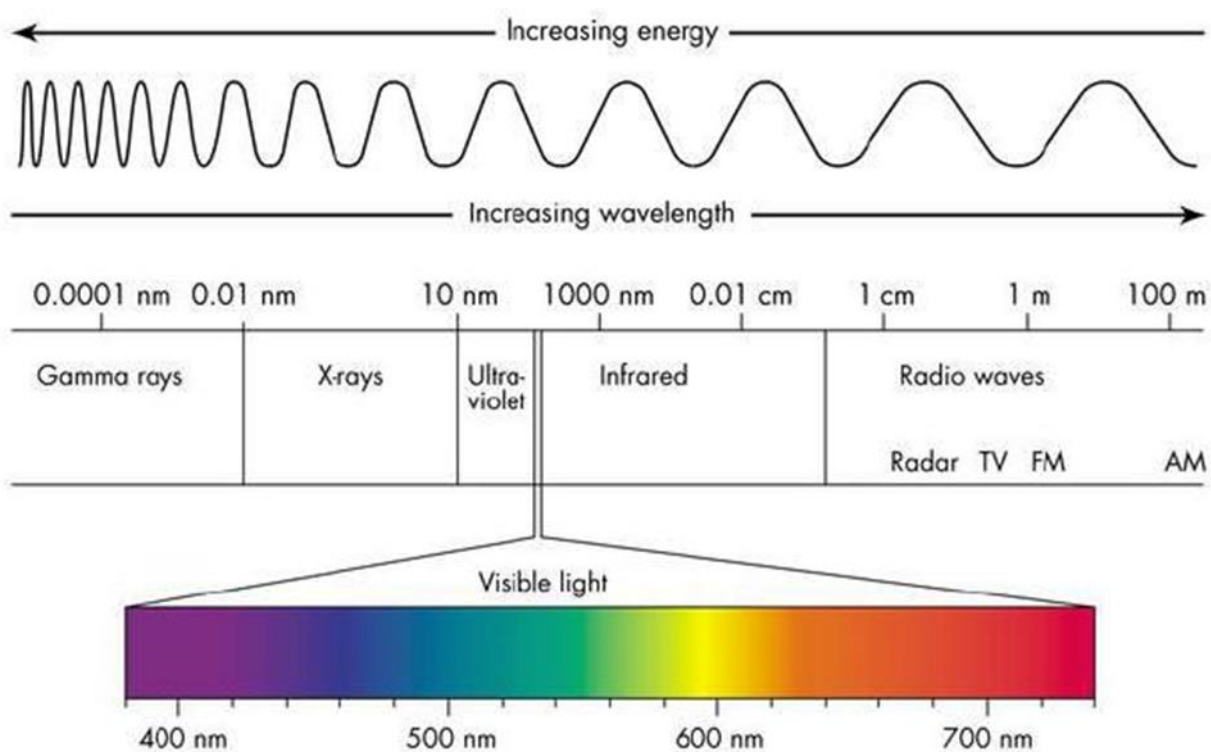


Figure 21 | Light spectrum.

Diagram displaying the visible light spectrum with its wavelength and energy level. The visible spectrum is located between the energetic and shorted-wavelength ultraviolet, and the low energy and long wavelength infrared. The visible light spectrum includes wavelength from 400 to 750 nm.

Image from: <https://munsell.com/color-blog/chemistry-fireworks-colors/>

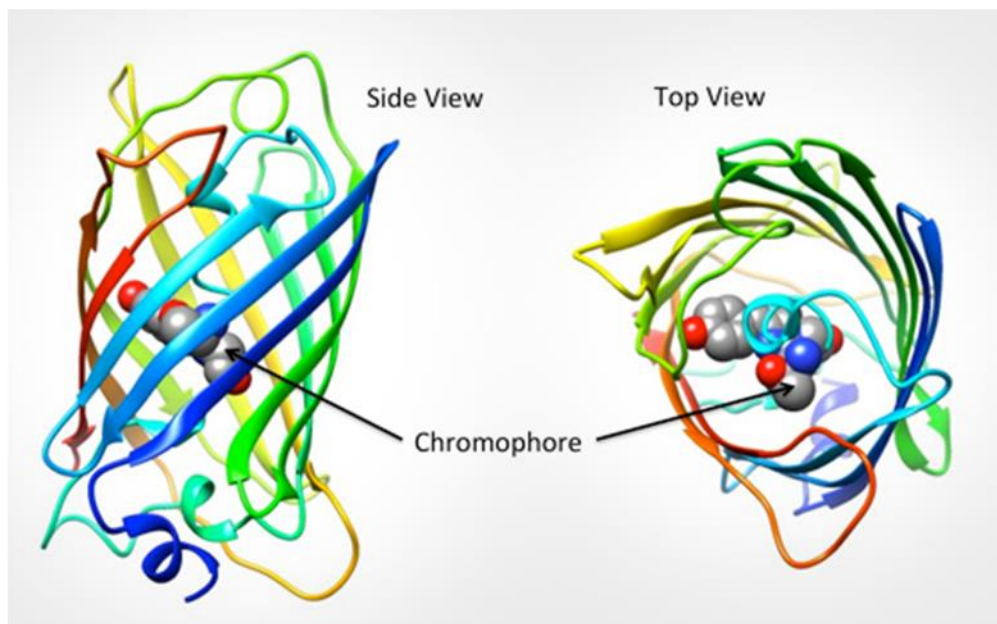
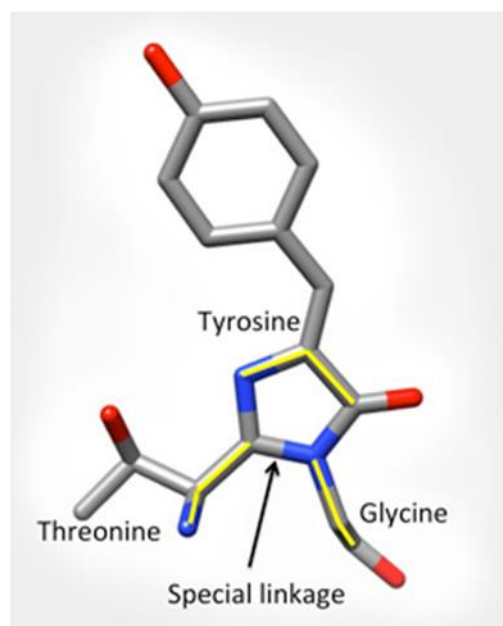
A**B**

Figure 22 | Green fluorescent protein (GFP) structure.

- A. Three-dimensional representation of the GFP structure. The GFP is shaped like a cylinder with all its amino acid side chains pointing toward the center of the cylinder, creating the adequate condition to induce the chemical reaction allowing the chromophore maturation.
- B. Chromophore structure resulting from the chemical reaction between the Serine 65, Tyrosine 66, and Glycine 67

Image from: <https://munsell.com/color-blog/chemistry-fireworks-colors/>

cylinder creates the adequate chemical conditions allowing the formation of the chromophore (*i.e* the part of the protein responsible for its fluorescence). Specifically, the side chains of 3 consecutive amino acids (Ser-65, Tyr-66, Gly-67) are reacting together to form the GFP chromophore (**Figure 22**) (Niwa *et al*, 1996). This specific structure, in which the side chains of the amino acids are pointing inside of the β -barrel, provides the advantage of decreasing the possibility of the GFP to interact with other proteins. This characteristic allows the creation of chimeric proteins where the GFP is fused to virtually any protein of interest without affecting its functionality nor the fluorescence mechanism of the GFP. In addition, scientists quickly realized that the GFP structure could be engineered to meet criteria required for specific microscopic applications. Thus, a myriad of random mutations was induced in the original GFP sequence, leading to the generation of a multitude of GFP variants presenting different characteristics than the original one (**Figure 23**). Nonetheless, even though an impressive number of GFP variants was created, the color spectra of these GFP mutants are limited to the blue-yellow range. Fortunately, several other species displaying fluorescent proteins were identified and thus expanded the color palette of fluorescent proteins (FP) to the whole visible spectra (**Figure 24**) (Wouters, 2006).

1.3.3.2.3. Properties of fluorescent proteins (FP)

Because of the variety of available FPs, one should carefully choose the most suited to its specific experiment. In fact, FP do not only differ by their “fluorescent color” but also possess several features that make them more or less suited for specific imaging techniques. These characteristics can be separated in two categories: optical properties and physicochemical properties.

1.3.3.2.3.1. Physicochemical properties

The physicochemical properties of FP include:

- **Oligomerization state.** Most of the FP derived from the original GFP were shown to be dimeric. As such, fusion of the non-monomeric GFP to a protein of interest might affect the experiment outcome. Fortunately, the propensity to dimerization of FP can be abolished with a single mutation (A206K) (Zacharias *et al*, 2002). This propensity to dimerize is not restricted to FP derived from the GFP but is also displayed by most of the red-shifted FP that tend to form tetramer, nonetheless following round of genetic engineering, monomeric forms were made available (Campbell *et al*, 2002; Bulina *et al*, 2003; YG *et al*, 2002). Of note, the evaluation of the tendency of a specific FP to oligomerize can be tested by fusing a desired FP to an ER resident protein. In case the tested FP is oligomerizing, the pattern of ER will be distorted into a specific structure named organized smooth endoplasmic reticulum (OSER) (**Figure 25**). Thus, the OSER assay became the method of choice to determine the tendency of newly created or engineered FP to dimerize (Costantini *et al*, 2012).

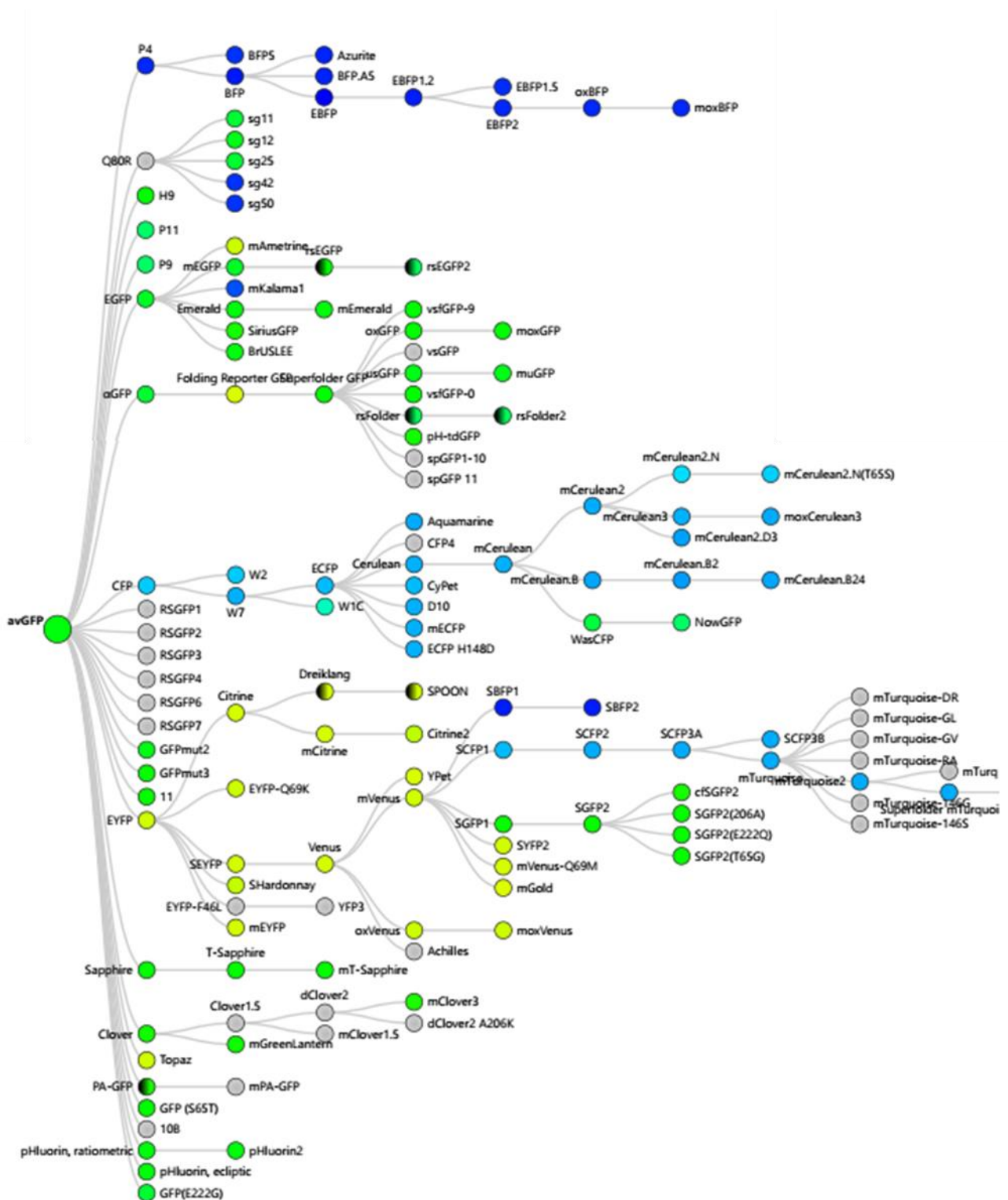


Figure 23 | Green fluorescent protein (variants).

Graphical representation of the GFP variants from the initial *Aequorea Victoria* jellyfish. Variants were generated by mutagenesis of the initial sequence. This graphic do not represent a phylogenetic tree, but a manually-compiled list of directed protein evolution.

Image from: <https://www.fpbases.org/lineage/>, Lambert, 2019

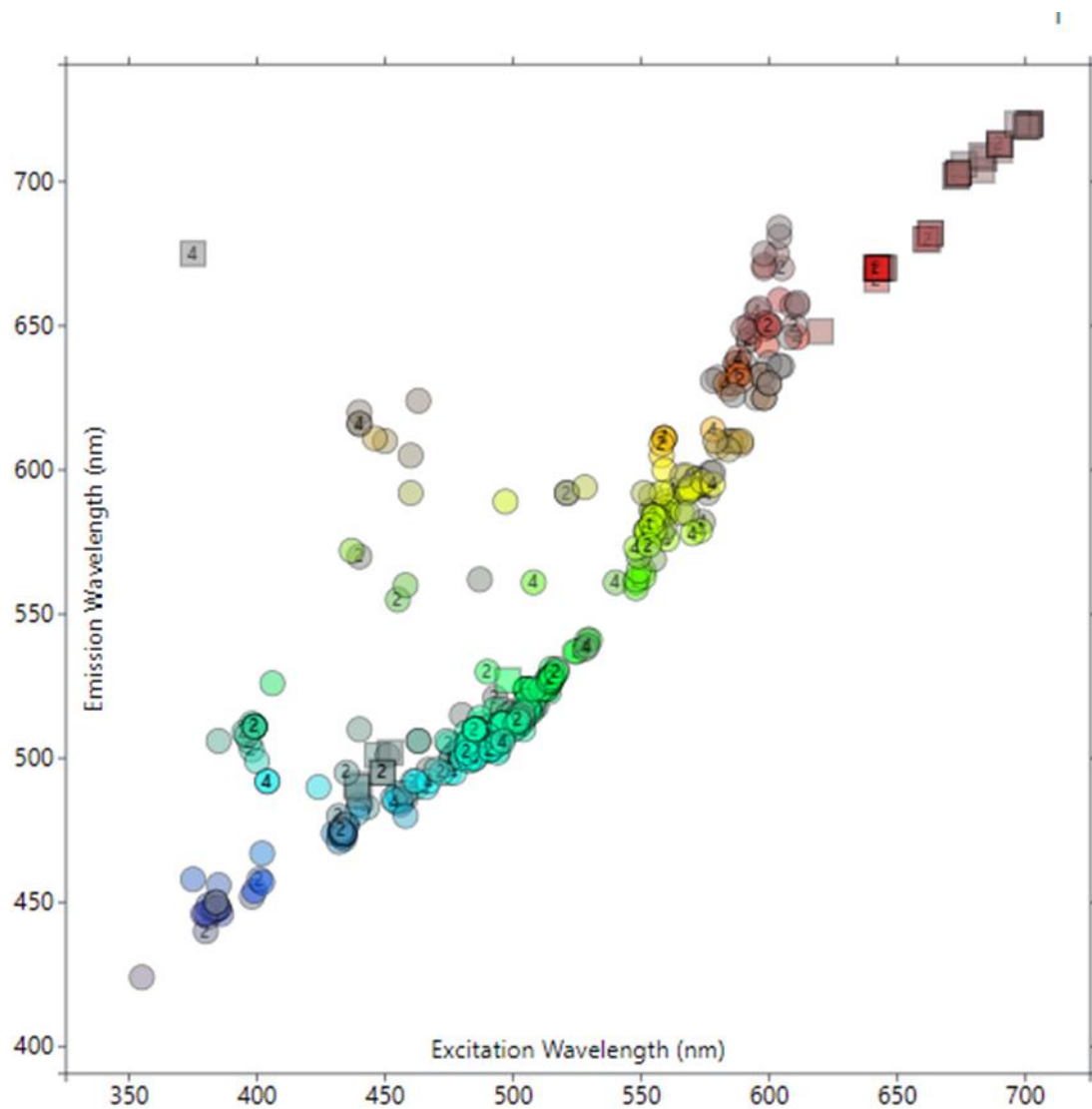


Figure 24 | Chart of emission and excitation wavelength of fluorescent proteins (FP).

Plot of the excitation and emission wavelength (in nm) of different FP. The FP color palette spans the entire visible spectrum.

Image from: <https://www.fpbases.org/chart/>, Lambert, 2019

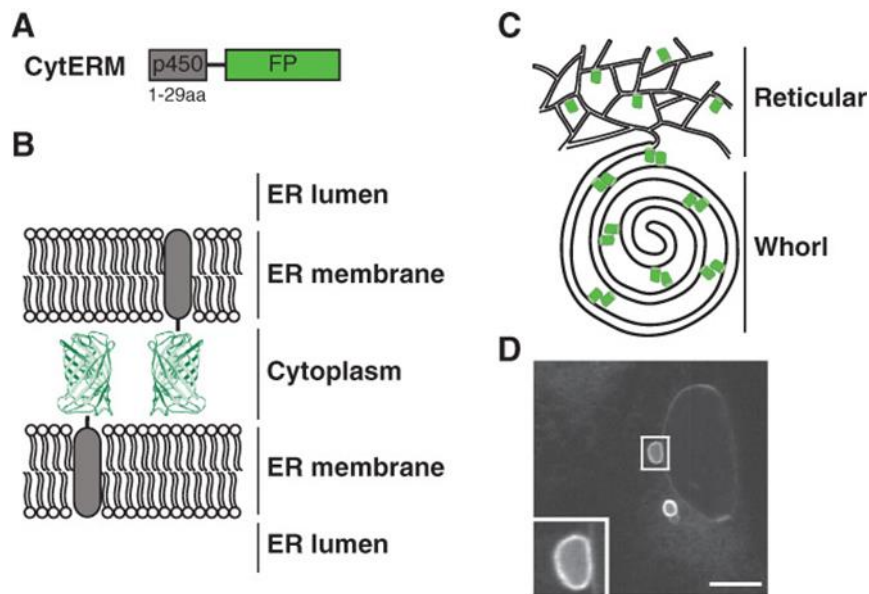


Figure 25 | The principle of the organized smooth endoplasmic reticulum (OSER) assay.

- A. Typical structure of the fusion protein for performing the OSER assay.
- B. Following transfection, in case of dimeric (or higher oligomeric) assembly of the FP, the ER adopts a specific structure due to the interaction between FP.
- C. Schematic representation of the OSER following transfection of dimeric FP targeted to the ER.
- D. Microscopic image of a typical OSER structure.

Adapted from Costantini et al, 2012

- Maturation process. Most of the FP were identified in jellyfishes. Thus, their optimal thermal stability and folding properties are adapted to the temperature of their living environment (usually below room temperature). Codon optimization procedure or mutation of few amino acids were introduced in the FP sequences in order to obtain thermostable and properly folded FP at 37°C (Yang *et al*, 1996; Nagai *et al*, 2002). Nonetheless, disparities exist from a specific FP to another, and the speed of maturation can be an important factor to account for depending on the experiment performed. Of note, presence of oxygen (O₂) is a pre-requisite to the chromophore formation within the GFP structure. Thus, experiments performed in anaerobic bacteria or in O₂-deprived environment should be carefully designed before conducting fluorescent microscopy experiment.
- pH stability. The pH affects the properties of the FP (Griesbeck *et al*, 2001; Shaner, 2014). Thus, fusion protein targeting acidic compartment should be fused to FP resistant to low pH. Of note, the sensitivity of certain FP to pH was used to create pH sensors (M *et al*, 2011).

1.3.3.2.3.2. Optical properties

The optical properties of FP represent another set of important characteristics to be considered when one wants to perform fluorescence microscopy experiment. Several features are included within the optical properties of a given FP:

- The excitation/emission spectra. The excitation spectrum defines the set of wavelengths allowing the excitation of a given FP. The emission spectrum represents the set of wavelengths from which a photon can be emitted by the FP. Of note, in databases it is not unusual to see single values given to describe FP excitation, they represent the “peak” excitation/emission, meaning, the wavelength at which most of the photons will be absorbed/emitted. The choice of FP spectrum is dictated by the set of filters equipped on the microscope where the experiment will be performed. In addition, in the case of multiple labelling, one should choose fluorophores with minimal crosstalk between their specific spectra. Thus, FP with narrow excitation and emission spectra are usually preferred. Additionally, because excitation and emission spectra of a given FP are usually overlapping, one would want to choose FP presenting a large Stokes shift. Finally, autofluorescence of the sample to be imaged should be taken into account in order to obtain the best contrast.
- The brightness. Brightness of a FP represents the efficiency with which it will convert the energy it absorbs into a fluorescent photon emission. On the one hand, the capacity of the FP to absorb a photon (and thus its energy) is represented by the extinction coefficient (ϵ), expressed in M⁻¹.cm⁻¹. On the other hand, the quantum yield (ϕ) is the ratio between the

number of photons absorbed and emitted by the FP (equation 1). The molecular brightness of a FP is calculated as follow (equation 2):

$$\phi = \frac{\text{Absorbed photons}}{\text{Emitted photons}} \quad (1)$$

$$\text{brightness} = \frac{\varepsilon \times \phi}{1000} \quad (2)$$

Of note, the extinction coefficient is specific to a given chromophore. Nonetheless, because the maturation of the chromophore within the FP depends on its proper folding, the effective extinction coefficient is susceptible to variation within experiments (Shaner, 2014). Noteworthy, quantum yield (ϕ) is comprised between 0 and 1. This suggests that a photon absorption by a FP is not obligatory leading the emission of the fluorescent. In fact, the emission of a photon represent the radiative pathway of energy release and competes with non-emissive or nonradiative pathways which includes heat production, collision to another molecule (for example, quenching) or intersystem crossing (leading to delayed fluorescence of phosphorescence) (**Figure 20**) (Shaner, 2014; Wolf, 2013).

- **The lifetime.** The lifetime of a given FP is a constant value expressed in nanoseconds (ns). In fact, fluorescence emission is a stochastic process. As such, considering a group of excited molecules, they will not return to their ground energy stated at the same time. The lifetime of a specific FP, represent the time for which 36.8% (1/e) of the excited population will have returned to their ground energy state. Noteworthy, we described above that non-radiative de-excitation pathways are competing with the fluorescence emission pathway of relaxation (Wolf, 2013). In fact, some specific microscopic applications (such as Fluorescence lifetime imaging - Förster resonance energy transfer [FLIM-FRET]) are specifically modifications in the lifetime of fluorescent proteins due to FRET in order to perform quantitative measurement of the distance between fluorescent molecules.
- **Photostability.** The photostability is a critical parameter of the FPs. It represents the amount of energy a FP can absorb before getting photobleached (*i.e.*, being unable to produce fluorescence). Photostability depends both on the FP characteristics and on the imaging conditions such as the temperature, the pH, and the illumination intensity. Interestingly, photobleaching can occur in several pathways and not all of them are leading to permanent fluorescence deactivation. For example, physical breakage of the chromophore (cleavage of the peptide bonds within the chromophore) is irreversible, while other mechanisms (such as entry of the chromophore in a triplet state, or chromophore protonation) are reversible (Shaner, 2014). Because of the variability of photobleaching events, it is usually recommended to test different FPs in a given experimental condition before performing a series of experiment.

Of note, the FPBase online tool lists 711 different FP together with their optical properties, and probably represent the most complete database to date enabling to choose a FP (Lambert, 2019). To conclude, FP are extremely complex, and their properties are greatly affected by their environmental and experimental condition. Thus, the choice of the adequate FP for a given experiment should not only be dictated by properties from database but should also result from testing different FP in the experimental condition.

1.3.3.3. Types of fluorescence microscopy

The use of fluorescence to acquire images of biological samples presents several advantages over the classic brightfield microscopy such as a very high contrast, sensitivity, specificity, and selectivity. Nonetheless, in order to perform fluorescence microscopy acquisitions, several adaptations need to be implemented in a classic light microscope. From the many types of fluorescent microscopes available, only the microscopy techniques used in this PhD will be described thereafter.

1.3.3.3.1. Widefield fluorescence microscopy

Widefield fluorescence microscopy, is performed on the simplest type of fluorescent microscope. The term widefield signifies that the whole sample is illuminated by the microscope. In that regard, widefield fluorescence is similar to the classic brightfield microscope. Nonetheless, the major difference between the two configurations arises from the presence of a filter that will deviates most of the incoming light preventing it to reach the detector (**Figure 26**). Specifically, the filter allows exclusively the passage of the wavelength corresponding to the excited fluorochrome. Additionally, one should mention that most fluorescent microscopes are using epi- illumination. This mode of illumination is opposed to the classic trans- illumination, where the incoming light is transmitted through the sample, as it is instead reflected by the sample. Specifically, the incident light passes through the observation objective, and is reflected by the sample (**Figure 26**). The reflected light is subsequently collected back the objective. The fluorescent epi- illumination mode dictates the implementation of an additional element in the microscope: the dichroic mirror.

1.3.3.3.1.1. Dichroic mirrors and filters

The dichroic mirror also called beam splitter is reflecting a specific set of wavelengths onto the sample and allows the transmission of a different set of wavelengths into to microscope. Classically, in epi- fluorescent microscopes, the light produced by the source is reflected by the dichroic mirror, enters the objective through its back rear aperture, and is focused on the sample where it excites the fluorochromes. This configuration implies that only an extremely reduced fraction of the incident light is reflected by the sample back to the objective lens, thus providing a better contrast. The subsequent fluorescent light emitted by the sample enters the objective, passes through the dichroic mirror to reach the detector. In addition, two supplementary filters are usually located up- and down-stream the dichroic

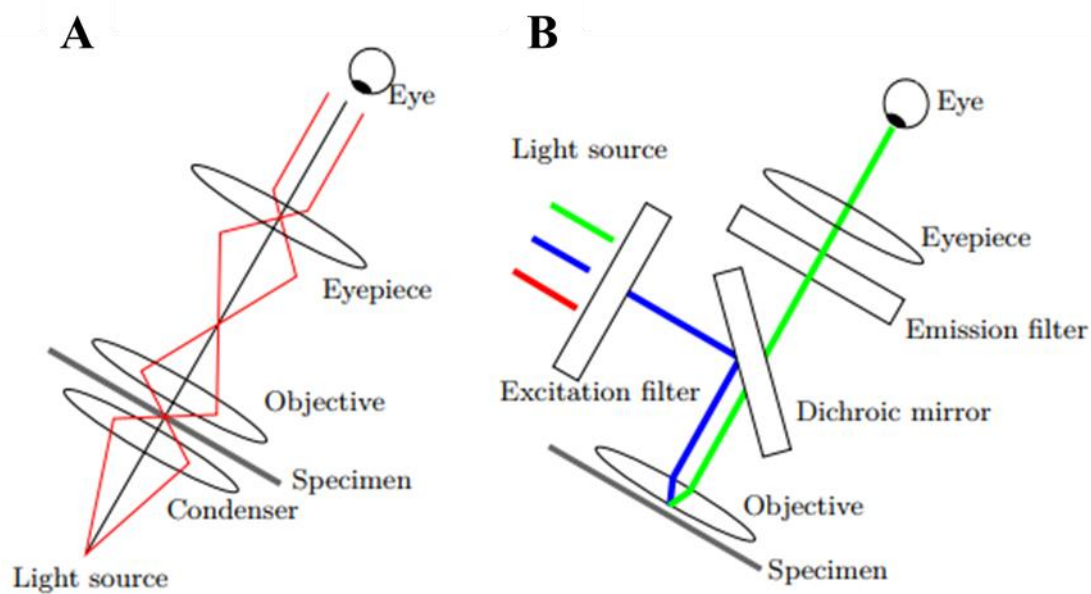


Figure 26 | Diagram of brightfield and fluorescence microscopes.

- A. Scheme of the light path in a brightfield microscope. The incoming light from the source, is focused on the sample by the condenser lens, it is then transmitted through the specimen and collected and magnified by its passage through the objective lens and the eyepiece.
- B. Scheme of the light path in a fluorescent microscope. The light source is filtered by the excitation filter and directed on the sample by the dichroic mirror. The excited molecules within the specimen are emitting fluorescence at a specific wavelength capable of diffusing through the dichroic mirror from where they reach the emission filter and the eyepiece. Note that the incoming light is not transmitted but reflected by the sample.

Adapted from Mualla et al, 2018

mirror to refine the incoming and outgoing light wavelength (**Figure 26**). This allows the light to be specifically fitted to the emission and excitation spectra of the desired FP (Lichtman & Conchello, 2005). Of note, the dichroic mirrors and the filters are usually assembled in a single element named the cube which can be changed depending on the specific fluorochrome being illuminated (**Figure 27**).

1.3.3.3.1.2. Light sources

Another important feature of the fluorescent microscope is represented by the light source used to illuminate the sample. Classic filament lights are not suited for fluorescence microscopy because a great part of the produced light is in the infrared (IR) range. In addition, because the different fluorochrome possess specific excitation spectra, the light source needs to provide a light with an even coverage all over the ultraviolet (UV), visible and IR spectra. Moreover, light sources need to produce powerful and stable illumination during all the time of the experiment. Three main types of illumination meet these criteria: mercury, xenon and metal halide arc lamps. They all possess the qualities mentioned above, nonetheless, they can present discrepancies on their emitted wavelength intensities and thus the fluorochrome should be chosen accordingly to the specificities of the light source (**Figure 28**). Finally, light emitting diode (LED) are slowly being used as light sources since they present the advantage of being compact, long lasting, extremely stable in time and the ability to be turned on and off extremely rapidly without affecting their properties of lifetime. In the meantime, LED lights possess specific wavelength and usually suffers from a lower power compared to arc lamps.

1.3.3.3.1.3. Detectors

Fluorescent microscopy not only allows to obtain qualitative images of a sample but also grants the obtention of quantitative information about the sample observed. Such quantitative interpretation of images cannot be realized through visual inspection. Thus, recording of images is performed by specific light detector depending on the type of fluorescent microscopy used. For widefield fluorescent microscopy, light detection is commonly operated by a camera. The most commonly equipped cameras are the charge-coupled device (CCD). Nonetheless, depending on the microscopic technique used and on the intensity of the signal recorded to be recorded, different camera types can be used such as the electron-multiplying CCD (EMCCD), the complementary-metal-oxide semiconductor (CMOS) and the scientific CMOS (sCMOS). The basic principle of all these cameras is to transform light signal into an electric signal due to the photoelectric effect. The generated electric signal is then read by a computer and transformed into an image.

- A CCD-camera consists of an array of light-sensitive elements (*i.e* pixels or photodiode). This array converts the photons into photoelectrons. During the image acquisition, the photons hitting the light sensitive surface are transformed into photoelectrons. These photoelectrons are accumulated in the specific picture elements of the array usually described as a bucket. This accumulation of photoelectrons creates an electric charge of a

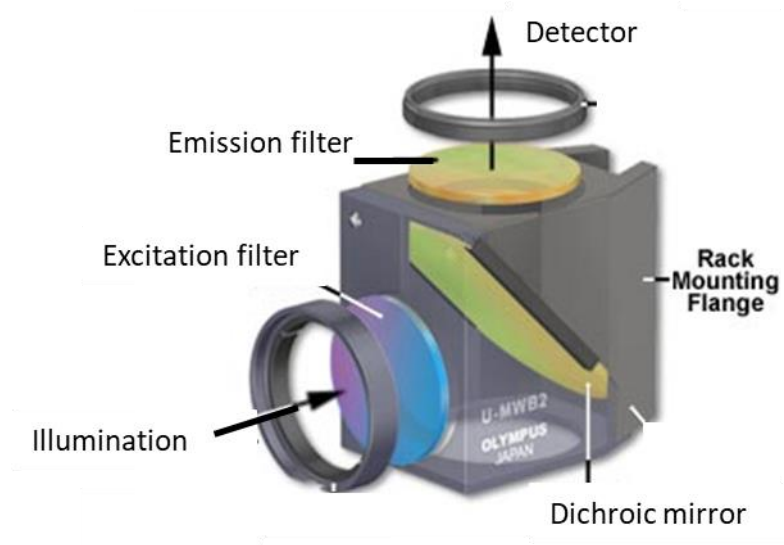
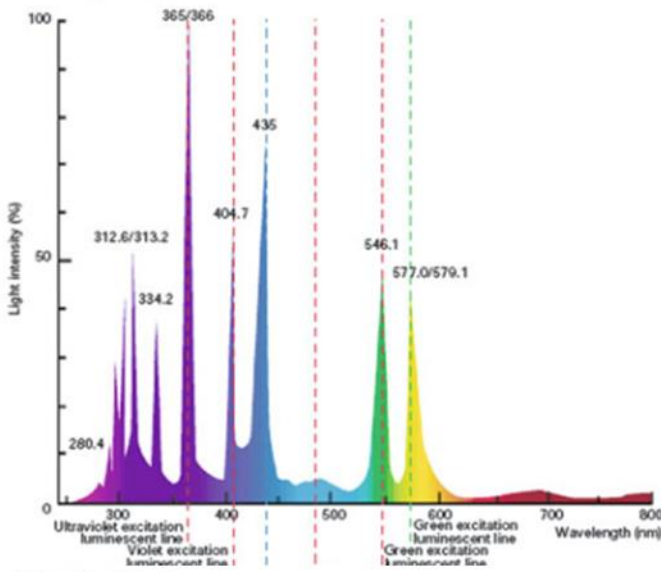


Figure 27 | Scheme of a filter cube.

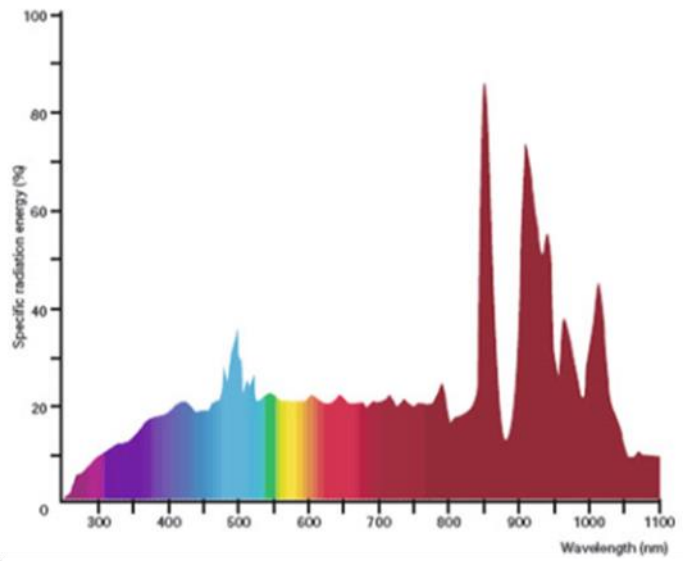
The filter cubes gather the excitation filter, the dichroic mirror and the emission filter in a single element block.

Adapted from <https://www.olympus-lifescience.com/en/microscope-resource/primer/techniques/fluorescence/filters/>

Mercury lamp



Xenon lamp



Metal halide lamp

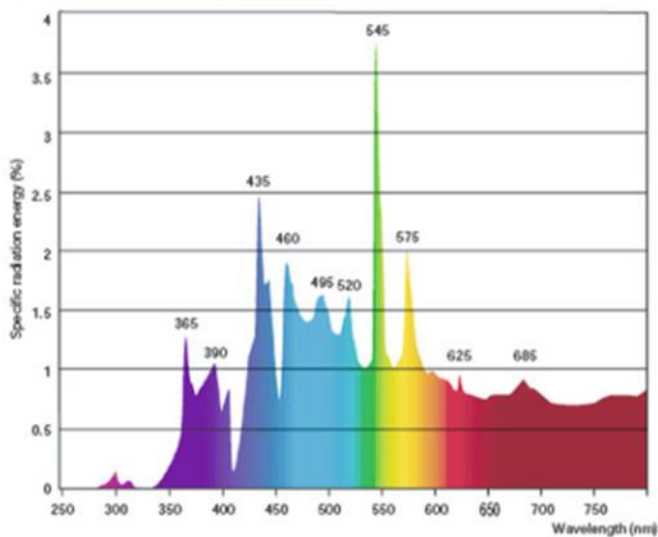


Figure 28 | Spectral characteristics of different light types.

The light intensities are displayed on the Y axis, and the wavelengths on the X axis. Each light type possess its own peaks of intensity through the visible light spectrum.

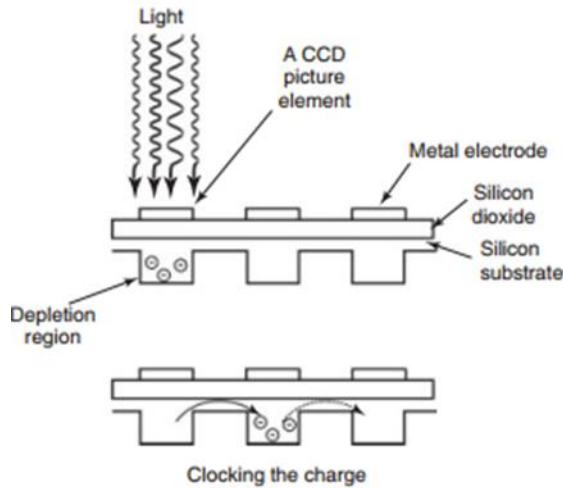
Adapted from Ghiran, 2011

specific value for each pixel (**Figure 29A**). During readout, the incoming light is stopped thanks to a shutter or due to the specific architecture of the array (such as frame transfer or interline transfer architecture (**Figure 29C**)). Finally, the charges of each pixel are transferred one by one -serially- to the amplifier that converts the photoelectrons in a voltage signal (**Figure 29B**). The voltage values obtained for each pixel are further converted into numbers (representative of the voltage value) which are ultimately translated into levels of greys (representing intensity of incident light). Because of the readout process, where pixels values are read one-by-one, CCD are usually slow to acquire images resulting in lower frame per second rate (fps) compared to other camera types. Of note, it is possible to increase the acquisition speed by increasing the rate at which the amplifier converts photoelectron into charges value, but this ultimately leads to an increase of the noise. An improved version of the classic CCD camera is the Electron-Multiplying CCD (EMCCD), which possesses an additional element called the multiplication register. Specifically, the multiplication register will multiply the photoelectrons before their conversion into voltage by the readout sensor. This allows a better sensitivity but introduces a new source of noise called noise factor. In addition, EMCCD usually possess an frame transfer architecture which enables all the photoelectrons stored during image acquisition to be transferred to a frame protected from light, thus allowing faster image acquisition (**Figure 29 C**) (Dobrucki, 2013).

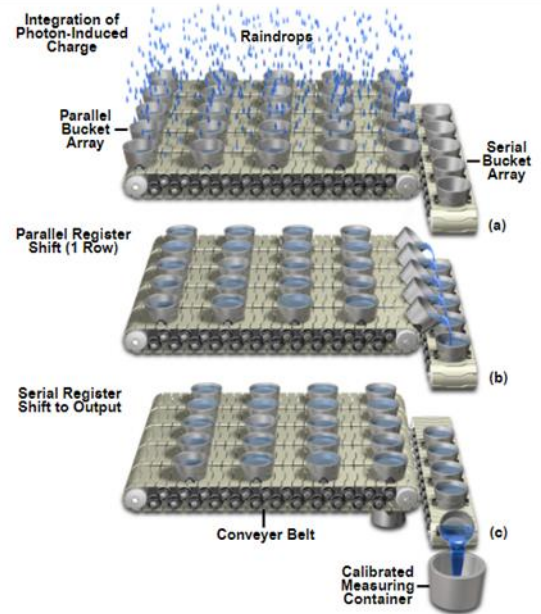
- The other major type of camera is represented by the complementary-metal-oxide semiconductor (CMOS) camera. While the principle of light detection is similar between CCD and CMOS camera (i.e the photoelectric effect), they differ by the specific architecture of their structural element (pixel or photodiode). In CMOS, each photodiode possesses its own amplifiers that converts photoelectron into voltage signal and this specific element is called the active pixel sensor (**Figure 30**). This element allows a very fast frame rate due to the absence of readout time. In addition, CMOS allows the control of individual pixels or group of pixels (imaging of a specific region of interest). The downside is that a big part of the array consists of electronic elements which do not detect incident light. Nonetheless, improvement in technology and implementation of micro lenses in scientific CMOS (sCMOS) made them a choice alternative to CCD camera.

Of note, the sensitivity of a camera is defined by its ability to detect faint signal (low number of photon). Importantly, the light-sensitive element of the camera is not able to produce an electron for every single photon hitting its surface. Thus, the ratio between the number of photons hitting the camera and the number of photons leading to the generation of an electron is called the quantum efficiency. Finally, cameras present the possibility of increasing the time during which the sensitive array is exposed to the incoming light thus, allowing the recording of weak signals. Nonetheless, electrons may occur randomly during image acquisition leading to “false” light

A



B



C

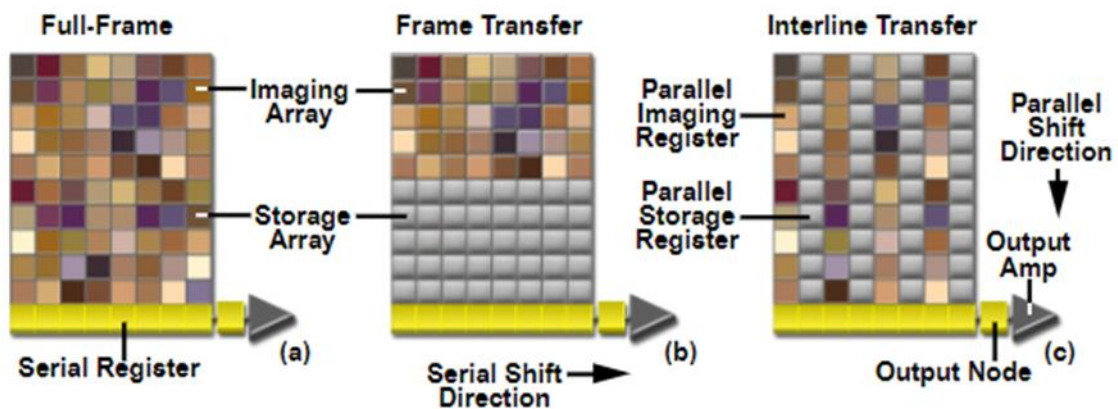


Figure 29 | Charge-coupled device (CCD) camera principle.

- A. Architecture of the CCD camera array.
- B. Conveyor belt analogy for the readout process of CCD camera. The raindrops represent the incoming photons, and the buckets represent the picture elements accumulating the photoelectrons.
- C. Common architecture of CCD arrays. The full-frame model (a) requires a shutter to stop the light recording during readout, while the frame transfer (b) and interline transfer architecture (c) do not.

Images adapted from Dobrucki, 2013 and Hazelwood et al, 2007

signal. As their apparition is stochastic, increasing the exposure time also increases the camera noise.

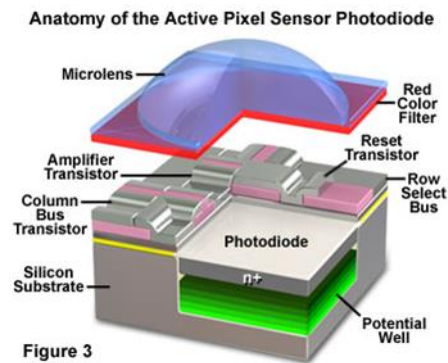


Figure 30 | complementary-metal-oxide semiconductor (CMOS) photodiode.

In a CMOS camera, each photodiode possess all the electronic component allowing the readout of the signal.

Image adapted from <https://www.olympus-lifescience.com/en/microscope-resource/primer/digitalimaging/cmosimagesensors/>

1.3.3.3.2. Confocal microscopy

In a widefield epi-fluorescent microscope, the sample is evenly illuminated by the incident light. Therefore, any part of the sample being under the light beam is emitting fluorescence. This often results in a noisy image. Especially, because the light coming from the unfocused background is reaching the detector. Confocal microscopy allows the removal of the light coming from unfocused parts of the sample, resulting in a lower background. The original idea of confocal microscopy is attributed to Marvin Minsky who had the idea to, 1-focus coincidentally the excitation light and the detected light to decrease the amount out-of-focus light reaching the detector, and 2-scan the sample point by point before reconstructing the image (Nikolaus Naredi-Rainer, Jens Prescher, Achim Hartschuh, 2013). Specifically, the focusing of the light was obtained by the addition of two pinholes: an illumination pinhole located right after the light source, allowing to focus the incident light on a diffraction limited spot, and a detection pinhole, preventing the out-of-focus light to reach the detector. The scanning of the sample was executed by shifting sample under the light beam. Minsky presented a prototype of his confocal microscope in 1958, and patented it 1961 (**Figure 31**) (Nikolaus Naredi-Rainer, Jens Prescher, Achim Hartschuh, 2013). Nonetheless, the general endorsement on the technique occurred in 1987 due to two papers showing that confocal microscopy was greatly improving contrast and resolution compared to classic widefield microscopy. In addition these papers demonstrated that confocal microscopy allows the observation of dynamic processes (Amos et al, 1987; van Meer et al, 1987). Nowadays, technological development has led to the modification of the initial Minsky's prototype. Especially, the use of laser as light source has made the use of illumination pinhole obsolete. In addition, galvanometric mirror which enabled to displace the incident light over the sample instead of moving the sample under the light beam were implemented in confocal microscopes (**Figure 32**). Finally, because the sample is scanned point-by-point, the image acquisition process of a confocal microscope also differs from widefield microscope. Thus, CCD cameras are usually replaced by a photomultiplier tube (PMT), avalanche photo diode (APD) or a mixture between these two technologies named hybrid detectors (HyD). Overall, the differences between a widefield microscope and a confocal microscope can be resumed by the addition of four elements:

- The use of laser as illuminating source. Lasers are producing a collimated light, meaning that all light rays are parallel. The use of additional focusing lenses, allows the incident light to be highly collimated at a specific diffraction limited spot. Of note, lasers are specific to a set of wavelengths, thus confocal microscope scopes are usually equipped with several laser lines to give them the ability to excite fluorophores with different wavelength.
- The pinhole implemented before the detector prevents the light not originating from the focal plane or from the diffraction limited illuminated spot to reach the detectors, resulting in optical sectioning of thin layer of the sample. Of note, pinhole size can be adjusted to increase or reduce the optical sectioning (**Figure 32 A**).

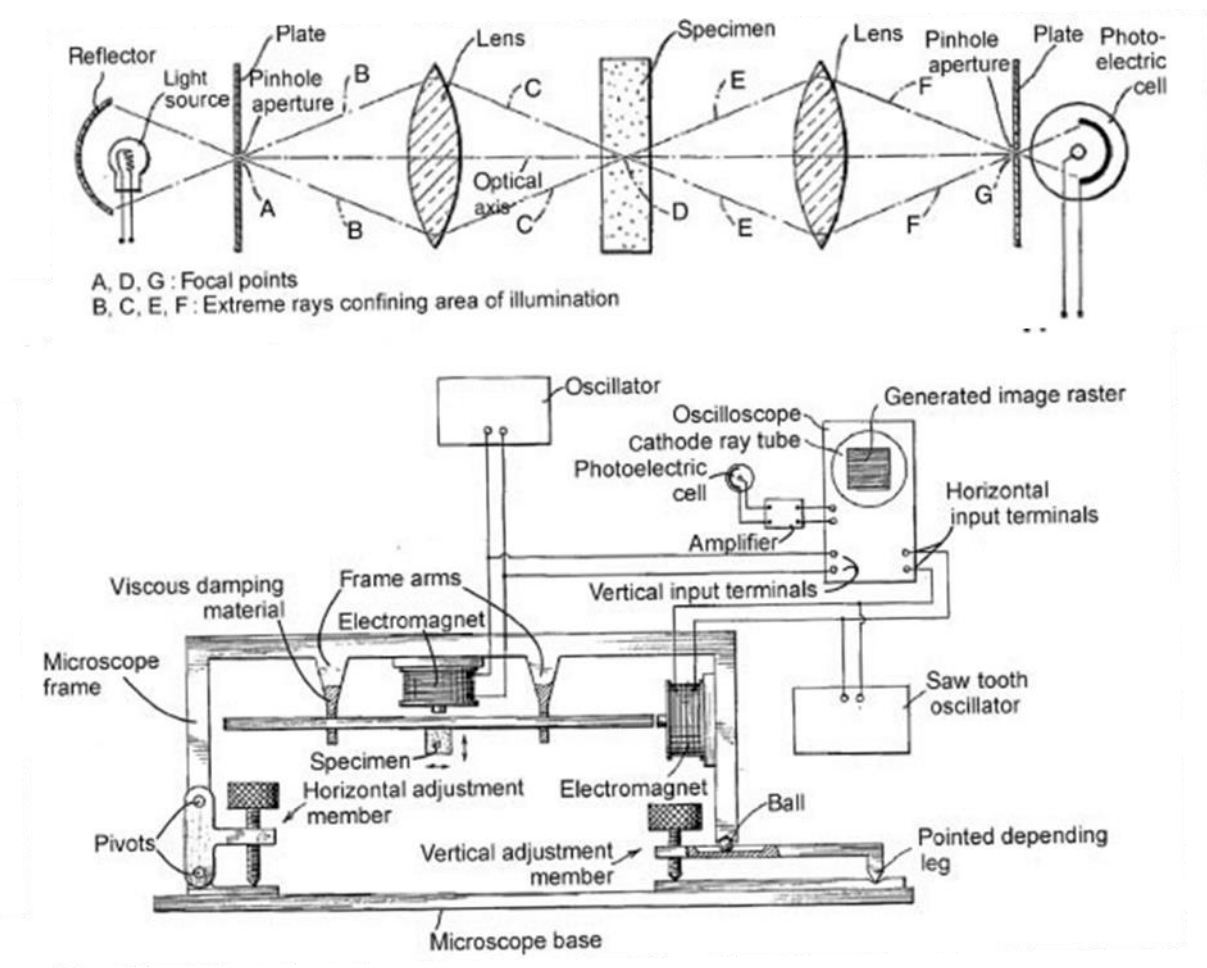


Figure 31 | Original confocal microscope prototype.

The prototype of confocal microscope proposed by Minsky. Top: the optical light path of a confocal, the two pinholes allows to coincidently focus the excitation and the detected light.

Bottom: Scheme of the Minsky scanner confocal

Image adapted from Nikolaus Naredi-Rainer, Jens Prescher, Achim Hartschuh, 2013

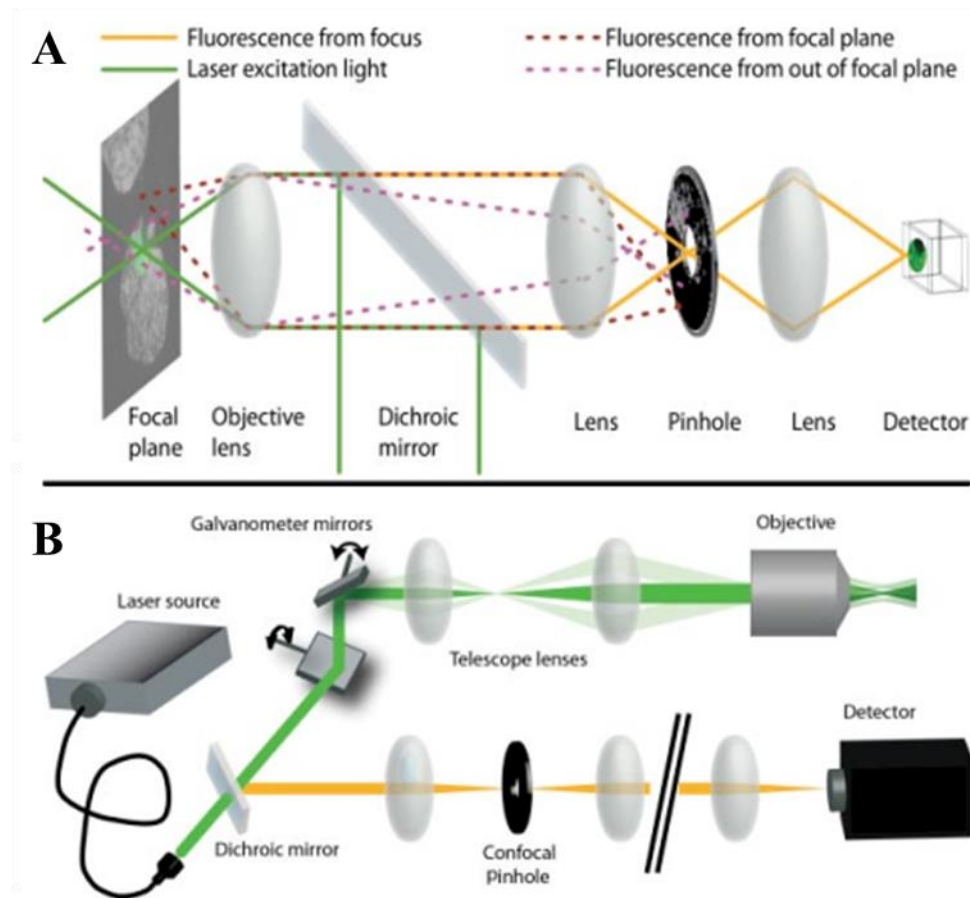


Figure 32 | Principle of confocal microscopy.

- A. Role of the pinhole. The incident light is focused on a specific spot within the sample (green). The fluorescent light originating from this spot passes through the pinhole, while the light originating from adjacent position or from out of focus position is filtered out by the pinhole.
- B. Laser scanning principle. A pair of galvanometer mirror are moving concertedly to allow scanning of the sample in user define pattern/

Image adapted from Nikolaus Naredi-Rainer, Jens Prescher, Achim Hartschuh, 2013

- The galvanometer mirrors are a pair of mirrors which are concertedly vibrating at high speed due to galvanometer motors. These vibrations allow the creation of a scanning pattern leading to the point-by-point scanning of the desired region's sample (**Figure 32 B**).
- The detectors of a confocal microscope possess different characteristic than the camera present on widefield epifluorescence microscopes. Indeed, because the sample is scanned point-by-point, the detector does not require to spatially discriminate the signal but rather respond very quickly to changes light intensity. In addition, since the pinhole restrict the passage of the light originating only from the focal plane, the recorded signals are usually of low intensity. Thus, highly sensitive photon detectors are required in confocal microscope.
 - On the one hand, PMT are amplifying the signal produced when a photon hits its photosensitive surface based on the photoelectric effect. The electrons produced in response to photons detection are accelerated in a vacuum chamber and amplified by a succession of electrodes (called dynodes). The current measured on the last dynode being proportional to the initial light intensity (**Figure 33A**). The advantages of PMT are their rapidity of detection (typical response time of a PMT is in the order of nanosecond) and their ability to detect single photons. However, they tend to be noisy because electrons are produced in the PMT even in the absence of light. In addition, they present a low gain between each multiplication step. Finally, their quantum efficiency is about 30% (Nikolaus Naredi-Rainer, Jens Prescher, Achim Hartschuh, 2013). Of note, confocal microscopes are usually equipped with multiple PMT to allow acquisition of different light wavelength (*i.e* colors).
 - On the other hand, APD, which are also based on the photoelectric effect, are silicon-based photodiode. Specifically, photodiode includes a “pn” junction consisting of two semi-conductor regions positively (p-) and negatively (n-) doped, and a neutral area (depletion region). When a voltage is applied to the semi-conductors the photons hitting the “pn” junction are generating electron-holes pairs which transit to the depletion zone where they generate a flow of electrons and electron holes (avalanche) proportional to the number of incident photons (**Figure 33B**)(Dobrucki, 2013). Of note, single-photon APD (SPAD) are able to detect single photon and are usually equipped on microscope used to perform low-light experiment such as fluorescence lifetime imaging (FLIM) or fluorescence correlation spectroscopy (FCS).
 - Finally, hybrid combination of both technologies allows to overcome their specific limitations (low gain for PMT, and restriction to lows signals for APD).

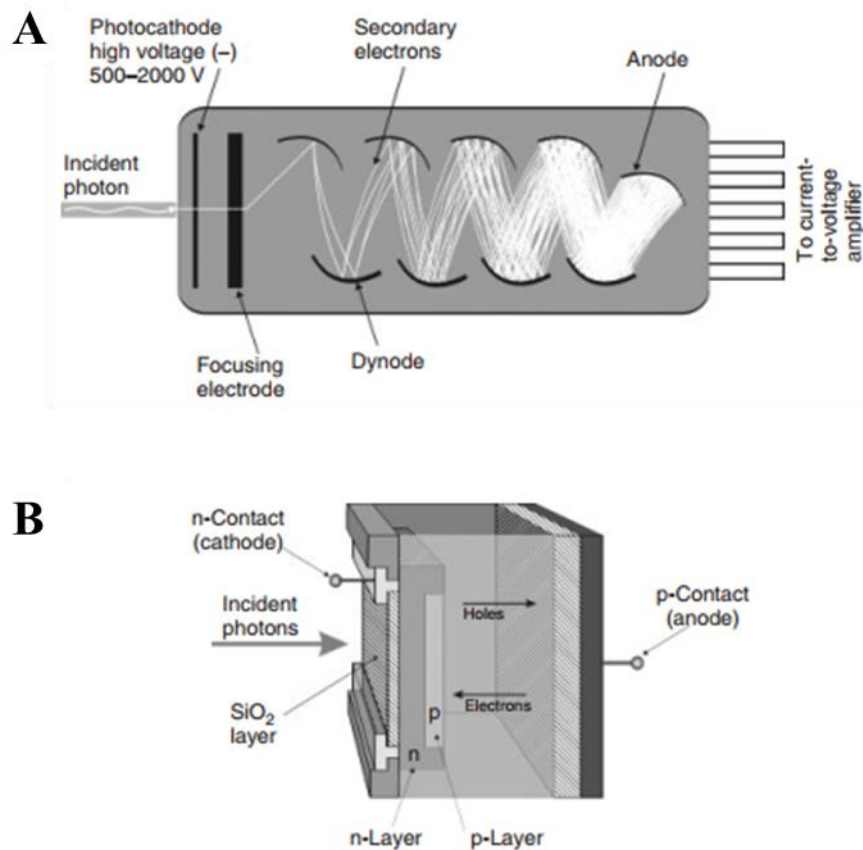


Figure 33 | Confocal microscope detectors.

- A. Photomultiplier (PMT). A PMT amplifies the signal created by the detection of photons due to acceleration of the incident electrons onto the dynode which leads to the creation of secondary electrons proportional to the incident electrons.
- B. Avalanche photodiode (APD). APD uses the properties of semi-conductor materials to generate electron-holes pairs amplifying the original signal.

Image adapted from Dobrucki, 2013

Overall, confocal microscopy produces high signal to noise ratio (SNR) and provides good resolution only limited by the light diffraction barrier. However, because the image is constructed point-by-point through the sample's scanning, the speed of image acquisition is limited (around 10 frames by second), thus limiting its application for live cellular process of fast kinetic.

1.3.3.3. Total internal reflection fluorescence (TIRF) microscopy

As mentioned above, widefield fluorescence microscopy suffers from an important noise due to out-of-focus light reaching detectors. TIRF microscopy allows to drastically decrease out-of-focus light by taking advantage of a specific light property indicating that light rays can be totally reflected at the interface between two media displaying different refractive indexes when shined at a specific angle. This technique allows break of the diffraction limit of the light, and to significantly improve the SNR of widefield microscopes. Specifically, in biological application a light beam is shined at a specific angle toward two media possessing different refractive indices represented by the glass bottom petri dish and the cell's media. The specific angle allowing total reflection is called the critical angle. Importantly, the reflection of the light beam is accompanied by the creation of a very thin evanescent wave that diffuses towards the cell medium for 60 to 200nm (below the light's diffraction limit) (**Figure 34A**). Thus, in biological application, TIRFm allows the specific excitation of fluorescent molecules located right above the bottom of the dish and thus, this technique is especially suited for the observation of membranes proteins. The main difference between TIRF microscopes and classic widefield fluorescent microscope, is the obligation to shine the light on the sample through a specific angle. As for classic widefield microscopy, the excitation light passes through directly from the objective. However, critical angle of illumination is obtained by deviating the laser from the center to the sides of the objective back focal plane (**Figure 34B**). Thanks to this deviation, the incident angle of the light beam can be controlled and adjusted the critical angle. Of note, the modulation of the deviation level from the back focal plane, allows to adjust the illumination angle, and thus allow an easy transition from widefield to TIRF modality. In addition, surpassing the critical angle induces a lower penetration of the evanescent wave in the sample and thus reduced the depth of illumination. In order for the angle of incidence to be greater than the critical angle TIRFm objective should present a $NA > 1.45$. Finally, while lasers are preferentially used to perform TIRFm, arc lamp can be used but requires the addition of mask in incidental optical path. Overall, TIRFm possess the advantage of both, widefield microscopes (speed of acquisition), and confocal microscopes (good SNR and optical sectioning). Nonetheless, it is limited to region illuminated by the evanescent wave, and thus its use is usually restricted to imaging and studying of membrane proteins.

1.3.3.4. Summary of the advantage and limitations of fluorescence microscopy techniques

We have seen above that each microscopy technique presents its own advantages and limitations. For example, widefield microscopy allows the study of fast and dynamic processes due to its rapidity in

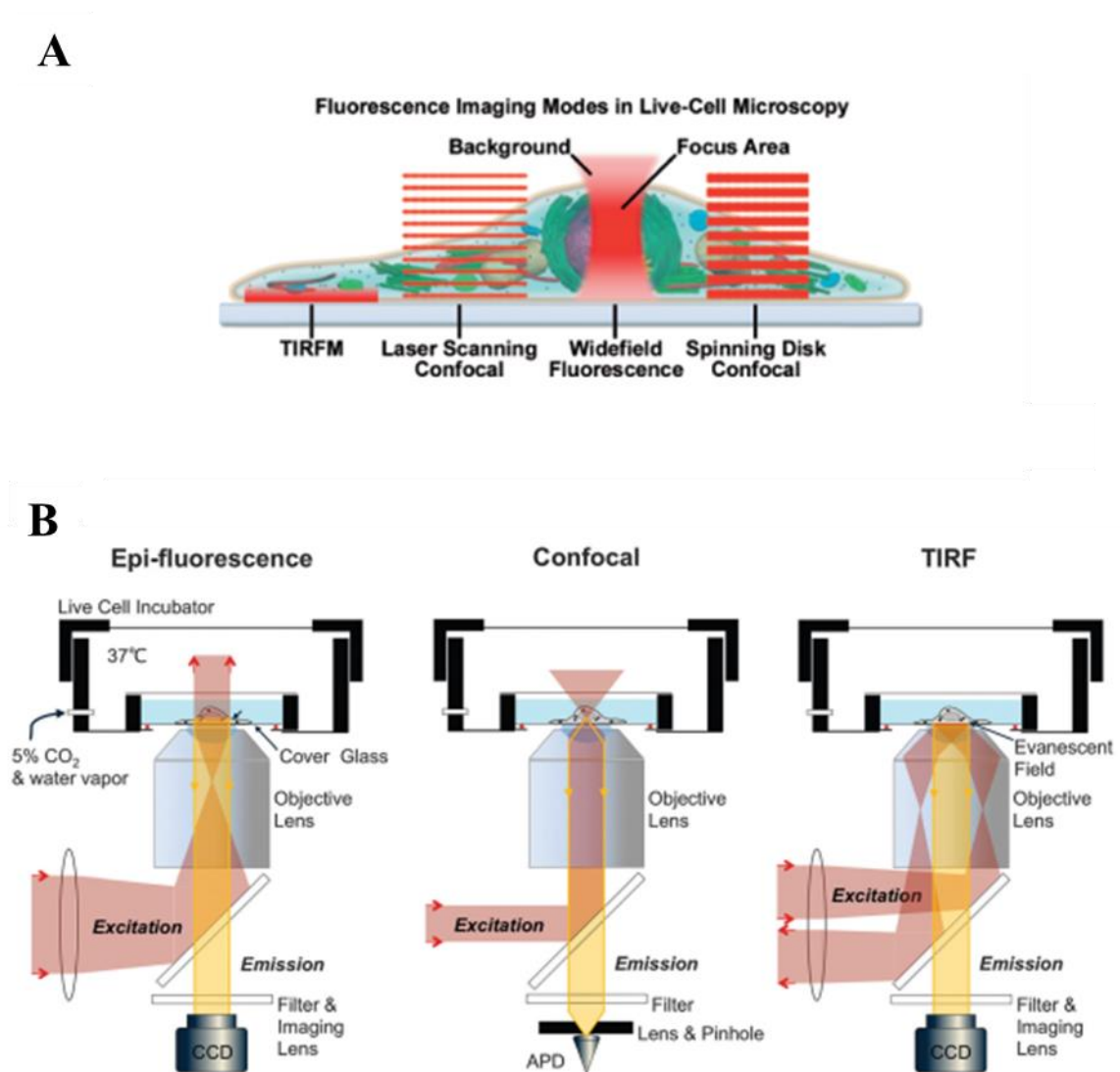


Figure 34 | Comparison between widefield, confocal, and total internal reflection microscopy (TIRF) techniques .

A. Representation of the excitation volume of different microscopy techniques.

B. Comparison of the light paths in widefield, confocal, and TIRF microscopy.

Image adapted from Park et al, 2015; Hazelwood et al, 2007

image acquisition, while confocal microscopy, allow the detection of faint signal and better resolution, but is slower in acquiring images. In the meantime, TIRFm present a good SNR and as well as a fast image acquisition but is restricted to phenomenon occurring within the few hundred of nanometers following the PM. Thus, all these techniques have allowed the visualization and the description of different cellular processes. Importantly, a variety of theses microscopy techniques have been used to describe the properties of ORAI protein and will be discussed below.

1.3.4. Study of properties of ORAI proteins with microscopy techniques

The specific features of ORAI channels, made them good subjects to be studied with microscopy techniques. For example, because CRAC channels is Ca^{2+} selective, the SOCE activation was studied with Ca^{2+} imaging techniques using chemical dyes or genetically encoded Ca^{2+} indicators (GECI). Additionally, the PM localization of ORAI channels as well as the clustering they undergo following SOCE activation has been assessed due to TIRF, fluorescence correlation spectroscopy (FCS) and single particle tracking (spt-) microscopy techniques. Finally, FRET microscopy as well as bimolecular fluorescence complementation (BiFC), were also used to study the interactions between ORAI and STIM proteins, but also the interactions within ORAI homologues (homo- and heteromeric channels formation).

1.3.4.1. Calcium entry

The main physiological function of the CRAC channel is to provide Ca^{2+} entry in the cells following SOCE activation. Since Ca^{2+} is a crucial second messenger involved in a myriad of cellular processes, several techniques were elaborated to measure its concentration inside the cell. Importantly, Ca^{2+} concentration is tightly regulated in the cell and its concentration is modulated depending on the stimulation received by the cell. Thus, several dyes were developed to enable the measurement of Ca^{2+} concentration in the cell with widefield fluorescence microscopy. On the one hand, measuring the absolute Ca^{2+} concentration (or any other compound) using fluorescent dyes is an extremely complex task due to the existence of several factor that might affect the fluorescent properties of the dyes independently from the Ca^{2+} concentration such as local dye concentration variation, dye leakage, changes in cell volume, and variations in illumination conditions between experiments. On the other hand, ratiometric dyes enable the evaluation of relative Ca^{2+} concentration independently of the aforementioned limitations. As such they are commonly used for in Ca^{2+} imaging studies. Structurally, chemical Ca^{2+} dyes are derived from Ca^{2+} chelators (Paredes *et al*, 2008). Especially, BAPTA (bis(2-aminophenoxy) ethane tetraacetic acid) derived structures are the most common because of its high Ca^{2+} affinity and selectivity over Mg^{2+} , and fast kinetic of Ca^{2+} binding and release. Importantly, excitation or emission spectra of ratiometric Ca^{2+} dyes are modified upon Ca^{2+} binding. Several dyes exists but Fura-2 is one of the most popular and thus its properties will be described below. In addition, several GECI were developed to study local Ca^{2+} variation, they will be described thereafter.

1.3.4.1.1. Ca^{2+} imaging with Fura-2

Fura-2 was developed by Tsien's team and shares common structural elements with BAPTA (**Figure 35**) (Grynkiewicz *et al*, 1985). This compound is hydrophilic, and cannot naturally cross the cell's PM. Thus, to facilitate its incorporation in cells, the commercially available form of Fura-2 possesses an additional acetoxymethyl (AM) ester allowing its diffusion through the PM inside the cell. Importantly, once internalized, the AM ester group bound to Fura-2 is cleaved by intracellular esterases and thus traps the dye inside the cell. Fura-2 affinity for Ca^{2+} is similar to endogenous Ca^{2+} levels (K_d 145mM). In addition, in its Ca^{2+} free state Fura-2 is excited at 380nm while its Ca^{2+} bound state excitation peak is at 340 nm. The fluorescence emission peak is around 500nm independently from its Ca^{2+} bound status (**Figure 36**)(Grynkiewicz *et al*, 1985; Paredes *et al*, 2008). Finally, due to its ratiometric properties, a simple normalization of fluorescence intensity acquired in Ca^{2+} bound state (340nm) versus Ca^{2+} free state (380nm) allow comparison between cells and between experiments (Paredes *et al*, 2008). If the first calcium experiments conducted with the aim of identifying ORAI as effector of SOCE were performed with the non ratiometric dye Fura-5F (Mercer *et al*, 2006a), several subsequent publications successfully used the ratiometric Fura-2 dye to observe Ca^{2+} entry induced by ORAI channel opening. For example, Forsell and al., performed Ca^{2+} measurement using Fura-2 dye and demonstrated that D vitamin was inducing SOCE in human enterocytes (Forsell *et al*, 2006). In line with these results, Barritt *et al*., confirmed by using a combination of Ca^{2+} imaging technique as well as patch clamp recording that SOCE in rat liver cell is provided by ORAI proteins (Barritt *et al*, 2009). In addition, Ca^{2+} imaging techniques were useful in the identification of pharmacological compounds altering SOCE entry. For instance, it was shown that pyrazole compounds enable the selective activation of either SOCE or receptor activated Ca^{2+} entry (ROCE) (Schleifer *et al*, 2012). Of note, evaluation of pharmacological activators of SOCE with Ca^{2+} imaging using Fura-2 were also successfully performed in animal tissue such as retinal rat arteriolar smooth muscle (McGahon *et al*, 2012). Finally, Ca^{2+} imaging techniques were also used to demonstrate that the modulation of ORAI expression affects the SOCE level which in turn modifies cell physiological properties (Abdullaev *et al*, 2008; Diez-Bello *et al*, 2017; Dubois *et al*, 2014c). To conclude, Ca^{2+} imaging in general is a very versatile tool used routinely to measure Ca^{2+} entries in cells or tissues. However, chemical dyes do not allow to target specific region since the dye is free in the cytoplasm. This is one of the reasons that lead to the creation of genetically encoded Ca^{2+} sensor that could be specifically targeted to subcellular regions or compartments.

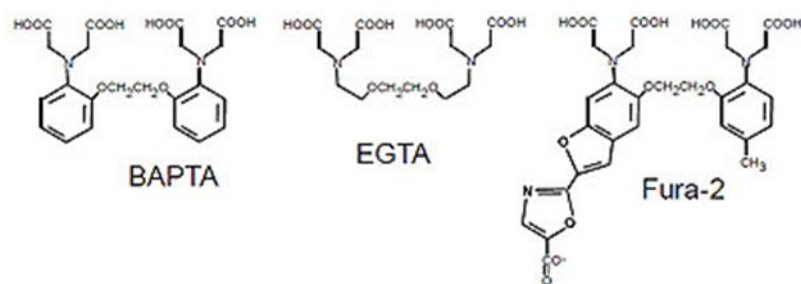


Figure 35 | Structure comparison between different Ca^{2+} chelators and Fura-2.

The Fura-2 structure is derived from the structure of Ca^{2+} chelators such as BAPTA and EGTA

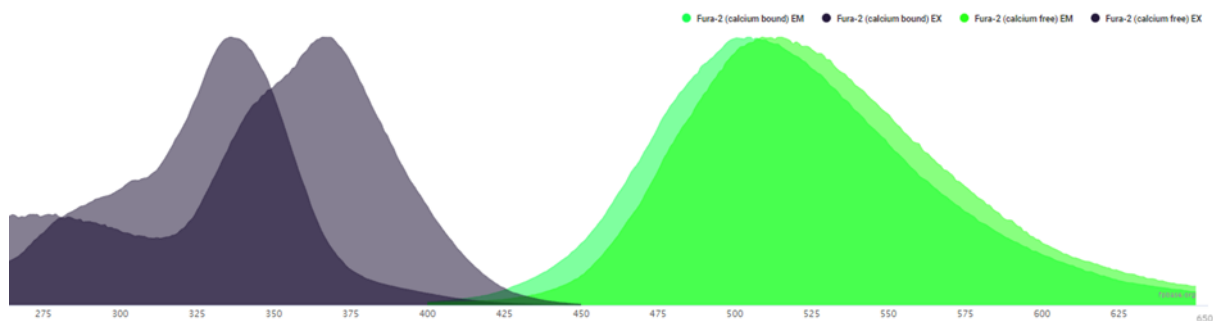


Figure 36 | Excitation and emission spectra of Fura-2 in Ca^{2+} -free and Ca^{2+} bound-states.

The Ca^{2+} -free Fura-2 excitation peak is located around 340 nm, while the peak excitation for the Ca^{2+} -bound form is located around 380 nm. The emission peak is located around 500 nm for both forms.

Graph generated from Fpbase (<https://www.fpbase.org/spectra/>)

1.3.4.1.2. Ca^{2+} imaging with genetically encoded Ca^{2+} indicators (GECI)

GECI were developed to address the main limitations of chemical Ca^{2+} dyes namely, the difficulty to target specific intracellular region and to observe calcium signal within living animals. GECIs are engineered fluorescent or luminescent proteins with the ability of binding Ca^{2+} . Due to the fusion of GECI to specific tags or addressing signal they can be targeted to specific organelles. In addition, since they are genetic tools, they allow the creation of transgenic animals allowing the monitoring of Ca^{2+} fluctuation within their tissues (Suzuki *et al*, 2016a) (Redolfi *et al*, 2021). One can distinguish three classes of GECI: bioluminescent probes derived from aequorin, single-fluorescent protein probes such as GCaMPs, and FRET-based probed. Importantly, members of the GCaMP family were fused to ORAI proteins allowing the observation of Ca^{2+} signals induced by their specific opening. GCaMP proteins are based on chimeric construct including the GFP sequence, a partial calmodulin sequence and a M13-peptide sequence. The development of GCaMP proteins was allowed due to the discovery made by Tsien's team that rearrangements within GFP structure were changing its ability to fluoresce. Specifically, they demonstrates that circularly permuted GFP (cpGFP), a construct where the C-terminal and N-terminal of the GFP are inverted (the protein sequence starts with the C-terminal sequence and finishes by its N-terminal7), can reconstitute the fluorescent GFP chromophore following a conformational change (Baird *et al*, 1999). Fusion of the M13 peptide (i.e., the binding domain of Ca^{2+} -calmodulin, a 13 amino acid sequence issued from the myosin light chain kinase), and N-terminal segment of Calmodulin (a ubiquitous Ca^{2+} binding protein) on each extremity of cpGFP enables, following Ca^{2+} detection, the induction of a conformational change reconstituting the original structure of the GFP protein. The reconstituted structure of GFP allows the formation of the classic β -barrel structure where the formation of chromophore is allowed (**Figure 37**) (Nakai *et al*, 2001). Thus, following Ca^{2+} detection GFP fluorescence intensity increases drastically. Successive rounds of genetic engineering led to specific improvement of the properties of GCaMPs, such as increase of their dynamic range (the ratio of the lowest fluorescent signal to the highest one), or refinement of their calcium affinity and kinetics, leading to the generation of a whole palette of GCaMPs with different properties allowing their use in several different applications (Redolfi *et al*, 2021). Interestingly, fusion construct associating ORAI to GCaMP were used to monitor the localization and specific activity of channels formed by ORAI. Specifically, Dynes *et al*. revealed that optical recordings of calcium entry through single ORAI channels were possible (Dynes *et al*, 2016a, 2020). This ability was further confirmed by other teams (Maneshi *et al*, 2020; Son *et al*, 2020). Additionally, constructs associating ORAI3 and GECO (red-shifted equivalent of GCaMP) were also used to visualize specific Ca^{2+} entry du to Orai3 channels in rat neonatal cardiomyocytes (Gammons *et al*, 2021), and to demonstrate the absence of ARC channel in breast cancer cell despite the expression of all its components (Cantonero *et al*, 2020).

A



B

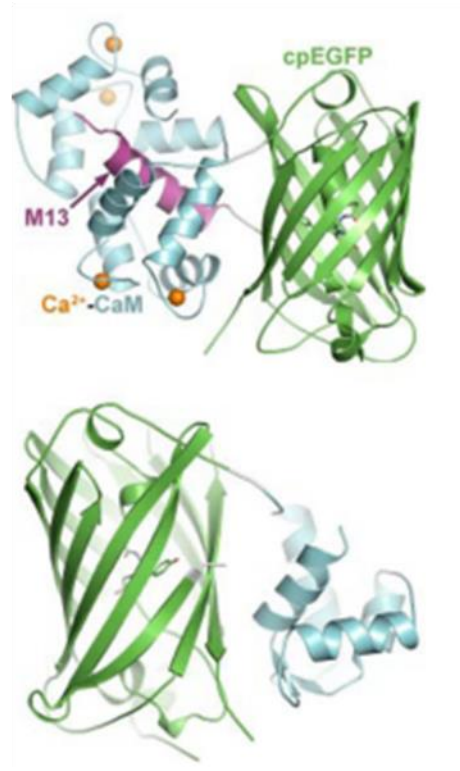


Figure 37 | Structure of GCaMP.

- A. Schematic representation of the GCaMP fusion protein, including the 13 amino acids from the myosin light chain kinase (M13, light blue), the circularly permuted eGFP sequence (green), and the the N-terminal extremity of the calmodulin protein (CaM, violet). Of note, linker sequences between each fusion are omitted.
- B. Three-dimensional structure of the GCaMP in the presence (top) and absence of Ca^{2+} (bottom), with the same color coed as above for each fragment.. Note that in the absence of Ca^{2+} , the GFP chromophore is not reconstituted

Modified from Akerboom et al, 2009

1.3.4.2. Localization and diffusion properties of ORAI proteins

1.3.4.2.1. Usage of TIRF microscopy

TIRF microscopy (TIRFm) allows the specific illumination of extremely thin space above coverslip that correspond to the evanescent field, and which includes around 200 nanometers above the PM. Therefore, this technique is particularly well suited for the study of membrane proteins. Thus, it is not surprising that ORAI channel properties were investigated using this method. In fact, following the identification of SOCE components, combination of TIRFm and patch-clamp techniques revealed that STIM and ORAI were in close proximity in during CRAC activation. The detection of ORAI1 through TIRFm was not a surprise since it was quickly identified as a PM protein. Nonetheless, the detection of both STIM and ORAI due to TIRFm confirmed the hypothesis that STIM was specifically located in the ER-PM junctions following Ca^{2+} store depletion. (Luik *et al*, 2006; Mercer *et al*, 2006a). Later, other studies tried to use TIRFm microscopy to elucidate the stoichiometry of ORAI protein through single molecule photobleaching (Demuro *et al*, 2011). Importantly, when fluorescent proteins are exposed to an exciting light of strong intensity, or for a long period of time, the atomic structure of the chromophore becomes altered resulting in the abolition of light emission called bleaching. This process was used in order to identify the number of “steps” required to fully extinct the fluorescence of a single CRAC channel and thus extrapolate the stoichiometry of the channel (**Figure 38**). While this technique has been used several times to determine stoichiometry of other ion channels (Yamamura *et al*, 2015), its use to determine the stoichiometry of the CRAC channel did not allow to demonstrate a hexamer stoichiometry. In fact, studies concluded on the existence of dimers of ORAI1 in non-active channel and of tetramers in activated channels (Ji *et al*, 2008b; Penna *et al*, 2008; Demuro *et al*, 2011). These results argue with the hexameric stoichiometry observed in dORAI1 crystallography and cryo-EM. These divergences might be explained by the difficulty of analyzing photobleaching steps for high oligomeric structures due to the different types of photobleaching (reversible vs irreversible), and the presence of endogenous non-tagged ORAI protein in these studies. Nonetheless, it is interesting to note that transitions from dimeric to tetrameric states were observed following SOCE activation, suggesting the existence of dynamic associations between ORAI proteins. Noteworthy, TIRFm has also been used to study interaction within ORAI homologs (Alansary *et al*, 2015; Inayama *et al*, 2015a), as well as with STIM protein (McNally *et al*, 2013). Finally, TIRFm confirmed that ORAI proteins can be located in vesicles under PM (Hodeify *et al*, 2015; Wu *et al*, 2021).

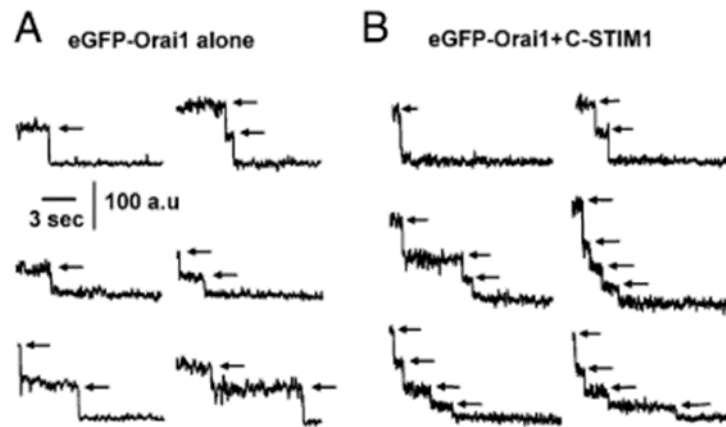


Figure 38 | TIRF photobleaching of CRAC channel.

- A. Fluorescence intensity decay of diffraction limited spots in cells transfected with ORAI1 fused to eGFP. The number of steps required before reaching the background fluorescent level indicates on the number of ORAI-eGFP units within the illuminated spot.
- B. Same as A, in cells transfected with STIM1 in addition of ORAI1-eGFP. Note that the number of steps increases between A and B.

Modified from Demuro et al, 2011

1.3.4.2.2. Usage of FRAP and FCS

One of the specificities of ORAI channels is the clustering they undergo following their activation by STIM. Specifically, ORAI are trapped and gathered by STIM following SOCE activation, and this mechanism has been studied due to microscopy techniques. In fact, fluorescence recovery after photobleaching (FRAP) and FCS are two techniques aiming to study the diffusion properties of proteins. In addition, they are widely used to study membrane proteins because these proteins present the advantage of diffusing in only 2 dimensions, while cytosolic protein are diffusing in 3 dimensions which complexify the analysis process of their diffusion properties. For these reasons, the mobilities of the SOCE components were studied with such techniques. The first studies using FRAP techniques were mainly focusing on STIM1 protein, and the results obtained led to the hypothesis that STIM activation was gradual and could be separated in several steps (*i.e.*, oligomerization, diffusion to ER-PM junctions, binding on ORAI1 and activation of CRAC channel) (Liou *et al*, 2007; Covington *et al*, 2010). Further, studies focusing on the ORAI protein demonstrated that they were in majority diffusing in the PM and that the simple binding of STIM1 CAD/SOAR was decreasing their mobility. This result was at the basis of the hypothesis suggesting the bind and trap model for the STIM1-activation of CRAC channels (**Figure 39**) (Park *et al*, 2009a). Additionally, some FRAP experiments are performed in TIRF modality to obtain a better SNR. Thus, while studying ORAI diffusive properties with FRAP technique, Madl *et al.*, took advantage of the TIRF modality to demonstrate that ORAI1 localization was not limited to PM but also existed in cytosolic vesicles that could be integrated in the PM (Madl *et al*, 2010a). In addition to FRAP, fluorescence correlation microscopy (FCS) techniques have also been used to study the behavior of ORAI and STIM. FCS technique allows the specific study of the diffusive properties of single molecules within the confocal volume (*i.e.*, the cellular volume being illuminated by the laser beam of the confocal microscope). Especially, this technique is based on the level of fluorescence intensity fluctuations observed in the restricted area of a confocal volume. The correlation of the fluorescence intensity signal over time allow to establish the diffusion properties of the observed molecules. This technique was used in TIRF modality to show that cholesterol level within PM was affecting the ORAI1 diffusive behavior. Specifically, this study demonstrated that reduction of plasmalemmal cholesterol induces internalization of ORAI prior to SOCE activation, thus decreasing SOCE level. In addition, the authors also demonstrated that cholesterol depletion from PM alters the diffusion of ORAI1 protein. Indeed, in normal condition (*i.e.*, non-cholesterol depleted) ORAI1 was mostly diffusive within confined compartments, while following cholesterol depletion from PM, the proportion of ORAI residing in confined structure was drastically reduced (Bohórquez-Hernández *et al*, 2017). These findings were confirmed by Qin *et al*, through the use of single particle tracking (spt-) techniques and simulations (**Figure 40**)(Qin *et al*, 2020). Another study using combination of super resolution techniques, FRAP, TIRFm and electron microscopy claimed that STIM and ORAI are

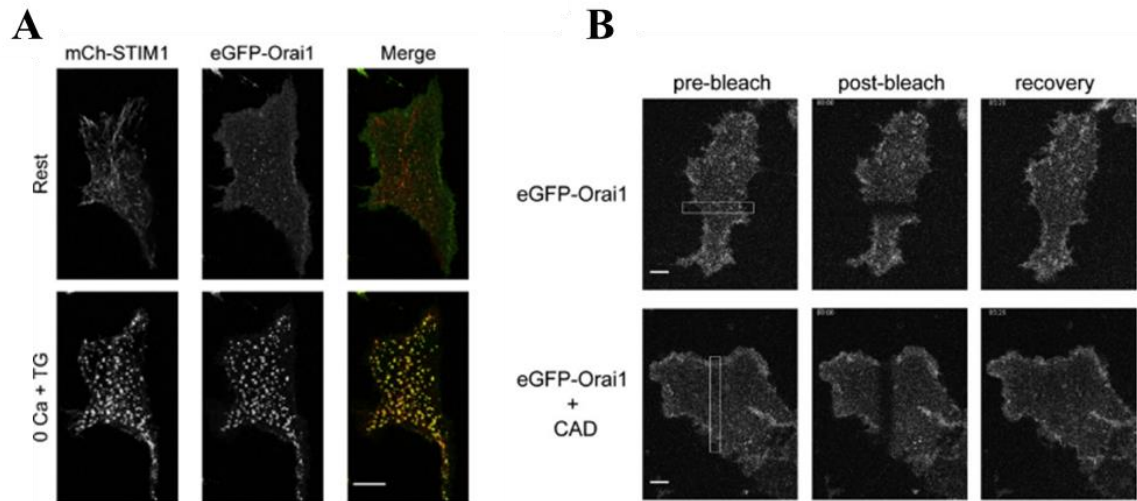


Figure 39 | STIM1-activation of CRAC channel traps and binds ORAI1 protein.

- A. Confocal images of HEK-293 overexpressing mCherry-STIM1 and eGFP-ORAI1 protein before and after store depletion by thapsigargin (TG)
- B. Fluorescence recovery after photobleaching (FRAP) experiment performed on HEK-293 expressing eGFP-ORAI1 and STIM1-CRAC-activating domain (CAD).

Modified from Park et al, 2009

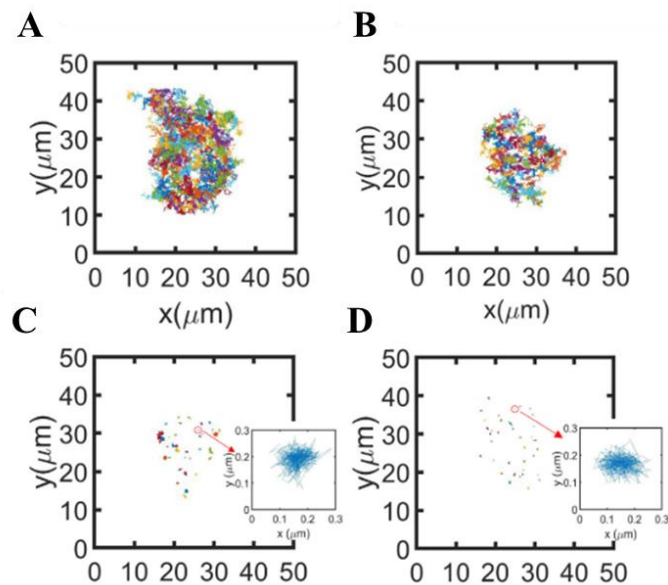


Figure 40 | Store depletion reduces the mobility of ORAI1 and STIM1.

Representative trajectories acquired during single particle experiment for

- A. ORAI1-GFP before store depletion
- B. ORAI1-GFP after store depletion
- C. STIM1-GFP before store depletion
- D. STIM1-GFP after store depletion

Blue inserts are zoomed trajectories of STIM1-GFP.

Modified from Qin et al, 2020

interacting through the unimolecular model where one STIM dimer interacts with ORAI units of distinct SOCE channels leading to cross linking of these channels. In addition, they confirmed that crosslinked CRAC channels were displaying different mobilities compared to the non-activated channels. Of note, they also suggested that addition of fluorescent tag in C-terminal extremity of ORAI1 might create a steric hindrance preventing the detection of unimolecular model but not affecting the ORAI1 function (Zhou *et al*, 2018a).

1.3.4.2.3. Usage of super resolution microscopy techniques

1.3.4.2.3.1. Principle of single particle tracking technique.

Following the initial studies using FRAP microscopy, new details on the ORAI-STIM coupling and motility were revealed using more advanced microscopy techniques such as super resolution microscopy. In fact, early TIRFm studies investigating ORAI oligomerization through photobleaching steps could be defined as super resolution microscopy as they enabled the imaging of single channels and single ORAI molecules. Nonetheless, more sophisticated super resolution techniques such as single particle tracking were applied to the SOCE components only recently. In fact, the identification and development of photoactivable and photoswitchable FP greatly contributed to the development of single particle tracking technique. Importantly, photoactivable FPs are able to undergo a switch from a dark state (unable to provide fluorescence) to a bright state due to UV illumination (Henderson *et al*, 2009), and photoswitchable FP see their emission spectra switched after being illuminated by UV light (Wiedenmann *et al*, 2004). In fact, single particle tracking techniques rely on the sequential illumination of fluorophores within a sample to allow their individual localization. Specifically, if one manages to illuminate a single fluorescent particle, the observed result is a diffraction limited dot (roughly a 200nm diameter dot) within the image. Nonetheless, the 3D shape of this diffraction limited spot is known and corresponds to the point spread function (PSF). Mathematical operation performed on the PSF such as deconvolution and fitting of Gaussian equation according to the shape of the PSF enables to localize precisely the origin of the light signal (**Figure 41**). On the one hand, single particle modality can be achieved with classic FP, however it is limited to region where single molecules are located within a diffraction limited region. Of note, this configuration is usually hardly reachable because protein needs to be expressed at a low level. Nonetheless, some strategies inducing photobleaching of molecule until reaching a low concentration of the fluorescent protein were successfully used. On the other hand, the proportion of detectable photoswitchable and/or photoactivated FP can be modulated through modification of the intensity of the switching light (UV light) and thus eases the obtention of images where single molecules are localized within a diffraction limited space (Manley *et al*, 2010). The use of these specific FP allowed the development of the single-particle tracking photoactivated localization microscopy (sptPALM), which allows the obtention of information about the behavior of studied molecules (Bayle *et al*, 2021).

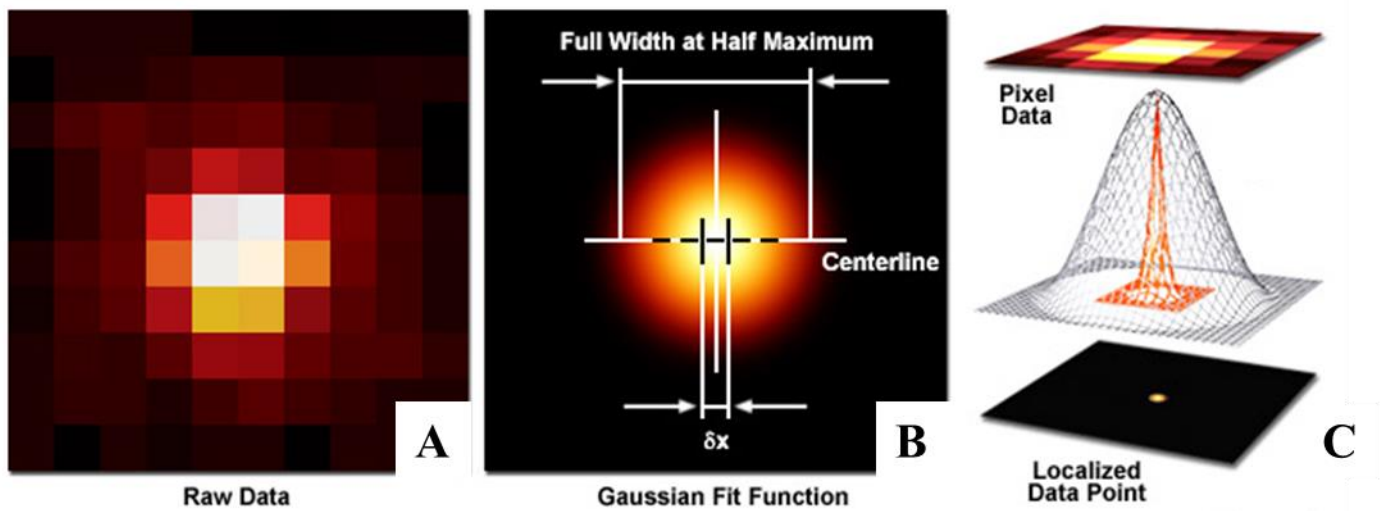


Figure 41 | Fitting a single molecule signal to obtain the fluorescent protein localization.

- A. A single molecule signal acquired during fluorescent microscopy equipment.
 - B. Fitting of a Gaussian function to the experimental data.
 - C. Representation of the method allowing the localization of the initial fluorescent protein
- Modified from <http://zeiss-campus.magnet.fsu.edu/print/superresolution/palm/practicalaspects-print.html>.*

1.3.4.2.3.2. Single particle tracking of STIM and ORAI

Tracking of ORAI1 and STIM1 single molecules before and after ER Ca^{2+} depletion enabled the refining the mechanisms describing their interactions and diffusion. For example, Wu and al., confirmed that STIM1-ORAI1 complexes are trapped in ER-PM junctions but also revealed that even after store depletion mobile fraction of ORAI1 and STIM1 are still present. Furthermore, they indicated that STIM1-ORAI1 complexes are dynamic assemblies and that ORAI1 and STIM1 molecule are able to diffuse between mobile and immobile pools (Wu *et al*, 2014). In 2016, Li et al., used the photoswitchable FP mEOS fused to ORAI1 to study the oligomerization level of ORAI1 proteins in cells originating from ORAI1 KO mice. They showed that under resting condition ORAI1 are mainly dimeric and that following SOCE activation their stoichiometry evolves up to hexameric assemblies (**Figure 42**). In addition, they show that a cytosolic protein, α -SNAP, is modulating the assembly of ORAI proteins channel and the interaction between ORAI channel and STIM protein. Finally, they concluded that ORAI channels might be assembled on site due to a mechanism involving α -SNAP protein, and suggested that these assembly is dynamic depending on the stimuli received by the cell (Li *et al*, 2016b).

1.3.4.3. Protein-protein interactions

Another specificity of ORAI proteins is their mode of activation through the interaction with STIM. In addition, ORAI proteins are also interacting within themselves to form functional channels and some data are suggesting the existence of dynamic processes in the assembly of the ORAI channels. Once again, investigation of protein-protein interactions in living cells can be investigated with microscopy techniques. Especially, FRET is considered as the main microscopy method allowing the study of protein-protein interactions, and as such has been used to study and demonstrate the existence of interactions within ORAI proteins and between STIM and ORAI. Nonetheless, other microscopy techniques also demonstrated their interest in the study of protein-protein interactions such as the bimolecular fluorescence complementation (BiFC) that has been used to study the interaction between SOCE components.

1.3.4.3.1. Usage of Bimolecular fluorescence complementation (BiFC)

BiFC is based on ability of circularly permuted FP to reconstitute their intact structure and thus produce fluorescence. Specifically, BiFC refers to the fact that a given FP split in the middle of its sequence in two individual fragments can assemble when brought in close proximity and reconstitute the chromophore of the FP. Therefore, by fusing the circularly permuted fragments to different protein of interest, one can assess their interaction level depending on the fluorescence displayed by the split FP (**Figure 43**) (Kodama & Hu, 2012). This technique presents the advantage to be relatively simple to

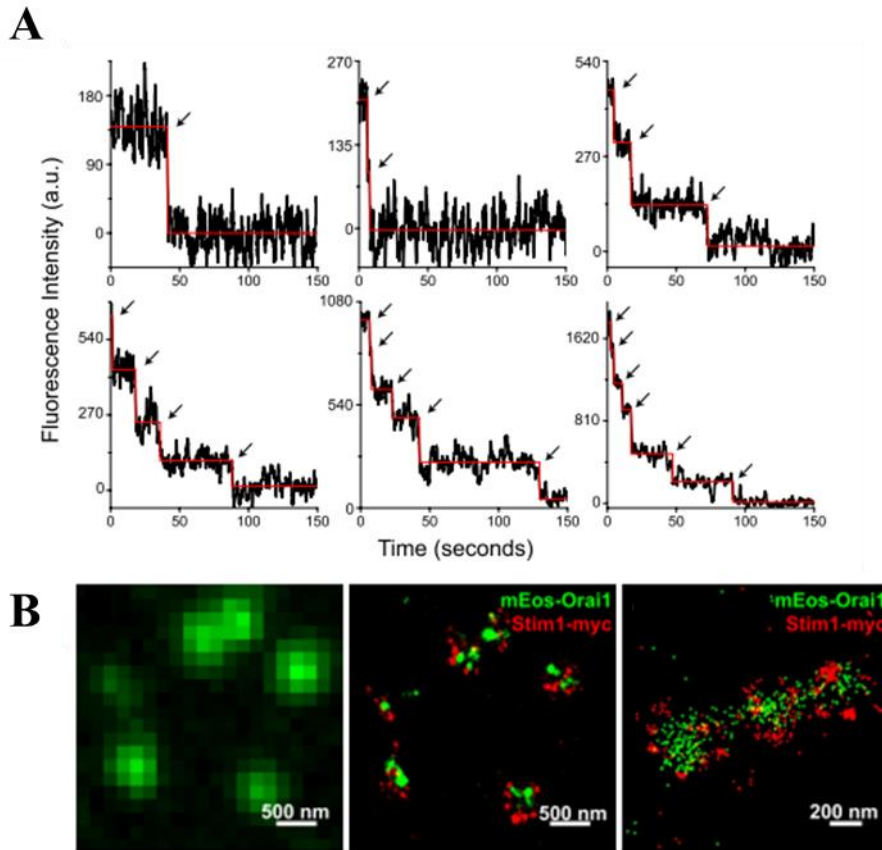


Figure 42 | Single particle experiment performed in ORAI1 and STIM1 proteins.

- A. Photobleaching steps experiment performed with mEOS-ORAI1 fusion protein.
- B. STIM1, ORAI1 and are co-clustering. Top row: images of classic confocal image of mEOS-ORAI1 (zoom into diffraction limited spots top left), and mEOS-ORAI1 / STIM1-myc. Bottom rows.

Modified from Li et al, 2016.

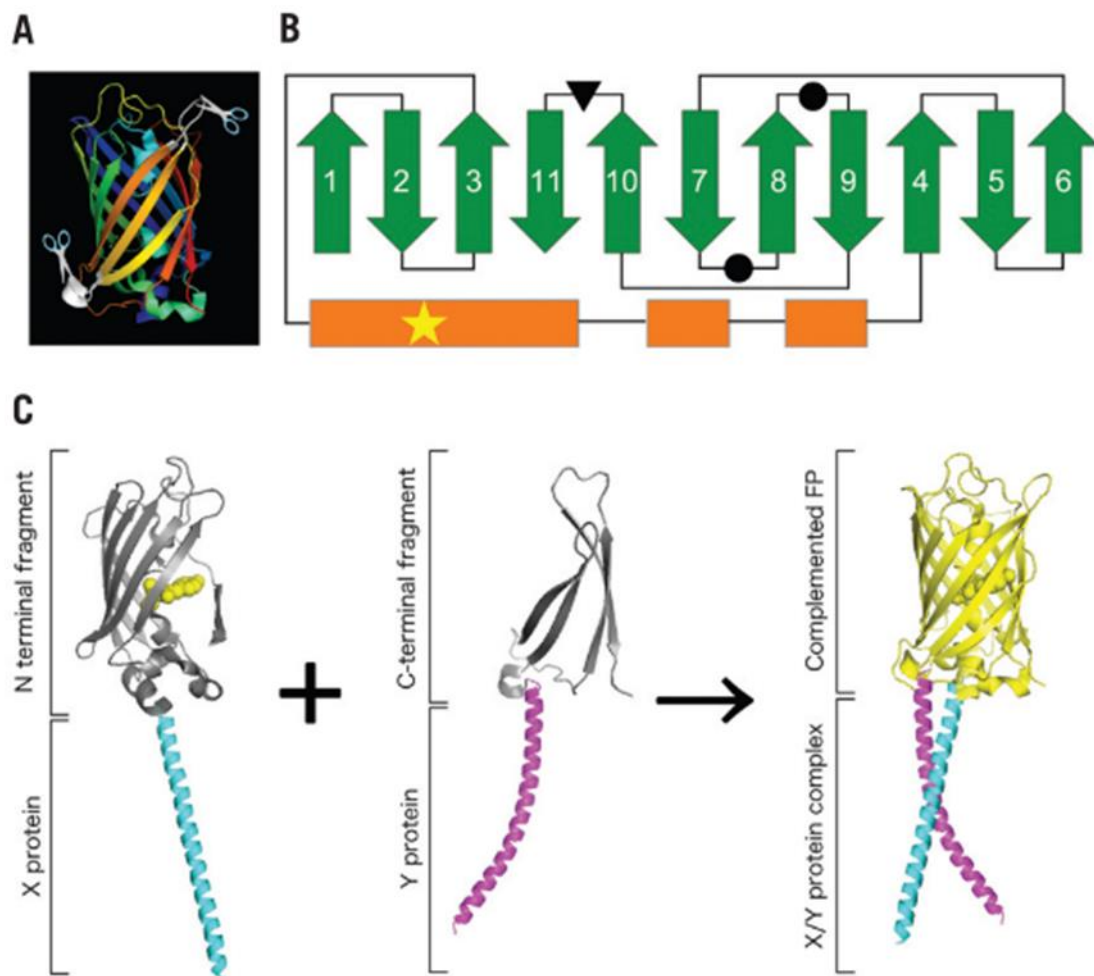


Figure 43 | Bimolecular fluorescence complementation (BiFC) assay.

- A. Structure of a hypothetical fluorescent protein (FP), the scissors indicates the site where the FP might be cut to induce the creation of split FP allowing to perform a BiFC experiments.
- B. Representation of the folding topology of FP. Green arrows are indicating β -strands and orange rectangle α -helices. The circles and the triangle represent the potential cutting site for generating circularly split FP, the star indicates the fluorochrome.
- C. Graphical representation of BiFC experiment. Each protein of interest (X, and Y) is fused to one part of the FP. The interaction between the two protein of interest, allow the formation of the classic FP structure and the chromophore formation, and ultimately produces fluorescence.

Modified from Kodama & Hu, 2012.

implement and interpret compared to FRET. Nevertheless, the irreversibility of the reaction prevents its use to study dynamic interactions. Importantly, BiFC was successfully used in the context of SOCE studies. For example, it was used to demonstrate that STIM protein are oligomeric in their resting state and that their interaction was mediated by their C-terminal domain (**Figure 44**) (He *et al*, 2012). This technique was also used to invalidate the theory that in skeletal muscle ORAI and STIM are pre-assembled (Wei-Lapierre *et al*, 2013). Of note, this technique was also used to study ORAI-STIM interaction in the context of ARC channel. Specifically, the authors used the cytosolic part of STIM protein fused to the C-terminal extremity of the eGFP, and an ORAI3 protein fused to N-terminal part the eGFP. With these constructs, they demonstrate that ORAI3 and STIM are interacting in the cell PM (Thompson & Shuttleworth, 2013). In addition, BiFC was used to demonstrate that ORAI1 and ORAI2 are forming a functional CRAC channel in chondrocyte cell line. Specifically, ORAI1 and ORAI2 were fused to YFP fragment and fluorescence resulting from YFP complementation was detectable in basal condition. Moreover, following Ca^{2+} store depletion, YFP signal was overlapping with STIM-mCherry signal suggesting that ORAI1/2 heteromers were activated by STIM to provide SOCE in this cell line (Inayama *et al*, 2015b). Finally, a BiFC-derived super resolution technique named reconstituted fluorescence-based stochastic optical fluctuation imaging (refSOFI), has been developed, and tested on the specific interaction between ORAI and STIM during SOCE interaction. Specifically, fragments of the Venus FP were fused to N-terminal and C-terminal extremities of ORAI1 and STIM1 respectively. The authors compared the results of TIRFm and refSOFI technique to evaluate the size of ORAI-STIM interaction sites. Due to refSOFI technique they improved measurements obtained with TIRFm, and demonstrated that the activation of SOCE leads to an increase in the interaction site number between ORAI1 and STIM1 and not in a size expansion of pre-existing interaction puncta (Hertel *et al*, 2016).

1.3.4.3.2. Usage of Förster resonance energy transfer (FRET)

1.3.4.3.2.1. FRET principle

FRET is a non-radiative energy transfer process that occurs between two fluorescent molecules in close proximity. Specifically, considering two fluorescent molecules (*i.e.*, donor and acceptor molecules), if the emission spectrum of the donor overlaps the excitation spectrum of the acceptor molecule, and if the two molecules are in close proximity (*i.e.*, <10 nm), then an excited donor molecule can transmit its energy to the acceptor fluorophore through non-radiative process (*i.e.*, without the emission of a photon from the excited molecule). This phenomenon ultimately leads to the emission of fluorescence by the acceptor molecule (**Figure 45**). While simple in principle, mastering the use of FRET technique requires to understand the physical principles allowing its existence.

The theoretical demonstration of the FRET phenomenon was proposed by Dr Förster, and the phenomenon was later named after him (Piston & Kremers, 2007; Förster, 1946; Förster, 1948). To

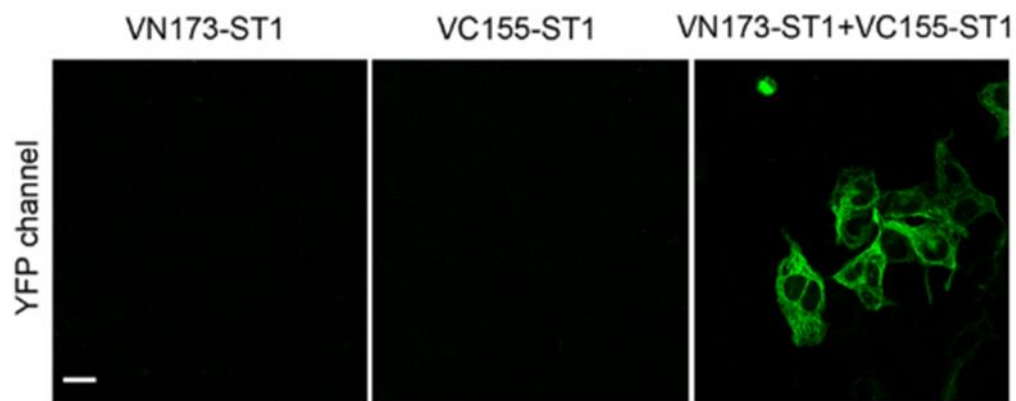


Figure 44 | Bimolecular fluorescence complementation (BiFC) assay with STIM1 protein.

The STIM1 protein were fused to circularly permuted Venus fluorescent protein fragments (VN173 and VC155). The single transfection of one or another construct do not display fluorescence while the transfection of both construct allow the visualization of a bright signal, indicating on the interaction of STIM proteins.

Modified from He et al, 2012.

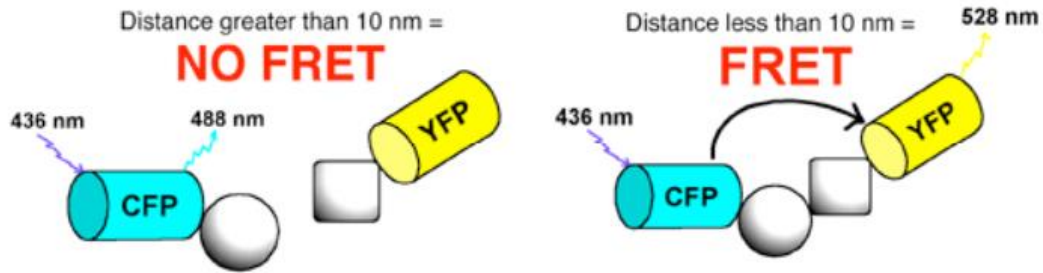


Figure 45 | Förster resonance energy transfer principle (FRET).

Considering two fluorescent proteins for which the emission spectrum of the donor (CFP) overlaps the excitation spectrum of the acceptor (YFP), if the distance between the two fluorescent proteins (FP) is lower than 10 nm, then excitation of the donor allow non-radiative transfer of energy between donor (CFP) and acceptor FP leading to the emission of fluorescent by the acceptor molecule (YFP, right image).

Modified from Swift & Trinkle-Mulcahy, 2004.

detail the mechanism of FRET, one should assimilate the fluorophores to dipoles, and understand that the resonance transfer is occurring through dipole-dipole coupling. Specifically, when two dipoles are meeting some specific criteria (described further) a long-range dipole-dipole coupling can arise. In term of fluorescence, this coupling provides an additional non-radiative de-excitation pathway for the excited molecule to return to its ground state energy level. This additional way is represented by the non-radiative energy transfer to the non-excited dipole (i.e, the acceptor molecule) leading to its excitation and to the emission of a fluorescent photon. The specific criteria allowing the development of long-range dipole-dipole interaction are the distance between the dipoles, their respective orientation one to another, and the sharing of a similar resonance frequency. Of note, for fluorescent proteins, the resonance frequency is linked to the excitation and emission spectra of the donor and acceptor fluorophores. Therefore, it explains the requirement of overlapping between the emission and excitation spectra of the donor and acceptor molecules respectively, to observe FRET (Wouters, 2013a).

In biological terms, as described earlier, when a fluorophore is hit by a photon of an appropriate wavelength, it will enter in an excited state. Subsequently, the excited molecule will return to its ground state energy level. Of note, this de-excitation can occur, either by non-radiative process (such as intersystem crossing), or through radiative process leading to the emission of a fluorescent photon (**Figure 20**). The FRET represents an additional non radiative de-excitation pathway for the excited molecule. Since FRET ultimately lead to emission of photon by the donor molecule and to the return to the ground state by the acceptor molecule without photon emission, the visual consequence of FRET is a decrease in donor fluorescence intensity accompanied by an increased fluorescence of the acceptor molecule.

Importantly, FRET is not directly measured but it is rather deduced from the modification of the photophysical properties of the donor and acceptor molecules. Especially, the modifications of the donor and acceptor properties allow the calculation of the FRET efficiency (E_{FRET}) which permit the quantification of FRET. Of note, the FRET efficiency is simply the ratio of the number of donor molecule that have transferred energy to the acceptor by the number of photons absorbed by the acceptor (3):

$$E_{FRET} = \frac{\text{Number of donor molecules transferring energy to the acceptor}}{\text{Number of photon absorbed by the donor}} \quad (3)$$

The FRET theory stipulates that FRET efficiency varies with distance between the fluorophore according to the following equation [4, (Piston & Kremers, 2007)], where R_0 represent the Förster radius: the distance for which half of the excited donor molecule are transferring energy to the acceptor molecule (i.e 50% FRET efficiency, for a specific couple of fluorophore), and r represent the effective distance between the donor and the acceptor during the experiment.

$$E_{FRET} = \frac{R_0^6}{R_0^6 + r^6} \quad (4)$$

with:

$$R_0 = [2.8 \cdot 10^{17} \cdot k^2 \cdot Q_D \cdot \varepsilon_A \cdot J(\lambda)]^{1/6} \quad (5)$$

Thus, from the equation (3), one can observe that E_{FRET} allows to measure distance between donor and acceptor molecule. In addition, because of the 6th order of magnitude applied to R_0 and r , distances between donor and acceptor to allow FRET decreases extremely sharply as a function of the distance, in the order of few nm (**Figure 46**). Importantly, R_0 depends on several factors (equation 5) including the quantum yield of the donor (Q_D), the extinction coefficient of the acceptor (ε_A), and the overlap integral between the emission spectrum of the donor and excitation spectrum of the acceptor ($J(\lambda)$). The aforementioned values are constant for a given couple of fluorophores, thus with a careful experiment design and fluorophore choice, one can expect to optimize FRET between two fluorophores. In addition, considering the strong dependency of FRET efficiency to the distance between the fluorophores one could hypothesize that the FRET efficiency value could be used to accurately measure distances between proteins in the cells. However, this is not the case because of the dependency between the FRET efficiency and the orientation factor k^2 . Importantly, k^2 is not a constant and represents the angle between the two fluorophore dipoles. In fact, dipole orientation bears a major influence on FRET efficiency: a colinear orientation of the dipoles is the best orientation to induce FRET (value of $k^2 = 4$), a parallel orientation being less optimal (value of $k^2 = 1$), and a perpendicular orientation preventing FRET ($k^2 = 0$) (**Figure 47**). Of note, databases are usually indicating a R_0 of a typical FRET pair assuming the value of k^2 being 2/3 as the results of the average of all possible orientations taken by a fluorophore during the time of a FRET experiment (Wouters, 2006). While this is valid for small fluorophores in solution, FP are large structure where the chromophore is embedded within the protein structure preventing rapid movements of the chromophore on the time scale of FRET. Unfortunately, it is almost impossible to arbitrary fix the orientation of FP in biological systems. Therefore, the possibility to measure precise distances between proteins due to FRET efficiency variations is limited. Nonetheless, the strict presence or absence of FRET between two molecules is a valid indicator of the existence or the absence of interaction between two proteins. In addition, in the cases where two FP are linked on the same polypeptidic chain, changes in E_{FRET} within this complex allows to identify conformational changes, this property led to the development of several biosensors based on FRET level modifications.

Finally, considering a hypothetical experiment, the calculated FRET efficiency, also called apparent efficiency, is the product between the real FRET efficiency between two individual fluorophores (strictly defined by the distance and orientation between the fluorophores), and the number of interacting

molecules within the volume imaged (*i.e.*, pixels). Thus, the FRET efficiency provides information about the localization of the interactions within the cell as well as an estimation of the number of molecules

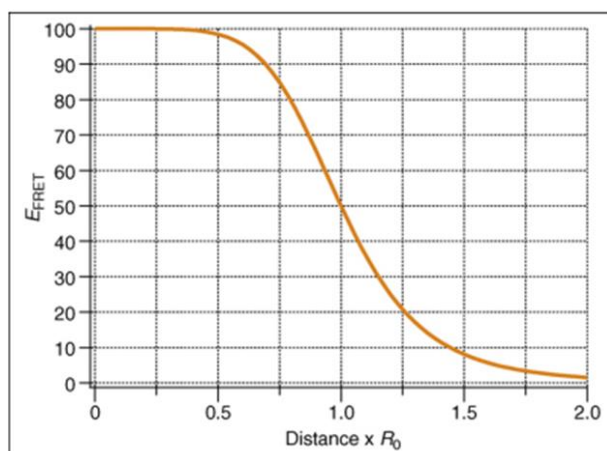


Figure 46 | FRET efficiency as a function of the distance.

The FRET efficiency is tightly dependent on the distance between the two fluorochromes.
Modified from Swift & Trinkle-Mulcahy, 2004.

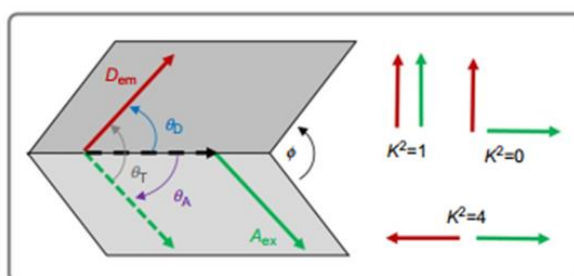


Figure 47 | FRET dependency to the orientation factor K^2 .

The relative orientation of the dipoles in a FRET experiment is of utmost importance for FRET efficiency. A colinear alignment of the dipoles leading to a value of the orientation factor of 4, a parallel orientation leading to a value of 1, and a perpendicular orientation to a value of 0 preventing FRET.

Modified from Swift & Trinkle-Mulcahy, 2004.

interacting together within each pixel. In addition, it allows the visualization of dynamic association between proteins which are not easily detectable by traditional biochemical techniques. For these reasons, FRET has been widely used in biological studies.

1.3.4.3.2.2. Intensity based FRET measurements

FRET principle is based on the transfer of energy from a donor fluorophore to an acceptor fluorophore. This transfer leads to a decreased in the fluorescence intensity of the donor associated to an increase in the fluorescence intensity of the acceptor. Thus, the simplest way to measure FRET between to molecules is represented by the ratiometric imaging, where the ratio between the acceptor (F_A) and donor (F_D) fluorescence intensities is calculated within each pixel of the image. Nonetheless, because of the spectral properties of the FPs, it is practically impossible to excite only the donor fluorophore, and to detect only the acceptor fluorescence (**Figure 48**). In addition, the concentrations of donor and acceptor molecules affects the intensity-based FRET measurements. Thus, its use is restricted to experiments where the stoichiometry between acceptor and donor is fixed (*i.e* attached on the same polypeptidic chain) (Yasuda, 2006). A good example of such use is represented by sensors such as the FRET-based sensor Cameleon where the change in FRET intensity can be directly related to conformational modification. Despite these limits, the application of corrections to account for 1- the direct excitation of the acceptor during donor excitation, and 2- the bleedthrough from donor emission into the acceptor emission channel allow to measure E_{FRET} through intensity-based techniques. The corrected ratiometric imaging of FRET is called sensitized emission FRET. It enables to access semi-quantitative information on the level of interaction between molecules. In brief, in sensitized emission FRET, one need to account for: 1-the excitation of the acceptor molecule when exciting the donor molecule, and 2- the amount of donor emission in spilling over the emission spectrum of the acceptor. To do so, images of the donor and of the acceptor alone needs to be recorded. Specifically, the donor alone should be excited at its specific excitation wavelength (D_{ex}), and its fluorescence emission should be recorded at both its specific emission peak (D_{em}), and the emission peak of the acceptor (A_{em}). Calculating the ratio of the fluorescence emission ($D_{ex}A_{em} / D_{ex}D_{em}$) provides a factor to correct for bleedthrough (β). On a similar principle, to compensate for the direct excitation of the acceptor, one need to record the emission of the acceptor (A_{em}) when excited both at its peak absorption wavelength (A_{ex}), and at the peak absorption wavelength of the donor (D_{ex}). The ratio of the emissions intensities ($D_{ex}A_{em}/A_{ex}A_{em}$) gives a factor to correct for direct excitation (δ). Therefore, the final calculation of E_{FRET} for sensitized emission is resumed in the following equation (6):

$$E_{FRET} = \frac{D_{ex}A_{em} - \beta \cdot D_{ex}D_{em} - \delta \cdot A_{ex}A_{em}}{A_{ex}A_{em}} \quad (6)$$

With, $\beta \cdot D_{ex}D_{em}$ corresponding to the correction for donor bleedthrough, and $\delta \cdot A_{ex}A_{em}$ corresponding to the correction for direct acceptor excitation. Thus, sensitized emission requires the

recording of three images: a donor excitation/acceptor emission image ($D_{ex}A_{em}$); a donor excitation/donor emission image ($D_{ex}D_{em}$); and an acceptor excitation/acceptor emission (image $A_{ex}A_{em}$). In addition, images of donor and acceptor alone in separate experiments to obtain the correction factors (β and δ). On the one hand, this type of measurement is easy to implement on a widefield or a confocal microscope, and it allows fast acquisitions to study dynamic interactions in live cells, explaining its wide usage in biological studies. On the other hand, sensitized emission is only semi-quantitative, and requires to perform several calibration measurements leading to an increased risk of error as well as an increase in the background noise (Ishikawa-Ankerhold *et al*, 2012a). Of note, other intensity-based FRET measurements exist such as acceptor photobleaching but are limited to fixed sample, thus it they will not be developed here.

1.3.4.3.2.3. Study of SOCE with intensity-based FRET measurements.

FRET technique has been widely used to study the interaction between ORAI and STIM during SOCE. Importantly, first studies using FRET techniques aimed to validate, localize and follow ORAI1-STIM1 interactions within cells were SOCE was activated (Barr *et al*, 2008; Navarro-Borelly *et al*, 2008; N *et al*, 2009). In addition, Frischauf *et al.*, used FRET to demonstrate that STIM1 was able to interact with the three ORAI homologues (Frischauf *et al*, 2009b). Later, fluorescently labeled mutant and/or truncated STIM1 proteins were used and their FRET level with ORAI1 protein were measured. This allowed to define the specific regions and even to identify the specific amino acids involved in ORAI channel binding and gating (Muik *et al*, 2009, 2011; Park *et al*, 2009a; Covington *et al*, 2010; McNally *et al*, 2013). Following the confirmation that ORAI1 and STIM1 are interacting during SOCE, and the definition of the specific domains involved in this interaction, FRET technique was used to study ORAI/STIM stoichiometry. While the specific mode of interaction and stoichiometry is still under debate, FRET data suggest that ORAI1 and STIM1 are interacting among the unimolecular coupling model where one STIM dimer binds two ORAI1 proteins belonging to two independent ORAI-channels. Thus, Zhou *et al.*, measured the FRET efficiency between dimers of STIM1 C-terminal extremities (bearing the SOAR domain) and ORAI1. By introducing a point-mutation preventing their association to ORAI1 in one or two of the units from the STIM construct they observed a reduction in the FRET efficiency, and an almost complete abolition of FRET when mutation was introduced in both units of the STIM1 dimer. This result suggest that each unit of STIM1 is interacting with different ORAI1 units and thus confirms an unimolecular binding model between ORAI1 and STIM1 (Zhou *et al*, 2015). This hypothesis of unimolecular coupling was further confirmed by Baraniak *et al.*, who used a similar strategy where the mutation were located in ORAI C-terminal fragments instead of STIM (Baraniak *et al*, 2021). Finally, FRET experiments were performed to assess interaction level between all ORAI homologs and STIM1 during SOCE induction. For example, using C-terminally tagged version of the ORAI protein, Yeast *et al.*, revealed that ORAI2 and ORAI3 present higher E_{FRET} with STIM1 protein in basal level compared to ORAI1-STIM1. In addition, they showed that activation of SOCE lead to an

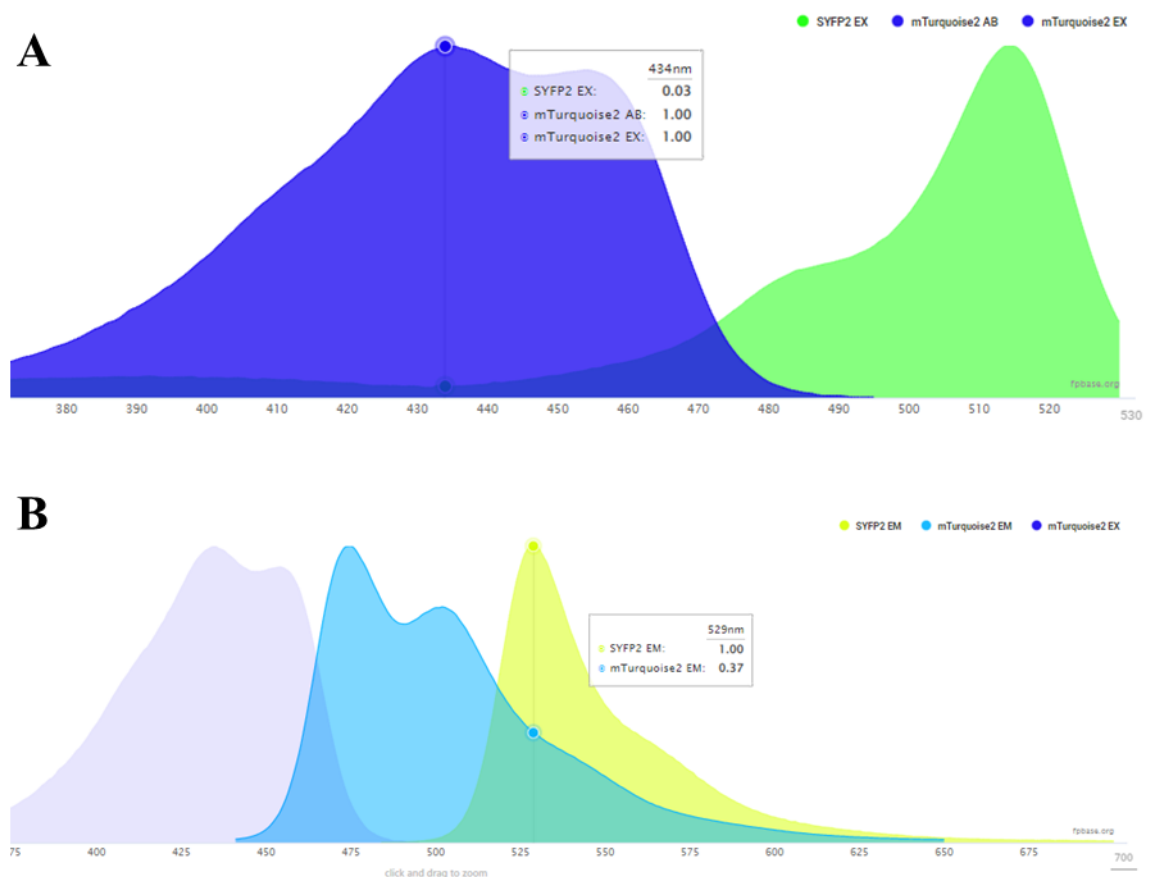


Figure 48 | Excitation and emission spectra of a FRET pair.

- Excitation of the donor (mTurquoise2, in blue) also excites the donor molecule (see insert for values), a phenomenon known as the direct excitation of the acceptor during donor excitation.
- Emission of the donor molecule overlaps with the emission of the acceptor molecules (see insert for values), a phenomenon known as bleedthrough from donor emission into the acceptor emission channel.

Graph generated from Fpbase (<https://www.fpbase.org/spectra/>).

increase of FRET for all ORAI homologs. Nonetheless, the extend of this increase was more pronounced for ORAI2-STIM1 than for ORAI1-STIM1, while ORAI3-STIM1 showed the smallest increase in FRET efficiency following SOCE induction. The same group performed similar experiments with STIM2, and revealed that STIM2 interaction with ORAI1 and ORAI2 is more pronounced than with ORAI3 in basal condition and that store depletion does not affect their interaction level (Emrich *et al*, 2021).

1.3.4.3.2.4. Study of ORAI-ORAI intensity-based FRET measurements

FRET studies were also conducted to study level of interaction within ORAI homologues. For examples, Navarro-Borelly *et al.*, studied the interaction level between ORAI1 proteins during SOCE activation. They demonstrated that ORAI1 proteins are interacting in basal condition. In addition, they observed a reduction in E_{FRET} when SOCE was activated and attributed this decrease to molecular rearrangement (Navarro-Borelly *et al*, 2008). Of note, the E_{FRET} decrease was strictly dependent on the overexpression of the STIM protein in the model. In addition, Schindl *et al.*, used ORAI1 and ORAI3 fusion proteins fluorescently labeled in their N-terminal extremities to perform FRET. They showed that ORAI1 and ORAI3 were displaying strong FRET level albeit lower than within ORAI3 proteins but higher than within ORAI1 proteins (Schindl *et al*, 2009). The specific interaction between ORAI1 and ORAI2 was also investigated by FRET and confirmed by BiFC technique in chondrocyte cell-line by Inyama *et al.*, (Inayama *et al*, 2015a). Finally, Yeast *et al.*, showed that all ORAI isoforms are interacting in basal conditions and that SOCE induction with carbachol or ionomycin as not modifying FRET levels (Yeast *et al*, 2020b).

Overall, FRET technique has been widely used to study ORAI proteins. Nonetheless, as explained earlier ratio imaging FRET and sensitized FRET experiments presents limitations in analysis of FRET intensities that might limit the conclusions that one could draw from experiments. Importantly, fluorescence lifetime imaging FRET enables to overcome these limitations and to quantify FRET between two proteins., as a consequence the specificity of this type of FRET measurement will be developed thereafter.

1.3.5. Fluorescence lifetime imaging (FLIM) – FRET

1.3.5.1. FLIM-FRET principles

Due to the limitation of the intensity-based method in evaluating E_{FRET} , alternative methods have been developed such as measuring the fluorescence lifetime of the donor molecule to calculate E_{FRET} . As described earlier, fluorescence lifetime is specific for a considered fluorophore. Nonetheless, it is affected by pH, temperature, or FRET. Indeed, when a fluorophore is excited, it enters a higher energy level state, the return to the ground state energy level can occur through radiative (photon emission, Γ) or non-radiative processes (k_{NR}) (equation 7). The time an excited molecule will spend in the higher

energy state is dependent on the possible ways of de-excitation. Thus, for an excited fluorophore, FRET represents an additional way of de-excitation (equation 5), leading to a decrease of lifetime.

$$\tau_D = \frac{1}{\Gamma + k_{NR}} \geq \frac{1}{\Gamma + k_{NR} + k_{FRET}} = \tau_{FRET} \quad (7)$$

The return of the fluorescent molecule to the non-excited state is a stochastic process. Thus, if one considers a single molecule excited by repeated laser pulses, the time this molecule spends in higher energy will vary between each measurement following an exponential decay. The specific average lifetime of a fluorophore represents the time for which a decrease in fluorescence intensity of 1/e of its initial intensity is observed (**Figure 49**). In case of FRET, the decrease in lifetime corresponds to an increased decay of the fluorophore lifetime. Importantly, the fluorescence lifetime is independent on, local concentration of fluorophores, excitation intensity, and fluorescence intensity. In addition, when measuring FRET by FLIM, one should carefully choose a donor molecule presenting a single exponential decay lifetime. Indeed, multiples exponential decay lifetime increases drastically the analysis processes. Finally, one would observe that during FLIM-FRET experiment, only the lifetime of the donor is measured. Thus, FLIM-FRET present the advantage of eliminating excitation and bleed through cross-contamination, as well as variation induced by changes in the fluorophores concentration (Yasuda, 2006; Ishikawa-Ankerhold *et al*, 2012b).

1.3.5.2. FLIM-FRET measurements

Considering a system where the donor molecules are not interacting with the acceptor molecules, the lifetime of the chosen donor molecule follows a single exponential decay allowing the calculation of its lifetime that will corresponds to the lifetime indicated in databases. Considering the opposite system, where all the donor molecules are interacting with acceptor, the lifetime will still follow a single exponential decay, but will display a shorter characteristic decay time because the probability of the donor molecule de-excitation is increased due to the presence of the additional de-excitation pathway represented by the FRET. In a cellular context when a population of donor is excited, some of the donor molecules will be interacting, while other will not. In this case, the measured lifetime is not the average of not-interacting and interacting lifetimes, instead it follows a double exponential decay (equation 8). Thus, the signal intensity for each pixel in time ($I_i(t)$) corresponds to the double exponential function relative to the decays of the donor alone (τ_D) and the decay of the donor interacting with the acceptor (τ_{DA}). Since the two lifetimes are constant, the only variable in the equation is represented by the number of interacting molecules within the cell (α_i , also called local parameter) for each pixel.

$$I_i(t) = (1 - \alpha_i) \cdot e^{-t/\tau_D} + \alpha_i \cdot e^{-t/\tau_{DA}} \quad (8)$$

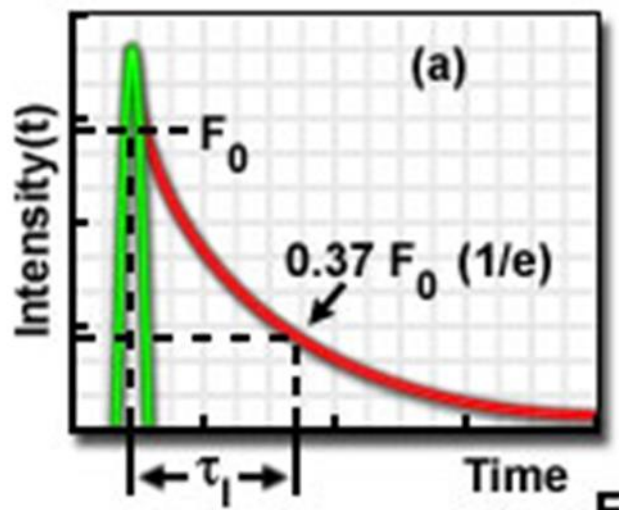


Figure 49 | Fluorescence lifetime decay.

Following excitation by a laser pulse (green), the fluorescent molecules will stochastically return to their ground energy state. The recording of the time spend in the excited state by each single excited molecule leads to the creation of an exponential decay curve (red). The time value for which the intensity value reaches $1/e$ of its initial intensity ($0.37 F_0$) represent the fluorophore lifetime.

Image modified from <https://www.olympus-lifescience.com/en/microscope-resource/primer/techniques/fluorescence/fret/fretintro/>.

Thus, considering the FLIM efficiency equation (9):

$$E_{FRET} = 1 - \frac{\tau_{DA}}{\tau_D} = \frac{R_0^6}{R_0^6 + r^6} \quad (9)$$

In a single FLIM measurement of FRET, one can obtain both the efficiency of FRET which is characteristic of the conformation of the complex, and the local parameter indicating for each pixel the proportion of interacting molecules. Of note, measurement of lifetime decay profiles can be performed in two ways named the time domain (TD) and the frequency domain (FD). Because TD-FLIM represents the easiest and more straight forward way to measure fluorescence lifetime, and because it was the measuring technique used throughout this PhD work, it will be the only method described thereafter. In order to measure the exponential decay in the TD, one needs to build a histogram of the number of photons detected as a function of the time. This type of measurement is performed with specific equipment. Especially a pulsed laser coupled to a time correlated single photon counting (TCSPC) board. In brief, laser pulses are exciting donor molecules, while single-emitted photon arrival times are recorded to build a histogram of time arrival (**Figure 50** (Sipietier *et al*, 2013)). From this histogram, the decay of the fluorescence lifetime can be extracted.

1.3.5.3. FLIM-FRET analysis

During a TD-FLIM experiment, the samples are excited by light pulses several times. As a result, histograms of the fluorescent intensity decay are established for each pixel. The classical way of extracting lifetimes from these histograms has been represented by fitting methods, where each the lifetimes are deduced by adjusting each histogram with an exponential model (**Figure 50**) (Verveer *et al*, 2000; Peter & Ameer-Beg, 2004). However, such method requires a high level of expertise and an important computational time. Because such methods are hardly exploitable for non-expert, non-fitting methods were developed, such as the phasor approach (also called polar representation approach). In brief, the lifetime image is converted into a two-dimensional histogram due to the application of sine and cosine Fourier transform to each experimentally constructed histogram. In this new two-dimensional histogram, called phasor or polar, each pixel from the original image corresponds to a point in the phasor define by its coordinates $[u; v]$ and *vice versa* (**Figure 51**) (Leray *et al*, 2012). In addition, the phasor representation allows the deduction of phase and modulation lifetimes (τ_ϕ , and τ_m , respectively) which are well known parameters of frequency domain FLIM measurements. Of note, for a fluorescent emitter presenting a mono-exponential decay, the values of the phase, modulation, and the true lifetime (τ) are all equal (10), while in the case a multi-exponential decay, which can be represented by FRET, the phase lifetime is shorter than the modulation lifetime (11):

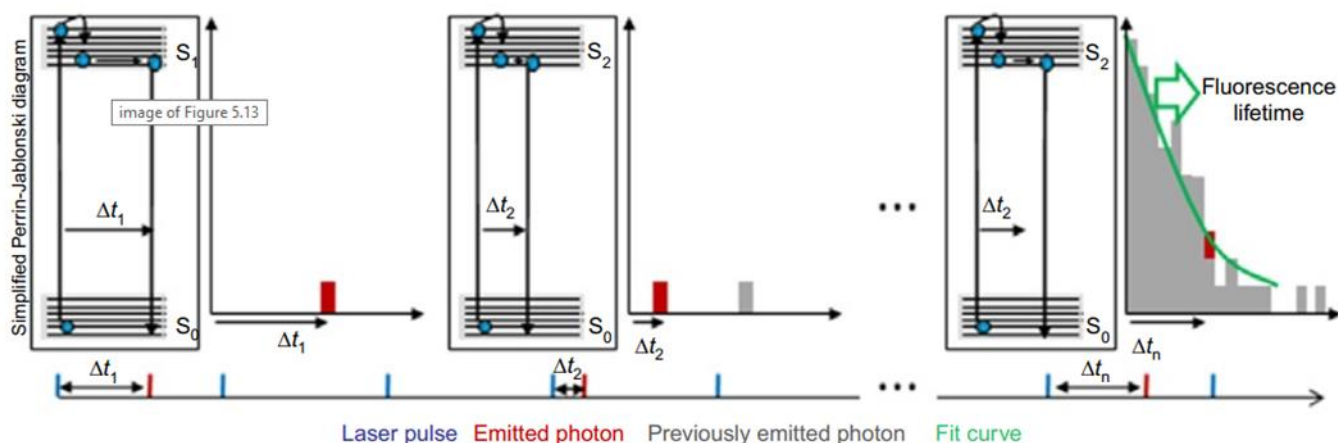


Figure 50 | Principle of fluorescence lifetime measurement.

A pulsed laser is used to excite the fluorophore (laser pulse blue lane), the time between the excitation pulse and the emission of a photon is measured (Δt) for each photon and leads to the building of a histogram of the photon time arrival (left). The calculation of the lifetime usually involves the fitting of a curve to the experiment data.

Image modified from Sipietter et al, 2013/.

$$\text{Mono exponential decay: } \tau = \tau_{\phi} = \tau_m \quad (10)$$

$$\text{Multi exponential decay: } \tau_{\phi} < \tau_m \quad (11)$$

Moreover, on the phasor diagram, mono-exponential decay lifetimes will be plotted along a semi-circle centered at [0.5, 0] with a radius of 0.5, with longer lifetimes located close to the origin of the diagram (coordinates [0, 0]), and short lifetimes located closer to the coordinates [1, 0]. Of note, multiple lifetime decays are located inside of the semi-circle (**Figure 51**). Thus, on the one hand, the phasor diagram presents the advantage of providing a visual representation of the fluorescence lifetimes measured in an image. In addition, one can calculate the mean lifetime value for the original image averaging the values of phase and modulation lifetimes (12) (Leray *et al*, 2011):

$$\tau = \frac{(\tau_{\phi} + \tau_m)}{2} \quad (10) \quad (12)$$

On the other hand, the fraction of donor molecule interacting is not easily extracted from these data (Sipiet *et al*, 2013). Nonetheless, for most cases, the FRET efficiency estimated from the average lifetime, provides sufficient information to evaluate interaction level within proteins (Wouters, 2013b). Of note, another non fitting approach was developed by Padilla-Parra *et al.*, introducing the minimal fraction of interacting donor. This method can be applied to TD FLIM technique and provides an indicator of the minimal interacting proportion of the donor when the lifetime of the donor alone is determined in a separate experiment (Padilla-Parra *et al*, 2008).

To conclude, while powerful, FLIM-FRET was never applied for the study of ORAI and STIM. This might be imputed to the specific equipment required to perform this type of experiment as well as the relative degree of specialization required to assimilate and perform analysis of the data obtained. Nonetheless, it enables a more precise measurement of the interaction level between proteins than the classic intensity-based method FRET, and thus might allow to obtain better pictures of the mechanism of interaction between ORAI proteins.

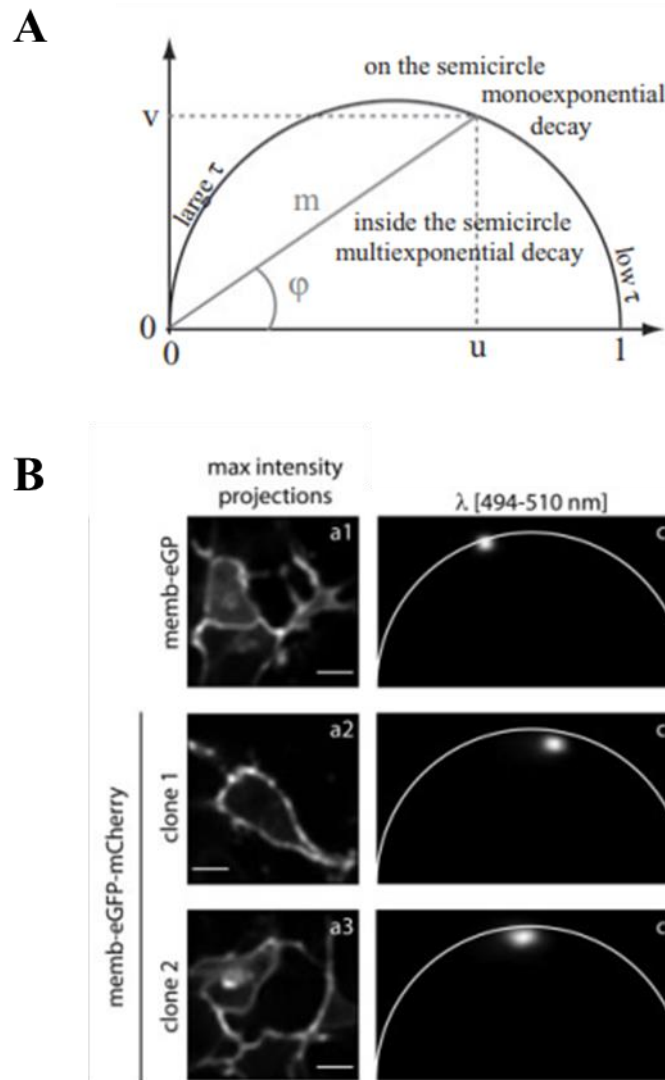


Figure 51 | Fluorescence lifetime analysis with the polar representation.

- A. Phasor or polar diagram representation. Each pixel from an image presenting a single exponential decay will fall on the semi-circle, with the shorter lifetime next to coordinate point [0,1] and the longer lifetimes next to the coordinated [0,0]. The multiexponential decay times will be displayed inside the semi circle. Of note, the coordinates of each points allow the determination of the phase (ϕ) and modulation (m) lifetimes characteristics from the frequency domain measurement of lifetime.
- B. Examples of phasor representation from an experiment. On top, the measured lifetime of eGFP molecule are represented on the semi-circle indicated a mono exponential lifetime. On the bottom row, the eGFP-is fused to a mCherry tag leading to FRET. As a consequence, the lifetime value is modified and the phasor diagram displays data points inside of the phasor semicircle, indicating a multi-exponential decay

Image modified from <https://www.olympus-lifescience.com/en/microscope-resource/primer/techniques/fluorescence/fret/fretintro/>.

1.3.6. Summary on the use of microscopy techniques for the study of ORAI proteins

As developed above, several microscopy techniques were used to study ORAI proteins and their associated channels. In the year following the ORAI proteins discovery and until the determination of the *Drosophila* CRAC channel structure by crystallization, several microscopy techniques such as counting of fluorescence photobleaching steps in TIRF modality, FRAP, and FRET techniques were used to assess the stoichiometry of ORAI channels. Even though a considerable amount of data were generated by these techniques, no consensus on the exact ORAI channel composition could be reached. This might be explained by one of the biggest limitations of imaging techniques: the rely on the overexpression of fluorescently labelled protein or on antibodies whose specificity, and capability of identifying all protein with a cell are limited. This limitation leads to the presence of an “invisible” population of protein of interest during the imaging experiment that complexify the interpretation of the results obtained. Of note, the recent revolution caused by the genome engineering technique CRISPR/Cas9 open the possibility of get rid of the aforementioned limitation by tagging virtually all the protein of interest within a cell through the insertion a genomic sequence coding for a fluorescent protein in frame with the sequence of the protein of interest. Thus, in addition to our initial aim of studying the ORAI1-ORAI3 protein interaction with FLIM-FRET technique, we also aimed to use the CRISPR/Cas9 technique to generate cell line displaying endogenous ORAI1 and ORAI3 protein fused to different FP. Therefore, a short introduction of the CRISPR/Cas9 system and its application for genome editing will be described thereafter.

1.4. The CRISPR-Cas9 system

1.4.1. Discovery of the CRISPR-Cas system

The identification of Clustered regularly interspaced palindromic repeats (CRISPR) is dated 1987 when Dr Ishino identified in *Escherichia coli* arrays of interspaced and partially palindromic DNA repeats (Ishino *et al*, 1987). Subsequently, several sequences sharing this pattern were observed in different bacteria species, and the acronym CRISPR, to refer to these sequences, was coined in 2002 (Jansen *et al*, 2002). In 2005, it was proposed, by three different groups, that the CRISPR sequences could represent a prokaryotic adaptive immunity system (Bolotin *et al*, 2005; Pourcel *et al*, 2005; Mojica *et al*, 2005). The confirmation, and identification of the role of CRISPR sequences together with the CRISPR-associated sequence (Cas) proteins in prokaryotic immunity was established in 2007 (Barrangou *et al*, 2007). Finally, the beginning of the CRISPR revolution is dated from 2012, with the repurposing of an engineered CRISPR/Cas9 system as a genome editing tool for eukaryotic cells (Jinek *et al*, 2012).

1.4.2. Mechanism of CRISPR-Cas9 system

1.4.2.1. Physiological mechanism of CRISPR-Cas9

In prokaryotes, the CRISPR-Cas system serves as an adaptive immunity system. CRISPR-Cas system are bacterial loci encompassing: an array of repetitive sequence interspaced by non-repetitive sequences (CRISPR), a set of Cas genes, and sometimes a *trans*-activating CRISPR RNA (tracrRNA) gene (**Figure 52A**) (Amitai & Sorek, 2016). The mechanism of action of this locus in bacterial immunity is divided in three stages: adaptation, expression and maturation, and interference.

- The adaptation stage (**Figure 52B**). In brief, when a phage infects a prokaryote (bacteria or archaea for instance), its DNA can be recognized as foreign by the RecBCD nuclease which breaks it down into single-stranded DNA (ssDNA) pieces. It is suggested that these ssDNA pieces represent the material recognized by the Cas1-Cas2 protein complex which will integrate these sequences, called spacer sequences, into the CRISPR array. The initial “choice” of the sequences to be integrated is dictated by the presence of a specific short nucleotide sequences (2 to 5 base pairs [bp]), named the protospacer adjacent motif (PAM). The spacer sequences acquired by the Cas1-Cas2 system are further integrated (without the PAM sequence) in the bacterial chromosome between the repetitive sequences of the CRISPR array. This process leads to the insertion of spacer sequences (foreign DNA pieces) every time a foreign DNA piece is identified by the bacteria. Therefore, the CRISPR array represent the memory of infections encountered by the bacteria (Amitai & Sorek, 2016).

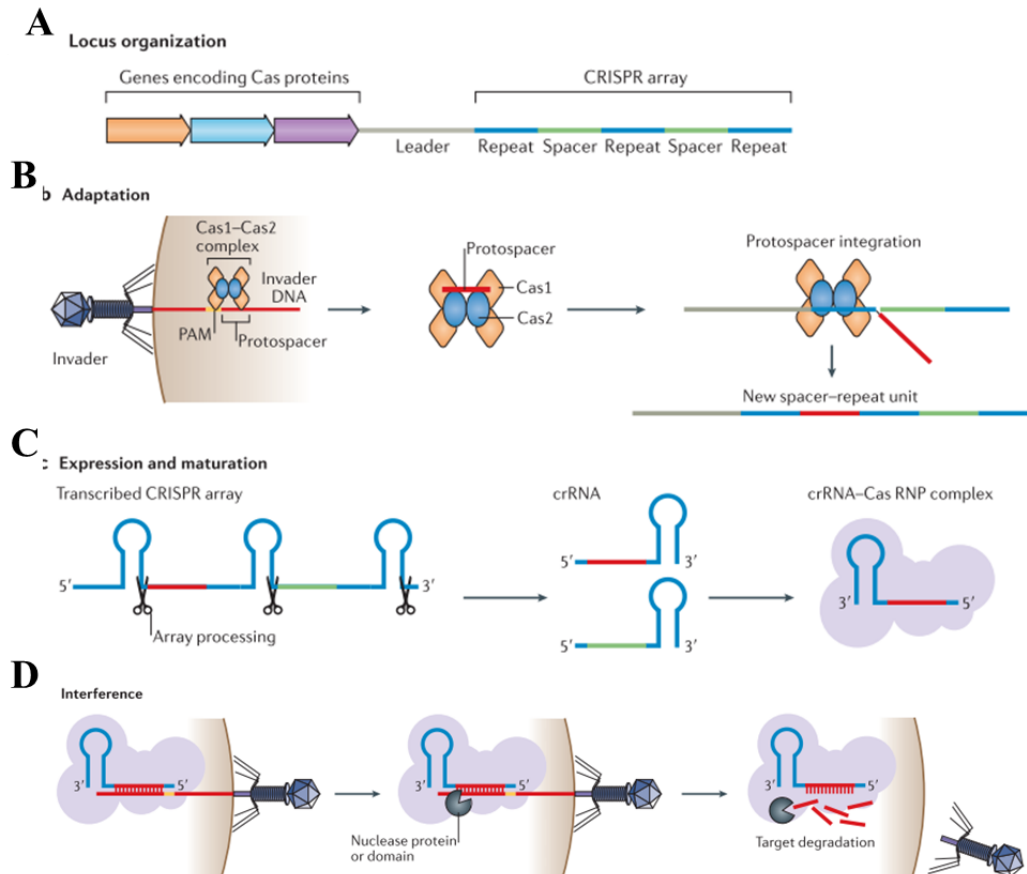


Figure 52 | The three stages of CRISPR-Cas immunity.

- A. Classic organization of a prokaryote CRISPR-Cas locus. The colored arrows represent the different Cas genes. Blue and green lanes symbolize the repeat and the spacer sequences, respectively. The succession of repeat and spacer sequences represent the CRISPR array. (Please note that, the numbers, the identities, the order of the genes as well as number of spacer-repeats units, are variable depending on the CRISPR-Cas system considered).
- B. During the adaptation stage, the Cas1-Cas2 complex acquires a protospacer from a foreign DNA element and integrates it into the CRISPR array.
- C. During the expression and maturation stage, the CRISPR array is transcribed as a precursor CRISPR RNA (pre-crRNA). Then, the crRNA is processed into mature crRNAs (crRNAs). Each crRNA display a unique spacer sequence and a portion of the repeat sequence. crRNAs and Cas protein are forming the ribonucleotide complex (crRNA-Cas RNP complex). The number of Cas proteins and the structure of the crRNA are variable depending on the CRISPR system considered.
- D. During the interference stage, the CRISPR-Cas complex identifies foreign DNA due to protospacer-adjacent motif (PAM), and homology between the crRNA and the target sequence following the PAM. Following complementary base pairing, the DNA is degraded by the Cas protein. The positions and sequences of the PAM vary depending on the CRISPR-Cas system considered.

Modified from Amitai & Sorek, 2016.

- The expression and maturation stage (**Figure 52C**). During this stage the whole CRISPR array is transcribed into a precursor CRISPR-RNA (pre-crRNA) which will be processed into several mature CRISPR-RNA (crRNA), each representing a single spacer motif (homologue to the initial foreign DNA element encountered), and a repeat sequence. These crRNA sequences are assembled with one or more Cas protein to form the Cas-crRNA complex (Amitai & Sorek, 2016).
- The interference stage (**Figure 52D**). Following its formation, the Cas-crRNA complex will scan the cell for foreign DNA sequences presenting a PAM motif. Following a PAM detection, the protospacer aligns with the foreign DNA, and case of matching between both sequences, the DNA piece will be cleaved by the Cas protein, leading to its final destruction and thus stopping the infection process of the bacteria (Amitai & Sorek, 2016).

Several types of CRISPR-Cas system have been identified since the initial discovery of CRISPR-Cas9. They are separated in two main classes, themselves divided in several subclasses (Types I, III, and IV for the class one; and Types II, V, VI for the Class 2, [**Figure 53**]). Of note, in the class one system the interference stage is performed by multiple Cas proteins associated together in a complex. At the opposite, in the class two systems (from which the Cas9 system belongs), a single Cas protein is sufficient to perform the whole interference process (Makarova *et al*, 2020). Importantly, the existing diversity in the CRISPR-Cas systems allowed the identification of specific properties that were selected for improving the capacities CRISPR derived genome editing techniques (different double strand break (DSB) induction mechanism, change in the PAM sequence required for cleavage, etc.).

1.4.2.2. Usage of CRISPR-Cas9 for genome editing

As mentioned previously, the advent of CRISPR-Cas9 for genome editing is due to the demonstration in 2012 that the system could be repurposed and used in eukaryotic cells. In fact, in the native CRISPR-Cas9 system the Cas9-RNA complex is constituted of two RNA sequences: the crRNA, described above, and the transactivating crRNA (tracrRNA). The tracr RNA is specific to Class two CRISPR-Cas system. This tracr RNA possess a specific structure allowing, first, its association with the Cas protein, and second, its association with the crRNA due to homology to the repetitive sequence present in crRNA sequence (Makarova *et al*, 2020). Part of the engineering applied to the original CRISPR-Cas system consisted in generating a single RNA molecule that would serve as a guide to induce DSB at a specific location. This single RNA molecule is named single-guide RNA (sgRNA) or simply guide RNA (gRNA) (**Figure 54A**). Of note, the gRNA is designed by the user such as it is complementary to a (ideally) unique 20-nucleotides sequence (for the Cas9 system) targeting the genomic loci of interest to edit. Overall, the mechanism of genome edition in eukaryote cells greatly relates to the original interfering mechanism described in prokaryotes. Specifically, following the introduction of Cas protein and gRNA in the cell, the Cas9-gRNA complex is assembled and scans the cellular genome for PAM sequences. Subsequently, for every PAM sequence located by the Cas9-gRNA

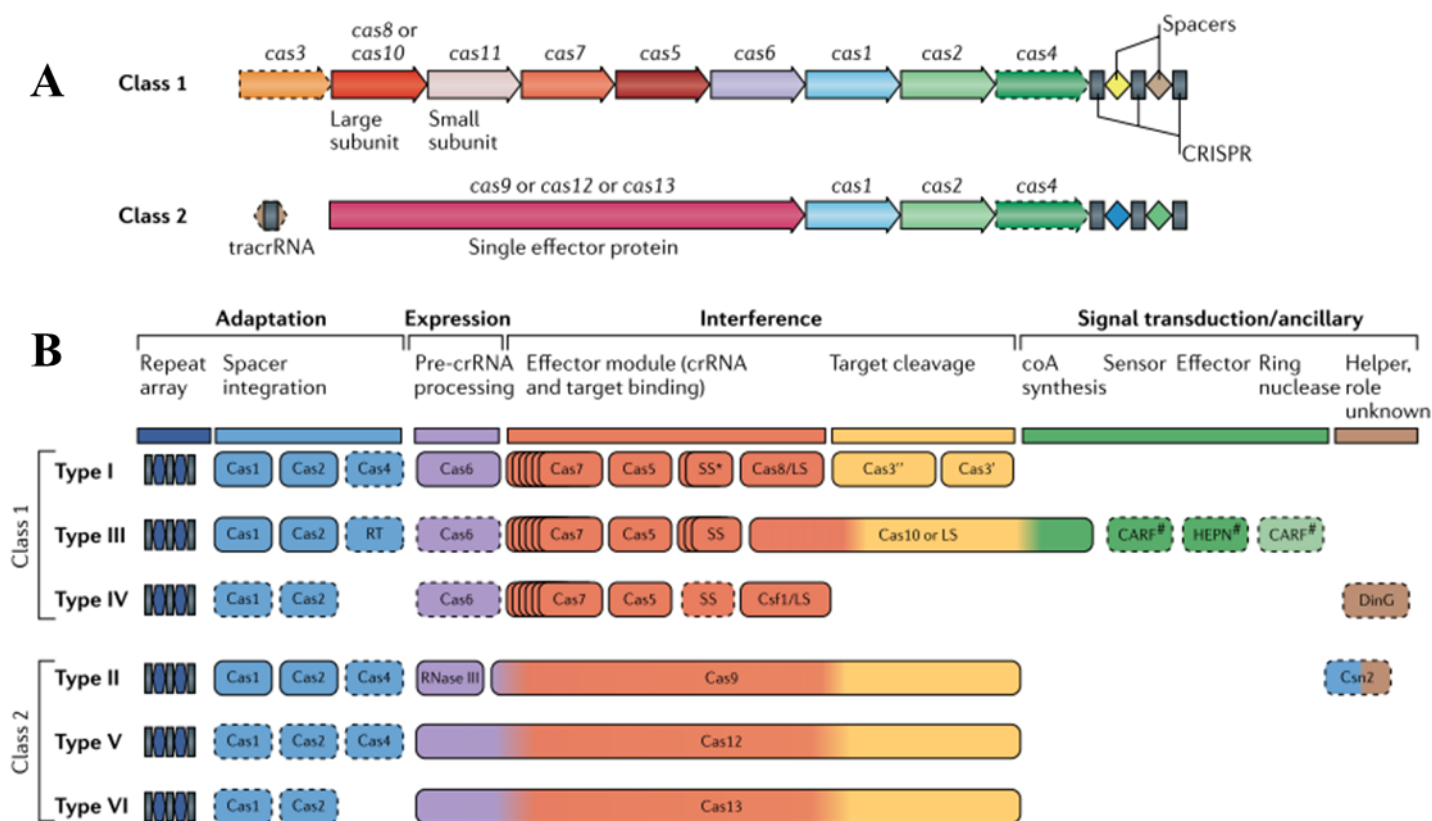


Figure 53 | Classification of the identified CRISPR-Cas systems.

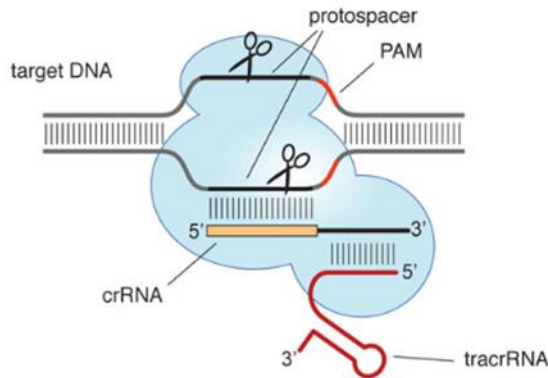
- A. Representation of the loci from the two classes of CRISPR-Cas systems. The CRISPR-Cas systems belonging to class 1 are characterized by the multiple Cas proteins required to degrade foreign DNA sequences. Class 2 systems possess a single effector protein (Cas9, 12 or 13) as well as a transactivating CRISPR RNA (tracrRNA) sequence.
- B. The subtypes of CRISPR-Cas systems. The names of the proteins involved in each phase of the CRISPR-Cas immunity are displayed in different colors. The dashed outlines indicates dispensable components. The pound symbols (#) indicates that unknown protein might be involved in the process.

Modified from Makarova et al, 2020.

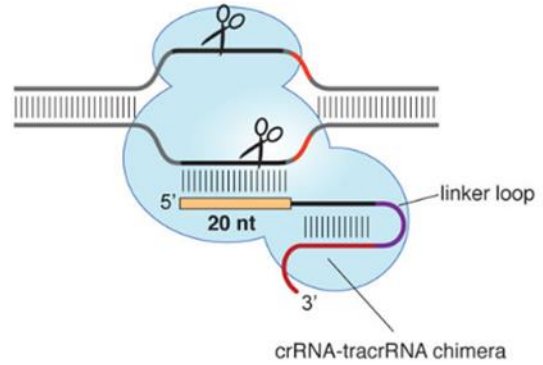
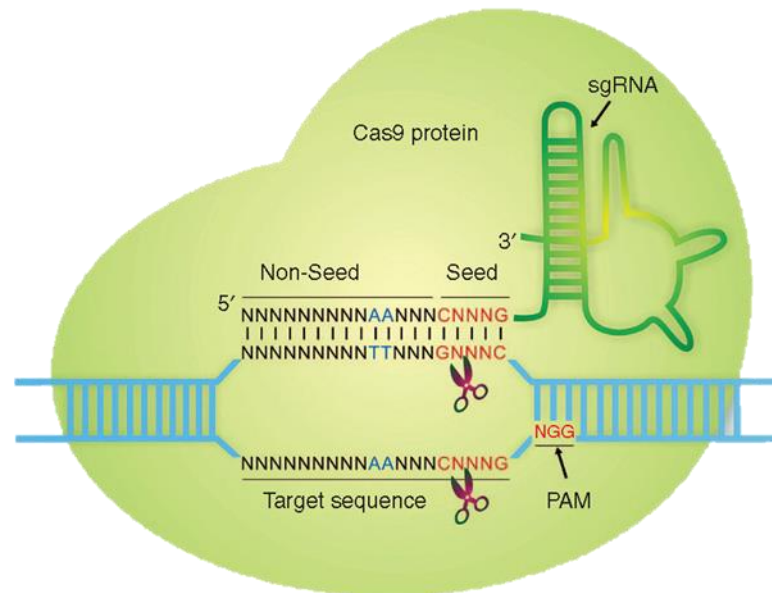
complex, the gRNA aligns to the genomic DNA (gDNA) sequence. If the gDNA sequence is homologous to the gRNA the Cas9 protein will cleave the double stranded DNA at the position -3 relative to the PAM (**Figure 54B**) (Zhang *et al*, 2015b).

A

Cas9 programmed by crRNA:tracrRNA duplex



Cas9 programmed by single chimeric RNA

**B****Figure 54 | | Mechanism of CRISPR-Cas9 double strand break (DSB) induction.**

- A. Comparison between the original CRISPR-Cas9 ribonucleotide complex (left) and the engineered system for genome editing (right). In the engineered version, the tracrRNA and crRNA were replaced by a single RNA molecules (crRNA-tracrRNA chimera)
- B. Detailed action mechanism of CRISPR-Cas9 DSB induction. First, the CRISPR-Cas9 complex locates PAM sequence (NGG, in red). Then the 5' extension of the single-guide RNA (sgRNA) matches the target sequence following the PAM. The perfect matching of the seed sequence is of peculiar importance for induction of DSB. Finally, the Cas9 protein induces DSB between the positions -3/-4 relative the PAM sequence.

Modified from (A) Jinek et al, 2012; (B) Zhang et al, 2015.

2. Aim and scope of the PhD

As developed throughout the introduction, there is an accumulation of evidence indicating that CRAC channels are heteromeric in their native form. In addition, their composition modulates the level of SOCE displayed by the cells with several phenotypic consequences. Moreover, in addition to the CRAC channels, ORAI1 and ORAI3 proteins are able to form a specific channel, namely the ARC channel, presenting a different stoichiometry than the CRAC channel as well as a specific mode of activation. The study of the ORAI channel composition is still an emerging topic, and not much is yet known about the mechanisms of association between ORAI proteins to form functional channels. In this PhD we proposed to study the specific interaction between the ORAI1 and the ORAI3 proteins by using the quantitative microscopy technique FLIM-FRET. To do so, we decided to implement the genome editing technique CRISPR-Cas9, in order to avoid the limitations induced by the overexpression of fluorescent protein of interest. Thus, our specific aims were:

- To implement the CRISPR/Cas9 technique to generate:
 - Knockin (KI) cells in order to fluorescently label ORAI1 and ORAI3 proteins.
 - Knockout (KO) cells for ORAI1 and ORAI3 proteins.
- Study the fundamental physiological role of ORAI1 protein in the KO cell line
- Study the interactions between ORAI1 and ORAI3 proteins with the FLIM-FRET technique in order to determine the mode of association of these protein in a functional channel., and to establish if this association is resulting from a dynamic process.

3. Materiel and methods

3.1. Stocks solution

3.1.1. Buffers and standard solutions

Recipes of the buffers and standard solutions used in this study are indicated in the table below. When needed buffers and standard solutions were autoclaved at 120°C or sterilized with 0.22 µm filters.

Name	Composition
0 Ca ²⁺ solution	150 mM NaCl, 5 mM KCl, 3 mM MgCl ₂ , 10 mM HEPES, 10 mM Glucose, pH=7.4
4 mM Ca ²⁺ solution	150 mM NaCl, 5 mM KCl, 4 mM CaCl ₂ , 1 mM MgCl ₂ , 10 mM HEPES, 10 mM Glucose, pH=7.4
8 mM Ca ²⁺ solution	150 mM NaCl, 5 mM KCl, 8 mM CaCl ₂ , 10 mM HEPES, 5.6 mM Glucose, pH=7.4
Hank's balanced salt solution (HBSS)	150 mM NaCl, 5 mM KCl, 2 mM CaCl ₂ , 1 mM MgCl ₂ , 10 mM HEPES, 10 mM Glucose, pH=7.4
Lysogeny Broth (LB)	1% tryptone, 0.5% Yeast extract, 1% NaCl, pH=7.0
Phosphate buffered saline (PBS)	137 mM NaCl, 2.7 mM KCl, 0.2 mM KH ₂ PO ₄ , 1.42 mM Na ₂ HPO ₄ •2H ₂ O, pH=7.4
Radioimmunoprecipitation assay buffer (RIPA)	15 mM KH ₂ PO ₄ , 100 mM Na ₂ HPO ₄ , 100 mM NaH ₂ PO ₄ , pH=7.2
Tris buffered saline-Tween (TBS-T)	1.5 mM Tris, 14 mM NaCl, 0,05% Tween20, pH=7.4

3.1.2. Pharmacological agents

Pharmacological agents were used as indicated in the table below.

Name	Mode of action	Final working concentration
Acetylcholine (ACh)	Agonist of cholinergic receptors	100 µM
Arachidonic acid	Agonist of ARC channel	8 µM
Carbachol (CCh)	Agonist of cholinergic receptors	100 µM
Thapsigargin (TG)	Irreversible inhibitor of SERCA	1 µM
Brefeldin A	Unknown	

3.1.3. Antibiotics

The antibiotics used in this study are indicated in the table below.

Name	Used for	Final working concentration
Carbenicilin	Bacterial selection	30 µg/mL
Kanamycin	Bacterial selection	50 µg/mL

3.2. Molecular biology

3.2.1. NEBuilder Cloning

Cloning experiments were performed using the NEBuilder cloning kit. This kit enables the cloning of multiple cDNA fragment in a single reaction due to the use of PCR primers presenting overlaps (15 to 80 bp) in their 3' and 5' extremities (Fig X). Specifically, the kit includes: an exonuclease creating 3' overhangs allowing annealing of fragments sharing sequence complementarity; a polymerase that will fill the gaps in the annealed 3' overhangs; a ligase that seals the nicks. Fragments used for the assemblies were PCR amplified with specific primers containing homology sequences one-to-another. Primer designed were performed using the NEB online tool (<https://international.neb.com/external-links/nebuilder-assembly-tool>). The list of the primers used to generate these assemblies are presented in the Table X. Classic assembly mixes were set up as follow: 1- For assemblies of 2 to 3 fragment, the recommended amount of fragment per reaction should be included between 0.03 and 0.2 pmols, with an ideal ratio vector to fragment of 1:2. In addition the fragments, master mix containing enzymes required for assembly was added to the tube with its specific buffer, and reaction was performed by an incubation of 15 minutes at 50°C in a thermocycler. Following cool down of the tube, 2µl of the assembly were used to transform competent cells. 2- For assemblies of 4 or more fragments, the quantity of fragments was ranging from 0.2 to 0.5 pmols and the ration insert to vector was 1:1. In addition, reaction was carried-out at 50°C for 60 minutes.

3.2.2. Classic expression cloning

3.2.2.1. Bacterial transformation

Transformation of bacteria was performed with the heat shock method. In brief, 50µL of chemically competent bacteria were mixed with the appropriate quantity of plasmid (5 to 50 ng) and incubated on ice for 20 minutes. Heat-shock procedure included a 45seconds incubation at 42°C in a water bath, before a resting period of 2 minutes on ice. Next, 100µML of pre-warmed (37°C) Super Optimal Broth with Catabolite repression (SOC) media was added on the bacteria and left shaking in orbital shaker at 200rpm/minutes for 1 hours at 37°C. The mixture was then spread on agar plates and incubated at 37°C overnight or until apparition of bacteria colonies. Bacteria colonies were further inoculated in LB media for plasmid amplification and extraction procedures.

3.2.2.2. Plasmid isolation

Plasmid isolation was performed by using NucleoBond Xtra Midi Plasmid DNA purification kit (Macherey-Nagel) according to the manufacturer's instructions.

3.2.2.3. Sequencing

DNA sequencing were performed by Eurofins genomics company.

3.2.2.4. Restriction digest

The restriction digest was performed by using restriction enzymes from NEB according to the manufacturer's instructions.

3.2.2.5. Agarose gel electrophoresis

Agarose gels of different concentration (from 0.5 to 2.5%) were prepared in 0.5x Tris/Borate/EDTA (TBE) for classic experiments, or 0.5x Tris/Acetate/EDTA (TAE) for cloning experiments. SYBR safe (Fisher scientific) was added to the gels to allow DNA visualization under UV exposure. Samples and 1 kb Plus DNA ladder were mixed with loading buffer and loaded into gel. Gels were migrated in 0.5x TBE or TAE buffer in a RunOne™ Electrophoresis Cell (EmbiTec) at 100 mV for an appropriate time allowing resolving of the bands. The gel visualization was performed by using MiniLumi (Bio-Imaging Systems) machine.

3.2.2.6. DNA extraction from agarose gel

NucleoSpin® Gel and PCR Clean-up (Macherey-Nagel) were used to extract DNA fragments from the gels according to manufacturer's instructions.

3.2.2.7. Ligation

Ligation reactions were performed using T4 DNA ligase from NEB according to manufacturer's instructions.

3.2.3. Polymerase chain reaction (PCR)

3.2.3.1. RNA extraction

RNA extractions were performed using NucleoSpin RNA, mini Kit from Machery-Nagel according to manufacturer's instructions.

3.2.3.2. DNase treatment

Degradation of DNA contaminant was performed using RNase-free DNase I (Ambion) according to the manufacturer's instructions.

3.2.3.3. Genomic DNA extraction (gDNA)

gDNA was extracted by using the QuickExtract DNA extraction solution (Euromedex). Cellular pellets were incubated in an appropriate volume of extracting solution, vortexed for 30 seconds, and incubated for 6 minutes at 65°C. Next, tubes were vortexed for 30 seconds and incubated for 2 minutes at 95°C. The gDNA concentration was determined by using a spectrophotometer. gDNA was stored at –20 °C or directly used for polymerase chain reaction (PCR).

3.2.3.4. Reverse transcription

The generation of complement DNA (cDNA) from the extracted mRNA was performed with the use of Moloney Murine Leukemia Virus (M-MuLV) reverse transcriptase, in the presence of RNase inhibitor. In brief, mRNA was annealed with random hexamers at 70°C for 10 minutes. Next, 0.5 mM dNTP, Moloney Murine Leukemia Virus (M-MuLV) reverse transcriptase, RNase inhibitor, and appropriate buffers were mixed and were incubated at room temperature for 15 minutes and then at 42°C for 30 minutes, enzymes were degraded by 70°C for 10 minutes. Samples were stored at -20°C.

3.2.3.5. Conventional PCR condition

Conventional PCR were performed using two different polymerases from NEB. These enzymes, their properties, and their usages are recapitulated in the table below:

Enzyme Name	Proof-reading	Usage	Buffers
OneTaq 2X mastermix	No	Screening procedures	Standard buffer and GC-rich buffer
Q5 High-fidelity 2X mastermix	Yes	Sequencings T7E1 Cloning	Standard

Because PCR were performed on gDNA extract, several adjustments were made to obtain only specific amplification products. Specifically, touchdown PCR protocol were used, where the initial annealing temperature is higher than the optimal T_m of the primers. After every cycle, the annealing temperature is decreased until it reaches the specific T_m of the primers. The amplification conditions mainly used throughout this study are recapitulated below:

Target: ORAI1/ORAI3. Enzyme: OneTaq polymerase. Buffer: GC buffer

	Step	Temperature	Time
	Initial denaturation	94°C	3 minutes
Cycles 1 to 10	Denaturation	94°C	20 seconds
	Primer annealing	65°C (-1°C/cycle)	30 seconds
	Elongation	68°C	1 minute / kb
Cycles 11 to 42	Denaturation	94°C	20 seconds
	Primer annealing	55°C (-1°C/cycle)	30 seconds
	Elongation	68°C	1 minute / kb
	Final elongation	68°C	5 minutes
	Hold	12°C	∞

Target: ORAI1. Enzyme: Q5 polymerase.

	Step	Temperature	Time
	Initial denaturation	98°C	3 minutes
Cycles 1 to 3	Denaturation	98°C	45 seconds
	Primer annealing	72°C	45 seconds
	Elongation	72°C	30 second / kb
Cycles 4 to 6	Denaturation	98°C	45 seconds
	Primer annealing	71°C	45 seconds
	Elongation	72°C	30 second / kb
Cycles 7 to 9	Denaturation	98°C	45 seconds
	Primer annealing	70°C	45 seconds
	Elongation	72°C	30 second / kb
Cycles 10 to 42	Denaturation	98°C	45 seconds
	Primer annealing	69°C	45 seconds
	Elongation	72°C	30 second / kb
	Final elongation	72°C	3 minutes
	Hold	12°C	∞

Target: ORAI3. Enzyme: Q5 polymerase.

	Step	Temperature	Time
	Initial denaturation	98°C	3 minutes
Cycles 1 to 3	Denaturation	98°C	45 seconds
	Primer annealing	72°C	45 seconds
	Elongation	72°C	30 second / kb
Cycles 4 to 6	Denaturation	98°C	45 seconds
	Primer annealing	71°C	45 seconds
	Elongation	72°C	30 second / kb
Cycles 7 to 9	Denaturation	98°C	45 seconds
	Primer annealing	70°C	45 seconds
	Elongation	72°C	30 second / kb
Cycles 10 to 12	Denaturation	98°C	45 seconds
	Primer annealing	69°C	45 seconds
	Elongation	72°C	30 second / kb
Cycles 13 to 42	Denaturation	98°C	45 seconds
	Primer annealing	68°C	45 seconds
	Elongation	72°C	30 second / kb
	Final elongation	72°C	3 minutes
	Hold	12°C	∞

3.2.3.6. Quantitative real-time PCR (qPCR)

qPCR was performed using SsoFast™ EvaGreen® Supermix polymerase (Bio-Rad) on CFX C1000 instrument (Bio-Rad). Primer sequences used in this study are indicated in the oligonucleotide section. Glyceraldehyde-3-phosphate dehydrogenase (GAPDH) and TATA-box-binding protein (TBP) were used as housekeeping genes. Each experiment was repeated four times. RT-qPCR data were analyzed with the common base method, which accounts for the specific qPCR efficiency of each analyzed gene (Ganger *et al*, 2017).

3.3. CRISPR/Cas9 related techniques

3.3.1.gRNA design

The gRNAs used in this study were designed using the CRISPOR website (<http://crispor.tefor.net/>) (Concordet & Haeussler, 2018). For the *ORAI1* and *ORAI3* gene knockin (KI) experiment, the input sequence consisted in a 100 base pair region surrounding the *ORAI1* or *ORAI3* start codon. The genome chosen for identification of potential off-target sequences was the human genome assembly (GRCh38/hg38). The protospacer motif (PAM) selected for identification gRNAs was NGG sequence (With N for any nucleotide, and G for guanine). From the selection of gRNAs proposed by the algorithm (53 gRNAs for *ORAI1*; 63 for *ORAI3*), the final choice of gRNAs was dictated by: 1- the localization of the double strand break site induction; 2- the specificity score; 3- the predicted efficiency score.

For the *ORAI1* knockout (KO) experiment, input sequence corresponded to a 114 base pair sequence ranging from alternative start codon of *ORAI1* until the end of the first exon (+189 to +303 from CDS).

For the *ORAI3* (KO), input sequences corresponded to a 115 base pair sequence equivalent (+114 to +229 from CDS). From the selection of gRNAs proposed by the algorithm (14 gRNAs for *ORAI1*; 63 for *ORAI3*), the final choice of gRNAs was dictated by: 1- the specificity score; 2- the predicted efficiency score.

For the *ORAI1* and *ORAI3* expression enhancement experiments, the putative promoting region were identified *via* e!Ensembl website (<https://www.ensembl.org/index.html>). For *ORAI1*, a 350 bp region located above the *ORAI1* mRNA was used as input. For *ORAI3*, a 500 bp region located above the *ORAI3* mRNA was used as input. From the potential gRNA obtained, criteria for selection were the specificity and the localization across the targeted regions.

Sequences of gRNAs used in the study are presented in the table below:

Name	Sequences	Type of experiment
ORAI1 KI gRNA1	Fw: 5'- <u>CACC</u> GCGGGGCGGGCTCCGGATGCA -3' Rv: 5'- <u>AAAC</u> TGCATCCGGAGCCCGCCCCGC -3'	Knockin
ORAI1 KI gRNA2	Fw: 5'- <u>CACC</u> GGCGGCGTGCTCCATGCATC-3' Rv: 5'- <u>AAAC</u> GATGCATGGAGCACGCCGCC-3'	Knockin
ORAI1 KI gRNA3	Fw: 5'- <u>CACC</u> GATGCATGGAGCACGCCGCCG-3' Rv: 5'- <u>AAAC</u> CGGCGGCGTGCTCCATGCATC-3'	Knockin
ORAI3 KI gRNA1	Fw: 5'- <u>CACC</u> GCGCCCCCCCCCAGGATGAA -3' Rv: 5'- <u>AAAC</u> TTCATCCTGGGGGGGGGGCGC -3'	Knockin
ORAI3 KI gRNA2	Fw: 5'- <u>CACC</u> GCCGCCCCCCCCCAGGATGA -3' Rv: 5'- <u>AAAC</u> TCATCCTGGGGGGGGGGCGGC -3'	Knockin
ORAI3 KI gRNA3	Fw: 5'- <u>CACC</u> GCCCTCGCCGCCCTTCATCCT -3' Rv: 5'- <u>AAAC</u> AGGATGAAGGGCGGCGAGGGC -3'	Knockin
ORAI1 KO gRNA1	Fw: 5'- <u>CACC</u> GAAGCCGGAGAGCAGAGCCG -3' Rv: 5'- <u>AAAC</u> CGGCTCTGCTCTCCGGCTTC -3'	Knockout

ORAI1 KO gRNA2	Fw: 5'- <u>CACC</u> GTGGAGGCTTTAAGCTTGGCG -3' Rv: 5'- <u>AAAC</u> CGCCAAGCTTAAAGCCTCCAC -3'	Knockout
ORAI1 KO gRNA3	Fw: 5'- <u>CACC</u> GATGCATGGAGCACGCCGCCG -3' Rv: 5'- <u>AAAC</u> CGGCGGCGTGCTCCATGCATC -3'	Knockout
ORAI3 KO gRNA1	Fw: 5'- <u>CACC</u> GGGCCAGTCAGCACTCGCTG -3' Rv: 5'- <u>AAAC</u> CAGCGAGTGCTGACTGGCCC -3'	Knockout
ORAI3 KO gRNA2	Fw: 5'- <u>CACC</u> G CCGAGAGCAAGGCAGACGTG -3' Rv: 5'- <u>AAAC</u> CACGTCTGCCTTGCTCTCGGC -3'	Knockout
ORAI3 KO gRNA3	Fw: 5'- <u>CACC</u> GTGGCCCGGCTGAGGTAGAGG -3' Rv: 5'- <u>AAAC</u> CCTCTACCTCAGCCGGGCCAC -3'	Knockout
Act ORAI1 gRNA1	Fw: 5'- <u>ACAC</u> GCTTCCAGGAAAAGTGGCGGG G -3' Rv: 5'- <u>AAAA</u> CCCC GCCACTTTCTCTGGAAGC-3'	Expression enhancement
Act ORAI1 gRNA2	Fw: 5'- <u>ACAC</u> GAGTGACCAGAGACTGCGCGCG G -3' Rv: 5'- <u>AAAA</u> CGCGCGCAGTCTCTGGTCACTC-3'	Expression enhancement
Act ORAI1 gRNA13	Fw: 5'- <u>ACAC</u> GACGTGACCCGCCCGCTCCGAG G -3' Rv: 5'- <u>AAAA</u> CTCGGAGCGGGCGGGTCACTC-3'	Expression enhancement
Act ORAI3 gRNA1	Fw: 5'- <u>ACAC</u> GAGTTCGTGTGTGTATCTGCG G -3' Rv: 5'- <u>AAAA</u> CCGCAGATACACACGAAC T C-3'	Expression enhancement
Act ORAI3 gRNA2	Fw: 5'- <u>ACAC</u> GCAAGCGCCCGGACCCACCG G -3' Rv: 5'- <u>AAAA</u> CCGGTGGGGTCCGGGCGCTTGC-3'	Expression enhancement
Act ORAI3 gRNA3	Fw: 5'- <u>ACAC</u> GAAGAACGTTATCCAAGCGCC G -3' Rv: 5'- <u>AAAA</u> CGGCGCTTGATAACGTTCT T C-3'	Expression enhancement
Underlined sequence represents the overhangs for cloning. Bold nucleotides represent the addition of guanine for increasing efficiency of U6 transcription initiation		

3.3.2.gRNA cloning

gRNA oligonucleotides sequences were cloned either in pX330 derived plasmids (addgene N°71814, 79145, 48138, 62988 ,48873, 48140, 62987) or in MLM3636 (addgene N° 43860). Specifically, plasmids were digested with Type IIS restriction enzyme (BbsI and BsmBI, for pX330-derived, and MLM3636 plasmids, respectively). Following digestion, plasmids were presenting the following overhangs: 5'-GTTT and 3'-GTGG, for pX330 derived plasmids; 5'-GTTT and 3'-TATC for MLM3636. As a consequence, complementary sequences of the overhangs were added to the gRNA sequences from above. Of note, because transcripts made under the control of the eukaryotic U6 promoters generally start with a guanine (G), this nucleotide was added in the beginning of the gRNA sequences when not naturally present. In addition, gRNA sequences were inspected for the absence of termination signal (TTTT).

To proceed to the cloning, a pair of oligonucleotides (sense and anti-sense) with appropriate overhangs (5'CACC or 5'-ATAG and 3'-CAAA) were ordered through Eurogentec.

3.3.2.1. Phosphorylation and annealing of the oligonucleotides

Prior to cloning, annealing and phosphorylation of the oligonucleotide was performed as follow: 100µM of each oligo were added in a PCR tube together with the T4 polynucleotide kinase (New England Biolabs [NEB]) and its buffer. In the thermocycler, phosphorylation step was performed due to a 30 min incubation at 37°C. The annealing step was performed due to a 5-minute incubation at 95°C followed by a ramp down to 25°C at 5°C/minute. Annealed oligonucleotides were subsequently diluted 250-fold (1:250) prior to ligation in the desired plasmid.

3.3.2.2. Ligation of oligonucleotides into CRISPR/Cas plasmids

Ligation of annealed oligo into the desired plasmid was performed in a single digestion-ligation reaction prepared as follow: 100ng of the appropriate vector were added in a PCR tube with 2µl of the diluted annealed oligonucleotides, 0.5µl of T7DNA ligase, 1µl of the appropriate restriction enzyme (BbsI or BsmBI), 2 µl of 10X buffer corresponding to the enzyme used and 1µl of a 1mM solution of DTT and ATP. This mixture tube was submitted to 6 cycles of 5 minutes incubation at 37°C and 5 minutes incubation at 23°C. Finally, 1 µl of the ligation product was transformed in competent bacteria.

3.3.3. T7 Endonuclease 1 (T7E1) assay

The T7Endonuclease1 (T7E1, NEB) assay allows the identification of mismatches in double stranded DNA. It is commonly used to report the level of activity of CRISPR-cas9 DSB induction. The principle of this assay is based on the fact that cellular reparation mechanisms through non homologous end joining (NHEJ) is error prone. Thus, following CRISPR-Cas9 and gRNA transfection in the cells targeted gDNA region will display “random scares” of the DSB. The region of interest is amplified by PCR and the PCR products are denatures and re-annealed. This lead to the annealing of DNA fragments that present different scares and thus presenting mismatches which are detected and cleaved by the endonuclease (**Figure 55**). Specifically, two days after the transfection of cells with the CRISPR-Cas9 plasmid and gRNA, gDNA was extracted. The region of DSB induction was amplified by PCR with the

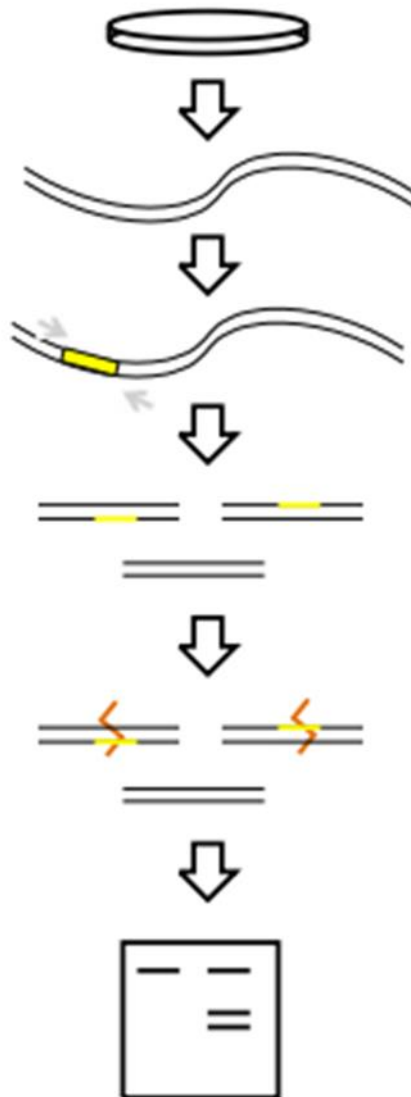


Figure 55 | T7 Endonuclease I (T7E1) assay principle.

From top to bottom:

- Cells are subjected to transfection with a plasmid coding for CRISPR/Cas9 plasmids and gRNA.
- Few days after transfection the genomic DNA (gDNA) is extracted.
- A PCR targeting the site of double strand break induction (DSB) is performed on the gDNA.
- The PCR products are denatured and re-annealed due to incubation at high temperature followed by cooling down. This procedure leads to the creation of double strand DNA presenting mismatches in their sequences (at the site of the initial DSB induction).
- The PCR products are incubated with the T7E1, which will specifically cleave the double stranded DNA presenting mismatches.
- Migration of PCR product on the gel allows the visualization of the proportion of DSB initially induced in the cells.

use of primers surrounding the region of interest (See primer list for details). Of note, since the result of the assay is representative of the level of mismatches present in the sample, this assay requires the use of proof-reading taq polymerase to avoid introduction of polymerization errors. In addition, PCR need to be robust and clean (conditions reported in table). PCR products are denatured by a two-minutes incubation at 95°C and subsequently re-annealed by a ramp down protocol as follow: a decrease from 95°C to 85°C at -2°C per second, followed by a decrease of 0.1°C per second until reaching 25°C. 1µg of the denatured/re-annealed PCR product is then incubated with the 0.5µl of T7E1 enzyme and its buffer for 20 minutes at 37°C. Cleaved product are subsequently loaded on a 2% agarose gel and visualized under UV light.

3.3.4. CRISPR-Cas9 related plasmids construction

3.3.4.1. CRISPR-Cas9 plasmids

Most of the CRISPR-cas9 plasmid used throughout this study were derived from the pX330 plasmid created by Zhang's team (Slaymaker *et al*, 2016). This plasmid contains two expression cassettes: 1- the engineered Cas9 sequence (eSsCas9[1.1]) linked to FLAG and (nuclear localization signal) NLS sequences under the control of CMV promoter; 2- the chimeric gRNA (engineered tracrRNA) which can be digested by the BbsI enzyme to allow insertion of specific gRNA sequence, under the control of U6 promoter. Variations of this plasmid used in this study are described in the table below.

Name	Difference with pX330	gRNA cloned:	Reference
eSpCas9 (1.1)	Original pX330 plasmid	ORAI1 KI gRNA1	Addgene 71814
		ORAI1 KI gRNA2	
		ORAI1 KI gRNA3	
		ORAI3 KI gRNA3	
		ORAI3 KI gRNA3	
		ORAI3 KI gRNA3	
pSpCas9(BB)-2A-GFP (PX458)	Cas9 expression cassette present 2A « self-cleavable » peptide before GFP sequence	ORAI1 KI gRNA3	Addgene 48138
		ORAI3 KI gRNA2	
		ORAI1 KO gRNA1	
		ORAI1 KO gRNA2	
		ORAI1 KO gRNA3	

		ORAI3 KO gRNA1	
		ORAI3 KO gRNA2	
		ORAI3 KO gRNA3	
pSpCas9n(BB)-2A-GFP (PX461)	Same as above, with mutated Cas9 (nCas9) leading to DNA nicks instead of DSB	ORAI1 KI gRNA3	Addgene 62987
		ORAI3 KI gRNA2	
pSpCas9(BB)-2A-Puro (PX459) V2.0	Cas9 expression cassette present 2A « self-cleavable » peptide before Puromycin resistance gene sequence	ORAI1 KI gRNA3	Addgene 48873
		ORAI3 KI gRNA2	
		ORAI1 KO gRNA2	
		ORAI3 KO gRNA3	
pSpCas9n(BB)-2A-Puro (PX462) V2.0	Same as above, with mutated Cas9 (nCas9) leading to DNA nicks instead of DSB	ORAI1 KI gRNA3	Addgene 66950
		ORAI3 KI gRNA2	

Plasmids non-derived from the pX330 plasmids are presented below:

Name	Specificity		Reference
pcDNA-dCas9-p300_Core	Inactive Cas9 (dCas9) unable to induce DSB, fused to transcriptional activating factor p300 Core		Addgene 61357
SP-dCas9-VPR	Inactive Cas9 (dCas9) unable to induce DSB, fused to transcriptional activating factor VPR		Addgene 63798
MLM3636	gRNA expression vector	ORAI1 activating gRNA 1	Addgene 43860
		ORAI1 activating gRNA 2	
		ORAI1 activating gRNA 3	
		ORAI3 activating gRNA 1	
		ORAI3 activating gRNA 2	

		ORAI3 activating gRNA 3	
pCAG-eCas9-GFP-U6-gRNA	Double expression cassette: eSpCas9 (1.1) fused to FLAG sequence and GFP sequence, and gRNA expression	ORAI1 gRNA3	Addgene 79145
		ORAI3 gRNA2	

3.3.4.2. Recombination plasmids

Recombination plasmids were constructed using the NEBuilder kit. Four different plasmids were constructed to perform homologous recombination experiments (HR): HR-ORAI1-sYFP2, HR-ORAI1-mT2, HR-ORAI3-mT2, HR-ORAI3-sYFP2. The structure of the HR plasmids included 4 elements (**Figure 56**):

- One backbone plasmid. pUC19 backbone was chosen because of its small size and because it does not allow expression of the sequence in contains in eukaryotic cells.
- Two homology sequences. The homologue sequences were stretches of 800 bp flanking the site of DSB induction of ORAI1 or ORAI3
- The fluorescent protein tags. The fluorescent proteins chosen were mTurquoise2 and sYFP2.

To obtain the homology sequences for ORAI1 and ORAI3, a PCR on gDNA extracted from HEK-293 was performed. The sequence amplified corresponded to the region -1000 / +1000 relative the ATG of *ORAI1* or *ORAI3* gene. This PCR product was purified and NEBuilder PCR were performed using this template. The primer used for the creation of HR plasmid with the NEBuilder kit are shown in the primer section.

3.3.4.3. PITCh plasmids

The PITCh systems for generating KI requires the use of two plasmids (**Figure 57** (Sakuma *et al*, 2016)):

- The CRISPR/Cas9 plasmid coding for the Cas9 protein and inducing the transcription of two gRNAs. The first gRNA sequence corresponding to the desired sequence of KI induction, and the second gRNAs named PITCh gRNA leading to the induction of DSB in the recombination plasmid (PITCh plasmid).
- The PITCh plasmid containing the following elements: the backbone plasmids, the specific gRNA sequences of the PITCh system, of the microhomology domains (25 nucleotides) corresponding to the 3' and 5' sides of the DSB induction site for ORAI1 or ORAI3 sequence, a cassette coding for the puromycin resistance gene followed by a self-cleavable T2A sequence followed by the desired fluorophore to insert.

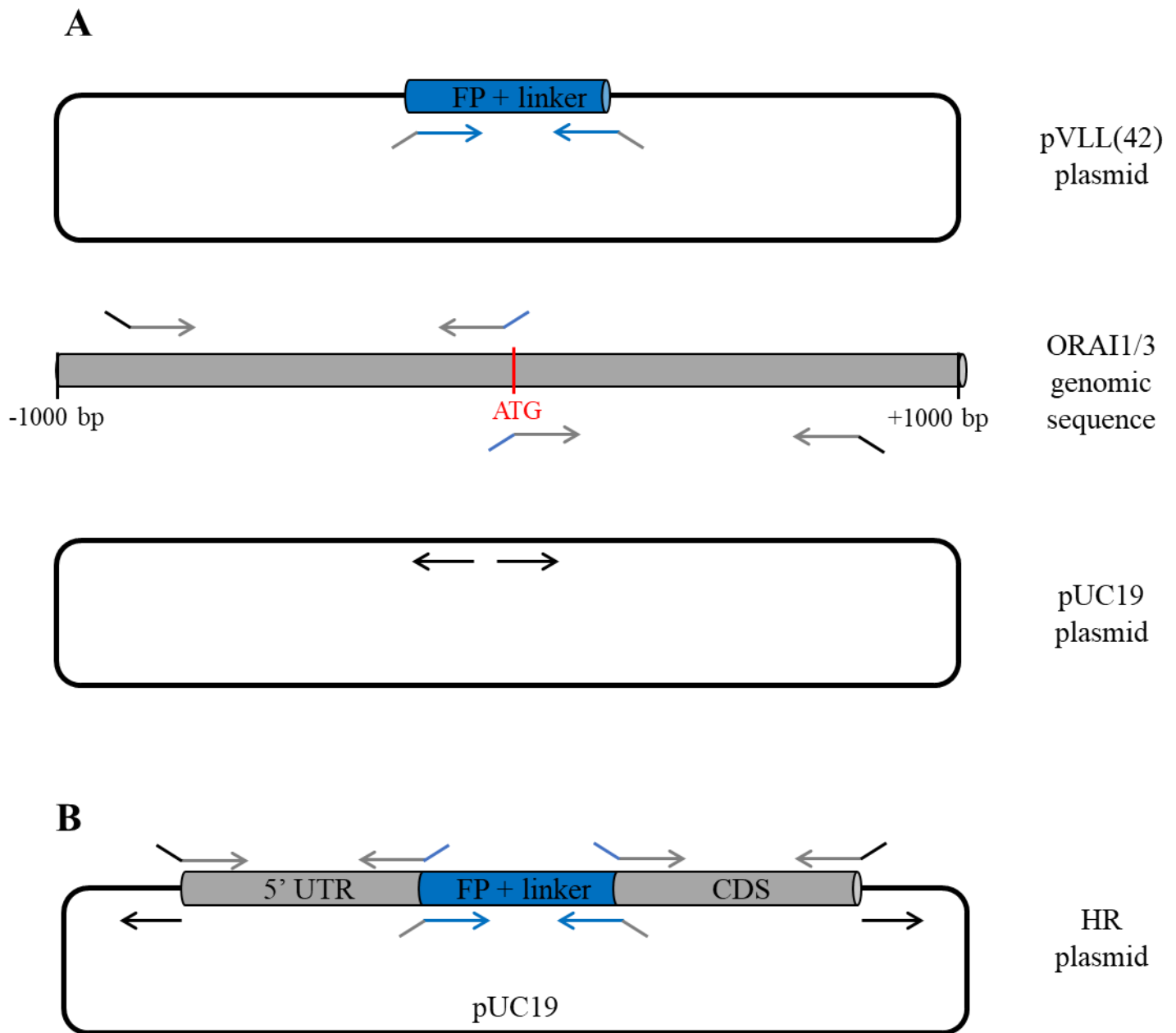


Figure 56 | Construction of Homologous Recombination (HR) plasmid using the NEBuilder kit.

- A. Representation of the initial PCR performed to obtain fragments to assemble for the HR plasmid construction. The primer pairs are represented as arrows. For the construction of HR plasmids, four PCR were performed: 1st a PCR amplifying the desired fluorescent tag (top scheme); 2nd and 3rd a PCR amplifying the desired region spanning the site of double strand break induction by the CRISPR/Cas9 system; 4th a PCR amplifying the desired backbone plasmid (pUC19).
- B. Scheme representing the final assembled HR plasmid. The primers pairs used during the initial PCR are spanning over each fragment junctions.

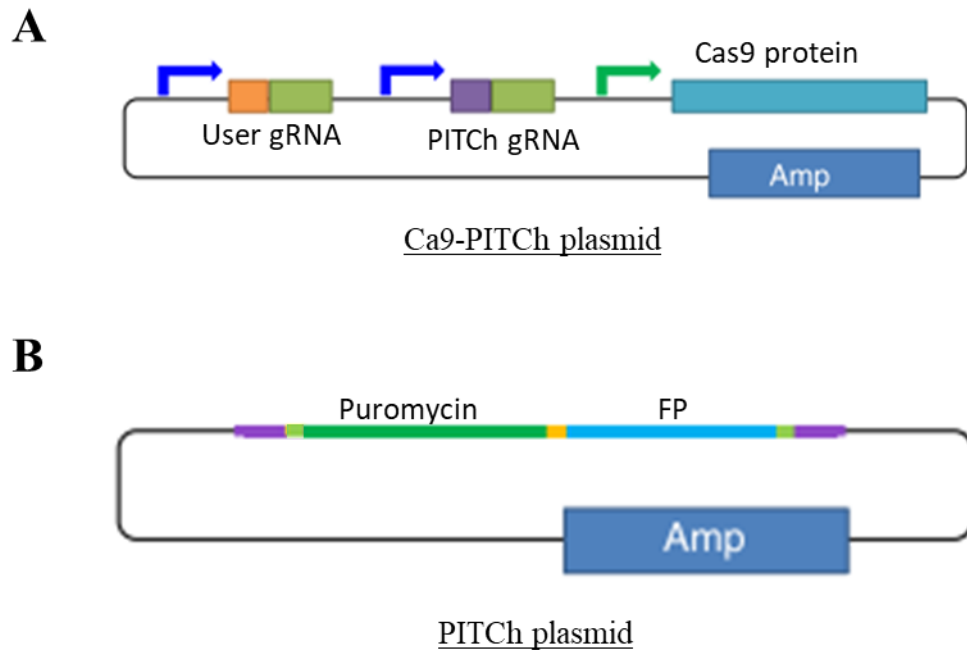


Figure 57 | Precise integration into target chromosome (PITCh) experiment design.

The PITCh requires the use of two plasmids

- A. The Cas9-PITCh plasmid possess sequences coding for: a user define gRNA (orange), a specific PITCh gRNA (violet) both under the control of the U6 promoter (blue arrow) , and the Cas9 protein under the control of CBh promoter (green arrow).
- B. The PITCh plasmid possess sequences corresponding to the PITCh gRNA (violet), microhomology domain corresponding to the 3' and 5' regions of the double strand break induction site in the genomic DNA (light green), a puromycin resistance cassette (dark green), a self-cleavable 2A sequence (yellow), and the sequence of the desired fluorescent protein (FP, blue).

Adapted from Sakuma et al, 2016.

Thus following, the transfection of both plasmids in the cell, DSB are induced at the location of desired insertion in the genomic DNA as well as in the donor PITCh plasmid leading. The KI generation is induced due to the presence of the microhomology domains, and the selection of the correctly edited cells is achieved *via* puromycin selection.

3.3.4.4. mCherry-eGFP Surrogate plasmids

In brief this method is based on the co-transfection of a Cas9-gRNA plasmid, and of a second plasmid designed as follow: a first expression cassette coding for mCherry is followed by the target gRNA sequence together with its PAM sequence. Further away an out-of-frame (relative to the initial mCherry) eGFP coding sequence is inserted after the PAM sequence (**Figure 58**). Thus, in case of successful induction of DSB in the cell, the plasmid will be cut. Since cellular reparation mechanisms aiming to repair DBS are error prone and are targeting all DSB, the plasmid might be repaired. In addition, due to error prone reparation mechanism, the repaired plasmid might display the eGFP cassette in frame with mCherry, as a consequence, successful DSB induction and reparation should results in cells displaying eGFP and mCherry fluorescence.

3.3.5. Genomic sequencing

Genomic sequencing was performed to validate the generation of KO cells. PCR region of the desired gene was amplified with proof-reading high-fidelity polymerases (Q5, NEB). PCR products were loaded on agarose gels and purified, before being cloned in pMiniT vector using the PCR cloning kit from NEB. In brief, the pMiniT vector allows blunt cloning in the open pMiniT vector. This vector is encoding a toxic minigene, positive insertion of genomic products in this sequence, breaks the reading frame and allow the bacteria to grow. The PCR products cloned into the vector were sequenced to verify the induction of KO from the CRISPR/Cas9 experiment.

3.4. Oligonucleotides

3.4.1. Primers

All oligonucleotides used in this work were purchased from Eurogentec.

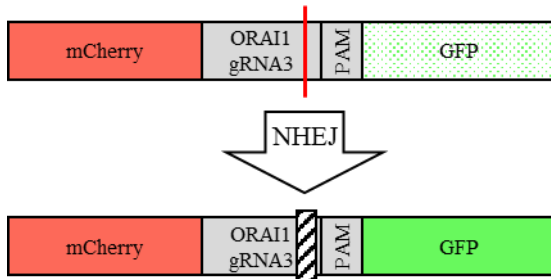
3.4.1.1. PCR

Several couples of primers were designed and tested throughout this study. The following table recapitulates:

- The target gene and as well as the annealing area within the gene target.
- The forward (FW) and reverse (RV) sequences of the primers.
- The expected sizes of the PCR product in base pair (bp). When two sizes are indicated, the *italicized* corresponds the size expected for the specific experiment (*i.e*, recombination or KO screening)

- The type of experiment for which primers were used (T7E1 assay, Recombination assessment, knockout assessment). In case the primers were used for T7E1, the number between parenthesis indicates the expected size of cleaved bands following T7E1 cleavage.

pBS SK mCherryROSAeGFP
ORAI1 gRNA3



pBS SK mCherryROSAeGFP
ORAI3 gRNA2

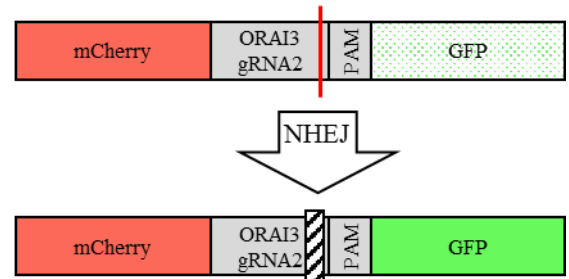


Figure 58 | Surrogate reporter system for visualizing gRNA efficiency.

Strategy of surrogate reporter system. The system is based on a plasmid coding for the mCherry gene (red rectangle) followed by an out-of-frame GFP gene sequence (dotted green rectangle). In between these sequence is inserted the target gRNA sequence (ORAI1gRNA3 or ORAI3gRNA2) together with the protospacer adjacent motif (PAM). Following CRISPR-Cas9 cutting of the surrogate plasmid, the cellular non homologous end joining (NHEJ, black arrow) system repairs the plasmid. This error prone reparation mechanism leads to shift of the GFP sequence reading frame potentially placing both mCherry and GFP sequences in the same reading frame (potential shift is represented by the black hatched rectangle, in frame GFP is represented by the green rectangle). Left, plasmid representation for ORAI1gRNA3. Right, plasmid representation for ORAI3 gRNA2.

Target	Sequence	Sizes (bp)	Usage
ORAI1 (5'UTR – Exon1)	FW 5'-GGCACTTCTTCGACCTCGTC-3' RV 5'- CTTGTCACCACCCCAGATCG-3'	647	T7E1 KI (507+140 bp)
		1487 / 647	Recombination (gDNA level)
		647 / 381	Knockout
FP – ORAI1 (Exon 2)	FW 5'- GAAGGGCATCGACTTCAAGGA-3' RV 5'- TGATCATGAGCGCAAACAGG-3'	866	Recombination (mRNA level)
ORAI1 (Upstream 5'UTR – Intron 1)	FW 5'- TCCCTCAGCGTAGCACGTAAT-3' RV 5'- AAAACTGAGGGGGGACTGGTTG-3'	1922	HR plasmid construction
ORAI1 (5'UTR – Intron 1)	FW 5'- TTCTTCGACCTCGTCCTCCT-3' RV 5'- GGTACGTGACCTGCTCTGAC-3'	1633	T7E1 KO (914+719 bp)
ORAI3 (5'UTR – Intron1)	FW 5'- GACGCTGCTTTTCTTGCTCC -3' RV 5'- GCCCCCTTTAACCTGTCTCC-3'	505	T7E1 KI (298+207 bp)
		1340 / 505	Recombination (gDNA level)
ORAI3 (5'UTR – Exon 1)	FW 5'- CGCAGACGCTGCTTTTCTTG-3' RV 5'- TTCCCCCTTTGACGAAAGCC-3'	526 / 328	Knockout
FP – ORAI3 (Exon 2)	FW 5'- GAAGGGCATCGACTTCAAGGA-3' RV 5'- GCTCACAGCTTCAATGTGGG-3'	843	Recombination (mRNA level)
ORAI3 (Upstream 5'UTR – Intron 1)	FW 5'- TGGAAATAGCAGCCAACGGA -3' RV 5'- CCATCCCCTTCCTGTGAGG-3'	1845	HR plasmid construction
ORAI3 (5'UTR – Intron 1)	FW 5'- CCGGGTCTGTACAATACGGTT-3' RV 5'- GGTACGTGACCTGCTCTGAC-3'	1633	T7E1 KO (914+719 bp)

5' UTR: 5' untranslated region.

FP: fluorescent protein (mTurquoise2/sYFP2).

gDNA : genomic DNA

mRNA : messenger RNA

KI: TE71 experiment to assess gRNA efficiency for knockin experiment

KO: TE71 experiment to assess gRNA efficiency for knockout experiment

The following table display the primer couples that did not lead to robust PCR signal. Thus, they were tested but not used in the experiment due to, absence of PCR products, or high level of nonspecific amplifications.

Target	Sequence	Sizes (bp)	Usage
ORAI1 (5'UTR – Exon 1)	FW 5'- CAACAACGCCCACCTTCTTGG-3' RV 5'- CGGAGTAACTCTGGCCGATC-3'	521	T7E1
ORAI1 (5'UTR - Intron 1)	FW 5'- TTCTTCGACCTCGTCCTCCT-3' RV ₍₁₎ 5'-GTTTCTCCCAGCTCTTCCCC-3' RV ₍₂₎ 5'-AGCCCATTCAACGGGAACAT- 3'	558 ₍₁₎ 1057 ₍₂₎	T7E1
ORAI1 (5'UTR – Exon 2)	FW 5'- CCAAAGGGGATATGGGCCTC-3' RV 5'- TGATCATGAGCGCAAACAGG-3'	977	Recombination (gDNA)
ORAI1 (Upstream 5'UTR – Intron 1)	FW 5'- TCCTGGAATCCCTCAGCGTA-3' RV 5'- TCTCGGAAAATGCGGTGGAA-3'	1889	HR plasmid construction
ORAI3 (5'UTR - Intron 1)	FW 5'- TGGAAATAGCAGCCAACGGA -3' RV 5'- CCATCCCCTTCCTGTGAGG-3'	1250	T7E1
ORAI3 (5'UTR - Intron 1)	FW 5'- GTTCTTGGTGGGTAGGGGTC-3' RV 5'- GCCCCCTTTAACCTGTCTCC-3'	1504	Recombination (gDNA)
ORAI3 (5'UTR – Exon 1)	FW 5'- CCGGGTCTGTACAATACGGTT-3' RV 5'- GCTCACAGCTTCAATGTGGG-3'	939	Recombination (mRNA)

3.4.1.2. qPCR

The qPCR primers used in this study are shown in the table below:

Target	Sequence	Sizes (bp)
ORAI1	FW 5'- ATGGTGGCAATGGTGGAG -3' RV 5'- CTGATCATGAGCGCAAACA -3'	122
ORAI2	FW 5'- ACCTGGAACCTGGTCACCTCT -3' RV 5'- ATGGCCACCATGGCAAAGC -3'	133
ORAI3	FW 5'- GGCCAAGCTCAAAGCTTCC -3' RV 5'- CCTGGTGGGTACTCGTGGT -3'	105
GAPDH	FW 5'- ACCCACTCCTCCACCTTTG -3' RV 5'- CTCTTGTGCTCTTGCTGGG -3'	178
TBP	FW 5'- CTTGACCTAAAGACCATTGCACTTC -3' RV 5'- GTTCTTCACTCTTGGCTCCTGTG -3'	266

3.4.1.3. Cloning primers

Most of the cloning experiments were performed using NEBuilder system (described thereafter) which involves the use of primers annealing to the target sequence and overlapping to the sequences to be joined. In the following tables, the sequences indicated in uppercase correspond to sequences annealing to the target, while lowercase sequences correspond to the overlapping part.

HR-ORAI1-FP		
Annealing target	Sequence 5'→ 3'	Overlapping target
pUC19	TACCCAACCTTAATCGCCTTG	
	ACGCCAGGGTTTTCCAG	
ORAI1 5'UTR	tgctgcaaggcgattaagttgggtaAGAATTGCTTGAACCCAG TAATAAAAAATAATAAATCAGGAACCGGTCACCTCAATAC	pUC19
	ccttgctcaccatGGAGCACGCCGCCGAGGC	FP
FP plasmid	ggcggcgtgctccATGGTGAGCAAGGGCGAGGAG	ORAI1 5'UTR
	gggctcgggatgcCCGCGGCCAACACCACCG	ORAI1 CDS
ORAI1 CDS	gtgttgccgcgggCATCCCGAGCCCGCCCC	
	gtcgtgactgggaaaaccctggcgtAAAATGCGGTGGAAAAGGGGTGT CAGG	
HR-ORAI3-FP		
Annealing target	Sequence 5'→ 3'	Overlapping target
pUC19	TACCCAACCTTAATCGCCTTG	
	ACGCCAGGGTTTTCCAG	
ORAI3 5'UTR	atgtgctgcaaggcgattaagttgggtaGGTCCCGCCCCTCCGCGC	pUC19
	ccttgctcaccatCCTGGGGGGGGGGCGGCA	FP
FP plasmid	ccccccccaggATGGTGAGCAAGGGCGAGGAG	ORAI3 5'UTR
	ctgcgcgccttcCCGCGGCCAACACCACCG	ORAI3 CDS
ORAI3 CDS	gtgttgccgcggGAAGGGCGGCGAGGGGGA	
	gtcgtgactgggaaaaccctggcgtTTGAGACTCGCTTATCAGTTTCCT CATCAGCC	

3.4.2.Expression plasmid

The expression plasmids coding for ORAI1 and ORAI3 fused to mTurquoise2, and sYFP2 respectively, used in this study were a generous gift from Dr Bidaux. In brief, ORAI1 and ORAI3 coding sequence were cloned in frame with mTurquoise2 or sYFP2 sequences into a pVLL vector (Bidaux *et al*, 2018). These vectors were designed in order to improve FRET occurrence by facilitating the modification of the linker size between the FP and GOI sequences. In addition, the linker sequence is enriched in glycine and valine residues to limit misfolding of the chimera and increase the flexibility. The amino acids sequences of the linkers used in this study was: 5'-TGGVGAGGGGGLPVVGGVVGGGVVGGVVGVGLPGGAGGVGRG-3' (VLL42). The other plasmids used in the study are presented in the table below:

Name	Initial purpose	Cloning method	Reference
pCMV-Myc-ORAI1	Ca ²⁺ imaging	/	/
pCMV-Myc-ORAI3	Ca ²⁺ imaging	/	/
STIM1-mCherry	FLIM-FRET	/	/
mTurquoise2-VLL-ORAI1	FLIM-FRET	Restriction cloning	Dr Bidaux
sYFP2-VLL-ORAI3	FLIM-FRET	Restriction cloning	Dr Bidaux
eGFP-ORAI1	TIRF	Restriction cloning	Bokhobza
eGFP-ORAI3	TIRF	Restriction cloning	Bokhobza
mCherry-ORAI1	TIRF	Restriction cloning	Bokhobza
mCherry-ORAI3	TIRF	Restriction cloning	Bokhobza
CLIP-ORAI1	spt	NEBuilder cloning	Bokhobza
CLIP-ORAI3	spt	NEBuilder cloning	Bokhobza
SNAP-ORAI1	spt	NEBuilder cloning	Bokhobza
SNAP-ORAI3	spt	NEBuilder cloning	Bokhobza
HaloTag-ORAI1	spt	NEBuilder cloning	Bokhobza
HaloTag-ORAI3	spt	NEBuilder cloning	Bokhobza
mEOS2-ORAI1	TIRF	NEBuilder cloning	Bokhobza
mEOS2-ORAI3	TIRF	NEBuilder cloning	Bokhobza
Dendra-ORAI1	TIRF	NEBuilder cloning	Bokhobza
Dendra-ORAI3	TIRF	NEBuilder cloning	Bokhobza
ddGFP-A-ORAI1	BiFC	NEBuilder cloning	Bokhobza
ddGFP-B-ORAI1	BiFC	NEBuilder cloning	Bokhobza
ddYFP-A-ORAI1	BiFC	NEBuilder cloning	Bokhobza
ddYFP-B-ORAI1	BiFC	NEBuilder cloning	Bokhobza
ddGFP-A-ORAI3	BiFC	NEBuilder cloning	Bokhobza
ddGFP-B-ORAI3	BiFC	NEBuilder cloning	Bokhobza
ddYFP-A-ORAI3	BiFC	NEBuilder cloning	Bokhobza
ddYFP-B-ORAI3	BiFC	NEBuilder cloning	Bokhobza
Venus-N173-ORAI1	BiFC	NEBuilder cloning	Bokhobza
Venus-C173-ORAI1	BiFC	NEBuilder cloning	Bokhobza
Venus-N173-ORAI3	BiFC	NEBuilder cloning	Bokhobza
Venus-C173-ORAI3	BiFC	NEBuilder cloning	Bokhobza
STIM1-Venus-N173	BiFC	Restriction cloning	(Hertel <i>et al</i> , 2016)
STIM1-Venus-C173	BiFC	Restriction cloning	(Hertel <i>et al</i> , 2016)
STIM1-VLL-mTurquosie2	FLIM-FRET	NEBuilder cloning	Bokhobza

STIM1-VLL-sYFP2	FLIM-FRET	NEBuilder cloning	Bokhobza
ORAI1-GCaMP6f	Ca ²⁺ imaging	Restriction cloning	(Dynes <i>et al</i> , 2016b)
G-GECO-ORAI3	Ca ²⁺ imaging	Restriction cloning	(Dynes <i>et al</i> , 2016b)

3.5. Cell lines, bacterial strains, and growth condition

3.5.1. Cell lines and growth conditions

HEK-293 cell lines were cultured in Modified Eagle Medium (DMEM) + GlutaMAX™ (31966, Gibco™) supplemented with 10% fetal bovine serum (10270, Gibco™). PC-3 cell lines were cultured in Roswell Park Memorial Institute 1640 media supplemented with 10% fetal bovine serum and 2 mM L-Glutamine (25030, Gibco™). Both cell lines were split twice per week by using 0,05% Trypsin-EDTA (25300, Gibco™) and left to grow at 37°C in a humidified incubator with 5% CO₂. Mycoplasma check was performed by using Hoechst staining.

3.5.2. Bacterial strains and growth conditions

DH5- α and OneShot™ Stbl3™ *E.coli* strains were cultured in LB at 37°C while shaking at 200 rpm for around 16 hours. If needed, bacterial strains were conserved at 25% glycerol at -80°C.

3.6. Cell culture assay

3.6.1. Cell count

Direct cell counting was performed on cell suspension by using counting chamber Malassez (Marienfeld, Germany) according to the manufacturer's instructions. The cell doubling was calculated as according to the formula:

$$\text{Doubling time (hours)} = \frac{\text{Time between measurements (hours)} \times \log 2}{\log(\text{Cell number [Day } x]) - \log(\text{Cell number [Day } x - 1])}$$

3.6.2. Proliferation

Proliferation was assessed by using colorimetric assay. Initially, 1x10³ cells per well were plated into 96-well plate and left to settle overnight. Cells were fixed with 50% trichloroacetate and total proteins were stained with 0.4% sulforhodamine B. Stain was fixed with 1% acetic acid and dye was released by applying 10mM unbuffered Tris-base solution (pH=10.5). Wells without cells were considered as blank. Absorbance was measured at 485 nm with TriStar² Multimodal Reader LB942 (Berthold Technologies).

3.6.3. Cell cycle analysis

For cell cycle analysis, cells were fixed with ice-cold 70% methanol, resuspended in 100 μ L of PBS with 500 μ g/mL Ribonuclease A and stained with 50 μ g/mL of propidium iodide for 1 hour at 4°C.

Afterwards, cells were analysed with CyAn™ ADP Analyser FACScan flow cytometer (Beckton-Dickinson).

3.6.4. Adhesion Assay

For the adhesion assays, 96-well plates were coated with fibronectin as follow: 1 mg of lyophilized fibronectin (Sigma-Aldrich) was reconstituted in 1 mL of ddH₂O, this solution was diluted in PBS to a final concentration of 10 µg/mL. 20 µL of this solution were distributed in the 96-well plate and incubates for 5 minutes at room temperature. Next, fibronectin solution was removed by aspiration and remaining liquid was left to air-dry for 30 minutes under the hood. Following coating, 1×10^3 cells were loaded in each well and incubated at 37°C for one hour. After one hour, medium was discarded and the cells carefully washed twice with PBS before being fixed with ice-cold ethanol. The cell nuclei were stained with incubation in Hoechst solution (2.5 µg/mL) for 15 minutes at room temperature. Fluorescent signal from the nuclei was recorded with Nikon Eclipse Ti-E microscope. 4X objective was used to record the image of the whole well. Cell nuclei were counted automatically with an ImageJ macro. Data were plotted by using the SuperPlotsOfData webapp; for each individual experiment, 6–8 wells were used, and the experiments were repeated 4 times.

3.6.5. Video microscopy migration assay (Wound healing)

For the wound healing assay, culture insert from Ibidi were used to generate wound of a constant size throughout experiments. The silicon inserts delimitate two cell-containing compartments separated by a 500 µm cell-free space (± 100 µm). The inserts were placed in 12-well plates, 9×10^4 cells suspended in 70 µL of DMEM were added in each cell compartment, and 1 mL of DMEM was added in the well. 48 hours after seeding, inserts were removed creating a cell-free gap between the two compartments. 12-well plates were placed on the automated stage of a Nikon Eclipse Ti-E microscope equipped with a chamber to maintain the temperature at 37 °C and 5% CO₂. Pictures of the center of the wound were taken with the 4× objective lens every hour for a period of 48 hours. Wound closure was analyzed using a FiJI macro code modified from BioImage Informatics Index (<https://biii.eu/>). Time-series data representation was performed using PlotTwist webapp, quantitative data plotted using SuperPlotsOfData webapp

3.6.6. Boyden chamber migration assay (Transwell®)

Boyden chamber assay were performed using Transwell® inserts with 8 µm pore-size. 2×10^5 cells in 500 µL of DMEM were added on the top part of the insert. 24 hours post-seeding, insert were collected and the cells from the upper part of the membrane were removed by scraping. Cells migrated on the lower part of the insert were fixed with ice-cold methanol bath, washed with ddH₂O bathes and stained with crystal violet (1% crystal violet solution in 20% methanol). Counting of migrated cells was performed was performed using the 10× objective lens of a Nikon Eclipse TS100 microscope. Five

randomly selected fields of the insert were captured, and cells were counted manually using ImageJ software. Data obtained were plotted using SuperPlotsOfData webapp.

3.7. Transfections

Transfections were performed using PEI Max 40X. A 1mg/mL stock solution was prepared in ddH₂O and filtered-sterilized using 0.22µm pore-size filter. For transfections, the stock solution was diluted to obtain a 1µg/µL solution. Transfection solutions were prepared in FBS-free medium, and a ratio of plasmid quantity to PEI Max volume of 1µg for 2 µL was used. Transfection solutions were gently mixed by tube flicking and following a 15-minute incubation, the solution was added on the cells in a dropwise manner. Of note, the cell's medium was refreshed before addition of transfection mixes.

3.8. Macromolecule blotting

3.8.1. Protein extraction

The cells were lysed in 1x RIPA buffer supplemented with protease inhibitors. Next, the cell lysates were sonicated for 10 seconds, and centrifuged at 10000 g for 10 minutes to eliminate the nuclei fraction. The protein lysate concentration was measured with Pierce® BCA Protein Assay (Thermo Fisher Scientific).

3.8.2. Immunoblotting

For sodium dodecyl sulfate–polyacrylamide gel electrophoresis (SDS-PAGE), 50 µg of total protein lysate were loaded on polyacrylamide gels and submitted to electrophoresis. Next, separated proteins were transferred to methanol-activated polyvinylidene fluoride (PVDF) membranes with the Pierce G2 Fast Blotter (Thermo Fischer Scientific). Subsequently, the membranes were incubated in 5% nonfat milk in TBS-T buffer (15 mM Tris-HCl, 140 mM NaCl, 0.05% Tween20®, pH 7.4) for 1 hour at room temperature to prevent nonspecific protein binding. The blocked membranes were then incubated with primary antibodies overnight at 4°C. The next day, the membranes were incubated for 1 hour with horseradish peroxidase (HRP)-conjugated anti-mouse or anti-rabbit secondary antibodies diluted at 1/100,000 (Chemicon). Chemiluminescent detection of bound secondary antibodies was captured with Amersham Imager 600 (GE Healthcare Life Sciences) using the SuperSignal™ West Femto Maximum Sensitivity Substrate and the SuperSignal™ West Dura Maximum Sensitivity Substrate (Thermo Fischer Scientific). The antibodies used in the study are shown in the table below:

Target	Working concentration	Secondary antibody	Expected size	Source (reference)
ORAI1	0.5µg/mL (1/500)	Rabbit	35kDa	ProteinTech (13130-1-AP)

ORAI1	3.23 $\mu\text{g/mL}$ (1/200)	Rabbit	35kDa	Alomone (ACC-006)
ORAI1	1 $\mu\text{g/mL}$ (1/500)	Rabbit	35kDa	Abcam (ab115558)
ORAI1	0.4 $\mu\text{g/mL}$ (1/250)	Rabbit	35kDa	Sigma (HPA 016583)
ORAI1	1 $\mu\text{g/mL}$ (1/500)	Rabbit	35kDa	GeneTex (85057)
B-ACTINE	1/1000	Mouse	42 kDa	Sigma (A5441)

3.9. Calcium imaging

For calcium experiments, cells were plated on glass-bottom dishes pre-coated with Poly-L-Lysine (Ibidi) 3 days before the experiment. The ratiometric dye Fura-2-acetoxymethyl ester (AM) (Interchim) was used to measure cytosolic Ca^{2+} concentration variations. Specifically, Fura-2-AM was diluted in the 2 mM Ca^{2+} HBSS solution to a final concentration of 1 μM . The cells were incubated in this solution for 45 minutes in the dark at 37°C. Following this incubation, the cells were washed twice with the 0 mM Ca^{2+} HBSS solution. The experiments were performed in 1 ml of 0 mM Ca^{2+} HBSS solution. At the desired time, 100 μL of 0 mM Ca^{2+} HBSS containing 10 μM of thapsigargin (TG) was added (final TG concentration = 1 μM) to induce Ca^{2+} store depletion. Next, 1 mL of 8 mM Ca^{2+} HBSS was added upon the previous solution into the dish.

Acquisitions were performed on a Superfluor Nikon Eclipse Ti-series inverted microscope equipped with a 510/84 emission filter (wavelength/bandwidth) and coupled to an Rolera EM-C2 (Qimaging), under the objective 20x. A xenon lamp light (300 W) was used to excite Fura-2 and fluorescence was recorded after wavelength filtering due to the following filter pairs (wavelength/bandwidth): 340/26 and 387/11 nm. The acquisition software was Metafluor; the data obtained were exported to Microsoft Excel. Time-series graphics were generated by using the PlotTwist webapp for each individual experiment. Integral measurements were performed with Microsoft Excel, and data were plotted by using the SuperPlotsOfData webapp.

3.10. FLIM-FRET

3.10.1. Fluorophore choice

For the FLIM-FRET experiments, the mTurquoise2 and sYFP2 fluorescent protein were used as donor and acceptor molecules, respectively. Of note, in order to conduct successful FRET experiment, the FP chosen should possess some specific characteristics such as, a good overlap between the donor emission spectrum, and the acceptor excitation spectra, an important quantum yield of donor molecule,

and a good extinction coefficient of the acceptor molecule. All these characteristics are displayed by the chosen FP (**Figure 59**). In addition, because FRET efficiency was measured due to changes in donor lifetime, it is required that the donor present a mono exponential decay which the case of the mTurquoise2.

3.10.2. Experimental procedure

The microscope equipped for FLIM-FRET experiment was located in distant building. Because transportation of the cells from one building to another induced stress (changing of temperature, movements...) to the cells, optimization procedures for plating, transfection, transportation and acquisition were implemented. Thus, the cells plating in 30mm glass-bottom dishes pre-coated with Poly-L-Lysin was performed in the resident building. Following cell spreading in the dishes, cells were

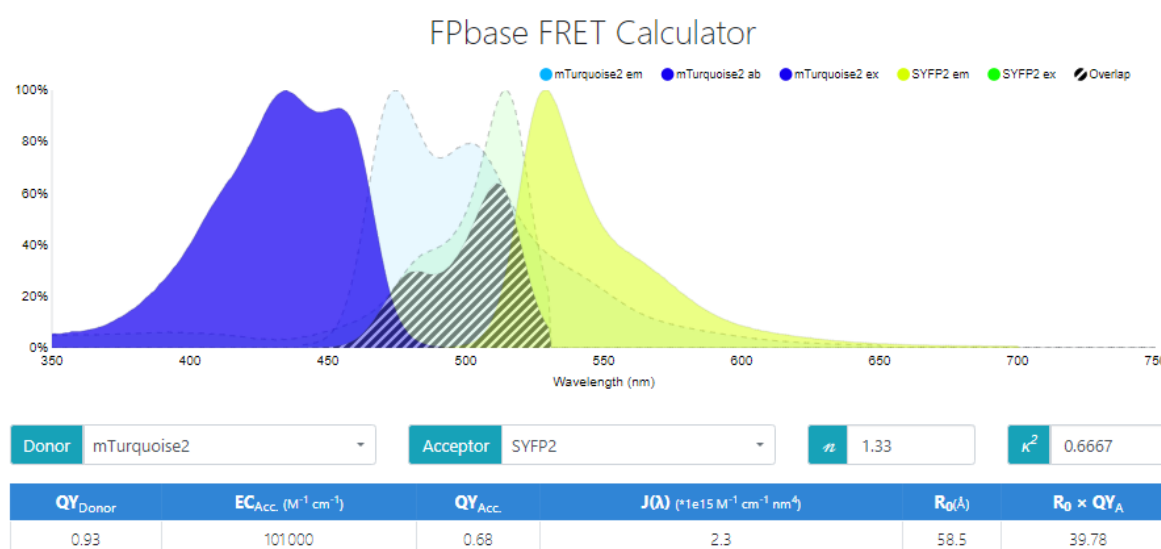


Figure 59 | mTurquoise2 – s Yellow Fluorescent Protein 2 (sYFP2) properties.

The mTurquoise2 and sYFP2 fluorescent protein were chosen as FRET pairs, because of the large overlap between the emission spectrum of mTurquoise2 (donor) and the excitation spectrum of sYFP2 (acceptor) (hatched surface), the good quantum yield of mTurquoise 2 (QY Donor), and the good extinction coefficient of sYFP2 (EC_{Acc.}).

Graphic generated from Fpbase (<https://www.fpbase.org/fret/>).

directly brought to the building equipped for FLIM-FRET experiment. One day later, cells were transfected, and imaging experiments were performed two days after transfection. For HEK-293, 1.5×10^5 cells were plated per dish. For PC3, 1.2×10^5 cells were plated per dish. Following their adhesion, the cells were transfected with different ratio of ORAI1-mTurquoise2, ORAI3-sYFP2, and STIM1-mCherry plasmids. Because the detector used during the FLIM measurements can be saturated by high levels of fluorescence, the quantity of plasmids transfected by condition was maintained low. The quantities of plasmid used for the different ratio are displayed in the table below.

Condition (ratio)	ORAI1-mT2	ORAI3-sYFP	STIM1-mCherry
Donor only (1:0:0)	0.3µg	0µg	0µg
Donor only (1:0:1)	0.3µg	0µg	0.3µg
Donor + Acceptor (1:1:0)	0.3µg	0.3µg	0µg
Donor + Acceptor (1:1:1)	0.3µg	0.3µg	0.3µg
Donor + Acceptor (1:3:0)	0.3µg	0.9µg	0µg
Donor + Acceptor (1:3:1)	0.3µg	0.9µg	0.3µg

3.10.3. Acquisition conditions

Before imaging, the cell medium was discarded, and cells were washed twice with 2 mM Ca^{2+} HBBS pre-warmed at 37°C. During the recordings, cells were incubated in 2 mM Ca^{2+} HBSS, treatment with TG or AA were performed 5 minutes before acquisition. Before fluorescence lifetime recording, expression of the different plasmid was confirmed by visual inspection of the fluorescent signal on the confocal microscope. During imaging, cells were maintained at 37°C using stage incubator.

FLIM experiments were performed with a Nikon A1 Eclipse Ti confocal, operated with NIS software. A pulsed diode laser, PDL 800-B (PicoQuant), delivered 20-MHz repetitive rate pulses at 405 nm. Single photons were collected through a 63x objective and detected through a 483/32 single-bandpass filter (Semrock) on single photon avalanche photodiodes (PDM Series; PicoQuant). Arrival time of single photons was measured with a time correlated single photon counting (TCSPC) counting card (HydraHarp 400; PicoQuant). The data were acquired with the SymPhoTime software (PicoQuant). Because the statistical determination of the distribution of single photon arrival times requires a minimum of 100 photons per pixel that was reached in ~120 frames, therefore 120 frames were acquired at 2 Hz for each TCSPC recording.

3.11. Statistical analysis and data presentation

Whenever possible, data were represented using superplots. Superplots, allow the visualization of all every data point performed within each experiment replicate and thus allow a better representation of the dispersion of the data. Super plots were generated using the SuperPlotsOfData webapp. Times series data were generated using the PlotTwist webapp and whenever possible traces corresponding to single data point were displayed. For all experiments and within technical replicates, median values

were used whenever the distribution of the data was considered non-normal (evaluated with the Shapiro–Wilk test, $p < 0.05$); otherwise, mean values were used. For statistical analysis, the means of the biological replicates was used. Error bars represent the 95% confidence interval (CI), except when stated otherwise. Of note, the 95% CI represents the interval in which the real value for a specific experiment is included, thus giving a visual interpretation of the significance of a result. The 95% CI was calculated from the mean of biological replicates [27]. Statistical analysis was performed by using the differences between the means of the conditions, except if stated otherwise. T.test were used for statistical analysis except if stated otherwise.

4. Results

4.1. Consideration before performing CRISPR-Cas experiment

The first aim of this PhD work was to generate knock-in in the *ORAI1* and *ORAI3* genes sequences. Specifically, it was decided to insert fluorescent tags at the N-terminal extremities of these genes because preliminary experiments and literature demonstrated that this location was not interfering with their functional roles. In order to generate KI one should: 1-create DSB in the genomic region where the foreign DNA piece wants to be inserted, and 2- provide a recombination template from which the DSB will be repaired by the cell that contain the foreign DNA piece to be inserted. Both mechanisms will be described in their specific section thereafter.

4.1.1. Model cell line to edit

The cell line to edit plays a crucial role in a successful CRISPR-Cas9 genome edition experiment. Because plasmids coding for Cas9 and gRNA need to be transfected and its coding sequence transcribed and translated into protein, it is required to use a proliferative cell line. In addition, a cell line that possesses a good transfection rate represents a good choice. Finally, one should pay attention to the cell line ploidy. Indeed, the rate of successful KI in the cell line will depend on the number of recombination event that occur within one cell, in case of haploid cells, a single HDR event per cell is required, while in diploid cell line, two HDR event will be required and so on for cell lines displaying higher ploidy. As a consequence, the HAP-1 haploid cell line was tested, but their cultivation and transfection rates turned out to be not optimal. Therefore, we used the HEK-293 cell line because: 1- it was routinely cultivated in the laboratory; 2- it is easily transfected; 3- it is a classic model used in the study of ORAI protein properties; 4- they are hypotriploid with a modal chromosome number of 64 in 30% of cells, and higher ploidy occurring in 4.2% of cells, meaning that around 65% of the cells are diploid.

4.1.2. Choice of the Cas protein to induce double strand break (DSB)

Nowadays, performing a genome editing experiment with the CRISPR-Cas9 is relatively simple but requires a careful design. Especially, one should consider the presence and the type of PAM present next to the desired target sequence. In addition, the best way of introducing both the Cas9 protein and gRNA sequences in the cell should be evaluated depending on the cellular type that one wants to edit. Moreover, the screening procedure for successful genome edition should also be taken into account. Finally, the existence of potential off-target effect (*i.e* induction of DSB at a non-desired location) should be studied, and if possible, evaluated. As described in the introduction, several CRISPR-Cas system were identified and have expanded the possibilities offered by genome editing techniques. Nonetheless, at the starting time of this project (*i.e* 2015) the number of CRISPR-Cas system available were more scarce. Thus, two different systems using different nucleases were available and considered:

- eSpCas9, engineered version of the classic Cas9 identified in *Streptococcus pyogenes*. Presenting an increased cutting specificity and efficiency developed by Zhang's lab (Slaymaker *et al*,

2016). Of note, this version uses the classic CRISPR-Cas9 PAM: NGG (where N denotes any nucleotide and G denotes guanine).

- hAsCpf1, humanized *acidaminococcus sp.* enzyme which generates staggered DSB and requires a TTT(A/C/G) PAM (where T, A, C, G denotes Thymine, Adenine, Cytosine, and Guanine respectively) (Zetsche *et al*, 2015). Because the DSB induced is staggered with this enzyme, the risk of deleterious off-target effect is decreased compared to the classic Cas9.

Thus, we faced the choice to use eSpCas9 or hAsCpf1 to perform our experiments. The final choice between these two systems was dictated by the presence of the required PAM in the 5'UTR regions of *ORAI1* and *ORAI3* genes as well as the number of potential off-target sites. Of note, when one wants to perform recombination, the DSB should be located as close as possible from the desired insertion point. Thus, the search for PAM motif was restricted to 100pb up- and down-stream of the start codon for both genes. Note that, at the time the search was performed, PAM sequence required for hAsCpf1 DSB induction was defined as: TTN, *ORAI1* region of interest present a single location for this motif, while *ORAI3* region of interest display six locations for this motif. At the opposite, more than 30 PAM motif corresponding to the eSpCas9 requirements were found next to our target region. Because of low number of potential gRNA to be used with the hAsCpf1 enzyme compared to the eSpCas9, the later was chosen for our experiments.

4.1.3.Delivery of the Cas9 protein in the cells

Following the choice of using eSpCas9 to induce the DSB, the best method for introducing the Cas9 protein and gRNA was considered. Currently, three main ways co-exist: the direct introduction of the complex Cas9-gRNA in the cells *via* microinjection; the transfection of two plasmids leading the expression of the Cas9 and the sgRNA independently; the transfection of a single plasmid coding for both the Cas9 and the sgRNA. The first solution is mainly proposed by specialized companies (selling lyophilized Cas9 proteins to be injected in the cells) and was marginal at the time of this work and thus was not considered. We choose to use the single plasmid method because it presents the advantage of performing a single transfection per experiment. Of note, the first experiments (*i.e.*, cutting efficiency assessment of the gRNAs) were conducted using a plasmid coding for eSpCas9. Nonetheless, the rapid development of CRISPR plasmids led us to use different plasmids throughout the PhD. Especially, plasmids encoding Cas9 protein linked via a self-cleavable T2A-peptide to a GFP or puromycin resistance cassette were used for genome editing experiments.

4.2. Generating gene knockin (KI) with CRISPR-Cas9

4.2.1.Design of gRNA

Design of the gRNA is probably the most crucial point of the genome editing experiment. Indeed, inattentive design might lead to low cutting efficiency preventing or delaying the obtention of edited genome, or to generation of off-target cuts that might affect the outcome of the totality of the experiment

performed on edited cells. Thus, two crucial points for design of gRNA to consider are the cutting efficiency and the off-target probability. The design of gRNA used were performed with the CRISPOR website (<http://crispor.tefor.net/crispor.py>) (Concordet & Haeussler, 2018).

4.2.1.1. Cutting efficiency

The cutting efficiency of a given gRNA is a predicted value (ranging from 0 to 100) relative to the probability of DSB induction at the specific site. This score is susceptible to variation for reasons not clearly defined. Secondary structure of chromatin is suggested to play a role as well as method of gRNA introduction in the cell (transfection of the plasmid and transcription inside the cell, versus direct modified gRNA injection). Of note, the predicted efficiency is not very accurate and constitute a simple indication (Haeussler *et al*, 2016). In addition, the DSB induction efficiency can be assessed by specific tests such as the T7 endonuclease assay (T7E1, used in this PhD). Importantly, the T7E1 assay is also inaccurate and does enable to discriminate very well between different efficiencies. Nonetheless, its results provide a visual representation of the absence or presence of DSB induction. The predicted efficiencies of the selected gRNA are presented in **Table 4**.

4.2.1.2. Cutting specificity

The second crucial parameter to be assessed when planning a CRISPR/Cas9 experiment is the specificity of the DSB. The specificity is defined by the probability that the Cas9 enzyme will create DSB at off-target site. Few parameters are important the establishment of the probability of cutting at non-target sites:

- The number of mismatches between the gRNA and the off-target site. The higher is the number of mismatches the lower is the probability of non-desired cuts.
- The localization of these mismatch on the gRNA. Mismatches located next the PAM decreases the probability of off-target cuts (12 adjacent to PAM, known as the seeding area).
- The localization of the off-target sites. Off-targets sites located on the same chromosome as the desired cutting site are more likely to be off-target.

A specificity score ranging from 0 to 100 is computed taking in to account the above parameters. Of note, because cutting efficiency of the enzymes for a specific location is computationally assessed but might vary in real conditions, it as a general advice to test different gRNA sequences before performing the genome editing experiment. As a consequence, the efficiencies of three different gRNA were tested for each gene with the T7E1 assay. The predicted efficiencies of the gRNA used are displayed in the **Table 4**.

Gene	gRNA	Sequence 5' → 3'	PAM	Cutting site (relative to ATG)	Predicted efficiency	Specificity score 1	Specificity score 2	Off-target sites	Next to PAM	Exon only	Chromosome 12/16 only
ORAI1	gRNA1	CGGGGCGGGCTCCGGATGCA	TGG	-2	38	77	90	0-0-3-13-109	0-0-2-0-0	40	3
	gRNA2	GGCGGCGTGCTCCATGCATC	CGG	4	50	74	88	0-0-0-7-121	0-0-0-3-1	12	4
	gRNA3	ATGCATGGAGCACGCCGCCG	AGG	-11	50	93	95	0-0-0-0-49	0-0-0-0-0	6	2
ORAI3	gRNA1	CGCCCCCCCCCAGGATGAA	GGG	2	47	74	86	0-0-1-9-142	0-0-1-2-1	25	8
	gRNA2	CCGCCCCCCCCCAGGATGA	AGG	1	37	60	75	0-0-1-25-256	0-0-1-3-2	38	23
	gRNA3	CCCTCGCCGCCCTTCATCCT	GGG	0	29	73	89	0-0-3-13-142	0-0-1-2-3	19	10

Table 4 | gRNA sequences chosen for knockin (KI) generation and their main characteristics.

Three gRNA sequences were designed for each gene. The predicted efficiency and the two specificity scores are ranging from 0 to 100 and were computed using Doench et al., and Hsu et al., publications. The number of off-target sites are displayed as follow: the first number represents the number of off-target sites presenting no mismatches with the target sequence, the second number represents the off-target sites presenting a single mismatch with the target sequence, the third number represents the off-target sites presenting two mismatches with the target sequence, and so on until 4 mismatches. The column: Next to PAM, resumes the preceding column but display the off-target sites which do not present mismatches in the gRNA seeding region (next to the PAM). The exon only column displays the number of predicted off-target sites present in exon exclusively. The column chromosome 12/16 only display the number of off-target sites present on the same chromosome as the target (chromosome 12 for ORAI1 and 16 for ORAI3). The gRNAs used in for this study are highlighted in golden).

4.2.2. Assessment of gRNA efficiencies

The cutting efficiencies of the gRNA designed above were assessed by T7E1 assay as described in the material and method section. In brief this test the T7E1 nuclease cleaves the double stranded DNA sequences when detecting mismatches. Of note, this technique does not display strong sensitivity but enables to verify that gRNAs are inducing DSB. Several sets of experiment were required to obtain reliable results. Indeed, even though transfection rate of HEK cells is usually high, in the absence of enrichment in positively transfected cells before performing T7E1 cells, the DSB induction could not be detected (**Figure 60A**). Thus, enrichment due to puromycin selection following the transfection of the Cas9-2A-Puro plasmid was tested (**Figure 60B**), but T7E1 results were not satisfying probably because of the lower cell number resulting from antibiotic selection. Therefore, enrichment due to GFP selection by FACS following transfection of Cas9-A-GFP plasmid was performed before extracting cells gDNA and performing T7E1 test. This enrichment method allowed us to obtain acceptable T7E1 results (**Figure 60C**) and to select the ORAI1 gRNA3 and ORAI3 gRNA2 to conduct the recombination experiments. In order to confirm that our selected gRNAs were inducing DSB in our cells, and that these DSB could be efficiently repaired by the cells, we used a surrogate strategy (Niccheri *et al*, 2017). In brief, this technique enables the visual validation of DSB induction through recording of green and red signal originating from eGFP and mCherry expression cassette (Please see material and method for full description of the assay). The result of this experiment confirmed that DSB were induced in our cells (**Figure 61**).

4.2.3. Recombination method

DSB are one of the most harmful type of DNA lesion. They can happen randomly during process such as mitosis or be induced due the exposure to deleterious element such as radiations or reactive oxygen species. Importantly, unrepaired DSB ultimately leads to cell death. As a consequence, cellular process evolved to specifically repair DSB. They can be divided in two mains pathways: the non-homologous end joining (NHEJ) and the homology direct repair (HDR) pathway. While genome editing techniques aiming to induce gene KO mostly rely on NHEJ mechanisms, gene KI techniques are usually taking advantage of HDR mechanisms. Specifically, HDR pathway requires the presence of long stretches of sequences homologous to the region where the DSB took place to repair the lesion. Of note, the natural frequency of HDR occurrence in cells is considered to be significantly lower level than NHEJ. Especially, because NHEJ mechanisms are functionally throughout the cell cycle (excluding mitosis), while HDR mechanism is active only during G2/S phase. In addition, NHEJ process is faster than HDR and the NHEJ process induces the inhibition of HDR pathways (Yang *et al*, 2020). Despite these limitations, the number of studies depicting strategies leading to successful integration of foreign DNA through HDR mechanism with impressive success rate, lead us consider that KI *ORAI1* and *ORAI3*

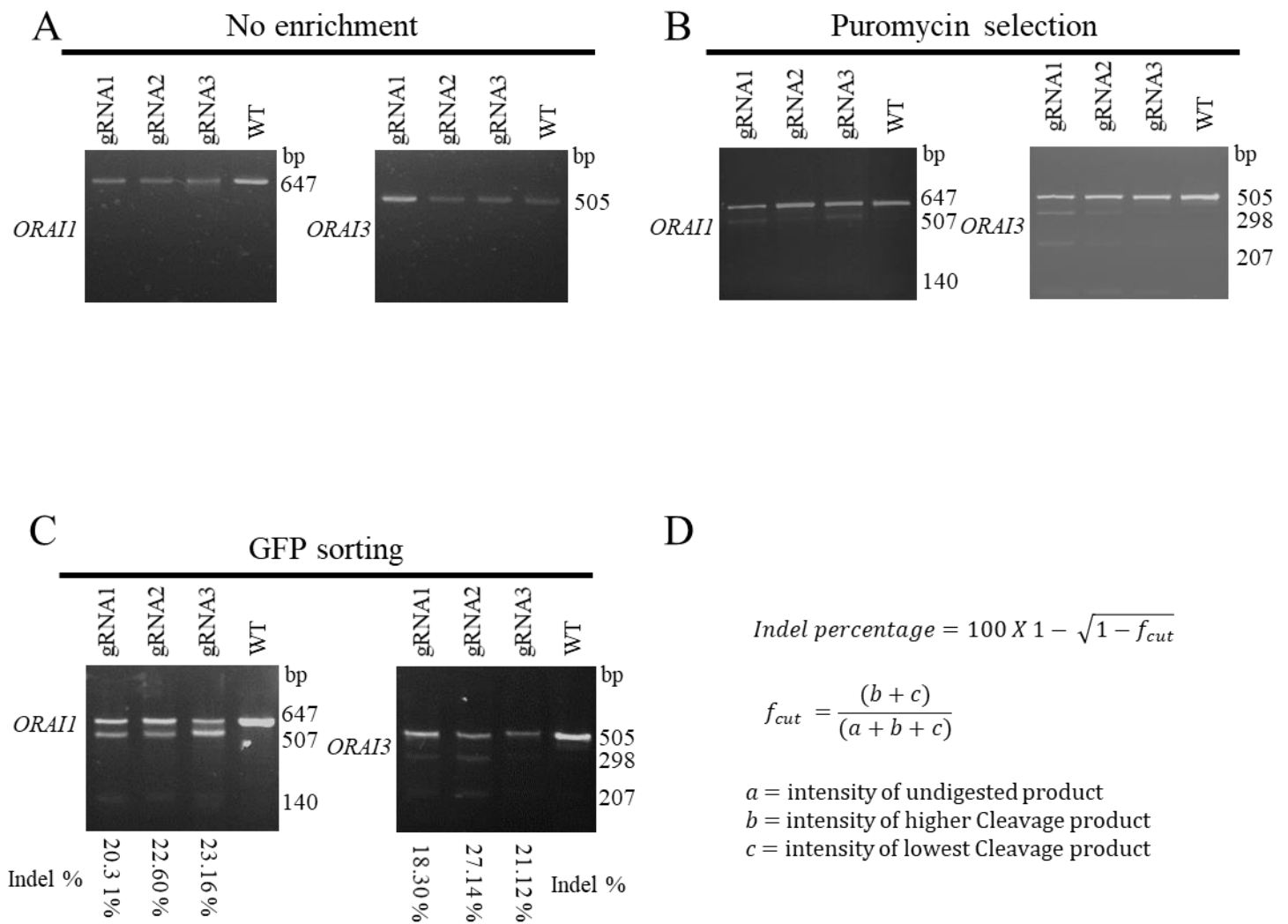


Figure 60 | Results of T7 Endonuclease I (T7EI) assay.

- T7EI assays performed on HEK-293 cells transfected with Cas9 protein and gRNA1, 2, or 3 for ORAI1 and ORAI3 gene KI. PCR were performed on the gDNA extracted from the whole cell population transfected. WT HEK-293 cells display PCR band at the expected size (647 pb for ORAI1 and 505 pb for ORAI3). HEK-293 cells transfected with gRNA do not display additional bands, indicating that T7EI assay did not induce any cut.
- Similar experiment as in (A), with selection of transfected cells due to puromycin addition in the cell culture medium. The faint bands detected in the gRNA wells indicates that T7EI assay performed poorly.
- Similar experiment as in (A). Specifically transfected cells were selected by FACS due to GFP signal. The presence of additional bands (507 + 140 bp for ORAI1, and 298 + 207 pb for ORAI3) allowed to select the most efficient gRNA for subsequent experiments (ORAI1 gRNA3 and ORAI3 gRNA2).
- Calculation method of the percentage of Indel following T7EI experiment).

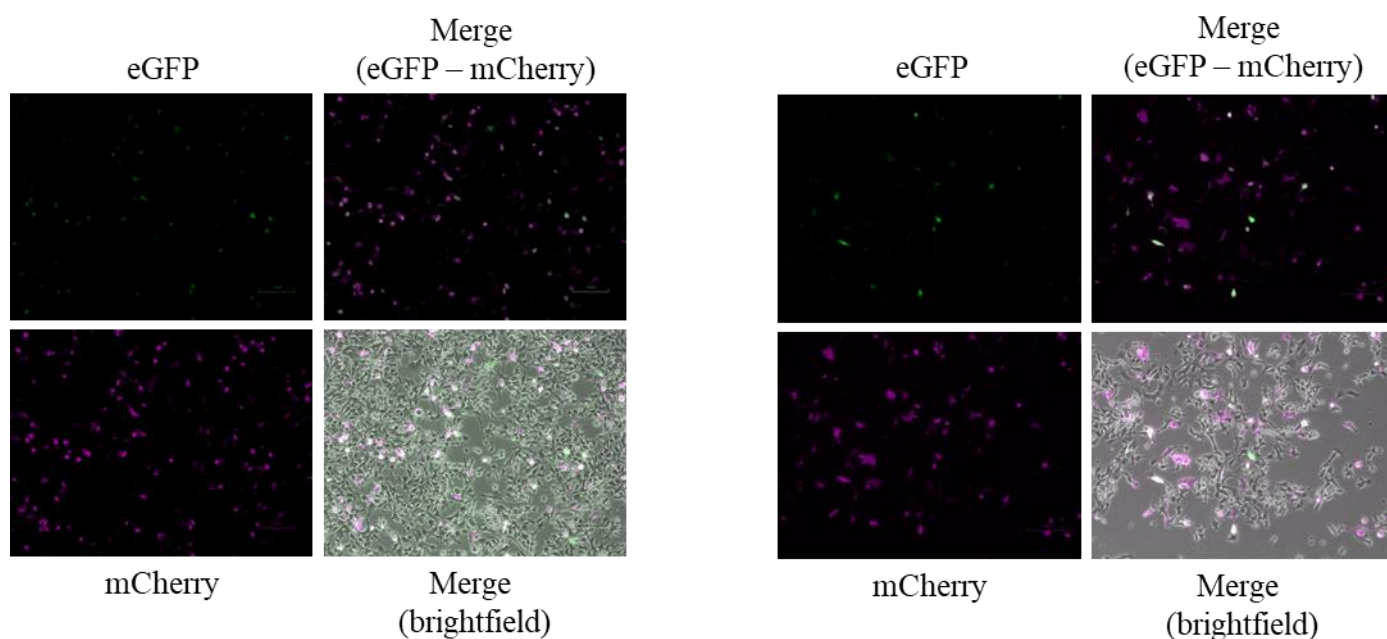


Figure 61 | Surrogate reporter system for visualizing gRNA efficiency.

Result of the surrogate reporter experiment. Magenta signal represent the cells displaying mCherry fluorescence indicating of effective transfection . Green signal represent the cells the cells displaying eGFP fluorescence. Green signal indicates that the surrogate strategy was effective and that CRISPR/Cas9 DSB induction and NHEJ reparation mechanism are functional in the cell population. Note that the probability of in-frame restoration of the GFP sequence relative the mCherry sequence is equal to 1/3. Efficiency of the surrogate strategy is higher for ORAI1gRNA3 (left, calculated efficiency $\approx 34\%$) than for ORAI3gRNA1 (right, calculated efficiency $\approx 18\%$).

genes with HDR were realistic goals to achieve. In addition, working with the easy-to-transfect cells HEK-293 and aiming to fluorescently tag protein led us to believe that even if only few cells would display fluorescence within millions of non-fluorescent cells, FACS would allow us to identify and select the desired cell clone. Thus, we tested different strategies to generate KI HEK-293 cells.

4.2.3.1. Considerations before conducting homologous direct repair (HDR) experiment

In almost any case, the induction of a recombination event aiming to insert a piece of DNA at a specific genomic location, requires the use of a donor template (donor plasmid) displaying sequence homology with the DSB induction site. In order to obtain the best efficiency during the KI procedure, the donor plasmid should respect few criteria. Ideally, the homologue region should perfectly match the DSB induction point. A distance superior 10 base pair between the beginning of the homologue region from the donor plasmid and the DSB induction drastically reduces the chances of homologous recombination events (HR) (Boel *et al*, 2018). In addition, the design of the donor plasmid should be carefully studied. Indeed, if the donor plasmid displays the PAM as well as the intact targeting gRNA sequence, the CRISPR-Cas might degrade the plasmid before it could be used for the HR process. In a similar way, if following a successful HR event, the edited gDNA presents the PAM and the gRNA sequences, it is not excluded that CRISPR-Cas9 might induce a new DSB and thus ruins the outcome of the experiment (**Figure 62**). Thus, it is common practice to introduce one (or several) silent mutation(s) in the donor plasmid sequence corresponding to the PAM or gRNA sequence of the target gene.

4.2.3.2. Donor plasmid

The most common and most described way to generate homologous recombination for generating KI is represented by the co-transfection of a donor plasmid together with the Cas9-gRNA plasmid complex. The specific designs of both donor plasmids used for inducing HR in *ORAI1* and *ORAI3* genes sequences are presented in **Figure 63**. Specifically, for *ORAI1* gene, the donor plasmid was designed as follow: the mTurquoise2 sequence was surrounded by an 800 base pair sequence corresponding to the *ORAI1* 5'UTR region, and by an 800 base pair sequence corresponding the genomic region following the *ORAI1* start codon (including the totality of the *ORAI1* first exon and part of its first intron). A similar design was used for *ORAI3* gene, with the sYFP2 sequence as fluorescent tag and with regions corresponding the *ORAI3* start codon surroundings.

In our first attempts to generate KI in HEK-293 cells, the Cas9-gRNA plasmids (coding for *ORAI1*gRNA3 or *ORAI1*gRNA2) were transfected together with the donor plasmids (*ORAI1* HR mTurquoise2 or *ORAI1* HR sYFP2) in HEK-293. Assessment of a successful insertion of fluorescent tags was performed by FACS one week after transfection. However, no fluorescent signal could be detected and thus HR recombination could not be identified. Due to the low expected number of HR event in the cells, we hypothesized that performing FACS without confirmation of the occurrence of HR event was not the best strategy. Therefore, in the following experiments we decided to assess the

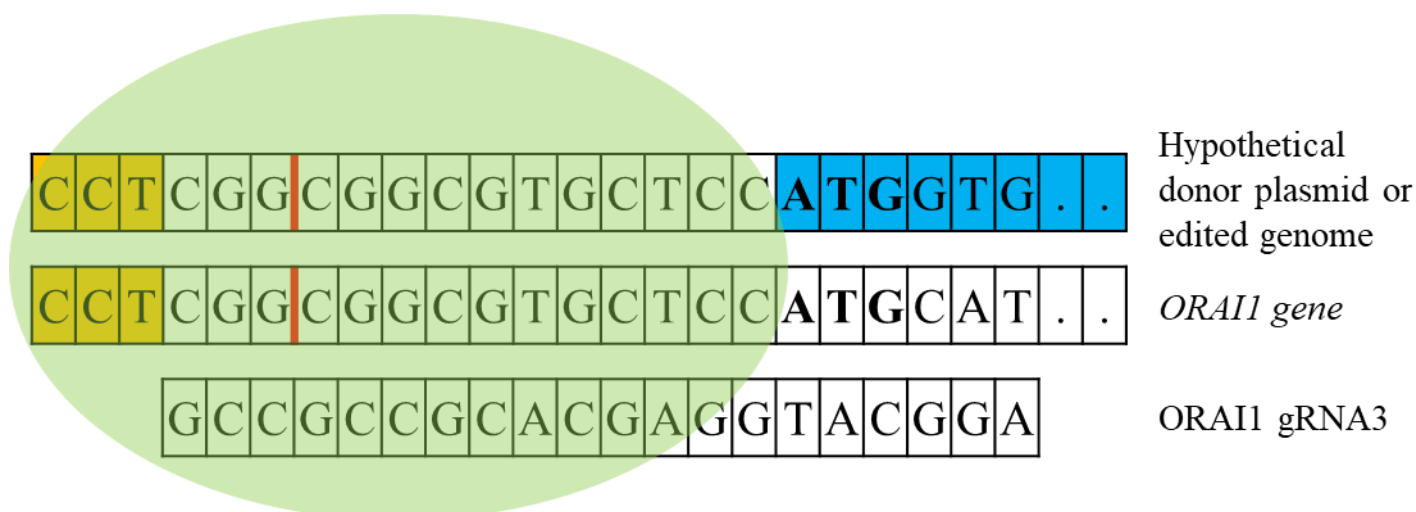


Figure 62 | Hypothetical design of CRISPR-Cas9 recombination experiment.

On top is represented the hypothetical sequence of a donor plasmid aiming to insert fluorescent tag in 5' extremity of the *ORAI1* gene. In the middle is shown the sequence of the *ORAI1* gene. On the bottom is displayed the sequence of the *ORAI1* gRNA3 used in the study. Note that successfully edited genome would present the same sequence as the donor plasmid. Yellow boxes represent the PAM, red lanes represent the cutting sites of the Cas9 protein; Bold letters represent start codon of *ORAI1* or fluorescent tag. Blue boxes represent the sequence aimed to be inserted by homologous recombination. Green shadow represent the Cas9 protein.

Note that the donor plasmid/edited genome present the PAM followed by a sequence partially similar to the sequence targeted by the gRNA, potentially leading to DSB induction.

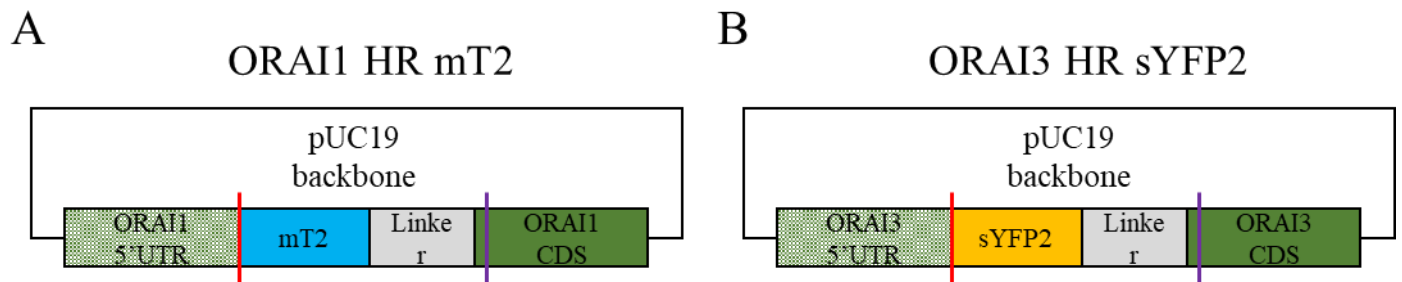


Figure 63 | Schematic representation of donor plasmids used in the homologous recombination (HR) experiments.

- A. Structure of the HR plasmid used to insert the mTurquoise2 fluorescent tag in ORAI1 N-terminal extremity. pUC19 was used as backbone plasmid because it does not allow for eukaryotic expression of its sequence. The mTurquoise2 sequence ([mT2], blue rectangle) and linker sequence (linker, grey box) were cloned between stretches of 800 bp regions corresponding to the ORAI1 5' untranslated region ([UTR] green dotted box) and the ORAI1 coding sequence ([CDS] green box). The red line represents the newly inserted start codon (ATG), the purple line represents the silent single-nucleotide mutation inserted to deleted the protospacer adjacent motif (PAM) sequence, preventing the cutting of edited genome by the Cas9 protein.
- B. Structure of the HR plasmid used to insert the sYFP2 fluorescent tag in ORAI3 N-terminal extremity. pUC19 was used as backbone plasmid because it does not allow for eukaryotic expression of its sequence. The sYFP2 sequence ([sYFP], yellow rectangle) and linker sequence (linker, grey box) were cloned between stretches of 800 bp regions corresponding to the ORAI3 5' untranslated region ([UTR] green dotted box) and the ORAI3 coding sequence ([CDS] green box). The red line represents the newly inserted start codon (ATG), the purple line represents the silent single-nucleotide mutation inserted to deleted the protospacer adjacent motif (PAM) sequence, preventing the cutting of edited genome by the Cas9 protein.

successful insertion of fluorescent sequences by PCR. Indeed, in case of successful integration of fluorescent tag, PCR performed with primers surrounding the region of integration should display an additional band of higher molecular weight compared to WT HEK-293. Nonetheless, using the strategy described above, we remained unable to identify positive HR event on gDNA level (**Fig 64A**). Some studies reported that HR rate was improved due to transfection of linearized plasmid (Ran *et al*, 2013). Therefore, we tested this approach, by performing restriction digest and purification of the donor plasmid before transfecting it together with the Cas9-gRNA plasmid. Interestingly, PCR performed on gDNA displayed bands of a high molecular weight corresponding to successful recombination event (**Fig 64B**). Nevertheless, because PCR were performed on gDNA extracted from cells transfected with the donor plasmid, we could not exclude that PCR bands correspond to plasmid amplification. Thus, we performed PCR experiment on mRNA extracted from the transfected cells and detected extremely faint bands corresponding to successful HR (**Fig 64C**). Nonetheless, no fluorescence signal could be detected, and no cells could be isolated by FACS. Because of the low intensity of the PCR bands indicating a potential successful HR, we reasoned that the absence of fluorescent detection in the cell population could be attributed due a low level of HR events. Thus, we looked for way to improve it. Importantly, some publications reported that small molecules could increase the rate of HR event in the cells, by unknown mechanism (Yu *et al*, 2015). Therefore, we used one of the mentioned molecules (Brefeldin A) in our subsequent experiments. In addition, we decided to select only cells transfected by the CRISPR-Cas9 system. To achieve this selection, we used two strategies:

- The first strategy tested was to transfect CRISPR-Cas9 plasmid encoding for a puromycin resistance cassette. Unfortunately, addition of puromycin to the transfected cells resulted in a high death rate, and PCR results were negative. In addition, we hypothesized that using a selection agent might lead to the creation of cellular clone constantly expressing the Cas9 protein and thus abandoned this way of selection.
- The second strategy tested was to transfect CRISPR-Cas9 plasmid coding for GFP. Thus, following transfection, GFP-positive cells were sorted using FACS. They were further expanded, and their mRNA were extracted to perform PCR and assess for successful HR event (**Fig 64D**). The results of this experiment indicated on the existence of potential successful HR event at a substantially higher rate.

Nevertheless, detection of fluorescence in confocal microscopy or cell sorting due to FACS remained impossible.

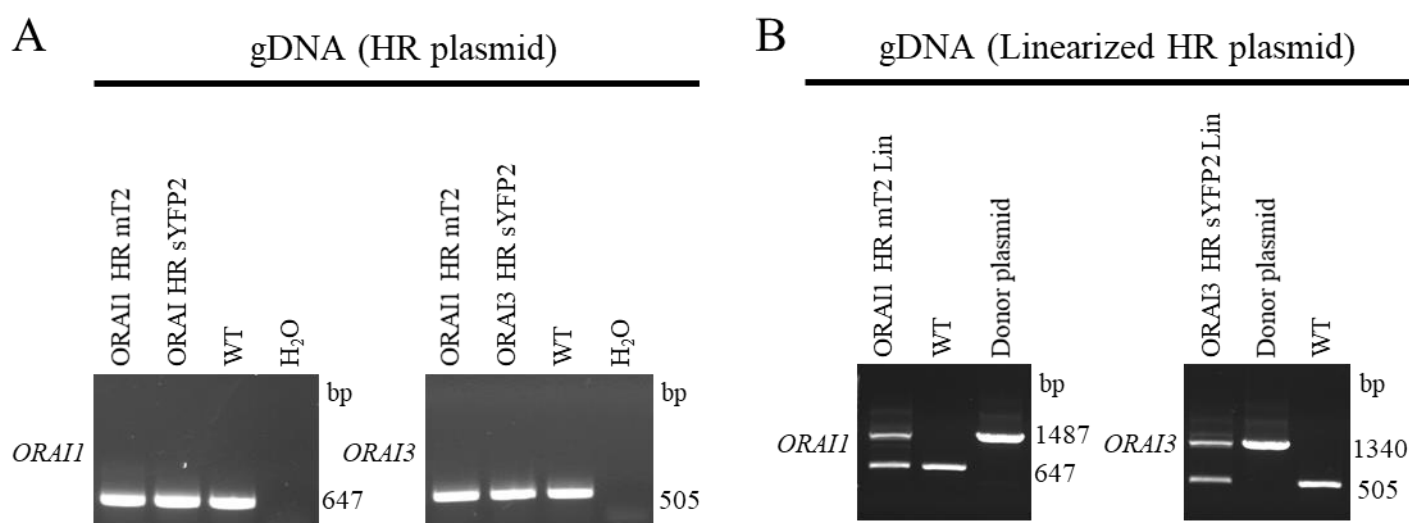


Figure 64 | PCR assessment of homologous recombination (HR) event.

- A. PCR performed on gDNA from the whole population of HEK-293 treated with a combination of CRISPR-Cas9 plasmid and HR plasmid. In case of successful HR event, bands at 1487 bp for ORAI1 and 1340 bp for ORAI3 are expected. PCR bands correspond to the expected size of the HEK-293 WT amplicon (647 bp for ORAI1; 505 bp for ORAI3), indicating on the absence of HR event. ORAI1 HR mT2 and ORAI1 HR sYFP2 corresponds to HEK-293 cells transfected with the CRISPR-Cas9 plasmid (ORAI1gRNA3) and the ORAI1 HR mTurquoise2 or ORAI1 HR sYFP2 donor plasmids; ORAI3 HR mT2 and ORAI3 HR sYFP2 corresponds to HEK-293 cells transfected with the CRISPR-Cas9 plasmid (ORAI3gRNA2) and the ORAI3 HR mTurquoise2 and ORAI3 HR sYFP2 donor plasmid. WT corresponds to HEK-WT; H₂O correspond to no template control.
- B. Similar experiment to A but using a linearized plasmid. ORAI1 HR mT2 Lin corresponds to HEK-293 cells transfected with the CRISPR-Cas9 plasmid (ORAI1gRNA3) and the linearized ORAI1 HR mTurquoise2. ORAI3 HR sYFP2 Lin corresponds to HEK-293 cells transfected with the CRISPR-Cas9 plasmid (ORAI3gRNA2) and the linearized ORAI3 HR sYFP2. WT corresponds to HEK-WT. Donor plasmid lanes indicate PCR performed on the donor plasmid used in the experiment (ORAI1 HR mT2 or ORAI3 HR sYFP2). The presence of two bands for ORAI1 HR mT2 and ORAI3 HR sYFP2 indicate on the potential successful HR recombination event.

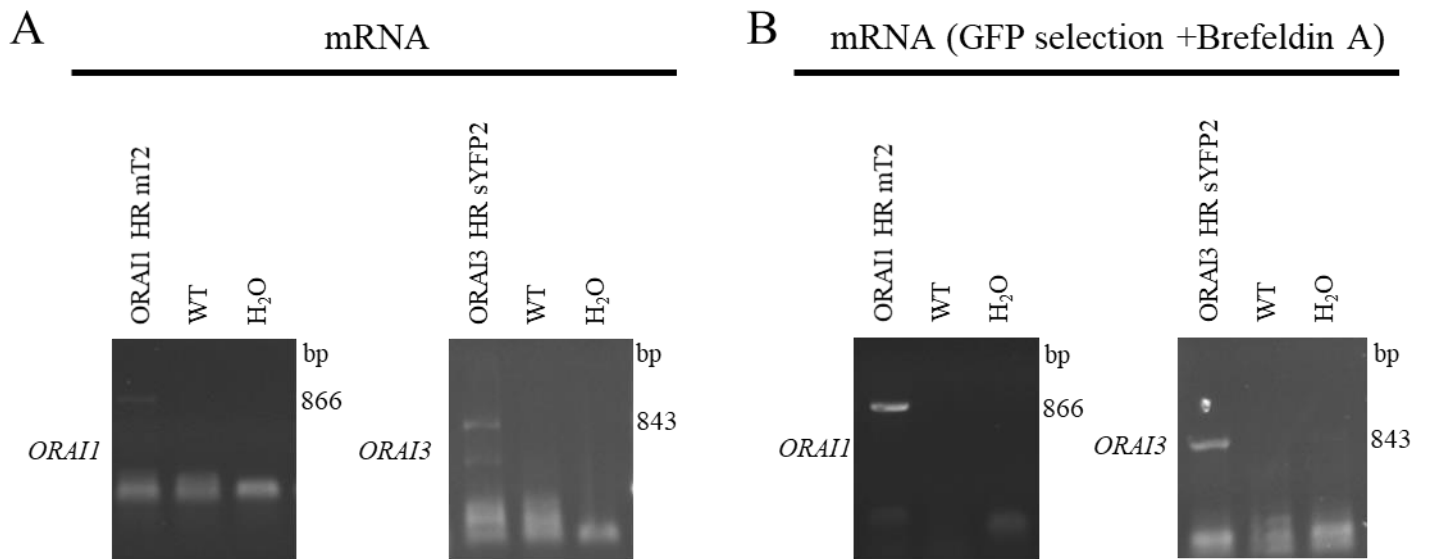


Figure 65 | PCR assessment of homologous recombination (HR) event.

- A. PCR performed on mRNA extracted from the experiment shown in the figure 64B. Primer couple used annealed in the fluorescent tag sequence and in the ORAI1 or ORAI3 coding sequence. Presence of band at 866 bp (for ORAI1) or 843 bp (for ORAI3) indicates a potential successful HR experiment. WT corresponds to HEK-WT; H₂O correspond to no template control. ORAI1 HR mT2 Lin and ORAI3 sYFP2 Lin correspond to HEK-293 cells transfected with the CRISPR-Cas9 plasmid (ORAI1gRNA3 / ORAI3gRNA2) and the linearized ORAI1 HR mT2 / ORAI3 HR sYFP2.
- B. Similar experiment as in C, transfected cells were selected by FACS due to GFP signal and Brefeldin A (0,1μM) was added in the medium to promote HR event. WT corresponds to HEK-WT; H₂O correspond to no template control. ORAI1 HR mT2 Lin and ORAI3 sYFP2 Lin correspond to HEK-293 cells transfected with the CRISPR-Cas9 plasmid (ORAI1gRNA3 / ORAI3gRNA2) and the linearized ORAI1 HR mT2 / ORAI3 HR sYFP2.

4.2.3.3. Increasing the endogenous expression level of *ORAI1* and *ORAI3*

PCR results indicated that recombination events were occurring in HEK-293 cells, but fluorescence could not be detected neither by FACS nor by confocal imaging. We hypothesize that the fluorescence level might be too dim to be effectively detected and hypothesized that it could be attributed to a low expression level of ORAI protein. Thus, we tried to increase ORAI1 and ORAI3 endogenous expression level. Importantly, publications showed that inactive Cas9 protein (which do not present cleavage activity) fused to transcriptional activating factor such as VP64-p65-Rta (VPR) or to the core of the human acetyltransferase p300 (p300) could be used to enhance expression of genes targeted by gRNAs (Hilton *et al*, 2015; Chavez *et al*, 2015). Thus, we set out to design new gRNA targeting 5'UTR regions of ORAI1 and ORAI3 with the aim of increasing expression level of these proteins. Unfortunately, we could not detect any increase in expression level of ORAI1 or ORAI3 following transfection with these plasmids.

4.2.3.4. Precise Integration into Target Chromosome (PITCh) technique

Because KI experiments using the HDR repair mechanism were not successful, we thought of using a strategy relying on the microhomology-mediated end-joining (MMEJ) to perform gene KI. Specifically, an experimental approach named precise integration into target chromosome (PITCh) was considered. This technique relies on the insertion of short sequences (5 to 25 bp) identical to the DSB induction region on each side of a template plasmid bearing the desired sequence to inset. In addition, plasmid linearization is induced through DSB induced by the Cas9-gRNA plasmid. Plasmids enabling this approach were constructed. Nonetheless, these plasmids were constructed in parallel to the experiments where we could detect HR event with the classic HR donor plasmid, and by lack of time, they were not use for trying to generate KI in HEK-293 cells.

4.2.4. Conclusion on the gene KI experiments with CRISPR-Cas9 system.

While quite straightforward in theory, the generation of gene KI remained in our hand a complex task. Obviously, the CRISPR/Cas9 revolution offered the possibility to virtually any scientist to attend gene KI, nonetheless several pitfalls are still present. Specifically, during our attempts to generate KI we faced three main difficulties:

- First, the design, induction, and verification of the successful induction of DSB at the desired gene location were already well described at the beginning of this PhD. Nonetheless, several protocol adaptations were required in order to succeed in these tasks.
- Second, following the DSB induction, one desire to specifically insert a sequence of interest at the specific genomic location. When starting this work, the main technique described to reach this goal was to take advantage of HDR process. However, the low rate of success

described with the classic technique of providing a plasmid template for recombination led us to adapt our initial strategy. Thus, we specifically selected positively transfected cells, tried to use a linearized donor plasmid, and tested drugs supposedly able to enhance the rate of recombination. In addition, several other techniques were considered such as the PITCH technique. These adjustments allowed us to detect by PCR the presence of recombination event. Nonetheless positively edited cells could not be identified.

- The final difficulty we faced the identification and selection of positively edited cells. Of note, most of the publications describing successful KI did not highlight this point probably for two main reasons. First, while generating KI, several publications used a donor plasmid bearing a selection cassette that would ease the selection of positively edited cells. Second, works describing fluorescent labeling of endogenous proteins were targeting high expression level proteins. In our case, the low expression level of ORAI protein prevented us to easily identify KI cells. As a consequence, we attempted to use the newly developed CRISPR tools allowing for specific increase of protein expression., which unfortunately remained unsuccessful.

As a conclusion, the field of gene KI with CRISPR/Cas9 system has continuously developed through the year, with roughly a 3-fold expansion in the number of publications reporting gene KI with CRISPR since 2017. Thus, several strategies have been developed that should ease the process of generating KI and are worth to be tested when trying to generate KI. Of note, the most appealing of these strategies will be briefly described in the discussion section. Anyway, due to time pressure and to our inability to select and identify cells that underwent recombination event, we had to adapt our strategy for reaching our aim to study ORAI protein remodeling. Therefore, because during our attempts to generate KI we had successfully induced DSB, we thought that knocking out *ORAI1* and *ORAI3* protein before re-expressing them due to transfection would be a valid strategy.

4.3. Generating knockout (KO) with CRISPR-Cas9 system.

4.3.1. General consideration for creating KO with CRISPR-Cas9

4.3.1.1. Identification of a suitable screening method for KO identification

Since KI generation turned out to be unsuccessful, we decided to modify our strategy and to generate KO cells for *ORAI1* and *ORAI3* in which fluorescently labelled protein will be later re-expressed. Creation of gene KO due to CRISPR-Cas9 technique takes advantage of the NHEJ repair mechanism. Specifically, NHEJ mechanism takes place following the induction of DSB in the cell and will ligate the DNA extremities together. This mechanism is useful when intending to create KO, because it is error prone. In fact, NHEJ leads to the creation of small insertions or deletion (Indels) in the region surrounding the DSB. The size of the Indels usually ranges from 1 to 10 bp, nonetheless they are extremely heterogeneous. The overall proportion of out-of-frame repair is about 2/3, thus it

represents an efficient way to generate KO. The T7E1 assay performed while attempting to generate KI, demonstrated that NHEJ mechanism were taking place in our cells and thus one could hypothesize that KO cells for ORAI1 and ORAI3 were effectively created. Nevertheless, we had to think of a way to select our KO cells from the whole population of transfected cells. To do so, we considered screening single-cell clones by immunoblotting, or by Ca^{2+} imaging techniques. However, we did not possess a reliable antibody allowing to screen for the absence of ORAI1 or ORAI3 protein at endogenous level. In addition, screening hundreds of clones through Ca^{2+} imaging technique would be expensive and time consuming. Therefore, we find another way to screen for knockout generation. Interestingly, Chen et al., proposed a dual gRNA method enabling to screen for edited cell by PCR performed on gDNA (Chen et al., 2014). The procedure involves the use of two gRNAs targeting the same gene but separated by hundreds of base pairs. The induction of two DSB would lead to the excision of the small portion of DNA located between the DSB induced by gRNA. Thus, a simple PCR amplifying the gDNA region targeted by the gRNA allows for identifying cellular clone that experienced genomic fragment excision.

4.3.1.2. Design of gRNA for *ORAI1*- and *ORAI3*- KO

Since our strategy involved the use of two gRNAs per target gene, and because we had already established that the gRNA created for the KI generation were effective, we created a second set of gRNAs located in the end of *ORAI1* and *ORAI3* first exons. As a reminder, the gRNA selected for our KI experiment were inducing DSB 11bp prior to the start codon of *ORAI1*, and on the start codon of *ORAI3*. Therefore, successful fragment excision would delete the start codon eliminating the possibility of creating an ORAI1 or ORAI3 protein presenting an “in-frame” deletion. The CRISPOR website was used to generate a set 3gRNAs to test per gene. The selected gRNAs with their efficiency and specificity characteristics are displayed in **Table 5**. The strategy and localization of gRNAs used for this study are displayed in **Figures 66 and 67**.

4.3.1.3. Assessment of gRNA efficiencies

The gRNAs were cloned in plasmids coding for Cas9 protein fused to GFP via 2A peptide. As a consequence, transfected cells were selected by FACS. Therefore, the PCR performed on gDNA and subjected to T7E1 assays were enriched in positively transfected cells. The T7E1 assay results indicated that the ORAI1-KO gRNA2 and ORAI3-KO gRNA3 were the most efficient and thus they were selected for the KO generation (**Fig 68**).

4.3.2. Generation of *ORAI1* KO HEK-293 cells

The most efficient ORAI1-KO gRNA were cloned into the Cas9-2A-Puro plasmid. This plasmid was used because the generation of KO cells required the transfection of two Cas9-gRNA plasmids. We thought of using two different backbones plasmids so we could select double transfected cells. Indeed, the plasmid coding for Cas9-2A-GFP allowed for sorting of transfected cells by FACS, while the

Gene	gRNA	Sequence 5' → 3'	PAM	Cutting site (relative to ATG)	Predicted efficiency	Specificity score 1	Specificity score 2	Off-target sites	Next to PAM	Exon only	Chromosome 12/16 only
ORAI1	gRNA1	GAAGCCGGAGAGCAGAGCCG	AGG	+280	60	64	71	0-0-2-23-262	0-0-1-2-5	43	8
	gRNA2	TGGAGGCTTTAAGCTTGGCG	CGG	+251	58	82	88	0-0-0-12-96	0-0-0-0-1	10	3
	gRNA3	CCTGCATGGAGTGCTCGTTG	AGG	+200	54	84	91	0-0-2-5-102	0-0-0-0-0	18	7
ORAI3	gRNA1	GGGCCAGTCAGCACTCGCTG	CGC	+135	59	74	85	0-0-2-16-169	0-0-0-3-3	18	5
	gRNA2	CCGAGAGCAAGGCAGACGTG	CGG	+200	65	74	89	0-0-1-15-110	0-0-0-1-3	10	9
	gRNA3	TGGCCCGGCTGAGGTAGAGG	CGG	+161	58	70	79	0-0-0-20-212	0-0-0-4-7	28	17

Table 5 | gRNA sequences chosen for knockout (KO) generation and their main characteristics.

Three gRNA sequences were designed for each gene. The predicted efficiency and the two specificity scores are ranging from 0 to 100 and were computed using Doench et al., and Hsu et al., publications. The number of off-target sites are displayed as follow: the first number represents the number of off-target sites presenting no mismatches with the target sequence, the second number represents the off-target sites presenting a single mismatch with the target sequence, the third number represents the off-target sites presenting two mismatches with the target sequence, and so on until 4 mismatches. The column: Next to PAM, resumes the preceding column but display the off-target sites which do not present mismatches in the gRNA seeding region (next to the PAM). The exon only column displays the number of predicted off-target sites present in exon exclusively. The column chromosome 12/16 only display the number of off-target sites present on the same chromosome as the target (chromosome 12 for ORAI1 and 16 for ORAI3). The gRNAs used in for this study are highlighted in golden.

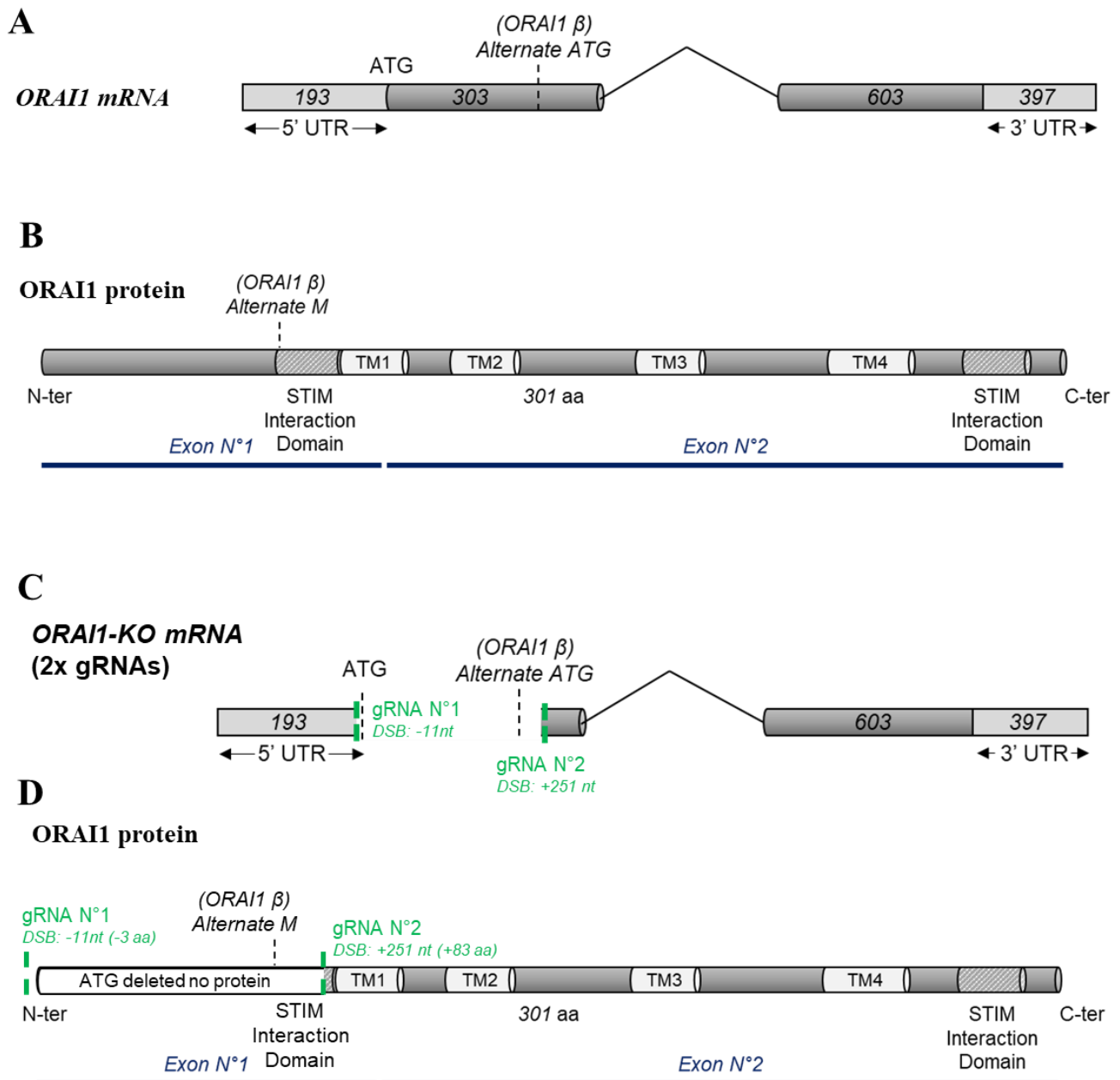
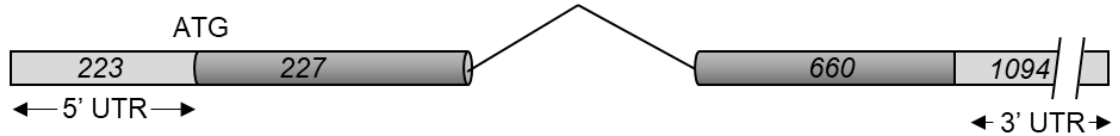


Figure 66 | Experimental design of the strategy used to create total knockout of Orail protein (ORAI1 KO).

- Structure of ORAI1 mRNA including non-coding region (light grey), coding sequence (dark grey), original start codon (ATG, full-length ORAI1 origin) and alternative start codon (ATG, ORAI1- β isoform).
- Structure of ORAI1 protein including transmembrane domain (white boxes) and STIM interaction domain (hatched boxes).
- sgRNAs strategy used to generate ORAI1 complete knockout (ORAI1 KO). The green dotted lines represent the localization of the two sgRNAs used (sgRNA N°1 and sgRNA N°2).
- Protein sequence of ORAI1 following successful KO generation

A

ORAI3 mRNA

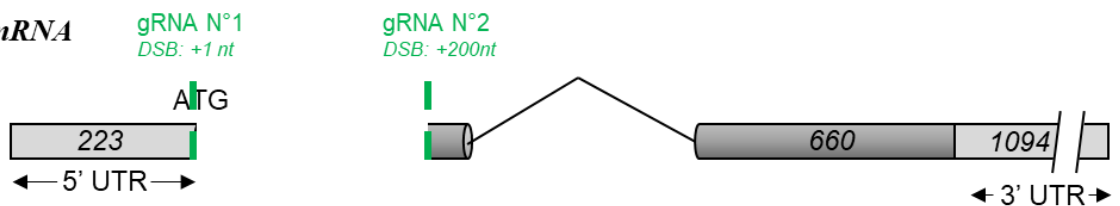


ORAI3 protein



C

ORAI3-KO mRNA
(2x gRNAs)



D

ORAI3 protein

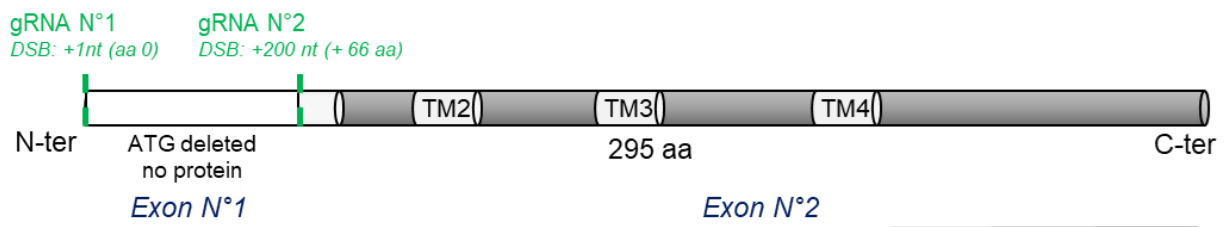


Figure 67 | Experimental design of the strategy used to create total knockout of Orai3 protein (ORAI3 KO).

- Structure of ORAI3 mRNA including non-coding region (light grey), coding sequence (dark grey), original start codon (ATG, full-length ORAI3 origin).
- Structure of ORAI3 protein including transmembrane domain (white boxes).
- sgRNAs strategy used to generate ORAI3 complete knockout (ORAI3 KO). The green dotted lines represent the localization of the two sgRNAs used (sgRNA N°1 and sgRNA N°2).
- Protein sequence of ORAI3 following successful KO generation

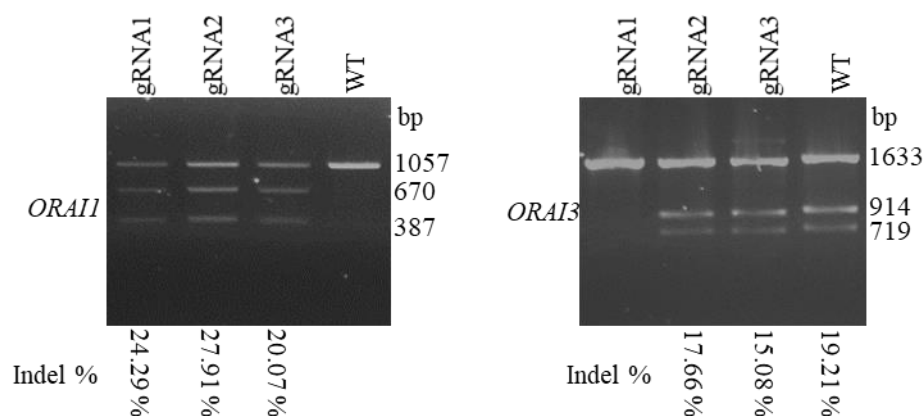


Figure 68 | Results of T7 Endonuclease I (T7EI) assay for KO gRNAs.

T7EI assays performed on HEK-293 cells transfected with Cas9 protein and gRNA1, 2, or 3 for ORAI1 or ORAI3 gene KO. PCR were performed gDNA extracted from the whole cell population transfected. WT HEK-293 cells display PCR band at the expected size (1057 bp for ORAI1 and 1250 bp for ORAI3). Cells transfected with gRNAs presented additional bands (670 + 387 bp for ORAI1, 914 + 719 bp for ORAI3) indicating that DSB were induced. Calculation of the percentage of Indel following T7EI experiment led to the selection of ORAI1KO gRNA2 and ORAI3KO gRNA3 for subsequent experiments.

plasmid coding for Cas9-2A-Puro allowed us to use puromycin for selecting only double transfected cells. To validate our double gRNA strategy, we performed PCR on gDNA extracted from the double transfected cells. Our results validated our strategy since we could visualize that HEK-293 cells underwent ORAI1 gene excision (**Figure 69A**). Therefore, in a subsequent experiment, the similar strategy was used, and double transfected cells were further isolated by limit dilution in 96 well-plates. Once single-cell colonies became visible, their gDNA were extracted and PCR were performed to identify cell clone displaying excision of ORAI1 fragment (**Figure 69B**). The positive clones were stored for further analysis.

4.3.2.1. Validation of *ORAI1* KO in HEK-293 cells

To validate the effective ORAI1 KO in the HEK-293 clones selected, we performed Ca^{2+} imaging experiments as well as immunoblotting and gene sequencing.

4.3.2.1.1. Ca^{2+} imaging experiments

First, we performed Ca^{2+} imaging experiment on the three clones displaying gene excision. As ORAI1 is known to be the main effector of SOCE, we used a protocol mimicking ER store depletion and measured the subsequent Ca^{2+} entry in the cell. Specifically, we used Thapsigargin (TG), an irreversible inhibitor of sarco/endoplasmic reticulum Ca^{2+} -ATPase (SERCA) pump, to induce ER store depletion. TG was added on HEK-293 cells in a Ca^{2+} -free medium leading store depletion (**Figure 70, grey inserts**). Subsequent addition of Ca^{2+} in the medium led to the generation of SOCE in the WT cells, while in ORAI1 KO cells, Ca^{2+} entry was strongly decreased (**Figure 70, yellow inserts**).

4.3.2.1.2. Immunoblotting

Several ORAI1 antibodies were available in the laboratory at the time of the study, but their ability to detect endogenous level of ORAI1 in HEK-293 cells was not demonstrated. Even though results of Ca^{2+} imaging experiment demonstrated that ORAI1 protein was absent in our cells, we decided to test these antibodies with the aim of identifying the most suitable for later studies. Of note, the expression level of ORAI1 in HEK-293 is relatively low. Thus, PC3 cells, supposedly expressing higher level of ORAI1, were used as a positive control in the experiment. Unfortunately, all the antibodies tested failed to provide clear evidence for the effective ORAI1 KO. Indeed, antibodies purchased from Abcam and ProteinTech, were clearly not functional as they exhibited an apparent random signal all over the membranes (**Figure 71A**). Other antibodies tested (purchased from Alomone, GeneTex and Sigma) displayed more convincing but not perfect signal. In fact, the three antibodies were effectively lacking bands compared to WT HEK-293 and PC3 cells. Nonetheless, the molecular weight of these bands was not identical between antibodies, with some antibodies displaying bands at 50 kilodaltons, corresponding to glycosylated form of ORAI1, or 35 kDa (**Figure 71B**), corresponding to the expected size of ORAI1.

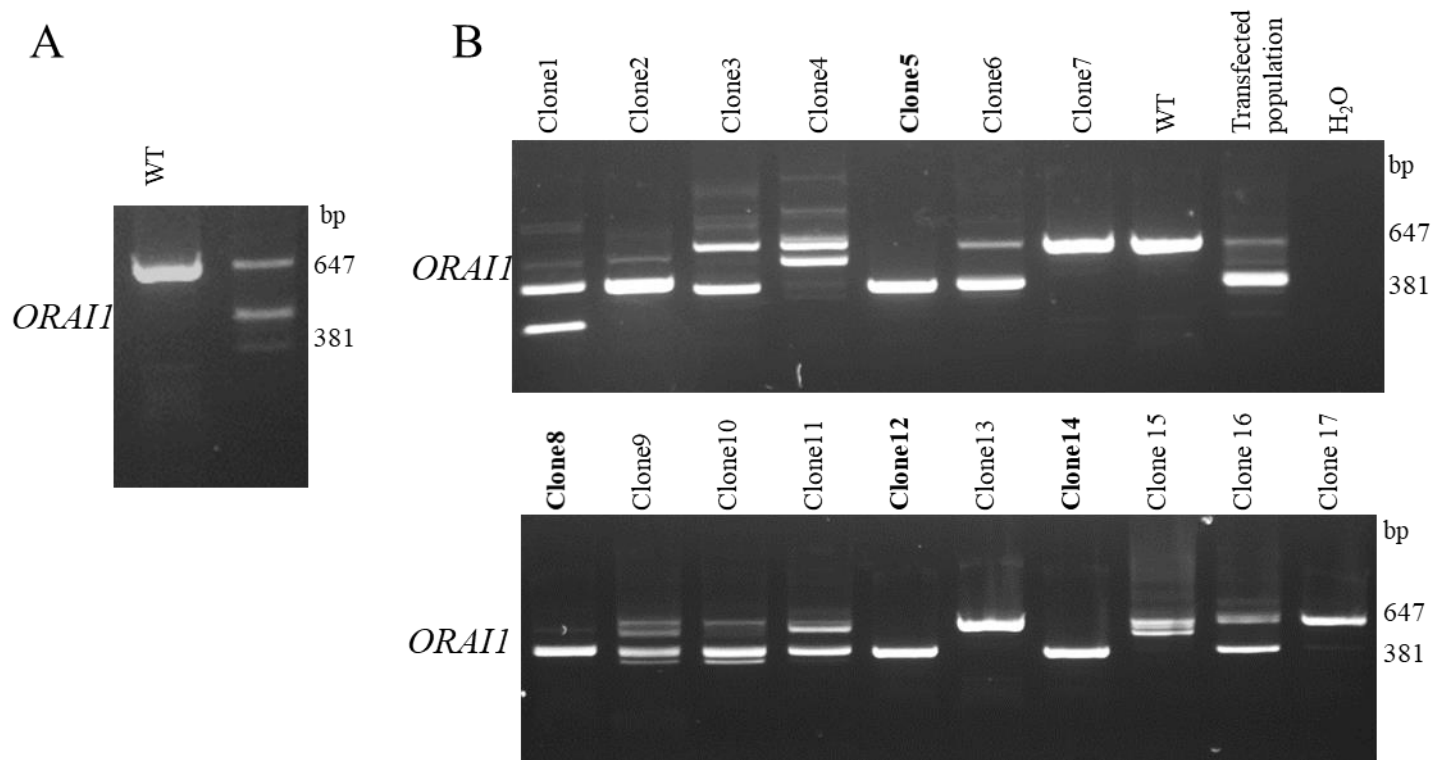


Figure 69 | Screening for ORAI1 KO HEK-293.

- A. PCR targeting ORAI1 deletion region performed on WT HEK-293 and on HEK-293 transfected with two gRNAs. WT HEK-293 display a single band at the expected PCR size of 647 bp, while the cells transfected with the two gRNAs are exhibiting two bands at 647 pb and 381 pb, indicating that some cells underwent partial ORAI1 gene excision.
- B. Same as in A, performed on single-cell clones. The WT HEK-293 displays a single band at the expected PCR size of 647 bp. The single-cells clones are exhibiting several bands indicating of genome edition. Clones 5, 12, 14 presenting a single band at the expected size for ORAI1 gene excision (381 bp) were selected for further experiments.

Note: the screening results presented do not represent the totality of the clones screened for KO

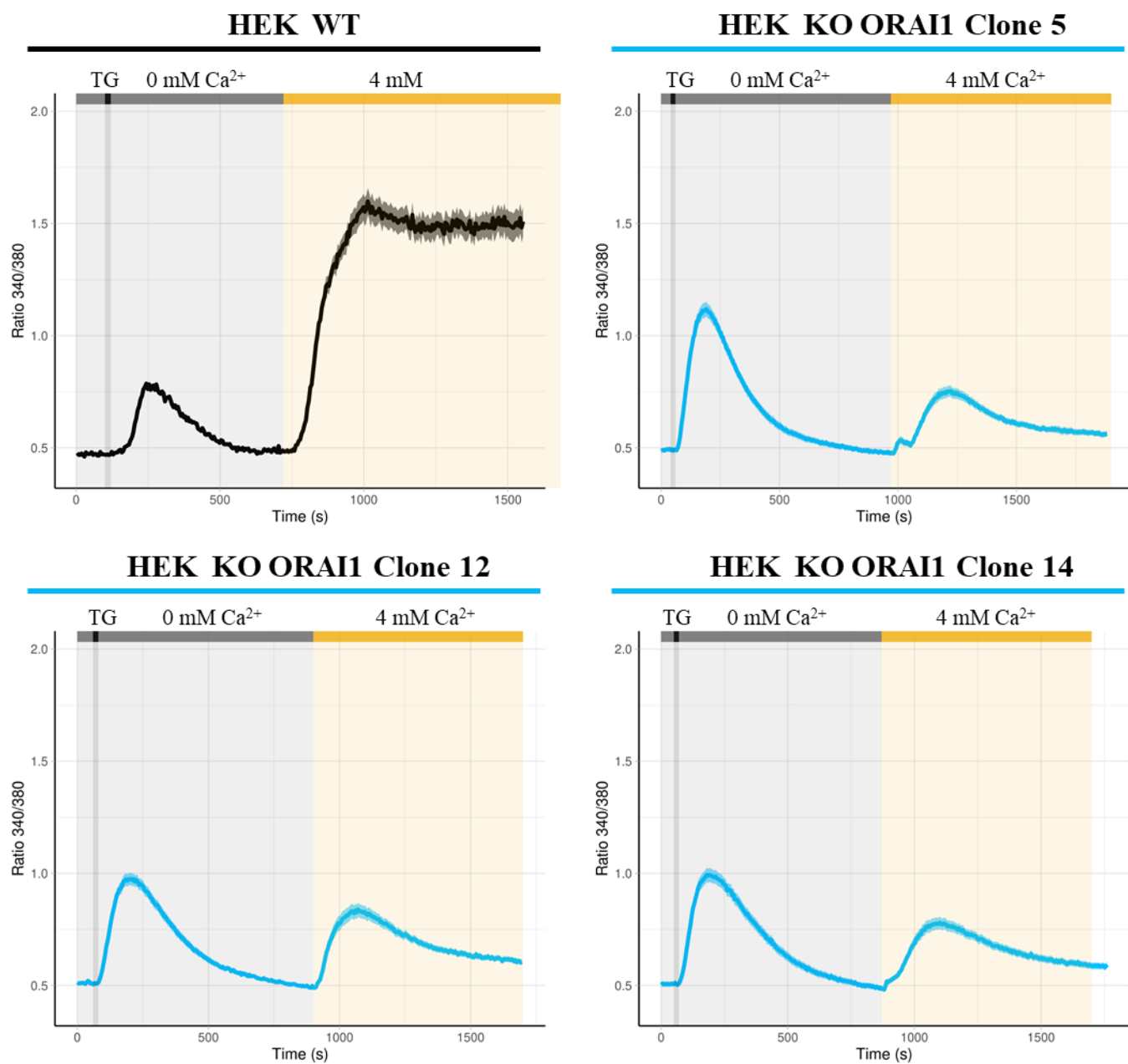


Figure 70 | SOCE level in ORAI1 KO HEK-293.

For every panel, a classic SOCE induction experiment was carried-out: cells were incubated in a Ca²⁺ free medium (grey insert) and TG was added to the medium (black bar) leading to ER store depletion (black inserts). Following ER store depletion, Ca²⁺ was added in the medium leading to SOCE generation (yellow inserts). Curves represent the mean value of the fluorescence intensity displayed by the cells with their 95% confidence interval (CI) in transparent colors. WT HEK-293 present a strong SOCE level while ORAI1 KO clones are exhibiting a greatly reduced but non-null SOCE level.

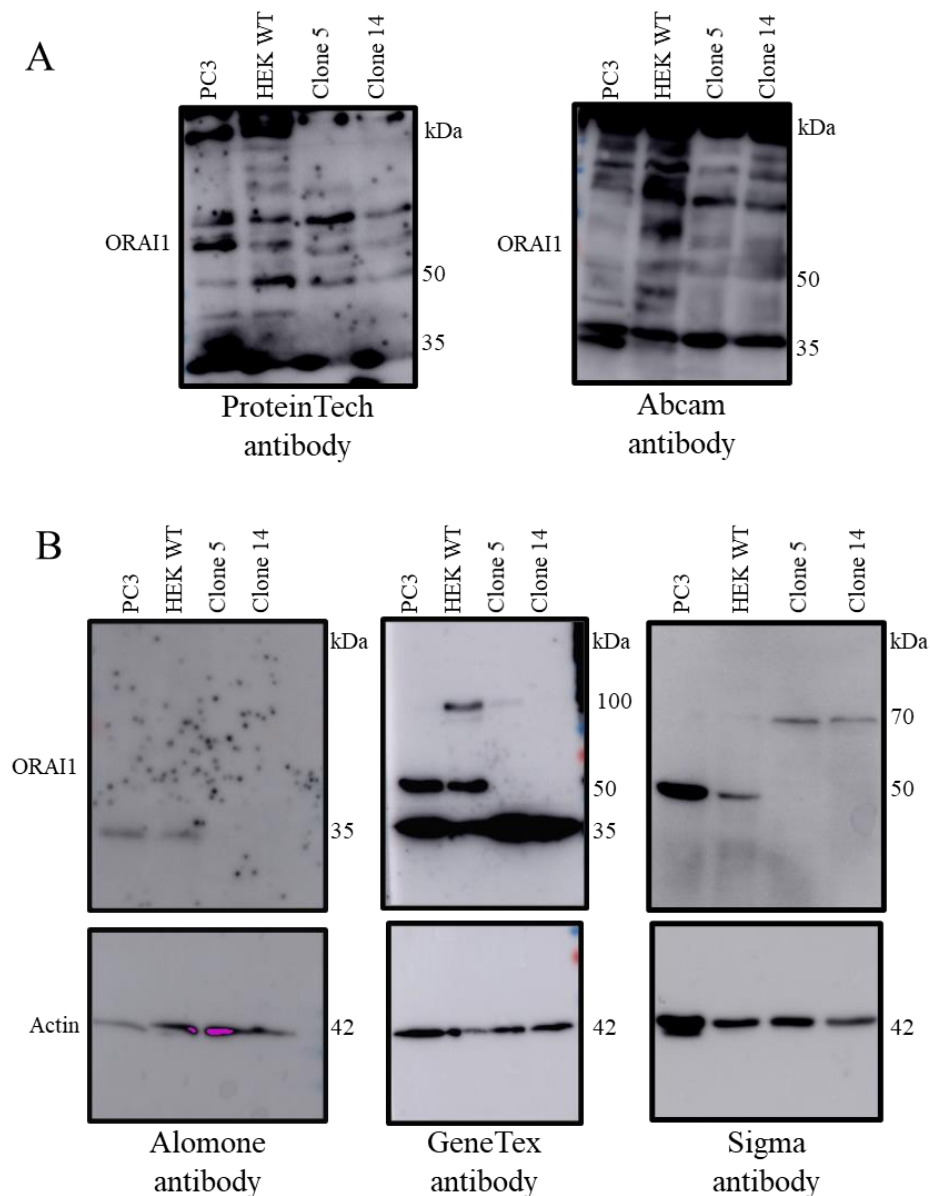


Figure 71 | Anti-ORAI1 antibody testing.

- A. Immunoblots targeting ORAI1 protein performed with antibodies purchased from Abcam and ProteinTech. These antibodies were nonfunctional as they display multiple bands all over the membrane for every conditions.
- B. Immunoblots targeting ORAI1 protein performed with antibodies purchased from Alomone, GenTex, and Sigma. Alomone antibody display bands corresponding to the ORAI1 expected size (35kDa) for HEK-WT and PC3, while ORAI1 KO clone do not show any bands. Gentex antibody shows bands around 50kDa corresponding to glycosylated form of ORAI1 for PC3 and WT HEK-293. These bands are lacking in ORAI1 KO clones. Nonetheless, nonspecific bands are present in all conditions at the ORAI1 expected size (35 kDa). Sigma antibody present a similar pattern as GeneTex antibody but does not display nonspecific bands at 35 kDa.

In addition, some nonspecific bands were present at the expected size for ORAI with the GenTex antibody. Taken together the results of immunoblotting confirmed that ORAI1 protein was effectively deleted in our cells. Nonetheless, because of the lack of quality of the available antibodies we decided to avoid using them for the conduction of the study.

4.3.2.1.3. Gene sequencing

As a final verification of ORAI1 effective KO, the area surrounding the deleted portion of ORAI1 was sequenced. The region of interest was amplified by PCR with proof-reading polymerase, and PCR products were cloned into pMiniT2.0 plasmid (NEB) and send for sequencing. Thus, the genomic sequencing results indicated that the ORAI1 gene presented a deletion including both *ORAI1* start codons (*i.e.*, ATG corresponding to the classic full length ORAI1 and to the ORAI1- β isoform). The exact coordinates of the induced deletion are displayed in the **Figure 72**.

4.3.2.2. Conclusion on the generation of HEK ORAI1 KO

The generation of ORAI1 KO was a surprisingly straightforward procedure. In addition, the double gRNA strategy greatly facilitated the screening procedure for the detection of potential KO and thus accelerated the obtention of KO cell clones. Of note, the main aim of this PhD was to study dynamic remodeling of ORAI1 and ORAI3 proteins. The hypothesis of the existence of such mechanism was developed due to results obtained in cancer model cell line PC3 and LNCaP. Because of the relative efficiency of KO generation in HEK, we thought that applying the same strategy in the PC3 cancer cell line would be successful and provide a more relevant model for our study. As a consequence, we did not develop ORAI1-ORAI3 double KO HEK-293 cells as initially planned, but we rather decided to generate this double KO in PC3 cells. In addition, we decided to take advantage of the ORAI1 KO HEK-293 cells to study the physiological effect of ORAI1 KO in this cell line.

4.3.3. Generation of double KO for *ORAI1* and *ORAI3* in PC3 cells.

The previous study from our laboratory suggested the existence of a dynamic remodeling between ORAI1 and ORAI3 proteins was performed using two different cancerous cell lines: LNCaP and PC3. On the one hand, LNCaP cells present a modal number of 76 to 91 chromosomes. On the other hand, PC3 presents a modal number of 62 chromosomes. Thus, we decided to use the PC3 cells to create double KO for ORAI1 and ORAI3 genes. We used the same strategy to induce KO in the PC3 cells as the one designed for HEK-293 cells. Specifically, we intended to create ORAI1 KO PC3 and to use these KO cells to generate a second KO for the ORAI3 gene. Indeed, we rationalized that the generation of ORAI1 KO could be quickly confirmed through Ca^{2+} imaging experiment and would allow us to quickly select ORAI1 KO cell clones to generate the double KO. Conversely, using a strategy where ORAI3 KO would be generated first would force us to confirm ORAI3 KO through genomic sequencing before generating double KO for ORAI1, and thus would be more time consuming.

HEK ORAI1-KO (clone5)

g. 183_445del

c. -12_252del

p. 1Met_84Ala del

g [..CCTCGG-----CAAGCTTAAAGCCTCCAG..CCTAG..] allele N°1
g [..CCTCGGCG-----AGCTTAAAGCCTCCAG..CCTAG..] allele N°2

Figure 72 | ORAI1 gene sequencing in HEK KO ORAI1.

Light green inserts are displaying genomic (g.) CDS (c.) and protein (p.) coordinates of the induced deletion. In the dark green insert are presented the sequences surrounding the deletion on genomic DNA level (g) for both alleles (underlined signs indicates the position of original ORAI1 start codon).

4.3.3.1. Screening and validation of ORAI1 KO in PC3 cells

The same strategy as previously described as used to generate ORAI1 KO in PC3 cells. The results of the PCR screening procedure are shown in **Figure 73A**. Validation of effective ORAI1 KO was performed through Ca^{2+} imaging experiments **Figure 74**. Clones displaying gene deletion as well as SOCE impairment were selected for ORAI3 KO generation or stored for further experiment. Final validation of effective ORAI1 KO was established by ORAI1 gene sequencing **Figure 75 A**. Four ORAI1 KO clones were used to induce ORAI3 KO and thus generate double KO for ORAI1 and ORAI3. The procedure for generating ORAI3 KO similar to the one used for ORAI1. PCR screening for ORAI3 gene deletion allowed us to select three clones double KO for ORAI1 and ORAI3 (**Figure 73B**). Final verification of effective ORAI3 deletion was established by ORAI3 gene sequencing (**Figure 75 B**).

4.3.3.2. Screening and validation of ORAI3 KO in PC3 cells

In addition to ORAI1 KO and ORAI1-ORAI3 double KO cell line, we thought of generating ORAI3 KO cell line in order to later compared the physiological functions of these protein in PC3 cells. The procedure for generating ORAI3 KO was reiterated and allowed us to generate four clones displaying ORAI3 gene partial excision (**Figure 76**). The confirmation of effective ORAI3 deletion was established by ORAI3 gene sequencing (**Figure 75 C**).

4.3.4. General conclusions on the generation of KO cells

KO generation in both HEK-293 and PC3 cells was a relatively straightforward task. Contrarily to generation of KI, the process of KO generation is well established and clearly defined, and several protocols are readily available to ensure success with the KO generation. At the start of this PhD, the most problematic task was the screening for KO step. Indeed, without the double gRNA strategy, this step is time consuming and would rely on expensive technique such as Ca^{2+} imaging experiment, or on the existence of reliable antibody. Overall, the crucial points of KO generation involved: the design of specific gRNAs, the assessment of their efficiency, the screening procedure for identifying KO cells. To conclude, the generation of KO did not present strong difficulties. During this PhD, several other teams generated HEK cells knocked out for ORAI proteins demonstrating the global usage of CRISPR-Cas9 for generating KO. However, generation of ORAI KO in cancer cell lines was not described by other teams, probably because of a more complex genotype than the classic HEK-293 cell line.

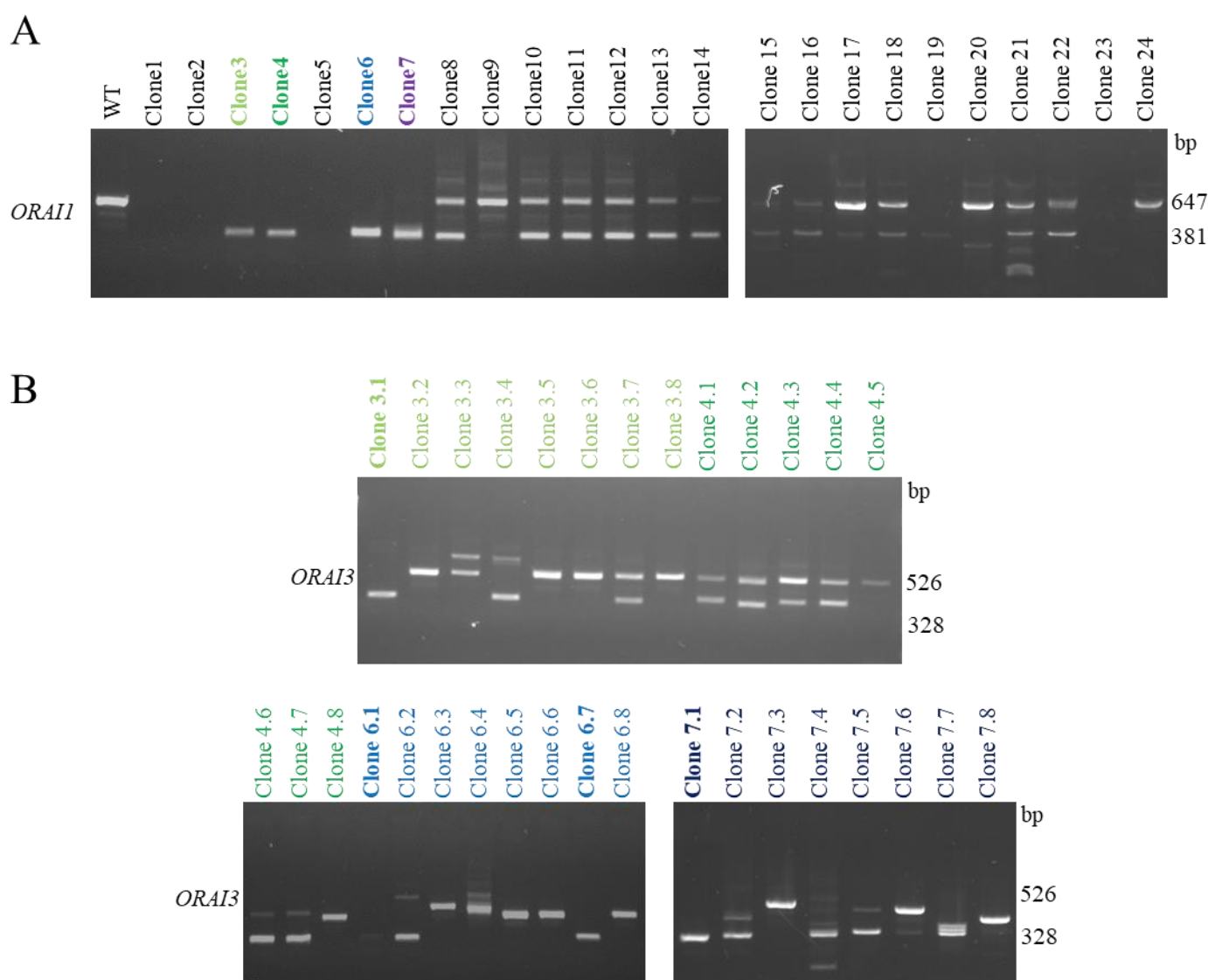


Figure 73 | Screening for ORAI1 and ORAI1-ORAI3 KO in PC3 cells.

- A. PCR targeting ORAI1 deletion region performed on WT PC3 as a and on PC3 transfected with two gRNAs. The WT PC3 displays a single band at the expected PCR size of 647 bp. The single-cells clones are exhibiting several bands indicating of genome edition. Clones 3, 4, 6, and 7 presenting a single band at the expected size for ORAI1 gene excision (381 bp) were selected for ORAI3 KO generation.
- B. PCR targeting ORAI3 deletion region performed on ORAI1 KO clones (3, 4, 6, and 7). The single-cells clones are exhibiting several bands indicating of genome edition. Clones 3.1, 6.1, and 7.1 presenting a single band at the expected size for ORAI3 gene excision (328 bp) were selected for further experiments.

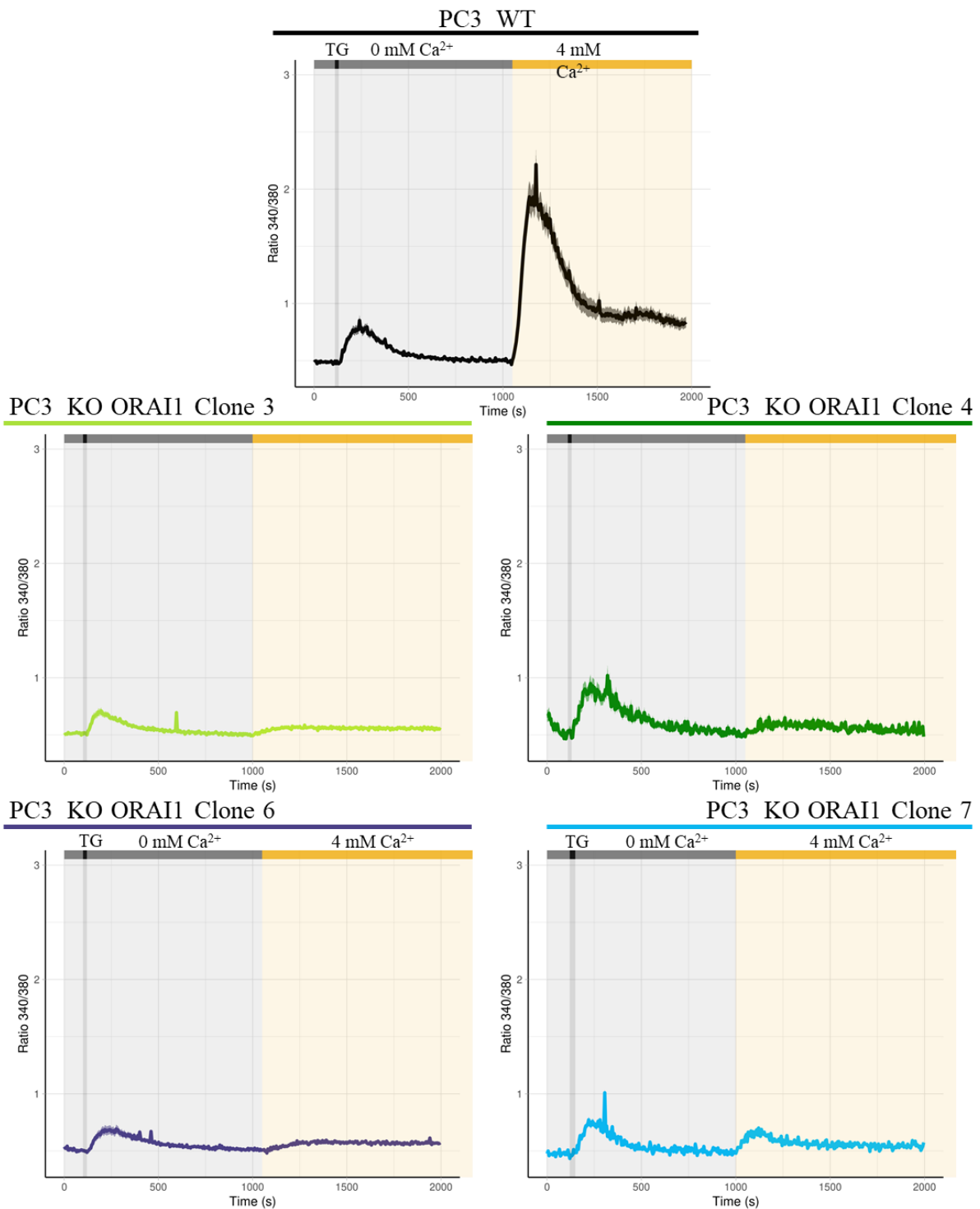


Figure 74 | SOCE level in ORAI1 KO PC3 cells.

For every panel, a classic SOCE induction experiment was carried-out. Cells were incubated in a Ca^{2+} free medium (grey insert) and TG was added to the medium (black bar) leading to ER store depletion (black inserts). Following ER store depletion, Ca^{2+} was added in the medium leading to SOCE generation (yellow inserts). Curves represent the mean value of the fluorescence intensity displayed by the cells with their 95% confidence interval (CI) in transparent colors. WT PC3 present a strong SOCE level while ORAI1 KO clones are exhibiting a greatly reduced but non-null SOCE level.

A PC3 double KO (ORAI1 + ORAI3)

ORAI1

g. 186_445del
c. -9_252del
p. 1Met_84Ala del

g[...CCTCGGCG-----CAAGCTTAAAGCCTCCAG..CCTAG..] allele N°1
g[...CCTCGGCG-----AAGCTTAAAGCCTCCAG..CCTAG..] allele N°2

ORAI3

g. 207_406del
c. 1_200del
p. 1Met_66Thr del

g[...CGCCCCCCCCCAGGA-----GTCTGCCTTG..TAG..] allele N°1
g[...CGCCCC-----TCTGCCTTG..TAG..] allele N°2

B PC3 KO ORAI1

ORAI1

g. 192_442del
c. -6_254del
p. 1Met_83Arg del

g[...CCTCGGCGCGT-----GCCAAGCTTAAAGCCTCCAG..CCTAG..] allele N°1
g[...CCTCGGCG-----CAAGCTTAAAGCCTCCAG..CCTAG..] allele N°2

C PC3 KO ORAI3

ORAI3

g. 208_405del
c. 2_199del
p. 1Met_65Arg del

g[...CGCCCCCCCCCAGG-----CGTCTGCCTTG..TAG..] allele N°1
g[...CGCCCCCCCCCA-----GCTGCCTTG..TAG..] allele N°2
g[...CGCCCCCCCCCAGGAT-----TCTGCCTTG..TAG..] allele N°3

Figure 75 | ORAI1 and ORAI3 gene sequencings in PC3.

Light green inserts are displaying genomic (g.) CDS (c.) and protein (p.) coordinates of the induced deletion for *ORAI1* gene. In the dark green insert are presented the sequences surrounding the deletion on genomic DNA level (g) for both alleles (underlined signs indicates the position of original *ORAI1* start codon).

Light violet inserts are displaying genomic (g.) CDS (c.) and protein (p.) coordinates of the induced deletion for *ORAI3* gene. In the dark violet insert are presented the sequences surrounding the deletion on genomic DNA level (g) for both alleles (underlined signs indicates the position of original *ORAI3* start codon).

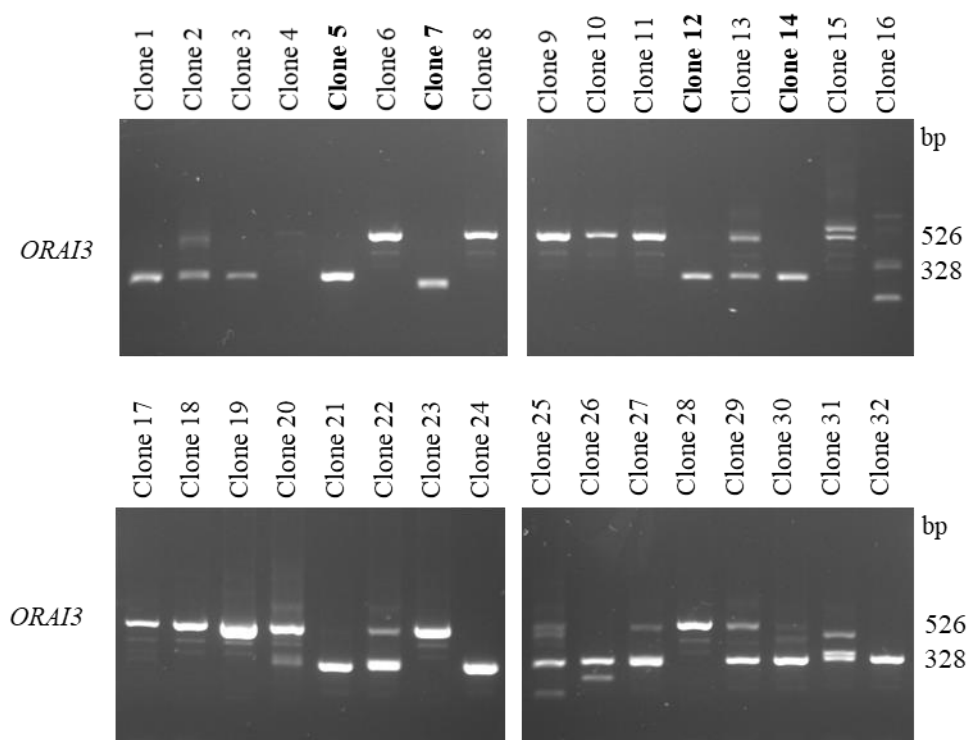


Figure 76 | Screening for ORAI3 KO in PC3 cells.

PCR targeting ORAI3 deletion region performed on PC3 transfected with two gRNAs. Non-edited cell clones are displaying a PCR band at 526 bp, successfully edited cell clones are displaying band at 328 bp. The clones 5, 7, 12, and 14 showing a single band at the expected size were selected for further experiments

Note: the screening results presented do not represent the totality of the clones screened for KO

4.4. Impact of ORAI1 deletion on the HEK-293 physiology

4.4.1. Different roles for ORAI1 in HEK-293 physiology

ORAI1 is identified as the main effector of the SOCE. In addition, SOCE represent the main Ca^{2+} entry pathway in non-excitabile cells (Prakriya & Lewis, 2015). Because Ca^{2+} is a central intracellular second messenger controlling several cellular functions such as proliferation and migration (Clapham, 2007; Berridge *et al*, 2003), we hypothesize that ORAI1 deletion and SOCE impairment should affect HEK-293 physiological properties. Of note, it was already shown that ORAI1 and SOCE are altered in cancer (Jardin & Rosado, 2016). Nonetheless, their role in the control of cancerous properties of the cells seems to be dependent on the type of cancer studied. For example, it was shown that SOCE does not control the proliferation of primary cultures of human metastatic renal cellular carcinoma (Dragoni *et al*, 2014) while other studies reported that ORAI1 and STIM1 downregulation were inducing cell cycle arrest in multiple myeloma cells (Wang *et al*, 2018b). Similar contradictions were described for the role of ORAI1 and SOCE in migration, as breast cancer cells display migration impairment due to ORAI1 downregulation (Yang *et al*, 2009) while colorectal carcinoma cells migrative properties were not affected by the downregulation of SOCE components (Zuccolo *et al*, 2018). In a physiological context, ORAI1 function is also cell type dependent as it is involved in the proliferation of endothelial cells (Abdullaev *et al*, 2008), inhibits the migration of myeloblastic cells ((Diez-Bello *et al*, 2017), and controls the differentiation of myoblasts (Darbellay *et al*, 2009). In addition, studies from our laboratory suggested that ORAI1 was involved in HEK-293 cells proliferation, but that this role was SOCE independent (El Boustany *et al*, 2010; Borowiec *et al*, 2014). Finally, patients with loss of function (LoF) or gain of function mutation (GoF) leading to absence or constitutive activation of SOCE present syndromes mostly affecting specific tissues or organs (Lacruz & Feske, 2015b). These data question the general assumption that ORAI1 and SOCE are controlling most of the cellular function. Overall, the different conclusion on the role of ORAI1 and SOCE in the control of cellular processes can be attributed to the techniques that were used to study their role. Indeed, downregulation as well as pharmacological inhibition of SOCE represent so far, the most widely tolls used to determine the roles of ORAI1 and SOCE. Although these techniques have proven to be powerful, pitfalls such as residual endogenous ORAI1 protein after knockdown, lack of specificity of pharmacological agents inhibiting SOCE, and potential compensation due to the expression of other ORAI isoforms might prevent the identification of clear roles for ORAI1 and SOCE. Therefore, our ORAI1 KO HEK-293 cells present a new model to study the fundamental role of ORAI1 in the HEK physiology.

4.4.2. Ca^{2+} signaling

First, we assessed the effect of the ORAI1 KO on the SOCE level displayed by HEK-293 cells. We used TG to induce store depletion and measured and compared the level of SOCE in our cell lines. As

anticipated, ORAI1 KO strongly impaired SOCE level in our cells. Nonetheless, it was not totally abolished. Quantification of SOCE entry by integration of the curve area following Ca^{2+} addition in the extracellular medium revealed that SOCE amplitude was decreased about 80% in ORAI1 KO cells (**Figure 77**).

4.4.3. ORAI homologues expression

It was demonstrated that all ORAI homologues are able to provide SOCE when overexpressed. Since we observed a small but non-null SOCE in the ORAI1 KO cells, we hypothesized that this Ca^{2+} entry could be attributed to ORAI2 and ORAI3. Thus, we verified their expression level in our cell line by RT-qPCR. Surprisingly, our results indicated that both genes are downregulated in our ORAI1 KO HEK-293 (**Figure 78**). Other studies using HEK-293 cells where ORAI protein were knocked out reported that only overexpression of ORAI2 and/or ORAI3 was able to restore SOCE in small proportion (Kar *et al*, 2021; Yeast *et al*, 2020b). In addition, patch-clamp recordings performed in ORAI1 KO HEK-293 cells demonstrated the absence of ORAI current in these cells. Taken together these data suggest that the remaining SOCE observed in our cells is not due to ORAI2 and ORAI3.

4.4.4. Proliferation

We hypothesized that the strong impairment of SOCE observed in ORAI1 KO cells should have physiological consequences on the HEK-293 properties. Thus, we first compared the level of proliferation between WT HEK-293 and ORAI1 KO cells. First, the doubling time of both cell lines was established by manual and automated counting. The result of this experiment indicated that the doubling time of HEK-293 was not modified by ORAI1 KO (25.7 hours for WT HEK-293, versus 26.8 hours for ORAI1 KO cells) (**Figure 79A**). To confirm this result, we measured the proliferative rate of these cell lines with SRB assay. In agreement with the result of doubling time we observed that the proliferative rate of ORAI1 KO cell line was not affected (**Figure 79B**). Finally, we measured the DNA content of our cells due to propidium iodide (PI) staining and cell-cycle analysis. This experiment proved that ORAI1 did not control proliferation of HEK-293 cells as no differences were observed in the proportion of cells in each phase of the cycle between WT HEK-293 and ORAI1 KO HEK (**Figure 79C**).

4.4.5. Adhesion

Following the assessment of the role of ORAI1 and SOCE in the control of HEK-293 proliferation we considered studying the impact of ORAI1 deletion on their migrative properties. Cell migration is a multi-step process involving release of cell adhesion spots from the substrate, creation of protrusion, renewal of adhesion spots, and cytoskeletal contraction (Ridley *et al*, 2003). Thus, we first set out to compare if our two cell lines were displaying differences in their adhesion level. Adhesion experiment revealed that adhesion properties were not affected by ORAI1 KO (**Figure 80**).

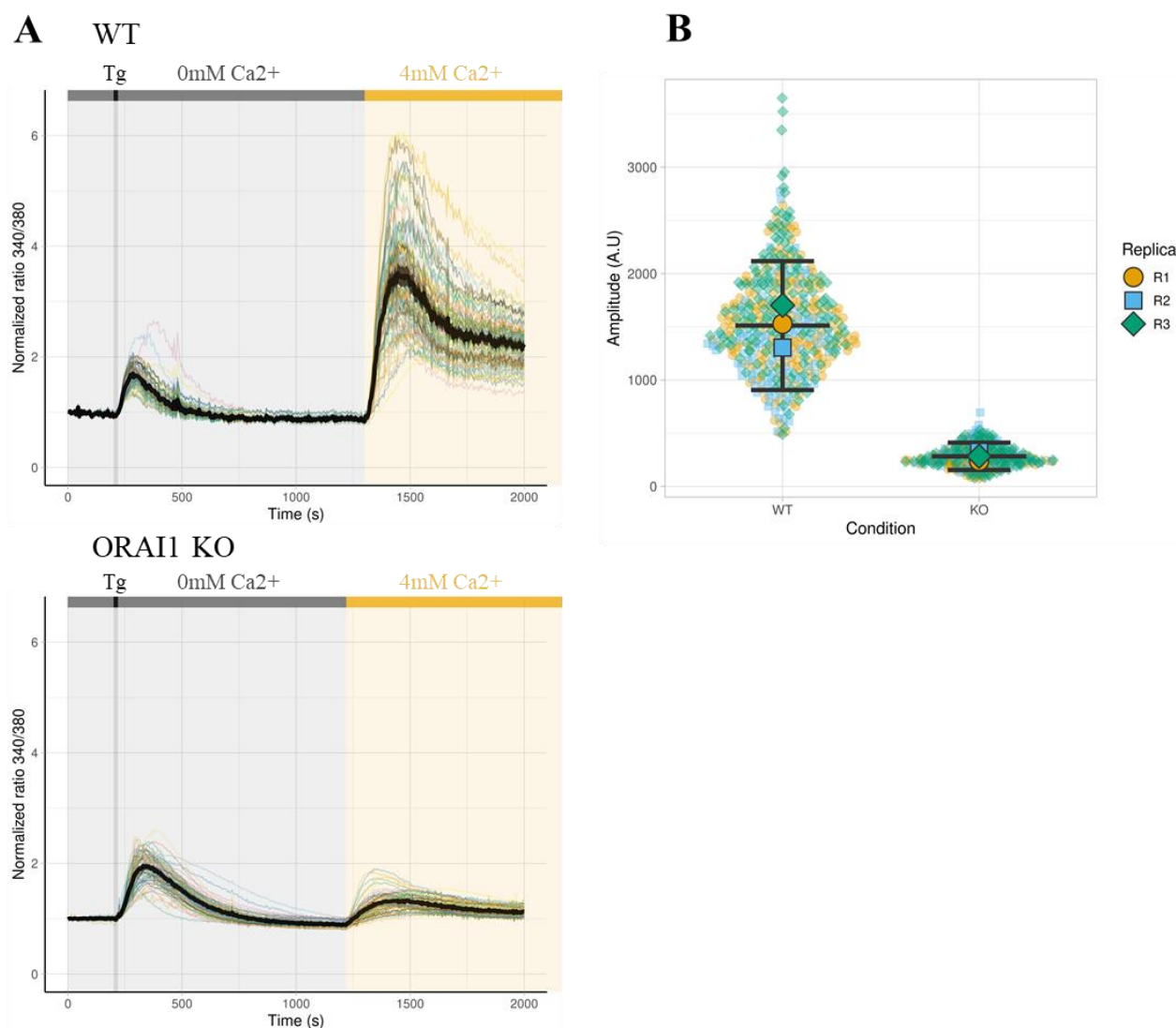


Figure 77 | Functional validation of ORAI1 KO generation.

- A. Representative traces of a single calcium imaging experiment. For both panels all recorded cells are represented with different colors, mean value is presented in black and the 95% confidence interval is shown in grey. Each experiment was repeated at least 3 times. ORAI1 KO cells present a greatly reduced SOCE compared to WT.
- B. SOCE amplitude measured for 800 seconds following Ca²⁺ addition. SOCE amplitude was calculated with an integral approximation of the area under the curve following Ca²⁺ addition in the medium. The values from each individual cells from 3 independent experiments are displayed in semi-transparent colors (Replica N°1 yellow rounds, Replica N°2 blue squares, Replica N°3 green diamond). For each replica, the mean values are displayed in plain shapes (Replica N°1 yellow rounds, Replica N°2 blue squares, Replica N°3 green diamond). Data generated for each experiment were considered non-paired. Black bars represent the mean and the 95% confidence interval of the three independent experiments. The difference in SOCE amplitude between WT-HEK (mean= 1511 with 95% CI ranging from 906 to 2117) compared to ORAI1 KO HEK cells (mean = 282 with 95% CI ranging from 154 to 411) was assessed by Welch's t-test and was significant (p=0,007).

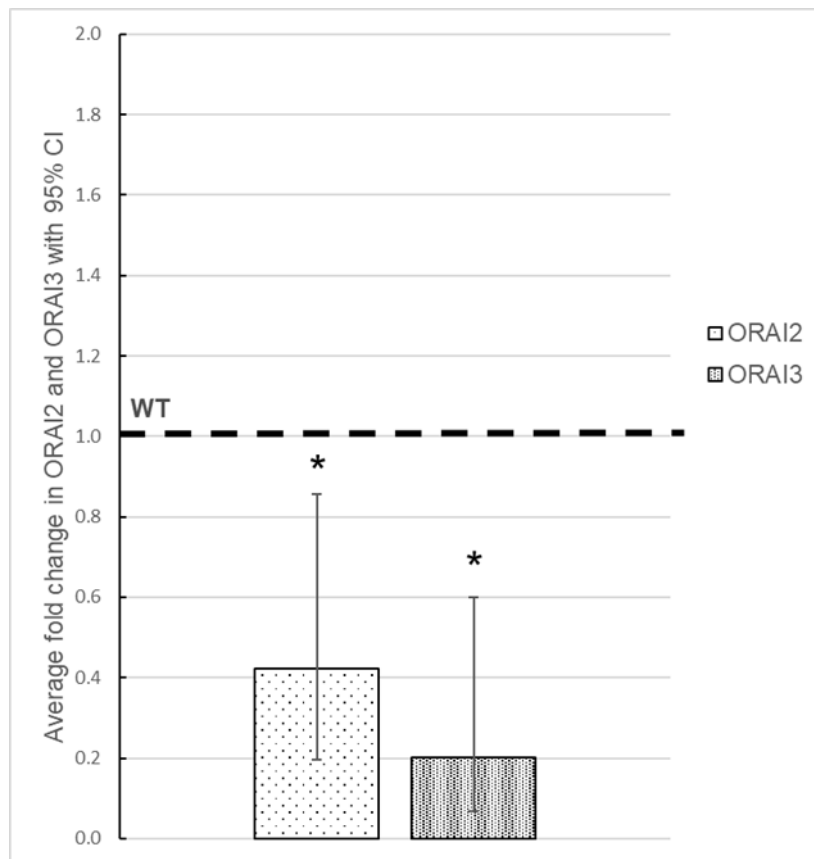


Figure 78 | ORAI1 KO leads to the downregulation of *ORAI3* and *ORAI2* expression.

The histogram represents the mean expression level of *ORAI2* and *ORAI3* mRNA measured by RT qPCR in 4 independent experiments. The expression level of *ORAI2* and *ORAI3* in WT HEK was arbitrary setup at 1. In *ORAI1* KO cells, the expression level of *ORAI2* (low density dots, left histogram) was significantly lower (expression level of 0,42 with 95% confidence interval [CI] ranging from 0,19 to 0,87) than in WT HEK cells. The *ORAI3* (dotted black line) expression level was also downregulated (expression level of 0,20 with 95% CI ranging from 0,07 to 0,60) compared to WT HEK-293. The significance of results was assessed by unpaired T.test (p= 0,02 for *ORAI2* and 0,01 for *ORAI3*).

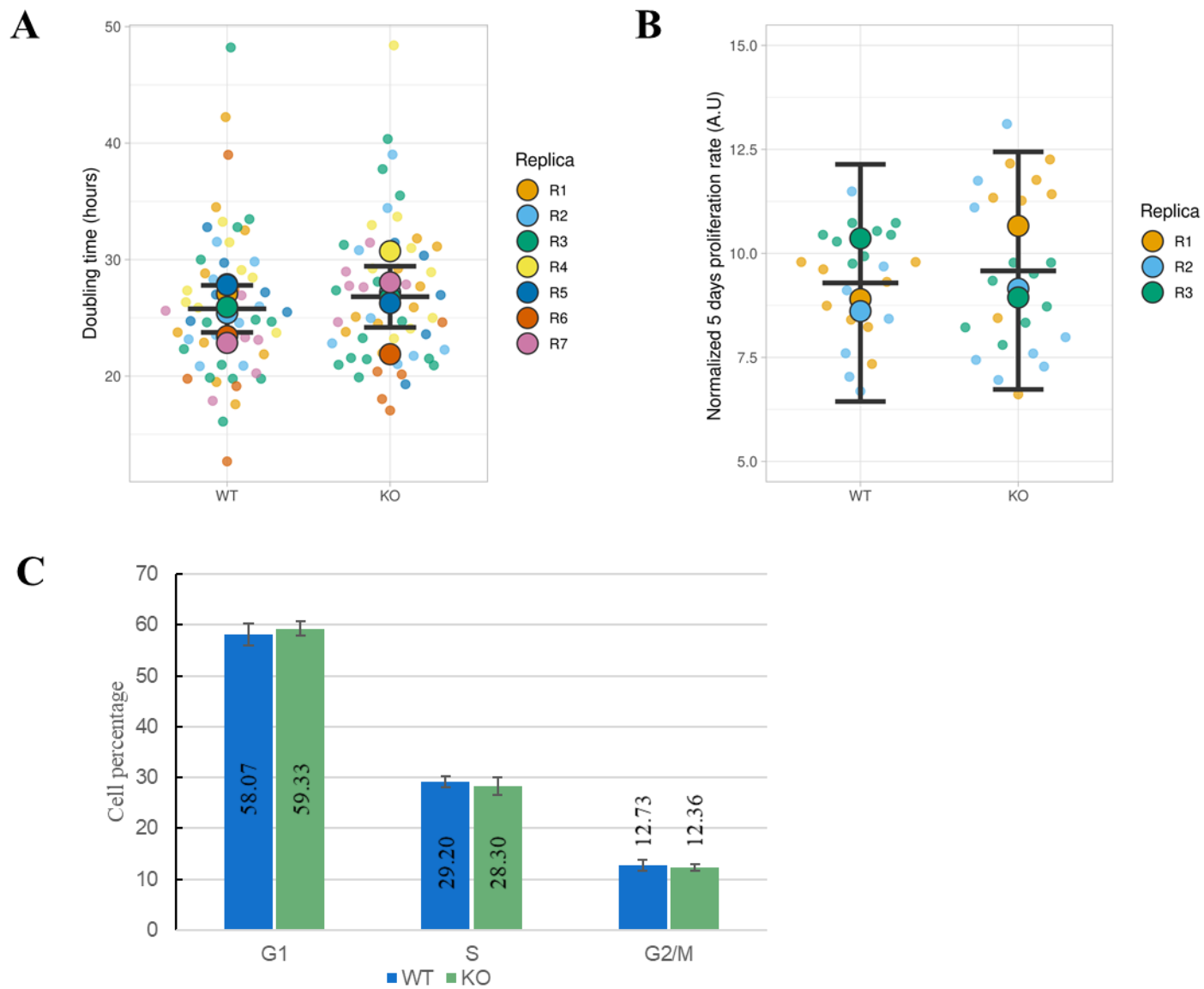


Figure 79 | ORAI1 knockout (KO) does not affect proliferation of HEK-293 cells.

- A. The doubling time of wild type (WT) and ORAI1 KO (KO) HEK-293 was measured by cell counting over a 5-to-6-day period. Semitransparent dots represent each doubling time calculated from one experiment (6–14 points per experiment). Plain colored circles display the mean of seven independent experiments. The black lanes represent the median value of each individual experiment and their 95% confidence interval (CI). The difference in the mean doubling time between condition was calculated by using Welch's t-test and was not significant (WT doubling time of 25.77 h with a 95% CI of 23.75–27.79 h; ORAI1 KO doubling time of 26.81 h with a 95% CI of 24.18–29.43 h; difference between the conditions = 1.04 h; Welch's t-test $p = 0.426$).
- B. The normalized cell proliferation rate assessed by the SRB assay 5 days after seeding WT and ORAI1 KO HEK-293 cells. The semitransparent dots represent single values obtained within each experiment (eight measurements). The median values of three independent experiments are displayed in plain colored circles. The black lanes indicate the mean value of the three individual experiments and their 95% CI (WT = 9.29 with a 95% CI of 6.44–12.14; ORAI1 KO = 9.58 with a 95% CI of 6.73–12.44). The significance of the difference between conditions (-0.29 with a 95% CI of 1.83–2.42) was calculated with Welch's t-test ($p = 0.721$).
- C. Cell-cycle analysis of the DNA content determined by propidium iodide staining for WT (blue) and ORAI1 KO (green) HEK-293 cells. The histograms represent the percentage of cells in each phase of the cell cycle (exact value indicated within the histogram bars) with error bars indicating the standard deviation. Experiments were repeated six times, and no significant differences between conditions were identified by using Welch's t test.

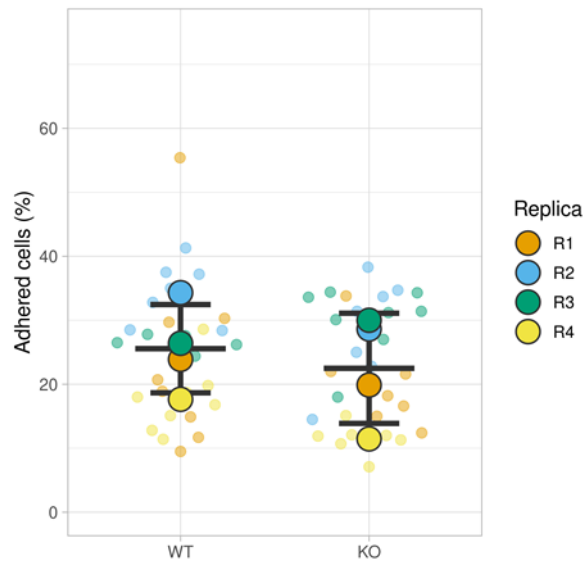


Figure 80 | ORAI1 knockout (KO) does not modify the adhesive properties of HEK-293 cells.

Comparison of the adhesive properties between wild type (WT) and ORAI1 KO cells. Data points represent the percentage of adhered cells after an incubation for 1 h at 37 °C. Plain circles represent the mean values of individual replicates (R1, R2, R3, and R4); semitransparent circles display individual data points within each replicate. The mean values of the four replicates are indicated as black bars \pm standard deviation (CI). The difference in adhesion between WT cells (25.56% \pm standard deviation [SD] 6.90%) and KO ORAI1 cells (22.49% \pm 8.61%) was assessed with Welch's t-test for nonpaired data and was not significant ($p = 0.6$; mean difference between conditions = -3.07% with a 95% CI of -16.73 to 10.59).

4.4.6.Migration

We continued investigating the role of ORAI1 in the migration of HEK-293 by performing the collective migration cell assay represented by the wound healing experiment. We analyzed several features of the collective migration. First, we determined that the collective speed migration was increased for ORAI1 KO cells only during the first 10 hours of the experiment. Further measurements of the collective migration speed from the 10th hours until total wound closure did not show any differences (**Figure 81A**). Second, we compared the time of total wound closure between our cell line and observed that there was no difference (**Figure 81B, left**). Nonetheless, because we observed that migration speed was different in the beginning of our experiment, and because the initial size of the wound is susceptible to variation, we performed a ratio between the half- and full- wound closure time. This analysis confirmed that the collective migration speed of HEK-293 was significantly slower than for ORAI1 KO in the beginning of the experiment (**Figure 81B, right**). Finally, we measured the leading-edge migration speed of our cell lines. Specifically, we measured the shortest distance between the two migration front every five hours period (**Figure 82**). This analysis demonstrated that ORAI1 KO cells are migrating faster than WT HEK-293 during the 1st-5th hours and 5th-10th hours periods. Altogether, our data of wound healing experiment indicates that collective WT HEK-293 migration present a delay in the migration initiation compared to ORAI1 KO cells. Finally, we wanted to assess whether the effect observed was restricted to collective migration, or if ORAI1 KO was also affective single cell migration. Therefore, we performed Transwell ® assay on our cell line. Our results indicate that single-cell migration is not affected by ORAI1 KO (**Figure 83**). Thus, we concluded that ORAI1 is involved in the control of HEK-293 cell collective migration.

4.4.7.Conclusions

In this study we have confirmed that ORAI1 is the main SOCE effector in HEK-293. In addition, we revealed that a small proportion of SOCE is not attributed to ORAI1 channel. RT-qPCR data suggest that the remaining SOCE observed is not due to ORAI 2 and ORAI3 overexpression. Further we demonstrate that ORAI1 does not control the proliferation of HEK-293. Similarly, ORAI1 does not impact the adhesion level of HEK-293. Finally, we establish that ORAI1 is partially involved in the control of HEK-293 migration. Specifically, we demonstrated that the collective cell migration properties are affected by ORAI1 KO while single-cell migration is unaffected by ORAI1-KO. As a conclusion, we demonstrated that ORAI1 and SOCE are dispensable in the maintenance of HEK-293 physiology. Whether the absence of an effect of ORAI1 deletion is the result of compensatory mechanisms or whether the impact of SOCE in HEK-293 physiology is indeed limited remain to be investigated.

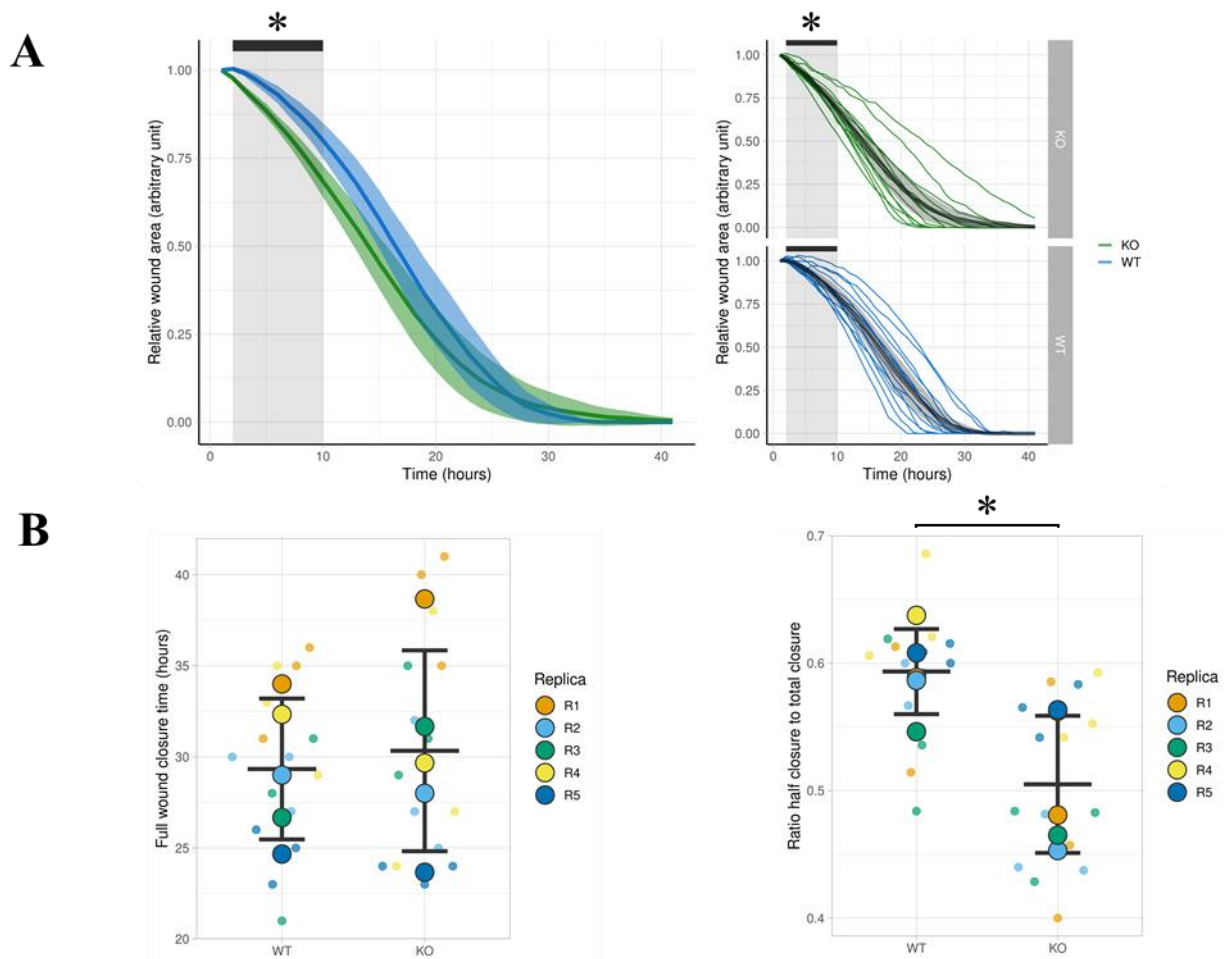


Figure 81 | ORAI1 KO increase collective migration speed of HEK-293.

- A. Relative wound area as a function of time (WT in blue, ORAI1 KO in green). The curves represent the means of five independent experiments with their 95% CI (semitransparent colors). Right panels: Relative wound area as a function of time with each repeat presented individually (down panel: WT in blue; top panel: KO in green). Black lines represent the mean value of the experiments with the 95% CI in semitransparent color; the thin colored lanes represent repeats of every experiment performed. Wound closure area analysis performed for each time point (*i.e.*, every hour) indicates that ORAI1 KO cells migrated significantly faster than WT cells during hours 1–9 of the experiment (* $p < 0.05$ at hours 1–9, assessed based on the wound closure mean value difference between WT and ORAI1 KO cells with Welch's t-test, nonpaired data).
- B. For both panels: The mean of each replicate is represented as a plain circle; semitransparent circles represent individual data points for each replicate. The mean of the five replicates is displayed as black bars \pm SD. Left panel: Time of complete wound closure, the difference in full closure time between WT cells ($29.33\text{h} \pm 3.87\text{ h}$) and KO ORAI1 cells ($30.33\text{ h} \pm 5.51\text{ h}$) was assessed with Welch's t-test for nonpaired data and was not significant ($p = 0.75$; mean difference between conditions = 1 h with a 95% CI of -6 to +8 h). Right panel: ratio of the half closure time to the total closure time. The difference in the ratio between WT cells (0.59 ± 0.03) and ORAI1 KO cells (0.50 ± 0.05) was assessed by Welch's t-test for nonpaired data and was significant ($p = 0.018$; mean difference between conditions = -0.09 with a 95% CI from -0.16 to -0.02).

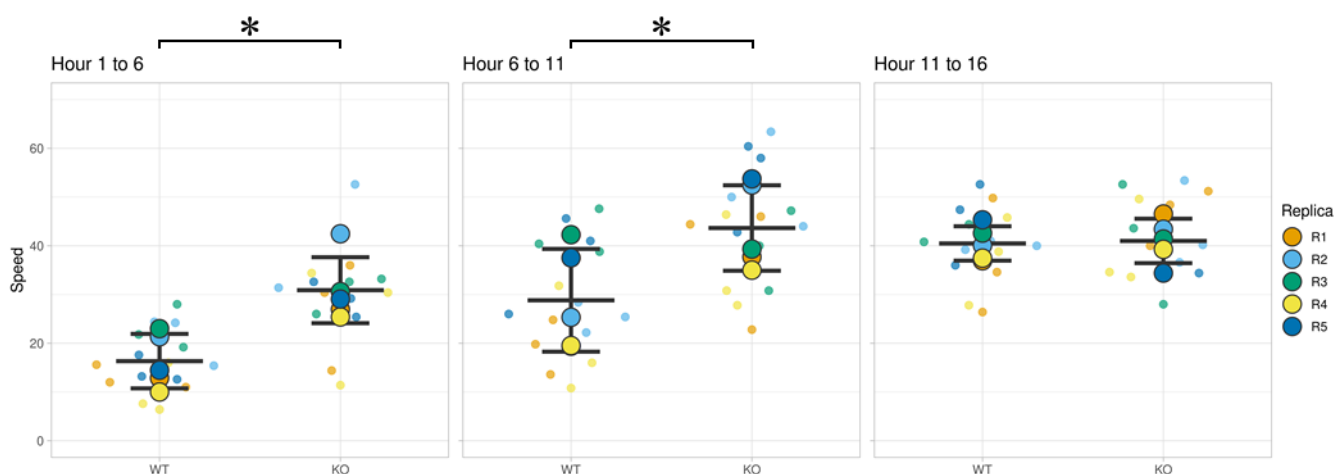


Figure 82 | ORAI1 KO increase collective migration speed of HEK-293.

Evolution of leading-edge migration speed over 5 h periods. Hours 0–5 are presented on the left panel, hours 5–10 are presented on the central panel, and hours 10–15 are presented on the right panel. The mean of each replicate is represented as a plain circle; semitransparent circles represent individual data points for each replicate. The mean of five replicates is displayed as black bars \pm SD. For hours 1–5, the difference in leading-edge migration speed between WT cells (16.33 ± 5.59 pixel/hours) and ORAI1 KO cells (30.89 ± 6.77 pixel/hours) was assessed by Welch's t-test for nonpaired data and was significant ($p = 0.006$; mean difference between conditions = 14.56 pixel/hours with a 95% CI of 5.45–23.67). For hours 5–10, the difference in leading-edge migration speed between WT cells (28.81 ± 10.53 pixel/hours) and ORAI1 KO cells (43.65 ± 8.77 pixel/hours) cells was assessed by Welch's t-test for nonpaired data and was significant ($p = 0.043$; mean difference between conditions = 14.84 pixel/hours with a 95% CI of 0.62–29.06). For hours 10–15, the difference in leading-edge migration speed between WT cells (40.48 ± 3.53 pixel/hours) and ORAI1 KO cells (41 ± 4.56 pixel/hours) cells was assessed by Welch's t-test for nonpaired data and was not significant ($p = 0.84$; mean difference between conditions = 0.52 pixel/hours with a 95% CI of -5.49 to 6.53).

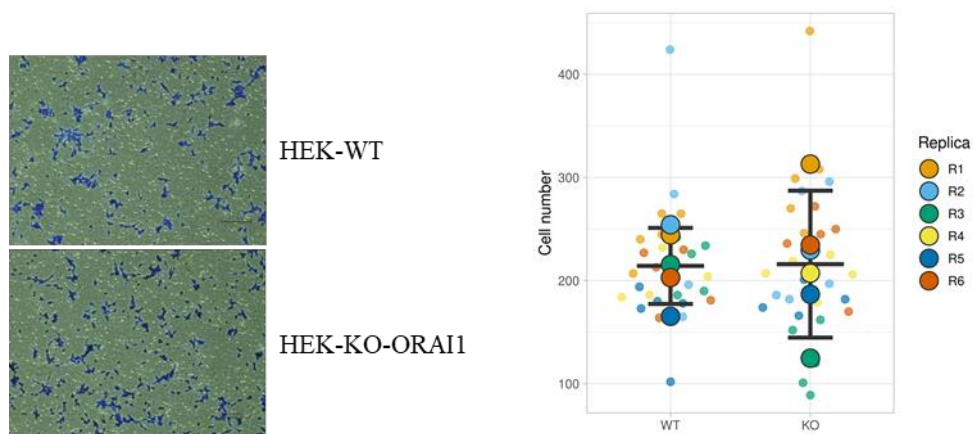


Figure 83 | ORAI1 KO does not modify the single-cell migration speed of HEK-293.

Transwell® migration assay. Left panel: representative picture of the bottom side of Transwell® insert following 24 h incubation with either WT or ORAI1 KO HEK-293 cells. Right panel, statistical analysis of Transwell® migration experiment: semitransparent circles display the number of cells of each counting performed for each replicate. Plain circles represent the mean value for a single experiment. Black lines show the median value of the six independent experiments performed with their 95% CI. ORAI1 KO cells (mean cell number = 208 with a 95% CI of 139–278) showed no significant difference in the migrating cell number compared with WT cells (mean cell number = 211 with a 95% CI of 185–238). The significance of the difference between WT and ORAI1 KO cells (-3 cells) was assessed with Welch's t-test ($p = 0.91$)

4.5. Study of ORAI1 - ORAI3 interactions with FLIM-FRET

4.5.1. Hypotheses on the existence of a dynamic re-arrangement of ORAI protein

The last part of the PhD work was devoted to the study of ORAI1-ORAI3 interactions. Specifically, we aimed to use the FLIM-FRET technique to determine if the interaction between ORAI1 and ORAI3 was modified due to ORAI channel activation. This work originates from one of the hypotheses suggested by the publication of Dubois et al. (Dubois *et al*, 2014a). Specifically, the authors demonstrated that the disruption of the equilibrium between ORAI1 and ORAI3 expression represents an oncogenic switch. In particular, the authors showed that ORAI3 is overexpressed in prostatic primary tumors. Moreover, they overexpressed ORAI3 in prostate cancer cell line, to resemble the remodeling observed during cancer progression, and demonstrated that ORAI3 overexpression promotes its association with ORAI1 and leads to the formation of heteromeric ORAI1-ORAI3 channel. The association between these two proteins induces a modification in the cellular Ca^{2+} answers provided by the cell thereby promoting cancerization processes. Finally, the authors proposed that ORAI channel composition as homo- or hetero- multimers depends on the expression level of the different ORAI proteins, but also on the specific stimulation received by the cells (Dubois *et al*, 2014b). The later proposition suggests that ORAI channel composition is susceptible to undergo a dynamic remodeling depending on the stimulation received by the cells. This suggestion led us to hypothesize that ORAI proteins could undergo an on-site assembly leading to the creation of specific ORAI channels. Of note, such a mechanism of an “on site” assembly of the ORAI channel, while highly hypothetical, was also proposed by Li and al (Li *et al*, 2016b). Alternatively, one can consider the existence of pre-assembled channel of different composition which would be specifically activated depending on the signal received by the cells. To address these possibilities, we took advantage on a collaboration with a team specialized in the use of FLIM-FRET technique to identify if ORAI protein interaction level was modified during activation of ORAI channels.

4.5.2. Impact of ORAI1 and ORAI3 overexpression modulation on SOCE level

4.5.2.1. Effect of transient overexpression of ORAI1 and ORAI3 on SOCE

The previous publication from our laboratory demonstrated that ORAI3 overexpression was impairing SOCE in PC3 cells. Of note, this result was obtained in PC3 cells stably overexpressing ORAI3. However, the expression level of ORAI3 in the cells was 20 times higher than in WT PC3 cells. Of note, this large overexpression of ORAI3 might have allowed detection of ORAI3 effect of SOCE which are marginal in physiological conditions. In addition, the creation of stable clones potentially induced compensatory mechanisms affecting the SOCE process. Therefore, we decided to confirm and extend their results by transiently overexpressing ORAI3 in WT PC3 cells. We hypothesized that transient overexpression would prohibit the apparition of compensatory mechanisms and would result in a cellular population overexpressing various level of ORAI3. Hence, the recording of SOCE from the

whole cell population might depict a more accurate picture of ORAI3 impact on SOCE. In addition, we decided to assess if the overexpression of ORAI1 would also affect SOCE.

Accordingly, we transfected PC3 cells with ORAI3 or ORAI1 plasmids and performed Ca^{2+} imaging experiments where store depletion was induced with TG. The results of the Ca^{2+} imaging experiment indicated that the transient ORAI3 overexpression decreased the level of SOCE compared to PC3 WT, while ORAI1 seemed to enhance SOCE (**Figure 84**). The quantification of the amplitude of SOCE revealed that ORAI3 transient overexpression was significantly decreasing SOCE (**Figure 85**). However, ORAI1 overexpression did not significantly affected the level of SOCE compared to WR cells (**Figure 85**). Thus, these results confirmed the previous data obtained by the laboratory that ORAI3 impairs SOCE. To extend further these results, we decided to use the ORAI1 and ORAI3 KO cells and to measure their SOCE level. In addition, we aimed to perform rescue experiment where the deleted protein (ORAI1 or ORAI3) would be re-expressed in order to verify that the effect observed in the KO cells could not be attributed compensatory mechanisms.

4.5.2.2. Effect ORAI1 deletion on SOCE

We started by measuring the level of SOCE in ORAI1 KO PC3 cells. As expected, ORAI1 deletion almost totally abolished SOCE, confirming that ORAI1 is the major effector of SOCE (**Figure 86 A, C**). Further we performed rescue experiments, where a plasmid coding for ORAI1 was transfected in ORAI KO cells. Unexpectedly, the rescue of ORAI1 did not allow a restoration of SOCE level comparable to the one observed in PC3 WT (**Figure 86 A, D**). Nonetheless, inspection of single cell Ca^{2+} traces allowed us to identify that some cells were displaying SOCE of a similar intensity to the one observed in PC3 WT (**Figure 86 B, D**). Therefore, we assumed that the difference observed in the mean intensity of SOCE level between PC3 WT and rescued ORAI1 KO cells could be attributed to a low transfection level.

4.5.2.3. Effect of ORAI3 deletion on SOCE

Next, we measured the level of SOCE in ORAI3 KO cells. With this experiment, we intended to determine if endogenous ORAI3 was affecting the amplitude of the SOCE in the PC3 cells. Ca^{2+} imaging experiment revealed that SOCE was enhanced following ORAI3 deletion, suggesting that endogenous ORAI3 impairs SOCE in PC3 WT (**Figure 87 A**). Quantification of the SOCE amplitude allowed us to determine that the improvement of SOCE following ORAI3 deletion was statistically significant (**Figure 87 B**). Further, we re-expressed ORAI3 in the cells where it was deleted. The Ca^{2+} traces as well as quantification of SOCE level demonstrated that ORAI3 rescue in ORAI3 KO cells significantly decreased the SOCE amplitude (**Figure 88**).

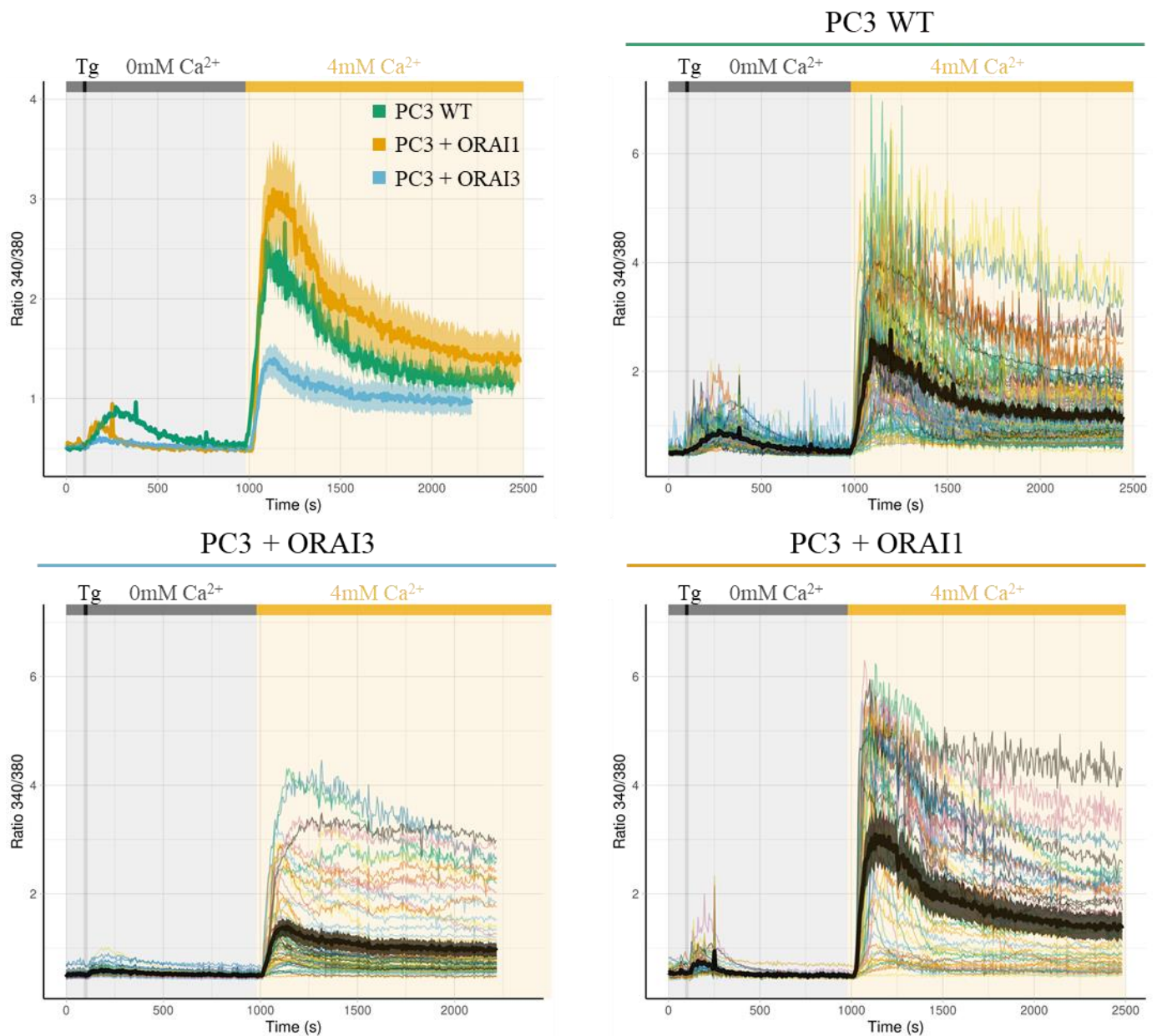


Figure 84 | ORAI1 and ORAI3 overexpression effect on SOCE level.

Representative traces of single Ca^{2+} imaging experiments. Top left: mean fluorescent signal recorded for PC3 WT (green), PC3 transfected with ORAI1 plasmid (PC3 + ORAI1, yellow), and PC3 transfected with ORAI3 plasmid (PC3 + ORAI3 blue). Solid lines represent the mean intensity, semi-transparent colors represent the 95% confidence interval (CI). ORAI3 transfection decreases SOCE amplitude. The top right, bottom left, and bottom right panels are displaying all the single cell Ca^{2+} traces corresponding to a single condition. For each panel, the mean signal of the corresponding condition is displayed in black with the 95% CI in grey. Single-cell traces are displayed in different colors. Please note that scales were kept similar to simplify comparison between all conditions.

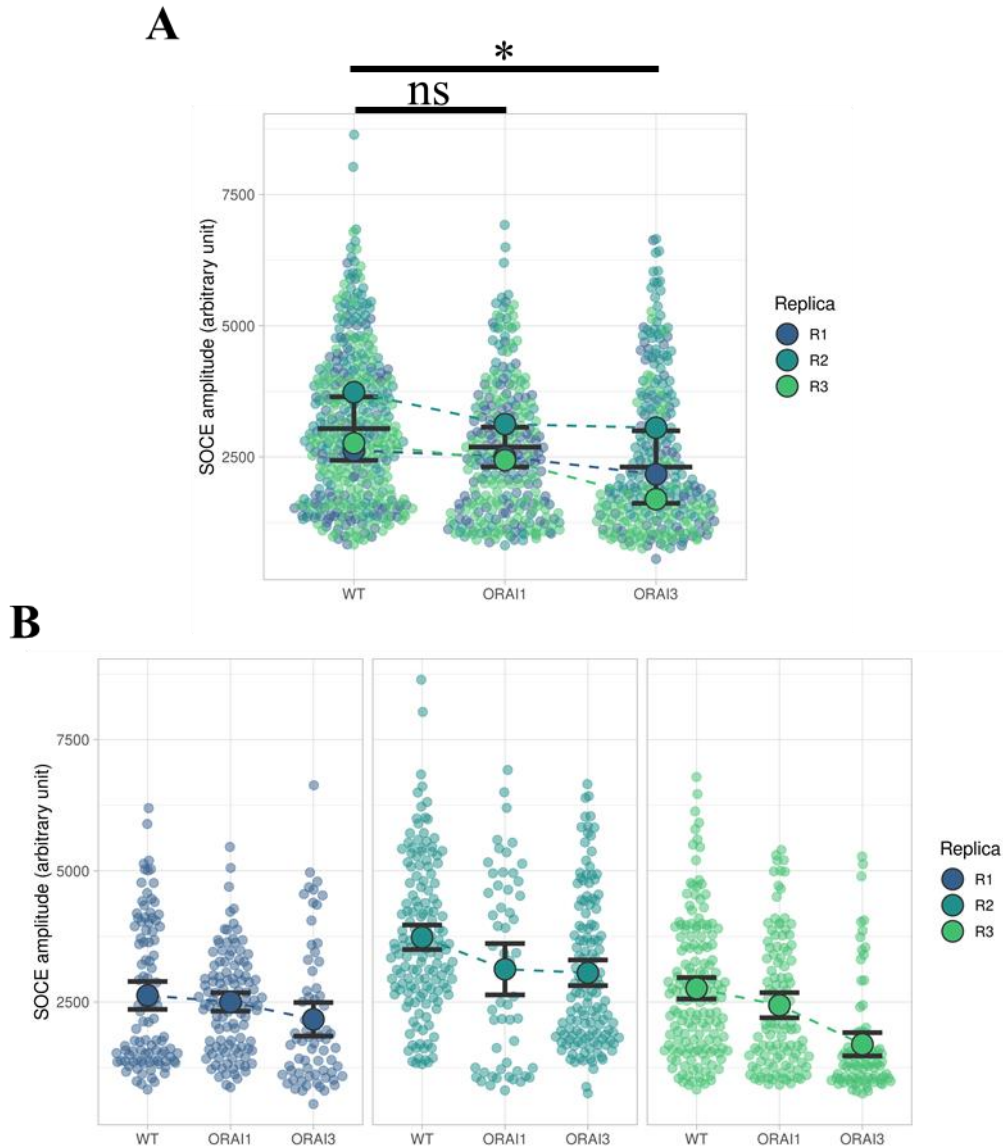


Figure 85 | ORAI3 overexpression impairs SOCE in PC3 WT.

- A. Quantification of SOCE level from Ca^{2+} traces of Figure 84. Quantification was performed due to integration of the curve area following Ca^{2+} addition in the medium. Semi-transparent circles represent the value calculated for each individual cell. Solid dots represent the mean value for each individual repeat. Black bars represent the mean value of the three experiments with their respective standard deviation (SD). SOCE level in PC3 + ORAI3 ($2206 \pm \text{SD } 530$) was significantly lower than in PC3 WT ($3040 \pm \text{SD } 604$): $p = 0.049$ calculated from the difference between condition. No differences were found between PC3 WT and PC3 + ORAI1 ($2689 \pm \text{SD } 379$) $p = 0.13$. p -values were calculated using paired t-test, * $p < 0.05$.
- B. Data from A represented for each replicate. Solid dot represent the mean value per condition for the experiment with the black bars representing the 95% confidence interval.

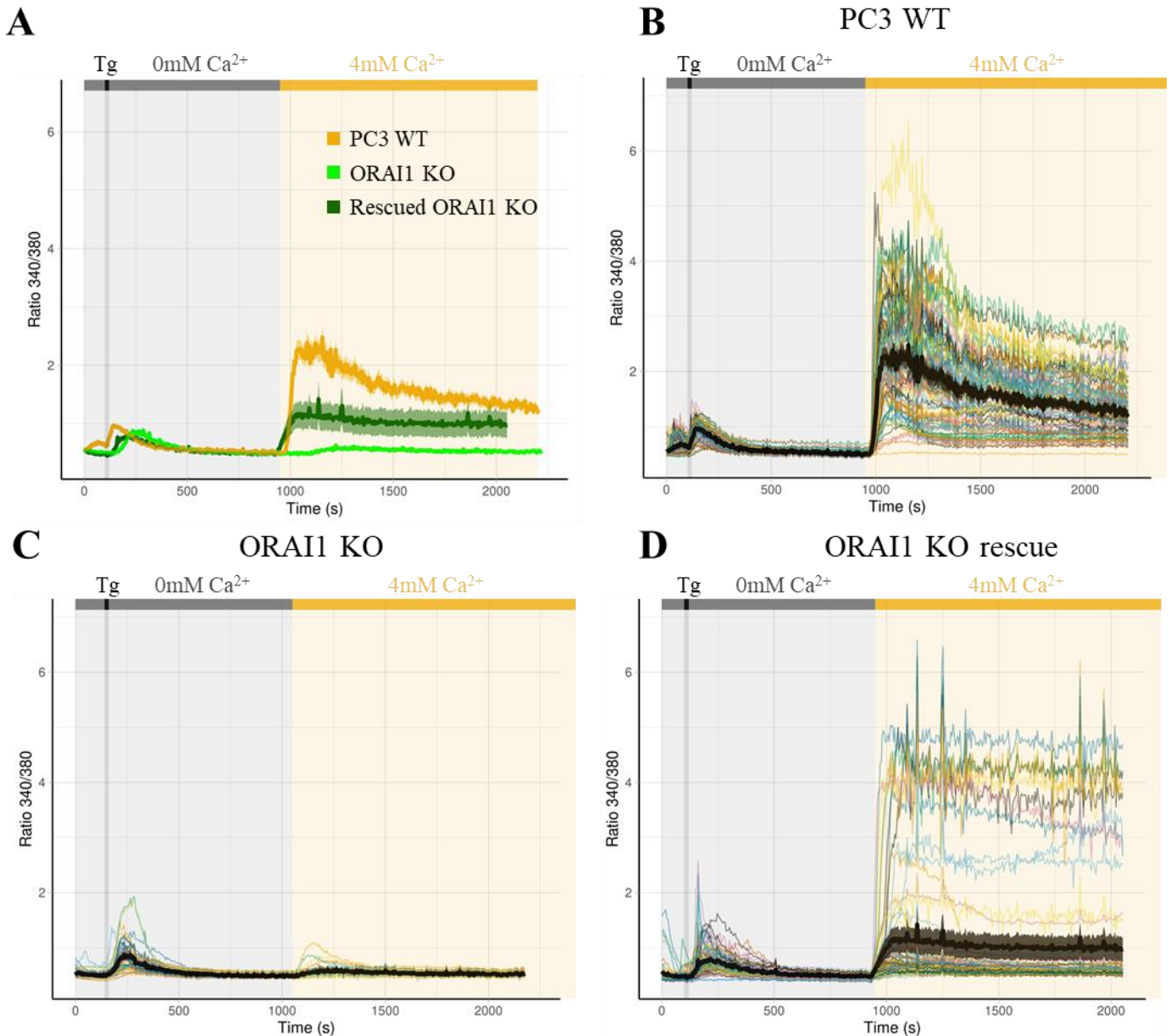


Figure 86 | ORAI1 is the main SOCE effector in PC3 WT.

- A. Representative Ca^{2+} traces of a single Ca^{2+} imaging experiment, corresponding to PC3 WT (yellow), ORAI1 KO PC3 (light green), and rescued ORAI1 KO PC3 (dark green). The mean fluorescent signal is represented by the solid line, with the 95% confidence interval (CI) displayed in semi-transparent color.
- B. Single-cell Ca^{2+} traces corresponding to the WT PC3 condition.
- C. Single-cell Ca^{2+} traces corresponding to a the ORAI1 KO PC3 condition
- D. Single-cell Ca^{2+} traces corresponding to a the rescued ORAI1 KO PC3 condition
- For B., C., and D. The mean signal is represented by the solid black line, with 95 CI in semi-transparent color, and single-cell traces are displayed in different colors.

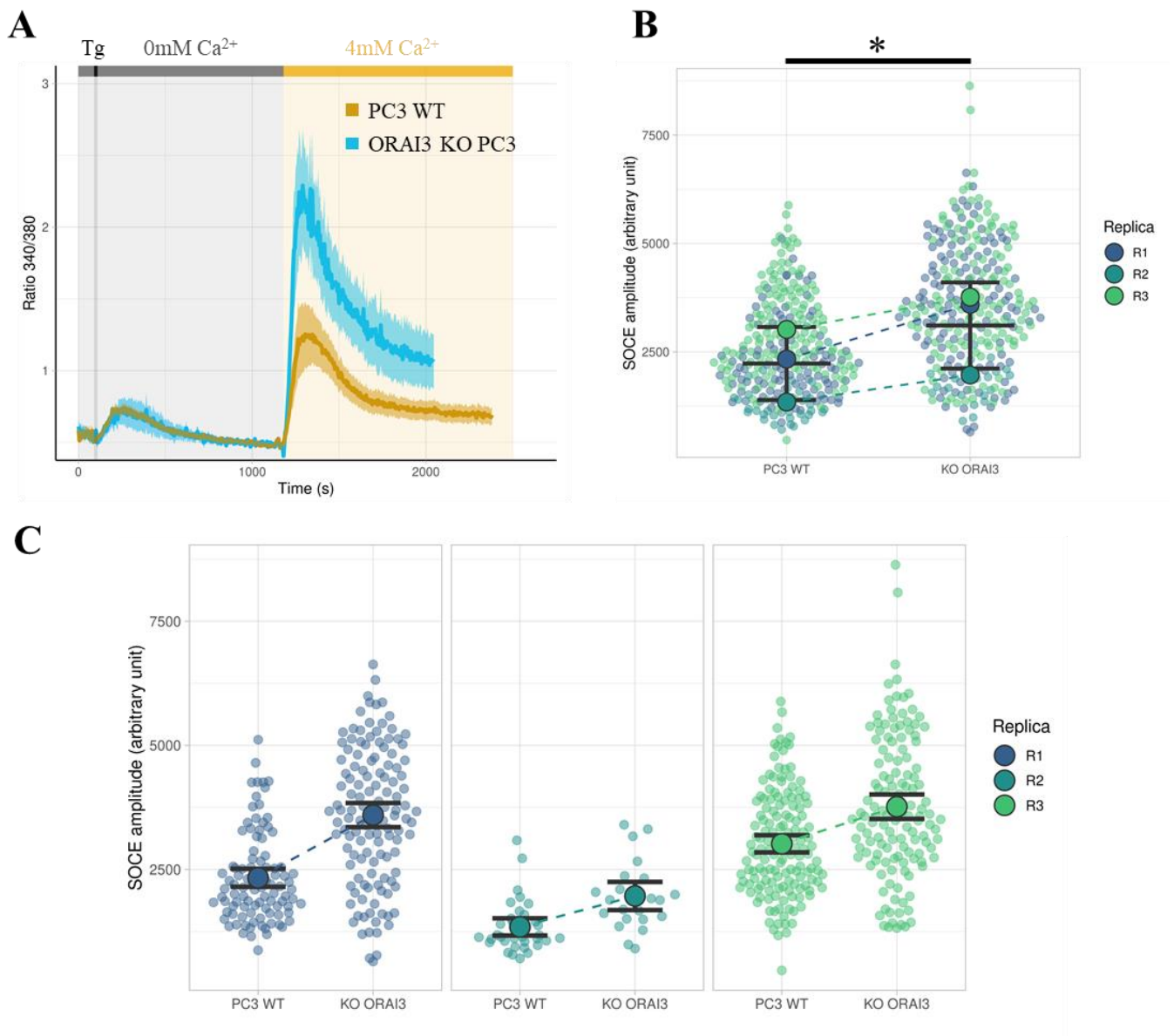


Figure 87 | Endogenous ORAI3 impairs native SOCE in PC3 WT.

- A. Representative Ca²⁺ traces of a single Ca²⁺ imaging experiment, corresponding to PC3 WT (yellow), ORAI3 KO PC3 (light blue). The mean fluorescent signal is represented by the solid line, with the 95% confidence interval (CI) displayed in semi-transparent color.
- B. Quantification of SOCE in WT PC3, and ORAI3 KO PC3, calculated by integrated the area under the curve following Ca²⁺ addition in the medium for 800 seconds. Semi transparent dots represent the SOCE amplitude measured for each single cell within each replica. Solid dots, represent the mean value for each replica. Black bars represent the mean of the three replica and their standard deviation (SD). The SOCE level in PC3 WT (2231 \pm SD 481) was significantly lower than in ORAI3 KO PC3 (3109 \pm SD 993). * p= 0,046 calculated from the difference between condition.
- C. Data from B represented for each replicate. Solid dot represent the mean value per condition for the experiment with the black bars representing the 95% confidence interval.
- p-values were calculated using paired t-test, * p<0.05

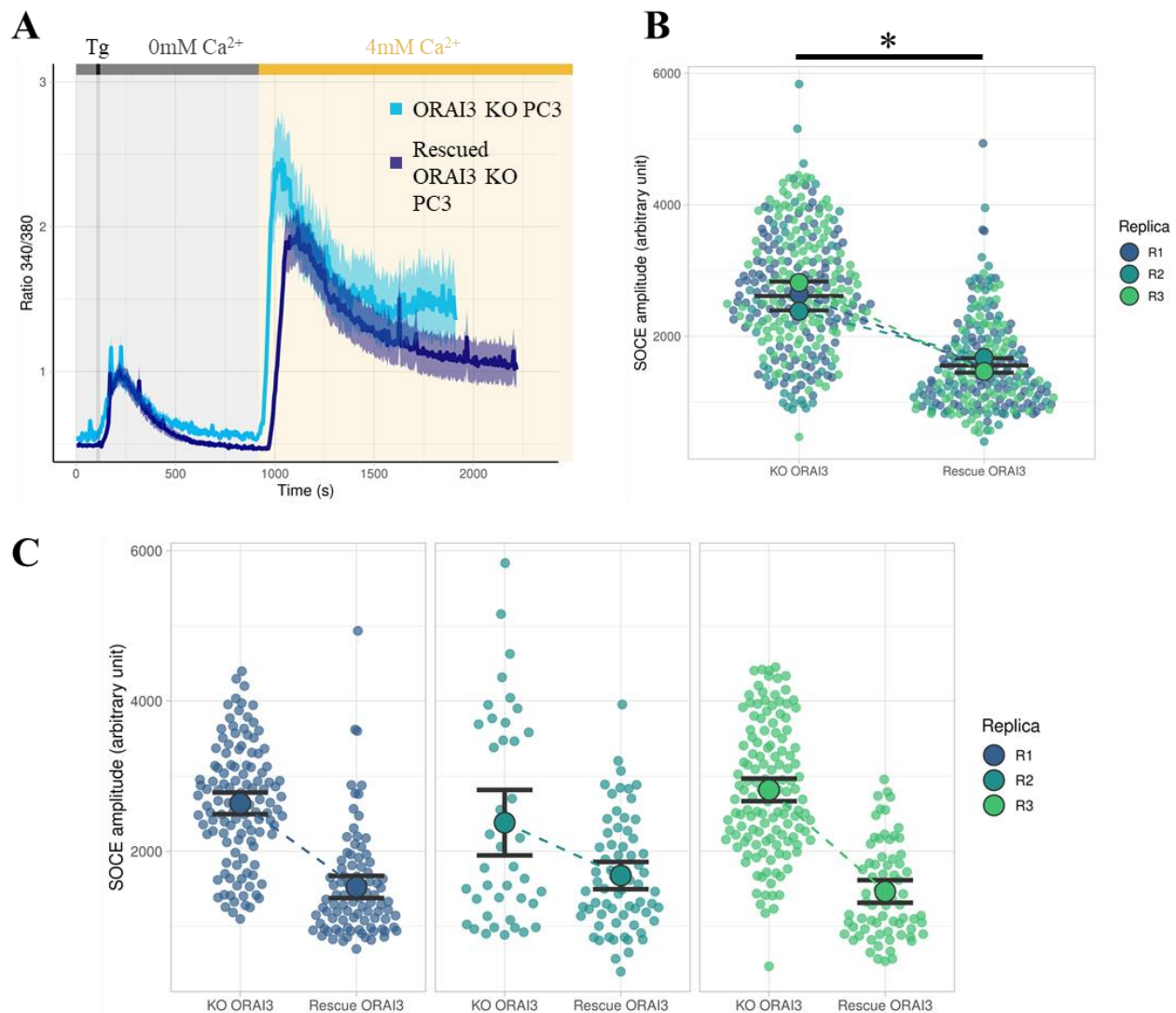


Figure 88 | ORAI3 rescue in ORAI3 KO cells, impairs SOCE.

- A. Representative Ca²⁺ traces of a single Ca²⁺ imaging experiment, corresponding to ORAI3 KO PC3 (light blue), and rescued ORAI3 KO PC3 (dark blue). The mean fluorescent signal is represented by the solid line, with the 95% confidence interval (CI) displayed in semi-transparent color.
- B. Quantification of SOCE in ORAI3 KO PC3, and rescued ORAI3 KO PC3, calculated by integrating the area under the curve following Ca²⁺ addition in the medium for 800 seconds. Semi transparent dots represent the SOCE amplitude measured for each single cell within each replica. Solid dots, represent the mean value for each replica. Black bars represent the mean of the three replicates and their standard deviation (SD). The SOCE level in ORAI3 KO PC3 ($2611 \pm \text{SD } 219$) was significantly higher than in rescued ORAI3 KO PC3 ($1555 \pm \text{SD } 109$). * $p = 0.031$ calculated from the difference between conditions.
- C. Data from B represented for each replicate. Solid dot represents the mean value per condition for the experiment with the black bars representing the 95% confidence interval.
- p-values were calculated using paired t-test, * $p < 0.05$

4.5.2.4. Conclusion on the roles of ORAI1 and ORAI3 in endogenous SOCE

Our results confirm and extend the finding of Dubois et al. indicating that ORAI3 impairs SOCE. Indeed, we used a transient overexpression model to show that ORAI3 impairs SOCE in PC3-WT. In addition, we demonstrate that the deletion of ORAI3 in PC3 cells leads to a SOCE enhancement indicating that endogenous ORAI3 expression possess an inhibitory role on SOCE level. In addition, we show that this effect is not the consequence of compensatory mechanisms since re-expression of ORAI3 in ORAI3 KO cells, leads to a decrease of the SOCE amplitude. We have also studied the effect of ORAI1 expression modulation on the SOCE level. The absence SOCE modulation following ORAI1 overexpression might be explained by a low expression level of STIM proteins compared to the overexpressed ORAI1, preventing the activation of all ORAI channel present in the cells. Finally, the experiments performed in ORAI1 KO cell line demonstrates that ORAI1 is the major effector of SOCE in PC3 cells. In addition, rescue experiments demonstrated that ORAI1 re-expression restored SOCE in PC3 cells. Overall, these data demonstrate the involvement of ORAI3 and ORAI1 in the SOCE in PC3. Thus, these results suggest the existence of heteromeric ORAI channels composed of ORAI1 and ORAI3 proteins. Since we showed that ORAI3 was modulating SOCE entry we decided to study the interaction level between ORAI1 and ORAI3 following ORAI channel activation.

4.5.3.Measurement of ORAI1-ORAI3 interaction with FLIM-FRET

4.5.3.1. In HEK-293

At the beginning of this PhD work, we considered studying ORAI1-ORAI3 interaction in HEK-293 cells bearing endogenously tagged ORAI proteins with FLIM-FRET technique. Even though, we could not establish this cell line, we had started performing FLIM-FRET experiments in HEK-293. Specifically, HEK-293 were transfected with different ratio of ORAI1-mTurquoise2 (ORAI3-mT2) and ORAI3-sYFP2 plasmids (*i.e.*, ratio 1:1 and ratio 1:3 for ORAI1-mT2:ORAI3-sYFP2. Indeed, the publications from Dubois et al., identified that ORAI3 expression level was three time higher to ORAI1 in prostate cancer tissue. In their work they used these transfections ratio to mimic the cancerous phenotype. Therefore, we used the same strategy to compare the interaction level between the two proteins depending on their relative expression level. Of note, for all the FLIM-FRET experiments, ORAI1-mT2 was used as the donor molecule, while ORAI3-sYFP2 was used as the acceptor molecule. In addition, only the donor lifetime (ORAI1-mT2 only transfection) was measured for each experiment to allow the calculation of the FRET efficiency. Finally, because lifetime is sensitive to external condition such as the temperature, and pH, the data obtained for each experiment were statistically treated as paired because they were performed in the exact same conditions (same solutions for example).

4.5.3.1.1. Basal interaction

In a first set of experiment, we evaluated the interaction level between ORAI1 and ORAI3 before activation of ORAI channels. Specifically, ORAI1-mT2 and ORAI3-sYFP2 were transfected in WT HEK-293 as the acceptor molecule with different ratios (1:1 and 1:3), and changes in the ORAI1mT2 lifetime were measured. Of note, in case of FRET, the lifetime of ORAI1-mT2 is expected to decrease because FRET represent an additional pathway for de-excitation of the excited molecule. First, we measured lifetime of ORAI1-mT2 alone and in the presence of ORAI3-sYFP2 in equimolar quantity (*i.e.*, transfection, ratio of 1:1) and in a three-fold higher expression rate (*i.e.*, transfection ratio of 1:3). ORAI1-mT2 lifetime alone was measured at 3.97 ns, which is consistent with the lifetime of the “free” mTurquoise2 fluorescent protein (4 ns) (**Figure 89A**). When ORAI3-sYFP was transfected together with ORAI1-mT2, a significant lifetime decrease was observed, revealing the existence of FRET and thus the existence of basal interaction between ORAI1 and ORAI3 (**Figure 89A**). Increasing the ratio of ORAI3-sYFP2 expression (ratio 1:3), decreased even further the ORAI1 mTurquoise2 lifetime indicating that the level of interaction between ORAI1 and ORAI3 was increased (**Figure 89A**). Thus, we demonstrated that ORAI1 and ORAI3 are interacting in basal condition. In addition, we demonstrated that the level of interaction between these two proteins is dependent on ORAI3 level of expression. In the subsequent experiments we wanted to evaluate the ORAI1-ORAI3 interaction following ORAI channel activation. Because STIM1 can be limiting during ORAI channel activation and thus its overexpression might be required. We performed the same experiment as above with the additional overexpression of the STIM1-mCherry plasmid to determine if this overexpression was affecting the basal interaction between ORAI1 and ORAI3. The measured lifetime of ORAI1-mT2 in the presence of STIM1 not deeply modified in the presence or absence of STIM (**Figure 89B**).

4.5.3.1.2. Arachidonic acid activated interaction

Next, we assessed if the activation of ORAI channels was modifying the interaction level between ORAI1 and ORAI3 proteins. First, we used arachidonic acid (AA) to specifically activate the ARC channel. Of note ARC channel is hypothesized to be constituted by a pentameric assembly of three ORAI1 proteins and two ORAI3 proteins. Because it was shown that STIM1 is required for ARC activation, measurements were performed both with endogenous STIM1 expression, and overexpressed STIM1. Using the same ratio strategy as described above we observed that in the 1:1 expression ratio, the addition of AA on the cells did not influence the lifetime of ORAI1mT2, independently on the overexpression presence of STIM1 (**Figure 90 A and B**). At the opposite, using a 1:3 transfection ratio, we observed that addition of AA on the cells was increasing the interaction level between ORAI1 and ORAI3, only when STIM was not overexpressed (**Figure 91 A and B**). Because AA is a highly unstable molecule, we thought that the difference in the effect observed when using AA might be attributed to its degradation when experiments were performed using a non-freshly open vial. Thus, we inspected

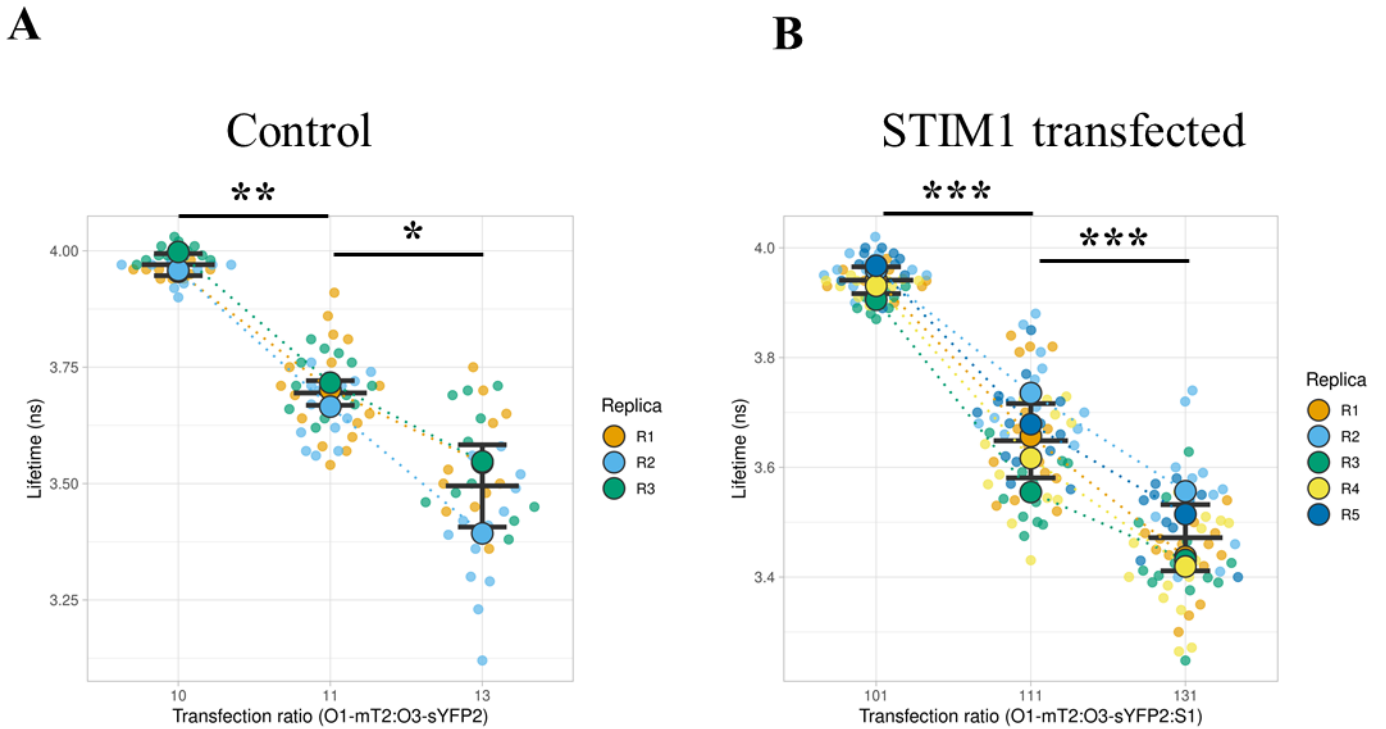


Figure 89 | ORAI1 and ORAI3 are interacting in basal condition in HEK-293.

For all panels: The semi-transparent circles represent the individual measurements performed for each experiment. Solid dots represent the mean measured lifetime of the condition for each replica; black bars represent the mean value of the three replica with the standard deviation (SD). Dotted lines are linking the data from the same experiment and indicate that data were treated as paired for statistical analysis.

- A. ORAI1-mTurquoise2 (O1-mT2) lifetime measurements performed in HEK-293 without STIM1 overexpression. The lifetime of O1-mT2 for the transfection ratio 1:1 was significantly lower ($3.69 \text{ ns} \pm \text{SD } 0.03 \text{ ns}$) than the lifetime of O1mT2 alone (transfection ratio 1:0; $3.97 \text{ ns} \pm \text{SD } 0.02 \text{ ns}$), $p = 0.002$. The lifetime of O1-mT2 for the transfection ratio 1:1 was significantly higher than the lifetime of O1mT2 for the transfection ratio 1:3 ($3.5 \text{ ns} \pm \text{SD } 0.09 \text{ ns}$), $p = 0.032$.
- B. O1-mT2 lifetime measurements performed in HEK-293 with STIM1 overexpression. The different transfection ratio between O1-mT2, ORAI3-sYFP2, and STIM1 were: 1:0:1, 1:1:1, 1:3:1. The lifetime of O1-mT2 for the transfection ratio 1:1:1 was significantly lower ($3.65 \text{ ns} \pm \text{SD } 0.07 \text{ ns}$) than the lifetime of O1mT2 alone (transfection ratio 1:0:1; $3.94 \text{ ns} \pm \text{SD } 0.02 \text{ ns}$), $p < 0.001$. The lifetime of O1-mT2 for the transfection ratio 1:1:1 was significantly higher than the lifetime of O1mT2 for the transfection ratio 1:3:1 ($3.47 \text{ ns} \pm \text{SD } 0.06 \text{ ns}$), $p < 0.001$.

Paired t-test were used to calculate the p-value between the compared conditions. * $p < 0.05$; ** $p < 0.01$; *** $p < 0.001$

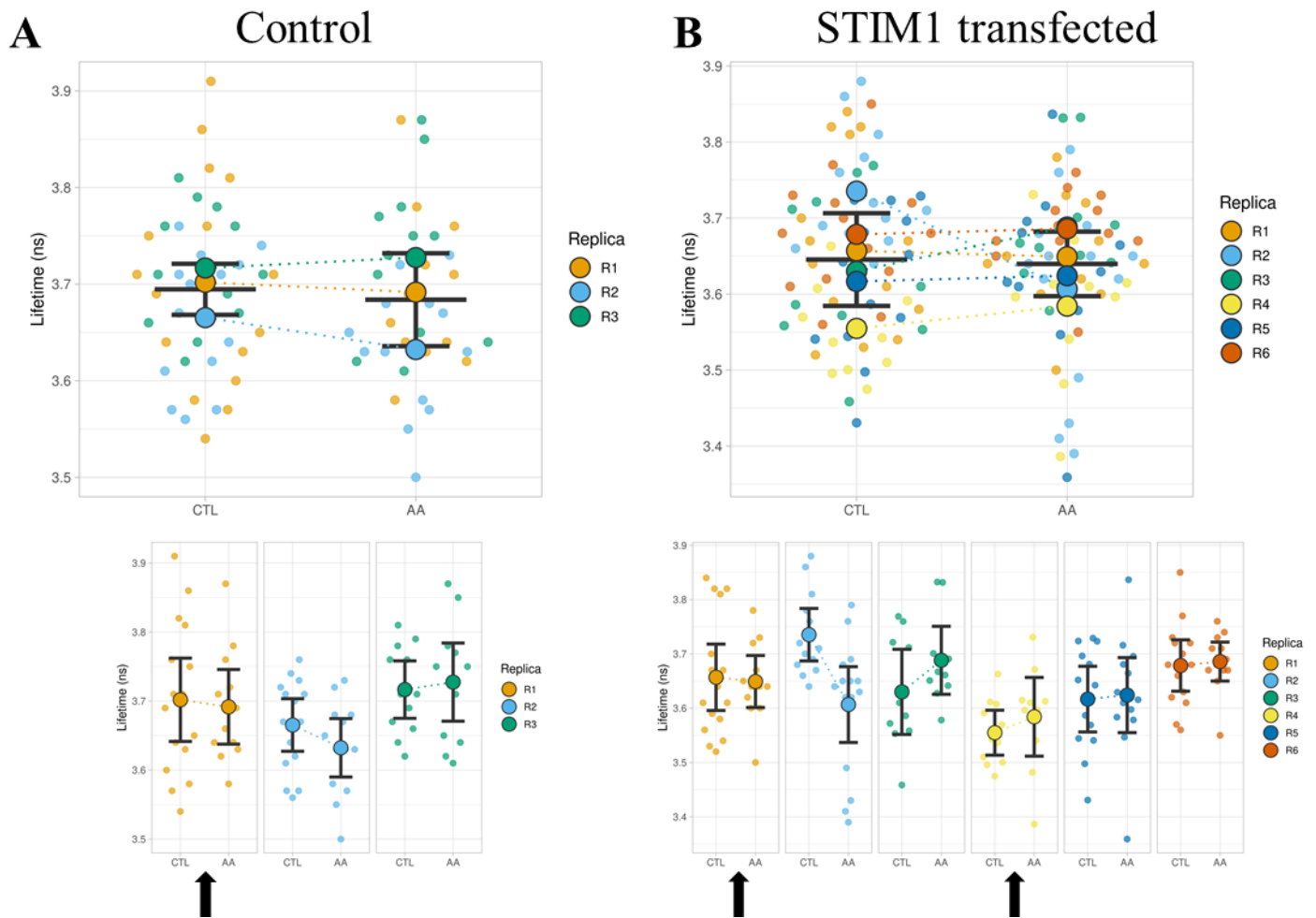


Figure 90 | Arachidonic acid does not affect ORAI1-3 interaction in 1:1 ratio.

For all panels: The semi-transparent circles represent the individual measurements performed for each experiment. Solid dots represent the mean measured lifetime of the condition for each replica; black bars represent the mean value of the three replica with the standard deviation (SD). Dotted lines are linking the data from the same experiment and indicate that data were treated as paired for statistical analysis. Lifetime measurements were performed before (CTL), and after arachidonic acid (AA) addition to the cell's medium (AA).

A. ORAI1-mTurquoise2 (O1-mT2) lifetime measurements performed in 1:1 ratio (ORAI1:ORAI3) without STIM1 overexpression in HEK-293. No significant differences in O1-mT2 lifetime between CTL ($3.69 \text{ ns} \pm \text{SD } 0.03 \text{ ns}$) and AA ($3.68 \text{ ns} \pm \text{SD } 0.05 \text{ ns}$) conditions were found, $p = 0.48$. Bottom panel: split individual replicate view from above. Black bars represent the 95% confidence interval of a given experiment. Black arrows represent indicate experiments for which a new vial of AA was used.

B. ORAI1-mTurquoise2 (O1-mT2) lifetime measurements performed in 1:1:1 ratio (ORAI1:ORAI3:STIM1) including STIM1 overexpression in HEK-293. No significant differences O1-mT2 lifetime between CTL ($3.65 \text{ ns} \pm \text{SD } 0.06 \text{ ns}$) and AA ($3.64 \text{ ns} \pm \text{SD } 0.04 \text{ ns}$) conditions were found, $p = 0.84$. Bottom panel: split individual replicate view from above. Black bars represent the 95% confidence interval. Black arrows indicate experiments for which a new vial of AA was used.

Paired t-test was used to calculate the p-value between the compared conditions.

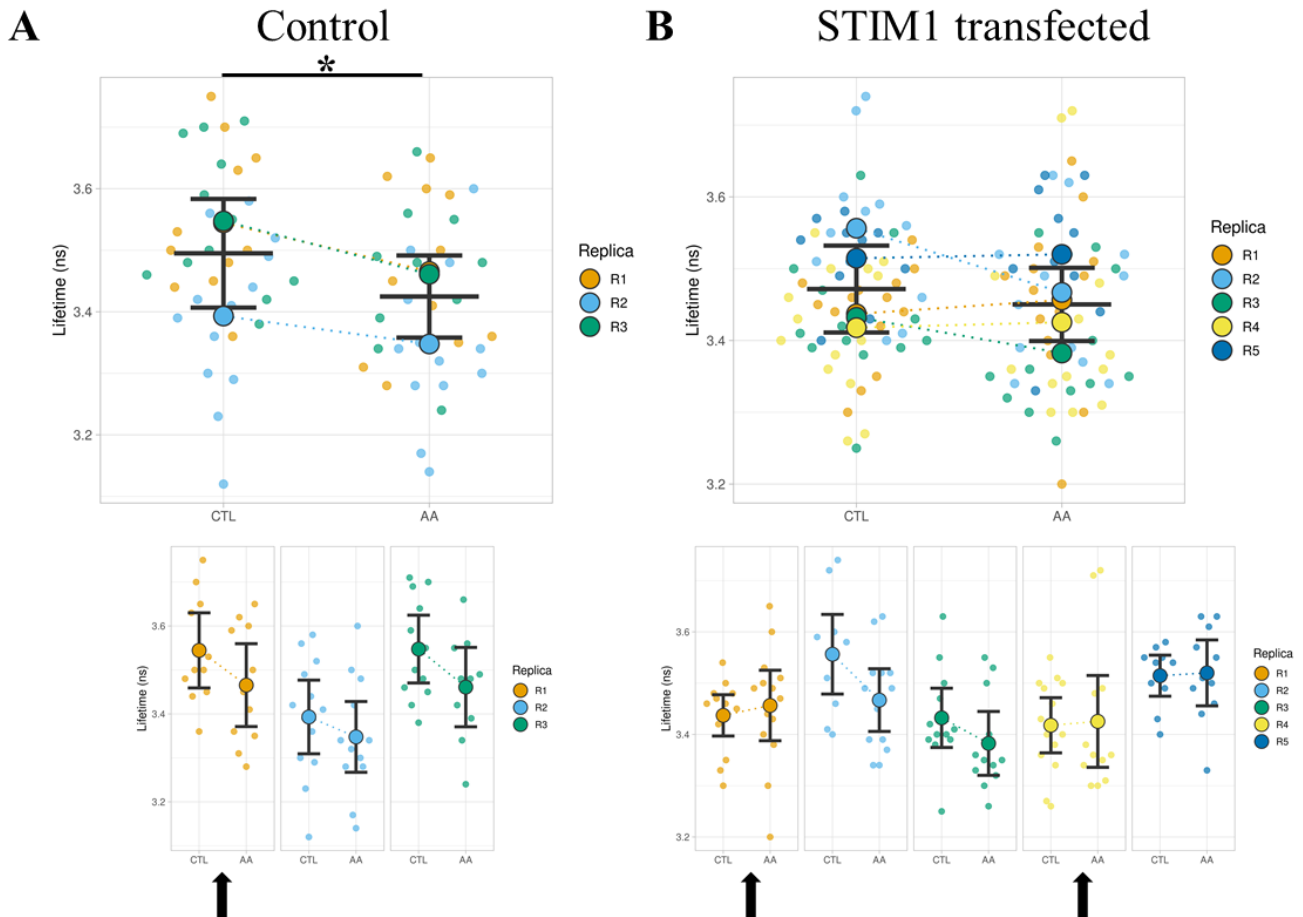


Figure 91 | Arachidonic acid increases ORAI1-3 interaction in 1:3 ratio.

For all panels: The semi-transparent circles represent the individual measurements performed for each experiment. Solid dots represent the mean measured lifetime of the condition for each replica; black bars represent the mean value of the three replica with the standard deviation (SD). Dotted lines are linking the data from the same experiment and indicate that data were treated as paired for statistical analysis. Lifetime measurements were performed before (CTL), and after arachidonic acid (AA) addition to the cell's medium (AA).

- A. ORAI1-mTurquoise2 (O1-mT2) lifetime measurements performed in 1:1 ratio (ORAI1:ORAI3) without STIM1 overexpression in HEK-293. The O1-mT2 lifetime was significantly higher in the CTL ($3.5 \text{ ns} \pm \text{SD } 0.09 \text{ ns}$) compared to the AA ($3.42 \text{ ns} \pm \text{SD } 0.07 \text{ ns}$) condition, $p = 0.03$. Bottom panel: split individual replicate view from above. Black bars represent the 95% confidence interval of a given experiment. Black arrows represent indicate experiments for which a new vial of AA was used.
- B. ORAI1-mTurquoise2 (O1-mT2) lifetime measurements performed in 1:1:1 ratio (ORAI1:ORAI3:STIM1) including STIM1 overexpression in HEK-293. No significant differences in the O1-mT2 lifetime between the CTL ($3.47 \text{ ns} \pm \text{SD } 0.06 \text{ ns}$) and the AA ($3.45 \text{ ns} \pm \text{SD } 0.05 \text{ ns}$) conditions were found, $p = 0.36$. Bottom panel: split individual replicate view from above. Black bars represent the 95% confidence interval. Black arrows indicate experiments for which a new vial of AA was used.

Paired t-test was used to calculate the p-value between the compared conditions.

single experiments result to determine if experiment performed on the day vial-opening were displaying different result than other repeats, but it was not the case (**Figure 90 and 91 low panels**). Overall, our results indicate that the addition of AA on the cells modifies the interaction level between ORAI1 and ORAI3 only when ORAI3 is overexpressed and that this increased interaction is prevented when STIM1 overexpressed.

4.5.3.1.3. Store dependent interaction

Further, we decided to measure the interaction between ORAI1 and ORAI3 following SOCE activation. Indeed, the Ca^{2+} imaging experiments performed in overexpression system, and in KO models suggest that ORAI3 is involved in the SOCE. Because STIM1 is known to be a limiting factor for SOCE development when ORAI1 is overexpressed, all the experiment were carried out with STIM1 overexpressed together with ORAI1 and ORAI3. Our results indicate that SOCE activation leads to an increased interaction between ORAI1 and ORAI3 when these proteins were expressed at the same level (ratio 1:1) (**Figure 92A**). On the contrary, when ORAI3 was overexpressed (ratio 1:3), SOCE activation did not modify their interaction level (**Figure 92B**).

4.5.3.1.4. Sequential activation of ARC and CRAC

Overall, our results demonstrate that ORAI1-ORAI3 interaction is modified by 1- AA when ORAI3 is overexpressed compared to ORAI1 (ratio1:3) in the absence of STIM1 overexpression; 2- TG when ORAI1 and ORAI3 are expressed in the same quantity and with STIM1 overexpressed. In order to obtain a better understanding of these opposite effects, we performed experiments where AA was added on the cell to induce activation of ARC channels, followed by the addition of TG to induce SOCE. Because we planned to focus on the SOCE activated interaction between ORAI1 and ORAI3, we performed these experiments only when STIM1 was overexpressed. Interestingly, the sequential activation of ARC channel followed by SOCE channel activation indicates that when expressed in the same proportions (ratio 1:1), neither the activation of ARC, nor the activation of SOCE modified the interaction level between ORAI1 and ORAI3 (**Figure 93A**). Nonetheless, it is interesting to note that ARC activation prevented the increase of interaction between ORAI1 and ORAI3 that was observed following SOCE activation (**Figure 92A**). The same experiment carried-out when ORAI3 was overexpressed compared to ORAI1 (ratio 1:3) did not lead to any significant differences in the lifetime of ORAI1mT2 (**Figure 93B**). These data demonstrate that AA pre-treatment prevents modification of the ORAI1-ORAI3 interaction induced by SOCE activation.

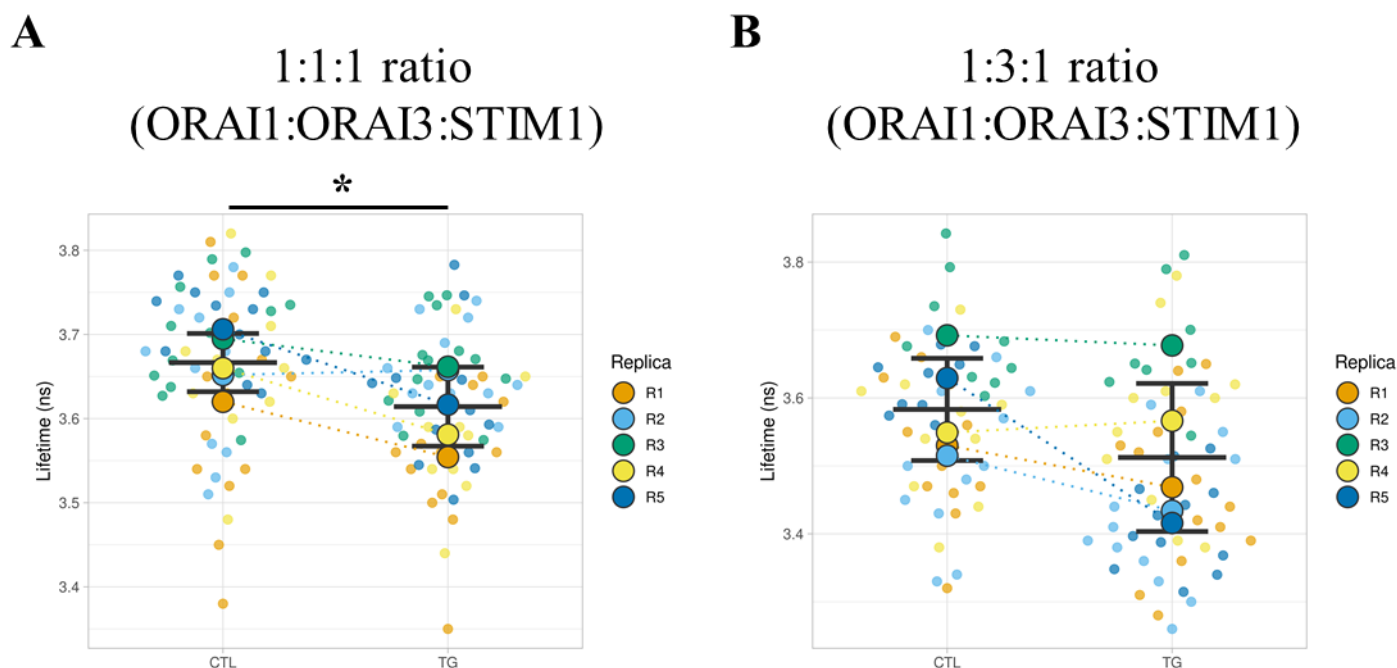


Figure 92 | Thapsigargin increases the ORAI1-ORAI3 interaction only for 1:1:1 ratio.

For all panels: The semi-transparent circles represent the individual measurements performed for each experiment. Solid dots represent the mean measured lifetime of the condition for each replica; black bars represent the mean value of the three replica with the standard deviation (SD). Dotted lines are linking the data from the same experiment and indicate that data were treated as paired for statistical analysis. . Lifetime measurements were performed before (CTL), and after thapsigargin (TG) addition to the cell's medium (TG).

A. ORAI1-mTurquoise2 (O1-mT2) lifetime measurements performed in 1:1:1 ratio (ORAI1:ORAI3:STIM1) in HEK-293. The O1-mT2 lifetime was significantly higher in the CTL ($3.67 \text{ ns} \pm \text{SD } 0.03 \text{ ns}$) compared to the TG ($3.61 \text{ ns} \pm \text{SD } 0.05 \text{ ns}$) condition, $p=0.04$.

B. ORAI1-mTurquoise2 (O1-mT2) lifetime measurements performed in 1:3:1 ratio (ORAI1:ORAI3:STIM1) in HEK-293. No significant differences in the O1-mT2 lifetime between the CTL ($3.58 \text{ ns} \pm \text{SD } 0.08 \text{ ns}$) and the TG ($3.51 \text{ ns} \pm \text{SD } 0.11 \text{ ns}$) conditions were found, $p=0.149$.

Paired t-test was used to calculate the p-value between the compared conditions, * $p < 0.05$.

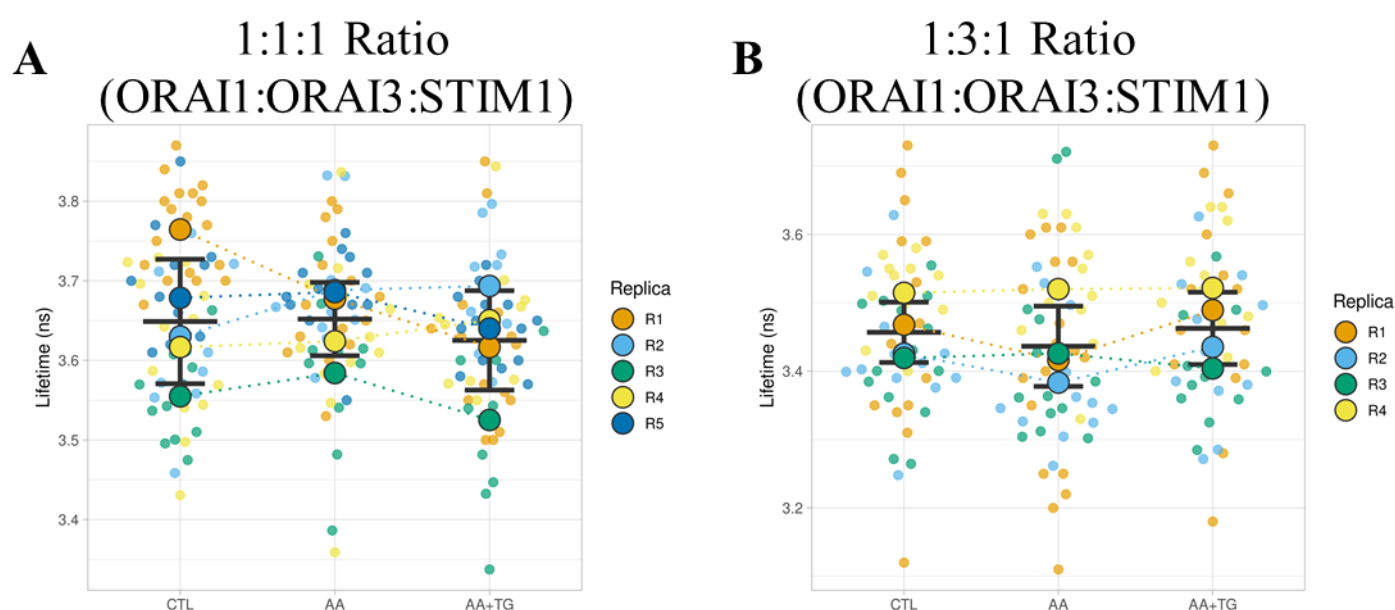


Figure 93 | Consecutive addition of AA and TG prevents ORAI1-ORAI3 interaction modulation in 1:1:1 ratio.

For all panels: The semi-transparent circles represent the individual measurements performed for each experiment. Solid dots represent the mean measured lifetime of the condition for each replica; black bars represent the mean value of the three replica with the standard deviation (SD). Dotted lines are linking the data from the same experiment and indicate that data were treated as paired for statistical analysis. Lifetime measurements were performed in control condition (CTL), following arachidonic acid treatment (AA), and after consecutive addition of thapsigargin (AA+TG) in the cell's medium.

- A. ORAI1-mTurquoise2 (O1-mT2) lifetime measurements performed in 1:1:1 ratio (ORAI1:ORAI3:STIM1) in HEK-293. The lifetime of O1-mT2 in the AA treated condition was not significantly different ($3.65 \text{ ns} \pm \text{SD } 0.05 \text{ ns}$) than the lifetime of the control condition ($3.65 \text{ ns} \pm \text{SD } 0.08 \text{ ns}$), or the AA+TG treated condition ($3.65 \text{ ns} \pm \text{SD } 0.05 \text{ ns}$) $p = 0.94$ and 0.46 , respectively.
- B. ORAI1-mTurquoise2 (O1-mT2) lifetime measurements performed in 1:3:1 ratio (ORAI1:ORAI3:STIM1) including STIM1 overexpression in HEK-293. The lifetime of O1-mT2 in the AA treated condition was not significantly different ($3.44 \text{ ns} \pm \text{SD } 0.06 \text{ ns}$) than the lifetime of the control condition ($3.46 \text{ ns} \pm \text{SD } 0.04 \text{ ns}$), or the AA+TG treated condition ($3.46 \text{ ns} \pm \text{SD } 0.04 \text{ ns}$) $p = 0.28$ and 0.51 , respectively.

Paired t-test was used to calculate the p-value between the compared conditions.

4.5.3.1.5. Conclusion on the ORAI1-ORAI3 interaction in HEK-293

Overall, the results obtained on the measurement of interaction level between ORAI1 and ORAI3 obtained in HEK-293 demonstrate a complex level of regulation between ORAI1 and ORAI3 as suggested by the publication of Dubois et al. (Dubois *et al*, 2014a). While it is clear that ORAI1-ORAI3 are interacting in basal condition and that their interaction level is dependent on the expression level of ORAI3, the data obtained in ORAI channel activated condition are more complex to interpret. On the one hand, ARC activation due to AA addition modified the interaction between ORAI1 and ORAI3 only for the 1:3 transfection ratio. In addition, overexpression of STIM1 prevented this phenomenon. On the other hand, induction of SOCE due to TG addition led to an increase in the ORAI1-ORAI3 interaction only in the 1:1 ratio when STIM1 as overexpressed. A potential interpretation of these puzzling data will be described in the discussion.

4.5.3.2. In PC3

In a second set of experiment, we decided to use PC3 cells as we successfully created a model where ORAI1 and ORAI3 were deleted, and to focus on the study of interaction between ORAI1 and ORAI3 during SOCE activation. Using the same strategy with HEK-293, we overexpressed STIM1 together with different ratio of ORAI1-mT2 and ORAI3-sYFP2. We performed our experiments in PC3 WT as well as in the double KO PC3 (KO ORAI1 + ORAI3) to assess whether the deletion of endogenous background allowed better assessment of the ORAI1-ORAI3 interactions.

4.5.3.2.1. PC3 WT

4.5.3.2.1.1. Basal interaction in PC3 WT

We started by evaluating the interaction level of ORAI1 and ORAI3 in basal conditions in the PC3 WT. In line with the results obtained in HEK-293 WT, the measured lifetime of ORAI1-mT2 was within the range of the lifetime corresponding to the free mTurquoise protein (*i.e.*, 3.96 ns, **Figure 94A**). The transfection of the of ORAI1-mT2 and ORAI3-sYFP2 in the same proportion decreased the lifetime of ORAI1-mT2 indicating that ORAI1 and ORAI3 were interacting in basal condition (**Figure 94A**). However, increasing the proportion of ORAI3-sYFP due to the 1:3 transfection ratio did lead to a significant modification of the ORAI1-mT2 lifetime (**Figure 94A**).

4.5.3.2.1.2. Store dependent interaction in PC3 WT

Subsequently, we assessed if the interaction level between ORAI1 and ORAI3 was affected by SOCE activation. Surprisingly, no significant differences were observed following SOCE activation independently on the ORAI3 expression level in the cells (**Figure 94 B, C**). While surprising, we hypothesize that this result might be explained by the presence of endogenous ORAI1 and ORAI3,

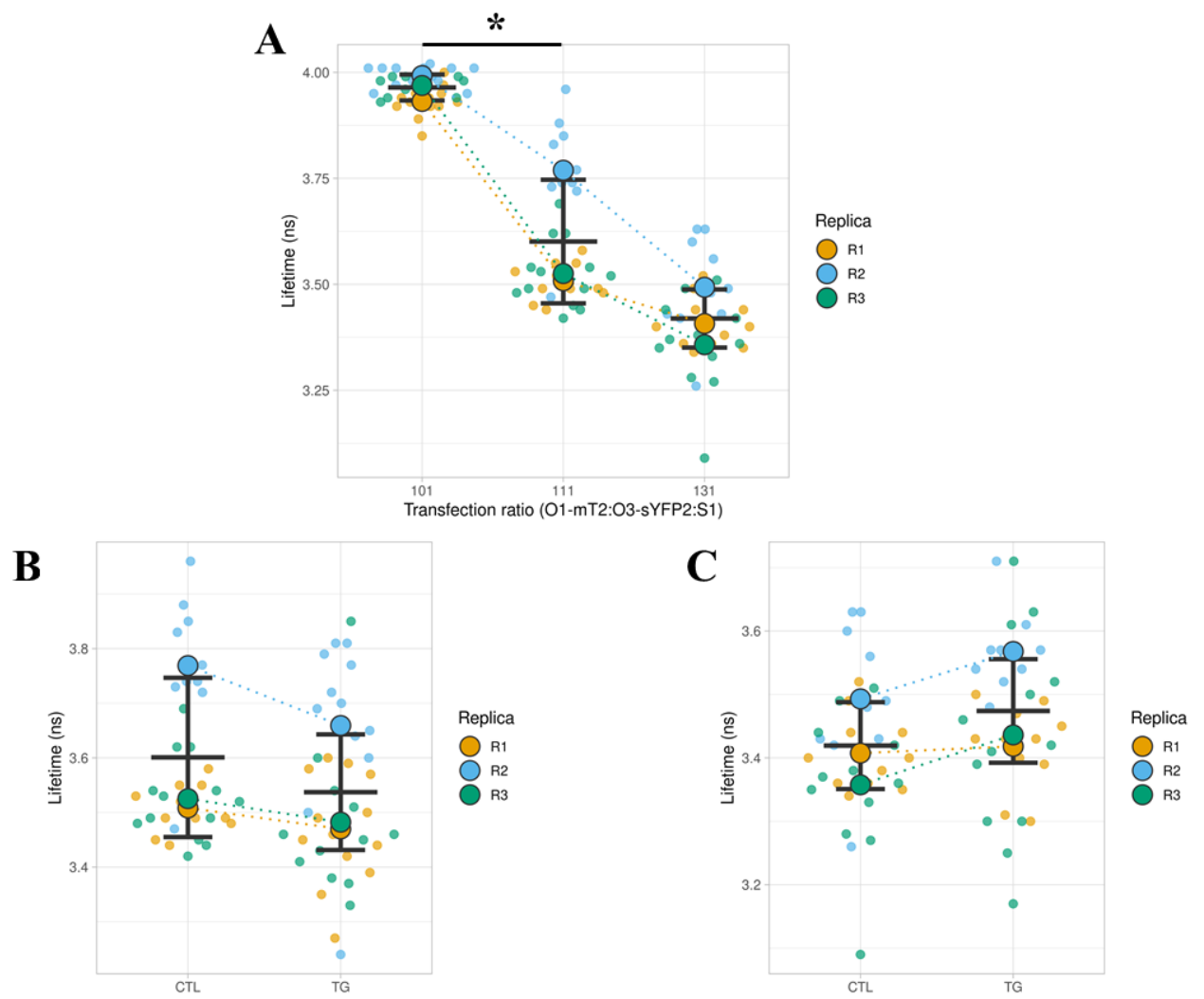


Figure 94 | ORAI1 and ORAI3 are interacting in basal condition in PC3.

For all panels: The semi-transparent circles represent the individual measurements performed for each experiment. Solid dots represent the mean measured lifetime of the condition for each replica; black bars represent the mean value of the three replica with the standard deviation (SD). Dotted lines are linking the data from the same experiment and indicate that data were treated as paired for statistical analysis.

- A. Lifetime measurements of ORAI1-mTurquoise2 with the following transfection ratio: 1:0:1, 1:1:1, 1:3:1 (O1-mT2 : O3-sYFP2 : STIM1). The lifetime of O1-mT2 for the transfection ratio 1:1:1 was significantly lower ($3.6 \text{ ns} \pm \text{SD } 0.14 \text{ ns}$) than the lifetime of O1-mT2 alone (transfection ratio 1:0:1; $3.96 \text{ ns} \pm \text{SD } 0.03 \text{ ns}$), $p = 0.003$. The lifetime of O1-mT2 for the transfection ratio 1:1:1 was not significantly different than the lifetime of O1-mT2 for the transfection ratio 1:3:1 ($3.42 \text{ ns} \pm \text{SD } 0.07 \text{ ns}$), $p = 0.07$.
- B. O1-mT2 lifetime measurements performed with the transfection ratio 1:1:1, in control condition (CTL) and after thapsigargin treatment (TG). The lifetime of O1-mT2 for the transfection ratio 1:1:1 ($3.6 \text{ ns} \pm \text{SD } 0.15 \text{ ns}$) in CTL condition was not significantly different than the lifetime of O1-mT2 after TG treatment ($3.54 \text{ ns} \pm \text{SD } 0.11 \text{ ns}$), $p = 0.11$.
- C. O1-mT2 lifetime measurements performed with the transfection ratio 1:3:1, in control condition (CTL) and after thapsigargin treatment (TG). The lifetime of O1-mT2 for the transfection ratio 1:3:1 ($3.42 \text{ ns} \pm \text{SD } 0.05 \text{ ns}$) in CTL condition was not significantly different than the lifetime of O1-mT2 after TG treatment ($3.47 \text{ ns} \pm \text{SD } 0.08 \text{ ns}$), $p = 0.13$.

Paired t-test was used to calculate the p-value between the compared conditions. * $p < 0.05$

especially because their endogenous expression is significantly higher in PC3 compared to HEK-293. Thus, we pursued our experiments in the PC3 double knockout cell line.

4.5.3.2.2. Double KO (ORAI1-ORAI3) PC3

4.5.3.2.2.1. Basal interaction

Following the same strategy as for HEK-293, we started by evaluating the level of interaction between ORAI1 and ORAI3 in basal condition. In addition, because ORAI1 and ORAI3 were deleted in our cells, we decided to verify if STIM1 overexpression was mandatory to observe any effect in the double KO cell line. First, we confirmed that ORAI1 and ORAI3 are interacting in basal condition and revealed that increasing the proportion of ORAI3 enhanced the interaction between ORAI1 and ORAI3 (**Figure 95 A**). This effect was reproducible independently on the overexpression of STIM1 (**Figure 95 B**).

4.5.3.2.2.2. Store dependent interaction

Subsequently, we induced SOCE with TG, and measured the interaction level between ORAI1 and ORAI3. We started by performing this experiment without overexpressing STIM1. Our results indicate that induction of SOCE leads to increased interaction between ORAI1 and ORAI3 when they are expressed in the same proportion (ratio 1:1) (**Figure 96 A**) but not when ORAI3 was overexpressed compared to ORAI1 (ratio 1:3) (**Figure 96 B**). Then, we repeated this experiment in cells overexpressing STIM1. In line with the former results, when ORAI1 and ORAI3 were expressed respecting the 1:1 ratio, their interaction level was reinforced upon SOCE induction (**Figure 97 A**). In addition, for the ratio 1:3 in the presence of STIM1, the induction of SOCE led to an increase of interaction between ORAI1 and ORAI3 (**Figure 97 B**).

4.5.3.2.2.3. Carbachol induced interactions

Finally, because TG is an irreversible blocker of SERCA pumps, its addition in the cell medium ultimately leads to a complete Ca^{2+} store depletion, which does not depict accurately physiological level of SOCE activation. Thus, we decided to use carbachol (Cch) to induce transient and reversible store depletion. Of note, carbachol is a ligand of muscarinic acetylcholine receptor, whose activation leads to activation of phospholipase C inducing the degradation of the phosphatidyl inositol phosphate into diacylglycerol and inositol triphosphate (IP3). The later activating the ER-residing IP3 receptor which leads to Ca^{2+} store release. We repeated one more time our classic protocol by replacing TG by Cch. As we demonstrated that STIM1 overexpression was mandatory to observe effects on interaction between ORAI1 and ORAI3, the experiments were performed with STIM1 overexpressed. Our results indicate that in the ratio 1:1, SOCE induction with Cch leads to an increased interaction between ORAI1 and ORAI3 (**Figure 98 A**), while no differences in interaction were visible when using the ratio 1:3 (**Figure 98 B**).

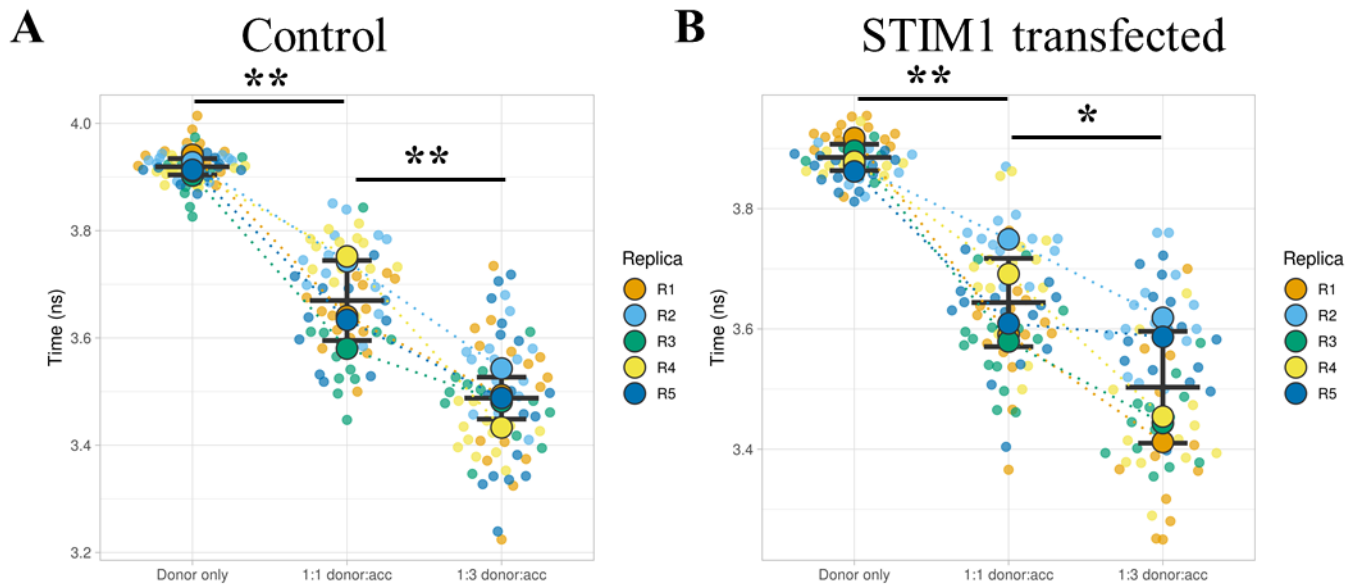


Figure 95 | ORAI1 and ORAI3 are interacting in basal condition in double KO PC3.

For all panels: The semi-transparent circles represent the individual measurements performed for each experiment. Solid dots represent the mean measured lifetime of the condition for each replica; black bars represent the mean value of the three replica with the standard deviation (SD). Dotted lines are linking the data from the same experiment and indicate that data were treated as paired for statistical analysis.

- A. Lifetime measurements of ORAI1-mTurquoise2 in PC3 double KO cells with endogenous level of STIM1. The different transfection ratio between O1-mT2, and ORAI3-sYFP2 (O3-sYFP2), were: 1:0, 1:1, and 1:3. The lifetime of O1-mT2 for the transfection ratio 1:1 was significantly lower ($3.67 \text{ ns} \pm \text{SD } 0.07 \text{ ns}$) than the lifetime of O1mT2 alone ($3.92 \text{ ns} \pm \text{SD } 0.02 \text{ ns}$), $p = 0.002$. The lifetime of O1-mT2 for the transfection ratio 1:3 was significantly lower ($3.49 \text{ ns} \pm \text{SD } 0.04 \text{ ns}$) than the lifetime of O1mT2 for the transfection ratio 1:1, $p = 0.009$.
- B. Lifetime measurements of ORAI1-mTurquoise2 in PC3 double KO cells with STIM1 overexpressed. The different transfection ratio between O1-mT2, STIM1, and O3-sYFP2 were: 1:0:1, 1:1:1, and 1:3:1. The lifetime of O1-mT2 for the transfection ratio 1:1:1 was significantly lower ($3.64 \text{ ns} \pm \text{SD } 0.07 \text{ ns}$) than the lifetime of O1mT2 alone ($3.89 \text{ ns} \pm \text{SD } 0.02 \text{ ns}$), $p = 0.003$. The lifetime of O1-mT2 for the transfection ratio 1:3:1 was significantly lower ($3.50 \text{ ns} \pm \text{SD } 0.09 \text{ ns}$) than the lifetime of O1mT2 for the transfection ratio 1:1:1, $p = 0.016$.

Paired t-test was used to calculate the p-value between the compared conditions. * $p < 0.05$, ** $p < 0.01$.

Control

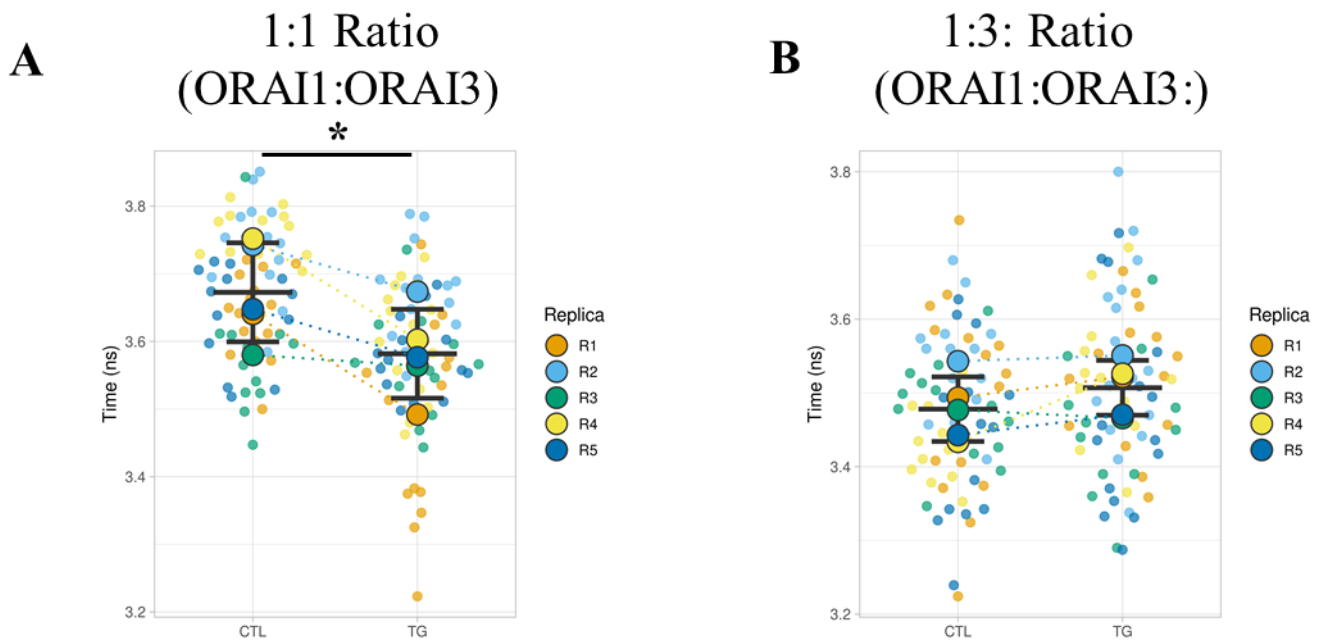


Figure 96 | SOCE activation increases the ORAI1-ORAI3 interaction in PC3 double KO in the 1:1 ratio with endogenous level of STIM1.

For all panels: The semi-transparent circles represent the individual measurements performed for each experiment. Solid dots represent the mean measured lifetime of the condition for each replica; black bars represent the mean value of the three replica with the standard deviation (SD). Dotted lines are linking the data from the same experiment and indicate that data were treated as paired for statistical analysis.

- A. Lifetime measurements of ORAI1-mTurquoise2 in PC3 double KO cells with endogenous level of STIM1, and for transfection ratio between O1-mT2, and O3-sYFP2 of 1:1, before (CTL) and after thapsigargin treatment (TG). The lifetime of O1-mT2 in the control condition was significantly lower ($3.67 \text{ ns} \pm \text{SD } 0.07 \text{ ns}$) than after TG treatment ($3.58 \text{ ns} \pm \text{SD } 0.07 \text{ ns}$), $p = 0.02$.
- B. Lifetime measurements of ORAI1-mTurquoise2 in PC3 double KO cells with endogenous level of STIM1, and for transfection ratio between O1-mT2, and O3-sYFP2 of 1:3, before (CTL) and after thapsigargin treatment (TG). The lifetime of O1-mT2 in the control condition was not significantly different ($3.48 \text{ ns} \pm \text{SD } 0.04 \text{ ns}$) than after TG treatment ($3.51 \text{ ns} \pm \text{SD } 0.04 \text{ ns}$), $p = 0.17$.

Paired t-test was used to calculate the p-value between the compared conditions. * $p < 0.05$.

STIM1 transfected

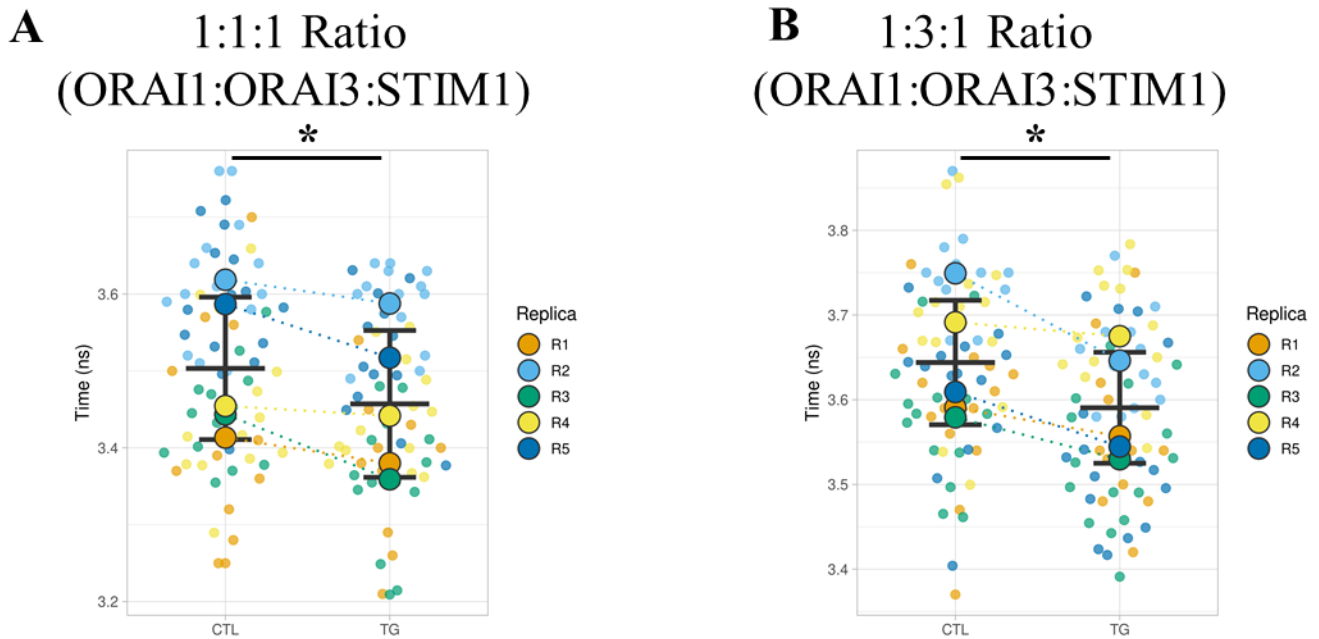


Figure 97 | SOCE activation increases the ORAI1-ORAI3 interaction in PC3 double KO in 1:1, and 1:3 ratio with overexpressed STIM1.

For all panels: The semi-transparent circles represent the individual measurements performed for each experiment. Solid dots represent the mean measured lifetime of the condition for each replica; black bars represent the mean value of the three replica with the standard deviation (SD). Dotted lines are linking the data from the same experiment and indicate that data were treated as paired for statistical analysis.

- A. Lifetime measurements of ORAI1-mTurquoise2 in PC3 double KO cells with overexpressed STIM1, and for transfection ratio between O1-mT2, and O3-sYFP2 of 1:1, before (CTL) and after thapsigargin treatment (TG). The lifetime of O1-mT2 in the control condition was significantly lower ($3.64 \text{ ns} \pm \text{SD } 0.07 \text{ ns}$) than after TG treatment ($3.59 \text{ ns} \pm \text{SD } 0.07 \text{ ns}$), $p = 0.02$.
- B. Lifetime measurements of ORAI1-mTurquoise2 in PC3 double KO cells with overexpressed STIM1, and for transfection ratio between O1-mT2, and O3-sYFP2 of 1:3, before (CTL) and after thapsigargin treatment (TG). The lifetime of O1-mT2 in the control condition was significantly higher ($3.50 \text{ ns} \pm \text{SD } 0.05 \text{ ns}$) than after TG treatment ($3.46 \text{ ns} \pm \text{SD } 0.05 \text{ ns}$), $p = 0.02$.

Paired t-test was used to calculate the p-value between the compared conditions. * $p < 0.05$.

STIM1 transfected

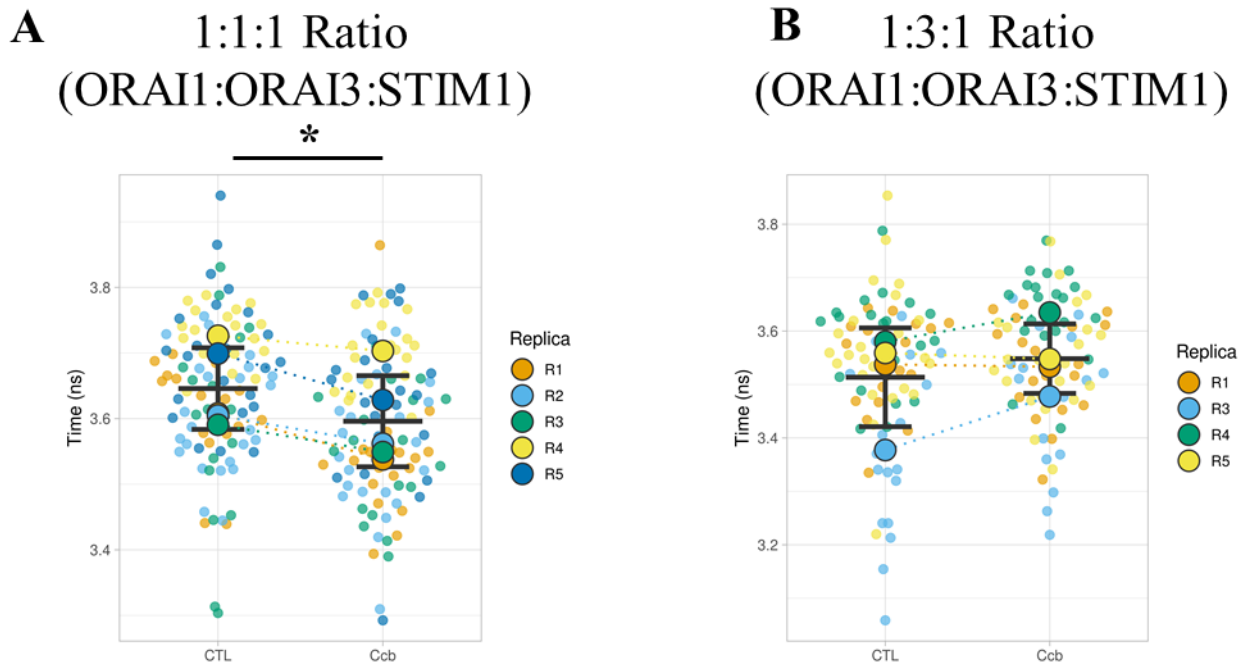


Figure 98 | SOCE activation with carbachol increases the ORAI1-ORAI3 interaction in PC3 double KO only in 1:1 with overexpressed STIM1.

For all panels: The semi-transparent circles represent the individual measurements performed for each experiment. Solid dots represent the mean measured lifetime of the condition for each replica; black bars represent the mean value of the three replica with the standard deviation (SD). Dotted lines are linking the data from the same experiment and indicate that data were treated as paired for statistical analysis.

- A. Lifetime measurements of ORAI1-mTurquoise2 in PC3 double KO cells with overexpressed STIM1, and for transfection ratio between O1-mT2, and O3-sYFP2 of 1:1, before (CTL) and after carbachol treatment (Cch). The lifetime of O1-mT2 in the control condition was significantly lower ($3.65 \text{ ns} \pm \text{SD } 0.06 \text{ ns}$) than after Cch treatment ($3.60 \text{ ns} \pm \text{SD } 0.07 \text{ ns}$), $p = 0.04$.
- B. Lifetime measurements of ORAI1-mTurquoise2 in PC3 double KO cells with overexpressed STIM1, and for transfection ratio between O1-mT2, and O3-sYFP2 of 1:3, before (CTL) and after carbachol treatment (Cch). The lifetime of O1-mT2 in the control condition was not significantly different ($3.51 \text{ ns} \pm \text{SD } 0.07 \text{ ns}$) than after Cch treatment ($3.55 \text{ ns} \pm \text{SD } 0.09 \text{ ns}$), $p = 0.28$.

Paired t-test was used to calculate the p-value between the compared conditions. * $p < 0.05$.

4.5.3.3. Conclusion on the interactions between ORAI1 and ORAI3 in PC3 cells

Our data on PC3 cells demonstrate the importance of ORAI1 and ORAI3 deletion to detect fine variation in their interaction level. Indeed, no difference in the interaction level between ORAI1 and ORAI3 due to ORAI3 overexpression was identified in PC3 WT, but the deletion of these endogenous protein in our KO model allowed to identify that ORAI1 and ORAI3 interaction level was dependent on ORAI3 expression level. In line with these results, SOCE activation did not alter the interaction level between ORAI1 and ORAI3 in PC3 WT but increased their interaction in the double KO cells. In addition, in store-depleted condition, we showed that ORAI1 and ORAI3 were displaying an increased interaction when they were expressed at the same level (1:1 ratio) or when ORAI3 was overexpressed (1:3 ratio). Moreover, we showed that this effect was dependent on the STIM1 expression level. Finally, using a more physiological SOCE activator, we showed that the increased interaction between ORAI1 and ORAI3 was effective only when they were expressed in the same ratio.

5. Discussion and perspectives

5.1. Challenges in generating gene KI with the CRISPR/Cas9 system

In the first part of this PhD, we aimed to create gene KI to fluorescently label the ORAI1 and ORAI3 proteins. Through our different tentative, we were able to successfully induce a DSB on the desired genomic location, and we could identify HR recombination event by PCR screening. Nonetheless, we were unable to identify and select the cells that positively underwent recombination. The reasons of our inability to create gene KI are not clearly defined and are probably the consequences of multiple factors, that will be exposed thereafter.

5.1.1.HDR-based method of KI

First, the method we used to generate KI might not have been optimal. Indeed, HR techniques relying on the cellular reparation mechanisms HDR was considered being the standard technique to generate KI in the beginning of this PhD work. Nonetheless, diverse techniques using modified donor sequence were developed and reported better efficiencies than the classic HR method. For example, the easi-CRISPR method relying on single stranded donor (ssODN) bearing homology arms displayed efficiencies up to 100% depending on the loci considered (**Figure 99A**) (Miura *et al*, 2018). However, ssODN production is complicated and subject to mistake (*i.e.*, single nucleotide polymorphism) during production (kit for *in vitro* production of ssODN exists but are relying on reverse transcriptase which are not proof-reading). In addition, modification of the standard protocol for inducing HR with the use of a donor plasmids have been developed such as cell synchronization (HDR events are more frequent during G/S phase of the cycle), or inhibition of NHEJ mechanisms. Nonetheless, it appears that success rates in generation of KI are cell type / loci / size and type of insertion dependent, and thus several techniques need to be tested for a specific desired application (Yamamoto & Gerbi, 2018).

5.1.2.Non-HDR based method for KI

Other techniques non relying on HDR mechanisms were proposed to generate KI. Of note, the PITCh method developed in 2014 represented an interesting alternative to the HDR-induced KI methods (**Figure 99B**)(Nakade *et al*, 2014; Sakuma *et al*, 2016). Especially, this strategy involves donor plasmid linearization performed *in vivo* due to specifically designed gRNA sequences as well as antibiotic selection of successful recombination event. Nonetheless, the original plasmid construct available were intended for KI of GFP tag in the C-terminal extremity of protein. Since our aim was to tag our protein of interest in the N-terminal extremity with the mTurquoise2 of sYFP2 protein, several rounds of cloning were required to obtain a construct allowing the tagging of N-terminal extremities with desired fluorescent tags. This laborious and time-consuming procedure were performed nonetheless, due to time pressure and modification of our global strategy (use of KO models instead of KI) the experiments for generating KI could not be performed (see material and method for detailed procedure). Alternative methods including the incorporation of the target gRNA sequences on each side of the homologue

sequences leading to creation of a donor template bearing the same DSB-induced extremities as the targeted genome were proven successful for generating homology-independent targeted integration (HITI) through NHEJ (**Figure 99C**) (Suzuki *et al*, 2016b) with success rate up to 30-40 %. Alternatively the use of Cas9 variants leading to the creation of cohesive ends following DSB induction were proposed to induced incorporation of DNA fragment in the DSB site by designing donor plasmid bearing the same DSB induction site in its sequence (**Figure 99D**) (Yamamoto & Gerbi, 2018). Of note, several techniques homology-independent gene insertion technique were developed in the recent years such as the homology-independent universal genome engineering (HiUGE) using adenoviral vector to generate insertion at specific sites, or the CRISPR/Cas9-mediated Homology-independent PCR-product integration (CHoP-In) using PCR products as donor template, or the Open Resource for the Application of Neuronal Genome Editing (ORANGE), a modified HITI method developed to enable KI in neurons (Gao *et al*, 2019; Manna *et al*, 2019; Willems *et al*, 2020). The development of all these techniques indicates that improvement in efficiencies rate is required to generalize the use of the CRISPR-Cas9 method to generate KI.

5.1.3. Hypothesis on the non-detection of recombination events

The fact that PCR amplification of the targeted region for KI indicated a successful fluorescent tag insertion, suggest that the KI were achieved in our cells. Nonetheless, cells displaying such a positive recombination event could not be selected. Several reasons could explain this result. First, the HEK-293 being hypotriploid cells one can consider that HR events were occurring on a single allele and thus leading to a fluorescence intensity that would be below detection level of FACS. In addition, as discussed earlier, the endogenous level of expression of ORAI1 and ORAI3 protein might be too low to enable their detection with fluorescent tags. The CRISPR strategies allowing enhancement of protein expression, have been refined in the last years, and might present an interesting solution to increase expression level of ORAI proteins. Finally, while the HDR technique is reputed error-free it is not obligatory the case, and insertion of small insertion or deletion (InDels) at the junctions sites occurs due to the existence of NHEJ repair mechanisms concomitant to HDR mechanisms (Paquet *et al*, 2016). This might explain why PCR results indicated on successful KI while fluorescence ere not detectable, indeed, if InDels occurred and resulted in open reading frame (ORF) shift, fluorescent protein would not be expressed. Of note, a newly developed KI technique named, CRISPR-mediated insertion of exon (CRISPIE) includes the insertion of fluorescent tag in an intronic region leading to the splice out of InDels insertion, might present a good strategy to prevent the apparition of ORF shifted KI.

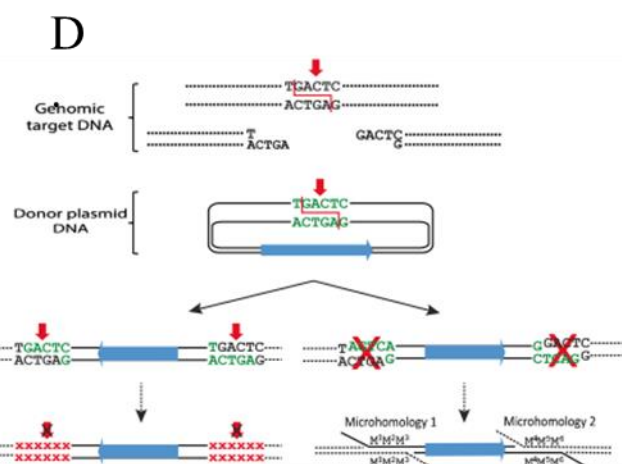
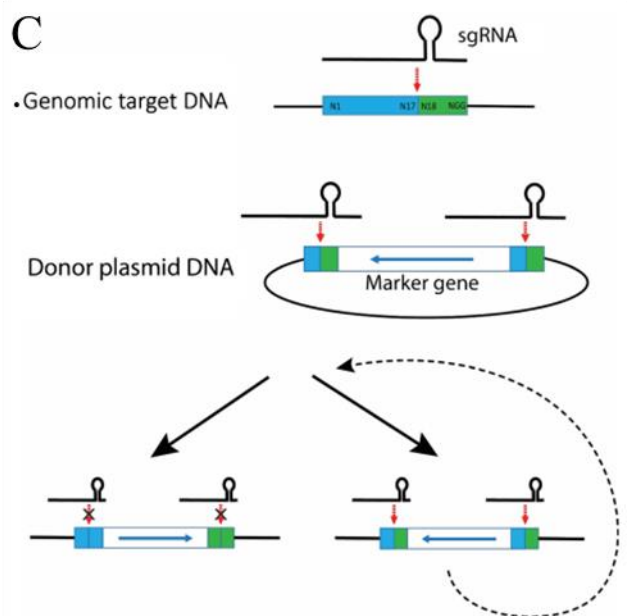
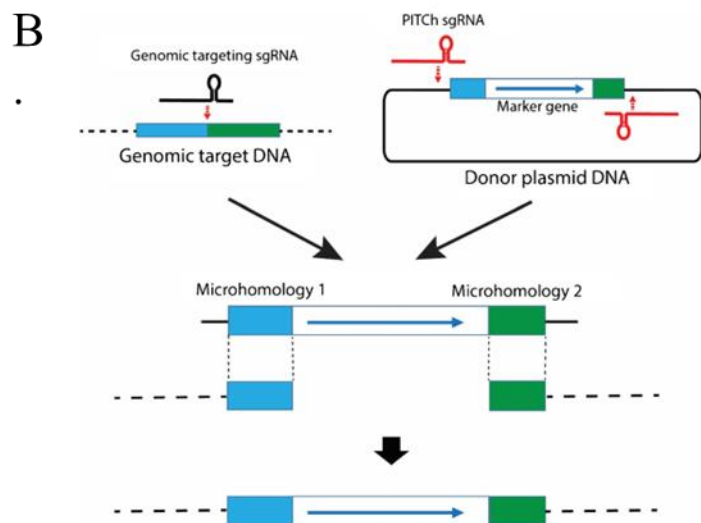
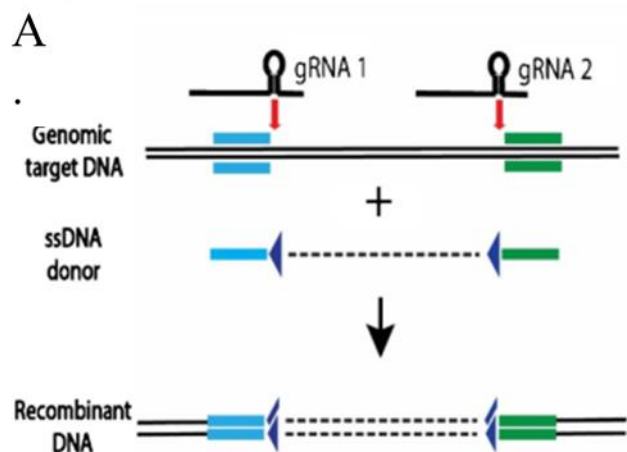


Figure 99 | Different strategies to induce gene knockin (KI).

- A. Easi-CRISPR recombination principle. A plasmid coding for the Cas9 protein and two gRNAs is transfected in the cells together with a single-stranded DNA donor bearing small homology arms.
- B. Precise integration into target chromosome (PITCh) recombination principle. A plasmid coding for the Cas9 protein and the targeting gRNA is transfected in the cell together with the PITCh donor. PITCh donor plasmid includes the sequence to insert in the genome flanked by microhomology domains (5 to 25 bp) and specific gRNA sequences. Following transfection of these elements, the gRNAs targeting the PITCh plasmid allow the liberation of the donor DNA fragment. Due to the presence of microhomology domain on each sides of this fragment, the microhomology mediated end joining (MMEJ) reparation process will ligate the donor sequence at the site of DSB in the genome.
- C. Homology-independent targeted integration (HITI) mechanism. The genomic sequence targeted by the gRNA is included on both extremities of the donor plasmid. Following transfection of the Cas9 and gRNA plasmid, the same DSB are induced on the donor plasmid and on the genomic locus, allowing reparation through NHEK mechanism. Specific design of the donor plasmid allow for reconstitution of normal gRNA sequence if the insertion occurs in the non-desired orientation. Thus, Cas9 might cleave again the DNA fragment until the correct orientation is reached.
- D. Example of strategy using Cpf1 for inducing recombination. Cpf1 enzymes creates overhangs while cutting DNA. Inclusion of specific gRNA sequence in the donor plasmid leads to the creation of specific overhangs allowing for precise reparation mechanism resulting in the incorporation of the desired sequence in the genome.

Adapted from Yamamoto & Gerbi, 2018

5.1.4. Conclusions and perspectives for the generation of gene KI

As a conclusion, the current abundance of methods allowing creation of KI cells might ease the process of conducting such experiments. Nonetheless, success rates described in scientific papers should be taken with precaution as modifications, of the cell line used, or the gene to integrated might greatly affect the outcome of the experiment. In addition, careful design of the experiment should be performed in order to avoid pitfall such as the low expression of the targeted gene to KI. In our specific case, one could probably achieve the labelling ORAI1 and ORAI3 with fluorescent tag with gene KI. An adequate strategy would probably involve: 1-the use of a cell line bearing a high expression of ORAI protein and displaying a diploid genome. Alternatively, using HEK-293 cells would require to successfully increase the expression level of ORAI proteins; 2-the creation and the use of several methods for inducing gene recombination. Especially, conducting experiments relying on different reparation mechanisms such as NHEJ (like the HITI method), MMEJ (like the PITCH method), and HDR (like the easi-CRISPR method) should allow to successfully create knockin to fluorescently label the ORAI proteins.

5.2. Challenges in generating gene KO with the CRISPR/Cas9 system

The generation of ORAI KO in HEK-293 and PC3 cell lines was achieved relatively easily. Indeed, the experimental design of the experiment, especially the use of dual gRNA strategy allowing for an easy screening procedure, and the experience acquired with the use of CRISPR/Cas9 system during the KI experiments allowed us to create KO cell line for ORAI proteins in HEK-293, but also in cancerous PC3 cells. While our strategy was successful, there are still rooms for improvements for every step involved in the KO generation with CRISPR/Cas9 genome editing technique.

5.2.1. Design of gRNA

The French-based CRISPOR website (<http://crispor.tefor.net/>) was used to design gRNAs in this work. Nonetheless, several online tools are allowing the design of gRNA. Some of these tools are developed and maintained by public laboratory (For example: <https://chopchop.cbu.uib.no/>, and <https://portals.broadinstitute.org/gppx/crispick/public>), or by private companies specialized in CRISPR related products (such as Synthego: <https://design.synthego.com/>). Within all these tools, the computed efficiency and specificity scores for the proposed gRNA are somewhat similar. Nonetheless, each website displays different features (indication of the GC content of the gRNA, or self-complementarity of gRNA sequence), or enable to screen for gRNA to be used for specific usages (gene interference, gene enhancement of expression, nickase experiment). Thus, crossing their results might be useful to define the more suitable sequences required for a specific experiment.

5.2.2. Assessment of gRNA efficiency

Efficiency assessment of the gRNA represents another important procedure in the development of KO cell lines. In our case, the identification of suitable primers pairs allowing to perform robust PCR

on gDNA was complex. Of note, non-coding genomic sequences can display specific structures requiring longer denaturation times to allow polymerase to access the amplification site. In addition, these regions can display highly repetitive sequences or rich GC content where the polymerases are usually poorly performing. Finally, the design of primers amplifying specifically a defined region is sometimes complex due to the increased size of the genomic DNA compared the size of the transcriptome. In our case, several primer pairs were tested, and PCR protocol adaptations were required to obtain robust and reproducible PCR amplifications. While we cannot exclude that these difficulties were gene specific, we believe that a sufficient amount of time should be devoted to the primer design and PCR condition adjustments. On a similar note, the assessment of DSB induction efficiency with the T7E1 assay was also a time-consuming procedure. Indeed, the incubation time of the PCR products with the enzyme as well as the level of amplification of the target region, or the size of the amplicon to be digested required adjustments to allow the obtention of clear results. For this last point, we found that increasing the size of the PCR amplicon greatly helps to obtain more reliable results because of the stronger intensity displayed by the digested PCR products of high molecular weight. Thus, T7E1 assays performed with KO gRNAs, where the PCR product were in the range of a thousand kb, exhibited more reliable results than the T7E1 assays performed for the KI gRNAs, where the size of PCR product was around 500 pb. Overall, because the sensitivity of the assay is reputed quite low, this assay should mostly be seen as a tool to assess the induction of DSB by the designed gRNAs than a precise method allowing the clear identification the most efficient gRNA. Finally, other strategies such as the Tracking of Indels by Decomposition (<http://shinyapps.datacurators.nl/tide/>), might represent an interesting tool to assess the efficiency of Indels induction of a gRNA.

5.2.3. Screening method for selection of KO cell lines and validation of KO.

Due to the dual gRNA strategy, the screening of potential KO was greatly facilitated. In addition, the re-use of primers pairs designed for T7E1 assay allowed efficient PCR to be performed without additional difficulties. One of the limitations of this strategy is the multiplication of potential off-target sites, thus choosing highly specific gRNA is advised. In addition, one should keep in mind that the gene excision procedure might be inducing a higher rate of complex genomic recombination as several clones screened by PCRs were displaying additional bands of non-expected sizes.

Finally, KO validation through the use of antibodies was particularly complex as different antibodies were displaying bands at different sizes for ORAI1. These differences might be explained by the differences in the epitope binding of ORAI1 antibodies. Of note, ORAI1 exhibit glycosylation site on N223 (asparagine 223 on the 2nd extracellular loop or ORAI1). Importantly, Alomone antibody was raised with synthetic peptide sequence in close proximity with the glycosylation site. We believe that glycosylation prevents ORAI1 binding to its site and thus. On the contrary, Sigma and GeneTex antibodies were raised against N-terminal which are distant from the glycosylation site and thus

recognizes specifically this form (50kDa). Nonetheless, it is clear that reliable antibody for ORAI protein was not available during this study and thus their use was avoided.

5.2.4. Conclusion on the generation of gene KO with the CRISPR/Cas9 system

As a conclusion, due to the advent of CRISPR/Cas9 system, generation of KO cell line does not represent a big challenge anymore. However, one should bear in mind that a good transfection efficiency and a proliferative cell line are mandatory to generate KO. Overall, KO generation with CRISPR/Cas9 is low-priced, as several Cas9 plasmids are available through addgene, and the generation steps are involving classic techniques used in biological laboratory (cloning, and PCR techniques mostly). Nonetheless, it remains a time-consuming procedure as many steps require careful assessment of the results before proceeding to the following step. Of note, several companies are now proposing to generate KO for specific cell line and might represent an interesting alternative for obtaining KO cells. Finally, it is important to bear in mind, that the use of CRISPR/Cas9 system might generate off-target DSB, which might result in unwanted genomic modifications. While it can be considered of relatively low importance if conducting mechanistic studies, it might represent a burden if one wants to assess the physiological relevance of a specific KO. In our study we used two different clones for assessing the physiological role of ORAI1 KO in HEK-293 cells. However deeper studies might require a specific assessment of DSB induction at the potential off-target sites. The most evident technique for evaluating the generation of unwanted genomic modification is represented by next generation sequencing (NGS) methods allowing for the screening and sequencing of whole genomes or transcriptome. However, they represent expensive technique to conduct for simply ensuring the absence of off-target effect. Nonetheless, the development of affordable sequencing techniques such as Nanopore sequencing technology might represent an interesting alternative. In addition, using NGS techniques might allow to identify compensatory mechanisms and off-target effects in a single experiment. Finally, because a list of off-target sites is usually provided when identifying suitable gRNA, a simple amplification of these sites for off-target represents an easy method for assessing the induction of DSB at unwanted genomic sites but would allow to identify events involving relatively big insertion or deletion events (+/- 50 bp).

5.3. Dispensability of ORAI1 in the control of the HEK-293 physiology.

Following the establishment of the ORAI1 KO HEK-293 cell line, we set-out to study the effect of this deletion on the physiology of HEK-293 cells. Specifically, we identified that ORAI1 deletion was greatly impairing SOCE but was not totally abolishing it. In addition, we evaluated if this remaining SOCE could be attributed to compensatory mechanism involving modulation of expression of other ORAI homologues and concluded that it was not the case. Further, we evaluated the proliferative properties of the ORAI1 KO cells and compared them to WT HEK-293. We observed that the deletion of ORAI1 protein did not modify the proliferation of HEK293 cells. Finally, we studied the migrative properties of the ORAI1 KO cells in comparison the WT HEK-293. We noted that adhesive properties

were not modify following ORAI1 deletion. In addition, we demonstrated that ORAI1 deletion was increasing the speed at which HEK-293 cells are initiating their collective migration but was not affecting single cell migration.

5.3.1. ORAI1 deletion abolishes SOCE

We identified the existence of a residual SOCE following ORAI1 deletion. Of note, other studies have reported various level of SOCE in ORAI KO cells. For example, Cai *et al.*, as well as Yoast *et al.*, observed a total SOCE abolition in ORAI1 KO cells (Yoast *et al.*, 2020b; Cai *et al.*, 2016), while Alansary *et al.*, observed a residual SOCE entry following ORAI1 deletion in HEK-293, the latter attributed this remaining SOCE to the presence of ORAI3 protein (Alansary *et al.*, 2020). The differences in the SOCE level observed within these studies and ours might be explained by the strategies used to generate ORAI1 KO. Indeed, we are the only ones to use the double gRNA strategy to generate ORAI1 KO. This strategy allowed us to generate cell line displaying a total absence of the ORAI1 protein (due to ATG deletion). Others have used a single gRNA strategy leading the induction of an ORF shift toward the middle of the ORAI1 protein sequence. While the possibility that “half-ORAI1” protein could possess ill-function is hypothetical, it represents a potential explanation for the differences observed in SOCE level. Alternatively, we proposed that the remaining SOCE could be attributed to ORAI2 or ORAI3. Nevertheless, our RT-qPCR data indicate that the expression level of both genes is decreases in ORAI1 KO cells. Another hypothesis is that the observed SOCE entry is potentiated in our experiment due to the use of a supra physiological Ca^{2+} concentration (4mM) while Cai *et al.*, and Yoast *et al.*, used a physiological Ca^{2+} concentration (Cai *et al.*, 2016; Yoast *et al.*, 2020b). Finally, we cannot exclude that expression level of other channels might be altered to compensate for ORAI1 deletion such as TRCPs since they have been shown to interact with STIM and to participates in the SOCE entry.

5.3.2. ORAI1 deletion does not affect proliferative properties of HEK-293

In the second part of our work, we studied and demonstrated that ORAI1 did not control the proliferation of HEK-293 cells. Interestingly, in immune cells, it was demonstrated that SOCE control proliferation through Nuclear Factor of activated T-cells (NFAT) activation (Cai *et al.*, 2016; Yoast *et al.*, 2020b). Specifically, NFAT is known to regulate cell cycle proteins such as cyclins (Mognol *et al.*, 2016). Moreover, work from our laboratory demonstrated that ORAI1 knockdown was decreasing the expression level of cyclin D1 in a prostate cancer cell line. In addition, several studies established a role for ORAI1 and SOCE in the control of cancer cell proliferation (Dragoni *et al.*, 2014). Nonetheless, these results were obtained in cancerous model where ORAI1 and SOCE are dysregulated. On a physiological level, our laboratory demonstrated a role for ORAI1 and ORAI3 proteins in HEK-293 proliferation (El Boustany *et al.*, 2010; Borowiec *et al.*, 2014). However, these results were obtained due to transient downregulation and acute treatment, while we induced a stable deletion of the ORAI1 protein. We hypothesize that the total deletion of ORAI1 protein probably led to the apparition of compensatory

mechanisms allowing HEK-293 cells to assure their proliferation. Of note, other groups have demonstrated an impairment of NFAT translocation following ORAI KO in HEK-293 cells. Nonetheless the physiological consequences of these impairment were not studied. One can hypothesize that if ORAI1 deletion was inducing strong modifications in the behavior of their KO HEK-293 cells, these studies would have studied the physiological consequence of the NFAT translocation impairment. As a conclusion, our results demonstrate that ORAI1 is not a crucial regulator in the control of HEK-293 proliferation, even though a limited role for this protein cannot be excluded. Indeed, the creation of complete KO might have induced the apparition of compensatory mechanisms. In addition, since HEK-293 are cultivated in FBS-containing media, is it conceivable that the FBS-specific composition contributes to the variations observed in other studies about a role of ORAI1 in proliferation.

5.3.3. ORAI1 deletion is not fundamental for the control of HEK-293 migration

In the last part of our work, we demonstrate that ORAI1 affects the collective migration properties of HEK-293. Of note, Ca^{2+} has been shown to be involved in several migration processes through the control of proteases, phosphatases, and Ca^{2+} -dependent kinases (Wei *et al*, 2012; Sun *et al*, 2014). Therefore, it is not surprising that SOCE has also been shown to control the migration process. For example, it was demonstrated that SOCE and ORAI1 were controlling migration properties of melanoma and breast cancer cells (Umemura *et al*, 2014; Yang *et al*, 2009). Nonetheless, in a physiological context suppression of SOCE did not impair the migration of CD8⁺ cells (Weidinger *et al*, 2013). Our results suggest that ORAI1 is involved specifically in the collective migration but does not take part in the single-cell migration. More specifically, our data demonstrates that the initiation of the collective migration is accelerated in the absence of ORAI1. Interestingly, studies performed in *Xenopus* embryos demonstrated that during collective migration, the cells leading-edge migration was due to Ca^{2+} transients (Hayashi *et al*, 2018). Of note, cellular migration has been increasingly linked to Ca^{2+} transient (Li *et al*, 2018; Catacuzzeno & Franciolini, 2018; Tang *et al*, 2015), and a recent study using HEK-293 triple KO (for all ORAI homologues) demonstrated that ORAI1 did not prevent apparition of Ca^{2+} oscillations while ORAI2 and ORAI3 were crucial actors in the maintenance of such oscillations (Yeast *et al*, 2020b). Thus, the observed increase in the migration initiation speed due to ORAI1 KO could be attributed to a deregulation of Ca^{2+} oscillations induced by the *ORAI1* deletion, and the *ORAI2* and *ORAI3* down regulation. Taken together, these data are in line with our results indicating that ORAI1 is only playing a minimal role in the overall cell migration process.

5.3.4. Conclusion on the role of ORAI1 in HEK-293 physiology.

Overall, the results obtained in our ORAI1 KO cell line allows us to claim that ORAI1 is not an indispensable actor of HEK-293 cell physiology. Indeed, proliferative and migratory properties of HEK-293 cells were not fundamentally affected by ORAI1 deletion. While we cannot exclude those compensatory mechanisms allowed the maintenance of basic HEK-293 properties, it appears unlikely

that ORAI1 KO cellular clones would arise if the function of the protein was of utmost importance for HEK-293 cells. Nonetheless, it remains under question how ORAI1 KO HEK-293 cells are able to restore their Ca^{2+} store following depletion, and further experiments assessing for modulation of expression of channels would help elicits this mechanism.

5.3.5. Perspectives on the role of ORAI1 in HEK-293 physiology.

5.4. In addition to the data presented and discussed above, we noted that the Ca^{2+} content of the ER was surprisingly higher in the ORAI1-KO cells compared to the WT HEK-293 (**Annex 1**). These data indicates that the whole HEK-293 Ca^{2+} homeostasis is probably affected by ORAI1-KO. Thus, we also performed preliminary experiments using a physiological inducer of Ca^{2+} store depletion, carbachol. We realized during Ca^{2+} imaging experiment that the use of carbachol to induce ER store release was leading to the generation of regenerative oscillations. Of note, these oscillations were not abolished in ORAI1 KO, but they were clearly displaying a different pattern than the one from WT HEK-293 (**Annex 2**). These data led us to consider that the other minor Ca^{2+} stores compartments (such as mitochondria and nuclear envelop) might be affected due to ORAI1 KO. We considered studying the level of these stores due to targeted GECl. Because oscillations are important for NFAT translocation to the cell nuclei, we also assessed its translocation level to the nuclei following carbachol activation and our data indicated that its translocation was impaired in ORAI1 KO cells (**Annex 3**). Of note, part of the results discussed above were already published by other groups who showed in HEK-293 KO for ORAI proteins, that their Ca^{2+} oscillations pattern was modified upon by ORAI proteins deletion, and that these deregulations were impairing the translocation of NFAT to the cells nuclei (Yoast *et al*, 2020b; Kar *et al*, 2021). Nonetheless, the consequences of ORAI1 KO on the overall Ca^{2+} dialog between compartment has not been studied. Evidence of an ORAI1-ORAI3 dynamic remodeling

In the last part of the PhD work, we studied the dynamic interactions between ORAI1 and ORAI3. First, we performed a set of Ca^{2+} imaging experiments using PC3 WT and PC3 KO for ORAI1 and ORAI3. These experiments allowed us to confirm that ORAI3 overexpression was impairing SOCE. In addition, we demonstrated that endogenous ORAI3 was impairing the native SOCE in PC3. These data suggesting that ORAI1 and ORAI3 are component of a heteromeric ORAI channels. We further performed FLIM-FRET experiments to evaluate how the ORAI1-ORAI3 interaction was evolving in basal conditions and following activation of the ORAI channels. This study conducted in HEK-293 and in PC3 cells revealed that ORAI1 and ORAI3 are interacting in basal conditions and that the strength of this interaction was dependent on the expression level of ORAI3. Using HEK-293 cells, we tried to decipher the mode of association between ORAI proteins during the formation of ORAI channels. We proposed and tested few models, but the complexity of and diversity of potential association prevented

us to clearly identify whether ORAI proteins were able to associate on site to form functional channel or if pre-assembled ORAI channels were already present at the PM. Nonetheless, these results allowed us to determine that upon induction of SOCE, the interaction level between ORAI1 and ORAI3 is increased. We deepened these results by repeating the experiment in the cancer cell line PC3 where ORAI1 and ORAI3 were deleted. In this model, where background due to endogenous ORAI1 and ORAI3 expression was abolished, we confirmed that the ORAI1-ORAI3 interaction was reinforced by SOCE activation and that the level of SOCE activation was affecting the strength of their interaction.

5.4.1. Influence of ORAI1 and ORAI3 expression on SOCE level

5.4.1.1. Overexpression of ORAI in WT PC3

In our Ca^{2+} imaging experiments, we started by overexpressing ORAI1 and ORAI3 in WT PC3. The results obtained allowed us to confirm that ORAI3 overexpression decreases the level of SOCE in PC3 WT. Nonetheless, while we believe that transient overexpression of ORAI3 represent a refine approach compared to stable overexpression of ORAI3, we could not control the exact level of ORAI3 overexpression in our cells, and thus could not identify in which proportion ORAI3 overexpression impact SOCE. An interesting approach to accurately evaluate the involvement of ORAI3 in SOCE would be to use CRISPR transcription activating plasmid, which can be activated through the addition of small molecules in a dose-dependent manner, such a system would allow for a tighter control of ORAI3 overexpression level and allow the study of the consequences of modifications in ORAI3 expression level (Chiarella *et al*, 2019). Further, we showed that ORAI1 overexpression did not enhance SOCE amplitude. Although this result might seem surprising, other publications reported that STIM1 expression level could be limiting when trying to increase SOCE level (Liao *et al*, 2008). Thus, the lack of effect of ORAI1 overexpression on the measured SOCE level might be attributed to a low expression level of the STIM1 protein preventing the formation and the activation of the totality of the ORAI1 channel. Overall, it is interesting to note that on the one hand, STIM1 might be a limiting factor for increasing SOCE level when overexpressing ORAI1, while, on the other hand STIM expression level was not a limiting for the SOCE impairment observed with the ORAI3 overexpression. This is explained by the fact that ORAI3 overexpression leads to the creation of heteromeric ORAI channels, which possess different characteristic compared to purely ORAI1-channel, such as lower Ca^{2+} selectivity for example, which explains the impairment of SOCE observed (Yoast *et al*, 2020a).

5.4.1.2. Effect of ORAI proteins deletion on SOCE in PC3 cells

In the second part of our Ca^{2+} imaging experiments we used KO cell lines to determine the role of endogenous ORAI proteins in SOCE. The abolition of SOCE due to ORAI1 deletion was expected. Nonetheless, it is interesting to compare the results obtained in PC3 to the ones obtained in HEK-293 cells. Indeed, while ORAI1 KO HEK-293 cells were still displaying a limited SOCE, such a reminiscent Ca^{2+} entry is barely detectable in PC3. It seems evident that the channel expression pattern of these two

cell lines is different and might explain the difference observed between these two KO models. Yet, exploring the differences in channel expression between these two cell lines could allow the identification of specific actors of SOCE. The results obtained in the ORAI1 rescue experiment showed that ORAI1 re-expression did not restore a classic SOCE level. While we can explain this by a low transfection efficiency, we cannot exclude that ORAI1 deletion has affected other protein expression such as STIM1. For example, one could hypothesize that following ORAI1 deletion, the STIM1 protein is downregulated, in this case re-expression of ORAI1 would not allow a restoration of classic SOCE level due to a limited number of STIM1 protein available for activation. In addition, we established that endogenous ORAI3 impairs native SOCE level. On the one hand, similar reports on a deleterious effect of ORAI2 and/or ORAI3 on SOCE amplitude have been published (Yeast *et al*, 2020b; Vaeth *et al*, 2017; Eckstein *et al*, 2019b; Tsvilovskyy *et al*, 2017). Nonetheless, these observations were made in physiological context and not in cancer cell lines. On the other hand, studies reported altered expression of SOCE component during cancer (Chalmers & Monteith, 2018), thus it is not surprising that the expression of ORAI3 modulates SOCE. This demonstration that ORAI3 impairs SOCE confirms the conclusion from the study of Dubois *et al.*, suggesting that ORAI3 represents a new therapeutic target in prostate cancer.

5.4.2. Study of ORAI1-ORAI3 interaction with FLIM-FRET

5.4.2.1. ORAI1-ORAI3 interaction models in HEK-293

For evaluating the interaction between ORAI1 and ORAI3, we performed a first set of experiment using WT HEK-293 cells. The results obtained following ORAI channel activation were puzzling. While this complexity might be attributed to the existence of an endogenous background due to the presence of endogenously expressed ORAI1 and ORAI3 proteins. We have tried to imagine models that might explain the results observed. Thus, we considered two putative models based on our data and on suggestions from previous publications.

5.4.2.1.1. Putative model N°1: on site assembly of ORAI dimers.

First, in one model we consider that ORAI protein can assemble as channel “on site”. Of note, few publications suggested that ORAI channel could be assembled on site (Li *et al*, 2016b; Penna *et al*, 2008). In addition, early publications on ORAI channel structure using biochemical analysis, as well as microscopy techniques have demonstrated that ORAI protein could be found in different oligomeric states such as monomers, dimers, trimers, and tetramers (Maruyama *et al*, 2009; Gwack *et al*, 2007a; Zhou *et al*, 2010; Ji *et al*, 2008a). Nonetheless, from the different oligomeric states identified, dimeric state is believed to be the most represented, and in addition a dimeric association of ORAI proteins would explain the formation of higher oligomeric states of ORAI proteins (tetramers, hexamers) upon store depletion (Penna *et al*, 2008; Gwack *et al*, 2007a). Finally, Cai *et al.*, proposed that the SOCE activated ORAI channel is a ‘trimer of a ORAI dimer’(Cai *et al*, 2016), in this publication the authors

highlight that the crystal structure of the hexameric *Drosophila* ORAI channel is consistent with this hypothesis as it displays two adjacent ORAI1 protein interacting together through hydrophobic interaction between their C-termini (Hou *et al*, 2012b). Thus, in a first model we hypothesized that ORAI proteins were existing as dimers at rest and that depending on the cell stimulation they were assembled on site in distinct channels.

5.4.2.1.2. Putative model N°2: reorganization of pre-formed ORAI channels

A second putative model that might explain our result is the existence of pre-assembled channels that will be specifically activated depending on the type of stimulation received by the cell. In fact, while the structural data obtained from the *Drosophila* CRAC channel display an architecture constituted by trimer of dimers, nothing indicates the channels are not formed and assembled in the ER and exported as “channel units” to the PM. Similarly, the biochemical studies indicating on the existence of low oligomeric states of ORAI proteins did not decipher the localization of this oligomers in different cellular compartments. In addition, the microscopic experiments such as the counting of TIRFm photobleaching steps were performed in *Xenopus* oocytes, that might not possess all the required human proteins allowing the classic assembly of ORAI channel. Moreover, some of these experiments were performed in overexpression system where endogenous protein might have affected the counting. Also, contradictory microscopic studies identified that ORAI are diffusing as homotetramers in the PM questioning the possibility of “on site” assembly of dimers (Madl *et al*, 2010b). Finally, the original architecture of the ARC channel consisting of a pentamer assembly of three ORAI1 and two ORAI3 proteins does not fit with a model of an “on site” assembly of ORAI dimers (Mignen *et al*, 2009). Thus, in the second model, we hypothesized that ORAI protein are pre-assembled in ARC and CRAC channels. In addition, we considered that ARC channels were pentameric association of three ORAI1 and two ORAI3 channels (in a 31113 or 31311 stoichiometry) as proposed by Mignen *et al.*, and that CRAC channels were heteromeric assemblies of ORAI dimers (Mignen *et al*, 2009).

5.4.2.1.3. FLIM-FRET results in regard with the interaction models

We tried to explain the results obtained in HEK-293 cells by confronting the FLIM-FRET data obtained in HEK-293 to the two putative models presented above.

5.4.2.1.3.1. Basal interaction suggests a pre-assembled channel model

Our results clearly demonstrate that ORAI1 and ORAI3 are interacting in basal condition and that this interaction is dependent on the expression level of ORAI3. The data indicating that ORAI1 and ORAI3 are interacting in basal condition when expressed in the same quantity (1:1 ratio) do not allow to differentiate between our two hypothetical models. However, the data indicating that the interaction between ORAI1 and ORAI3 is increased when ORAI3 is overexpressed points toward a pre-assembled model of the ORAI channels. Indeed, considering the existence of ORAI dimers, and that the probability

of forming homo or heterodimer is equivalent, in a 1:1 transfection ratio one expects to observe 50% of heterodimers (ORAI1-ORAI3) displaying FRET, 25% of ORAI1-ORAI1 homodimers, and 25% of homodimers ORAI3-ORAI3, the two later not displaying FRET. For a 1:3 transfection ratio the proportion of ORAI3-ORAI3 homodimers would increase at the expense of both ORAI1-ORAI1 homodimers, but the amount of interacting donor and acceptor molecule should not be strongly affected as a consequence, one would expect that FRET level would not be modified (**Figure 100 A**). On the contrary, considering a mixture of pre-assembled ARC and CRAC channels, the increase of ORAI3 expression induced by the 1:3 transfection ratio would favor the creation of heteromeric CRAC channel leading to an increased number of FRET acceptor molecules (ORAI3-sYFP2) for a single donor molecule (ORAI1-mT2), and thus induce a general increase of FRET level observed (**Figure 100 B**).

5.4.2.1.3.2. AA-activated interaction does not agree with the proposed models

The data obtained following activation of ARC channel due to AA treatment indicates that in the 1:1 ratio, the interaction level between ORAI1 and ORAI3 is not modified while in the 1:3 ratio their interaction is reinforced. In addition, this effect is observed only when STIM1 is expressed at its endogenous level.

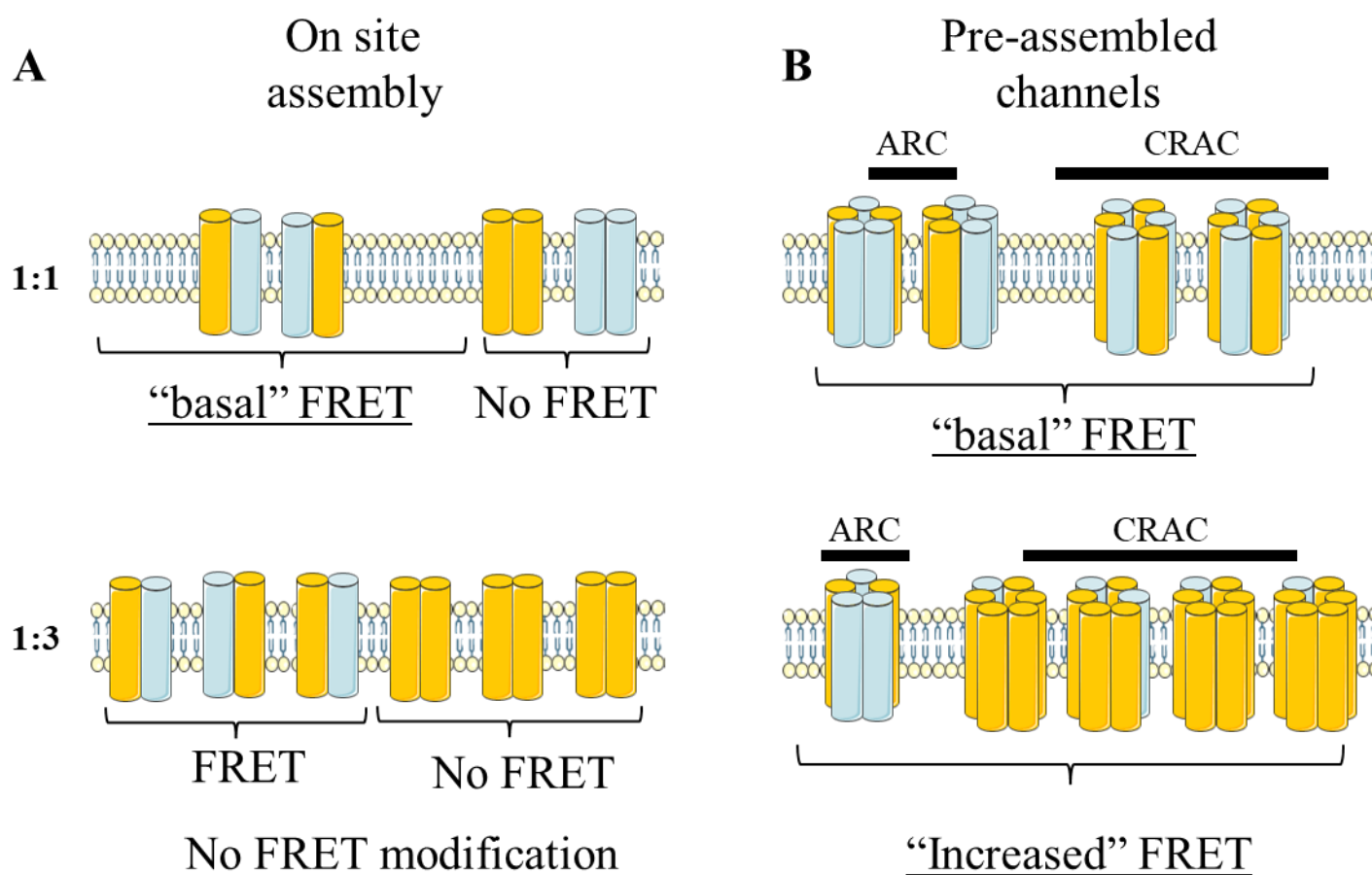


Figure 100 | Putative models for the basal interaction between ORAI1 and ORAI3 in HEK-293.

For both panels, ORAI3 proteins are represented by the yellow cylinders, and ORAI1 proteins by the blue cylinders. Underlined text, indicates that the data confirms the model. The different transfection ratio used are shown on the left of the schemes.

- A. The on-site assembly putative model, hypothesize the existence of ORAI dimers in the PM that are assembled in functional channels depending on the stimulation received by the cell. This model do not explain the increased interaction observed for the 1:3 ratio in our experiment.
- B. The pre-assembled channel putative model, hypothesize that CRAC and ARC channels are pre-assembled and selectively activated depending on the stimulation received by the cell. This model explains the increased interaction observed for the 1:3 ratio in our experiment.

Considering the 1:1 transfection condition for our two models, both can explain the absence of effect observed following AA treatment. If considering the “on site” channel assembly model, AA treatment would lead to the creation of ARC channel. The differences in FRET that would occur following ARC channel formation is not clear. Indeed, in the basal interaction, one can observe that half of the ORAI dimers are displaying FRET (ORAI1-ORAI3 heterodimers) and half of the dimer are not displaying FRET (25% of ORAI1-ORAI1 homodimer, and 25% of ORAI3-ORAI3 homodimers). Thus, the measured FRET would relate to a situation in which one donor molecule (O1-mT2) interacts with one acceptor molecule (O3-sYFP2). On the other hand, the assembled channels would bring together homodimers that were previously not able to display FRET, and thus would increase FRET. However, because of the specific architecture of ARC channel, the ratio of donor to acceptor molecule would be of three donor molecules (O1-mT2) for two acceptor molecules (O3-sYFP2), and so lower than in the condition basal condition (**Figure 101 A**). Thus, the observation that AA treatment does not modify the interaction between ORAI1 and ORAI3 might agree with this model. If considering the pre-assembled model, activation of ARC channel would not modify the proportion of ORAI molecules interacting together, and thus does not impact the measured lifetime of O1-mT2 (**Figure 101 B**). Of note, in such a scenario, our data would suggest that a conformational change due to ARC channel opening, would not be transmitted to the FP, as their interaction level is not modified. This is plausible due to the length and flexibility of the linker used in our experiment. Of note, in our experiment the presence of STIM1 protein at endogenous or overexpressed level did not modify the results and thus does not seem of utmost importance.

Considering the 1:3 transfection condition, both models fail to explain the results observed. Indeed, both of our models would lead to the same conclusion as for the 1:1 transfection ratio (**Figure 102**). The conduction of similar experiments in ORAI KO cells as well as the ability to define the exact proportion of ORAI1 and ORAI3 with the use of concatemers might help deepen this result and obtain a better understanding of the observed results.

5.4.2.1.3.3. CRAC-activated interaction indicates a pre-assembled channel model

Because our Ca^{2+} imaging data suggested that ORAI3 was involved in native SOCE, we have studied the interaction level of ORAI1 and ORAI3 following TG treatment. Our data indicate that the interaction between ORAI1 and ORAI3 was reinforced following SOCE activation only when the two proteins were expressed at the same level. These data can be explained exclusively by the pre-assembled channel models. Indeed, if for the 1:1 ratio, both models could explain an increase of FRET following store depletion; the absence of modification in the interaction level between ORAI1 and ORAI3 for a 1:3 expression ratio can be explained only with the pre-assembled channel model.

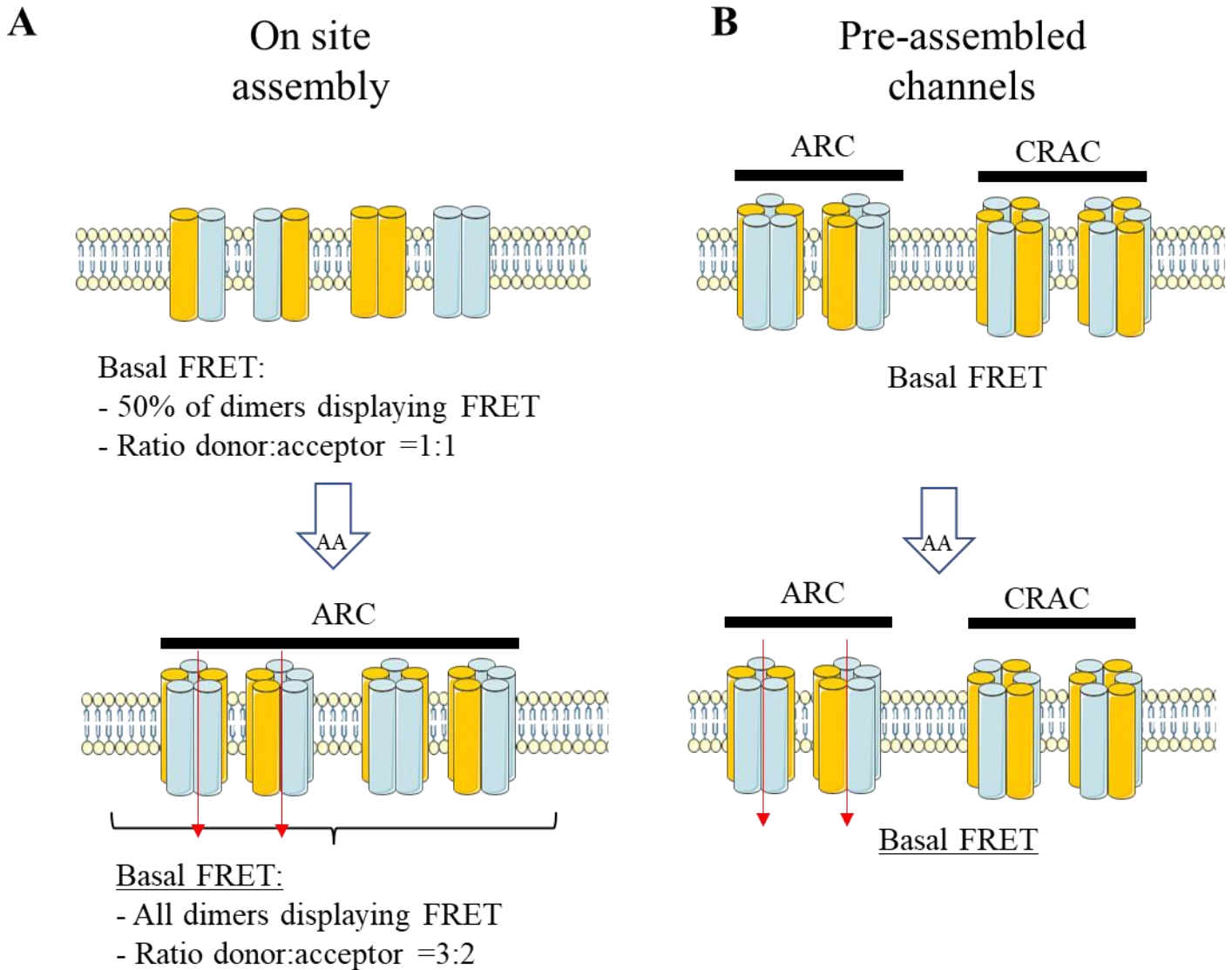
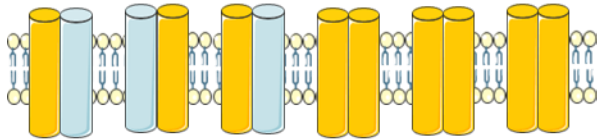


Figure 101 | Putative models for the AA-activated interaction (1:1 ratio) in HEK-293.

For both panels, ORAI3 proteins are represented by the yellow cylinders, and ORAI1 proteins by the blue cylinders. Underlined text, indicates that the data confirms the model. The blue arrows indicates the treatment by arachidonic acid (AA) leading to ARC activation. Red arrow indicates activated channels

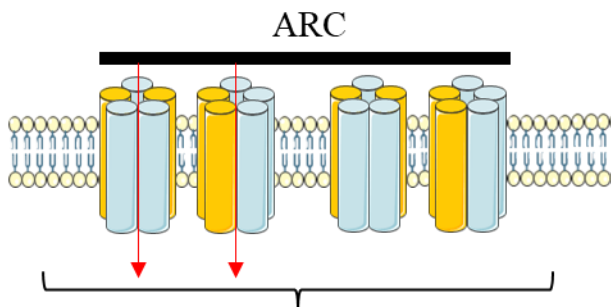
- A. The on-site assembly putative model, hypothesize the existence of ORAI dimers in the PM that are assembled in functional channels depending on the stimulation received by the cell. This model might explain the absence of modification in the interaction level between ORAI1 and ORAI3 observed for the 1:1 following AA treatment.
- B. The pre-assembled channel putative model, hypothesize that CRAC and ARC channels are pre-assembled and selectively activated depending on the stimulation received by the cell. This model might explain the absence of modification in the interaction level between ORAI1 and ORAI3 observed for the 1:1 following AA treatment.

On site assembly



Basal FRET:

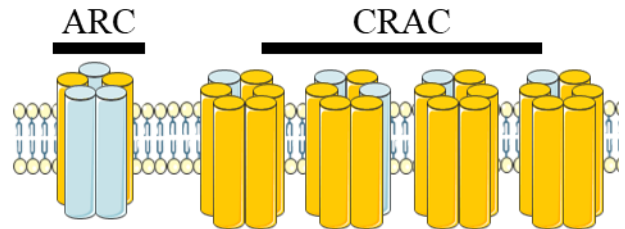
- 50% of dimers displaying FRET
- Ratio donor:acceptor = 1:1



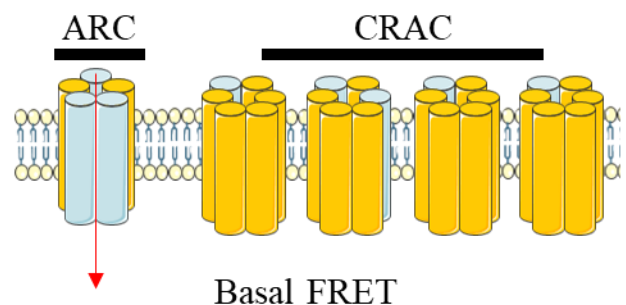
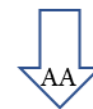
Basal FRET:

- All dimers displaying FRET
- Ratio donor:acceptor = 3:2

Pre-assembled channels



Basal FRET



Basal FRET

Figure 102 | Putative models for the AA-activated interaction (1:3 ratio) in HEK-293.

For both panels, ORAI3 proteins are represented by the yellow cylinders, and ORAI1 proteins by the blue cylinders. Underlined text, indicates that the data confirms the model. The blue arrows indicates the treatment by arachidonic acid (AA) leading to ARC activation. Red arrow indicates activated channels

- The on-site assembly putative model, hypothesize the existence of ORAI dimers in the PM that are assembled in functional channels depending on the stimulation received by the cell. This model can explain the increased interaction between ORAI1 and ORAI3 observed in the experiment.
- The pre-assembled channel putative model, hypothesize that CRAC and ARC channels are pre-assembled and selectively activated depending on the stimulation received by the cell. This model can explain the increased interaction between ORAI1 and ORAI3 observed in the experiment

Specifically, for the 1:1 expression ratio; considering the “on site” assembly model, association of ORAI dimers into a channel might not increase the FRET level, however the clustering of CRAC channels induced by store depletion would increase the proportion of interacting donor (O1-mT2) and acceptor (O3-sYFP) molecules. If considering the pre-assembled channels model, the same phenomenon would occur (**Figure 103**). As for the 1:3 transfection ratio, in the “on site” assembly model, the FRET level of the basal condition would be relative to the number of ORAI-ORAI3 dimers. Due to SOCE activation, ORAI3-ORAI3 dimers would be included in the CRAC channel and thus increase the acceptor/donor ratio ultimately leading to a FRET increase (**Figure 104A**). On contrary, if considering the pre-assembled channel model, one could consider that the high ratio of acceptor to donor molecules in the pre-assembled channels do not allow a further increased in FRET when channels are brought in close proximity by STIM1 proteins (**Figure 104 B**).

5.4.2.1.3.4. Consecutive activation of ARC and CRAC channels suggest an on site assembly model

The final experiment conducted in HEK-293 was to consecutively induce ARC formation followed by SOCE activation. The results of these experiments showed that AA treatment was preventing the modification of interaction observed when SOCE was activated for the 1:1 ratio of expression between ORAI1 and ORAI3. Still considering our two models, this last result finds an explanation with the “on site” assembly model. Indeed, we explained earlier that this model would allow an increase of FRET following SOCE activation due to the creation of clusters of ORAI channels. With the “on site” assembly model one could hypothesize that AA treatment leads to the creation of ARC channel, which as we detailed earlier did not modify FRET level. The creation of these ARC channels would have decreased the quantity of ORAI dimers available to create SOC channel and thus prevent the apparition of clusters and thus the FRET increase (**Fig 48 A**). In the case of pre-assembled channels, activation of ARC would not modify the number of pre-formed SOC channel and thus clustering of ORAI channel could develop and induce FRET increase (**Fig 48 B**). As for the transfection ratio 1:3, the same rationale as for the 1:1 ratio applies for the “on site” assembly domain explaining the absence of modification of the interaction level between ORAI1 and ORAI3 (**Fig 49A**). Nonetheless, in the case of ORAI3 overexpression compared to ORAI1, the “pre-assemble” channel model would also lead to the absence of effect of the consecutive treatment due to a supposedly maximal FRET interaction reached in the heteromeric SOC channel (**Fig 49B**).

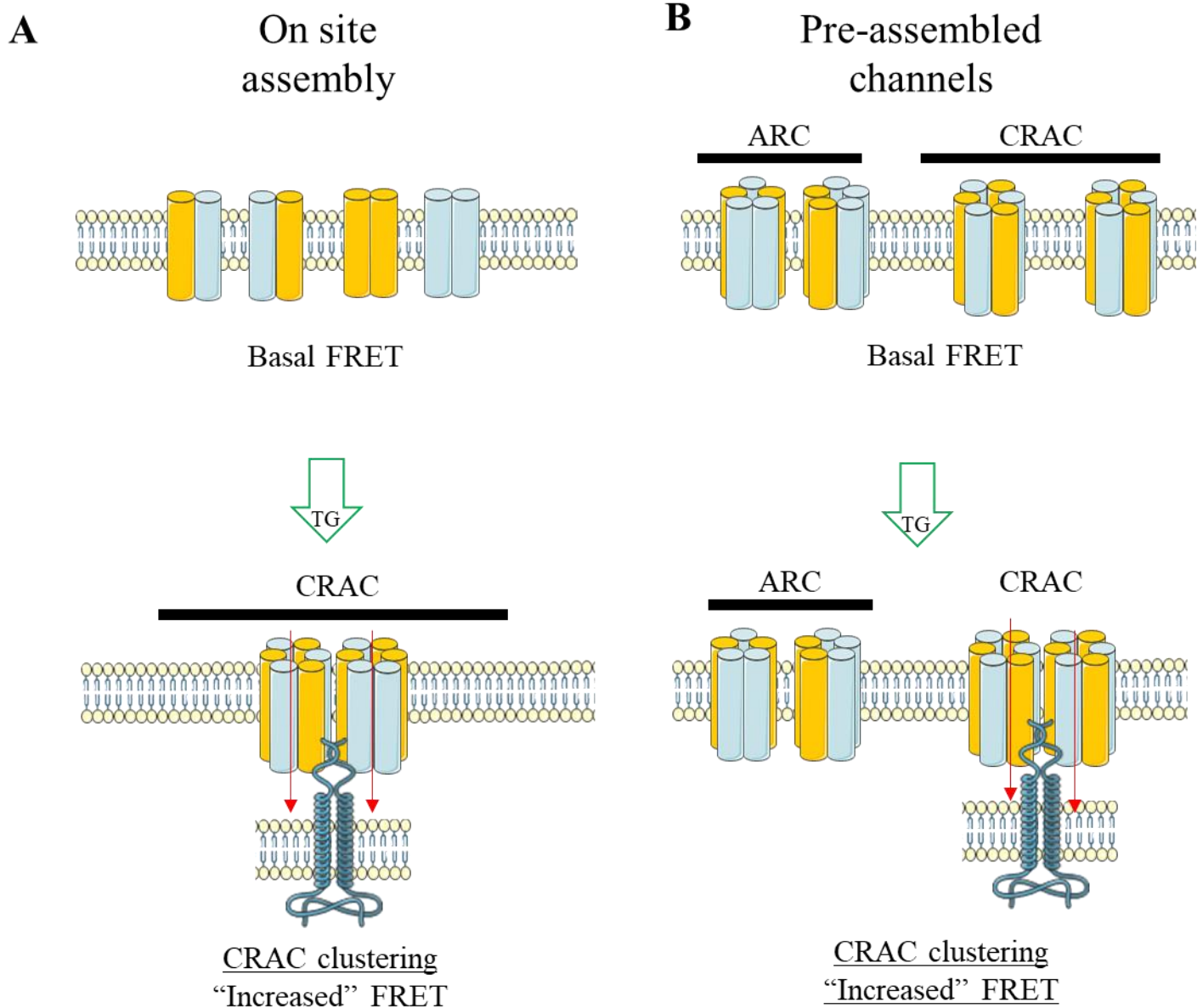


Figure 103 | Putative models for the store depleted interaction (1:1 ratio) in HEK-293.

For both panels, ORAI3 proteins are represented by the yellow cylinders, and ORAI1 proteins by the blue cylinders. Underlined text, indicates that the data confirms the model. The blue arrows indicates the treatment by thapsigargin (TG) leading to CRAC channel activation. Red arrow indicates activated channels. STIM1 protein from ER are represented in blue (helices).

- A. The on-site assembly putative model, hypothesize the existence of ORAI dimers in the PM that are assembled in functional channels depending on the stimulation received by the cell. This model can explain the increased interaction between ORAI1 and ORAI3 observed in the experiment.
- B. The pre-assembled channel putative model, hypothesize that CRAC and ARC channels are pre-assembled and selectively activated depending on the stimulation received by the cell. This model can explain the increased interaction between ORAI1 and ORAI3 observed in the experiment

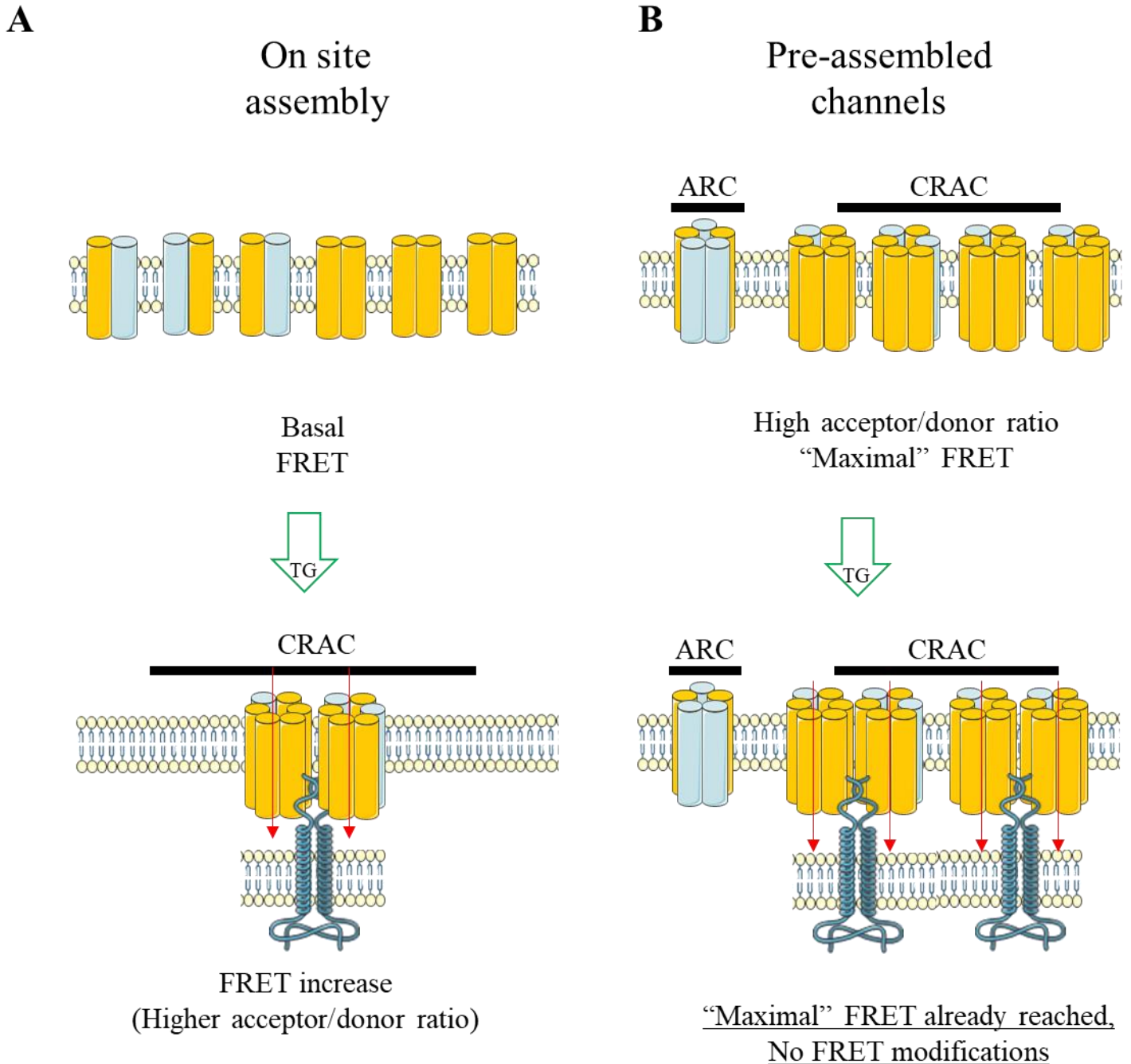
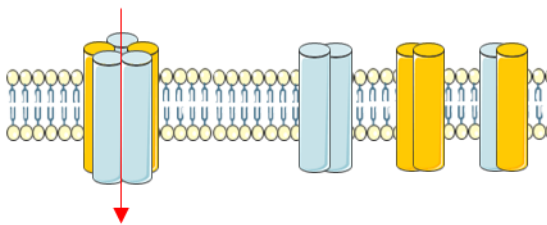
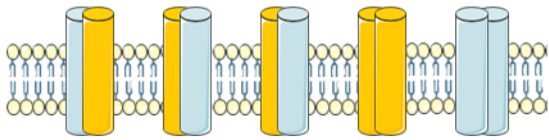


Figure 104 | Putative models for the store depleted interaction (1:3 ratio) in HEK-293.

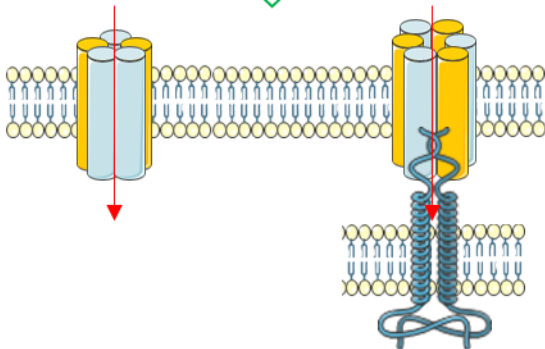
For both panels, ORAI3 proteins are represented by the yellow cylinders, and ORAI1 proteins by the blue cylinders. Underlined text, indicates that the data confirms the model. The blue arrows indicates the treatment by thapsigargin (TG) leading to CRAC channel activation. Red arrow indicates activated channels. STIM1 protein from ER are represented in blue (helices).

- A. The on-site assembly putative model, hypothesize the existence of ORAI dimers in the PM that are assembled in functional channels depending on the stimulation received by the cell. This model does not explain the absence of FRET level observed in the experiment.
- B. The pre-assembled channel putative model, hypothesize that CRAC and ARC channels are pre-assembled and selectively activated depending on the stimulation received by the cell. This model can explain the absence of interaction between ORAI1 and ORAI3 observed in the experiment

A On site assembly

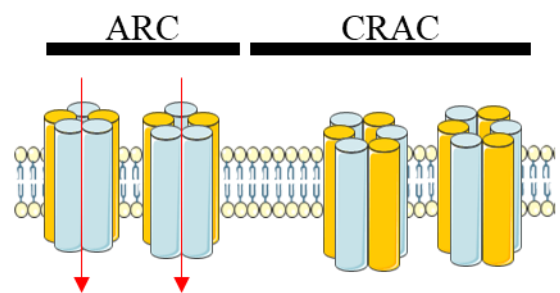
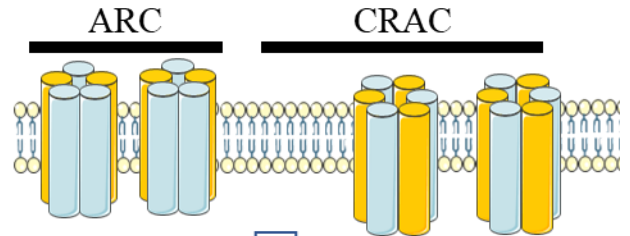


ARC activation
decrease of ORAI dimers availability

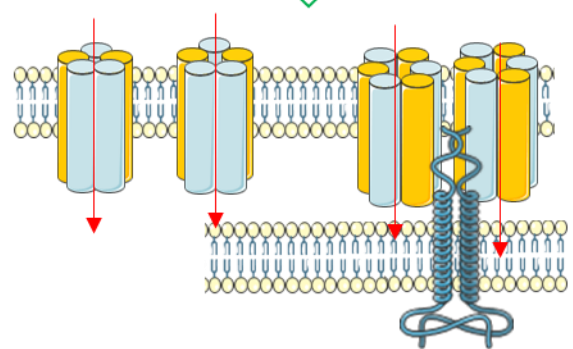


No clustering
(low availability in ORAI dimers)
No FRET changes

B Pre-assembled channels



No changes in ORAI
channels proportion



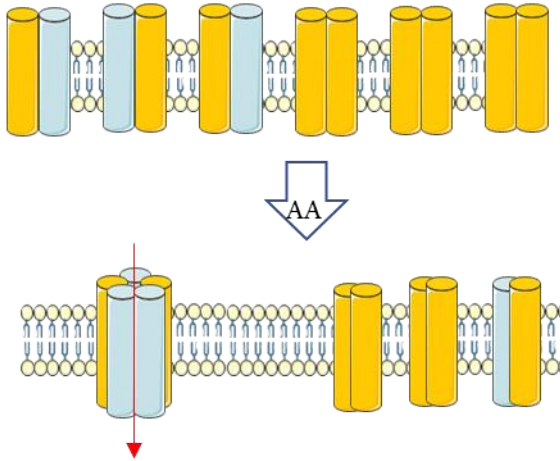
CRAC clustering,
FRET increase

Figure 105 | Putative models for consecutive AA-activated and store depleted interaction in HEK-293 (1:1 ratio).

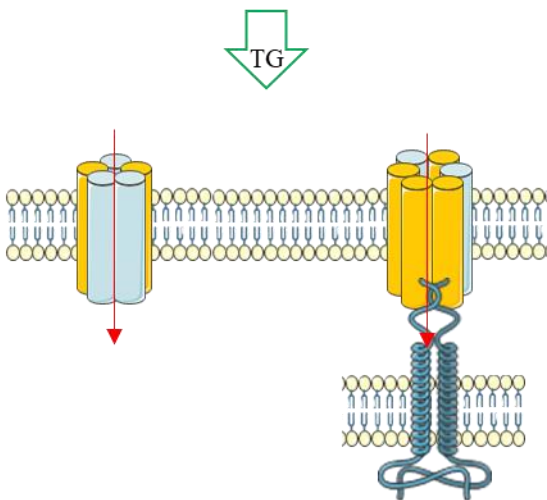
For both panels, ORAI3 proteins are represented by the yellow cylinders, and ORAI1 proteins by the blue cylinders. Underlined text, indicates that the data confirms the model. The blue arrows indicates the treatment by arachidonic acid (AA) leading to ARC channel activation, the green arrow indicates thapsigargin treatment (TG) leading to CRAC channel activation. Red arrow indicates activated channels. STIM1 protein from ER are represented in blue (helices).

- A. The on-site assembly putative model, hypothesize the existence of ORAI dimers in the PM that are assembled in functional channels depending on the stimulation received by the cell. This model agrees with our data indicating that consecutive treatments with AA and TG do not modify the interaction level between ORAI1 and ORAI3 for the 1:1 ratio.
- B. The pre-assembled channel putative model, hypothesize that CRAC and ARC channels are pre-assembled and selectively activated depending on the stimulation received by the cell. This model fail to explain our data indicating that consecutive treatments with AA and TG do not modify the interaction level between ORAI1 and ORAI3 for the 1:1 ratio.

A On site assembly

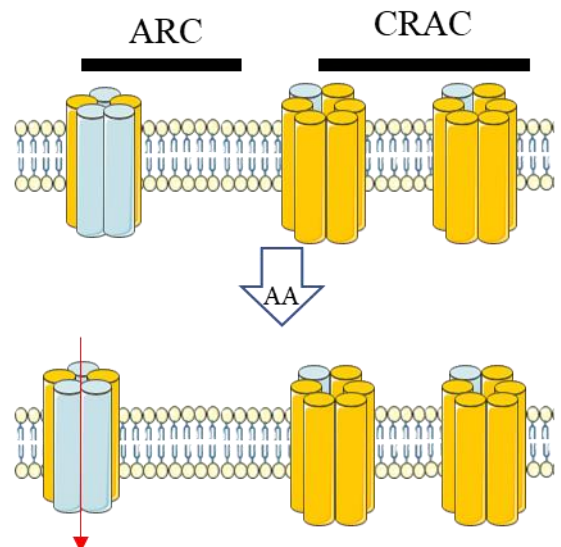


ARC activation
decrease of ORAI dimers availability

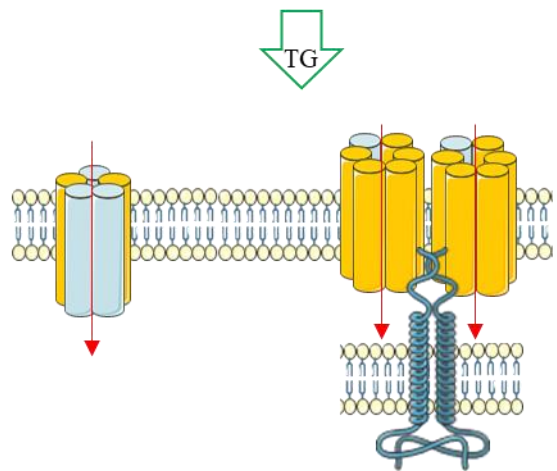


No clustering
(low availability in ORAI dimers)
No FRET changes

B Pre-assembled channels



No changes in ORAI
channels proportion



CRAC clustering,
“Maximal” FRET already reached

Figure 106 | Putative models for consecutive AA-activated and store depleted interaction in HEK-293 (1:3 ratio).

For both panels, ORAI3 proteins are represented by the yellow cylinders, and ORAI1 proteins by the blue cylinders. Underlined text, indicates that the data confirms the model. The blue arrows indicates the treatment by arachidonic acid (AA) leading to ARC channel activation, the green arrow indicates thapsigargin treatment (TG) leading to CRAC channel activation. Red arrow indicates activated channels. STIM1 protein from ER are represented in blue (helices).

- A. The on-site assembly putative model, hypothesize the existence of ORAI dimers in the PM that are assembled in functional channels depending on the stimulation received by the cell. This model agrees with our data indicating that consecutive treatments with AA and TG do not modify the interaction level between ORAI1 and ORAI3 for the 1:3 ratio.
- B. The pre-assembled channel putative model, hypothesize that CRAC and ARC channels are pre-assembled and selectively activated depending on the stimulation received by the cell. This model agrees with our data indicating that consecutive treatments with AA and TG do not modify the interaction level between ORAI1 and ORAI3 for the 1:3 ratio.

5.4.2.1.3.5. Conclusion on the hypothetical models of interaction

To conclude, most of the data obtained in our experiments can be explained by our simplified models. On the one hand, the ORAI1-ORAI3 basal interaction and its dependency on the ORAI3 expression level find an explanation with the pre-assembled channel model. In addition, the increased interaction between ORAI1 and ORAI3 following store depletion can also be explained by the pre-assembled channel scenario. On the other hand, the results of the consecutive treatment by AA and TG, are finding an explanation with the “on-site assembly” model. Finally, the data demonstrating that AA treatment increased ORAI1 - ORAI3 interaction only when ORAI3 is overexpressed cannot be explained by any of our model. Thus, we believe that 1-both models are not mutually exclusive, 2-our models are a simplification of complex processes occurring within cells which explains why we could not interpret the totality of the results obtained. In any case, further experiments are required to confirm the results obtained with the FLIM-FRET measurement, especially, Ca^{2+} imaging experiments demonstrating the successful activation of ARC channel due to acid arachidonic. Overall, because WT HEK-293, expressing endogenous ORAI1 and ORAI3 proteins, were used to perform the experiments, the interpretation of results is limited by the existence of “invisible” ORAI molecules that might affect the measurable interaction level between ORAI1 and ORAI3.

5.4.2.2. Study of ORAI1-ORAI3 interaction in PC3

5.4.2.2.1. ORAI1-ORAI3 interaction in PC3-WT

For the specific study of the ORAI1-ORAI3 interaction level following SOCE activation, we started by evaluating the basal interaction and store-depleted interaction levels between ORAI1 and ORAI3 in PC3 WT and verify whether we could reach the same conclusions as in HEK-293. On the contrary to what was observed in HEK-293, overexpressing ORAI3 compared to ORAI1 did not allow to increase their interaction level. In addition, SOCE activation did not allow to observe modification of FRET level between ORAI1 and ORAI3. These differences might be explained by the different expression level of endogenous ORAI1 and ORAI3 protein in the two cell lines. Indeed, both ORAI1 and ORAI3 protein display a higher expression level in PC3 than HEK-293. As a consequence, we hypothesize that the higher proportion of non-tagged ORAI proteins in PC3 cells prevented us from detecting modification in the interaction level between ORAI1 and ORAI3.

5.4.2.2.2. ORAI1-ORAI3 interactions in double KO (ORAI1+ORAI3) PC3

Using the double KO (ORAI1+ORAI3) PC3 cells we demonstrated that the interaction level between ORAI1 and ORAI3 was dependent on the expression level of ORAI3. In addition, we demonstrated that the interaction level between both molecules was increased by the maximal activation

of SOCE induced by TG for ORAI1:ORAI3 transfection ratio of 1:1, and 1:3. Finally, we demonstrated, using the more physiological activator carbachol, that the increased interaction observed following SOCE activation when ORAI3 was overexpressed (*i.e.*, ratio 1:3) was limited to the maximal SOCE activation only. Taken together our data indicates that the modification of interaction observed cannot be attributed to the ORAI channel opening. Indeed, FLIM-FRET is an extremely sensitive method allowing to evaluate distance between proteins. As it was demonstrated that store depletion leads to STIM1 binding to ORAI1 inducing a conformational change in ORAI1 allowing CRAC channel opening, one could hypothesize that the change in lifetime observed following SOCE activation is the consequence of this conformational change. If this would be the case, changes in lifetimes would occur for any expression ratio and with any type of agent leading to store depletion, which is not the case in our experiments. Our results rather suggest that ORAI1-ORAI3 interactions are dynamic as they evolve depending on, 1-their relative expression level, and 2-the type of activation of the CRAC channel. Of note, other FRET experiments were performed to study the interaction level between ORAI proteins during SOCE activation. On the one hand, a study evaluating the interaction level between ORAI1 protein during SOCE activation concluded that CRAC activation was decreasing FRET (Navarro-Borelly *et al.*, 2008). Nonetheless, the author indicated that changing the location of the fluorescent tag from the C-terminal extremity to the N-terminal extremity of ORAI1 was almost abolishing the decrease of FRET associated with SOCE activation. On the other hand, another study conducted in triple KO (for ORAI1, ORAI2, and ORAI3) HEK-293 have concluded on the absence of changes in interaction level between ORAI and ORAI3 following SOCE activation (Yeast *et al.*, 2020b). Of note, in these works the FRET measurement were performed based on signal intensity due to sensitized emission, which is sensible to the donor and acceptor concentration and less accurate than FLIM-FRET measurements in resolving level of FRET interaction. In addition, the latter publication used ORAI proteins tagged in their C-terminal extremity while we used N-terminally tagged ORAI proteins which might also explain the difference observed between our two studies.

5.4.2.3. Perspectives on the study of ORAI1-ORAI3 interactions

5.4.2.3.1. Additional analysis of the results

Our results have highlighted that, while we could measure and detect variations in the interaction level between ORAI1 and ORAI3 in various condition, the interpretation of the data turned out to be complex. Indeed, during the FLIM-FRET experiment we are measuring the lifetime of the donor molecule (O1-mT2), which is directly related the FRET efficiency between the donor molecule and the acceptor molecule (equation 7). As described in the introduction, FLIM-FRET measurements allow the determination of the proportion of interacting molecules α_i (equation 6), which in our case would help getting a better understanding of the measured lifetime changes. Nonetheless, the use of phasor representation which eases the calculation of the mean lifetime for each condition, makes difficult the

determination of the proportion of interacting molecules in each pixel of the image. Thus, additional analysis of our data might ease the interpretation of our data. For example, an updated version of software used in our study to determine the mean lifetime of images allows the determination of the MFD (minimal fraction of interacting donor) and represent an additional analysis to be performed, that would allow us to map the interaction level pixel by pixel for each cell. In addition, performing new experiments for which images of O1-mT2 and O3-sYFP2 intensities would be performed in addition to lifetime measurement would allow to correlate the signal intensity of each fluorophore to the measured lifetime and might allow detection a better understanding of the proportion of ORAI molecule interacting depending on the transfection ratio used or of the treatment applied on the cells. Finally, new analysis developments specifically accounting for specific FRET phenomenon such as the FRET antenna effect would be of great interest to get better understanding of our results (Bunt & Wouters, 2017).

5.4.2.3.2. Additional experimental procedures

Finally, several additional experiments considered in order to obtain a better understanding of our results. For example, some publications hypothesized that ORAI channels could be located in pre-membranaire vesicles and be exported to the PM following store-depletion. Such a mechanism could provide better understanding of the model indicating on the existence of pre-assembled ORAI channels that would undergo rearrangement following SOCE activation. Due to the acquisition in the laboratory of a microscope equipped to perform TIRF, preliminary experiments were performed using ORAI1 and ORAI3 tagged protein transfected in PC3 double KO cells (**Annex 4**). While only preliminary (a single repeat, allowing the visualization of two cells), we could observe in these experiment that ORAI1 and ORAI3 signals were not totally overlapping, both before and after TG treatment (**Annex 5**). In addition, visual inspection of the acquired images did not allow us to detect any “apparition” of signal that would indicate fusion of ORAI-containing vesicles to the membrane. Unfortunately, we could not proceed further with experimental acquisitions. Nonetheless, we believe that adjusting the experimental TIRF conditions (level of transfections, laser power for instance) in order to obtain single molecule signal would allow us to decipher if the non-localized signals were corresponding to ORAI1-ORAI3 molecules or to ORAI1 or ORAI3 oligomers (photobleaching steps). In addition, single particle tracking of ORAI1 and ORAI3 proteins was also considered, and few preliminary experiments were performed through a collaboration. Unfortunately, we faced several problems in the determination of optimal conditions allowing to perform the spt experiments. Especially, we used the SNAP- / CLIP- technology allowing the tag proteins with a chemical dye, unfortunately addition of this chemical dye to our cells resulted in a strong impairment of the adhesion of the PC3 cells and thus preventing us to obtain reliable data. Finally, to obtain a better understanding on the association between ORAI1 and ORAI3 protein we also used BifC strategy. Specifically, we used two different constructs, the dimerization-dependent fluorescent proteins (dd-FP) and the split Venus proteins. The dd-FP, allow the reconstitution of

fluorescent signal between the two parts a split FP if they are in close proximity (Alford *et al*, 2012). We cloned the dd-FP in frame to the ORAI1 and ORAI3 sequences and transfected them in our PC3 double KO cells but could not identify signal. Thus, we used the split Venus system with the aim to study how CRAC activation was modifying, ORAI1-STIM1, ORAI3-STIM1, and ORAI1-ORAI3 interactions, nonetheless, only preliminary data on ORAI1-STIM1 and ORAI3-STIM1 interactions could be obtained (**Annex 6**). Finally, we also thought of using GCaMP and GECO constructs fused to ORAI1 and ORAI3 to study the Ca^{2+} signal generated by the CRAC activation in our double KO PC3 cells transfected with ORAI1 / ORAI3 or both homologues, while the constructs were generated only preliminary experiments were performed on WT PC3(**Annex 7**).

The general idea with these constructs was to confirm and deepen our understanding of the modification of the ORAI1-ORAI3 interaction due to CRAC channel activation:

- The TIRF experiments in which eGFP-ORAI1 and mCherry-ORAI3 would be transfected in PC3 double KO cells would allow us to perform photobleaching steps experiments before and after CRAC channel activation to determine the oligomeric state of these proteins before and after channel activation.
- The spt experiments would allow us to follow single ORAI1 and ORAI3 molecules and to verify if their movement following CRAC activation were synchronous or not. Indeed, a synchronous movement would suggest that the proteins are already interacting before the channel activation
- The split FP experiments would allow us to visualize if ORAI1-ORAI3 interaction were effectively increased following CRAC channel activation.
- Finally, we planned to transfect GECI fused to ORAI1 together with a second plasmid coding for mCherry-ORAI3 (and *vice versa*) in order to observe the Ca^{2+} signal intensity resulting from homomeric versus heteromeric CRAC channel activation.

6. General conclusion

The main objective of this PhD was to study the interaction between ORAI1 and ORAI3 proteins and to determine the existence of a dynamic remodeling between these proteins. Throughout this work, several milestones and auxiliary aims were defined:

6.1. Generation of KI cell lines with CRISPR/Cas9

Our specific aim was to generate HEK-293 knocked-in in such a way that the mTurquoise2 and sYFP2 fluorescent sequences would be inserted in frame with the ORAI1 and ORAI3, respectively. Despite the use different strategies, the generation of KI cells remained unsuccessful. Of note, we used a strategy relying on the HDR cellular reparation mechanism, and thus intended to induce HR between a donor plasmid and the genomic sequence cleaved by the CRISPR/Cas9 system. While we could successfully detect HR event by PCR, we were unable to identify and specifically select edited cells, highlighting the overall difficulty of generating KI cells.

6.2. Generation of KO cell lines with CRISPR/Cas9

Using the CRISPR/Cas9 system, we were able to successfully generate the following KO cell lines: HEK-293 KO for ORAI1; PC3 KO for ORAI1; PC KO for ORAI3; PC3 double KO for ORAI1 and ORAI3. The generation of these cell lines was facilitated by the implementation of the double gRNA strategy leading to the creation of genomic deletion facilitating the screening procedures for KO. Of note, the relative efficiency of KO generation could be attributed to the dominance of NHEJ reparation mechanisms compared to HR in our cell lines.

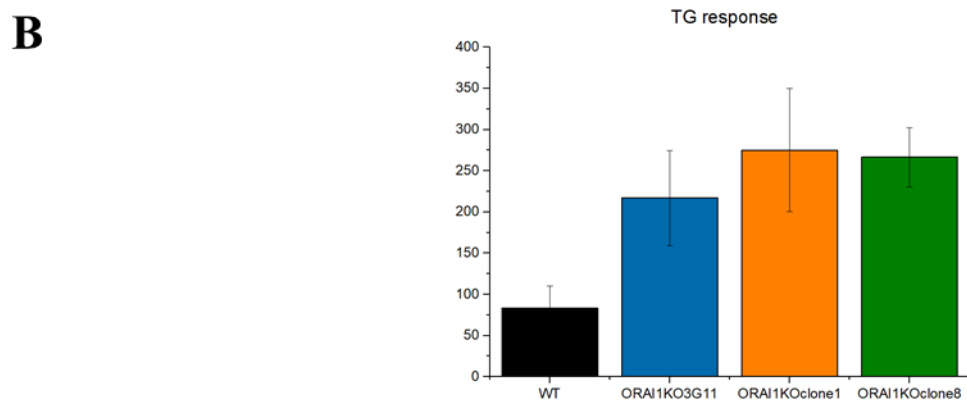
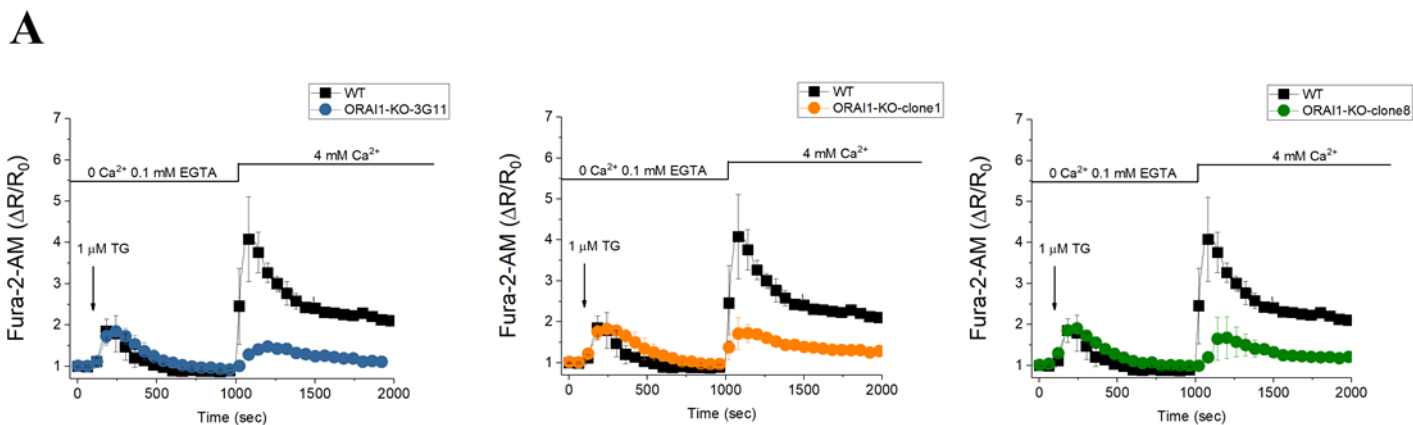
6.3. Study of ORAI1 role in fundamental physiology of HEK-293

Using the ORAI1 HEK-293 cells, we could evaluate the role of ORAI1 in the physiology of this cell line. We demonstrated that ORAI1 was the main effector of SOCE in HEK-293, but not the only one as a slight remaining SOCE could be detected following ORAI1 deletion. In addition, we showed that its deletion was leading to the downregulation of ORAI2 and ORAI3 expression, and thus we suggest that the remaining SOCE observed is probably not due to these homologues. Further, we demonstrated that the role of ORAI1 in the maintenance of HEK-293 physiology was marginal, as its deletion did not modify the proliferative nor the adhesive properties of HEK-293. In addition, we showed that ORAI1 KO only slightly influences the HEK-293 migrative properties by increases the speed of the initiation of collective cell migration. This study put in perspective the assumed fundamental role of ORAI1 in the maintenance of cellular physiology and highlight the probable existence of alternative pathway in providing Ca^{2+} entry to the cells following store depletion.

6.4. Study of ORAI1-ORAI3 interaction with FLIM-FRET

In order to investigate the interaction between ORAI1 and ORAI3, different cellular models were used. First, experiments performed in HEK-293 led us to imagine two potential models describing the mode of formation of the ORAI channels. Confronting our results to our hypothetical models, we concluded that ORAI proteins might exist in a pre-assembled channel state as well as in a lower oligomeric state allowing on site assembly into functional channels. Second, we used the double KO PC3 cells to demonstrate that the CRAC channel in these cells is a heteromeric assembly of ORAI1 and ORAI3 proteins. In addition, we studied the interaction level of ORAI1 and ORAI3 in this KO model and established that maximal SOCE activation was increasing their interaction, strengthening our conclusion that ORAI1 and ORAI3 form a heteromeric channel in PC3.

7. Annexes

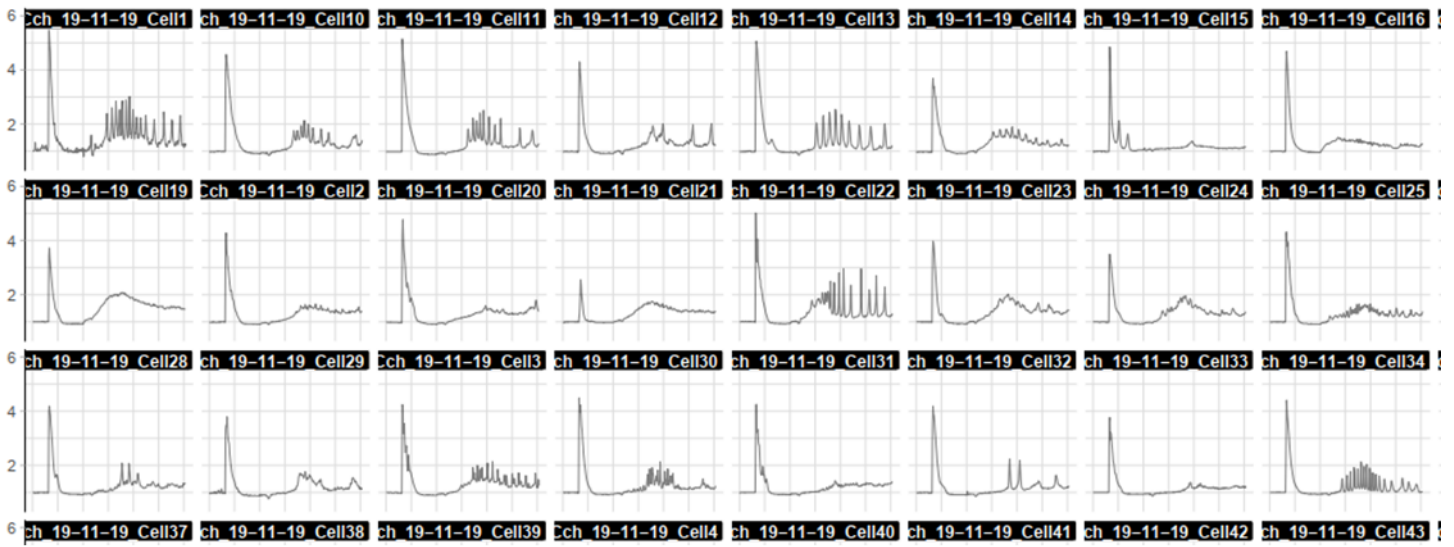


8.

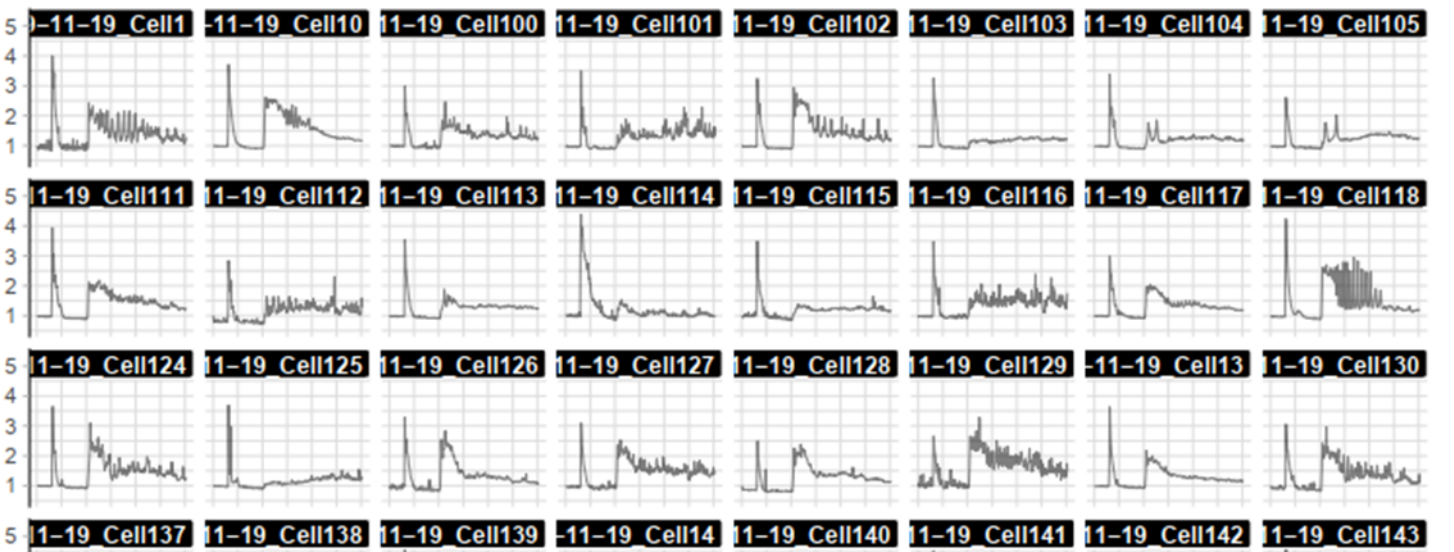
Annex 1 | Ca^{2+} store content in ORAI1 KO and WT HEK-293.

- Ca^{2+} traces from a single experiment performed on WT HEK-293 (black lane) and three different ORAI1 KO clones (blue, orange, green). Solid lines represent the mean fluorescent value of the cell population within the experiment, with their standard deviation as errors bars.
- Quantification of the Ca^{2+} store release from A. calculated by integration of the area under the curve following thapsigargin (TG) addition.

A



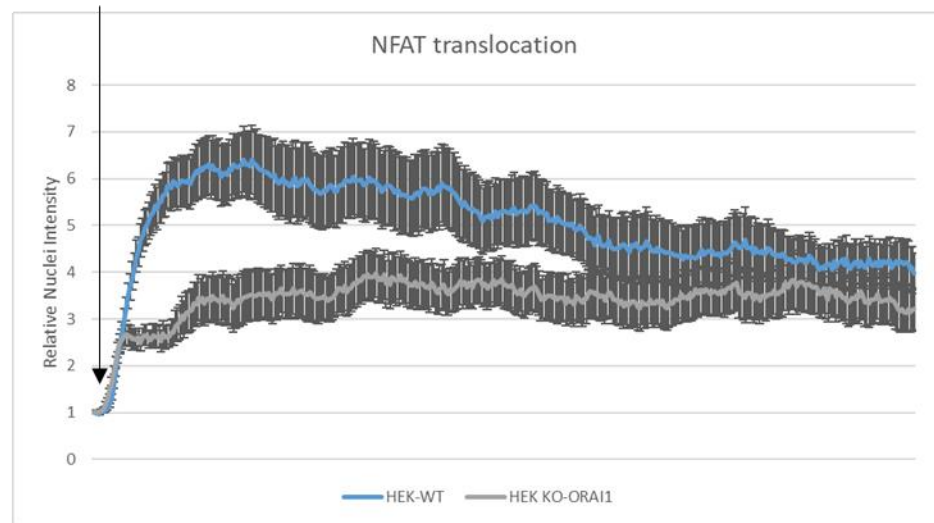
B



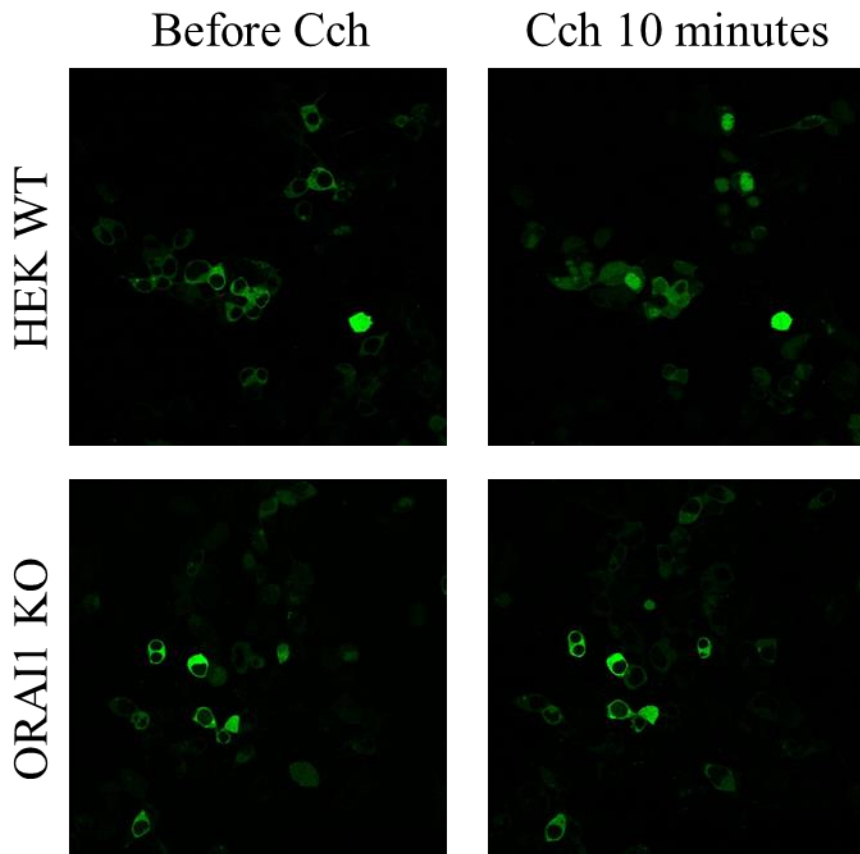
Annex 2 | Carbachol-induced Ca^{2+} oscillations in ORAI1 KO and WT HEK-293.

- A. Single-cell Ca^{2+} traces from ORAI1 KO HEK-293. The first peak corresponds to carbachol addition in the cell's medium. Experiments were carried out in a medium without Ca^{2+} .
- B. Ca^{2+} traces from WT HEK-293 single cells. The first peak corresponds to carbachol addition in the cell's medium. Experiments were carried out in a medium without Ca^{2+} .
- Note the different shapes of Ca^{2+} oscillations between ORAI1 KO and WT cells.

A Cch (100 μ M)

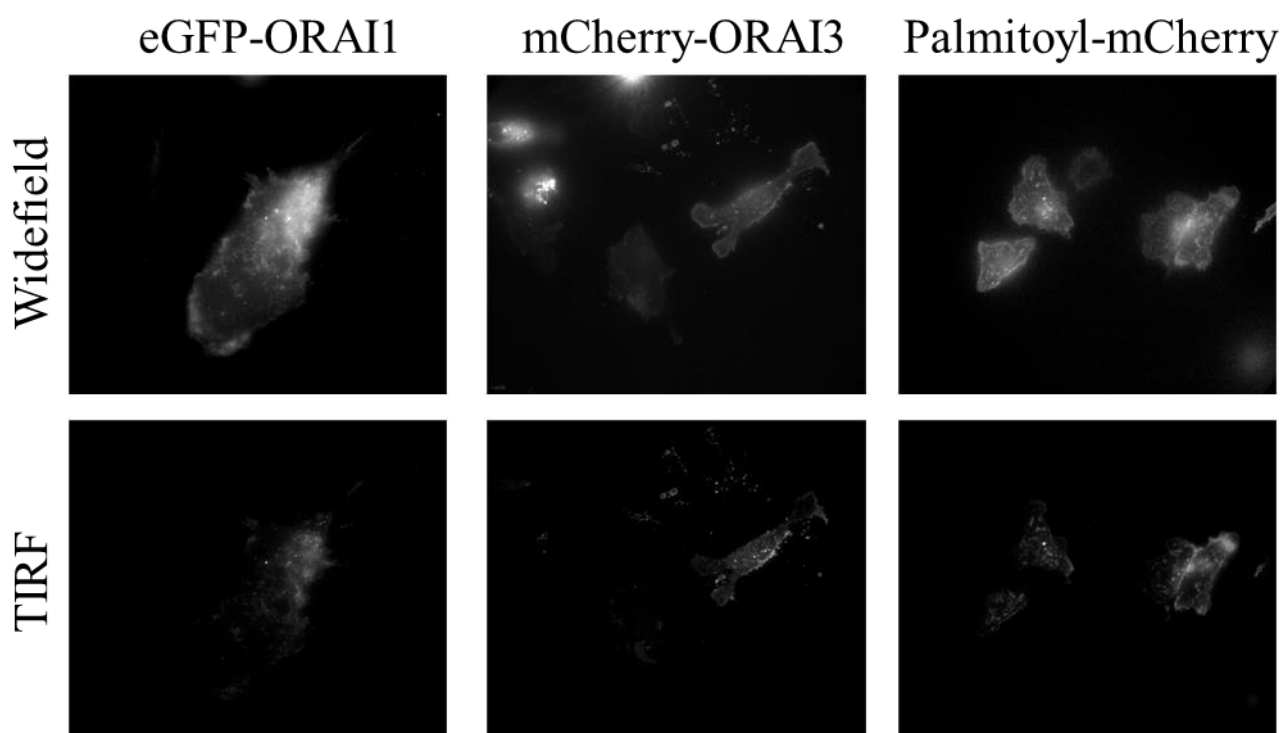


B



Annex 3 | NFAT translocation in ORAI1 KO and WT HEK-293.

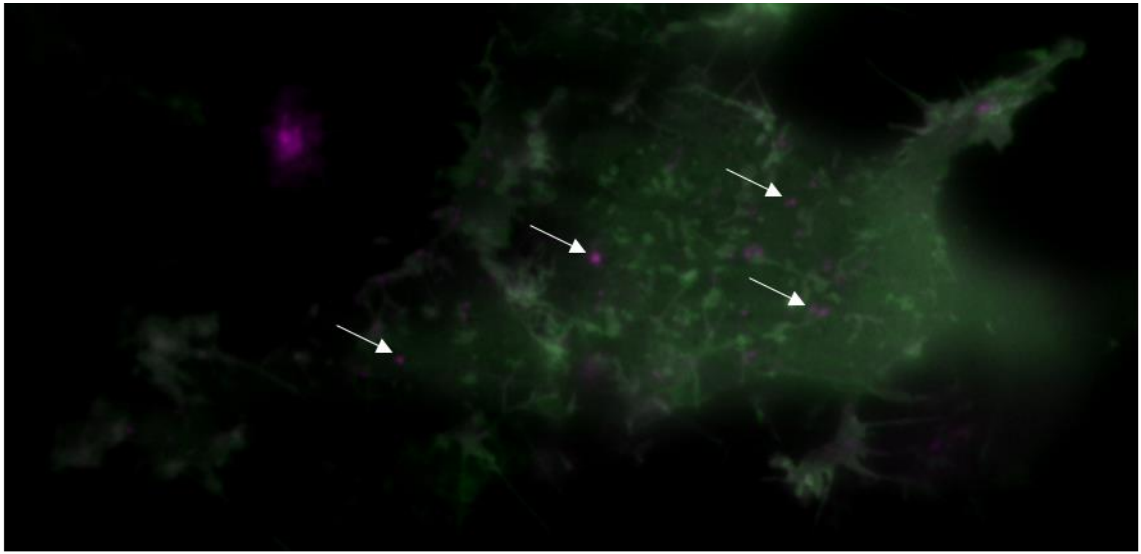
- A. The solid lanes represent the level of NFAT translocation into the cell nucleus following carbachol (Cch) addition in the cell medium.
- B. Representative image of the NFAT translocation experiment. ORAI1 KO and WT HEK cells were treated with 100 μ M carbachol (Cch) in a 2mM Ca^{2+} solution. The level of nuclear translocation of the NFAT-GFP reporter is lower in ORAI1 KO compared to WT HEK-293



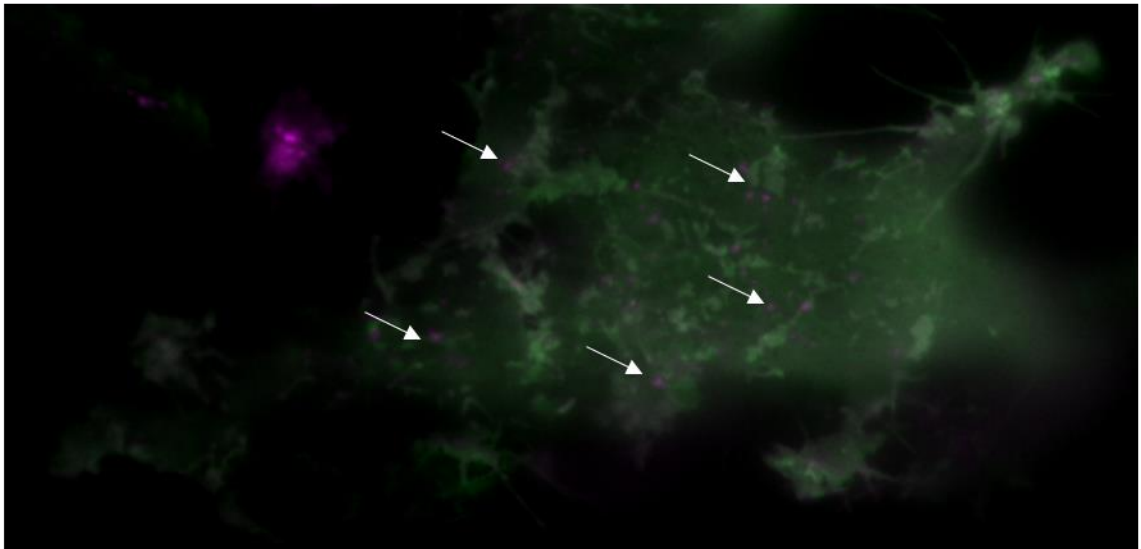
Annex 4 | Adjustments for TIRF microscopy.

Images of double KO PC3 (ORAI1+ORAI3) transfected with mGFP-ORAI1, mCherry-ORAI3, Palmitoyl-mCherry (membrane marker). Top lane: widefield microscopy images; Bottom lane: TIRF images.

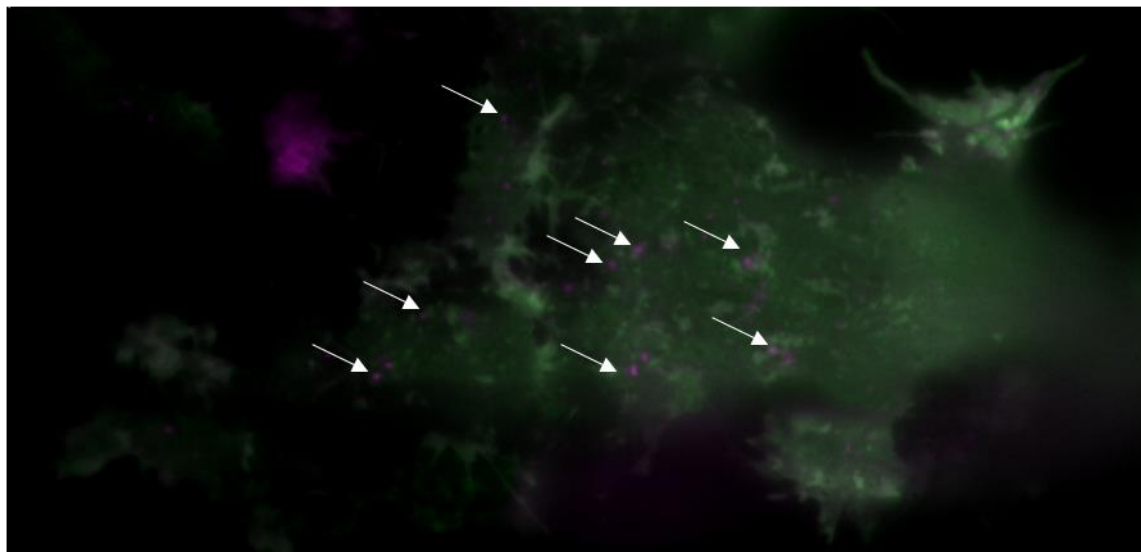
Before TG



TG (250 seconds)



TG (500 seconds)



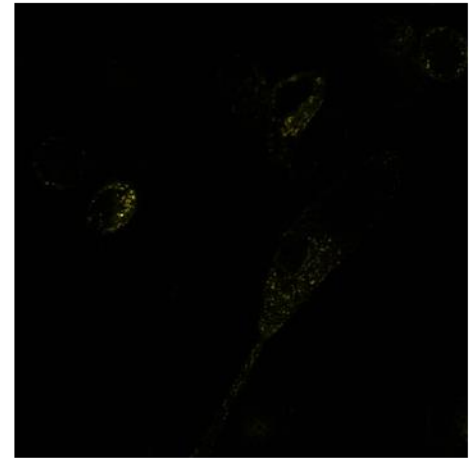
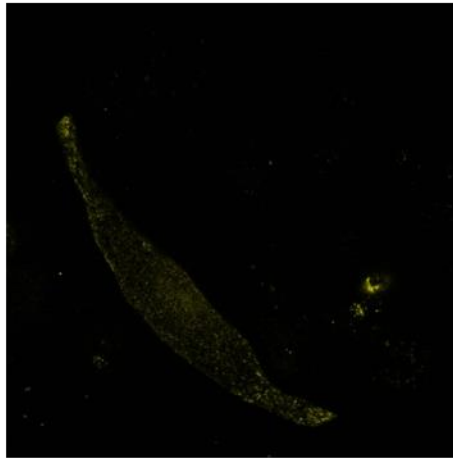
Annex 5 | TIRF microscopy thapsigargin treatment on double KO PC3.

Representative images of TIRF experiment performed on double KO PC3 (ORAI1+ORAI3) transfected with eGFP-ORAI1 and mCherry-ORAI3 plasmids, and treated with thapsigargin (TG). eGFP-ORAI1 and mCherry-ORAI3 signals are not totally colocalized. Following TG treatment, the number of isolated mCherry-ORAI3 spots seem to increase (white arrows)/

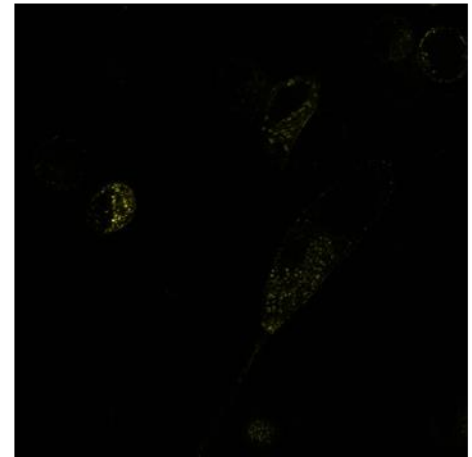
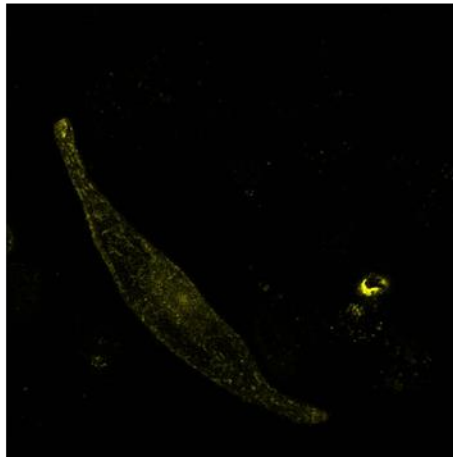
Venus 173C ORAI1
STIM1 Venus 173C

Venus 173C ORAI3
STIM1 Venus 173C

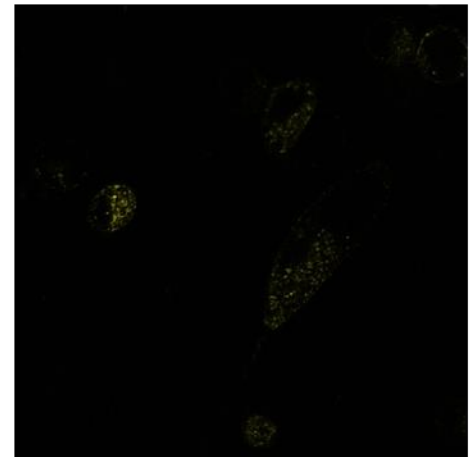
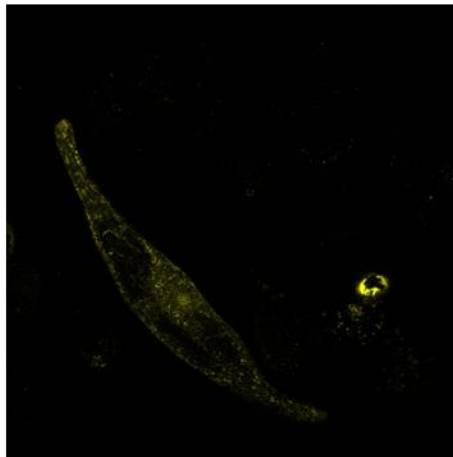
Before TG



TG 5
minutes

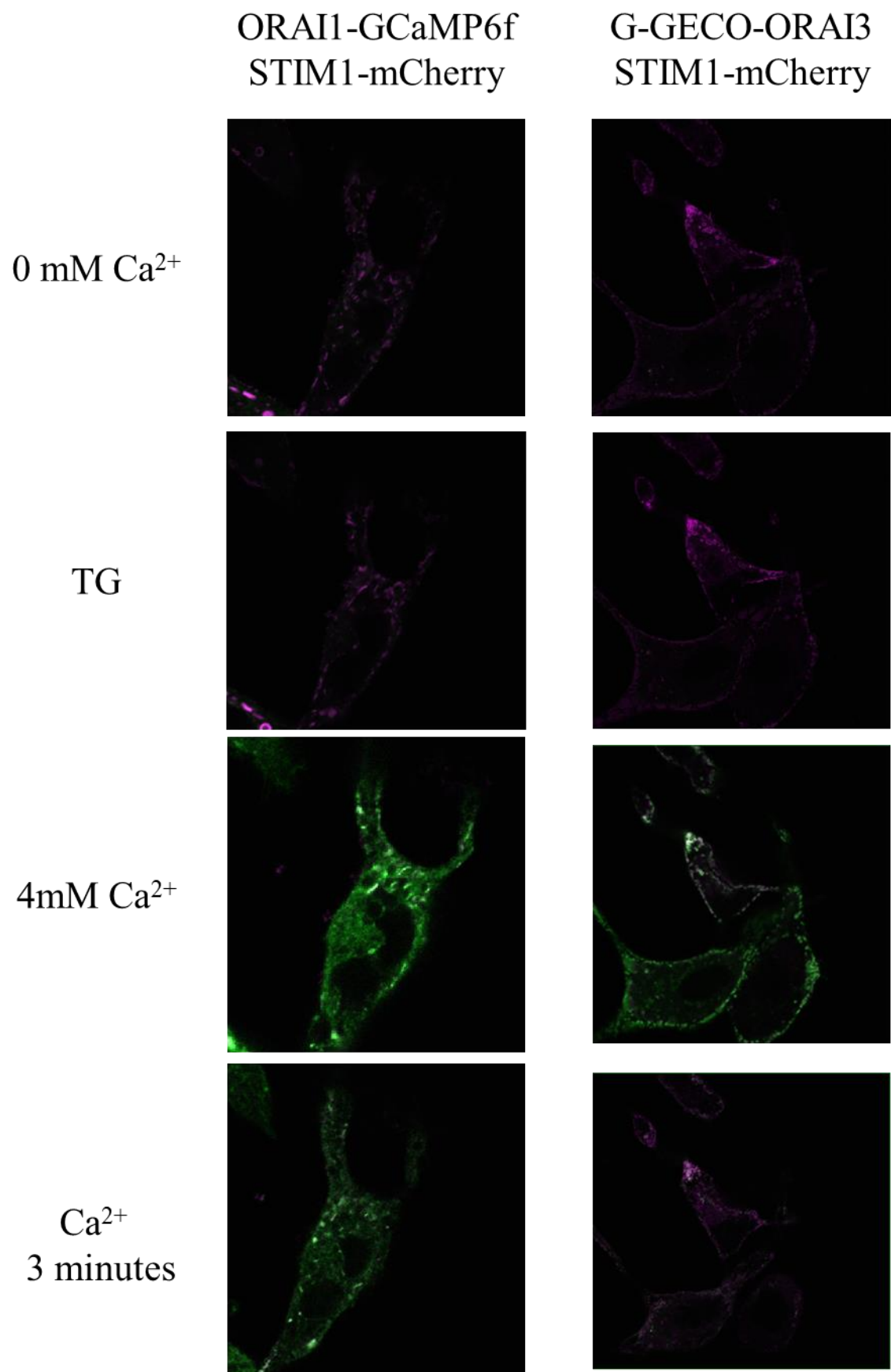


TG 10
minutes



Annex 6 | BifC experiment on double KO PC3 (ORAI1+ORAI3).

BiFC experiments were performed to assess the interaction level between ORAI1 and STIM1, and ORAI3 and STIM1 following CRAC activation by thapsigargin (TG). Both ORAI homologues are interacting with STIM in basal conditions. TG treatment seems to slightly increase the fluorescence intensity due to ORAI1 and STIM1 interaction, but not between ORAI3 and STIM1.



Annex 7 | CRAC activation visualization with ORAI-GECI.

The same protocol as for Ca^{2+} imaging experiment was used to induce store depletion and activate SOCE. PC3 WT were transfected with ORAI1-GCaMP6f and STIM1mCherry or with G-GECO-ORAI3 and STIM1mCherry plasmids. Cells were incubated in 0 mM Ca^{2+} calcium solution (0mM Ca^{2+}), thapsigargin (TG) was added to induce store-depletion. 4mM Ca^{2+} was added to visualize SOCE (4mM Ca^{2+}). Note Ca^{2+} release from ER store did not reach the ORAI1-GCaMP6f nor the G-GECO-ORAI3 protein. Addition of Ca^{2+} in the extracellular medium led to strong fluorescent signal indicating of Ca^{2+} transiting next to ORAI proteins. The Ca^{2+} quickly disappeared in the G-GECO-ORAI3 transfected cells while it was maintained in ORAI1-GCaMP6f transfected cells.

9. Bibliography

- Abdullaev IF, Bisailon JM, Potier M, Gonzalez JC, Motiani RK & Trebak M (2008) Stim1 and orai1 mediate crac currents and store-operated calcium entry important for endothelial cell proliferation. *Circ. Res.* **103**: 1289–1299
- Acuña AU, Amat-Guerri F, Morcillo P, Liras M & Rodríguez B (2009) Structure and formation of the fluorescent compound of lignum nephriticum. *Org. Lett.* **11**: 3020–3023
- Alansary D, Bogeski I & Niemeyer BA (2015) Facilitation of Orai3 targeting and store-operated function by Orai1. *Biochim. Biophys. Acta - Mol. Cell Res.* **1853**: 1541–1550 Available at: <http://dx.doi.org/10.1016/j.bbamcr.2015.03.007>
- Alansary D, Peckys DB, Niemeyer BA & De Jonge N (2020) Detecting single ORAI1 proteins within the plasma membrane reveals higher-order channel complexes. *J. Cell Sci.* **133**:
- Alford SC, Abdelfattah AS, Ding Y & Campbell RE (2012) A fluorogenic red fluorescent protein heterodimer. *Chem. Biol.* **19**: 353–360 Available at: <https://pubmed.ncbi.nlm.nih.gov/22444590/> [Accessed November 28, 2021]
- Alicia S, Angélica Z, Carlos S, Alfonso S & Vaca L (2008) STIM1 converts TRPC1 from a receptor-operated to a store-operated channel: Moving TRPC1 in and out of lipid rafts. *Cell Calcium* **44**: 479–491
- Amitai G & Sorek R (2016) CRISPR-Cas adaptation: Insights into the mechanism of action. *Nat. Rev. Microbiol.* **14**: 67–76
- Amos WB, White JG & Fordham M (1987) Use of confocal imaging in the study of biological structures. *Appl. Opt.* **26**: 3239 Available at: <https://pubmed.ncbi.nlm.nih.gov/20490049/> [Accessed October 17, 2021]
- Anderson PA V & Greenberg RM (2001) Phylogeny of ion channels: Clues to structure and function. *Comp. Biochem. Physiol. - B Biochem. Mol. Biol.* **129**: 17–28
- Antigny F, Sabourin J, Saüc S, Bernheim L, Koenig S & Frieden M (2017) TRPC1 and TRPC4 channels functionally interact with STIM1L to promote myogenesis and maintain fast repetitive Ca²⁺ release in human myotubes. *Biochim. Biophys. Acta - Mol. Cell Res.* **1864**: 806–813 Available at: <https://linkinghub.elsevier.com/retrieve/pii/S0167488917300289> [Accessed October 5, 2021]
- Ay A, Benzerdjeb N, Sevestre H, Ahidouch A & Ouadid- H (2015) Erratum: Orai3 Constitutes a Native Store-Operated Calcium Entry That Regulates Non Small Cell Lung Adenocarcinoma Cell Proliferation (PLOS ONE (2015) 10:4 (e0124201) 10.1371/journal.pone.0124201). *PLoS One* **10**: 1–11
- Bacon R (1267) Opus majus
- Baird GS, Zacharias DA & Tsien RY (1999) Circular permutation and receptor insertion within green fluorescent proteins. *Proc. Natl. Acad. Sci. U. S. A.* **96**: 11241–11246
- Ball CS (1966) The Early History of the Compound Microscope. *Bios* **37**: 51–60 Available at:

- <https://www.jstor.org/stable/4606667?origin=JSTOR-pdf> [Accessed October 12, 2021]
- Ball CS (2018) The Early History of the Compound Microscope. *Bios* **37**: 51–60
- Banach M, Konieczny L & Roterman I (2019) Secondary and Supersecondary Structure of Proteins in Light of the Structure of Hydrophobic Cores. In *Artificial Chemistries* pp 347–378. Available at: http://link.springer.com/10.1007/978-1-4939-9161-7_19
- Bandara S, Malmersjo S & Meyer T (2013) Regulators of Calcium Homeostasis Identified by Inference of Kinetic Model Parameters from Live Single Cells Perturbed by siRNA. *Sci. Signal.* **6**: ra56–ra56 Available at: <https://www.ncbi.nlm.nih.gov/pmc/articles/PMC3624763/pdf/nihms412728.pdf>
- Baraniak JH, Zhou Y, Nwokonko RM, Jennette MR, Kazzaz SA, Stenson JM, Whitsell AL, Wang Y, Trebak M & Gill DL (2021) Orai channel C-terminal peptides are key modulators of STIM-Orai coupling and calcium signal generation. *Cell Rep.* **35**: 109322 Available at: <https://doi.org/10.1016/j.celrep.2021.109322>
- Bardell D (2004) The Biologists' Forum: The invention of the microscope. *Bios* **75**: 78–84
- Barr VA, Bernot KM, Srikanth S, Gwack Y, Balagopalan L, Regan CK, Helman DJ, Sommers CL, Oh-hora M, Rao A & Samelson LE (2008) Dynamic Movement of the Calcium Sensor STIM1 and the Calcium Channel Orai1 in Activated T-Cells: Puncta and Distal Caps. *Mol. Biol. Cell* **19**: 2802 Available at: <https://www.ncbi.nlm.nih.gov/pmc/articles/PMC2441672/> [Accessed October 21, 2021]
- Barrangou R, Fremaux C, Deveau H, Richards M, Boyaval P, Moineau S, Romero DA & Horvath P (2007) CRISPR Provides Acquired Resistance Against Viruses in Prokaryotes. *Science* (80-.). **315**: 1709–1712 Available at: <https://www.science.org/doi/abs/10.1126/science.1138140> [Accessed November 5, 2021]
- Barrera NP, Ormond SJ, Henderson RM, Murrell-Lagnado RD & Edwardson JM (2005) Atomic force microscopy imaging demonstrates that P2X2 receptors are trimers but that P2X6 receptor subunits do not oligomerize. *J. Biol. Chem.* **280**: 10759–10765
- Barritt GJ, Litjens TL, Castro J, Aromataris E & Rychkov GY (2009) Store-Operated Ca²⁺ Channels and Microdomains of Ca²⁺ in Liver Cells. *Clin. Exp. Pharmacol. Physiol.* **36**: 77–83 Available at: <https://onlinelibrary.wiley.com/doi/10.1111/j.1440-1681.2008.05095.x>
- Bayle V, Fiche JB, Burny C, Platre MP, Nollmann M, Martinière A & Jaillais Y (2021) Single-particle tracking photoactivated localization microscopy of membrane proteins in living plant tissues. *Nat. Protoc.* **16**: 1600–1628
- Benzerdjeb N, Sevestre H, Ahidouch A & Ouadid-Ahidouch H (2016) Orai3 is a predictive marker of metastasis and survival in resectable lung adenocarcinoma. *Oncotarget* **7**: 81588–81597
- Berridge MJ, Bootman MD & Roderick HL (2003) Calcium signalling: Dynamics, homeostasis and remodelling. *Nat. Rev. Mol. Cell Biol.* **4**: 517–529
- Bidaux G, Le Nézet C, Pisfil MG, Henry M, Furlan A, Bensaude O, Vandenbunder B & Héliot L (2018) FRET Image Correlation Spectroscopy Reveals RNAPII-Independent P-TEFb

- Recruitment on Chromatin. *Biophys. J.* **114**: 522–533
- Boel A, De Saffel H, Steyaert W, Callewaert B, De Paepe A, Coucke PJ & Willaert A (2018) CRISPR/Cas9-mediated homology-directed repair by ssODNs in zebrafish induces complex mutational patterns resulting from genomic integration of repair-template fragments. *Dis. Model. Mech.* **11**: dmm035352 Available at: <http://dmm.biologists.org/lookup/doi/10.1242/dmm.035352>
- Bohórquez-Hernández A, Gratton E, Pacheco J, Asanov A & Vaca L (2017) Cholesterol modulates the cellular localization of Orai1 channels and its disposition among membrane domains. *Biochim. Biophys. Acta - Mol. Cell Biol. Lipids* **1862**: 1481–1490 Available at: [file:///C:/Users/Carla Carolina/Desktop/Artigos para acrescentar na qualificação/The impact of birth weight on cardiovascular disease risk in the.pdf](file:///C:/Users/Carla%20Carolina/Desktop/Artigos%20para%20acrescentar%20na%20qualifica%C3%A7%C3%A3o/The%20impact%20of%20birth%20weight%20on%20cardiovascular%20disease%20risk%20in%20the.pdf)
- Bolotin A, Quinquis B, Sorokin A & Ehrlich SD (2005) Clustered regularly interspaced short palindrome repeats (CRISPRs) have spacers of extrachromosomal origin. *Microbiology* **151**: 2551–2561 Available at: <https://pubmed-ncbi-nlm-nih-gov.proxy.insermbiblio.inist.fr/16079334/> [Accessed November 5, 2021]
- Borowiec AS, Bidaux G, Tacine R, Dubar P, Pigat N, Delcourt P, Mignen O & Capiod T (2014) Are Orai1 and Orai3 channels more important than calcium influx for cell proliferation? *Biochim. Biophys. Acta - Mol. Cell Res.* **1843**: 464–472 Available at: <http://dx.doi.org/10.1016/j.bbamcr.2013.11.023>
- El Boustany C, Katsogiannou M, Delcourt P, Dewailly E, Prevarskaya N, Borowiec A-S & Capiod T (2010) Differential roles of STIM1, STIM2 and Orai1 in the control of cell proliferation and SOCE amplitude in HEK293 cells. *Cell Calcium* **47**: 350–359 Available at: <https://linkinghub.elsevier.com/retrieve/pii/S0143416010000175> [Accessed October 23, 2021]
- Brough GH, Wu S, Cioffi D, Moore TM, Li M, Dean N & Stevens T (2001) Contribution of endogenously expressed Trp1 to a Ca²⁺-selective, store-operated Ca²⁺ entry pathway. *FASEB J.* **15**: 1727–1738
- Bulina ME, Verkhusha V V, Staroverov DB, Chudakov DM & Lukyanov KA (2003) Hetero-oligomeric tagging diminishes non-specific aggregation of target proteins fused with Anthozoa fluorescent proteins. *Biochem. J* **371**: 109
- Bunt G & Wouters FS (2017) FRET from single to multiplexed signaling events. *Biophys. Rev.* **9**: 119–129
- Butorac C, Muik M, Derler I, Stadlbauer M, Lunz V, Krizova A, Lindinger S, Schober R, Frischauf I, Bhardwaj R, Hediger MA, Groschner K & Romanin C (2019) A novel STIM1-Orai1 gating interface essential for CRAC channel activation. *Cell Calcium* **79**: 57–67
- Cai X (2007) Molecular Evolution and Structural Analysis of the Ca²⁺ Release-Activated Ca²⁺ Channel Subunit, Orai. *J. Mol. Biol.* **368**: 1284–1291
- Cai X, Zhou Y, Nwokonko RM, Loktionova NA, Wang X, Xin P, Trebak M, Wang Y & Gill DL (2016) The Orai1 store-operated calcium channel functions as a hexamer. *J. Biol. Chem.* **291**:

- Campbell RE, Tour O, Palmer AE, Steinbach PA, Baird GS, Zacharias DA & Tsien RY (2002) A monomeric red fluorescent protein. *Proc. Natl. Acad. Sci.* **99**: 7877–7882 Available at: <https://www.pnas.org/content/99/12/7877> [Accessed October 27, 2021]
- Cantonero C, Sánchez-Collado J, Lopez JJ, Salido GM, Rosado JA & Redondo PC (2020) Arachidonic Acid Attenuates Cell Proliferation, Migration and Viability by a Mechanism Independent on Calcium Entry. *Int. J. Mol. Sci.* **21**: Available at: [/pmc/articles/PMC7247542/](https://pubmed.ncbi.nlm.nih.gov/3247542/) [Accessed October 19, 2021]
- Casteels R & Droogmans G (1981) Exchange characteristics of the noradrenaline-sensitive calcium store in vascular smooth muscle cells or rabbit ear artery. *J. Physiol.* **317**: 263–279
- Catacuzzeno L & Franciolini F (2018) Role of KCa3.1 channels in modulating Ca^{2+} oscillations during glioblastoma cell migration and invasion. *Int. J. Mol. Sci.* **19**: 1–15
- Cavalier-Smith T (2000) Membrane heredity and early chloroplast evolution. *Trends Plant Sci.* **5**: 174–182
- Chalfie M, Tu Y, Euskirchen G, Ward WW & Prasher DC (1994) Green fluorescent protein as a marker for gene expression. *Science* (80-.). **263**: 802–805
- Chalmers SB & Monteith GR (2018) ORAI channels and cancer. *Cell Calcium* **74**: 160–167 Available at: <https://doi.org/10.1016/j.ceca.2018.07.011>
- Chang C-L, Chen Y-J, Quintanilla CG, Hsieh T-S & Liou J (2018) EB1 binding restricts STIM1 translocation to ER–PM junctions and regulates store-operated Ca^{2+} entry. *J. Cell Biol.* **217**: 2047–2058 Available at: <https://doi.org/10.1083/jcb.201711151> [Accessed October 6, 2021]
- Chang Q, Gyftogianni E, Graaf SFJ van de, Hoefs S, Weidema FA, Bindels RJM & Hoenderop JGJ (2004) Molecular Determinants in TRPV5 Channel Assembly *. *J. Biol. Chem.* **279**: 54304–54311 Available at: <http://www.jbc.org/article/S002192581963190X/fulltext> [Accessed October 4, 2021]
- Chavez A, Scheiman J, Vora S, Pruitt BW, Tuttle M, P R Iyer E, Lin S, Kiani S, Guzman CD, Wiegand DJ, Ter-Ovanesyan D, Braff JL, Davidsohn N, Housden BE, Perrimon N, Weiss R, Aach J, Collins JJ & Church GM (2015) Highly efficient Cas9-mediated transcriptional programming. *Nat. Methods* **12**: 326–328 Available at: <https://pubmed.ncbi.nlm.nih.gov/25730490/> [Accessed November 7, 2021]
- Chen X, Xu F, Zhu C, Ji J, Zhou X, Feng X & Guang S (2014) Dual sgRNA-directed gene knockout using CRISPR/Cas9 technology in *Caenorhabditis elegans*. *Sci. Rep.* **4**: 1–7
- Cheng KT, Liu X, Ong HL, Swaim W & Ambudkar IS (2011) Local Ca^{2+} entry via Orai1 regulates plasma membrane recruitment of TRPC1 and controls cytosolic Ca^{2+} signals required for specific cell functions. *PLoS Biol.* **9**: 26–34
- Cheng KT, Ong HL, Liu X & Ambudkar IS (2013) Contribution and Regulation of TRPC Channels in Store-Operated Ca^{2+} Entry. In *Current topics in membranes* pp 149–179. NIH Public Access

- Available at: [/pmc/articles/PMC3824975/](https://pmc/articles/PMC3824975/) [Accessed October 10, 2021]
- Chiarella AM, Butler K V., Gryder BE, Lu D, Wang TA, Yu X, Pomella S, Khan J, Jin J & Hathaway NA (2019) Dose-dependent activation of gene expression is achieved using CRISPR and small molecules that recruit endogenous chromatin machinery. *Nat. Biotechnol.* 2019 381 **38**: 50–55 Available at: <https://www.nature.com/articles/s41587-019-0296-7> [Accessed November 28, 2021]
- Clapham DE (2007) Calcium Signaling. *Cell* **131**: 1047–1058
- Concepcion AR, Vaeth M, Wagner LE, Eckstein M, Hecht L, Jun Y, Crottes D, Seidl M, Shin HP, Weidinger C, Cameron S, Turvey SE, Issekutz T, Meyts I, Lacruz RS, Cuk M, Yule DI & Feske S (2016) Store-operated Ca²⁺ entry regulates Ca²⁺-activated chloride channels and eccrine sweat gland function. *J. Clin. Invest.* **126**: 4303–4318
- Concordet J-P & Haeussler M (2018) CRISPOR: intuitive guide selection for CRISPR/Cas9 genome editing experiments and screens. *Nucleic Acids Res.* **46**: W242–W245 Available at: <https://academic.oup.com/nar/article/46/W1/W242/4995687> [Accessed October 22, 2021]
- Costantini LM, Fossati M, Francolini M & Snapp EL (2012) Assessing the Tendency of Fluorescent Proteins to Oligomerize Under Physiologic Conditions. *Traffic* **13**: 643–649 Available at: <https://onlinelibrary.wiley.com/doi/full/10.1111/j.1600-0854.2012.01336.x> [Accessed October 27, 2021]
- Covington ED, Wu MM & Lewis RS (2010) Essential Role for the CRAC Activation Domain in Store-dependent Oligomerization of STIM1. *Mol. Biol. Cell* **21**: 1897–1907 Available at: <https://www.molbiolcell.org/doi/10.1091/mbc.e10-02-0145>
- D. Davenport and J. A. C. Nicol (1955) Luminescence in Hydromedusae. *Proc. R. Soc. London. Ser. B - Biol. Sci.* **144**: 399–411 Available at: <https://royalsocietypublishing.org/doi/abs/10.1098/rspb.1955.0066> [Accessed October 12, 2021]
- Darbellay B, Arnaudeau S, Bader CR, König S & Bernheim L (2011) STIM1L is a new actin-binding splice variant involved in fast repetitive Ca²⁺ release. *J. Cell Biol.* **194**: 335–346 Available at: www.jcb.org/cgi/doi/10.1083/jcb.201012157 [Accessed October 5, 2021]
- Darbellay B, Arnaudeau S, König S, Jousset H, Bader C, Demaurex N & Bernheim L (2009) STIM1- and Orai1-dependent store-operated calcium entry regulates human myoblast differentiation. *J. Biol. Chem.* **284**: 5370–5380
- Davidson MW & Abramowitz M (2002) Optical Microscopy. In *Encyclopedia of Imaging Science and Technology*, Hornak JP (ed) Hoboken, NJ, USA: John Wiley & Sons, Inc. Available at: <http://doi.wiley.com/10.1002/0471443395>
- DeCoursey TE (2013) Voltage-gated proton channels: Molecular biology, physiology, and pathophysiology of the HV family. *Physiol. Rev.* **93**: 599–652
- Al Deek M (2004) Ibn Al-Haitham Master of Optics, mathematics, Physics and Medecins. *Al Shindagah*

- DeHaven WI, Smyth JT, Boyles RR, Bird GS & Putney JW (2008) Complex actions of 2-aminoethyldiphenyl borate on store-operated calcium entry. *J. Biol. Chem.* **283**: 19265–19273
- DeHaven WI, Smyth JT, Boyles RR & Putney JW (2007) Calcium inhibition and calcium potentiation of Orai1, Orai2, and Orai3 calcium release-activated calcium channels. *J. Biol. Chem.* **282**: 17548–17556
- Demuro A, Penna A, Safrina O, Yeromin A V., Amcheslavsky A, Cahalan MD & Parker I (2011) Subunit stoichiometry of human Orai1 and Orai3 channels in closed and open states. *Proc. Natl. Acad. Sci.* **108**: 17832–17837 Available at: <http://www.pnas.org/cgi/doi/10.1073/pnas.1114814108>
- Derler I, Plenck P, Fahrner M, Muik M, Jardin I, Schindl R, Gruber HJ, Groschner K & Romanin C (2013) The extended transmembrane orai1 N-terminal (ETON) region combines binding interface and gate for orai1 activation by STIM1. *J. Biol. Chem.* **288**: 29025–29034
- Desai PN, Zhang X, Wu S, Janoshazi A, Bolimuntha S, Putney JW & Trebak M (2015) Multiple types of calcium channels arising from alternative translation initiation of the Orai1 message. *Sci. Signal.* **8**: ra74–ra74 Available at: <https://stke.sciencemag.org/lookup/doi/10.1126/scisignal.aaa8323>
- Dickson EJ, Duman JG, Moody MW, Chen L & Hille B (2012) Orai-STIM-mediated Ca²⁺ release from secretory granules revealed by a targeted Ca²⁺ and pH probe. *Proc. Natl. Acad. Sci. U. S. A.* **109**:
- Diez-Bello R, Jardin I, Salido GM & Rosado JA (2017) Orai1 and Orai2 mediate store-operated calcium entry that regulates HL60 cell migration and FAK phosphorylation. *Biochim. Biophys. Acta - Mol. Cell Res.* **1864**: 1064–1070 Available at: <http://dx.doi.org/10.1016/j.bbamcr.2016.11.014>
- Dobrucki JW (2013) 3 Fluorescence Microscopy.
- Dong H, Zhang Y, Song R, Xu J, Yuan Y, Liu J, Li J, Zheng S, Liu T, Lu B, Wang Y & Klein ML (2019) Toward a Model for Activation of Orai Channel. *iScience* **16**: 356–367 Available at: <https://click.endnote.com/viewer?doi=10.1016%2Fj.isci.2019.05.041&token=Wzg2MzksIjEwLjEwMTYvai5pc2NpLjIwMTkuMDUuMDQxIl0.Pr0njrOYX77k75vCpk7ftBx12iE> [Accessed November 24, 2021]
- Dörr K, Kilch T, Kappel S, Alansary D, Schwär G, Niemeyer BA & Peinelt C (2016) Cell type-specific glycosylation of Orai1 modulates store-operated Ca²⁺ entry. *Sci. Signal.* **9**: 1–15
- Dragoni S, Turin I, Laforenza U, Potenza DM, Bottino C, Glasnov TN, Prestia M, Ferulli F, Saitta A, Mosca A, Guerra G, Rosti V, Luinetti O, Ganini C, Porta C, Pedrazzoli P, Tanzi F, Montagna D & Moccia F (2014) Store-operated Ca²⁺ entry does not control proliferation in primary cultures of human metastatic renal cellular carcinoma. *Biomed Res. Int.* **2014**:
- Dubois C, Vanden Abeele F, Lehen'kyi V, Gkika D, Guarmit B, Lepage G, Slomianny C, Borowiec AS, Bidaux G, Benahmed M, Shuba Y & Prevarskaya N (2014a) Remodeling of Channel-

- Forming Orai Proteins Determines an Oncogenic Switch in Prostate Cancer. *Cancer Cell* **26**: 19–32 Available at: <http://dx.doi.org/10.1016/j.ccr.2014.04.025>
- Dubois C, Vanden Abeele F, Lehen'kyi V, Gkika D, Guarmit B, Lepage G, Slomianny C, Borowiec AS, Bidaux G, Benahmed M, Shuba Y & Prevarskaya N (2014b) Remodeling of Channel-Forming Orai Proteins Determines an Oncogenic Switch in Prostate Cancer. *Cancer Cell* **26**: 19–32 Available at: <http://dx.doi.org/10.1016/j.ccr.2014.04.025>
- Dubois C, Vanden Abeele F, Lehen'kyi V, Gkika D, Guarmit B, Lepage G, Slomianny C, Borowiec AS, Bidaux G, Benahmed M, Shuba Y & Prevarskaya N (2014c) Remodeling of Channel-Forming Orai Proteins Determines an Oncogenic Switch in Prostate Cancer. *Cancer Cell* **26**: 19–32 Available at: <http://dx.doi.org/10.1016/j.ccr.2014.04.025>
- Dubois C, Kondratska K, Kondratskyi A, Morabito A, Mesilmany L, Farfariello V, Toillon RA, Ziental Gelus N, Laurence E, Vanden Abeele F, Lemonnier L & Prevarskaya N (2021) Orai3 silencing alters cell proliferation and promotes mitotic catastrophe and apoptosis in pancreatic adenocarcinoma. *Biochim. Biophys. Acta - Mol. Cell Res.* **1868**: 119023 Available at: <https://doi.org/10.1016/j.bbamcr.2021.119023>
- Dynes JL, Amcheslavsky A & Cahalan MD (2016a) Genetically targeted single-channel optical recording reveals multiple Orai1 gating states and oscillations in calcium influx. **113**:
- Dynes JL, Amcheslavsky A & Cahalan MD (2016b) Genetically targeted single-channel optical recording reveals multiple Orai1 gating states and oscillations in calcium influx. *Proc. Natl. Acad. Sci.* **113**: 440–445 Available at: <http://www.pnas.org/lookup/doi/10.1073/pnas.1523410113>
- Dynes JL, Yeromin A V. & Cahalan MD (2020) Cell-wide mapping of Orai1 channel activity reveals functional heterogeneity in STIM1-Orai1 puncta. *J. Gen. Physiol.* **152**:
- Dyrda A, Koenig S & Frieden M (2020) STIM1 long and STIM1 gate differently TRPC1 during store-operated calcium entry. *Cell Calcium* **86**: 102134
- Eckstein M, Vaeth M, Aulestia FJ, Costiniti V, Kassam SN, Bromage TG, Pedersen P, Issekutz T, Idaghdour Y, Moursi AM, Feske S & Lacruz RS (2019a) Differential regulation of Ca²⁺ influx by Orai channels mediates enamel mineralization. *Sci. Signal.* **12**: 1–13
- Eckstein M, Vaeth M, Aulestia FJ, Costiniti V, Kassam SN, Bromage TG, Pedersen P, Issekutz T, Idaghdour Y, Moursi AM, Feske S & Lacruz RS (2019b) Differential regulation of Ca²⁺ influx by Orai channels mediates enamel mineralization. *Sci. Signal.* **12**: 1–13
- Emrich SM, Yoast RE, Xin P, Arige V, Wagner LE, Hempel N, Gill DL, Sneyd J, Yule DI & Trebak M (2021) Omnitemporal choreographies of all five STIM/Orai and IP3Rs underlie the complexity of mammalian Ca²⁺ signaling. *Cell Rep.* **34**: 108760 Available at: <https://doi.org/10.1016/j.celrep.2021.108760>
- Enoch JM (1999) Remarkable lenses and eye units in statues from the Egyptian Old Kingdom (ca. 4500 years ago): properties, timeline, questions requiring resolution.

- <https://doi.org/10.1117/12.354722> **3749**: 224–225 Available at: <https://www.spiedigitallibrary.org/conference-proceedings-of-spie/3749/0000/Remarkable-lenses-and-eye-units-in-statues-from-the-Egyptian/10.1117/12.354722.full> [Accessed October 26, 2021]
- Fahrner M, Muik M, Derler I, Schindl R, Fritsch R, Frischauf I & Romanin C (2009) Mechanistic view on domains mediating STIM1-Orai coupling. *Immunol. Rev.* **231**: 99–112 Available at: <https://pubmed.ncbi.nlm.nih.gov/19754892/> [Accessed October 6, 2021]
- Fahrner M, Muik M, Schindl R, Butorac C, Stathopoulos P, Zheng L, Jardin I, Ikura M & Romanin C (2014) A Coiled-coil Clamp Controls Both Conformation and Clustering of Stromal Interaction Molecule 1 (STIM1). *J. Biol. Chem.* **289**: 33231–33244 Available at: <https://pubmed.ncbi.nlm.nih.gov/25342749/> [Accessed October 6, 2021]
- Fahrner M, Pandey SK, Muik M, Traxler L, Butorac C, Stadlbauer M, Zayats V, Krizova A, Plenk P, Frischauf I, Schindl R, Gruber HJ, Hinterdorfer P, Ettrich R, Romanin C & Derler I (2018) Communication between N terminus and loop2 tunes Orai activation. *J. Biol. Chem.* **293**: 1271–1285 Available at: <https://pubmed.ncbi.nlm.nih.gov/29237733/> [Accessed October 7, 2021]
- Faouzi M, Hague F, Potier M, Ahidouch A, Sevestre H & Ouadid-Ahidouch H (2011) Down-regulation of Orai3 arrests cell-cycle progression and induces apoptosis in breast cancer cells but not in normal breast epithelial cells. *J. Cell. Physiol.* **226**: 542–551
- Feske S (2009) ORAI1 and STIM1 deficiency in human and mice: roles of store-operated Ca²⁺ entry in the immune system and beyond. *Immunol. Rev.* **231**: 189–209 Available at: <https://pubmed.ncbi.nlm.nih.gov/19754898/> [Accessed October 11, 2021]
- Feske S (2011) CRAC channelopathies Stefan. *Pflugers Arch* **460**: 417–435
- Feske S, Gwack Y, Prakriya M, Srikanth S, Puppel SH, Tanasa B, Hogan PG, Lewis RS, Daly M & Rao A (2006) A mutation in Orai1 causes immune deficiency by abrogating CRAC channel function. *Nature* **441**: 179–185
- Fetrow JS (1995) Omega loops; nonregular secondary structures significant in protein function and stability. *FASEB J.* **9**: 708–717
- Fiorio Pla A & Munaron L (2001) Calcium influx, arachidonic acid, and control of endothelial cell proliferation. *Cell Calcium* **30**: 235–244 Available at: <https://pubmed.ncbi.nlm.nih.gov.proxy.insermbiblio.inist.fr/11587547/> [Accessed October 11, 2021]
- Forsell P, Eberhardson M, Lennernas H, Knutson T & Knutson L (2006) Rapid modulation of Ca²⁺ uptake in human jejunal enterocytes. *Biochem. Biophys. Res. Commun.* **340**: 961–966
- Forster T (1946) Energiewanderung und Fluoreszenz. *Naturwissenschaften* 1946 336 **33**: 166–175 Available at: <https://link.springer.com/article/10.1007/BF00585226> [Accessed November 2, 2021]
- Förster T (1948) Zwischenmolekulare Energiewanderung und Fluoreszenz. *Ann. Phys.* **437**: 55–75 Available at: <https://onlinelibrary.wiley.com/doi/full/10.1002/andp.19484370105> [Accessed

November 2, 2021]

- Frischauf I, Muik M, Derler I, Bergsmann J, Fahmer M, Schindl R, Groschner K & Romanin C (2009a) Molecular determinants of the coupling between STIM1 and Orai channels: Differential activation of Orai1-3 channels by a STIM1 coiled-coil mutant. *J. Biol. Chem.* **284**: 21696–21706
- Frischauf I, Muik M, Derler I, Bergsmann J, Fahmer M, Schindl R, Groschner K & Romanin C (2009b) Molecular determinants of the coupling between STIM1 and Orai channels: Differential activation of Orai1-3 channels by a STIM1 coiled-coil mutant. *J. Biol. Chem.* **284**: 21696–21706
- Frischauf I, Muik M, Derler I, Bergsmann J, Fahrner M, Schindl R, Groschner K & Romanin C (2009c) Molecular Determinants of the Coupling between STIM1 and Orai Channels. *J. Biol. Chem.* **284**: 21696–21706
- Frischauf I, Schindl R, Bergsmann J, Derler I, Fahrner M, Muik M, Fritsch R, Lackner B, Groschner K & Romanin C (2011) Cooperativeness of Orai cytosolic domains tunes subtype-specific gating. *J. Biol. Chem.* **286**: 8577–8584
- Fujiwara Y, Kurokawa T, Takeshita K, Kobayashi M, Okochi Y, Nakagawa A & Okamura Y (2012) The cytoplasmic coiled-coil mediates cooperative gating temperature sensitivity in the voltage-gated H⁺ channel Hv1. *Nat. Commun.* 2012 31 **3**: 1–11 Available at: <https://www.nature.com/articles/ncomms1823> [Accessed October 4, 2021]
- Fukushima M, Tomita T, Janoshazi A & Putney JW (2012) Alternative translation initiation gives rise to two isoforms of Orai1 with distinct plasma membrane mobilities. *J. Cell Sci.* **125**: 4354–4361 Available at: <http://jcs.biologists.org/cgi/doi/10.1242/jcs.104919>
- Gammons J, Trebak M & Mancarella S (2021) Cardiac-specific deletion of orai3 leads to severe dilated cardiomyopathy and heart failure in mice. *J. Am. Heart Assoc.* **10**:
- Ganger MT, Dietz GD & Ewing SJ (2017) A common base method for analysis of qPCR data and the application of simple blocking in qPCR experiments. *BMC Bioinformatics* **18**: 1–11
- Gao Y, Hisey E, Bradshaw TWA, Erata E, Brown WE, Courtland JL, Uezu A, Xiang Y, Diao Y & Soderling SH (2019) Plug-and-Play Protein Modification Using Homology-Independent Universal Genome Engineering. *Neuron* **103**: 583-597.e8 Available at: <https://doi.org/10.1016/j.neuron.2019.05.047>
- Ghiran IC (2011) Light Microscopy Chiarini-Garcia H & Melo RCN (eds) Totowa, NJ: Humana Press Available at: <http://link.springer.com/10.1007/978-1-60761-950-5>
- González-Cobos JC, Zhang X, Zhang W, Ruhle B, Motiani RK, Schindl R, Muik M, Spinelli AM, Bisailon JM, Shinde A V., Fahrner M, Singer HA, Matrougui K, Barroso M, Romanin C & Trebak M (2013) Store-independent Orai1/3 channels activated by intracrine leukotriene₄: Role in neointimal hyperplasia. *Circ. Res.* **112**: 1013–1025
- Griesbeck O, Baird GS, Campbell RE, Zacharias DA & Tsien RY (2001) Reducing the Environmental Sensitivity of Yellow Fluorescent Protein: MECHANISM AND APPLICATIONS *. *J. Biol. Chem.* **276**: 29188–29194 Available at: <http://www.jbc.org/article/S0021925820803858/fulltext>

[Accessed October 27, 2021]

- Gross SA, Wissenbach U, Philipp SE, Freichel M, Cavalié A & Flockerzi V (2007) Murine ORAI2 splice variants form functional Ca^{2+} release-activated Ca^{2+} (CRAC) channels. *J. Biol. Chem.* **282**: 19375–19384
- Grynkiewicz G, Poenie M & Tsien RY (1985) A new generation of Ca^{2+} indicators with greatly improved fluorescence properties. *J. Biol. Chem.* **260**: 3440–3450
- Gunthorpe MJ, Harries MH, Prinjha RK, Davis JB & Randall A (2000) Voltage- and time-dependent properties of the recombinant rat vanilloid receptor (rVR1). *J. Physiol.* **525**: 747–759
- Gwack Y, Srikanth S, Feske S, Cruz-Guilloty F, Oh-hora M, Neems DS, Hogan PG & Rao A (2007a) Biochemical and functional characterization of orai proteins. *J. Biol. Chem.* **282**: 16232–16243
- Gwack Y, Srikanth S, Feske S, Cruz-Guilloty F, Oh-hora M, Neems DS, Hogan PG & Rao A (2007b) Biochemical and functional characterization of orai proteins. *J. Biol. Chem.* **282**: 16232–16243
- Haeussler M, Schönig K, Eckert H, Eschstruth A, Mianné J, Renaud JB, Schneider-Maunoury S, Shkumatava A, Teboul L, Kent J, Joly JS & Concordet JP (2016) Evaluation of off-target and on-target scoring algorithms and integration into the guide RNA selection tool CRISPOR. *Genome Biol.* **17**:
- Hayashi K, Yamamoto TS & Ueno N (2018) Intracellular calcium signal at the leading edge regulates mesodermal sheet migration during *Xenopus* gastrulation. *Sci. Rep.* **8**: 1–12 Available at: <http://dx.doi.org/10.1038/s41598-018-20747-w>
- He J, Yu T, Pan J & Li H (2012) Visualisation and identification of the interaction between STIM1s in resting cells. *PLoS One* **7**: 1–8
- Heim R, Cubitt AB & Tsien RY (1995) Improved green fluorescence. *Nature* **373**: 663–664 Available at: <https://www.nature.com/articles/373663b0> [Accessed October 12, 2021]
- Henderson JN, Gepshtein R, Heenan JR, Kallio K, Huppert D & Remington SJ (2009) Structure and mechanism of the photoactivatable green fluorescent protein. *J. Am. Chem. Soc.* **131**: 4176–4177
- Hertel F, Mo GCH, Duwé S, Dedeker P & Zhang J (2016) RefSOFI for Mapping Nanoscale Organization of Protein-Protein Interactions in Living Cells. *Cell Rep.* **14**: 390–400
- Hilton IB, D'Ippolito AM, Vockley CM, Thakore PI, Crawford GE, Reddy TE & Gersbach CA (2015) Epigenome editing by a CRISPR-Cas9-based acetyltransferase activates genes from promoters and enhancers. *Nat. Biotechnol.* **33**: 510–517 Available at: <https://pubmed.ncbi.nlm.nih.gov/25849900/> [Accessed November 7, 2021]
- Hirve N, Rajanikanth V, Hogan PG & Gudlur A (2018) Coiled-Coil Formation Conveys a STIM1 Signal from ER Lumen to Cytoplasm. *Cell Rep.* **22**: 72–83 Available at: <http://www.cell.com/article/S2211124717318399/fulltext> [Accessed October 6, 2021]
- History of Microscopes | Microscope.com Available at: <https://microscope.com/blog/microscope-101-6/history-of-microscopes-2> [Accessed October 26, 2021]
- Hodeify R, Selvaraj S, Wen J, Arredouani A, Hubrack S, Dib M, Al-Thani SN, McGraw T & Machaca

- K (2015) A STIM1-dependent ‘trafficking trap’ mechanism regulates Orai1 plasma membrane residence and Ca²⁺ influx levels. *J. Cell Sci.* **128**: 3143–3154
- Hogan PG & Rao A (2015) Store-operated calcium entry: Mechanisms and modulation. *Biochem. Biophys. Res. Commun.* **460**: 40–49
- Hoover PJ & Lewis RS (2011) Stoichiometric requirements for trapping and gating of Ca²⁺ release-activated Ca²⁺ (CRAC) channels by stromal interaction molecule 1 (STIM1). *Proc. Natl. Acad. Sci. U. S. A.* **108**: 13299–13304
- Horikawa K (2015) Recent progress in the development of genetically encoded Ca²⁺ indicators. *J. Med. Investig.* **62**: 24–28 Available at: https://www.jstage.jst.go.jp/article/jmi/62/1.2/62_24/_article
- Horinouchi T, Higashi T, Higa T, Terada K, Mai Y, Aoyagi H, Hatate C, Nepal P, Horiguchi M, Harada T & Miwa S (2012) Different binding property of STIM1 and its novel splice variant STIM1L to Orai1, TRPC3, and TRPC6 channels. *Biochem. Biophys. Res. Commun.* **428**: 252–258 Available at: <https://linkinghub.elsevier.com/retrieve/pii/S0006291X12019717> [Accessed October 5, 2021]
- Hoth M (1995) Calcium and barium permeation through calcium release-activated calcium (CRAC) channels. *Pflügers Arch. Eur. J. Physiol.* **430**: 315–322
- Hoth M & Niemeyer BA (2013) The Neglected CRAC Proteins: Orai2, Orai3, and STIM2 1st ed. Elsevier Inc. Available at: <http://dx.doi.org/10.1016/B978-0-12-407870-3.00010-X>
- Hoth M & Penner R (1992) Depletion of intracellular calcium stores activates a calcium current in mast cells. *Nature* **355**: 353–356 Available at: <http://www.nature.com/articles/355353a0> [Accessed October 8, 2021]
- Hou X, Burstein SR & Long SB (2018a) Structures reveal opening of the store-operated calcium channel Orai. *Elife* **7**: 1–28
- Hou X, Burstein SR & Long SB (2018b) Structures reveal opening of the store-operated calcium channel Orai. *Elife* **7**: 1–28 Available at: <https://elifesciences.org/articles/36758>
- Hou X, Outhwaite IR, Pedi L & Long SB (2020) Cryo-EM structure of the calcium release-activated calcium channel Orai in an open conformation. *Elife* **9**: 1–27 Available at: <https://elifesciences.org/articles/62772> [Accessed October 8, 2021]
- Hou X, Pedi L, Diver MM & Long SB (2012a) Crystal Structure of the Calcium Release–Activated Calcium Channel Orai. *Science (80-.).* **338**: 1308–1313 Available at: <https://www.ncbi.nlm.nih.gov/pmc/articles/PMC3624763/pdf/nihms412728.pdf>
- Hou X, Pedi L, Diver MM & Long SB (2012b) Crystal Structure of the Calcium Release-Activated Calcium Channel Orai. *Science (80-.).* **338**: 1308–1313 Available at: <http://www.sciencemag.org/cgi/doi/10.1126/science.1228757>
- Huang GN, Zeng W, Kim JY, Yuan JP, Han L, Muallem S & Worley PF (2006) STIM1 carboxyl-terminus activates native SOC, Icrac and TRPC1 channels. *Nat. Cell Biol.* **8**: 1003–1010

- Hwei LO, Kwong TC, Liu X, Bandyopadhyay BC, Paria BC, Soboloff J, Pani B, Gwack Y, Srikanth S, Singh BB, Gill D & Ambudkar IS (2007) Dynamic assembly of TRPC1-STIM1-Orai1 ternary complex is involved in store-operated calcium influx: Evidence for similarities in store-operated and calcium release-activated calcium channel components. *J. Biol. Chem.* **282**: 9105–9116
- Ikeya M, Yamanoue K, Mochizuki Y, Konishi H, Tadokoro S, Tanaka M, Suzuki R & Hirashima N (2014) Orai-2 is localized on secretory granules and regulates antigen-evoked Ca²⁺ mobilization and exocytosis in mast cells. *Biochem. Biophys. Res. Commun.* **451**: 62–67 Available at: <http://dx.doi.org/10.1016/j.bbrc.2014.07.060>
- Inayama M, Suzuki Y, Yamada S, Kurita T, Yamamura H, Ohya S, Giles WR & Imaizumi Y (2015a) Orai1-Orai2 complex is involved in store-operated calcium entry in chondrocyte cell lines. *Cell Calcium* **57**: 337–347 Available at: <http://dx.doi.org/10.1016/j.ceca.2015.02.005>
- Inayama M, Suzuki Y, Yamada S, Kurita T, Yamamura H, Ohya S, Giles WR & Imaizumi Y (2015b) Orai1-Orai2 complex is involved in store-operated calcium entry in chondrocyte cell lines. *Cell Calcium* **57**: 337–347 Available at: <http://dx.doi.org/10.1016/j.ceca.2015.02.005> [Accessed October 11, 2021]
- Ishikawa-Ankerhold HC, Ankerhold R & Drummen GPC (2012a) Advanced fluorescence microscopy techniques-FRAP, FLIP, FLAP, FRET and FLIM. *Molecules* **17**: 4047–4132
- Ishikawa-Ankerhold HC, Ankerhold R & Drummen GPC (2012b) Advanced fluorescence microscopy techniques-FRAP, FLIP, FLAP, FRET and FLIM. *Molecules* **17**: 4047–4132
- Ishino Y, Shinagawa H, Makino K, Amemura M & Nakata A (1987) Nucleotide sequence of the iap gene, responsible for alkaline phosphatase isozyme conversion in Escherichia coli, and identification of the gene product. *J. Bacteriol.* **169**: 5429–5433 Available at: <https://journals.asm.org/doi/abs/10.1128/jb.169.12.5429-5433.1987> [Accessed November 4, 2021]
- Jablonski A (1933) Efficiency of Anti-Stokes Fluorescence in Dyes. *Nat. 1933 1313319* **131**: 839–840 Available at: <https://www.nature.com/articles/131839b0> [Accessed October 12, 2021]
- Jaiteh M, Taly A & Hénin J (2016) Evolution of pentameric ligand-gated ion channels: Pro-loop receptors. *PLoS One* **11**: 1–24
- Jansen R, Embden JDA van, Gaastra W & Schouls LM (2002) Identification of genes that are associated with DNA repeats in prokaryotes. *Mol. Microbiol.* **43**: 1565–1575 Available at: <https://onlinelibrary-wiley-com.proxy.insermbiblio.inist.fr/doi/full/10.1046/j.1365-2958.2002.02839.x> [Accessed November 5, 2021]
- Jardin I & Rosado JA (2016) STIM and calcium channel complexes in cancer. *Biochim. Biophys. Acta - Mol. Cell Res.* **1863**: 1418–1426 Available at: <http://dx.doi.org/10.1016/j.bbamcr.2015.10.003>
- Jasti J, Furukawa H, Gonzales EB & Gouaux E (2007) Structure of acid-sensing ion channel 1 at 1.9 Å resolution and low pH. *Nature* **449**: 316–323
- Jentsch TJ, Stein V, Weinreich F & Zdebik AA (2002) Molecular structure and physiological function

- of chloride channels. *Physiol. Rev.* **82**: 503–568
- Ji W, Xu P, Li Z, Lu J, Liu L, Zhan Y, Chen Y, Hille B, Xu T & Chen L (2008a) Functional stoichiometry of the unitary calcium-release-activated calcium channel. *Proc. Natl. Acad. Sci.* **105**: 13668–13673 Available at: <http://www.pnas.org/cgi/doi/10.1073/pnas.0806499105>
- Ji W, Xu P, Li Z, Lu J, Liu L, Zhan Y, Chen Y, Hille B, Xu T & Chen L (2008b) Functional stoichiometry of the unitary calcium-release-activated calcium channel. *Proc. Natl. Acad. Sci. U. S. A.* **105**: 13668–13673
- Jiang Y, Lee A, Chen J, Ruta V, Cadene M, Chait BT & MacKinnon R (2003) X-ray structure of a voltage-dependent K⁺ channel. *Nat.* **423**: 33–41 Available at: <https://www-nature-com.proxy.insermbiblio.inist.fr/articles/nature01580> [Accessed October 4, 2021]
- Jinek M, Chylinski K, Fonfara I, Hauer M, Doudna JA & Charpentier E (2012) A programmable dual-RNA-guided DNA endonuclease in adaptive bacterial immunity. *Science* **337**: 816–21 Available at: <https://pubmed.ncbi.nlm.nih.gov/22761448/> [Accessed November 5, 2021]
- Kaczmarek-Hájek K, Lörinczi É, Hausmann R & Nicke A (2012) Molecular and functional properties of P2X receptors-recent progress and persisting challenges. *Purinergic Signal.* **8**: 375–417
- Kang M, Moroni A, Gazzarrini S, DiFrancesco D, Thiel G, Severino M & Van Etten JL (2004) Small potassium ion channel proteins encoded by chlorella viruses. *Proc. Natl. Acad. Sci. U. S. A.* **101**: 5318–5324
- Kar P, Lin YP, Bhardwaj R, Tucker CJ, Bird GS, Hediger MA, Monico C, Amin N & Parekh AB (2021) The N terminus of Orai1 couples to the AKAP79 signaling complex to drive NFAT1 activation by local Ca²⁺-entry. *Proc. Natl. Acad. Sci. U. S. A.* **118**: 1–11
- Kim JH, Lkhagvadorj S, Lee MR, Hwang KH, Chung HC, Jung JH, Cha SK & Eom M (2014) Orai1 and STIM1 are critical for cell migration and proliferation of clear cell renal cell carcinoma. *Biochem. Biophys. Res. Commun.* **448**: 76–82
- Kim MS, Zeng W, Yuan JP, Shin DM, Worley PF & Muallem S (2009) Native Store-operated Ca²⁺ Influx Requires the Channel Function of Orai1 and TRPC1. *J. Biol. Chem.* **284**: 9733–9741 Available at: <https://linkinghub.elsevier.com/retrieve/pii/S002192582032233X> [Accessed October 10, 2021]
- Kodama Y & Hu CD (2012) Bimolecular fluorescence complementation (BiFC): A 5-year update and future perspectives. *Biotechniques* **53**: 285–298
- Korzeniowski MK, Wisniewski E, Baird B, Holowka D & Balla T (2017) Molecular anatomy of the early events in STIM1 activation; oligomerization or conformational change? *J. Cell Sci.* **130**: 2821–2832 Available at: <https://journals.biologists.com/jcs/article/doi/10.1242/jcs.205583/265517/Molecular-anatomy-of-the-early-events-in-STIM1> [Accessed October 6, 2021]
- Kriss TC & Kriss VM (1998) History of the Operating Microscope: From Magnifying Glass to Microneurosurgery. *Neurosurgery* **42**: 907–907 Available at:

<https://academic.oup.com/neurosurgery/article/42/4/907/2846887>

- Kubitscheck U (2017) Principles of Light Microscopy. *Fluoresc. Microsc. From Princ. to Biol. Appl. Second Ed.*: 23–83
- Kwan CY, Takemura H, Obie JF, Thastrup O & Putney JW (1990) Effects of MeCh, thapsigargin, and La³⁺ on plasmalemmal and intracellular Ca²⁺ transport in lacrimal acinar cells. *Am. J. Physiol. - Cell Physiol.* **258**:
- Kwong TC, Liu X, Hwei LO & Ambudkar IS (2008) Functional requirement for Orai1 in store-operated TRPC1-STIM1 channels. *J. Biol. Chem.* **283**: 12935–12940
- Lacruz RS & Feske S (2015a) Diseases caused by mutations in ORAI1 and STIM1. *Ann. N. Y. Acad. Sci.* **1356**: 45–79 Available at: <https://onlinelibrary.wiley.com/doi/10.1111/nyas.12938>
- Lacruz RS & Feske S (2015b) Diseases caused by mutations in ORAI1 and STIM1. *Ann. N. Y. Acad. Sci.* **1356**: 45–79 Available at: <https://linkinghub.elsevier.com/retrieve/pii/S0031938416312148>
- Lambert TJ (2019) FPbase: a community-editable fluorescent protein database. *Nat. Methods* **16**: 277–278 Available at: <https://www.nature.com/articles/s41592-019-0352-8> [Accessed October 27, 2021]
- Lee KP, Choi S, Hong JH, Ahuja M, Graham S, Ma R, So I, Shin DM, Muallem S & Yuan JP (2014) Molecular determinants mediating gating of transient receptor potential canonical (TRPC) channels by stromal interaction molecule 1 (STIM1). *J. Biol. Chem.* **289**: 6372–6382
- Lee KP, Yuan JP, Hong JH, So I, Worley PF & Muallem S (2010) An endoplasmic reticulum/plasma membrane junction: STIM1/Orai1/TRPCs. *FEBS Lett.* **584**: 2022–2027
- Leon-Aparicio D, Pacheco J, Chavez-Reyes J, Galindo JM, Valdes J, Vaca L & Guerrero-Hernandez A (2017) Orai3 channel is the 2-APB-induced endoplasmic reticulum calcium leak. *Cell Calcium* **65**: 91–101 Available at: <http://dx.doi.org/10.1016/j.ceca.2017.01.012>
- Leray A, Spriet C, Trinel D, Blossey R, Usson Y & Héliot L (2011) Quantitative comparison of polar approach versus fitting method in time domain FLIM image analysis. *Cytom. Part A* **79 A**: 149–158
- Leray A, Spriet C, Trinel D, Usson Y & Héliot L (2012) Generalization of the polar representation in time domain fluorescence lifetime imaging microscopy for biological applications: Practical implementation. *J. Microsc.* **248**: 66–76
- Li A, Cho JH, Reid B, Tseng CC, He L, Tan P, Yeh CY, Wu P, Li Y, Widelitz RB, Zhou Y, Zhao M, Chow RH & Chuong CM (2018) Calcium oscillations coordinate feather mesenchymal cell movement by SHH dependent modulation of gap junction networks. *Nat. Commun.* **9**: 1–15 Available at: <http://dx.doi.org/10.1038/s41467-018-07661-5>
- Li J, Bruns A-F, Hou B, Rode B, Webster PJ, Bailey MA, Appleby HL, Moss NK, Ritchie JE, Yuldasheva NY, Tumova S, Quinney M, McKeown L, Taylor H, Prasad KR, Burke D, O'Regan D, Porter KE, Foster R, Kearney MT, et al (2015) Orai3 Surface Accumulation and Calcium Entry Evoked by Vascular Endothelial Growth Factor. *Arterioscler. Thromb. Vasc. Biol.* **35**:

- 1987 Available at: [/pmc/articles/PMC4548547/](https://pubmed.ncbi.nlm.nih.gov/11111111/) [Accessed October 11, 2021]
- Li P, Miao Y, Dani A & Vig M (2016a) α -SNAP regulates dynamic, on-site assembly and calcium selectivity of Orai1 channels. *Mol. Biol. Cell* **27**: 2542–2553
- Li P, Miao Y, Dani A & Vig M (2016b) α -SNAP regulates dynamic, on-site assembly and calcium selectivity of Orai1 channels. *Mol. Biol. Cell* **27**: 2542–2553 Available at: <https://www.molbiolcell.org/doi/10.1091/mbc.e16-03-0163>
- Li Z, Lu J, Xu P, Xie X, Chen L & Xu T (2007) Mapping the Interacting Domains of STIM1 and Orai1 in Ca^{2+} Release-activated Ca^{2+} Channel Activation. *J. Biol. Chem.* **282**: 29448–29456 Available at: <http://www.jbc.org/article/S0021925819514521/fulltext> [Accessed October 6, 2021]
- Liao Y, Erxleben C, Abramowitz J, Flockerzi V, Zhu MX, Armstrong DL & Birnbaumer L (2008) Functional interactions among Orai1, TRPCs, and STIM1 suggest a STIM-regulated heteromeric Orai/TRPC model for SOCE/Icrac channels. *Proc. Natl. Acad. Sci.* **105**: 2895–2900 Available at: <http://www.pnas.org/cgi/doi/10.1073/pnas.0712288105>
- Lichtman JW & Conchello JA (2005) Fluorescence microscopy. *Nat. Methods* **2**: 910–919
- Liou J, Fivaz M, Inoue T & Meyer T (2007) Live-cell imaging reveals sequential oligomerization and local plasma membrane targeting of stromal interaction molecule 1 after Ca^{2+} store depletion. *Proc. Natl. Acad. Sci. U. S. A.* **104**: 9301–9306
- Liou J, Kim ML, Won DH, Jones JT, Myers JW, Ferrell JE & Meyer T (2005) STIM is a Ca^{2+} sensor essential for Ca^{2+} -store- depletion-triggered Ca^{2+} influx. *Curr. Biol.* **15**: 1235–1241
- Lis A, Peinelt C, Beck A, Parvez S, Monteilh-Zoller M, Fleig A & Penner R (2007a) CRACM1, CRACM2, and CRACM3 Are Store-Operated Ca^{2+} Channels with Distinct Functional Properties. *Curr. Biol.* **17**: 794–800
- Lis A, Peinelt C, Beck A, Parvez S, Monteilh-Zoller M, Fleig A & Penner R (2007b) CRACM1, CRACM2, and CRACM3 Are Store-Operated Ca^{2+} Channels with Distinct Functional Properties. *Curr. Biol.* **17**: 794 Available at: [/pmc/articles/PMC5663639/](https://pubmed.ncbi.nlm.nih.gov/11111111/) [Accessed October 8, 2021]
- Liu X, Cheng KT, Bandyopadhyay BC, Pani B, Dietrich A, Paria BC, Swaim WD, Beech D, Yildirim E, Singh BB, Birnbaumer L & Ambudkar IS (2007) Attenuation of store-operated Ca^{2+} current impairs salivary gland fluid secretion in TRPC1(/) mice. *Proc. Natl. Acad. Sci.* **104**: 17542–17547 Available at: <http://www.pnas.org/cgi/doi/10.1073/pnas.0701254104> [Accessed October 10, 2021]
- Liu X, Groschner K & Ambudkar IS (2004) Distinct Ca^{2+} -permeable cation currents are activated by internal Ca^{2+} -store depletion in RBL-2H3 cells and human salivary gland cells, HSG and HSY. *J. Membr. Biol.* **200**: 93–104
- Liu X, O’Connell A & Ambudkar IS (1998) Ca^{2+} -dependent Inactivation of a Store-operated Ca^{2+} Current in Human Submandibular Gland Cells. *J. Biol. Chem.* **273**: 33295–33304 Available at:

<https://linkinghub.elsevier.com/retrieve/pii/S0143416016302184>

- Liu X, Wang W, Singh BB, Lockwich T, Jadowiec J, O'Connell B, Wellner R, Zhu MX & Ambudkar IS (2000) Erratum: Trp1, a candidate protein for the store-operated Ca^{2+} influx mechanism in salivary gland cells (Journal of Biological Chemistry (2000) 275 (3403-3411). *J. Biol. Chem.* **275**: 9890–9891
- Liu X, Wu G, Yu Y, Chen X, Ji R, Lu J, Li X, Zhang X, Yang X & Shen Y (2019) Molecular understanding of calcium permeation through the open Orai channel. *PLoS Biol.* **17**:
- Luik RM, Wu MM, Buchanan J & Lewis RS (2006) The elementary unit of store-operated Ca^{2+} entry: Local activation of CRAC channels by STIM1 at ER-plasma membrane junctions. *J. Cell Biol.* **174**: 815–825
- M T, YP H & G Y (2011) Imaging intracellular pH in live cells with a genetically encoded red fluorescent protein sensor. *J. Am. Chem. Soc.* **133**: 10034–10037 Available at: <https://pubmed.ncbi.nlm.nih.gov/21631110/> [Accessed October 27, 2021]
- Ma G, Wei M, He L, Liu C, Wu B, Zhang SL, Jing J, Liang X, Senes A, Tan P, Li S, Sun A, Bi Y, Zhong L, Si H, Shen Y, Li M, Lee M-S, Zhou W, Wang J, et al (2015) Inside-out Ca^{2+} signalling prompted by STIM1 conformational switch. *Nat. Commun.* **2015 61 6**: 1–14 Available at: <https://www.nature.com/articles/ncomms8826> [Accessed October 6, 2021]
- Ma X, Cheng K-T, Wong C-O, O'Neil RG, Birnbaumer L, Ambudkar IS & Yao X (2011) Heteromeric TRPV4-C1 channels contribute to store-operated Ca^{2+} entry in vascular endothelial cells. *Cell Calcium* **50**: 502–509 Available at: <https://linkinghub.elsevier.com/retrieve/pii/S0143416011001709> [Accessed October 10, 2021]
- Madl J, Weghuber J, Fritsch R, Derler I, Fahrner M, Frischauf I, Lackner B, Romanin C & Schütz GJ (2010a) Resting state Orai1 diffuses as homotetramer in the plasma membrane of live mammalian cells. *J. Biol. Chem.* **285**: 41135–41142
- Madl J, Weghuber J, Fritsch R, Derler I, Fahrner M, Frischauf I, Lackner B, Romanin C & Schütz GJ (2010b) Resting state Orai1 diffuses as homotetramer in the plasma membrane of live mammalian cells. *J. Biol. Chem.* **285**: 41135–41142
- Makarova KS, Wolf YI, Iranzo J, Shmakov SA, Alkhnbashi OS, Brouns SJJ, Charpentier E, Cheng D, Haft DH, Horvath P, Moineau S, Mojica FJM, Scott D, Shah SA, Siksnys V, Terns MP, Venclovas Č, White MF, Yakunin AF, Yan W, et al (2020) Evolutionary classification of CRISPR–Cas systems: a burst of class 2 and derived variants. *Nat. Rev. Microbiol.* **18**: 67–83
- Maneshi MM, Toth AB, Ishii T, Hori K, Tsujikawa S, Shum AK, Shrestha N, Yamashita M, Miller RJ, Radulovic J, Swanson GT & Prakriya M (2020) Orai1 Channels Are Essential for Amplification of Glutamate-Evoked Ca^{2+} Signals in Dendritic Spines to Regulate Working and Associative Memory. *Cell Rep.* **33**: 108464 Available at: <https://doi.org/10.1016/j.celrep.2020.108464>
- Manley S, Gillette JM & Lippincott-Schwartz J (2010) Single-Particle Tracking Photoactivated

- Localization Microscopy for Mapping Single-Molecule Dynamics. In pp 109–120. Available at: <https://linkinghub.elsevier.com/retrieve/pii/S0076687910750059> [Accessed October 20, 2021]
- Manna PT, Davis LJ & Robinson MS (2019) Fast and cloning-free CRISPR/Cas9-mediated genomic editing in mammalian cells. *Traffic* **20**: 974–982 Available at: <https://onlinelibrary.wiley.com/doi/10.1111/tra.12696>
- Maruyama Y, Ogura T, Mio K, Kato K, Kaneko T, Kiyonaka S, Mori Y & Sato C (2009) Tetrameric Orai1 is a teardrop-shaped molecule with a long, tapered cytoplasmic domain. *J. Biol. Chem.* **284**: 13676–13685
- Matias MG, Gomolplitinant KM, Tamang DG & Saier MH (2010) Animal Ca²⁺ release-activated Ca²⁺ (CRAC) channels appear to be homologous to and derived from the ubiquitous cation diffusion facilitators. *BMC Res. Notes* **3**:
- McGahon MK, McKee J, Dash DP, Brown E, Simpson DA, Curtis TM, McGeown JG & Scholfield CN (2012) Pharmacological Profiling of Store-Operated Ca²⁺ Entry in Retinal Arteriolar Smooth Muscle. *Microcirculation* **19**: 586–597
- Mcnelly BA, Somasundaram A, Jairaman A, Yamashita M & Prakriya M (2013) The C- and N-terminal STIM1 binding sites on Orai1 are required for both trapping and gating CRAC channels. *J. Physiol.* **591**: 2833–2850
- van Meer G, Stelzer EH, Wijnaendts-van-Resandt RW & Simons K (1987) Sorting of sphingolipids in epithelial (Madin-Darby canine kidney) cells. *J. Cell Biol.* **105**: 1623–1635 Available at: <https://pubmed.ncbi.nlm.nih.gov/3667693/> [Accessed October 17, 2021]
- Mercer JC, DeHaven WI, Smyth JT, Wedel B, Boyles RR, Bird GS & Putney JW (2006a) Large store-operated calcium selective currents due to co-expression of Orai1 or Orai2 with the intracellular calcium sensor, Stim1. *J. Biol. Chem.* **281**: 24979–24990
- Mercer JC, DeHaven WI, Smyth JT, Wedel B, Boyles RR, Bird GS & Putney JW (2006b) Large Store-operated Calcium Selective Currents Due to Co-expression of Orai1 or Orai2 with the Intracellular Calcium Sensor, Stim1. *J. Biol. Chem.* **281**: 24979–24990 Available at: <http://www.jbc.org/lookup/doi/10.1074/jbc.M604589200>
- Michelucci A, García-Castañeda M, Boncompagni S & Dirksen RT (2018) Role of STIM1/ORAI1-mediated store-operated Ca²⁺ entry in skeletal muscle physiology and disease. *Cell Calcium* **76**: 101–115 Available at: <https://doi.org/10.1016/j.ceca.2018.10.004>
- Miederer A-M, Alansary D, Schwär G, Lee P-H, Jung M, Helms V & Niemeyer BA (2015) A STIM2 splice variant negatively regulates store-operated calcium entry. *Nat. Commun.* **2015 61** **6**: 1–12 Available at: <https://www.nature.com/articles/ncomms7899> [Accessed October 5, 2021]
- Mignen O & Shuttleworth TJ (2000) I(ARC), a novel arachidonate-regulated, noncapacitative Ca²⁺ entry channel. *J. Biol. Chem.* **275**: 9114–9119
- Mignen O & Shuttleworth TJ (2001) Permeation of monovalent cations through the non-capacitative arachidonate-regulated Ca²⁺ channels in HEK293 cells. Comparison with endogenous store-

- operated channels. *J. Biol. Chem.* **276**: 21365–21374
- Mignen O, Thompson JL & Shuttleworth TJ (2007) STIM1 regulates Ca²⁺ entry via arachidonate-regulated Ca²⁺ -selective (ARC) channels without store depletion or translocation to the plasma membrane. *J. Physiol.* **579**: 703–715
- Mignen O, Thompson JL & Shuttleworth TJ (2008a) Both Orai1 and Orai3 are essential components of the arachidonate-regulated Ca²⁺-selective (ARC) channels. *J. Physiol.* **586**: 185–195
- Mignen O, Thompson JL & Shuttleworth TJ (2008b) Orai1 subunit stoichiometry of the mammalian CRAC channel pore. *J. Physiol.* **586**: 419–425
- Mignen O, Thompson JL & Shuttleworth TJ (2009) The molecular architecture of the arachidonate-regulated Ca²⁺ -selective ARC channel is a pentameric assembly of Orai1 and Orai3 subunits. *J. Physiol.* **587**: 4181–4197
- Miura H, Quadros RM, Gurumurthy CB & Ohtsuka M (2018) Easi-CRISPR for creating knock-in and conditional knockout mouse models using long ssDNA donors. *Nat. Protoc.* **13**: 195–215
Available at: <http://dx.doi.org/10.1038/nprot.2017.153>
- Mognol GP, Carneiro FRG, Robbs BK, Faget D V & Viola JPB (2016) Cell cycle and apoptosis regulation by NFAT transcription factors: new roles for an old player. *Cell Death Dis.* **7**: e2199–e2199 Available at: <http://www.nature.com/articles/cddis201697>
- Moitra A & Rapaport D (2021) The Biogenesis Process of VDAC – From Early Cytosolic Events to Its Final Membrane Integration. *Front. Physiol.* **0**: 1311
- Mojica FJM, Díez-Villaseñor C, García-Martínez J & Soria E (2005) Intervening Sequences of Regularly Spaced Prokaryotic Repeats Derive from Foreign Genetic Elements. *J. Mol. Evol.* **60**: 174–182 Available at: <https://link.springer.com/article/10.1007/s00239-004-0046-3> [Accessed November 4, 2021]
- Moran Y, Barzilai MG, Liebeskind BJ & Zakon HH (2015) Evolution of voltage-gated ion channels at the emergence of Metazoa. *J. Exp. Biol.* **218**: 515–525
- Moss GP (1996) Basic Terminology of Stereochemistry. *Pure Appl. Chem* **68**: 2193–2222 Available at: <http://www.iupac.org/publications/pac/pdf/2002/7405/7405x0793.html>
- Motiani RK, Abdullaev IF & Trebak M (2010) A novel native store-operated calcium channel encoded by Orai3: Selective requirement of Orai3 versus Orai1 in estrogen receptor-positive versus estrogen receptor-negative breast cancer cells. *J. Biol. Chem.* **285**: 19173–19183
- Mualla AF, Aubreville M & Maier A (2018) Microscopy. : 69–90
- Muik M, Fahrner M, Derler I, Schindl R, Bergsmann J, Frischauf I, Groschner K & Romanin C (2009) A Cytosolic Homomerization and a Modulatory Domain within STIM1 C Terminus Determine Coupling to ORAI1 Channels. *J. Biol. Chem.* **284**: 8421–8426 Available at: <https://pubmed.ncbi.nlm.nih.gov/19189966/> [Accessed October 6, 2021]
- Muik M, Fahrner M, Schindl R, Stathopoulos P, Frischauf I, Derler I, Plenk P, Lackner B, Groschner K, Ikura M & Romanin C (2011) STIM1 couples to ORAI1 via an intramolecular transition into an

- extended conformation. *EMBO J.* **30**: 1678–1689 Available at:
<http://dx.doi.org/10.1038/emboj.2011.79>
- Muik M, Frischauf I, Derler I, Fahrner M, Bergsmann J, Eder P, Schindl R, Hesch C, Polzinger B, Fritsch R, Kahr H, Madl J, Gruber H, Groschner K & Romanin C (2008) Dynamic coupling of the putative coiled-coil domain of ORAI1 with STIM1 mediates ORAI1 channel activation. *J. Biol. Chem.* **283**: 8014–8022
- Mullins FM, Chan YP, Dolmetsch RE & Lewis RS (2009) STIM1 and calmodulin interact with Orai1 to induce Ca²⁺-dependent inactivation of CRAC channels. *Proc. Natl. Acad. Sci. U. S. A.* **106**: 15495–15500
- N C, M V, JP K, D H & B B (2009) Molecular clustering of STIM1 with Orai1/CRACM1 at the plasma membrane depends dynamically on depletion of Ca²⁺ stores and on electrostatic interactions. *Mol. Biol. Cell* **20**: 389–399 Available at: <https://pubmed-ncbi-nlm-nih-gov.proxy.insermbiblio.inist.fr/18987344/> [Accessed October 21, 2021]
- Nagai T, Ibata K, Park ES, Kubota M, Mikoshiba K & Miyawaki A (2002) A variant of yellow fluorescent protein with fast and efficient maturation for cell-biological applications. *Nat. Biotechnol.* **20**: 87–90 Available at: <https://www.nature.com/articles/nbt0102-87> [Accessed October 27, 2021]
- Nakade S, Tsubota T, Sakane Y, Kume S, Sakamoto N, Obara M, Daimon T, Sezutsu H, Yamamoto T, Sakuma T & Suzuki KIT (2014) Microhomology-mediated end-joining-dependent integration of donor DNA in cells and animals using TALENs and CRISPR/Cas9. *Nat. Commun.* **5**: 1–8 Available at: <http://dx.doi.org/10.1038/ncomms6560>
- Nakai J, Ohkura M & Imoto K (2001) A high signal-to-noise Ca²⁺ probe composed of a single green fluorescent protein. *Nat. Biotechnol.* **19**: 137–141
- Navarro-Borelly L, Somasundaram A, Yamashita M, Ren D, Miller RJ & Prakriya M (2008) STIM1–Orai1 interactions and Orai1 conformational changes revealed by live-cell FRET microscopy. *J. Physiol.* **586**: 5383 Available at: <https://pmc/articles/PMC2655373/> [Accessed October 9, 2021]
- Nayak S, Batalov S, Jegla T & Zmasek C (2009) Evolution of the Human Ion Channel Set. *Comb. Chem. High Throughput Screen.* **12**: 2–23
- Niccheri F, Pecori R & Conticello SG (2017) An efficient method to enrich for knock-out and knock-in cellular clones using the CRISPR/Cas9 system. *Cell. Mol. Life Sci.* **74**: 3413–3423
- Nikolaus Naredi-Rainer, Jens Prescher, Achim Hartschuh and DCL (2013) Fluorescence Microscopy Kubitschek U (ed) Weinheim, Germany: Wiley-VCH Verlag GmbH & Co. KGaA Available at: <https://www.jaypeedigital.com/book/9789386150998/chapter/ch5>
- Niu L, Wu F, Li K, Li J, Zhang SL, Hu J & Wang Q (2020) STIM1 interacts with termini of Orai channels in a sequential manner. *J. Cell Sci.* **133**: Available at: <https://journals.biologists.com/jcs/article/doi/10.1242/jcs.239491/266305/STIM1-interacts-with-termini-of-Orai-channels-in-a> [Accessed October 9, 2021]

- Niwa H, Inouye S, Hirano T, Matsuno T, Kojima S, Kubota M, Ohashi M & Tsuji FI (1996) Chemical nature of the light emitter of the Aequorea green fluorescent protein. *Proc. Natl. Acad. Sci.* **93**: 13617–13622 Available at: <http://www.pnas.org/cgi/doi/10.1073/pnas.93.24.13617>
- Ong HL, De Souza LB & Ambudkar IS (2016) Role of TRPC channels in store-operated calcium entry. *Adv. Exp. Med. Biol.* **898**: 87–109
- Oritani K & Kincade PW (1996) Identification of stromal cell products that interact with pre-B cells. *J. Cell Biol.* **134**: 771–782
- Ouellette RJ & Rawn JD (2015) Amino Acids, Peptides, and Proteins. *Princ. Org. Chem.*: 371–396
- Padilla-Parra S, Audugé N, Coppey-Moisán M & Tramier M (2008) Quantitative FRET analysis by fast acquisition time domain FLIM at high spatial resolution in living cells. *Biophys. J.* **95**: 2976–2988
- Palty R, Fu Z & Isacoff EY (2017) Sequential Steps of CRAC Channel Activation. *Cell Rep.* **19**: 1929–1939 Available at: <http://www.cell.com/article/S2211124717306502/fulltext> [Accessed October 9, 2021]
- Paquet D, Kwart D, Chen A, Sproul A, Jacob S, Teo S, Olsen KM, Gregg A, Noggle S & Tessier-Lavigne M (2016) Efficient introduction of specific homozygous and heterozygous mutations using CRISPR/Cas9. *Nature* **533**: 125–129 Available at: <https://pubmed.ncbi.nlm.nih.gov/27120160/> [Accessed November 8, 2021]
- Paredes RM, Etzler JC, Watts LT, Zheng W & Lechleiter JD (2008) Chemical calcium indicators. *Methods* **46**: 143–151 Available at: <https://linkinghub.elsevier.com/retrieve/pii/S104620230800159X>
- Parekh AB & Putney JW (2005) Store-Operated Calcium Channels. *Physiol. Rev.* **85**: 757–810 Available at: <https://pubmed-ncbi-nlm-nih-gov.proxy.insermbiblio.inist.fr/15788710/> [Accessed October 10, 2021]
- Park CY, Hoover PJ, Mullins FM, Bachhawat P, Covington ED, Raunser S, Walz T, Garcia KC, Dolmetsch RE & Lewis RS (2009a) STIM1 Clusters and Activates CRAC Channels via Direct Binding of a Cytosolic Domain to Orai1. *Cell* **136**: 876–890 Available at: <http://dx.doi.org/10.1016/j.cell.2009.02.014>
- Park CY, Hoover PJ, Mullins FM, Bachhawat P, Covington ED, Raunser S, Walz T, Garcia KC, Dolmetsch RE & Lewis RS (2009b) STIM1 Clusters and Activates CRAC Channels via Direct Binding of a Cytosolic Domain to Orai1. *Cell* **136**: 876–890 Available at: <https://www.ncbi.nlm.nih.gov/pmc/articles/PMC2670439/>
- Parker NJ, Begley CG, Smith PJ & Fox RM (1996) Molecular cloning of a novel human gene (D11S4896E) at chromosomal region 11p15.5. *Genomics* **37**: 253–256
- Pathak MM, Tran T, Hong L, Tombola F, Joós B & Morris CE (2016) The Hv1 proton channel responds to mechanical stimuli. *J. Gen. Physiol.* **148**: 405–418
- Pauling L & Corey RB (1951) Configurations of Polypeptide Chains With Favored Orientations

- Around Single Bonds: Two New Pleated Sheets. *Proc. Natl. Acad. Sci.* **37**: 729–740
- Pauling L, Corey RB & Branson HR (1951) The structure of proteins: Two hydrogen-bonded helical configurations of the polypeptide chain. *Proc. Natl. Acad. Sci.* **37**: 205–211 Available at: <http://www.pnas.org/cgi/doi/10.1073/pnas.37.4.205>
- Penna A, Demuro A, Yeromin A V., Zhang SL, Safrina O, Parker I & Cahalan MD (2008) The CRAC channel consists of a tetramer formed by Stim-induced dimerization of Orai dimers. *Nature* **456**: 116–120 Available at: <http://www.nature.com/articles/nature07338>
- Penna A, Demuro A, Yeromin A V, Zhang SL, Safrina O, Parker I & Cahalan MD (2009) The CRAC channel consists of a tetramer formed by Stim- induced dimerization of Orai dimers. *Nature* **456**: 116–120
- Perni S, Dynes JL, Yeromin A V., Cahalan MD & Franzini-Armstrong C (2015) Nanoscale patterning of STIM1 and Orai1 during store-operated Ca²⁺ entry. *Proc. Natl. Acad. Sci.*
- Peter M & Ameer-Beg SM (2004) Imaging molecular interactions by multiphoton FLIM. *Biol. Cell* **96**: 231–236 Available at: <https://onlinelibrary.wiley.com/doi/full/10.1016/j.biolcel.2003.12.006> [Accessed November 20, 2021]
- Piston DW & Kremers GJ (2007) Fluorescent protein FRET: the good, the bad and the ugly. *Trends Biochem. Sci.* **32**: 407–414
- Poroca DR, Pelis RM & Chappe VM (2017) ClC channels and transporters: Structure, physiological functions, and implications in human chloride channelopathies. *Front. Pharmacol.* **8**: 1–25
- Potier M, Gonzalez JC, Motiani RK, Abdullaev IF, Bisailon JM, Singer HA & Trebak M (2009) Evidence for STIM1- and Orai1-dependent store-operated calcium influx through ICRC in vascular smooth muscle cells: Role in proliferation and migration. *FASEB J.* **23**: 2425–2437
- Pourcel C, Salvignol G & Vergnaud G (2005) CRISPR elements in *Yersinia pestis* acquire new repeats by preferential uptake of bacteriophage DNA, and provide additional tools for evolutionary studies. *Microbiology* **151**: 653–663 Available at: <https://pubmed.ncbi.nlm.nih.gov.proxy.insermbiblio.inist.fr/15758212/> [Accessed November 5, 2021]
- Pozo-Guisado E, Casas-Rua V, Tomas-Martin P, Lopez-Guerrero AM, Alvarez-Barrientos A & Martin-Romero FJ (2013) Phosphorylation of STIM1 at ERK1/2 target sites regulates interaction with the microtubule plus-end binding protein EB1. *J. Cell Sci.* **126**: 3170–3180
- Prakriya M, Feske S, Gwack Y, Srikanth S, Rao A & Hogan PG (2006) Orai1 is an essential pore subunit of the CRAC channel. *Nature* **443**: 230–233
- Prakriya M & Lewis RS (2015) Store-operated calcium channels. *Physiol. Rev.* **95**: 1383–1436
- Prasher DC, Eckenrode VK, Ward WW, Prendergast FG & Cormier MJ (1992) Primary structure of the *Aequorea victoria* green-fluorescent protein. *Gene* **111**: 229–233 Available at: <https://pubmed.ncbi.nlm.nih.gov/1347277/> [Accessed October 12, 2021]
- Putney JW (1986) A model for receptor-regulated calcium entry. *Cell Calcium* **7**: 1–12 Available at: <https://linkinghub.elsevier.com/retrieve/pii/0143416086900266>

- Putney JW (2007) Recent breakthroughs in the molecular mechanism of capacitative calcium entry (with thoughts on how we got here). *Cell Calcium* **42**: 103–110
- Putney JW, Steinckwich-Besançon N, Numaga-Tomita T, Davis FM, Desai PN, D’Agostin DM, Wu S & Bird GS (2017) The functions of store-operated calcium channels. *Biochim. Biophys. Acta - Mol. Cell Res.* **1864**: 900–906 Available at: <https://reader.elsevier.com/reader/sd/pii/S0167488916303238?token=970DB1203ECB9A05CAD051197C96D57C4D3FB725CBAF80E0E0911B1F0B37AA65DC3A14A180AFF2E1E02310AF2AE3C12D&originRegion=eu-west-1&originCreation=20211011133143> [Accessed October 11, 2021]
- Qin X, Liu L, Lee SK, Alsina A, Liu T, Wu C, Park H, Yu C, Kim H, Chu J, Triller A, Tang BZ, Hyeon C, Park CY & Park H (2020) Increased Confinement and Polydispersity of STIM1 and Orai1 after Ca²⁺ Store Depletion. *Biophys. J.* **118**: 70–84 Available at: <https://doi.org/10.1016/j.bpj.2019.11.019>
- Qiu R & Lewis RS (2019) Structural features of STIM and Orai underlying store-operated calcium entry. *Curr. Opin. Cell Biol.* **57**: 90–98 Available at: <https://doi.org/10.1016/j.ceb.2018.12.012>
- Ramesh G, Jarzembowski L, Schwarz Y, Poth V, Konrad M, Knapp ML, Schwärz G, Lauer AA, Grimm MOW, Alansary D, Bruns D & Niemeyer BA (2021) A short isoform of STIM1 confers frequency-dependent synaptic enhancement. *Cell Rep.* **34**: 108844
- Ran FA, Hsu PD, Wright J, Agarwala V, Scott DA & Zhang F (2013) Genome engineering using the CRISPR-Cas9 system. *Nat. Protoc.* **8**: 2281–2308 Available at: <http://www.nature.com/articles/nprot.2013.143>
- Rana A, Yen M, Sadaghiani AM, Malmersjö S, Park CY, Dolmetsch RE & Lewis RS (2015) Alternative splicing converts STIM2 from an activator to an inhibitor of store-operated calcium channels. *J. Cell Biol.* **209**: 653–670
- Redolfi N, García-Casas P, Fornetto C, Sonda S, Pizzo P & Pendin D (2021) Lighting up ca²⁺ dynamics in animal models. *Cells* **10**: 1–18
- Ridley AJ, Schwartz MA, Burridge K, Firtel RA, Ginsberg MH, Borisy G, Parsons JT & Horwitz AR (2003) Cell Migration: Integrating Signals from Front to Back. *Science (80-.).* **302**: 1704–1709
- Roos J, DiGregorio PJ, Yeromin A V., Ohlsen K, Lioudyno M, Zhang S, Safrina O, Kozak JA, Wagner SL, Cahalan MD, Velicelebi G & Stauderman KA (2005) STIM1, an essential and conserved component of store-operated Ca²⁺ channel function. *J. Cell Biol.* **169**: 435–445
- Rosado JA (2006) Discovering the mechanism of capacitative calcium entry. *Am. J. Physiol. - Cell Physiol.* **291**: 1104–1106
- Rosado JA, Brownlow SL & Sage SO (2002) Endogenously expressed Trp1 is involved in store-mediated Ca²⁺ entry by conformational coupling in human platelets. *J. Biol. Chem.* **277**: 42157–42163
- Ryazanova L V., Dorovkov M V., Ansari A & Ryazanov AG (2004) Characterization of the Protein

- Kinase Activity of TRPM7/ChaK1, a Protein Kinase Fused to the Transient Receptor Potential Ion Channel. *J. Biol. Chem.* **279**: 3708–3716 Available at: <http://dx.doi.org/10.1074/jbc.M308820200>
- Sakuma T, Nakade S, Sakane Y, Suzuki KIT & Yamamoto T (2016) MMEJ-Assisted gene knock-in using TALENs and CRISPR-Cas9 with the PITCh systems. *Nat. Protoc.* **11**: 118–133 Available at: <http://dx.doi.org/10.1038/nprot.2015.140>
- Saliba Y, Keck M, Marchand A, Atassi F, Cazorla O, Trebak M, Pavoine C, Lacampagne A & Lompre A (2015a) Emergence of Orai3 activity during cardiac hypertrophy. : 248–259
- Saliba Y, Keck M, Marchand A, Atassi F, Ouillé A, Cazorla O, Trebak M, Pavoine C, Lacampagne A, Hulot JS, Farès N, Fauconnier J & Lompré AM (2015b) Emergence of Orai3 activity during cardiac hypertrophy. *Cardiovasc. Res.* **105**: 248–259
- Schindl R, Bergsmann J, Frischauf I, Derler I, Fahrner M, Muik M, Fritsch R, Groschner K & Romanin C (2008) 2-Aminoethoxydiphenyl borate alters selectivity of Orai3 channels by increasing their pore size. *J. Biol. Chem.* **283**: 20261–20267
- Schindl R, Frischauf I, Bergsmann J, Muik M, Derler I, Lackner B, Groschner K & Romanin C (2009) Plasticity in Ca²⁺ selectivity of Orai1/Orai3 heteromeric channel. *Proc. Natl. Acad. Sci.* **106**: 19623–19628
- Schleifer H, Doleschal B, Lichtenegger M, Oppenrieder R, Derler I, Frischauf I, Glasnov TN, Kappe CO, Romanin C & Groschner K (2012) Modulation of cellular Ca²⁺ handling by pyrazoles. *Br. J. Pharmacol.* **167**: 1712–1722
- Shaner NC (2014) Fluorescent proteins for quantitative microscopy. In *Methods in Cell Biology* pp 95–111. Elsevier Inc. Available at: <http://dx.doi.org/10.1016/B978-0-12-420138-5.00006-9>
- Shimomura O, Johnson FH & Saiga Y (1962) Extraction, Purification and Properties of Aequorin, a Bioluminescent Protein from the Luminous Hydromedusan, Aequorea. *J. Cell. Comp. Physiol.* **59**: 223–239 Available at: <https://pubmed.ncbi.nlm.nih.gov/13911999/> [Accessed October 12, 2021]
- Shin DM, Son A, Park S, Kim MS, Ahuja M & Muallem S (2016) The TRPCs, OraIs and STIMs in ER/PM junctions. *Adv. Exp. Med. Biol.* **898**: 47–66
- Shuttleworth TJ (2012) Orai3 - the ‘exceptional’ Orai? *J. Physiol.* **590**: 241–257
- Sine SM & Engel AG (2006) Recent advances in Cys-loop receptor structure and function. *Nature* **440**: 448–455
- Sipietier F, Vandame P, Spriet C, Leray A, Vincent P, Trinel D, Bodart JF, Riquet FB & Héliot L (2013) From FRET imaging to practical methodology for Kinase activity sensing in living cells
- Skipper L (2005) PROTEINS | Overview. In *Encyclopedia of Analytical Science* pp 344–352. Elsevier Available at: <https://linkinghub.elsevier.com/retrieve/pii/B0123693977004933>
- Slaymaker IM, Gao L, Zetsche B, Scott DA, Yan WX & Zhang F (2016) Rationally engineered Cas9 nucleases with improved specificity. *Science (80-.).* **351**: 84–88 Available at:

- <https://pubmed.ncbi.nlm.nih.gov/26628643/> [Accessed November 5, 2021]
- Son GY, Subedi KP, Ong HL, Noyer L, Saadi H, Zheng C, Bhardwaj R, Feske S & Ambudkar IS (2020) STIM2 targets Orai1/STIM1 to the AKAP79 signaling complex and confers coupling of Ca²⁺ entry with NFAT1 activation. *Proc. Natl. Acad. Sci. U. S. A.* **117**: 16638–16648
- Spasova MA, Soboloff J, He L-P, Xu W, Dziadek MA & Gill DL (2006) STIM1 has a plasma membrane role in the activation of store-operated Ca²⁺ channels. *Proc. Natl. Acad. Sci.* **103**: 4040–4045 Available at: <https://pubmed.ncbi.nlm.nih.gov/16537481/> [Accessed October 6, 2021]
- Stathopoulos PB, Schindl R, Fahrner M, Zheng L, Gasmi-Seabrook GM, Muik M, Romanin C & Ikura M (2013) STIM1/Orai1 coiled-coil interplay in the regulation of store-operated calcium entry. *Nat. Commun.* **4**: Available at: [/pmc/articles/PMC3927877/](https://www.ncbi.nlm.nih.gov/pmc/articles/PMC3927877/) [Accessed October 9, 2021]
- Stokes GG (1852) On the change of refrangibility of light. *Philos. Trans. R. Soc. London* **142**: 463–562 Available at: <https://royalsocietypublishing.org/doi/abs/10.1098/rstl.1852.0022> [Accessed October 12, 2021]
- Subedi KP, Ong HL, Son G-Y, Liu X & Ambudkar IS (2018) STIM2 Induces Activated Conformation of STIM1 to Control Orai1 Function in ER-PM Junctions. *Cell Rep.* **23**: 522–534 Available at: <http://www.cell.com/article/S2211124718304261/fulltext> [Accessed October 5, 2021]
- Sun Y, Birnbaumer L & Singh BB (2015) TRPC1 regulates calcium-activated chloride channels in salivary gland cells. *J. Cell. Physiol.* **230**: 2848–2856 Available at: <https://pubmed-ncbi-nlm-nih.gov.proxy.insermbiblio.inist.fr/25899321/> [Accessed October 10, 2021]
- Sun Y, Sukumaran P, Varma A, Derry S, Sahmoun AE & Singh BB (2014) Cholesterol-induced activation of TRPM7 regulates cell proliferation, migration, and viability of human prostate cells. *Biochim. Biophys. Acta - Mol. Cell Res.* **1843**: 1839–1850 Available at: <https://www.ncbi.nlm.nih.gov/pmc/articles/PMC3624763/pdf/nihms412728.pdf>
- Suzuki J, Kanemaru K & Iino M (2016a) Genetically Encoded Fluorescent Indicators for Organellar Calcium Imaging. *Biophys. J.* **111**: 1119–1131 Available at: <http://dx.doi.org/10.1016/j.bpj.2016.04.054>
- Suzuki K, Tsunekawa Y, Hernandez-Benitez R, Wu J, Zhu J, Kim EJ, Hatanaka F, Yamamoto M, Araoka T, Li Z, Kurita M, Hishida T, Li M, Aizawa E, Guo S, Chen S, Goebel A, Soligalla RD, Qu J, Jiang T, et al (2016b) In vivo genome editing via CRISPR/Cas9 mediated homology-independent targeted integration. *Nature* **540**: 144–149
- Takahashi Y, Murakami M, Watanabe H, Hasegawa H, Ohba T, Muneishi Y, Nobori K, Ono K, Iijima T & Ito H (2007) Essential role of the N-terminus of murine Orai1 in store-operated Ca²⁺ entry. *Biochem. Biophys. Res. Commun.* **356**: 45–52
- Tang B-D, Xia X, Lv X-F, Yu B-X, Yuan J-N, Mai X-Y, Shang J-Y, Zhou J-G, Liang S-J & Pang R-P (2017) Inhibition of Orai1-mediated Ca²⁺ entry enhances chemosensitivity of HepG2 hepatocarcinoma cells to 5-fluorouracil. *J. Cell. Mol. Med.* **21**: 904–915 Available at:

- <https://onlinelibrary.wiley.com/doi/full/10.1111/jcmm.13029> [Accessed October 11, 2021]
- Tang Y, Wu S, Liu Q, Xie J, Zhang J, Han D, Lu Q & Lu Q (2015) MERTK deficiency affects macrophage directional migration via disruption of cytoskeletal organization. *PLoS One* **10**: 1–14
- Thompson JL & Shuttleworth TJ (2013) Molecular basis of activation of the arachidonate-regulated Ca^{2+} (ARC) channel, a store-independent Orai channel, by plasma membrane STIM1. **14**: 3507–3523
- Thompson MA, Prakash YS & Pabelick CM (2014) Arachidonate-regulated Ca^{2+} influx in human airway smooth muscle. *Am. J. Respir. Cell Mol. Biol.* **51**: 68–76
- Tiffner A & Derler I (2021) Isoform-specific properties of Orai homologues in activation, downstream signaling, physiology and pathophysiology. *Int. J. Mol. Sci.* **22**: 1–28
- Tiffner A, Maltan L, Weiß S & Derler I (2021) The Orai pore opening mechanism. *Int. J. Mol. Sci.* **22**: 1–33
- Tirado-Lee L, Yamashita M & Prakriya M (2015) Conformational changes in the Orai1 C-terminus evoked by STIM1 binding. *PLoS One* **10**: 1–17
- Tsvilovskyy V, Solís-López A, Schumacher D, Medert R, Roers A, Kriebs U & Freichel M (2017) Deletion of Orai2 augments endogenous CRAC currents and degranulation in mast cells leading to enhanced anaphylaxis. Available at: <https://doi.org/10.1016/j.ceca.2017.11.004> [Accessed October 11, 2021]
- Umemura M, Baljinnyam E, Feske S, De Lorenzo MS, Xie LH, Feng X, Oda K, Makino A, Fujita T, Yokoyama U, Iwatsubo M, Chen S, Goydos JS, Ishikawa Y & Iwatsubo K (2014) Store-operated Ca^{2+} entry (SOCE) regulates melanoma proliferation and cell migration. *PLoS One* **9**: 1–10
- Vaeth M, Yang J, Yamashita M, Zee I, Eckstein M, Knosp C, Kaufmann U, Karoly Jani P, Lacruz RS, Flockerzi V, Kacs Kovics I, Prakriya M & Feske S (2017) ORAI2 modulates store-operated calcium entry and T cell-mediated immunity. *Nat. Commun.* **8**: 14714 Available at: <http://www.nature.com/doi/10.1038/ncomms14714>
- Varadarajan S, Tanaka K, Smalley JL, Bampton ETW, Pellicchia M, Dinsdale D, Willars GB & Cohen GM (2013) Endoplasmic Reticulum Membrane Reorganization Is Regulated by Ionic Homeostasis. *PLoS One* **8**: 1–10
- Verveer PJ, Wouters FS, Reynolds AR & Bastiaens PIH (2000) Quantitative Imaging of Lateral ErbB1 Receptor Signal Propagation in the Plasma Membrane. *Science* (80-.). **290**: 1567–1570 Available at: <https://www-science-org.proxy.insermbiblio.inist.fr/doi/abs/10.1126/science.290.5496.1567> [Accessed November 3, 2021]
- Vig M (2006) CRACM1 Is a Plasma Membrane Protein Essential for Store-Operated Ca^{2+} Entry. *Science* (80-.). **312**: 1220–1223 Available at: <https://linkinghub.elsevier.com/retrieve/pii/S0031938416312148>

- Vig M, Beck A, Billingsley JM, Lis A, Parvez S, Peinelt C, Koomoa DL, Soboloff J, Gill DL, Fleig A, Kinet JP & Penner R (2006) CRACM1 Multimers Form the Ion-Selective Pore of the CRAC Channel. *Curr. Biol.* **16**: 2073–2079
- Vig M, DeHaven WI, Bird GS, Billingsley JM, Wang H, Rao PE, Hutchings AB, Jouvin M-H, Putney JW & Kinet J-P (2008) Defective mast cell effector functions in mice lacking the CRACM1 pore subunit of store-operated calcium release-activated calcium channels. *Nat. Immunol.* **9**: 89–96 Available at: <https://www.nature.com/articles/ni1550> [Accessed October 11, 2021]
- Walsh CM, Doherty MK, Tepikin A V & Burgoyne RD (2010) Evidence for an interaction between Golgi and STIM1 in store-operated calcium entry. **460**: 453–460
- Wang Q-C, Wang X & Tang T-S (2018a) EB1 traps STIM1 and regulates local store-operated Ca²⁺ entry. *J. Cell Biol.* **217**: 1899–1900 Available at: <https://doi.org/10.1083/jcb.201805037> [Accessed October 6, 2021]
- Wang W, Ren Y, Wang L, Zhao W, Dong X, Pan J, Gao H & Tian Y (2018b) Orai1 and Stim1 Mediate the Majority of Store-Operated Calcium Entry in Multiple Myeloma and Have Strong Implications for Adverse Prognosis. *Cell. Physiol. Biochem.* **48**: 2273–2285
- Wei-Lapierre L, Carrell EM, Boncompagni S, Protasi F & Dirksen RT (2013) Orai1-dependent calcium entry promotes skeletal muscle growth and limits fatigue. *Nat. Commun.* **4**: 1–12
- Wei C, Wang X, Zheng M & Cheng H (2012) Calcium gradients underlying cell migration. *Curr. Opin. Cell Biol.* **24**: 254–261 Available at: <http://dx.doi.org/10.1016/j.ceb.2011.12.002>
- Weidinger C, Shaw PJ & Feske S (2013) STIM1 and STIM2-mediated Ca²⁺ influx regulates antitumour immunity by CD8⁺ T cells. *EMBO Mol. Med.* **5**: 1311–1321
- West JB (2013) Marcello Malpighi and the discovery of the pulmonary capillaries and alveoli. <https://doi.org/10.1152/ajplung.00016.2013> **304**: Available at: <https://journals.physiology.org/doi/abs/10.1152/ajplung.00016.2013> [Accessed October 26, 2021]
- Wiedenmann J, Ivanchenko S, Oswald F, Schmitt F, Röcker C, Salih A, Spindler KD & Nienhaus GU (2004) EosFP, a fluorescent marker protein with UV-inducible green-to-red fluorescence conversion. *Proc. Natl. Acad. Sci. U. S. A.* **101**: 15905–15910
- Willems J, de Jong APH, Scheefhals N, Mertens E, Catsburg LAE, Poorthuis RB, de Winter F, Verhaagen J, Meye FJ & MacGillavry HD (2020) ORANGE: A CRISPR/Cas9-based genome editing toolbox for epitope tagging of endogenous proteins in neurons. *PLOS Biol.* **18**: e3000665 Available at: <http://dx.doi.org/10.1371/journal.pbio.3000665>
- Williams RT, Manji SSM, Parker NJ, Hancock MS, Van Stekelenburg L, Eid JP, Senior P V., Kazenwadel JS, Shandala T, Saint R, Smith PJ & Dziadek MA (2001) Identification and characterization of the STIM (stromal interaction molecule) gene family: Coding for a novel class of transmembrane proteins. *Biochem. J.* **357**: 673–685
- Wolf DE (2013) Fundamentals of fluorescence and fluorescence microscopy. *Methods Cell Biol.* **114**:

- Wouters FS (2006) The physics and biology of fluorescence microscopy in the life sciences. *Contemp. Phys.* **47**: 239–255
- Wouters FS (2013a) Förster Resonance Energy Transfer and Fluorescence Lifetime Imaging. *Fluoresc. Microsc. From Princ. to Biol. Appl.*: 245–291
- Wouters FS (2013b) Förster Resonance Energy Transfer and Fluorescence Lifetime Imaging. : 245–291
- Wu B, Woo JS, Vila P, Jew M, Leung J, Sun Z, Srikanth S & Gwack Y (2021) NKD2 mediates stimulation-dependent ORAI1 trafficking to augment Ca²⁺ entry in T cells. *Cell Rep.* **36**:
- Wu MM, Covington ED & Lewis RS (2014) Single-molecule analysis of diffusion and trapping of STIM1 and Orai1 at endoplasmic reticulum-plasma membrane junctions. *Mol. Biol. Cell* **25**: 3672–3685 Available at: <http://www.molbiolcell.org/cgi/doi/10.1091/mbc.E14-06-1107>
- Xia J, Wang H, Huang H, Sun L, Dong S, Huang N, Shi M, Liao W, Wang H, Bin J & Liao Y (2016) Elevated Orai1 and STIM1 expressions upregulate MACC1 expression to promote tumor cell proliferation, metabolism, migration, and invasion in human gastric cancer. *Cancer Lett.* **381**: 31–40 Available at: <http://dx.doi.org/10.1016/j.canlet.2016.07.014>
- Xiaowei Hou, Leanne Pedi, Melinda M. Diver and SBL (2012) Crystal structure of the calcium release-activated calcium channel Orai. **100**: 130–134
- Yamamoto Y & Gerbi SA (2018) Making ends meet: targeted integration of DNA fragments by genome editing. *Chromosoma* **127**: 405–420
- Yamamura H, Suzuki Y & Imaizumi Y (2015) New light on ion channel imaging by total internal reflection fluorescence (TIRF) microscopy. *J. Pharmacol. Sci.* **128**: 1–7 Available at: <http://dx.doi.org/10.1016/j.jphs.2015.04.004>
- Yang H, Ren S, Yu S, Pan H, Li T, Ge S, Zhang J & Xia N (2020) Methods favoring homology-directed repair choice in response to crispr/cas9 induced-double strand breaks. *Int. J. Mol. Sci.* **21**: 1–20
- Yang S, Zhang JJ & Huang XY (2009) Orai1 and STIM1 Are Critical for Breast Tumor Cell Migration and Metastasis. *Cancer Cell* **15**: 124–134 Available at: <http://dx.doi.org/10.1016/j.ccr.2008.12.019>
- Yang T-T, Cheng L & Kain SR (1996) Optimized Codon Usage and Chromophore Mutations Provide Enhanced Sensitivity with the Green Fluorescent Protein. *Nucleic Acids Res.* **24**: 4592–4593 Available at: <https://academic.oup.com/nar/article/24/22/4592/2386507> [Accessed October 27, 2021]
- Yang X, Jin H, Cai X, Li S & Shen Y (2012) Structural and mechanistic insights into the activation of Stromal interaction molecule 1 (STIM1). *Proc. Natl. Acad. Sci.* **109**: 5657–5662 Available at: <https://pubmed.ncbi.nlm.nih.gov/22451904/> [Accessed October 6, 2021]
- Yasuda R (2006) Imaging spatiotemporal dynamics of neuronal signaling using fluorescence

- resonance energy transfer and fluorescence lifetime imaging microscopy. *Curr. Opin. Neurobiol.* **16**: 551–561
- Yen M & Lewis RS (2018) Physiological CRAC channel activation and pore properties require STIM1 binding to all six Orai1 subunits. *J. Gen. Physiol.* **150**: 1373–1385 Available at: <https://doi.org/10.1085/jgp.201711985> [Accessed October 9, 2021]
- Yeromin A V, Zhang SL, Jiang W, Yu Y, Safrina O & Cahalan MD (2006) Molecular identification of the CRAC channel by altered ion selectivity in a mutant of Orai. *Nature* **443**: 226–229 Available at: <http://www.nature.com/articles/nature05108>
- YG Y, DB S, AP S, AF F, NG G, ME B, KA L & SA L (2002) A strategy for the generation of non-aggregating mutants of Anthozoa fluorescent proteins. *FEBS Lett.* **511**: 11–14 Available at: <https://pubmed.ncbi.nlm.nih.gov/11821040/> [Accessed October 27, 2021]
- Yoast RE, Emrich SM & Trebak M (2020a) The anatomy of native CRAC channel(s). *Curr. Opin. Physiol.* **17**: 89–95 Available at: </pmc/articles/PMC7521663/> [Accessed October 11, 2021]
- Yoast RE, Emrich SM, Zhang X, Xin P, Johnson MT, Fike AJ, Walter V, Hempel N, Yule DI, Sneyd J, Gill DL & Trebak M (2020b) The native ORAI channel trio underlies the diversity of Ca²⁺-signaling events. *Nat. Commun.* **11**: 2444 Available at: <http://dx.doi.org/10.1038/s41467-020-16232-6>
- Yu C, Liu Y, Ma T, Liu K, Xu S, Zhang Y, Liu H, La Russa M, Xie M, Ding S & Qi LS (2015) Small Molecules Enhance CRISPR Genome Editing in Pluripotent Stem Cells. *Cell Stem Cell* **16**: 142–147 Available at: <https://linkinghub.elsevier.com/retrieve/pii/S1934590915000041>
- Zacharias DA, Violin JD, Newton AC & Tsien RY (2002) Partitioning of Lipid-Modified Monomeric GFPs into Membrane Microdomains of Live Cells. *Science* (80-.). **296**: 913–916 Available at: <https://www.science.org/doi/abs/10.1126/science.1068539> [Accessed October 27, 2021]
- Zbidi H, Jardin I, Woodard GE, Lopez JJ, Berna-Erro A, Salido GM & Rosado JA (2011) STIM1 and STIM2 Are Located in the Acidic Ca²⁺ Stores and Associates with Orai1 upon Depletion of the Acidic Stores in Human Platelets. *J. Biol. Chem.* **286**: 12257–12270 Available at: <https://pubmed.ncbi.nlm.nih.gov/21321120/> [Accessed October 6, 2021]
- Zetsche B, Gootenberg JS, Abudayyeh OO, Slaymaker IM, Makarova KS, Essletzbichler P, Volz SE, Joung J, Van Der Oost J, Regev A, Koonin E V. & Zhang F (2015) Cpf1 Is a Single RNA-Guided Endonuclease of a Class 2 CRISPR-Cas System. *Cell* **163**: 759–771 Available at: <http://dx.doi.org/10.1016/j.cell.2015.09.038>
- Zhang W, Zhang X, González-Cobos JC, Stolwijk JA, Matrougui K & Trebak M (2015a) Leukotriene-C4 Synthase, a Critical Enzyme in the Activation of Store-independent Orai1/Orai3 Channels, Is Required for Neointimal Hyperplasia. *J. Biol. Chem.* **290**: 5015 Available at: </pmc/articles/PMC4335238/> [Accessed October 11, 2021]
- Zhang X, Gonzalez-Cobos JC, Schindl R, Muik M, Ruhle B, Motiani RK, Bisailon JM, Zhang W, Fahrner M, Barroso M, Matrougui K, Romanin C & Trebak M (2013) Mechanisms of STIM1

- Activation of Store-Independent Leukotriene C4-Regulated Ca²⁺ Channels. *Mol. Cell. Biol.* **33**: 3715–3723
- Zhang X, Pathak T, Yoast R, Emrich S, Xin P, Nwokonko RM, Johnson M, Wu S, Delierneux C, Gueguinou M, Hempel N, Putney JW, Gill DL & Trebak M (2019) A calcium/cAMP signaling loop at the ORAI1 mouth drives channel inactivation to shape NFAT induction. *Nat. Commun.* **10**: Available at: <http://dx.doi.org/10.1038/s41467-019-09593-0>
- Zhang X, Zhang W, González-Cobos JC, Jardin I, Romanin C, Matrougui K & Trebak M (2014) Complex role of STIM1 in the activation of store-independent Orai1/3 channels. *J. Gen. Physiol.* **143**: 3450–3359
- Zhang XH, Tee LY, Wang XG, Huang QS & Yang SH (2015b) Off-target Effects in CRISPR/Cas9-mediated Genome Engineering. *Mol. Ther. - Nucleic Acids* **4**: e264
- Zheng L, Stathopulos PB, Li GY & Ikura M (2008) Biophysical characterization of the EF-hand and SAM domain containing Ca²⁺ sensory region of STIM1 and STIM2. *Biochem. Biophys. Res. Commun.* **369**: 240–246
- Zheng S, Ma G, He L, Zhang T, Li J, Yuan X, Nguyen NT, Huang Y, Zhang X, Gao P, Nwokonko R, Gill DL, Dong H, Zhou Y & Wang Y (2018) Identification of molecular determinants that govern distinct STIM2 activation dynamics. *PLOS Biol.* **16**: e2006898 Available at: <https://pubmed.ncbi.nlm.nih.gov/30444880/> [Accessed October 5, 2021]
- Zhou Y, Nwokonko RM, Cai X, Loktionova NA, Abdulqadir R, Xin P, Niemeyer BA, Wang Y, Trebak M & Gill DL (2018a) Cross-linking of Orai1 channels by STIM proteins. *Proc. Natl. Acad. Sci. U. S. A.* **115**: E3398–E3407
- Zhou Y, Nwokonko RM, Cai X, Loktionova NA, Abdulqadir R, Xin P, Niemeyer BA, Wang Y, Trebak M & Gill DL (2018b) Cross-linking of Orai1 channels by STIM proteins. *Proc. Natl. Acad. Sci.* **115**: E3398–E3407 Available at: </pmc/articles/PMC5899466/> [Accessed October 9, 2021]
- Zhou Y, Ramachandran S, Oh-hora M, Rao A & Hogan PG (2010) Pore architecture of the ORAI1 store-operated calcium channel. *Proc. Natl. Acad. Sci.* **107**: 4896–4901 Available at: <http://www.pnas.org/cgi/doi/10.1073/pnas.1001169107>
- Zhou Y, Wang X, Wang X, Loktionova NA, Cai X, Nwokonko RM, Vrana E, Wang Y, Rothberg BS & Gill DL (2015) STIM1 dimers undergo unimolecular coupling to activate Orai1 channels. *Nat. Commun.* **6**: 8395 Available at: </labs/pmc/articles/PMC4598629/> [Accessed October 21, 2021]
- Zhu H, Zhang H, Jin F, Fang M, Huang M, Yang CS, Chen T, Fu L, Pan Z, Zhu H, Zhang H, Jin F, Fang M, Huang M, Yang CS, Chen T, Fu L & Pan Z (2014) Elevated Orai1 expression mediates tumor-promoting intracellular Ca²⁺ oscillations in human esophageal squamous cell carcinoma. *Oncotarget* **5**: 3455–3471 Available at: <https://www.oncotarget.com/article/1903/text/> [Accessed October 11, 2021]
- Zhu X, Jiang M, Peyton M, Boulay G, Hurst R, Stefani E & Birnbaumer L (1996) trp, a Novel

- Mammalian Gene Family Essential for Agonist-Activated Capacitative Ca^{2+} Entry. *Cell* **85**: 661–671 Available at: <http://www.cell.com/article/S0092867400812337/fulltext> [Accessed October 9, 2021]
- Zitt C, Zobel A, Obukhov AG, Harteneck C, Kalkbrenner F, Lückhoff A & Schultz G (1996) Cloning and Functional Expression of a Human Ca^{2+} -Permeable Cation Channel Activated by Calcium Store Depletion. *Neuron* **16**: 1189–1196 Available at: <http://www.cell.com/article/S0896627300801452/fulltext> [Accessed October 9, 2021]
- Zuccolo E, Laforenza U, Ferulli F, Pellavio G, Scarpellino G, Tanzi M, Turin I, Faris P, Lucariello A, Maestri M, Kheder DA, Guerra G, Pedrazzoli P, Montagna D & Moccia F (2018) Stim and Orai mediate constitutive Ca^{2+} entry and control endoplasmic reticulum Ca^{2+} refilling in primary cultures of colorectal carcinoma cells. *Oncotarget* **9**: 31098–31119
- Zweifach A & Lewis RS (1993) Mitogen-regulated Ca^{2+} current of. **90**: 6295–6299